ASME
SETTING THE STANDARD

Journal of Engineering for Gas Turbines and Power

Published Bimonthly by ASME

VOLUME 130 • NUMBER 6 • NOVEMBER 2008

Transactions of the ASME, Journal of Engineering for Gas Turbines and Power (ISSN 0742-4795) is published bimonthly (Jan., Mar., May, July, Sep, Nov.) by The American Society of Mechanical Engineers, Three Park Avenue, New York, NY 10016. Periodicals postage paid at New York, NY and additional mailing offices.
POSTMASTER: Send address changes to Transactions of the ASME, Journal of Engineering for Gas Turbines and Power, c/o THE AMERICAN SOCIETY OF MECHANICAL ENGINEERS, 22 Law Drive, Box 2300, Fairfield, NJ 07007-2300.
CHANGES OF ADDRESS must be received at Society headquarters seven weeks before they are to be effective. Please send old label and new address.
STATEMENT from By-Laws. The Society shall not be responsible for statements or opinions advanced in papers or ... printed in its publications (B7.1, par. 3).

RESEARCH PAPERS

Gas Turbines: Aircraft Engine

061201 Improving the Performance of a Bent Ejector With Inlet Swirl
Asim Maqsood and A. M. Birk

Gas Turbines: Ceramics

061301 Optical Nondestructive Condition Monitoring of Thermal Barrier Coatings
A. L. Heyes, J. P. Feist, X. Chen, Z. Mutasim, and J. R. Nicholls

Gas Turbines: Combustion, Fuels, and Emissions

061501 Pressure-Scaling of Pressure-Swirl Atomizer Cone Angles
D. R. Guildenbecher, R. R. Rachedi, and P. E. Sojka

061502 Laminar Flame Speeds and Strain Sensitivities of Mixtures of $H_2/O_2/N_2$ at Elevated Preheat Temperatures
J. Natarajan, T. Lieuwen, and J. Seitzman

Gas Turbines: Controls, Diagnostics, and Instrumentation

061601 A Real-World Application of Fuzzy Logic and Influence Coefficients for Gas Turbine Performance Diagnostics
Richard W. Eustace

061602 Influence of Force Field Direction on Pressure Sensors Calibrated at Up to 12,000 g
Wieland Uffrecht and Erwin Kaiser

Gas Turbines: Manufacturing, Materials, and Metallurgy

062101 Biaxial Thermomechanical-Fatigue Life Property of a Directionally Solidified Ni-Base Superalloy
Takashi Ogata

Gas Turbines: Structures and Dynamics

062501 Parametric Studies on Dynamic Performance of Hybrid Airfoil Bearing
Manish Kumar and Daejong Kim

062502 A Case Study for a Turbogenerator Accident Using Multiscale Association
Da-Ren Yu, Wei Wang, Zhi-Qiang Zhang, Qing-Hua Hu, and Xiao-Min Zhao

062503 Experimental Analysis of Air/Oil Separator Performance
K. Willenborg, M. Klingsporn, S. Tebby, T. Ratcliffe, P. Gorse, K. Dullenkopf, and S. Wittig

062504 An Energy-Based Uniaxial Fatigue Life Prediction Method for Commonly Used Gas Turbine Engine Materials
Onome E. Scott-Emuakpor, Herman Shen, Tommy George, and Charles Cross

062505 Hybrid Gas Bearings With Controlled Supply Pressure to Eliminate Rotor Vibrations While Crossing System Critical Speeds
Luis San Andrés and Keun Ryu

(Contents continued on inside back cover)

This journal is printed on acid-free paper, which exceeds the ANSI Z39.48-1992 specification for permanence of paper and library materials. ♾™
♻ 85% recycled content, including 10% post-consumer fibers.

(**Contents continued**)

Journal of Engineering for Gas Turbines and Power **NOVEMBER 2008**

Volume 130, Number 6

Internal Combustion Engines

062801 Spark-Ignition and Combustion Characteristics of High-Pressure Hydrogen and Natural-Gas Intermittent Jets
Ali Mohammadi, Masahiro Shioji, Yuki Matsui, and Rintaro Kajiwara

062802 Nonlinear Versus Linear Stress-Strain Relations in Engine Turbulence Modeling Under Swirl and Squish Flow Conditions
Mirko Baratta, Andrea E. Catania, and Stefano d'Ambrosio

062803 Analysis of the Interactions Between Indicated and Reciprocating Torques for the Development of a Torsional Behavior Model of the Powertrain
Fabrizio Ponti and Luca Solieri

062804 Controlling Backfire for a Hydrogen-Fueled Engine Using External Mixture Injection
T. C. Huynh, J. K. Kang, K. C. Noh, Jong T. Lee, and J. A. Caton

062805 Prediction of Combustion Parameters, Performance, and Emissions in Compressed Natural Gas and Gasoline SI Engines
Mirko Baratta, Andrea E. Catania, Stefano d'Ambrosio, and Ezio Spessa

062806 Investigation of Mixture Preparation Effects on Gasoline HCCI Combustion Aided by Measurements of Wall Heat Flux
Junseok Chang, Zoran S. Filipi, Tang-Wei Kuo, Dennis N. Assanis, Paul M. Najt, and Rodney B. Rask

062807 Simulating Area Conservation and the Gas-Wall Interface for One-Dimensional Based Diesel Particulate Filter Models
Christopher Depcik and Dennis Assanis

062808 An Improved Phenomenological Soot Formation Submodel for Three-Dimensional Diesel Engine Simulations: Extension to Agglomeration of Particles into Clusters
Joan Boulanger, W. Stuart Neill, Fengshan Liu, and Gregory J. Smallwood

062809 Development and Application of a Complete Multijet Common-Rail Injection-System Mathematical Model for Hydrodynamic Analysis and Diagnostics
Andrea E. Catania, Alessandro Ferrari, and Michele Manno

Power Engineering

063001 Comparison of Primary Flow Measurement Techniques Used During Combined Cycle Tests
W. Cary Campbell, Warren H. Hopson, and Mark A. Smith

i Author Index

The ASME Journal of Engineering for Gas Turbines and Power is abstracted and indexed in the following:

AESIS (Australia's Geoscience, Minerals, & Petroleum Database), Applied Science & Technology Index, Aquatic Sciences and Fisheries Abstracts, Civil Engineering Abstracts, Compendex (The electronic equivalent of Engineering Index), Computer & Information Systems Abstracts, Corrosion Abstracts, Current Contents, Engineered Materials Abstracts, Engineering Index, Enviroline (The electronic equivalent of Environment Abstracts), Environment Abstracts, Environmental Science and Pollution Management, Fluidex, INSPEC, Mechanical & Transportation Engineering Abstracts, Mechanical Engineering Abstracts, METADEX (The electronic equivalent of Metals Abstracts and Alloys Index), Pollution Abstracts, Referativnyi Zhurnal, Science Citation Index, SciSearch (The electronic equivalent of Science Citation Index), Shock and Vibration Digest

Improving the Performance of a Bent Ejector With Inlet Swirl

Asim Maqsood
e-mail: 1am21@queensu.ca

A. M. Birk
e-mail: birk@me.queensu.ca

Department of Mechanical and Materials Engineering,
Queen's University,
Kingston, ON, K7L3N6, Canada

Ejectors are commonly employed in gas turbine exhaust systems for reasons such as space ventilation and IR suppression. Ejectors may incorporate bends in the geometry for various reasons. Studies have shown that the bend has a deteriorating effect on the performance of an ejector. This work was aimed to investigate the effect of exhaust gas swirl on improving the performance of a bent ejector. Four short oblong ejectors with different degrees of bend in the mixing tube and four swirl conditions were tested in this study. The primary nozzle, in all cases, was composed of a circular to oblong transition. Testing was performed at ambient and hot primary flow with 0 deg, 10 deg, 20 deg, and 30 deg swirl angles. It was observed that the swirl had a strong affect on the performance of a bent ejector. Improvement of up to 55%, 96%, and 180% was obtained in the pumping ratio, pressure rise, and total efficiency, respectively, with a 20 deg swirl in the exhaust gas. [DOI: 10.1115/1.2943196]

Introduction

In aerospace applications, the bends are required to (i) avoid internal parts in the way of the exhaust or (ii) direct hot exhaust gases away from the structural components or (iii) hide hot engine parts from heat seeking missiles. The performance of a bent ejector is reduced because of flow separation and secondary flows. It may also cause localized heating on some parts of the bends. The optimum performance point of an ejector is changed by the degree of bend.

The exhaust of a gas turbine has a tangential component, causing a swirling flow. The degree of swirl depends on the design and operating speed of a gas turbine. Swirl has large-scale effects on the flow field. Jet growth and decay, which are measures of mixing and pumping, are affected by the degree of swirl imparted to the flow [1]. The swirling flow in the exhaust of a gas turbine may be utilized to improve the performance of a bent ejector.

Only limited data were available on the performance of bent ejectors with no data on the effect of swirl on improving the performance of oblong ejectors. Manganiello and Bogatsky [2] performed tests with bent ejectors. Their investigation included only a 15 deg bend and a 15 deg *S*-bent ejector. Also, the lengths of different ejectors were not kept constant; therefore, the effect of bend on the performance is not clear in their study. Toulmay [3] conducted tests on an ejector for a helicopter engine. By testing the ejector with an elbow, he concluded that the elbow in the mixing tube adversely affected the pumping ratio of the ejector.

Studies on flow through circular and square sectioned ducts with curvatures show the production of cross-stream counter-rotating vortices due to the imbalance of centrifugal force and radial pressure gradient [4]. By experiments on circular and square sectioned bent ducts, Sudo et al. [5,6] reported that the effect of the bend on the flow remains up to ten diameters downstream of the bend.

Ackeret [7,8] and Sprenger [9] performed a large number of experimental investigations on curved and straight diffusers in their individual studies. Their investigations showed that the diffuser efficiency decreases with the degree of bend and it is independent of the Reynolds number above $Re = 2.5 \times 10^5$ [10].

Often in aerospace applications, the exhaust ducts have a noncircular cross section, which leads to the requirement for rectangular or oblong ejectors. Noncircular jets have higher entrainment and mixing properties compared to the circular jets, as discussed by Gutmark and Grinstein [11]. Higher pumping may be obtained if a noncircular ejector is utilized in the exhaust system of a gas turbine.

The purpose of this study was to provide data to the aerospace community for designing of such devices and for comparison and validation with computational fluid dynamics (CFD) studies of such devices.

Test Setup and Components

Wind Tunnel. High Reynolds number and temperature flow were supplied by a wind tunnel capable of delivering air at a mass flow rate of about 2.0 kg/s at 500°C. The wind tunnel was composed of a blower, natural gas burner, settling chamber, and an annular pipe. The annulus height of the pipe was equal to 49 mm and the inner and outer radii were 57 mm and 106 mm, respectively. The annulus section of the wind tunnel changed to a circular with an ellipsoidal center body having a length equal to 80 mm. The nozzle of the ejector was attached to the wind tunnel pipe where the circular section of the wind tunnel started. A schematic of the wind tunnel is shown in Fig. 1.

Radially uniform swirl was generated by swirlers installed in the annulus. Each swirler was composed of 16 constant angle vanes. 10 deg, 20 deg, and 30 deg, angle swirlers introduced a swirl of a clockwise sense when looking in the downstream direction. The swirlers were positioned 12 annulus heights upstream of the nozzle and 10 annulus heights upstream of the seven-hole probes of the primary flow measurement station.

The swirl numbers associated with various swirl angles in the annulus of the wind tunnel are listed in Table 1. An approximate relationship between the vane angle of the swirler and the swirl number is given as [1]

$$S \cong \frac{2}{3}\left[\frac{1-(r_i/r_o)^3}{1-(r_i/r_o)^2}\right]\tan\phi \tag{1}$$

where r_i and r_o are the inner and outer radii of the annulus and

$$S = \frac{G_\phi}{G_x r} \tag{2}$$

For flow in an annular pipe, with r_i and r_o as inner and outer radii, we can write the axial flux of axial momentum and axial flux of swirl momentum as

Contributed by the International Gas Turbine Institute of ASME for publication in the JOURNAL OF ENGINEERING FOR GAS TURBINES AND POWER. Manuscript received March 26, 2008; final manuscript received April 25, 2008; published online August 22, 2008. Review conducted by Dilip R. Ballal. Paper presented at the ASME Turbo Expo 2008: Land, Sea and Air (GT2008), Berlin, Germany, June 9–13, 2008.

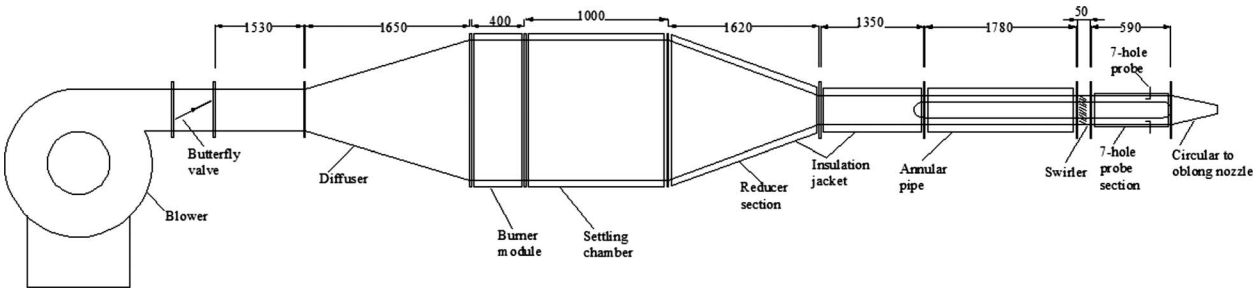

Fig. 1 Schematic of the wind tunnel (all dimensions are in millimeters—length shortened to highlight small details)

$$G_x = 2\pi \int_{r_i}^{r_o} (\rho V w + p) r dr \tag{3}$$

$$G_\phi = \int_{r_i}^{r_o} \rho V u_\phi r^2 dr \tag{4}$$

Instrumentation. Figure 2 shows the schematic of the instrumentation and the measurement planes. Measurements of the primary flow properties were taken two annulus heights upstream of the nozzle (Plane 1) and the combined flow properties were measured at the mixing tube exit plane (Plane 3) of the ejectors with the thermocouples and seven-hole probes. The amount of entrained air was calculated by subtracting the primary mass flow rate (m_1) from the combined-stream mass flow rate (m_3). Pressure at the inlet of the mixing tube was measured by radially traversing a Pitot static tube at the inlet plane of the mixing tube (Plane 2).

Four L-shaped seven-hole probes were traversed in the radial direction at four angular positions to measure inlet flow properties. Probe tips were located two annulus heights upstream of the nozzle entrance. Each probe was radially traversed in equal increments. Pressures from the seven holes of the probe were measured by seven pressure transducers. The pressure readings were converted to three velocity components, and static and total pressures by using the method described by Gerner et al. [12]. The mass flow rate was calculated by integrating the mass flow through incremental areas around the measurement points.

A seven-hole probe was traversed in the exit plane of the ejector (Plane 3) in a grid containing 1521 data points. The pressures and velocities were obtained by the procedure given by Gerner et al. [12]. The total combined-stream mass flow rate was calculated by the summation of the flow through the incremental areas around the data points.

K-type thermocouples were used to measure the temperature of the primary flow, ambient air, and the mixed flow at the exit of the ejector. Thermocouple TC_1, used to measure the primary flow temperature, was mounted upstream of the inlet seven-hole probes, in the annular pipe. A bare wire thermocouple (TC_3) was attached to the exit seven-hole probe to obtain the temperature distribution at the exit of the ejector. The thermocouple was mounted 0.010 m downstream of the seven-hole probe tip. Thermocouple TC_2, used for measuring the ambient temperature, was mounted outside the ejector close to the secondary inlet.

Single sample uncertainty analysis was performed by the procedure described by Moffat [13]. The propagation of errors in the

Table 1 Swirl number in the annular pipe of the test rig as a function of swirler vane angle

Vane angle φ (deg)	S
10	0.14
20	0.28
30	0.45

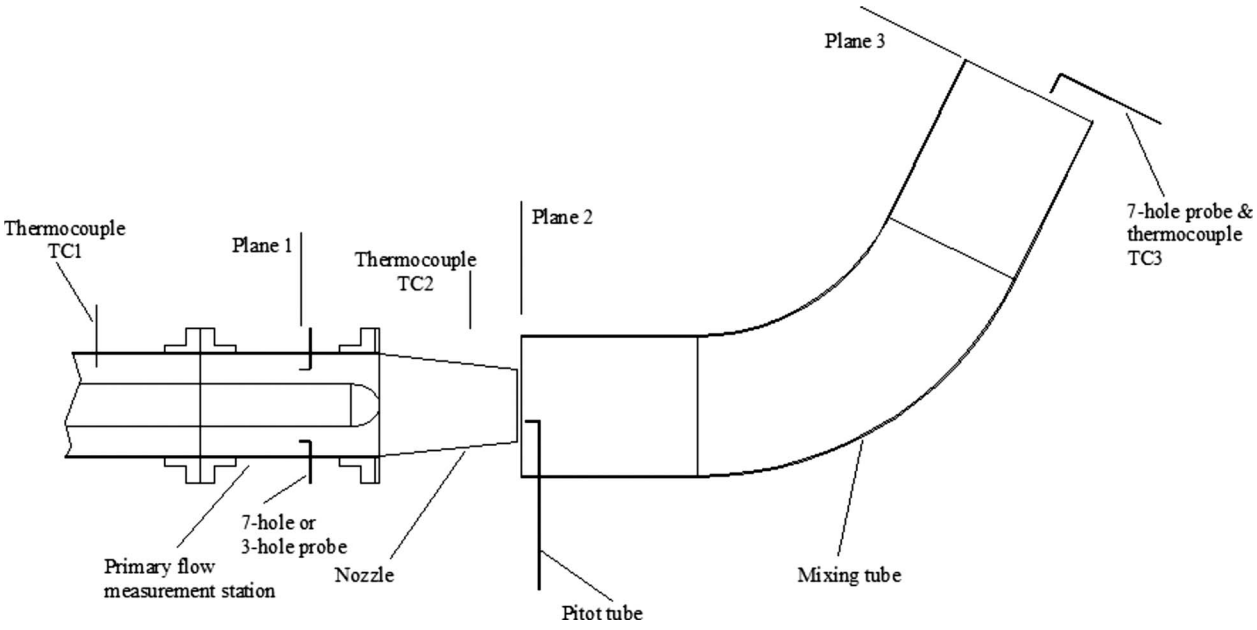

Fig. 2 Schematic showing instrumentation and measurement planes on the ejector and wind tunnel

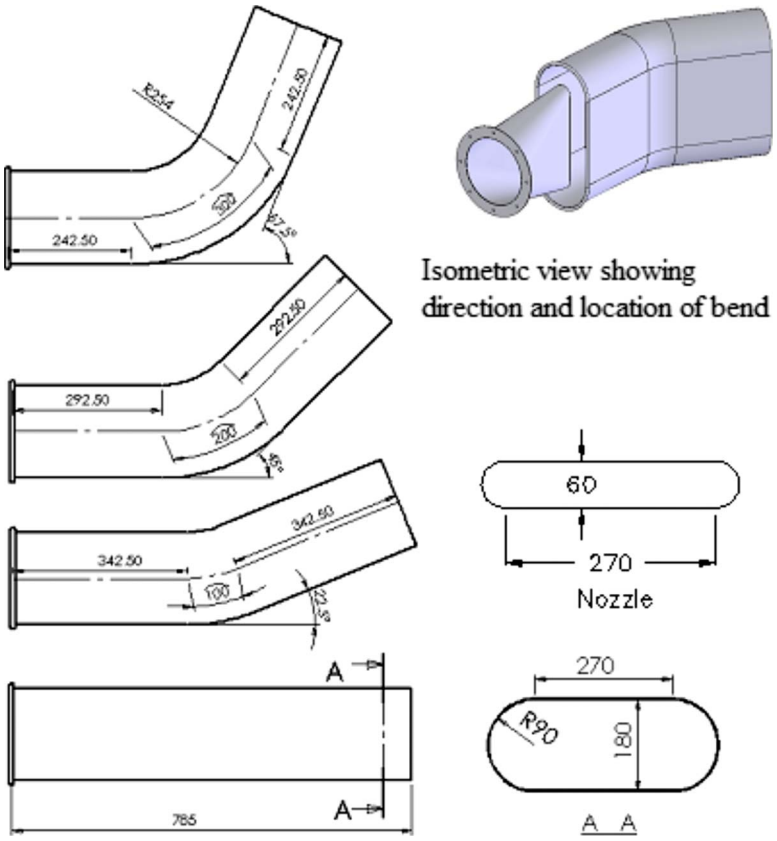

Fig. 3 Geometry detail of the test ejectors (all dimensions are in millimeters)

calculated results was estimated by the relationship proposed by Kline and McClintock [14]. The measuring instrument uncertainties in the velocity, pressure, and temperature were evaluated from the calibration programs of the seven-hole probe and manufacturer's data of the thermocouples. These uncertainties were combined with the uncertainties of the measuring process by the root sum squared (RSS) method, described by Moffat [13]. As the thermocouple TC_3 moved between regions of different temperatures (during the exit traverse) and was positioned just outside the ejector, radiation and the response time effects were considered for this thermocouple.

The uncertainty analysis was based on a 95% confidence interval. The uncertainty in the velocity, measured by the seven-hole probe, was ± 1.3 m/s and the uncertainties in the thermocouples TC_1, TC_2, and TC_3 were $\pm 3.6°C$, $\pm 1.0°C$, and $\pm 2.4°C$, respectively. The uncertainty in the static pressure was ± 44 Pa (absolute). The propagated uncertainty in the calculated result of mass flow rate was ± 0.048 kg/s.

Test Components. This study included three bent ejectors having different bends in the center of the mixing tubes and a base line straight ejector. The geometry detail of the test components is provided in Fig. 3. The length of the ejectors was equal to 2.5De, where De is the diameter of a round pipe whose cross-sectional area is equal to the area of the mixing tubes of current ejectors. The mixing tube inlet was positioned at the exit section of the nozzle (Plane 2), as shown in Fig. 2.

An oblong nozzle of 104.5 mm hydraulic diameter and 19,000 mm^2 cross-sectional area was used in each case. The nozzle was formed by a smooth transition from circular to oblong cross section over a length of 325 mm. The radius of the nozzle inlet was equal to 106 mm and the dimensions of the exit section are shown in Fig. 3. The mixing tube to nozzle area ratio (AR) was equal to 4. Mixing tube hydraulic diameter was equal to 268 mm. The inlet of the mixing tube was rounded by welding a 10 mm diameter stainless steel tube at the inlet lip.

The bend was located in the center of the mixing tube length with the radius of curvature (R_{CL}) equal to 254 mm. The length of the bent region was measured at the center of curvature of the bent ejectors. There was a straight length of the mixing tube before and after the bend. The total length of each mixing tube was equal to 785 mm measured at the centerline.

Results and Discussion

Primary flow properties are given in Table 2. The Reynolds number was in the range 4.5×10^5–4.6×10^5 during the cold cases and it was 1.9×10^5–2.0×10^5 during the hot flow cases. In all cases, the testing was performed in the Reynolds number independent region. Vyas and Kar [15] explained that the pumping ratio (Φ) of an ejector does not change if the Reynolds number is changed beyond 2×10^4. Therefore, the data of different tests can be compared if their Reynolds number is greater than 2×10^4.

Mach number was in the range 0.22 in cold flow cases and 0.27 in the hot flow tests. The Mach number remained below 0.3 and therefore the flow was considered incompressible in all cases.

Table 2 Primary and secondary flow properties

	Re_1	Ma_1	T_1 (°C)	p_1 (Pa)	p_2 (Pa)
Cold cases	4.5×10^5–4.6×10^5	0.22	39–42	750–1190	−1500–−500
Hot cases	1.9×10^5–2.0×10^5	0.27	460–464	1050–1650	−2000–−750

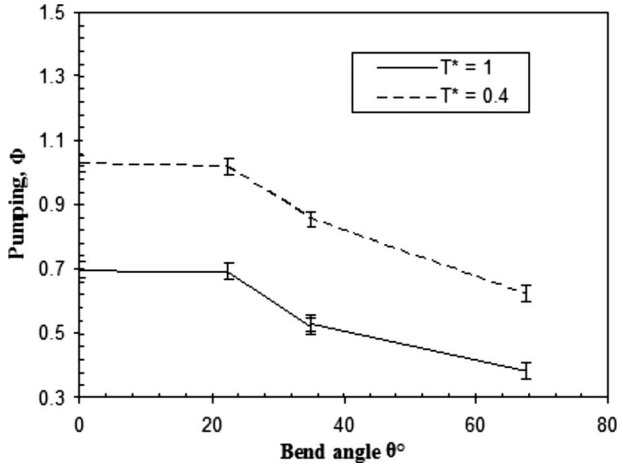

Fig. 4 Effect of the degree of bend in the mixing tube on the pumping ratio of the ejector; hot and cold flow testings presented without any swirl in the primary flow [16]

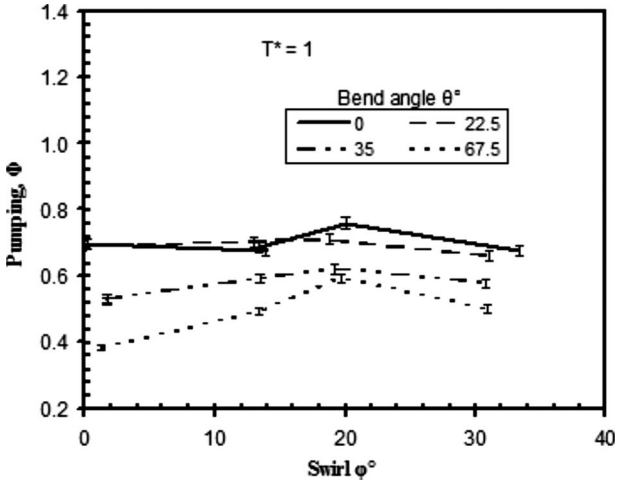

Fig. 5 Effect of swirl on the pumping ratio of ejectors having mixing tubes bent at various angles—cold primary flow presented ($T^*=1$)

Ambient temperature was in the range 20–30°C and the temperature of the hot primary flow measured upstream of the nozzle was 460°C. Static pressures at Planes 1 and 2 are listed in Table 2.

Pumping. Pumping of the ejector was normalized by dividing the secondary mass flow rate (pumped air) by the primary mass flow rate. Figure 4 (cf. Ref. [16]) shows the pumping ratio, Φ, as a function of mixing tube bend angle, θ, when there was no swirl in the primary flow.

It is observed that the entrainment ratio continuously decreases with the degree of bend. With the cold primary flow ($T^*=1$), the pumping ratios of the 35 deg and 67.5 deg bent ejectors are 25% and 45% less than the straight ejector, respectively. Similarly, the pumping ratios of the 35 deg and 67.5 deg bent ejectors are 17% and 39% less than the straight ejector in the hot flow ($T^*=0.4$) case. The pumping ratio of the 22.5 deg bent ejector is nearly equal to the straight ejector in both cases. It is highly desirable to improve the performance of highly bent ejectors.

Figure 6 shows the effect of swirl in the primary flow on the pumping ratio of the bent ejectors. In the cold flow cases, the pumping increases with the swirl angle and reaches maximum at 20 deg swirl. The pumping decreases slightly after the 20 deg swirl in all of the cold flow cases. These results are similar to the observations of cold flow cases with circular sectioned ejectors [17].

In the hot flow cases, a continuous improvement in pumping is observed for the straight ejector. This is due to the fact that a higher degree of mixing is obtained especially in the case of straight ejector. In the bent ejectors, the pumping increased from 0 deg to 20 deg swirl and slightly changed from 20 deg to 30 deg swirl.

From Figs 5 and 6, it is observed that the pumping ratios of the 35 deg and 67.5 deg bent ejectors increase with swirl with highest pumping achieved with the 20 deg swirl. This shows that the swirl in the primary flow helps the flow to attach to the walls of the ejector, which leads to a smaller separation region on the convex wall. This relatively smaller separation region leads to the higher flow area for the secondary air and also reduces the flow losses.

The pumping of the 35 deg bent ejector is improved by 19% and 15% for cold and hot primary flows, respectively, whereas the pumping of the 67.5 deg bent ejector is improved by 55% and 49% for cold and hot flows.

Pressure Rise. Pressure rise is the difference between the static pressures of Planes 3 and 2 measured by the seven-hole probe and Pitot static tube, respectively. The pressure rise is nondimensionalized by the inlet dynamic pressure, measured at Plane 1. This nondimensional pressure rise is denoted by Π. Figure 7 (cf. Ref. [16]) shows the variation of pressure rise with the degree of bend of the ejector when no swirl is present. The pressure rise of the 22.5 deg, 35 deg, and 67.5 deg bent ejectors were 9%, 54%, and 68% less than the straight ejector in the cold flow case and were 16%, 52%, and 70% less in the hot flow case.

Figure 8 shows that the swirl has an unfavorable effect on the pressure rise across the straight and low degree bent ejectors; however, a swirl angle up to 20 deg improves the pressure rise of a high degree of bent ejectors. It appears that the counter-rotating vortices formed due to the bend are somewhat reduced if the primary flow has a swirl component in it. The pressure rise of the 35 deg bent ejector is improved by 68% and 46% for cold and hot primary flows, respectively, whereas the pumping of the 67.5 deg bent ejector is improved by 96% and 71% for cold and hot flows.

The bend in the ejector causes secondary flows and flow nonuniformity, which reduce the performance of an ejector. The kinetic energy flux factor was used to measure the degree of nonuniformity of the flow with respect to a plug profile.

Figures 9 and 10 show the effect of swirl on the kinetic energy

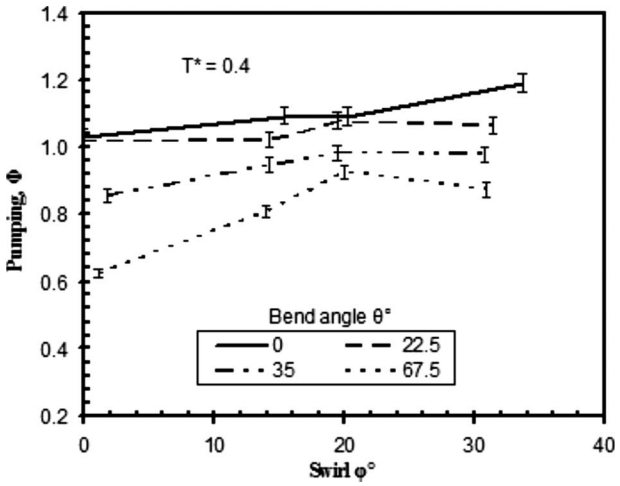

Fig. 6 The effect of swirl in the primary flow on the pumping ratio of ejectors having mixing tubes bent at various angles—hot primary flow presented ($T^*=0.4$)

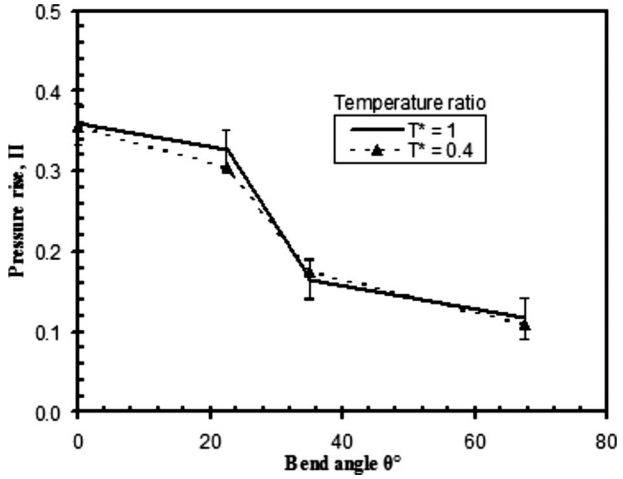

Fig. 7 The effect of bend angle of the mixing tube of the ejector on the pressure rise—no swirl in the primary flow [16]

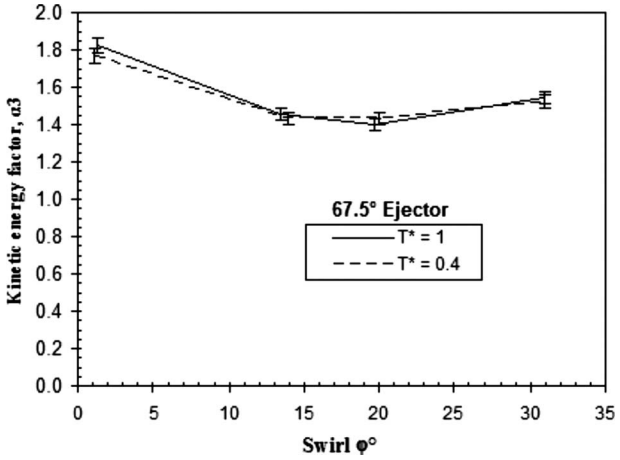

Fig. 10 The effect of swirl in the primary flow on the kinetic energy flux factor of the 67.5 deg bent ejector

flux factor in the 35 deg and 67.5 deg bent ejectors, respectively. The velocity nonuniformity caused by the high degree of bend is reduced by the introduction of swirl in the primary flow.

The lowest kinetic energy flux at the exit of the ejectors is obtained with 20 deg swirl in the primary flow, which clarifies the reason behind the improvement of pumping and pressure rise with the 20 deg swirl in the 35 deg and 67.5 deg bent ejectors. The smaller value of α is a measure of smaller losses in the ejectors. There is a very low momentum region seen in the center of the nozzle and mixing tube exit cross sections in the 30 deg swirl case, which are shown in Figs. 16 and 17 and will be discussed later. This low momentum region causes the increase of α when the primary flow swirl angle is increased from 20 deg to 30 deg.

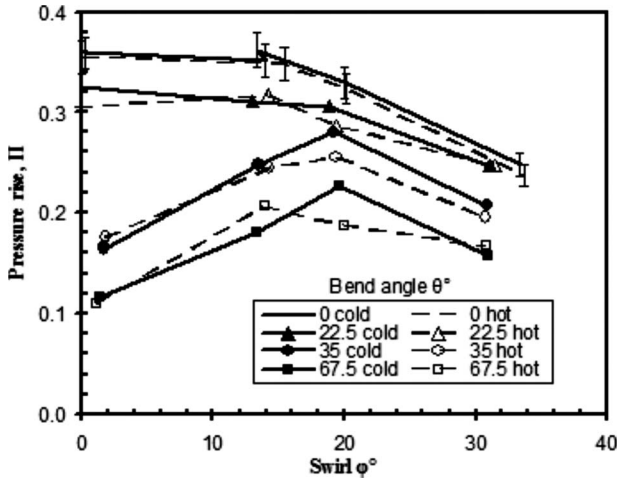

Fig. 8 The effect of swirl in the primary flow on the pressure rise of the bent ejectors

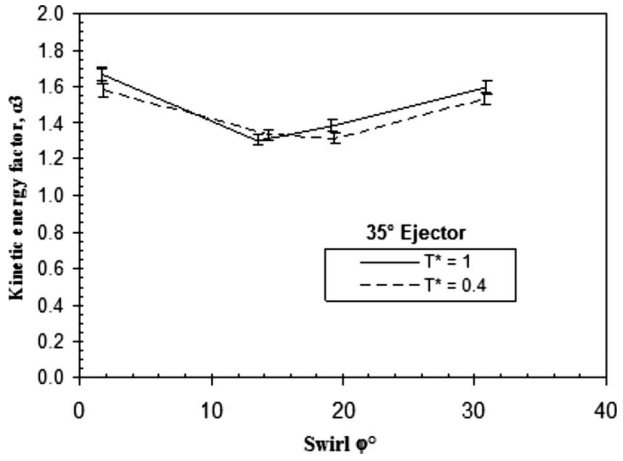

Fig. 9 The effect of swirl on the kinetic energy flux factor of the 35 deg bent ejector

Efficiency. Ejector efficiency is defined as the ratio of the increase in the flow work of the secondary fluid to the dynamic pressure of the primary fluid. Flow work is the product of the mass flow rate and the pressure rise. The relationship of efficiency is given in Eq. (5). Here, atmospheric pressure is used instead of p_3 due to the fact that at the exit of the ejector the pressure is nearly atmospheric

$$\eta_E = \Phi T^* \frac{(P_a - p_2)}{q_1 - (P_a - p_2)} \tag{5}$$

Figures 11 and 12 show the ejector efficiency against the primary flow swirl angle in the cold and hot flow cases, respectively. As could be expected, the efficiency reduces with the degree of bend of the ejector. Efficiency of the cold flow is higher than that of the hot flow cases due to the higher dynamic pressure of the hot

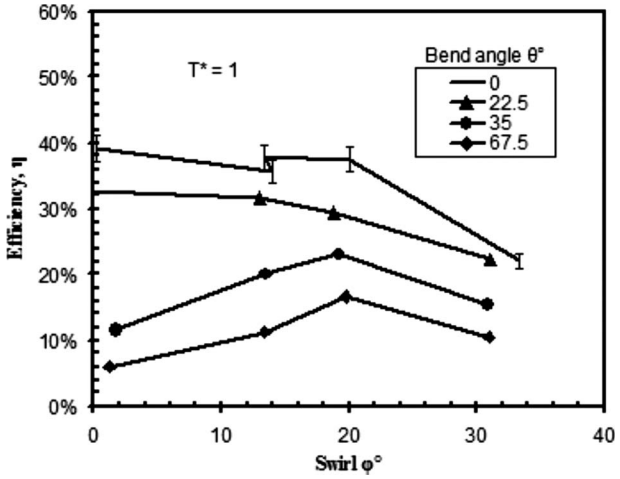

Fig. 11 The effect of swirl in the primary flow on the efficiency of the bent ejectors—cold primary flow ($T^*=1$)

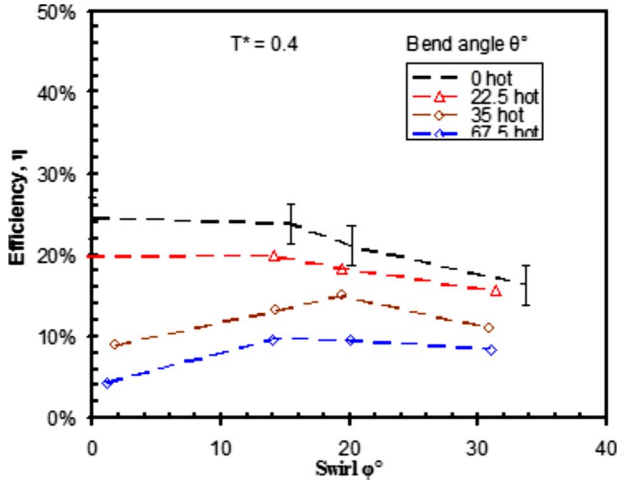

Fig. 12 The effect of swirl in the primary flow on the efficiency of the bent ejectors—hot primary flow ($T^*=0.4$)

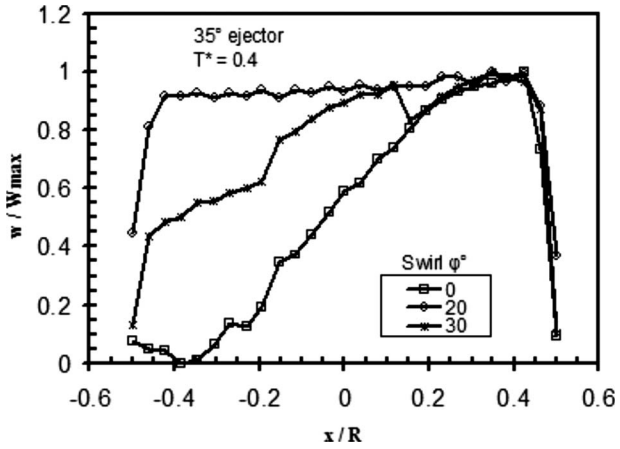

Fig. 14 Axial velocity profile at the horizontal centerline of the exit cross section of the 35 deg bent ejector—effect of swirl on the spreading of momentum

primary flow, which is the driving force of the ejector pumping and pressure rise.

The variation of the efficiency with the swirl angle is similar to the variation of pressure rise. The efficiency of the 35 deg bent ejector is improved by 101% and 69% for cold and hot primary flows, respectively, whereas the pumping of the 67.5 deg bent ejector is improved by 179% and 125% for cold and hot flows with a 20 deg swirl.

Mixing of Momentum. Figure 13 presents the normalized velocity profile at the horizontal centerline of the straight ejector exit plane. Presented in the figure are the data of the cold and hot primary flows at no swirl and 30 deg swirl conditions. The figure shows that the velocity profiles obtained with the cold and hot flows are very similar to each other despite the fact that the velocity magnitudes are different. The mixing of hot flow is slightly higher than the cold flow, the effect of which was seen on the pumping and pressure rise. This higher mixing was expected due to the higher viscosity of hot primary flow.

Figures 14 and 15 show the effect of swirl on the horizontal centerline velocity profile of the 35 deg and 67.5 deg bent ejectors, respectively. In the 35 deg bent ejector, the 20 deg swirl case shows much better mixed flow at the exit of the ejector. With the 30 deg swirl, the amount of mixing is decreased but it is still higher than the no swirl case.

The raised velocity profile in the 30 deg swirl case is due to the transport of high momentum flow from the outer (concave) wall to the center of the mixing tube with the cross-stream motion of the fluid. This transport of high momentum flow is clearly seen in the contour plots of velocity, which is shown in Fig. 17 later. In the 67.5 deg bent ejector, the 30 deg swirling flow has slightly higher mixing than the 20 deg swirl. The velocity profile is raised in the center for both 20 deg and 30 deg swirl cases due to the same reason.

Figure 16 shows the velocity contour plots at the exit of nozzle with 0 deg and 30 deg swirls in the primary flow. This figure explains the effect of geometry and swirl on the flow coming out of the nozzle. These contours were obtained by traversing a seven-hole probe at the exit section of the nozzle (Plane 2). The contour plots show the velocity distribution when looking upstream into the nozzle.

Due to the circular to oblong transition, the flow moves radially in along the minor axis and radially out along the major axis. In the case of swirling primary flow, the geometry driven flow interacts with the swirl driven flow. Due to this interaction, the flow at the exit of the nozzle has a symmetry plane at an angle to the vertical (y) axis.

Figure 17 shows the contours of axial velocity at the exit of ejectors with different swirl conditions for hot flow cases. The velocity contours of a 0 deg swirl show a high axial momentum region in the center of the straight ejector due to the primary jet. The top and bottom sides of the ejector have the maximum axial

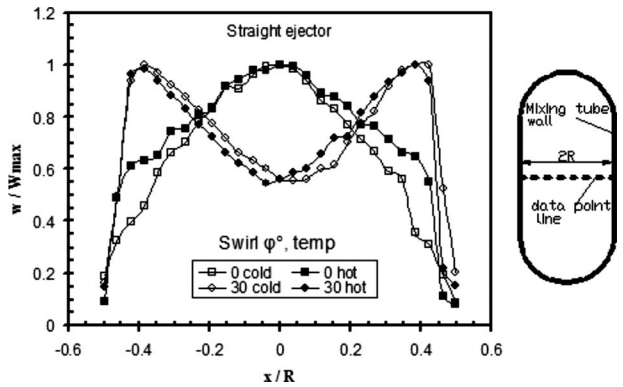

Fig. 13 Axial velocity profile at the horizontal centerline of the exit cross section of the straight ejector—the effect of different temperatures and swirls in the primary flow

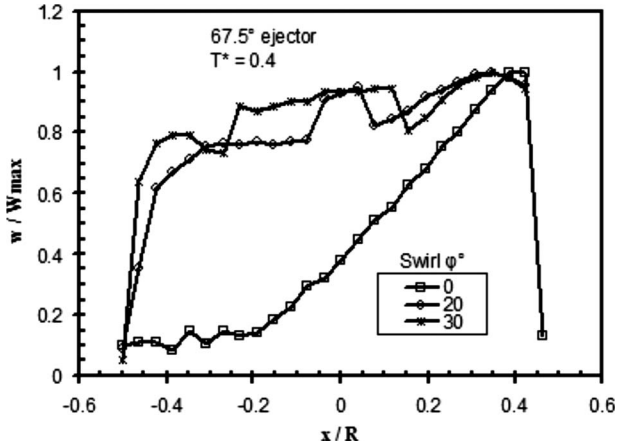

Fig. 15 Axial velocity profile at the horizontal centerline of the exit cross section of the 67.5 deg bent ejector—effect of swirl on the spreading of momentum

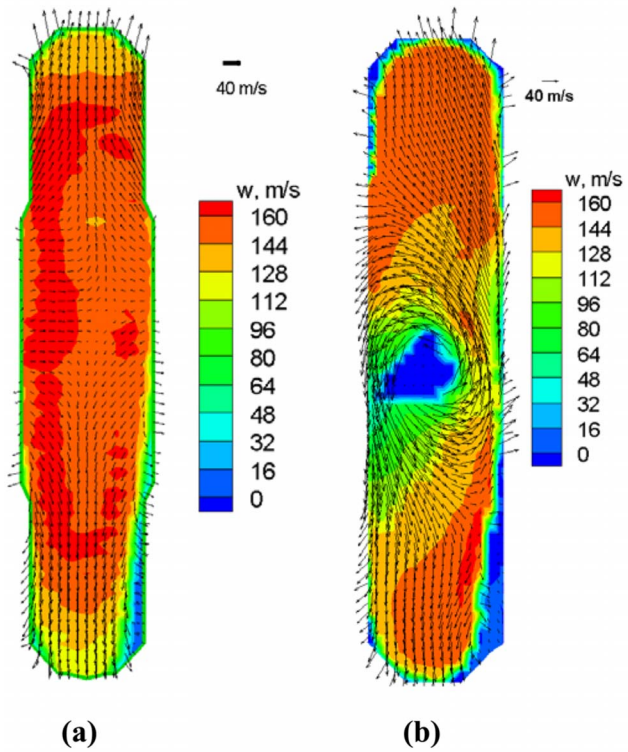

Fig. 16 Contours of axial velocity (*w*), overlaid by cross-stream velocity at the exit of the nozzle measured by a seven-hole probe in the hot flow mass conservation tests with (*a*) 0 deg swirl and (*b*) 30 deg swirl in the primary flow

momentum, which is due to the flow from the nozzle moving radially out in the vertical axis (seen in Fig. 16) and impinging the ejector walls where it makes counter-rotating vortices. Apart from the top and bottom sides, the thickness of the jet appears more in the center than the sides. This is expected because of the higher growth rate of the jet in the minor axis compared to the major axis, which is caused by the axis switching phenomenon of non-circular free jets. With the bend in the ejector, the high momentum flow attaches to the outside wall and the area near the inner wall of the bend shows very low momentum flow. A top-bottom asymmetry is also observed, which may be due to (i) buoyancy of the lighter primary flow with respect to the entrained air and (ii) minor misalignment between the mixing tube and nozzle.

In the 20 deg swirl case, the velocity contours of all the ejectors show better mixed combined flow due to the mutual interaction of swirl generated and bend generated vortices. The flow at the ejector exit is not symmetric about the horizontal (x-axis) or vertical (y-axis). This is because of the structure of flow coming out of the circular to oblong transition nozzle.

The asymmetric cross-stream flow on one hand moves the high momentum flow from the outer wall to the center (seen in high swirl cases, Fig. 17) and moves the low momentum wake region from center to the bottom wall of the mixing tube (seen in the 30 deg swirl cases of 35 deg and 67.5 deg bent ejectors).

In case of 30 deg swirl, the flow is not able to fill the wake region behind the annular to circular transition due to centrifugal force; hence, a velocity deficit zone appears at the exit of the nozzle. Contrary to the no swirl case, the center region of the exit cross section of the 30 deg swirl case has a very low axial momentum because of the wake of annular to circular transition. The effect of swirl on the axial velocity shows that the axial momentum in the center decreases continuously with the swirl. The contours show that the 20 deg swirl causes higher mixing than the 0 deg and 30 deg swirl cases.

Conclusions

The experimental investigation was directed to find the effect of swirl in improving the performance of oblong ejectors with short bent mixing tubes.

The conclusions can be divided into small bend angle ejectors, including the ejectors up to 22.5 deg bend angle in the mixing tube; and highly bent ejectors, which include the 35–67.5 deg bent ejectors of the current study.

In the small bend angle ejectors, the swirl in the primary flow is negligible, if any effect on the pumping ratio and the pressure rise degrades with the swirl in the primary flow. This leads to the decrease in the overall performance of the slightly bent ejectors with the primary swirl.

In the highly bent ejectors (35 deg and 67.5 deg), the swirl improves the pumping and pressure rise. Best performance was obtained with the 20 deg swirl ($S=0.28$). Further increasing the swirl angle decreased the ejector performance. It is believed that the increase in the swirl number of the primary flow increases the performance up to the point when center recirculation zone is formed. Further increasing the swirl increases the center recirculation zone, which reduces the flow area and hence performance of the ejector.

Better improvement was obtained in the ejector with a higher bend angle, which suggests that there is more opportunity for a improvement for a higher degree of bend ejectors. The improvement in the performance is obtained by the reduction of excess kinetic energy of the exit flow and better mixing of the two streams.

Acknowledgment

The authors are thankful to the Natural Sciences and Engineering Research Council of Canada (NSERC), the Canadian Department of National Defense (DND), and W. R. Davis Engineering Ltd., Ottawa, Canada for financial support of this research. The authors are also indebted to the Department of Mechanical and Materials Engineering, Queen's University. The authors also want to acknowledge D. Poirier for his help in the experimental testing process.

Nomenclature

D = diameter
dn = diameter at the exit of the nozzle
Gx = axial component of swirl momentum
G_Φ = tangential component of swirl momentum
L = length
Ma = Mach number
m = mass flow rate
P_a = atmospheric pressure
P_0 = total pressure
p = static pressure
q = dynamic pressure, $q=\frac{1}{2}\rho u^2$
R = half width of the exit section, $R=90$ mm
Re = Reynolds number
r = radius
S = swirl number
T = temperature (K)
T^* = secondary to primary temperature ratio, $T^*=T_2/T_1$ (based on Kelvin scale)
u_ϕ = tangential component of velocity
V = velocity
w = axial component of velocity, component of the velocity which is normal to the measurement plane
x = coordinate along the x-axis, with $x=0$ at the center of ejector cross section

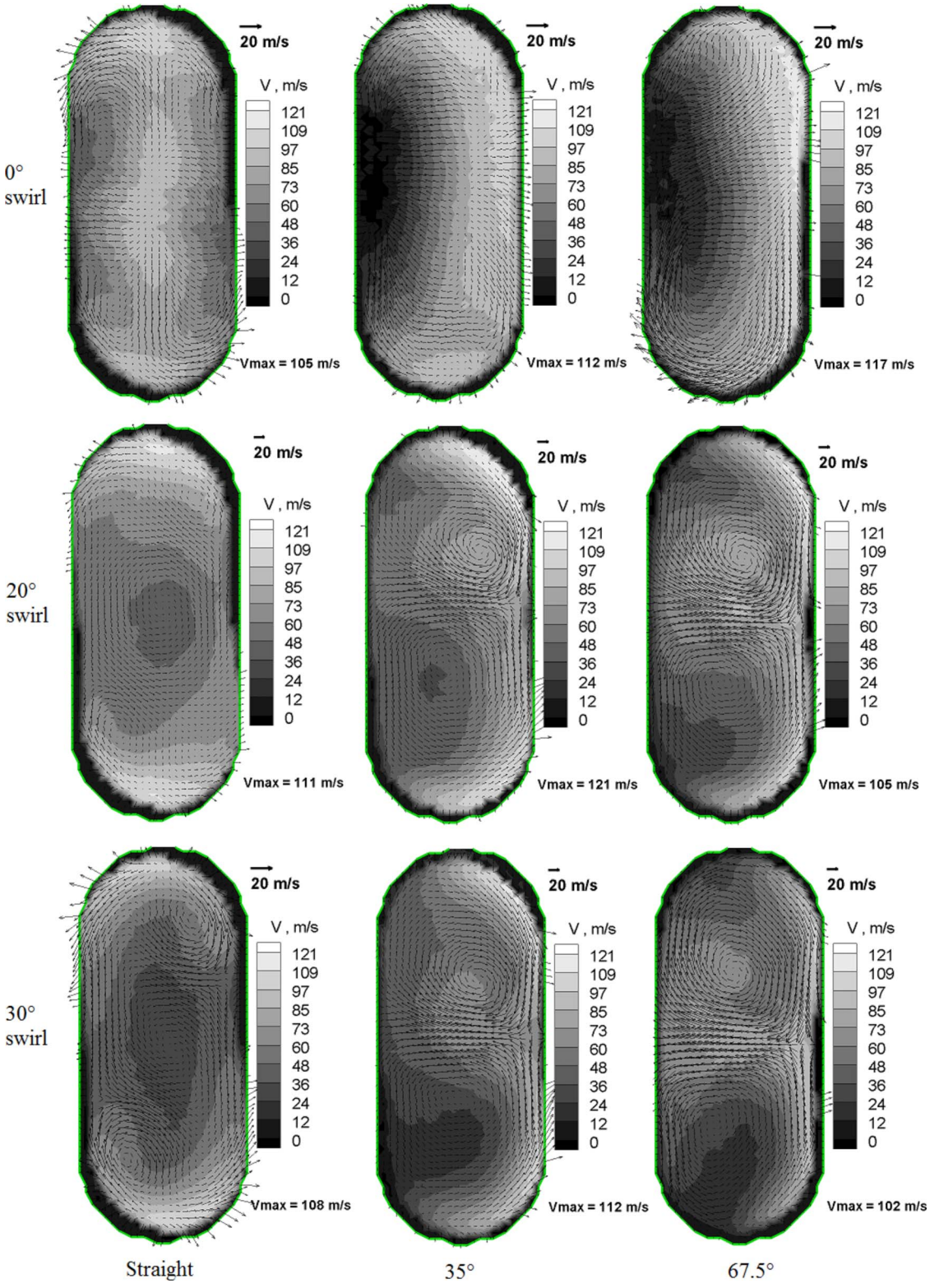

Fig. 17 Axial velocity contour plots at the exit of the straight, 35 deg and 67.5 deg bent ejectors, overlaid by vectors of cross-stream flow at different swirl conditions—measured by traversing a seven-hole probe at the exit sections of the ejectors

Greek Symbols

- α = kinetic energy flux factor, $\alpha = \int_A V^2 \rho V \hat{n} dA / \dot{m} \bar{V}^2$
- θ = bend angle
- Φ = entrainment ratio, $\Phi = m_2/m_1$
- Π = nondimensional pressure rise, $\Pi = (p_3 - p_2)/q_1$
- ρ = density

Subscripts

- a = atmospheric
- e = equivalent

m = mixing tube
max = maximum
n = nozzle
i = inner
o = outer
1 = nozzle inlet plane
2 = nozzle exit and mixing tube inlet plane
3 = mixing tube exit plane

References

[1] Gupta, A. K., Lilley, D. G., and Syred, N., 1984, *Swirl Flows*, Abacus.
[2] Manganiello, E. J., and Bogatsky, D., 1945, "An Experimental Investigation of Rectangular Exhaust Gas Ejectors Applicable for Engine Cooling," NACA-TR-818.
[3] Toulmay, F., 1988, "Internal Aerodynamics of Infrared Suppressors for Helicopter Engines," J. Am. Helicopter Soc., **33**(4), pp. 4–14.
[4] Humphrey, J. A. C., Whitelaw, J. H., and Yee, G., 1981, "Turbulent Flow in a Square Duct With Strong Curvature," J. Fluid Mech., **103**, pp. 443–463.
[5] Sudo, K., Sumida, M., and Hibara, H., 1998, "Experimental Investigation on Turbulent Flow in a Circular-Sectioned 90-Degree Bend," Exp. Fluids, **25**(1), pp. 42–49.
[6] Sudo, K., Sumida, M., and Hibara, H., 2001, "Experimental Investigation on Turbulent Flow in a Square-Sectioned 90-Degree Bend," Exp. Fluids, **30**(3), pp. 246–252.
[7] Ackeret, J., 1958, "Grenzschichten in Geraden und Gekrummten Diffusoren," IUTAM-Symposium, Freiburg/Br., pp. 22–37.
[8] Ackeret, J., 1967, "Aspects of Internal Flow," *Fluid Mechanics of Internal Flow*, pp. 1–24.
[9] Sprenger, H., 1959, "Experimentelle Untersuchungen an Geraden und Gekrummten Diffusoren," Inst. Aerodyn. ETH Zurich, Mitt. No. 27.
[10] Schlichting, H., 1968, *Boundary Layer Theory*, 6th ed., McGraw-Hill, New York.
[11] Gutmark, E. J., and Grinstein, F. F., 1999, "Flow Control With Noncircular Jets," Annu. Rev. Fluid Mech., **31**, pp. 239–272.
[12] Gerner, A. A., Maurer, C. L., and Gallington, R. W., 1984, "Non-Nulling Seven-Hole Probes for High Angle Flow Measurement," Exp. Fluids, **2**(2), pp. 95–103.
[13] Moffat, R. J., 1988, "Describing the Uncertainties in Experimental Results," Exp. Therm. Fluid Sci., **1**(1), pp. 3–17.
[14] Kline, S. J., and McClintock, F. A., 1953, "Describing Uncertainties in Single Sample Experiments," Mech. Eng. (Am. Soc. Mech. Eng.), **75**(1), p. 38.
[15] Vyas, B. D., and Kar, S., 1975, "Study of Entrainment and Mixing Process for an Air to Air Jet Ejector," Second Symposium on Jet Pumps and Ejectors and Gas Lift Techniques, Cambridge, England.
[16] Maqsood, A., and Birk, A. M., 2007, "Effect of a Bend on the Performance of an Oblong Ejector," ASME Turbo Expo, Montreal, Canada, pp. 37–45.
[17] Maqsood, A., and Birk, A. M., 2005 "Experimental and CFD Study of Exhaust Ejectors With Bent Mixing Tubes," ASME Turbo Expo, Reno-Tahoe, NV, pp. 155–165.

Optical Nondestructive Condition Monitoring of Thermal Barrier Coatings

A. L. Heyes
Department of Mechanical Engineering,
Imperial College London,
Exhibition Road,
London, SW7 2AZ, UK

J. P. Feist
Southside Thermal Sciences Ltd.,
c/o IC Innovations,
Imperial College London,
Exhibition Road,
London, SW7 2AZ, UK

X. Chen

Z. Mutasim

Solar Turbines Inc.,
2200 Pacific Highway,
P.O. Box 85376,
San Diego, CA 92186-5376

J. R. Nicholls
Cranfield University,
College Road,
Cranfield,
Bedfordshire, MK43 0AL, UK

This paper describes recent developments of the thermal barrier sensor concept for nondestructive evaluation (NDE) of thermal barrier coatings (TBCs) and online condition monitoring in gas turbines. Increases in turbine inlet temperature in the pursuit of higher efficiency will make it necessary to improve or upgrade current thermal protection systems in gas turbines. As these become critical to safe operation, it will also be necessary to devise techniques for online condition monitoring and NDE. The authors have proposed thermal barrier sensor coatings (TBSCs) as a possible means of achieving NDE for TBCs. TBSCs are made by doping the ceramic material (currently yttria-stabilized zirconia (YSZ)) with a rare-earth activator to provide the coating with luminescence when excited with UV light. This paper describes the physics of the thermoluminescent response of such coatings and shows how this can be used to measure temperature. Calibration data are presented along with the results of comparative thermal cycle testing of TBSCs, produced using a production standard air plasma spray system. The latter show the durability of TBSCs to be similar to that of standard YSZ TBCs and indicate that the addition of the rare-earth dopant is not detrimental to the coating. Also discussed is the manufacture of functionally structured coatings with discreet doped layers. The temperature at the bond coat interface is important with respect to the life of the coating since it influences the growth rate of the thermally grown oxide layer, which in turn destabilizes the coating system as it becomes thicker. Experimental data are presented, indicating that dual-layered TBSCs can be used to detect luminescence from, and thereby the temperature within, subsurface layers covered by as much as 500 μm of standard TBC material. A theoretical analysis of the data has allowed some preliminary calculations of the transmission properties of the overcoat to be made, and these suggest that it might be possible to observe phosphorescence and measure temperature through an overcoat layer of up to approximately 1.56 mm thickness. [DOI: 10.1115/1.2940988]

1 Introduction

The efficiency and specific power output of gas turbines is dictated by the turbine inlet temperature. Therefore, it would be desirable to find ways of increasing this and thereby reducing specific fuel consumption and carbon emissions. The maximum inlet temperature is restricted by the so-called metallurgical limit. New materials such as ceramics might allow the turbine inlet temperature to be increased, but for the moment nickel-based superalloys are likely to remain the materials of choice. Improvements in the short term may be best sought by the development of improved cooling and insulation systems. Drawing air from the main gas path for cooling purposes represents lost capacity. Therefore, improving and fully utilizing the insulating properties of ceramic thermal barrier coatings (TBCs) should be a primary goal in the pursuit of the desired improvements.

Current TBCs consist of an intermetallic bond coat to provide oxidation resistance overlaid with a ceramic, which is typically yttria-stabilized zirconia (YSZ). There are a number of features of the composition and structure that have made this the coating of choice, including phase stability, low thermal conductivity, and strain tolerance. However, the degradation processes associated with the coatings and the dependence of these on operating conditions still need to be better understood if their insulating properties are to be utilized in full. The durability of YSZ is strongly temperature dependent because most of the processes that can destabilize the coating, such as loss of phase stability, sintering, and rate of growth of the oxide layer at the bond coat interface, are temperature dependent.

In older generations of gas turbines, failure of the TBC results in an increase in the temperature of the underlying metal, but the operating conditions are such that the design limits are not exceeded. However, if in future designs the turbine inlet temperature is increased to fully exploit the insulating potential of TBCs, a similar failure would result in metal temperatures beyond design limits. The phase stability of YSZ breaks down at about 1200°C and this represents a practical limit to their utility. It may, therefore, be necessary to look for new materials and, indeed, research is already under way (e.g., Clarke and Levi [1]). Given the potentially severe consequences of coating failure, even if better materials become available and if lifetime characteristics and failure modes become better understood, it will be necessary to monitor coatings to ensure that temperature limits are not exceeded, to provide early detection of degradation, and to allow prediction of remaining life. Hence, new nondestructive evaluation (NDE) technologies are required. These may be used in development testing or in service and ideally should enable temperature to be measured at critical regions such as the surface and bond coat/thermally grown oxide (TGO) interface. In addition, measurements of degradation, online or offline, caused by erosion, or changes in phase composition or hot corrosion, for example, would help the remaining life to be estimated.

2 Thermal Barrier Sensor Coatings

The thermal barrier sensor coating (TBSC) concept was proposed by Choy et al. [2] as a way to meet the requirements set out

Contributed by the International Gas Turbine Institute of ASME for publication in the JOURNAL OF ENGINEERING FOR GAS TURBINES AND POWER. Manuscript received April 27, 2007; final manuscript received September 4, 2007; published August 28, 2008. Review conducted by Dilip R. Ballal. Paper presented at the ASME Turbo Expo 2007: Land, Sea and Air (GT2007), Montreal, QC, Canada, May 14–17, 2007.

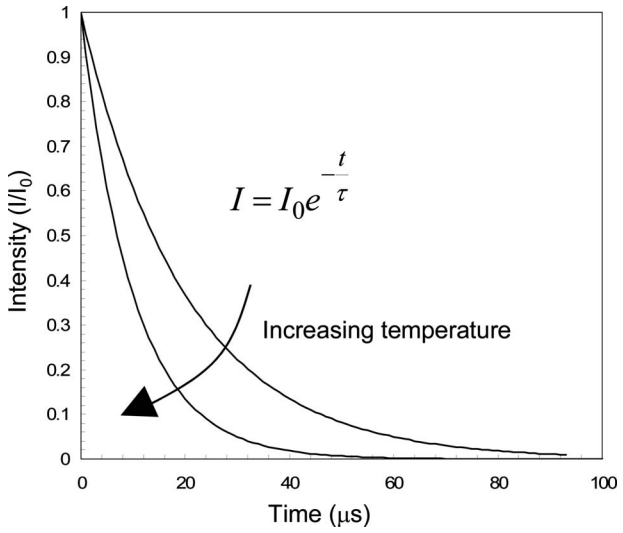

Fig. 1 Temperature dependent emission decay of thermographic phosphors. For each decay curve, an exponential decay function is fitted to the data and the decay characterized by the time constant τ.

above. Sensor coatings are made by modifying the composition of a TBC to include a small amount of a rare-earth element. These are the activators used in phosphors and hence provide the TBC with phosphorescent properties. Phosphor thermometry is a well-known technique by which temperature may be deduced from the phosphorescent response of certain "thermographic phosphors." For a thorough discussion of the method, the reader is referred to Allison and Gillies [3], Heyes [4,5], and Feist [6]; however, for the sake of completeness, a brief review is provided below.

The important characteristic of the rare-earth elements that causes them to bring about phosphorescence in ceramics is a partially filled $4f$ shell containing electrons not involved in bonding the ion to the host lattice and interacting only weakly with it. Light may be absorbed resulting in electron transfer to an excited state and it may be emitted as a result of relaxation back to the ground state. Transitions between $4f$ levels contravene the spectroscopic selection rules so that relaxation is relatively slow and the emission characterized as phosphorescence rather than fluorescence. Hence, after a short burst of exciting illumination, a relatively long-lived emission of decreasing intensity may be anticipated, just as is observed from the face of a phosphorescent timepiece. Not all electrons relax radiatively and some transfer their energy to the host lattice where it is dissipated by phonon emission. As the temperature increases, this process becomes increasingly likely so that the emission intensity decreases and the rate of decay in emission increases. The latter provides one of the measurement modes associated with thermographic phosphor thermometry. This is illustrated in Fig. 1, which shows how the exponentially decaying emission varies with temperature and how the exponential decay time constant, τ, may be used as a measure of the temperature. Other information may be obtained, and other modes of temperature measurement realized, by consideration of the emission spectrum. For further discussion of these, Heyes [4,5] should be consulted.

The authors and their colleagues have already demonstrated the viability of creating TBSCs. The first step involved production of a thermographic phosphor based on YSZ as the host material [7,8]. Samples of 8YSZ (zirconia stabilized with approximately 8% by weight of yttria) doped with approximately 1.4% by weight of Eu_2O_3 were prepared as powders and coatings were laid down using a vapor deposition technique. With these samples, temperatures could be measured up to around 830°C with both powder samples and coatings. Measurements were made at the substrate/TBC interface using a sample consisting of a layer of YSZ:Eu approximately 10 μm thick overlaid with about 50 μm of undoped YSZ. Hence the viability of subsurface temperature measurements was demonstrated. Finally, differences in the emission spectra of samples differently processed were noted. The differences are thought to have been attributable to different phase compositions leading to different phonon spectra. This result implies that, as suggested by Dexpert-Ghys et al. [9], the lanthanide activator ions may act as a structural microprobe to detect phase composition changes.

In the next phase, a YSZ:Dy coating was produced using electron beam physical vapor deposition (EBPVD) in an industry standard coating facility at Cranfield University (Feist et al. [10]). The coating was shown to be suitable for temperature measurements up to around 700°C. No changes to the emission spectra were noted, and it was concluded that the phase stability of the coating remained intact, at least to the temperatures tested.

In a subsequent investigation (Feist and Heyes [11]), the effect of the concentration of dysprosium in yttria-stabilized zirconia on luminescent response and temperature dynamic range was studied. Concentration quenching was shown to be an important factor in the performance of YSZ:Dy. The temperature dynamic range at the optimum concentration was shown to extend to 800°C. This is still too low for gas turbine applications, but new sensor coatings devised by Southside Thermal Sciences have now been shown to have a dynamic range extending to in excess of 1300°C although, unfortunately, at the time of writing the exact compositions of these materials are regarded as proprietary.

TBSCs have also been produced by a production standard air plasma spray (APS) process (Chen et al. [12]). These coatings consisted of a dysprosium doped YSZ layer overcoated with a layer of undoped YSZ. An analysis of the microstructure confirmed this to be very similar to that of conventional TBCs, demonstrating that the addition of the rare-earth dopant does not significantly affect the coating. Thermal cycling of these coatings to failure also showed them to have similar durability to standard TBCs. An examination of the thermoluminescent response showed the coatings to be suitable for temperature measurement up to almost 1000°C. The efficacy of the technique was also demonstrated in a survey of the temperature distribution on the wall of a laboratory combustor.

There are a number of possible embodiments of the TBSC concept that have been suggested by Choy et al. [2] and others (e.g., Eldridge et al. [13]) and that may be employed to realize a variety of measurement functions, as illustrated in Fig. 2. Figure 2(*a*) shows the simplest configuration wherein the ceramic topcoat is uniformly doped and is therefore phosphorescent throughout. This configuration could be used to provide an average temperature for the topcoat. It could also be used to detect location independent coating degradation by mechanisms such as hot corrosion or phase change, both of which affect the host lattice and hence the emission spectrum. Figure 2(*b*) shows a coating wherein a thin, doped layer is positioned at the bottom of the topcoat directly adjacent to the TGO layer with the aim of measuring the temperature in this region. The temperature at this location is important since it dictates the growth rate of the TGO. Instability of the TGO is linked to thickness so that knowledge of the temperature may enable life expectancy to be estimated. In addition, the close proximity of this region (probably within 10 μm) to the substrate means that this configuration should give a good estimate of the metal temperature. Figure 2(*c*) shows a multilayered coating with doped regions at the TGO interface and at the surface. By choosing different dopants for the two doped layers, the emission from them can easily be separated by optical filtration so that temperatures in the two regions can be simultaneously measured. By also providing a measure of the temperature drop across the topcoat, these data could be used to estimate the heat flux to the component assuming the thermal conductivity is known or to estimate the thermal conductivity in an experiment with a controlled and

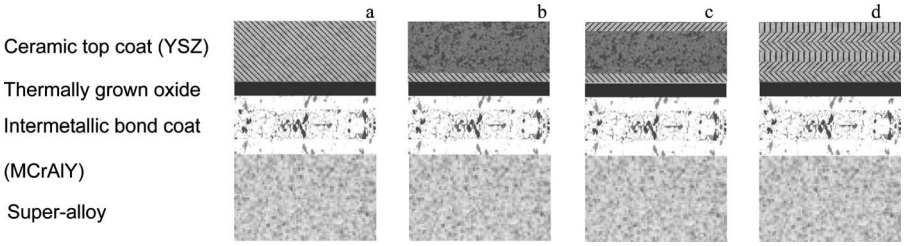

Fig. 2 Proposed embodiments of the thermal barrier sensor coating technology. (*a*) Average temperature/ location independent degradation. (*b*) Bond coat/TGO interface temperature or metal surface temperature. (*c*) Heat flux gauge or thermal conductivity measurement. (*d*) Erosion sensor.

known heat flux. The final concept is illustrated in Fig. 2(*d*), which shows a TBSC composed of differently doped layers throughout. This design could be used as an erosion detector, as suggested by Amano et al. [14]. As the coating thins because of foreign object damage or sintering and spallation, for example, the different layers are successively revealed. The high contrast provided by the different emission spectra of the successive layers will aid detection during routine boroscope inspection (provided that an UV light source is used to illuminate the surface). In addition, knowledge of layer thickness will provide a quantitative estimate of the extent of the damage and of the remaining coating thickness.

3 Research Objectives

The experiments and concepts described above have shown that TBSCs can be manufactured based on the current standard material used for TBCs, i.e., YSZ, and using both the EBPVD and APS industrial coating manufacturing methods. Surface and subsurface temperature measurements have been demonstrated to have the potential for phase change detection. Ongoing research is directed toward improving TBSCs to the point where they can be applied in an industrial setting on rotating or stationary components in a full-scale gas turbine. The technique is equally applicable in aero- and land-based gas turbines, but the latter would be more appropriate for a first application of the technology due to lower regulatory hurdles and the absence of weight restrictions. New TBC materials are under development, but it is not clear what material, if any, will eventually supersede YSZ. Our research is therefore currently concentrated on YSZ as the host material. Nevertheless, the same basic physics would apply for many ceramic host materials. Therefore when new compositions become known, the technique will be adapted to suit them. The research objectives associated with bringing the technology to the point of industrial application are outlined below.

3.1 Composition. Initial sensor materials and coatings based on YSZ showed a temperature dynamic range limited to around 800°C. More recently, compositions allowing temperatures in excess of 1300°C have been established. However, further composition optimization is desirable with a dynamic range extending to at least 1400°C of the target. Material composition affects the dynamic range primarily as a result of the temperature dependent phonon spectra of the host lattice. However, other variables include activator concentration and the inclusion of sensitizing agents. Concentration quenching is known to diminish luminescent output so that an optimum activator concentration should exist. Sensitizing agents may enhance performance by absorbing exciting radiation and pumping the activator by energy transfer.

3.2 Durability. TBC failure may occur as a result of phase instability, sintering, or delamination at the bond coat/TGO interface. The durability of coatings has been shown to be a strong function of operating temperature, ceramic and bond coat composition, substrate composition, and a number of variables related to the coating process. Hence any change in coating composition must be validated to ensure no degradation in durability. This involves testing by long-term exposure at typical operating temperatures and gradients and thermal cycling between ambient and operating conditions. In addition it may be necessary to redefine coating control parameters such as the substrate temperature to retain the desired morphology.

3.3 Instrumentation. Online application of the TBSC technology will require a means to deliver exciting radiation to components inside the engine and to collect and return the luminescence emission. This represents a significant technical challenge since any probe must survive the harsh environment inside hot sections of an engine while continuing to perform for thousands of hours.

4 Current Contribution

Herein we review the manufacture and testing of the first sensor coatings that have been produced using a commercial plasma spraying process. In particular we will consider the performance of functionally structured coatings with a twin layer composition consisting of a doped layer and a standard YSZ topcoat. Such coatings could enable depth selective temperature sensing, measurement of the temperature at the bond coat interface, and, if a three layer structure was manufactured, measurement of heat flux. The temperature dependent luminescent response of the coatings has been calibrated, and a sample of the results is given. A number of coatings have been subjected to long-term isothermal cyclic testing to establish their longevity relative to standard TBCs, and some initial results are presented.

5 Subsurface Temperature Measurements in Functionally Structured TBSCs

Temperature is the determining factor in the rate of several of the degradation mechanisms associated with TBCs including phase change, sintering, and growth of the TGO. In order to assess the risk posed by any or all of these processes, it is important to know the temperature and in some cases the specific locations in the coating. For phase change and sintering the maximum temperature is of interest and the location at which it occurs. For growth of the TGO the temperature at the bond coat interface must be known.

It is not sufficient to assume that the temperature within a TBC remains constant; indeed, there is a steep temperature gradient within the ceramic topcoat of around 500°C/mm with the temperature drop across the top layer being in excess of 100°C for most TBCs. Consequently temperature measured at the surface of the coating system is likely to be a poor indicator of the temperature at the bond coat interface and better spatial resolution is required. A thin layer of TBSC placed at the bond coat interface and overlaid with undoped YSZ, as shown in Fig. 2(*b*), might provide the necessary depth selective temperature measurement capability.

However, for this approach to be successful, the undoped layer must permit the incoming excitation and outgoing signal radiation to pass with minimum loss.

The optical properties of YSZ have been investigated by a number of researchers for a range of compositions and phases including the t' phase favored for TBCs; see, for example, Nakajima et al. [15] and Nychka et al. [16]. The bulk material is effectively transparent from the near infrared through the visible range and down to 248 nm—the wavelength associated with the band gap of YSZ (5 eV). This illustrates the problem of using pyrometry for depth selective temperature measurement since with this method it is difficult to know where the radiation originates so that the output will be some form of average over the thickness of the coating and the metal underneath. Unfortunately, knowledge of the bulk properties of YSZ is not enough to predict the optical properties of a TBC due to heterogeneities such as porosity that modify the properties of the coating. Porosity is an essential feature of TBCs as it affords them strain tolerance, reduces the thermal conductivity, and acts to scatter penetrating infrared radiation. However, in the context of thermoluminescent interrogation, it will at best render the coating translucent and at worst diminish signal strength to the point where it is undetectable and the coating effectively opaque.

Coating microstructure and the nature of the heterogeneities are functions of the manufacturing technique. In APS the coating is built up by a succession of droplet impacts or "splats" so that splat boundaries parallel to the surface may exist and could act to scatter light. EBPVD coatings have a columnar microstructure with the columns, and hence column boundaries, oriented normal to the surface. If total internal reflection can be assumed at the column boundaries, then these may act as light guides delivering excitation to the subsurface layer and returning the subsequent emission. From this discussion, one might expect EBPVD coatings to be a better prospect for subsurface temperature measurements. The coatings considered herein, however, were all manufactured using APS. In Secs. 6–8, the manufacture and endurance testing of the coatings will be described followed by a calibration of the temperature dependent luminescent properties of a range of coatings of different topcoat thicknesses. The effect of topcoat thickness on signal strength is then reported in order to provide an estimate of the degree of transparency of the undoped YSZ layer and to allow an assessment of the ability to measure subsurface temperatures by this method.

6 Coating Manufacture and Endurance Testing

The sensor TBC material was applied to 2.54 cm diameter by 0.635 cm thick buttons made from the Haynes 230 nickel-based superalloy. The coating system consisted of a NiCrAlY bond coating, a 50 μm dysprosium (Dy) doped YSZ layer followed by an overcoat of commercial 6–8 wt % YSZ at thicknesses of 50 μm, 125 μm, 205 μm, and 500 μm. The doped layer contained dysprosium at a concentration of 0.06 wt % and was laid down using a preprepared powder manufactured to the same specifications in terms of particle size and flowability as standard YSZ feedstock.

Endurance testing was carried out by subjecting the samples to thermal cycling in a CM Rapid Temp furnace at temperatures between 25°C and 1148°C. Holding time at the peak temperature (1148°C) was 10 h for each cycle. TBC failure was identified as having occurred when 20% of the area of the TBC or more had cracked and spalled from the substrate. A metallurgical evaluation was conducted using an optical microscope and a scanning electron microscope (SEM) with an energy dispersive X-ray spectrometer (EDS). The coating application, analysis, and furnace test were conducted at Solar Turbines Inc.

Figure 3(*a*) shows a micrograph of the sensor TBC in an as-coated condition and reveals that the microstructure was very similar to that of a conventional TBC. EDS spectra confirmed the presence of Dy in the intermediate layer and its absence from the overcoat suggesting little or no diffusion of the dysprosium. The sensor TBC failed after an average of 122 cycles. Figure 3(*b*) shows a micrograph of the sensor TBC after failure. The sensor TBC failed at the interface between TBC and bond coat. The failure mode and the coating life were very similar to those of conventional TBCs.

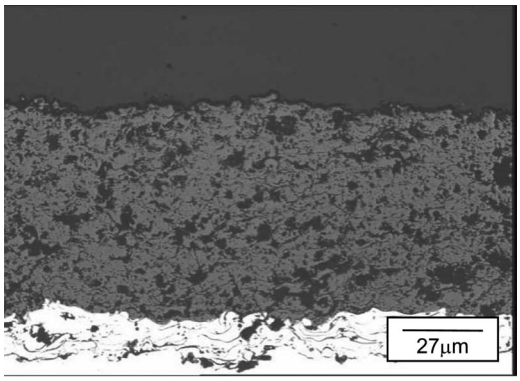

(*a*)

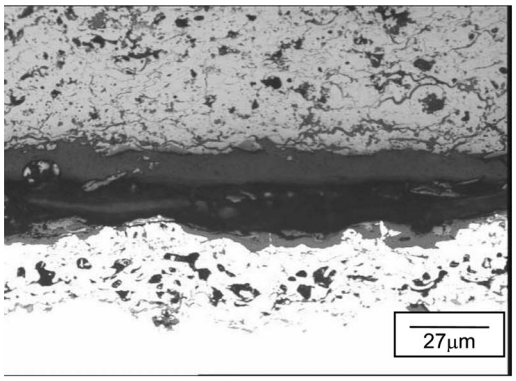

(*b*)

Fig. 3 (*a*) Microstructure of the sensor TBC in as-coated condition and (*b*) after failure along ceramic/bond coat interface

7 Temperature Response Calibration

The thermoluminescent response of the various coating samples was tested using the experimental setup shown in Fig. 4. A pulsed Nd:YAG (yttrium aluminum garnet) laser (Spectra Physics; Model GCR-201) was used to excite samples housed in a furnace (Lenton Furnace Ltd.) capable of reaching temperatures of 1600°C and specially modified to provide optical access. The coated coupons were placed onto a solid ceramic stand providing good thermal connection with the furnace. The temperature controller displayed the temperature in 1 deg steps. The laser was operated at 355 nm (Q-switch mode), at a repetition rate of 16 Hz, and was monitored continuously using a power meter as shown in Fig. 4. A beam dump was used to avoid accidental irradiation of the sample at 532 nm due to leakage. The beam was steered through a window into the furnace and the subsequent luminescence was observed through the same window using wavelength selective optics. The emission was collected using a 50 mm Nikkor lens, which focused an image of the sample on the entrance slit of a crossed Czerny–Turner spectrometer (Jarrell-Ash MonoSpec 18; $f=3.8$).

A photomultiplier tube (PMT) (Hamamatsu) was placed at the flexible exit slit of the spectrometer and used to measure the lifetime decay in phosphorescence emission. An analog/digital converter (PICO Technology; ADC-200; 50 MHz) transferred data simultaneously from the PMT and the power meter to a PC and an exponential decay was fitted to each single exposure using commercial software. The power meter data were used to monitor

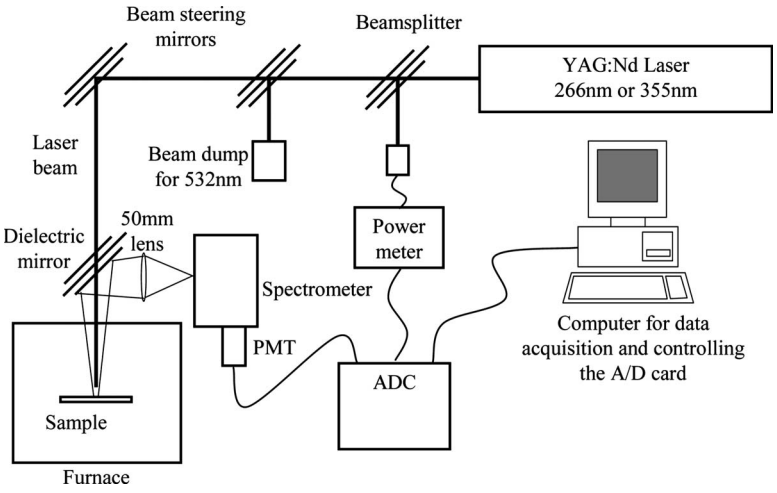

Fig. 4 Experimental setup for phosphor/sensor coating calibration

irradiation of the sample during testing and for triggering purposes. For an observation of the emission spectrum, the photomultiplier system could be replaced with a charge-coupled device (CCD) linear array (Alton LS2000).

8 Results and Discussion

Figure 5 shows the exponential decay time constant as a function of temperature for four different coatings each with a YSZ topcoat of different thickness. The data were all derived by considering phosphorescent emission at 584 nm, a wavelength shown in a previous study by Chen et al. [12], which exhibits the strongest emission for this material. To establish the time constant at a given point, an exponential function was fitted to a decay formed from the summation of the decays from 15 consecutive laser pulses (approximately 1 s). The process was then repeated ten times at each temperature to allow the uncertainty statistics to be derived. Figure 5 shows a response with a dynamic range extending from about 400°C (~600 μs) to at least 800°C (~3 μs). The upper limit is dictated by the signal intensity, which at 800°C was too weak to be processed reliably. In a previous study by Chen et al. [12], a YSZ:Dy coating with no overcoat was shown to have a dynamic range extending to around 950°C (~0.6 μs) so we may conclude that the reduction in the dynamic range observed in the current data was the result of the diminution of signal intensity caused by the overcoat layer. However, it is interesting to note that the thickness of the overcoat layer appears to have had no effect since the dynamic range is the same whether it is 500 μm or 50 μm thick.

In order to try and quantify the attenuating properties of the overcoat, two measures of signal intensity have been considered. First, the emission spectrum of the various samples was considered at room temperature and under constant excitation energy. The resulting spectra are shown in Fig. 6, which includes the spectrum of a YSZ:Dy layer with no overcoat. From Fig. 6, a substantial fall in intensity may be observed as a result of the existence of the YSZ topcoat. However, as suggested by the calibration data shown in Fig. 5, there is relatively little change in emission intensity with the topcoat thickness. This implies that the biggest factors associated with the reduction in signal intensity observed when an undoped YSZ overcoat is introduced are interface effects such as scattering and reflection. If these are concentrated at the surface, it would imply that the surface properties of a pure YSZ layer differ substantially from those of a rare-earth doped YSZ layer. Alternatively, the scattering/reflection could occur at the YSZ/YSZ:Dy interface. This is perhaps surprising, given the known compatibility of dysprosium and YSZ, the relatively low concentration of the former, and the consistent manufacturing process used for both layers. More data will be required

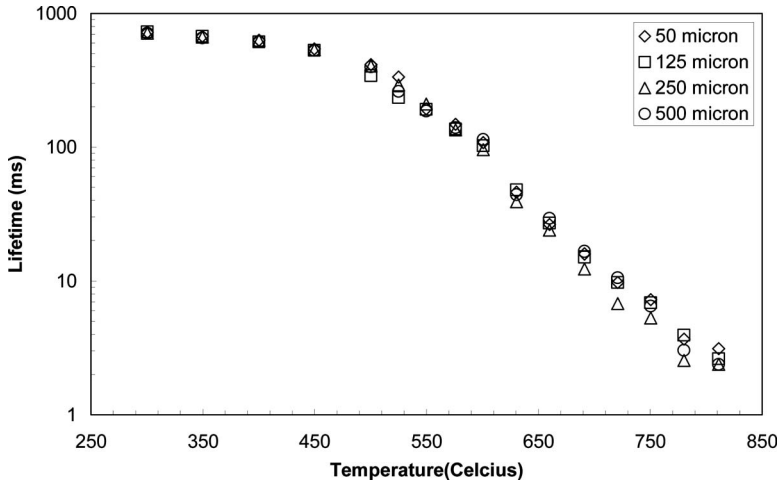

Fig. 5 Exponential decay time constant versus temperature for coatings with a YSZ overcoat of various thicknesses

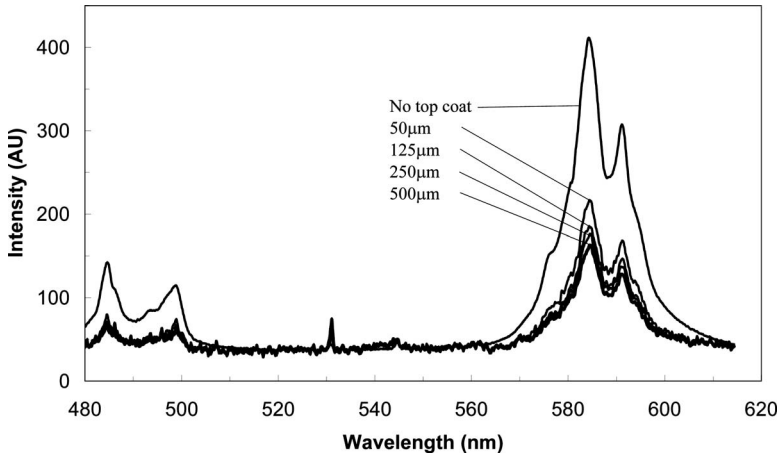

Fig. 6 Emission spectra of TBSCs at room temperature and excited at 355 nm

before this issue can be fully resolved, and it would be interesting to conduct further experiments to see if the dopant affects the refractive index, for example, and how temperature affects the coating performance.

A second analysis of the emission intensity designed to investigate in more detail the transmission properties of the YSZ layer is presented in Fig. 7. In Fig. 7, the abscissa, referred to as the "emission ratio," represents the average intensity of the exponential emission decay normalized by the background emission intensity B and was calculated using Eq. (1). B is composed primarily of blackbody radiation and was assumed to be constant at a given temperature. By normalizing the average emission intensity with B, the effect of system variations that might affect signal strength, such as optical component cleanliness, was minimized. Hence, by carefully maintaining the laser pulse energy and by adopting a fixed integration period at each temperature, E_R gives a reliable measure of the signal strength as a function of coating thickness,

$$E_R = \frac{\int_0^t E_0 e^{-t/\tau} dt}{B \,.\, t} \tag{1}$$

In Fig. 7, E_R is plotted for the four YSZ overcoat thicknesses and at temperatures ranging from 400°C to 750°C. The first thing that can be noted from Fig. 7 is the rapid decline in signal intensity relative to the background as temperature is increased. At 750°C, the average signal intensity is only around 2% of the background emission. This is, of course, due not only to a decrease in the signal intensity but also to an increase in the blackbody emission. This illustrates the signal strength problem that curtails the dynamic range of the TBSC at 800°C. At 400°C, the emission ratio shows that, as might be expected, the brightest emission was observed for the 50 μm overcoat and decreased monotonically as the overcoat thickness was increased to 500 μm. At the other temperatures the differences in the emission ratios are less marked and there is no monotonic decrease in the ratio as the overcoat thickness increases. Indeed at 600°C and 690°C, the weakest signal appears to have come from the coating with the 250 μm overcoat rather than that with the 500 μm overcoat. Such inconsistency may be due to experimental uncertainty, the maximum extent of which was $\pm 15\%$ (standard error) at 600°C for the 250 μm overcoat. However, this remains less than the spread of the data points at this temperature so that the inconsistency is not completely resolved by this hypothesis.

Notwithstanding the inconsistency at elevated temperatures, and since there is little or no information of this kind in literature, it was decided to try and derive an estimate of the extinction coefficient of the YSZ topcoat both to further evaluate the prospects for subsurface interrogation of functionally structured TBSCs and to quantify the effect of inhomogeneities on the transmis-

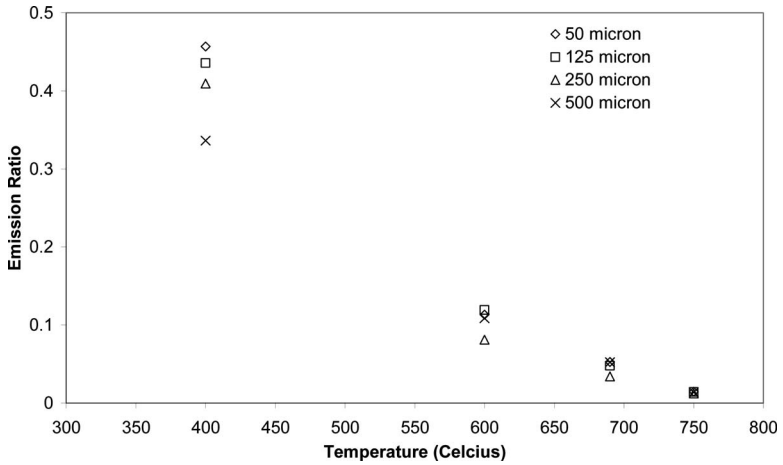

Fig. 7 Phosphorescent emission integrated over the emission period and normalized by the background radiation over the same period

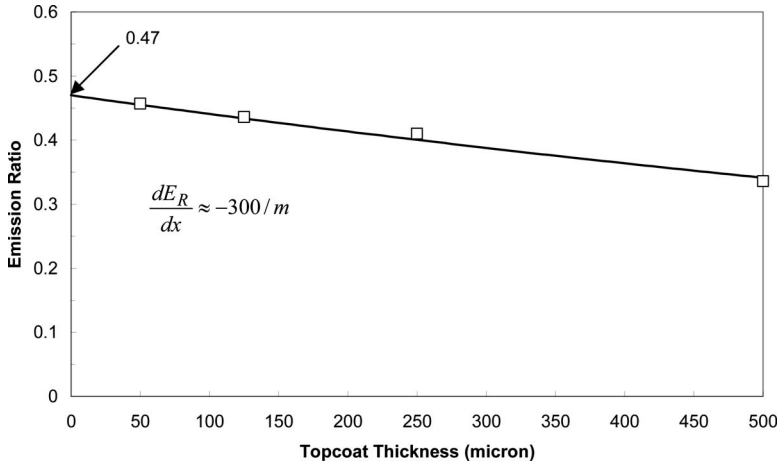

Fig. 8 Emission ratio as a function of coating thickness under constant illumination at 400°C.

sion properties of YSZ as compared with that of the bulk material. A preliminary analysis has therefore been conducted based on the emission ratio data obtained at 400°C.

The observed emission intensity is a function of the amount of excitation arriving at the phosphorescent layer so that the transmission properties of the YSZ topcoat should be considered at both the illumination and emission wavelengths. Using the *Beer–Lambert law* to describe the transmission process, and lumping together all the effects that diminish the transmitted light into a single extinction coefficient, we can write an expression for the maximum emission intensity as

$$E_0 = \eta I e^{-x(\alpha_I + \alpha_E)} \tag{2}$$

where I is the illumination intensity, η is a simple conversion efficiency of illumination to emission (a function of quantum efficiency but also of temperature and the duration of the exciting laser pulse), x is the thickness of the topcoat, and α_I and α_E are the extinction coefficients of the YSZ topcoat at the illumination and emission wavelengths, respectively. Substituting this expression into Eq. (1) for the emission ratio, we obtain

$$E_R = \eta I e^{-x(\alpha_I + \alpha_E)} \frac{\int_0^t e^{-t/\tau} dt}{Bt} \tag{3}$$

At a fixed temperature and under constant illumination conditions, E_R is a function of x only so that we can write

$$E_R = C e^{-x(\alpha_I + \alpha_E)} \tag{4}$$

where

$$C = \eta I \frac{\int_0^t e^{-t/\tau} dt}{Bt}$$

Figure 8 shows the variation of E_R with topcoat thickness at 400°C. By fitting a function of the form of Eq. (4), it may be deduced that at $x=0$, $E_R=C=0.47$ and that the overall extinction coefficient is

$$\alpha_I + \alpha_E \approx 640/\text{m} \tag{5}$$

We can obtain a further estimate of the extent of the indicated extinction by calculating the penetration depth, i.e., the depth at which the observed intensity falls by a factor of $1/e$ relative to that observed at $x=0$. This is simply the reciprocal of the absorption coefficient and equates to 1.56 mm for the case considered herein. This exceeds the thickness of most TBCs used in gas turbines and suggests that they can be regarded as optically thin. This would bode well for the application of the TBSC technology for subsurface temperature measurement.

There is no evidence in literature of absorption features at either the excitation wavelength (355 nm) or the emission wavelength (584 nm) and hence we conclude that the observed absorption is due to scattering promoted by the inhomogeneities of the APS coating. There is also currently no information in literature concerning the overall extinction coefficient for APS YSZ at the excitation and emission wavelengths used herein. However, Schlichting et al. [17] investigated the use of Cr^{3+} fluorescence for the measurement of residual stress in the TGO layer and in doing so considered signal strength as a function of the thickness of the YSZ topcoat for an excitation wavelength of 514 nm and a signal wavelength of 693 nm. They appear to have observed much greater signal attenuation due to the YSZ topcoat although due to the differences in optical configuration, it is not possible to compute an equivalent extinction coefficient for comparison with the one derived herein. Nevertheless it is worthwhile considering what might have caused the improved signal strength observed by the present authors. One explanation might be a different degree of inhomogeneity in the coatings used by the present authors relative to those used by Schlichting et al. However, given that the coatings described herein were produced by a production standard coating process, there seems to be no reason to expect any exceptional coating properties. Another explanation might be the diffusion of the dysprosium ions from the subsurface layer into the YSZ topcoat and the region near the surface. However, an evaluation of the as-coated TBSCs using a SEM with an EDS clearly showed the presence of dysprosium in the surface layer and its absence from the overcoat layer (Chen et al. [12]). Further work is required to quantify the extent of subsequent diffusion of the dopant ions and is ongoing. Preliminary results from a layered coating heated to 1200°C for 270 h suggest no significant diffusion process. If both the above factors can be excluded, then the reasons for the difference in signal quality remain, for the moment, unknown.

The results presented are very promising and bode well for the utility of functionally structured TBSCs, as proposed above and illustrated in Fig. 2. However, more work is required to confirm the findings presented herein and to further quantify the properties and performance of TBSCs.

9 Conclusions

Functionally structured TBSCs have been produced using the production standard APS technique. The coatings were examined and shown to have a microstructure similar to that of standard TBCs, and thermal cycling to failure showed them to have similar

durability. It is therefore indicated that inclusion neither of a rare-earth dopant nor of a layered construction affects the stability or longevity of TBCs.

Calibration of the thermoluminescent properties of the coatings showed them to be suitable for subsurface temperature measurement at the bond coat TGO interface at up 800°C and under an undoped overcoat of YSZ up to 500 μm thick.

An analysis of intensity data has suggested that there are two factors that affect the ability to interrogate subsurface layers in functionally structured TBSCs, namely, surface/interface effects such as scattering and reflection and extinction within the undoped overcoat layer. From the data presented, the former effect appears to be the dominant factor and indeed from the lifetime decay and spectral data no effect due to absorption could easily be discerned. This is in keeping with information in literature concerning the optical properties of bulk YSZ, which shows no absorption features at either the excitation or emission wavelengths. A more detailed analysis enabled an estimate of the extinction characteristics of the APS YSZ coating to be obtained with the translucence of the coating attributed to inhomogeneities such as porosity caused by the manufacturing process. A penetration depth of approximately 1.56 mm was calculated. This exceeds the thickness of most commercial TBCs and suggests that they can be regarded as optically thin. If so, the prospects for subsurface measurements in layered TBSCs are good.

The extinction coefficient calculated appears low when other optically based NDE methods reported in literature are considered. Furthermore, there was some inconsistency in the results relating to transmission through the undoped layer at elevated temperatures, and for both reasons it is recommended that more work be undertaken to investigate further the effect of temperature and to confirm all the findings reported herein.

Nomenclature

B = background emission
E_R = emission ratio
E_0 = maximum emission
I = illumination intensity
T = time (s)
α_I = excitation extinction coefficient
α_E = emission extinction coefficient
η = excitation/emission conversion efficiency
τ = decay time constant (s)

Acknowledgment

The research described in this paper was partly funded by the EU Framework VI ASTERIXE program under Contract No. 505953-1. A.L.H. was additionally funded by a Leverhulme Trust Fellowship.

References

[1] Clarke, D. R., and Levi, C. G., 2003, "Materials Design for the Next Generation Thermal Barrier Coatings," Annu. Rev. Mater. Res., **33**, pp. 383–417.
[2] Choy, K. L., Feist, J. P., and Heyes, A. L., 1998, "Smart Thermal Barrier Coatings for Gas Turbines," European Union Patent No. EU1105550.
[3] [Allison, S. A., and Gillies, G. T., 1997, "Remote Thermometry With Thermographic Phosphors: Instrumentation and Applications," Rev. Sci. Instrum., **7**(68), pp. 2615–2650.
[4] Heyes, A. L., 2004,"Thermographic Phosphor Thermometry—Physical Principles and Measurement Capability," *VKI Lecture Series on Advanced Measurement Techniques for Aero and Stationary Gas Turbines*, *Lecture Series 2004-04*, C. H. Sieverding and J.-F. Brouckaert, eds., von Karman Institute for Fluid Dynamics, Brussels.
[5] Heyes, A. L., 2004, "Thermographic Phosphor Thermometry—Applications in Engineering," *VKI Lecture Series on Advanced Measurement Techniques for Aero and Stationary Gas Turbines*, *Lecture Series 2004-04*, C. H. Sieverding and J.-F. Brouckaert, eds., von Karman Institute for Fluid Dynamics, Brussels.
[6] Feist, J. P., 2001, "Development of Phosphor Thermometry for Gas Turbines," Ph.D., thesis, Department of Mechanical Engineering, Imperial College, London.
[7] Feist, J. P., and Heyes, A. L., 2000, "Europium Doped YSZ for High Temperature Phosphor Thermometry," Proc. Inst. of Mech. Eng., Part L: J. Mater.: Des. Appl., **214**, pp. 7–12.
[8] Choy, K. L., Feist, J. P., Heyes, A. L., and Mei, J., 2000, "Microstructure and Thermoluminescent Properties of ESAVD Produced Eu Doped Y_2O_3-ZrO_2 Coatings," Surf. Eng., **16**(6), pp. 469–472.
[9] Dexpert-Ghys, J., Faucher, M., and Caro, P., 1984, "Site Selective Spectroscopy and Structural Analysis of Yttria-Doped Zirconias," J. Solid State Chem., **54**, pp. 179–192.
[10] Feist, J. P., Heyes, A. L., and Nicholls, J. R., 2001, "Phosphor Thermometry in an EBPVD Produced TBC Doped With Dysprosium," Proc. Inst. Mech. Eng., Part G: J. Aerosp. Eng., **215**(6), pp. 333–341.
[11] Feist, J. P., and Heyes, A. L., 2003, "Recent Developments in Thermal Barrier Sensor Coatings," *16th International Symposium on Airbreathing Engines*, Cleveland, OH, Paper No. AIAA-2003-1049.
[12] Chen, X., Mutasim, Z., Price, J., Feist, J. P., Heyes, A. L., and Seefeldt, S., 2005, "Industrial Sensor TBCs: Studies on Temperature Detection and Durability," Int. J. Appl. Ceram. Technol., **2**(5), pp. 414–421.
[13] Eldridge, J. I., Singh, J., and Wolfe, E., 2006, "Erosion-Indicating Thermal Barrier Coatings Using Luminescent Sublayers," J. Am. Ceram. Soc., **89**(10), pp. 3252–3254.
[14] Amano, K., Takeda, H., Suzuki, T., Tamatani, M., Itoh, M., and Takahashi, Y., 1987, *Thermal Barrier Coating*, Kabushiki Kaisha Toshiba, Tokyo, Japan.
[15] Nakajima, H., Mori, T., and Itoh, S., 2004, "Photoluminescence Properties of Yttria Stabilised Zirconia Single Crystal," J. Mater. Res., **19**(8), pp. 2457–2461.
[16] Nychka, J. A., Winter, M. R., Clarke, D. R., Naganuma, T., and Kagawa, Y., 2006, "Temperature Dependent Optical Reflectivity of Tetragonal Prime Yttria Stabilized Zirconia," J. Am. Ceram. Soc., **89**(3), pp. 908–913.
[17] Schlichting, K. W., Padture, P., and Klemens, P. G., 2001, "Thermal Conductivity of Dense and Porous Yttria-Stabilised Zirconia," J. Mater. Sci., **36**, pp. 3003–3010.

Pressure-Scaling of Pressure-Swirl Atomizer Cone Angles

D. R. Guildenbecher

R. R. Rachedi

P. E. Sojka
e-mail: sojka@ecn.purdue.edu

Maurice J. Zucrow Laboratories,
School of Mechanical Engineering,
Purdue University,
West Lafayette, IN 47906-2014

An experimental investigation was conducted to study the effects of increased ambient pressure (up to 6.89 MPa) and increased nozzle pressure drop (up to 2.8 MPa) on the cone angles for sprays produced by pressure-swirl atomizers having varying amounts of initial swirl. This study extends the classical results of DeCorso and Kemeny, (1957, "Effect of Ambient and Fuel Pressure on Nozzle Spray Angle," ASME Transactions, ***79****(3), pp. 607–615). Shadow photography was used to measure cone angles at* $x/D_0 = 10, 20, 40,$ *and 60. Our lower pressure results for atomizer swirl numbers of 0.50 and 0.25 are consistent with those of DeCorso and Kemeny, who observed a decrease in cone angle with an increase in nozzle pressure drop,* ΔP*, and ambient density,* ρ_{air}*, until a minimum cone angle was reached when* $\Delta P \rho_{air}^{1.6} \sim 100\ MPa(kg/m^3)^{1.6}$ *(equivalent to* $200\ psi(lbm/ft^3)^{1.6}$*). Results for atomizers having higher initial swirl do not match the DeCorso and Kemeny results as well, suggesting that their correlation be used with caution. Another key finding is that an increase in* $\Delta P \rho_{air}^{1.6}$ *to a value of* $600\ MPa(kg/m^3)^{1.6}$ *leads to continued decrease in cone angle, but that a subsequent increase to* $2000\ MPa(kg/m^3)^{1.6}$ *has little effect on cone angle. Finally, there was little effect of nozzle pressure drop on cone angle, in contrast to findings of previous workers. These effects are hypothesized to be due to gas entrainment.* [DOI: 10.1115/1.2939004]

Keywords: pressure swirl, cone angle, nozzle pressure drop, ambient pressure, entrainment

Introduction

Recent advances in gas turbine engine technologies have allowed for the creation of larger, more powerful units with pressure ratios higher than those found in the industry today. The increased combustion chamber pressures (40–60 atm) can have profound effects on the burning process, such as varying the injection characteristics of the fuel.

Previous researchers, in particular, DeCorso and Kemeny [1], have studied the effects of ambient pressure and nozzle pressure drop on spray cone angles produced by pressure-swirl nozzles. These authors proposed that air entrainment caused the spray expansion rate to decrease with increasing ambient pressure until a minimum cone angle was reached, at which point an increase in ambient pressure would have no effect on the spray expansion rate.

For ambient pressures up to 0.79 MPa, DeCorso and Kemeny [1] reported that changes in the normalized cone angle were well described by the following correlation:

$$\Delta P \rho_{\text{air}}^{1.6} \tag{1}$$

where ΔP is the pressure drop across the nozzle and ρ_{air} is the density of the ambient environment.

Ortman and Lefebvre [2] extended DeCorso and Kemeny's results [1] to include ambient pressures up to 2.2 MPa. They sprayed aviation kerosene into pressurized nitrogen and used a "patternator" to measure radial mass flux distribution 10 cm downstream of the nozzle exit. Four commercially available atomizers were tested.

Preussner et al. [3] performed companion numerical studies (a sophisticated numerical simulation of a Gasoline Direct Injection System for an internal combustion engine using the CFD code FIRE). Included in this analysis was the modeling of the influence of ambient effects on a hollow cone spray pattern. The model confirmed the explanation of entrained gas flow leading to a reduction in spray cone angle that was first put forth by DeCorso and Kemeny [1]. Momentum exchange between the spray and the ambient environment led to a reduced pressure within the spray cone. As a result, airflow into the spray cone developed. Aerodynamic drag resulting from this airflow accelerated the drops toward the center of the spray thus leading to a reduced cone angle. The computational model also showed that the amount of cone angle contraction is dependent on the ambient pressure.

While these two studies helped improve our ability to describe pressure-swirl atomizer sprays, they do not consider operating conditions typical of current, and future, gas turbine engines. That lack provided the motivation for this study.

Herein, we consider four issues germane to scaling pressure-swirl sprays to conditions typical of advanced gas turbine engines. We first considered the effect of an increase in ambient pressure on spray cone angle. We then studied how increasing nozzle pressure drop affected spray cone angle. These two sets of data were used to extend the correlation proposed by DeCorso and Kemeny [1]. Specifically, the correlation was extended to include pressures up to 6.89 MPa, comparable to a pressure ratio of 68–1. Finally, pressure-swirl nozzles with various amounts of initial swirl were tested to determine if the scaling behavior first reported by DeCorso and Kemeny [1] is independent of the magnitude of atomizer initial swirl.

Experimental Apparatus

DeCorso and Kemeny [1] studied the injection of diesel fuels into quiescent gas at room temperature. In contrast, we used a noncombustible surrogate fluid in our experiments to avoid the

Manuscript received June 29, 2007; final manuscript received March 1, 2008; published online August 22, 2008. Review conducted by Nader Rizk. Paper presented at the 2006 ASME International Mechanical Engineering Congress (IMECE2006), Chicago, IL, November 5–10, 2006.

Table 1 Properties of a 41:59 mixture of The Cooler™ and water

Density, ρ_{lig}	1015 kg/m^3
Dynamic viscosity, μ_{liq}	2.71 mPa s

dangers of explosions associated with the high pressures involved. This surrogate was Spartan Chemical Company's synthetic machine lubricant/coolant ("The Cooler™") mixed with water. Satapathy [4] showed that a mixture of The Cooler™ and water having a mass ratio of 41:59 exhibits properties similar to those of diesel fuel (see Table 1).

Figure 1 shows the pressure-swirl nozzle used in these experiments. It was originally designed by Zeaton [5], and includes a common exit orifice 1 mm in diameter, a common converging section having a total included angle of 118 deg, plus interchangeable swirl inserts having inlet port diameters of 0.5 to1.0 mm and outer diameters of 2 or 4 mm. The inserts are classified by swirl number, which represents the ratio of initial liquid angular momentum flux to initial liquid axial momentum flux, as defined by Syred [6,7]. Nozzles with swirl numbers of 0.25, 0.50, 0.75, and 1.00 were tested in this study. Atomizers having larger values of swirl number were not used because their wider cone angles would have caused spray development to be influenced by the pressure vessel walls.

Injection occurred within a pressure vessel originally designed by Satapathy [4] and later modified by Zeaton [5]. This vessel is designed to withstand pressures up to 10.3 MPa and includes flow straighteners to ensure a uniform (1D) flow. The vessel has two 5.72 cm diameter, diametrically opposed optical windows, and a traversable injector which allows for spray imaging at various locations downstream of the injector exit plane.

The injection pressure, ambient pressure, and coflow air streams are supplied to the pressure vessel by three systems. The liquid injection system, originally designed by Ohrn [8], injects the surrogate fluid at pressures ranging from 0.69 to 7.58 MPa into ambient air environments having pressures ranging between 0 and 0.89 MPa.

The ambient air pressure was controlled by a coflow system, designed by Zeaton [5]. It is capable of supplying air at pressures up to 10.3 MPa (1500 psi). The system is configured such that the ambient pressure can be set independently of the air mass flow rate. Finally, in-line electric heaters allow for temperature control.

Ambient air and fuel pressure data were acquired using Druck model PMP 1240 transducers. These units are rated up to 13.8 MPa (2000 psi) and have an accuracy of ±0.25% of full scale output. Omega model EMQSS-125G-6 type E thermocouples were used to measure ambient air and fuel injection temperatures. They have an accuracy of ±1°C.

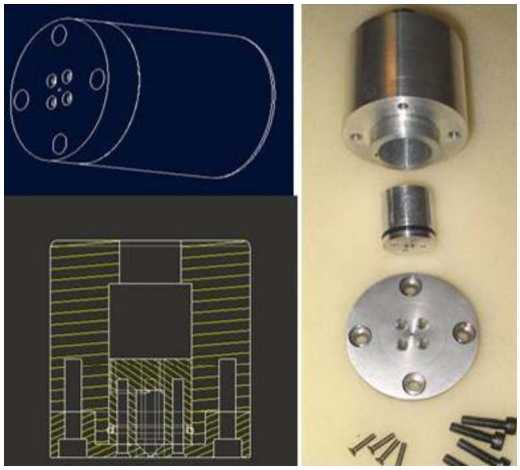

Fig. 1 Variable swirl injector

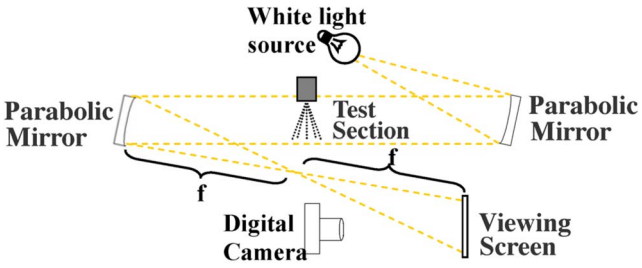

Fig. 2 Shadow graph optical setup

The air mass flow rate was measured using a Micro Motion D-25 Coriolis-type mass flowmeter. The liquid flow rate was measured using an orifice meter having an orifice diameter of 0.36 mm. A Validyne model DP360-56-N1-W-4-B pressure transducer measured the relevant pressure drop.

All quantities were recorded at a sampling rate of 1 kHz using a LABVIEW VI program.

Digital images of the sprays were obtained using the optical system shown in Fig. 2. Here, a white light source in the form of a theatrical stage lamp was used to illuminate an $f/8$ parabolic mirror, thereby creating a beam of parallel light which passed through the test section. A second parabolic mirror was used to focus that light onto a viewing screen. This resulted in a shadowgraph of the spray. Finally, a Sony MVC-FD95 digital camera was used to capture the image for postprocessing.

Results and Discussion

Complete sets of data were collected for nozzles with swirl numbers (Sn) equal to 0.25, 0.50, 0.75, and 1.00. The cone half-angles were measured from shadowgraphs taken of the spray geometry at ambient pressures ranging from 0.69 to 6.89 MPa, and nozzle pressure drops between 0.69 and 2.8 MPa. The cone half-angle was calculated by connecting the visual spray boundary at a given axial distance to the center of the atomizer exit orifice and then determining the angle formed with the spray axis of symmetry. This definition is similar to that of Dodge and Biaglow [9] and Jang et al. [10] and was chosen for its simplicity. The cone angles were measured at four axial locations, $x/D_0=10$, 20, 40, and 60, where x is the axial distance from the orifice and D_0 is the atomizer exit orifice diameter (1 mm). Table 2 summarizes the cone angle naming convention.

Figure 3 contains representative spray images and illustrates the effect of increased P_{air} (or ρ_{air}) and ΔP on spray structure for the Sn=0.75 nozzle. As predicted by previous researchers [1,2,10,11], the spray contracts significantly at increased ambient pressure ($\rho_{air}^{1.6}$) while the effect of increased nozzle pressure drop (ΔP) is less significant.

Figures 4 and 5 show full cone angle versus ambient pressure data for all four nozzles. Figure 4 shows full cone angles measured at $x/D_0=10$, 20, 40 and 60 (θ_{10}, θ_{20}, θ_{40}, and θ_{60}) for the

Table 2 Cone angle definitions

θ_{10}	Cone angle at $x/D_0=10$
θ_{20}	Cone angle at $x/D_0=20$
θ_{40}	Cone angle at $x/D_0=40$
θ_{60}	Cone angle at $x/D_0=60$

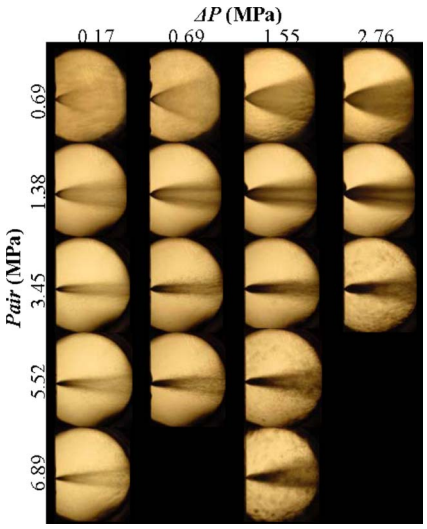

Fig. 3 Representative spray images for Sn=0.75

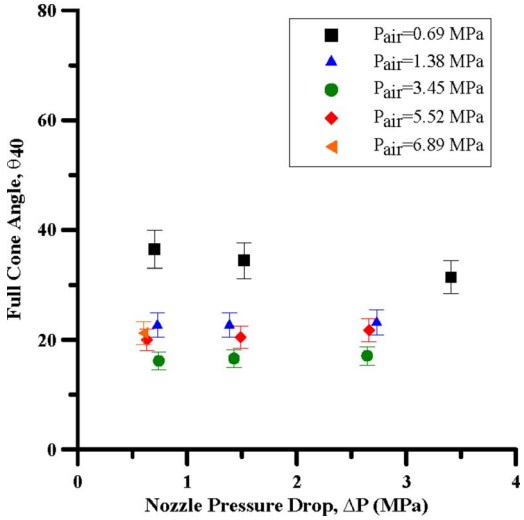

Fig. 5 θ_{40} versus ambient pressure for ΔP=0.69 MPa

Sn=0.25 injector operating at a pressure drop of 0.69 MPa, while Fig. 5 illustrates the influence of initial swirl by showing full cone angles for x/D_0=40 only. The data in Fig. 4 are representative of all nozzle geometries and operating conditions, and the data in Fig. 5 are representative of all nozzle pressure drops tested. Uncertainty bars represent the uncertainty in measurements calculated by a Kline and McClintock analysis [12].

The data in Fig. 4 show that beyond a certain pressure (between about 1.5 and 3.5 MPa) the cone angle is essentially independent of ambient pressure. This is consistent with the findings of Ortman and Lefebvere [2], who theorized that at sufficiently high ambient pressures the cone angles are so small that further increases in P_{air} do not increase the effects of gas entrainment.

It is important to note that different values of the threshold pressure above which the cone angle remains constant have been reported by other researchers—Wang and Lefebvre [13] gave a value of 0.4 MPa, while Ortman and Lefebvre [2] and Parsons and Jasuja [14] both suggested a value of 1.0 MPa.

At least two explanations exist for the different values of threshold pressures reported. First, the reduction in cone angle is an asymptotic function of ambient pressure. As a result, different researchers may have used different criteria for when the spray cone angle could be assumed to reach a constant value. In addition, researchers have defined the cone angle in different ways, which places a limitation on the ability to directly compare the data. Figure 4 data support this latter explanation since they demonstrate that the ambient pressure value for which a further increase has no effect on cone angle varies with measurement location—that value is near 3.5 MPa for cone angle measurements at x/D_0=10, but decreases to about 1.5 MPa for cone angle measurements at x/D_0=60. This experiment is the first to report the cone angle at various axial locations, and thus is the first to observe this phenomena.

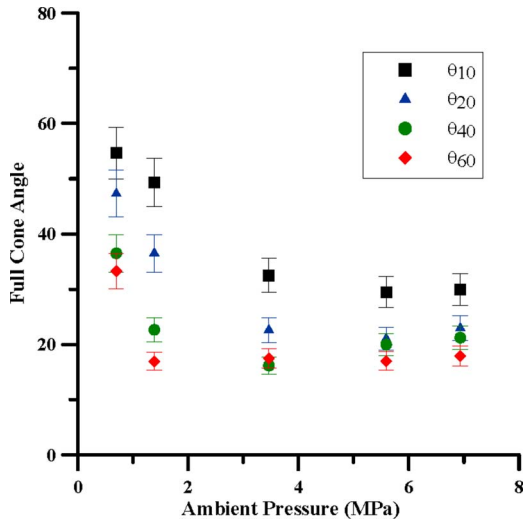

Fig. 4 Full cone angles versus ambient pressure for Sn=0.25 and ΔP=0.69 MPa

Figure 4 data also indicate that the difference between near-nozzle (θ_{10}) and downstream (θ_{60}) cone angles decreases as ambient pressure rises. This leads to the interesting conclusion that the effects of surrounding air entrainment on cone angle become important closer to the atomizer exit plane as ambient pressure increases.

Figure 5 data show the relationship between cone angle and ambient pressure for the four Sn cases. The results demonstrate that swirl number does have an effect on cone angle at low ambient pressures (up to about 1.3 MPa). However, at higher ambient pressures, the cone angles for all four Sn cases are equal (within experimental uncertainty). This suggests that entrainment of the surrounding air becomes the dominant factor for cone angle control at these higher pressures.

Figure 6 shows the measured full cone angle at x/D_0=40 versus nozzle pressure drop ΔP for the swirl nozzle having Sn =0.25. No significant variation in cone angle with pressure drop can be observed. This relation also held for the Sn=0.50, 0.75, and 1.00 nozzles. Our observation is in contrast to findings by most previous researchers who observed a reduction in cone angle with an increase in ΔP at pressures above ambient. Note, however, that previously reported reductions were of significantly smaller magnitude than the reductions observed for increases in ambient pressure. In this study, any reduction in cone angle with a change in ΔP is within the uncertainty of the measurements, as can be seen in Fig. 6, so current results are not inconsistent with those from previous studies.

Data collected during this study were used to determine if the scaling expression of DeCorso and Kemeny [1] could be extended to higher pressures. The following assumptions were needed to ensure that our results are consistent with their data.

The normalized effective spray angle, φ/φ_{atm}, used by DeCorso and Kemeny [1] was assumed equivalent to θ_{40}/θ_{atm} in our experiments. This assumption was necessary because the effective spray angle was not measured here. The effective spray angle

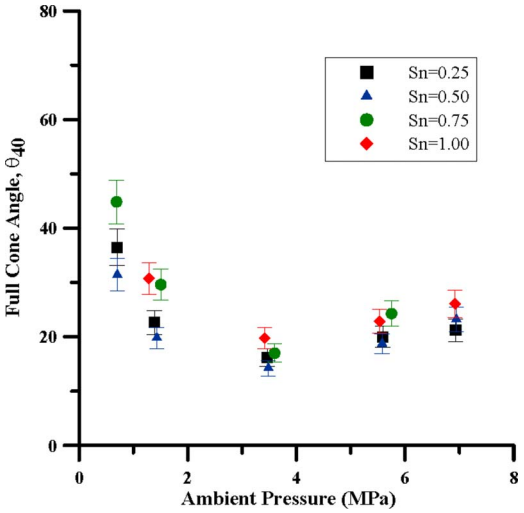

Fig. 6 θ_{40} versus nozzle pressure drop for Sn=0.25

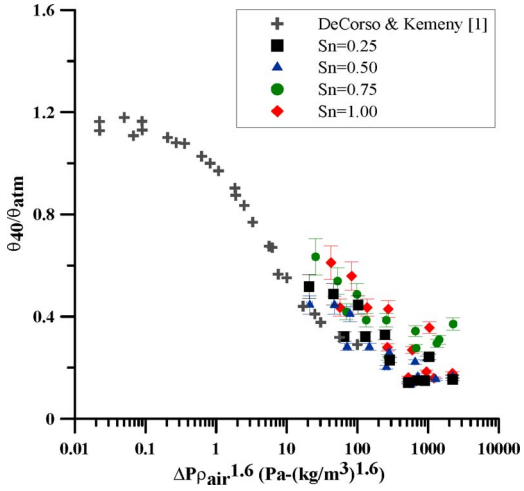

Fig. 7 Comparison of current results with those of DeCorso and Kemeny [1]

measured by DeCorso and Kemeny [1] gives an indication of the radial center of mass at a given axial distance, whereas θ_{40} is a measure of the visual spray boundary. The validity of this assumption requires that the entrained air causes uniform contraction of the jet without affecting the profile of the radial mass distribution. This would be approximated by a spray with a narrow drop size distribution, such that the aerodynamic drag force causes uniform inward acceleration of all the drops. Support for this assumption is provided by Chen et al. [11], who simultaneously measured the effective spray angle and visual cone angle for a pressure-swirl atomizer and found that the two angles scale in a similar manner with nozzle pressure drop. We also assume that θ_{40} is the appropriate cone angle for comparison purposes. This assumption was necessary to specify which axial distance would be used to define the cone angle. Our choice was driven by the DeCorso and Kemeny [1] test matrix, where they tested ten nozzles with different orifice diameters, each at an axial location of 11.4 cm (4.5 in.). As a result, x/D_0 ranged between 40 and 145. It was obviously desirable to use a similar axial distance in this study. The location $x/D_0=40$ was chosen because it is within the range studied by DeCorso and Kemeny [1], and because our results indicate minimal change in cone angle between $x/D_0=40$ and higher ($x/D_0=60$) values. Finally, cone angles were difficult to determine beyond this distance because the penetration length of the spray was reached.

Having made these assumptions, Fig. 7 was created using data from DeCorso and Kemeny [1], plus those acquired during this study. Several points are of interest.

First, this figure shows that Sn=0.5 and Sn=0.25 data from this study match those of DeCorso and Kemeny [1]. This lends support to our choice of cone angle (θ_{40}) for comparison.

Second, above $\Delta P\rho_{air}{}^{1.6}=100$ MPa$(kg/m^3)^{1.6}$ (200 psi$(lbm/ft^3)^{1.6}$), θ_{40}/θ_{atm} is approximately constant and equal to 0.20. Ortman and Lefebvre [2] also extended the DeCorso and Kemeny results to $\Delta P\rho_{air}{}^{1.6}=100$ MPa$(kg/m^3)^{1.6}$ and found that above $\Delta P\rho_{air}{}^{1.6}=60$ MPa$(kg/m^3)^{1.6}$ φ/φ_{air} was approximately constant and equal to 0.25. The discrepancy between our value and that of Ortman and Lefebvre [2] may be due to having used the visual spray boundary here, rather than the effective cone angle that was chosen by Ortman and Lefebvre [2].

Third, there is some influence of atomizer Sn on scaled cone angle for $\Delta P\rho_{air}{}^{1.6}<300$ MPa$(kg/m^3)^{1.6}$. This is evidenced by the systematically higher relative cone angle values for the Sn=1.00 and Sn=0.75 cases, and indicated that the DeCorso and Kemeny [1] correlation, which does not account for the effects of Sn on cone angle, should be used with caution.

Conclusions

Cone angles from pressure-swirl nozzles of Sn=0.25, 0.50, 0.75, and 1.00 were measured at $x/D_0=10$, 20, 40, and 60 over pressure ranges of 0.69 to 6.89 MPa with nozzle pressure drops varying between 0.69 and 2.76 MPa. A number of conclusions can be drawn from these results:

- Cone angle decreases with an increase in ambient pressure, regardless of measurement location. This finding extends the utility of previous investigations where cone angle was measured at only a single location.
- Cone angle is independent of ambient pressure after a value of between 1.5 and 3.5 MPa. The threshold value for this independence is a function of measurement location, with smaller pressure thresholds corresponding to further measurement locations.
- The difference between near-nozzle and downstream cone angle values decreases as ambient pressure rises. This suggests that the influence of air entrainment becomes important closer to the atomizer exit plane as ambient pressure is increased.
- Atomizer swirl number does have an effect on cone angle for ambient pressures below about 1.3 MPa. At higher pressures, measured cone angles are within experimental uncertainty of each another. This finding suggests that entrainment becomes the dominant factor controlling cone angle at pressures above about 1.4 MPa.
- An increase in nozzle pressure drop had little effect on the measured cone angle. While this finding contradicts those by previous researchers (who observed a reduction in cone angle when nozzle pressure drop was increased), the reduction they reported was significantly smaller in magnitude than the reduction observed with increases in ambient pressure. As such, our results are not inconsistent with theirs.
- Our lower pressure results for Sn=0.50 and Sn=0.25 are consistent with those of DeCorso and Kemeny [1], who observed a decrease in cone angle with an increase in an ambient pressure-density product until a minimum was reached at $\Delta P\rho_{air}{}^{1.6}\sim 100$ MPa$(kg/m^3)^{1.6}$.
- Our higher pressure results are consistent with those of Ortman and Lefebvre [2], in that a continued increase in $\Delta P\rho_{air}{}^{1.6}$ to a value of 600 MPa$(kg/m^3)^{1.6}$ leads to a de-

crease in cone angle, but that a subsequent increase to 2000 MPa$(kg/m^3)^{1.6}$ has little effect on cone angle. These data extend the useful range of DeCorso and Kemeny's [1] results to $\Delta P \rho_{air}^{1.6} \sim 2000$ MPa$(kg/m^3)^{1.6}$.

- There is some influence of atomizer Sn value on scaled cone angle for $\Delta P \rho_{air}^{1.6} < 300$ MPa$(kg/m^3)^{1.6}$. It indicates that the DeCorso and Kemeny [1] correlation, which does not account for the effects of Sn on cone angle, should be used with caution.

Nomenclature

D_0 = nozzle exit orifice diameter, m
P_{air} = ambient pressure, Pa
ΔP = pressure drop across nozzle, Pa
Sn = swirl number, dimensionless
x = distance downstream of injector exit plane, m
θ_0 = cone angle for atmospheric pressure, deg
θ_{10} = cone angle measured at $x/D_0=10$, deg
θ_{20} = cone angle measured at $x/D_0=20$, deg
θ_{40} = cone angle measured at $x/D_0=40$, deg
θ_{60} = cone angle measured at $x/D_0=60$, deg
μ = viscosity, Pa s
ρ_{air} = ambient gas density, kg/m^3
φ = effective cone angle of DeCorso and Kemeny [1], deg
φ_0 = effective cone angle at atmospheric pressure, deg

References

[1] DeCorso, D. E., and Kemeny, G. A., 1957, "Effect of Ambient and Fuel Pressure on Nozzle Spray Angle," Trans. ASME, **79**(3), pp. 607–615.
[2] Ortman, J., and Lefebvre, A. H., 1985, "Fuel Distributions from Pressure-Swirl Atomizers," J. Propul. Power, **1**(1), pp. 11–15.
[3] Preussner, C., Döring, C., Fehler, S., and Kampmann, S., 1998, "GDI: Interaction Between Mixture Preparation, Combustion System and Injector Performance," SAE Technical Paper No. 980498.
[4] Satapathy, M. R., 1997, "The Effect of Ambient Density on the Performance of an Effervescent Diesel Injector: A Thesis," MSME thesis, Purdue University, West Lafayette.
[5] Zeaton, G. W. P., 2004, "An Experimental Study of Supercritical Fluid Jets: A Thesis," MSME thesis, Purdue University, West Lafayette.
[6] Syred, N., Gupta, A. K., and Beer, J. M., 1954, "Temperature and Density Gradient Changes Arising With the Processing Vortex Core and Vortex Breakdown in Swirl Burners," *15th Symposium (International) on Combustion*, pp. 587–597.
[7] Lefebvre, A. H., 1989, *Atomization and Sprays*, Hemisphere, New York.
[8] Ohrn, T. R., 1989, "The Effects of Internal Geometry and Injection Pressure on the Flow and Spray Characteristics of a Plain Orifice Atomizer: A Thesis," MSME thesis, Purdue University, West Lafayette.
[9] Dodge, L. G., and Biaglow, J. A., 1986, "Effect of Elevated Temperature and Pressure on Sprays From Simplex Swirl Atomizers," ASME J. Eng. Gas Turbines Power, **108**, pp. 209–215.
[10] Jang, C., Bae, C., and Choi, C., 2000, "Characterization of Prototype High-Pressure Swirl Injector Nozzles—Part I: Prototype Development and Initial Characterization of Sprays," Atomization Sprays, **10**, pp. 159–178.
[11] Chen, S. K., Lefebvre, A. H., and Rollbuhler, J., 1992, "Factors Influencing the Effective Spray Cone Angle of Pressure Swirl Atomizers," ASME J. Eng. Gas Turbines Power, **114**, pp. 97–103.
[12] Kline, S. J., and McClintock, F. A., 1953, "Describing Uncertainties in Single-Sample Experiments," Mech. Eng. (Am. Soc. Mech. Eng.), **75**, pp. 3–9.
[13] Wang, X. F., and Lefebvre, A. H., 1987, "Influence of Ambient Air Pressure on Pressure-Swirl Atomization," ASME Paper No. 87-GT-55.
[14] Parsons, J. A., and Jasuja, A. K., 1986, "Effect of Air Pressure Upon Spray Angle/Width Characteristics of Simplex Pressure Swirl Atomizers," ASME Paper No. 88-GT-176.

Laminar Flame Speeds and Strain Sensitivities of Mixtures of $H_2/O_2/N_2$ at Elevated Preheat Temperatures

J. Natarajan

T. Lieuwen

J. Seitzman

School of Aerospace Engineering,
Georgia Institute of Technology,
Atlanta, GA 30332-0150

*Laminar flame speeds and strain sensitivities of mixtures of H_2 and air or air highly diluted with N_2 (O_2:N_2 1:9) have been measured for a range of equivalence ratios at high preheat conditions (~700 K) using a nozzle generated, 1D, laminar, wall stagnation flame. The measurements are compared with numerical predictions based on three detailed kinetic models (GRIMECH 3.0, a H_2/CO mechanism from Davis et al. (2004, "An Optimized Kinetic Model of H_2/CO Combustion," Proc. Combust. Inst., **30**, pp. 1283–1292) and a H_2 mechanism from Li et al. (2004, "An Updated Comprehensive Kinetic Model of Hydrogen Combustion," Int. J. Chem. Kinet., **36**, pp. 566–575)). Sensitivity of the measurements to uncertainties in boundary conditions, e.g., wall temperature and nozzle velocity profile (plug or potential), is investigated through detailed numerical simulations and shown to be small. The flame speeds and strain sensitivities predicted by the models for preheated reactants are in reasonable agreement with the measurements for mixtures of H_2 and standard air at very lean conditions. For H_2 and N_2 diluted air, however, all three mechanisms significantly overpredict the measurements, and the overprediction increases for leaner mixtures. In contrast, the models underpredict flame speeds for room temperature mixtures of H_2 with both standard and N_2 diluted air, based on comparisons with measurements in literature. Thus, we find that the temperature dependence of the hydrogen flame speed as predicted by all the models is greater than the actual temperature dependence (for both standard and diluted air). Finally, the models are found to underpredict the measured strain sensitivity of the flame speed for H_2 burning in N_2 diluted air, especially away from stoichiometric conditions.*
[DOI: 10.1115/1.2943180]

Keywords: hydrogen, laminar flame speed, strain sensitivity, N_2 dilution, reactant preheat

Introduction

One of the most extensively studied kinetic mechanisms is that of hydrogen combustion because of its relative simplicity and its importance in understanding combustion of hydrocarbon fuels in general. Hydrogen is also an interesting fuel from a practical standpoint due to its intense burning characteristics and because of its potential to reduce greenhouse gas emissions. For example, recent interest has been focused on synthetic fuel gas (syngas) combustion. Syngas is derived from coal through a gasification process, and it is a promising fuel source for low emission and high efficiency power generation. It is mainly composed of H_2, CO, N_2, and CO_2 in varying amounts, with typically lower levels of H_2O, CH_4, and other higher order hydrocarbons [1,2]. Extensive research has been conducted to understand the fundamental combustion properties of these fuel mixtures. These include experimental determination of laminar flame speed, ignition delay, and flame structure. Laminar flame speed is an important parameter of a combustible mixture as it contains fundamental information regarding reactivity, diffusivity, and exothermicity.

Laminar flame speeds of syngas-type mixtures have been measured with conical flames [3,4], spherically expanding flames [5], and flat flames [6]. Stretch-corrected laminar flame speeds for H_2/CO mixtures have been obtained with counterflow flames (CFF) [7] and spherically expanding flames [8–12]. In addition, various reaction mechanisms have been proposed for H_2/CO combustion [13,14] and used to predict laminar flame speeds for syngas fuels. Since most of the flame speed measurements were obtained for stoichiometric and fuel-rich mixtures, and most importantly with room temperature reactants, the applicability of the proposed kinetic models to low emissions, lean premixed gas turbine combustion is uncertain.

Recently, the laminar flame speeds of H_2/CO mixtures have been measured over a range of preheat temperature (up to 700 K) and fuel composition [15]. Figure 1 compares the measured flame speeds (using a Bunsen flame technique) for preheated, lean 50:50 H_2:CO fuel-air mixtures from Ref. [15] with predicted, unstrained, laminar flame speeds from two models (GRI MECH 3.0 [16] and a H_2/CO mechanism from Davis et al. [13]). The predicted flame speeds are in good agreement (~10%) with measurements for low preheat temperatures (less than ~500 K) for both lean equivalence ratios. For further increase in preheat temperature, the models overpredict the measured flame speeds by as much as 30%. Moreover for a given preheat temperature, the overprediction increases as the mixture becomes leaner. For instance, the GRI MECH overprediction increases from 14% at $\Phi=0.8$ to 26% at $\Phi=0.6$ for 700 K preheat temperature. It is also important to note that the H_2/CO mechanism overpredictions are larger than for GRI MECH, specifically 16% at $\Phi=0.8$ and 32% at $\Phi=0.6$ for 700 K

Contributed by the International Gas Turbine Institute of ASME for publication in the JOURNAL OF ENGINEERING FOR GAS TURBINES AND POWER. Manuscript received January 15, 2008; final manuscript received January 16, 2008; published online August 22, 2008. Review conducted by Dilip R. Ballal. Paper presented at the ASME Turbo Expo 2007: Land, Sea and Air (GT2007), Montreal, Quebec, Canada, May 14–17, 2007.

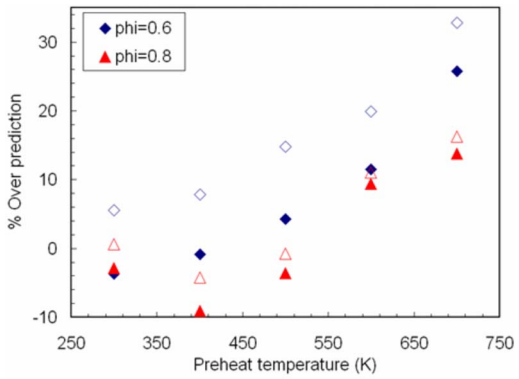

Fig. 1 Variation of the model (GRIMECH 3.0: closed symbols; Davis H_2/CO mechanism: open symbols) overprediction with preheat temperature for 50:50 H_2:CO fuel composition at 0.6 and 0.8 equivalence ratios

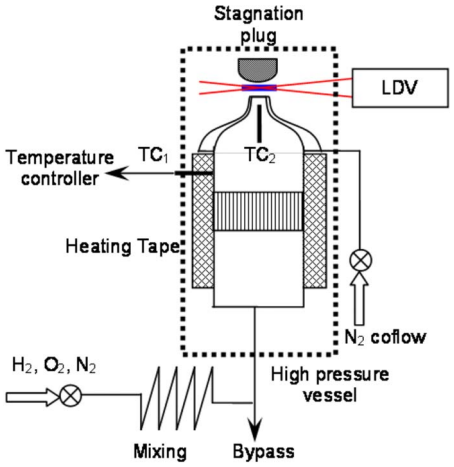

Fig. 2 Schematic of the experimental setup (TC =thermocouple); mixing is achieved through long flow lines

preheat temperature. In summary, the flame speeds predicted with the two mechanisms increase with preheat temperature faster than the measurements, especially for fuel lean conditions. Similar behavior was also observed for high H_2 content fuel mixtures [15]. Hence it is important to investigate the effect of preheat on flame speeds of pure H_2 fuels at lean conditions. As applications involving H_2 combustion can also entail significant levels of diluent gases, we also consider laminar flame speeds for reactant mixtures with high amounts of N_2 dilution.

Thus, the primary objective of the present study is to measure laminar flame speeds for $H_2/O_2/N_2$ fuel mixtures at high preheat temperature (700 K) and under lean conditions. A stagnation flame technique is employed in this work; it is a direct measure of flame speed and it allows us to obtain the sensitivity of the unburned flame speed to imposed strain rate. The measurements are compared with the predictions of leading chemical kinetic mechanisms in order to ascertain the accuracy of current models at the high preheat temperatures found in gas turbine combustors.

Experimental Facility and Measurement Method

Strained laminar flame data were acquired in a stagnation flow configuration. This configuration, like the more commonly employed opposed jet flow approach [17], allows for stretch-corrected flame speed measurements of a one-dimensional (1D) laminar flame. Furthermore, it is advantageous over the opposed flow arrangement for determining laminar flame speeds for the following reasons: (1) the use of a solid wall leads to more stable flames, (2) problems related to heating of the upper burner are eliminated, and (3) use of a single jet greatly simplifies burner operation.

A general schematic of the stagnation flow burner is shown in Fig. 2. The reactant (H_2, O_2, and N_2) flow rates are monitored with rotameters, and they are premixed in the mixing section ahead of the burner. The rotameters are calibrated with a bubble flow meter and wet test meter to better than $\pm 1\%$ accuracy, with fuel and air flows in the range of 0.1–50 slpm. The desired flow rate of the premixed fuel mixture is sent to the burner while the remainder is bypassed. With this arrangement, the average velocity of the mixture at the exit of the burner is easily adjusted without altering the equivalence ratio. The burner is formed from a smoothly contoured nozzle with high contraction ratio, in order to create a uniform velocity profile at the burner exit and a uniform flame stretch throughout the flame area. Moreover, the high contraction ratio contoured nozzle ensures laminar flow even at high Reynolds number based on the burner exit diameter.

Two nozzles with exit diameters (D) of 6.25 mm and 9 mm are employed to produce a stable flame, with higher flame speed mixtures requiring the smaller nozzle. Flow straighteners placed upstream of the contoured nozzle reduce any unsteadiness in the incoming flow. The exiting fuel/air mixture is surrounded by a N_2 coflow. Flow stagnation is achieved with a plug produced from a stainless steel rod (38 mm diameter). The end of the rod is first formed into a hemisphere and then machined to produce a flat surface with 12.5 mm diameter. The rounded plug, compared to a flat plate, greatly improves flame stability especially at high flame speed conditions (e.g., high preheating). The distance (L) between the burner exit and stagnation plug is adjusted depending on the burning velocity. For high burning velocities, smaller L and D lead to a stable stagnation flame. In the current measurements, L ranges from 5 mm to 6 mm. The corresponding L/D values are sufficiently large that the effect of finite domain on the measured flame speed can be considered small [18]. The use of a solid wall as a stagnation plane, as opposed to the counterflow configuration with adiabatic twin flames, is generally considered to have an insignificant effect on the measured unburned flame speed, provided that the flame is stabilized sufficiently away from the stagnation plane [19]. In all our experiments, the flame is located at least two flame thicknesses away from the plate. The effects of the solid wall are mainly downstream heat loss from the flame products to the wall and zero radial velocity gradient at the wall. A detailed numerical analysis of the influence of these effects on the unburned strained flame speed is reported in the Appendix.

The reactants are preheated by electrical resistance tape wrapped around the burner. Once the desired reactant temperature is achieved (as determined by a Type-K thermocouple, TC_2, placed at the center of the burner 25 mm below the exit), the surface temperature of the burner is monitored by a second thermocouple, TC_1, and held constant by a temperature controller. The mixture temperature at the exit of the burner has a nearly uniform radial profile ($\Delta T \approx 3-5$ K). The axial velocity along the stagnation streamline is measured using a laser doppler velocimetry (LDV) system. The fuel mixture is seeded with alumina (Al_2O_3) particles. The nominal size of these particles is chosen to be 1–2 μm in order to minimize thermophoretic effects [20].

To illustrate this method, the measured axial velocity along the stagnation streamline for a typical stagnation flame is shown in Fig. 3. The axial velocity decreases from the exit of the nozzle and reaches a minimum where the preheat zone starts. After reaching a local minimum, the axial velocity increases sharply inside the flame and then decreases to zero at the wall. Based on a standard approach [17], the minimum velocity before the preheat zone is considered as the reference strained unburned flame speed (S_u), and the maximum gradient of the axial velocity (as determined from the velocity measurements) ahead of the minimum velocity

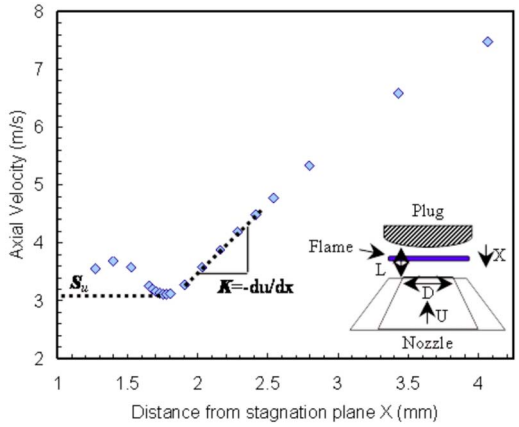

Fig. 3 Measured axial velocity along the stagnation streamline for H_2 with N_2 diluted air (O_2:N_2 1:9) mixture at Φ=0.8 and 700 K preheat temperature (D=9 mm; L=6 mm); figure insert shows a layout of the nozzle generated wall stagnation flame (WSF)

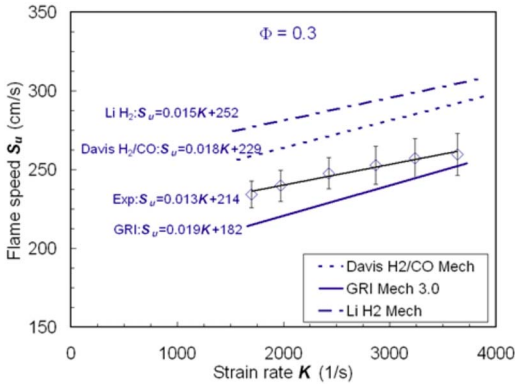

Fig. 4 Strained laminar flame speeds for mixture of H_2 with air at Φ=0.3 and 700 K preheat temperature; data (symbols and linear fits) and OPPDIF predictions (lines)

location is taken as the imposed strain rate (K) (see Fig. 3). The imposed strain rate is controlled by changing the nozzle exit velocity. As the nozzle exit velocity increases, the strain rate increases, and the flame moves closer to the stagnation surface. For each fuel mixture, the strain rates and corresponding strained flame speeds are measured for a range of nozzle exit velocities. The flame speeds were measured across a range of strain rates, with the lowest attained strain rates limited either by flashback or flame stability (unsteadiness). The uncertainty in the strained flame speed measurement can be estimated from the root-mean-square fluctuation of the axial velocity at the location where the average velocity is a minimum. At each location along the stagnation streamline, 10,000 measurements were acquired and the rms fluctuations are 2–4% at the minimum velocity location for the conditions reported here.

Flame Speed Modeling

The experimental results are compared to predictions of a standard (CHEMKIN) 1D flame model. The unstrained laminar flame speeds are calculated with the PREMIX algorithm, while the strained stagnation flames are simulated with OPPDIFF code. In the strained flame simulations, the distance between the nozzle and stagnation plane (L) was matched to the experimental value, since it can have a significant effect on the predicted strained flame speed. The plug flow boundary condition, which is a close representation of the measured nozzle data, is used at the nozzle exit. A detailed numerical analysis on the effect of nozzle exit boundary condition on the predicted flame speed is given in the Appendix. The predicted flame speed and strain rate are determined from the stagnation simulation with the same definitions that were applied to the experimental data (minimum axial velocity for flame speed and maximum preflame axial velocity gradient for strain). In all the flame simulations, the converged solution was obtained for a large number of grid points by considering the gradient and curvature to be 0.1.

Three reaction mechanisms are employed in the simulations: GRI MECH 3.0 [16], a H_2/CO mechanism from Davis et al. [13], and a H_2 mechanism by Li et al. [21]. The GRI mechanism has been tested and validated extensively for methane and natural gas combustion over a wide range of pressure and temperature conditions. It consists of 325 elementary chemical reactions with associated rate coefficients and thermochemical properties for the 53 species involved. The second, more recent mechanism was developed specifically for H_2/CO combustion. It consists of 14 species and 30 reactions, and incorporates recent updates for rate parameters and third body efficiencies of a few key reactions. It also includes modifications of thermodynamic and transport properties for species relevant to high temperature H_2 and CO oxidation. The third mechanism is an updated comprehensive kinetic model for hydrogen combustion. It consists of 19 elementary reactions and 11 species with associated rate coefficients and thermochemical properties. In all the simulations, multicomponent diffusion and Soret effects (thermal diffusion) have been included, as they have significant influence on the calculated flame speeds.

Results and Discussions

The prime objective of this study is to measure the laminar flame speeds and strain sensitivities of lean mixtures of H_2 at elevated preheat temperature and also compare the measurements to model predictions in order to ascertain the validity of the H_2 oxidation mechanism in the current models for syngas combustion. As noted above, the emphasis on lean mixtures is based on the earlier findings that the model predictions showed larger discrepancies for leaner mixtures of H_2/CO fuels with medium and high H_2 content [15]. The effect of N_2 dilution is also considered, as many practical syngas fuels have significant amounts of diluents. For these comparisons, the flame temperatures were maintained at similar values as that of the undiluted mixtures.

Elevated Preheat Temperature Results

H_2 *With Standard Air*. The strained flame speed for highly preheated H_2 air mixtures was measured for very lean conditions. The 6.25 mm diameter burner was used with a stagnation surface spacing of L/D=0.8. The measured strained flame speeds for various strain rates at Φ=0.3 and 700 K preheat temperature are shown in Fig. 4. The measured flame speed increases linearly as the strain rate increases. The unstrained flame speed (S_u^0) can be estimated by linearly extrapolating the measured strained flame speeds to zero strain rate. The mixture Markstein length (L_M) or strain sensitivity, a measure of the sensitivity of the flame speed to strain, is found from the slope of the linear fit, i.e., S_u=S_u^0−$L_M\kappa$, as shown in Fig. 4. The calculated unstrained flame speed and the strain sensitivity with this approach are 214 cm/s and −0.013 cm.

Figure 4 also shows the predicted strained flame speeds from the three models in the same strain rate range as that of the experiments. The H_2/CO and H_2 mechanisms overpredict the measurements by 10% and 16%, respectively, for the investigated strain rate range, while the GRI mechanism predictions fall below the measurements by about 6%. These discrepancies should be compared to the estimated uncertainties in the measurements and modeling. The measurement precision, as indicated by the error bars in Fig. 4, is within ~3% for most of the measurements. As described in the Appendix, uncertainties in the wall and nozzle

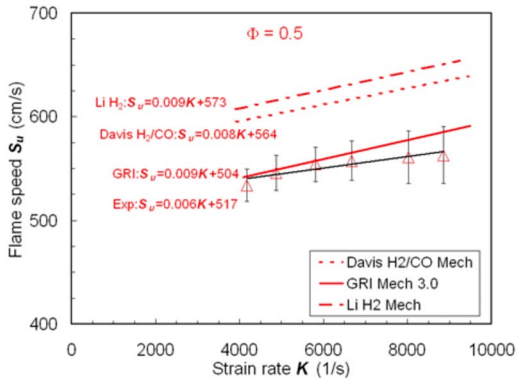

Fig. 5 Strained laminar flame speeds for mixture of H_2 with air at $\Phi=0.5$ and 700 K preheat temperature; data (symbols and linear fits) and OPPDIF predictions (lines)

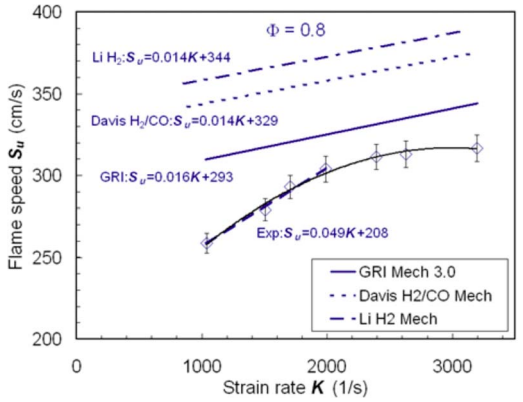

Fig. 6 Strained laminar flame speeds for mixture of H_2 with N_2 diluted air (O_2:N_2 1:9) at $\Phi=0.8$ and 700 K preheat temperature; data (symbols, dashed linear and solid nonlinear fits) and OPPDIF predictions (lines)

boundary conditions between the experiments and the 1D simulations could lower the model results by no more than ~2–3%. Thus the differences between the numerical and experimental results are larger than the combined uncertainty of ~4%. Yet the differences are not too large (mostly within ±10–15%), so it can be concluded that the model predictions are in reasonable agreement with the measurements. The predicted strain sensitivities (slopes in the equations of Fig. 4) from all the models are similar (–0.015 to –0.019 cm), and they are in reasonable agreement with the measured strain sensitivity (–0.013 cm), though somewhat higher (by 15–50%).

The measured and predicted flame speeds for various strain rates at $\Phi=0.5$ are shown in Fig. 5. The linearly extrapolated measured unstrained flame speed is 517 cm/s and the measured strain sensitivity is –0.006 cm. Compared to the $\Phi=0.3$ case, the unstrained flame speed increases and the strain sensitivity decreases as expected for the richer mixture. The decrease in the strain sensitivity is attributed to the decrease in the flame thickness and also the increase in the concentration of the highly diffusive deficient species (H_2) as the equivalence ratio increases. The strained flame speeds predicted by the GRI mechanism are now in excellent agreement with the measurements. As with the leaner mixture, the H_2/CO and H_2 mechanisms overpredict the measured flame speeds, by 12% and 15%, respectively, about the same amounts as in the $\Phi=0.3$ case. The predicted strain sensitivities are even closer to one another in this case (–0.08 cm and –0.09 cm) and are again somewhat higher (by 30–50%) than the measured strain sensitivity (–0.06 cm). Overall the agreement between the measurements and the predictions is good for the lean H_2 mixtures at elevated preheat temperature, with the GRI mechanism appearing to provide results that are in somewhat better agreement than the other two mechanisms. The flame speed results from the H_2 and H_2/CO mechanisms are quite close, though the H_2 mechanism tends to overpredict the measured flame speeds slightly more.

H_2 *With* N_2 *Diluted Air*. In order to investigate the effect of dilution on highly preheated H_2 mixtures, experiments were conducted for pure H_2 fuel with highly N_2 diluted air (O_2:N_2 volume ratio of 1:9). The burner diameter used for this fuel mixture was 9 mm with an L/D of 0.66. The fuel-air ratios are chosen in such a way that the adiabatic flame temperatures are similar as that of the undiluted cases. Figure 6 shows the measured strained flame speeds at $\Phi=0.8$ and 700 K preheat temperature for a range of strain rates. The measured flame speed increases nonlinearly with the imposed strain rate, though the data appear closer to linear at low strain. Also shown in Fig. 6 are the predicted strain flame speeds in the same strain rate range as the measurements. Unlike the measurements, the predicted flame speeds increase linearly with strain rate. All three models overpredict the measured flame speed. As in the undiluted cases, the GRI mechanism results are closest to the measurements, and the H_2 mechanism produces the highest flame speeds. The GRI mechanism results are higher than the measurements by ~20% at lower strains, with the overprediction decreasing to 10% as strain increases. The H_2/CO and H_2 mechanism results are higher than the measurements by 30% and 35%, respectively, at low strain rates, with the discrepancy again decreasing at high strain.

Though the measured flame speeds increase nonlinearly with strain, we can estimate the strain sensitivity by a linear fit to the experimental results in the low strain region (1000–2000 s^{-1}) where the data are close to linear (see Fig. 6). The magnitudes of the strain sensitivities predicted by the models are again similar to one another (0.014 cm and 0.016 cm), but nearly three times lower than the measured sensitivity (0.049 cm). Thus if the results are extrapolated back to zero strain (to produce estimates of the unstrained flame speed), this leads to even larger discrepancies between the extrapolated model values (293–344 cm/s) and the extrapolated measurements (208 cm/s).

Experiments and simulations were also conducted for stoichiometric and rich ($\Phi=1.6$) mixtures of H_2 and N_2 diluted air (Fig. 7). As in the lean case, all three models overpredict the measurements. Now, however, the model results are closer to one another than to the measurements. The GRI mechanism again has the

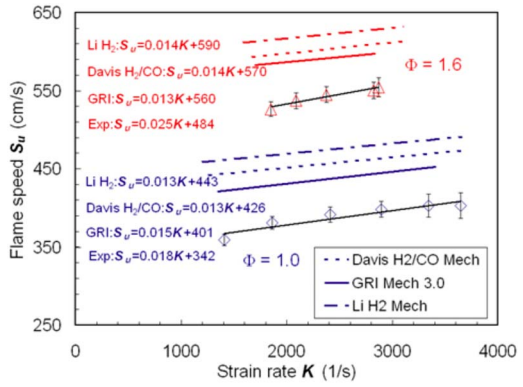

Fig. 7 Strained laminar flame speeds for stoichiometric and rich mixtures of H_2 with N_2 diluted air (O_2:N_2 1:9) at 700 K preheat temperature; data (symbols and linear fit) and OPPDIF predictions (lines)

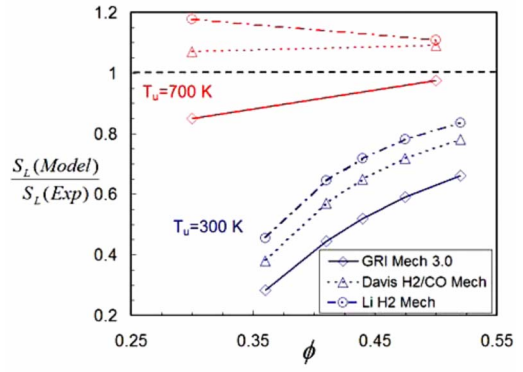

Fig. 8 Ratios of the models predicted (PREMIX) and measured unstrained laminar flame speeds for lean mixtures of H_2 with standard air at 300 K and 700 K preheat temperatures

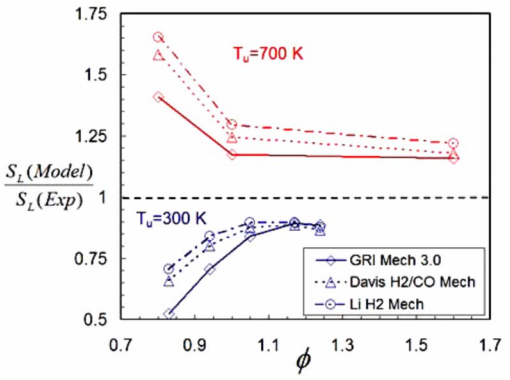

Fig. 9 Ratios of the models predicted (PREMIX) and measured unstrained laminar flame speeds for lean mixtures of H_2 with H_2 with N_2 diluted air at 300 K and 700 K preheat temperatures

smallest amount of overprediction (12% at $\Phi=1.0$ and 10% at $\Phi=1.6$), the H_2 mechanism produces the highest flame speeds (overprediction of 22% at $\Phi=1.0$ and 15% at $\Phi=1.6$), and the H_2/CO mechanism is in between (18% high at $\Phi=1$ and 12% at $\Phi=1.6$).

By comparing the results at $\Phi=0.8$, 1.0, and 1.6 (Figs. 6 and 7), we find that the difference between the model predictions and the measurements increases for the N_2 diluted mixtures as the mixture becomes leaner. This trend is very similar to the results for the 50:50 H_2:CO fuel mixture at elevated preheat temperatures observed in the earlier study [15]. It is also interesting to consider the change in strain sensitivity with equivalence ratio. The magnitude of the measured strain sensitivity decreases from 0.049 cm at $\Phi=0.8$ to 0.018 cm at $\Phi=1.0$, and then increasing to 0.025 cm as the equivalence ratio increases further to 1.6. This behavior is expected and can be explained by the variation of the flame thickness and the concentration of the deficient species (H_2 or O_2 in the fuel lean or rich conditions, respectively) as the equivalence ratio varies. In contrast to the measurements, the strain sensitivities predicted by the models change only slightly despite the significant variation in equivalence ratio.

Overall the results at elevated reactant temperature show that the measured flame speeds and strain sensitivities are in good agreement for undiluted lean H_2 mixtures. On the other hand, the measured flame speeds are overpredicted and the strain sensitivities are underpredicted for the N_2 diluted mixtures, even though the adiabatic flame temperatures are similar for both undiluted and diluted cases.

Comparison With Room Temperature Results

To elucidate the effect of the preheat temperature on these observed discrepancies between the measurements and the models, it is important to consider the models' performance at low preheat temperature. To this end, the predicted unstrained laminar flame speeds (from PREMIX) at room temperature are compared with measured, unstretched laminar flame speeds from Egolfopoulos and Law [22] for essentially the same fuel and oxidizer mixtures and equivalence ratios used in the high preheat results presented above. In their work, the unstretched laminar flame speed is calculated by linear extrapolation of the measured strained flame speeds determined in a counter flow flame (CFF).

H_2 *With Standard Air*. The ratio of the predicted unstrained flame speeds to the measured (linearly extrapolated) values, for all three models, is shown in Fig. 8 for both elevated preheat temperature (700 K) and room temperature reactants (300 K). For the elevated preheat temperature, the models only slightly under- or overpredict the measurements. Hence the predicted/measured flame speed ratio is close to unity. On the other hand, Fig. 8 reveals that all three models significantly underpredict the experimental results for the room temperature reactants. The H_2 mechanism, which was the farthest from the data at high preheat, now produces results that are closest to the measured room temperature flame speeds (15% too low at $\Phi=0.5$). The GRI mechanism, which produced predictions closest to the high temperature flame speeds, has the greatest discrepancy at room temperature, underpredicting the measurements by 35% at $\Phi=0.5$. In addition, the amount of underprediction increases as the mixture becomes leaner for all three models. For example, the H_2/CO mechanism underpredicts the measurements by 20% at $\Phi=0.5$ and 60% as the equivalence ratio decreases to 0.35. Comparing the low and high temperature results, it is evident that the predicted flame speeds increase with preheat temperature faster than the measured values, and the good agreement with the measurements at 700 K is somewhat fortuitous.

It is interesting to note that ignition delay studies have also found that the GRI and H_2/CO mechanisms have difficulty matching experimental results at "low" temperatures for high H_2 content fuels, though they do well at higher temperatures. Specifically the models were found to overpredict the ignition delay at ~900 K for lean, atmospheric pressure syngas fuel mixtures with high H_2 content [23].

H_2 *With* N_2 *Diluted Air*. The ratio of predicted and measured flame speeds for H_2 with N_2 diluted air is shown in Fig. 9. As indicated previously, the models overpredict the measurements for high preheat with the amount of overprediction decreasing as the equivalence ratio increases from 0.8 to 1.6. Like the undiluted results, all the mechanisms underpredict the measurements for room temperature reactants. In addition, the amount of underprediction increases as the mixture moves away from near stoichiometric conditions. For lean mixtures, as opposed to the elevated preheat case, the H_2 mechanism is closest to the measurements (within 10% and 30% at $\Phi=1.0$ and 0.8), and the GRI mechanism results are the farthest (15% and 50% at $\Phi=1.0$ and 0.8). As the mixture becomes fuel rich, all three mechanisms produce essentially the same flame speeds. Comparing the low and high temperature results, we again find that the models predict higher temperature dependence for the flame speed than is found from the measurements.

Summary and Conclusions

The effect of reactant preheating on the laminar flame speeds of H_2 mixed with air and with highly N_2 diluted air has been investigated. Strained laminar flame speeds and strain sensitivities were measured in a wall stagnation flame (WSF) with 700 K preheat temperature. The measurements are compared with numerical predictions based on three leading chemical kinetic mechanisms,

each with its own thermal and transport property database and each optimized for a different fuel system that includes oxyhydrogen reactions. It has been shown that the uncertainty in the experimental boundary conditions, mainly the downstream heat loss from the products to the wall and the velocity boundary condition at the wall, has insignificant effect (less than 3%) on the unburned flame speed and strain sensitivity for typical fuel mixtures and test conditions considered here.

For mixtures of H_2 and standard air, the modeled flame speeds and their sensitivity to strain are in reasonable agreement with the measurements, at least for the lean conditions studied here. However, for mixtures of H_2 and N_2 diluted air, the models overpredict the measured flame speeds and underpredict the strain sensitivities even though the flame temperatures are in the same range as that of the undiluted case. The amount of flame speed overprediction increases as the mixture becomes leaner. Moreover in contrast to the experimental results, all three models predict almost no variation in the strain sensitivity with equivalence ratio. These results for lean H_2 mixtures with N_2 dilution are especially relevant to low emission combustion applications involving syngas fuels that contain significant hydrogen and diluent fractions.

In contrast to the elevated reactant preheat case, comparisons of the model results to previous measurements for room temperature reactants indicate that all the models significantly underpredict the measured H_2 flame speeds for both standard and N_2 diluted air. Also the amount of underprediction is higher for H_2 with standard air than for N_2 diluted air. The model that produces the best results for high preheat temperature (GRIMECH 3.0) has the largest discrepancy at low temperature.

We therefore conclude that the temperature dependence of the hydrogen flame speed as predicted by the models is greater than the actual temperature dependence for both standard and diluted air. Since all three models exhibit this same behavior, it is likely that they share a common cause. The source could be an error in the temperature dependence of one or more reaction rates, or in transport properties; this is currently under investigation.

Acknowledgment

The authors would like to acknowledge the support of Siemens Power Generation (Dr. Scott Martin, contract monitor) under a subcontract from the U.S. Department of Energy.

Appendix

Effect of Wall Boundary Conditions

For all the strained flame speed predictions, the CHEMKIN opposed flow code was used with two premixed flames on either side of the stagnation plane; the simulation is adiabatic. In the experiments, however, a solid wall replaces one of the premixed jets, which makes the system nonadiabatic due to the loss of heat from the product gases to the solid wall. This could potentially reduce the unburned strained flame speeds. Moreover in the opposed flame (CFF) case, the radial velocity gradient at the stagnation plane is finite (due to a slip condition), while for the single-jet case it is zero at the plug wall (due to a no-slip condition). This zero radial velocity gradient changes the strain rate distribution in the product zone, which could change the unburned flame speed. In order to investigate the effects of both heat loss and no-slip condition at the wall, a detailed numerical analysis was conducted on a WSF configuration, and the results were compared with that of the CFF case.

The WSF was simulated with the CHEMKIN opposed flow code, but with modified boundary conditions. For the opposed flow code there are two nozzles separated by distance L. The boundary conditions at each nozzle exit are the same: $T=T_i$, $F=\rho u/2$, $G=\rho v/r$, and for the species, the sum of convection and diffusion is equal to the total inflow mass flux. Here, F and G are the parameters defining axial (u) and radial (v) velocities, respectively, and

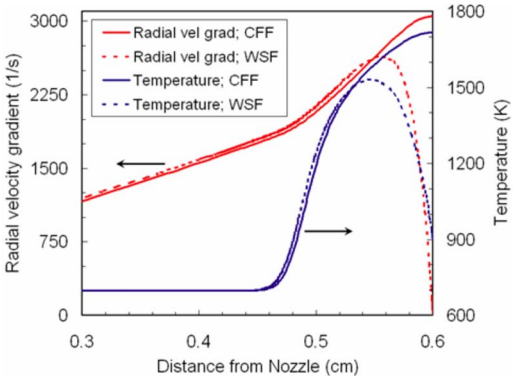

Fig. 10 Numerical simulation of CFF and WSF for H_2 with N_2 diluted air (O_2:N_2 1:9) at $\Phi=0.8$ and 700 K preheat temperature

they are functions of x only. To simulate the WSF, one of the nozzle boundary conditions is changed as follows: the axial velocity is zero ($F=0$), the temperature is $T=T_{wall}$, the radial velocity gradient is zero ($G=0$), and for the species the diffusive velocity is zero. All of these boundary conditions can be applied in the opposed flow code by considering the top nozzle as a solid wall and specifying $u=0$ and $T=T_{wall}$. The other two boundary conditions for the radial velocity gradient and the species are automatically satisfied. The distance between the nozzles has to be reduced from L to $L/2$. Figure 10 shows the variation of the temperature and radial velocity gradient along the axial direction for both CFF and WSF for the same mixture and single-jet flow rate. In this example, $L=0.6$ cm and the axial velocity at the nozzle exit is 1.2 m/s. The temperature of the wall is 900 K (for the WSF).

For both cases, the flame is located ~0.46 cm from the nozzle exit. The temperature for the CFF case increases and reaches a maximum (1717 K) at the stagnation plane. For the WSF case, the temperature rise is nearly identical in the preheat zone, but it reaches a lower maximum (1531 K) somewhere in the reaction zone, afterward decreasing due to heat loss to the wall (and reaching the specified 900 K at the wall stagnation plane). The radial velocity gradient, in a similar fashion to the temperature, increases and reaches maximum at the stagnation plane for the CFF case. For the WSF case, it increases and then decreases to zero at the wall in order to satisfy the no-slip condition at the stagnation plane. Thus there is a significant change in strain rate distribution in the product zone close to the wall. Moreover the WSF is slightly displaced further from the stagnation surface compared to the counterflow (twin flame) case.

Numerical simulations of CFF and WSF were carried out for H_2 with N_2 diluted air (O_2:N_2 1:9) at $\Phi=0.8$ and 700 K preheat temperature. This fuel composition is chosen for detailed investigation because it is expected to be more sensitive to heat loss for two reasons: (1) the flame is located closer to the wall (within about two flame thicknesses) compared to the other cases reported here, and (2) the temperature and velocity rise across the (weaker) flame are smaller. Figure 11 shows the strained flame speed predicted with GRI MECH over a range of strain rates for both the CFF and WSF. For the WSF, simulations were performed for two wall temperatures (900 K and 1700 K). The heat loss will clearly be very small for $T_{wall}=1700$ K, because the temperature at the stagnation plane for the CFF case is nearly of the same value. Hence the effect of no-slip boundary condition at the wall should dominate for this simulation. For the $T_{wall}=900$ K case, however, the amount of heat loss is much greater and hence the effect of both heat loss and no-slip boundary condition can be studied.

The predicted strained flame speeds increase linearly for all three cases over the range of strain rates simulated. Moreover the predicted strain sensitivities are almost the same for all three

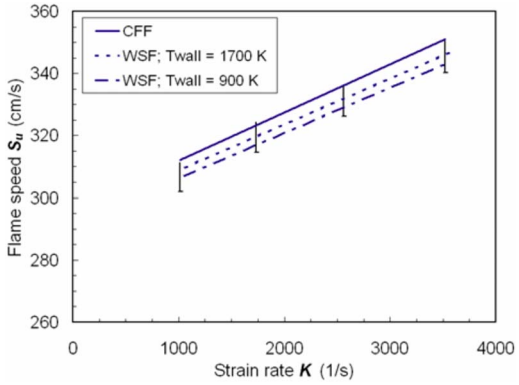

Fig. 11 Model predicted strained flame speeds for CFF and WSF with two different wall temperatures. The fuel mixture is H_2 with N_2 diluted air (O_2:N_2 1:9) at Φ=0.8 and 700 K preheat temperature. The vertical bars indicate 3% deviation from CFF.

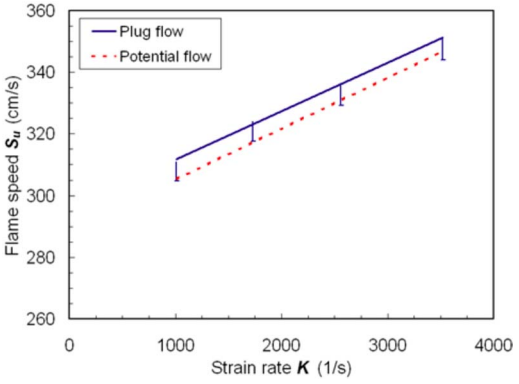

Fig. 13 Model predicted strained flame speeds with plug and potential flow boundary conditions. The vertical bars indicate 2% deviation.

cases. Comparing the strained flame speeds, the WSF predictions are always (slightly) lower than the CFF predictions. The WSF predictions with T_{wall}=1700 K underpredict the CFF by less than 2%. Since the temperatures at the stagnation plane are nearly the same for both cases, the zero radial velocity gradient at the wall is seen to slightly reduce the strained flame speed. When the wall temperature is reduced further, the predicted strained flame speed decreases a bit more. For T_{wall}=900 K, the predicted flame speeds are now below the CFF results by less than 3% throughout the strain rate range tested. Even though the flame (product) temperature is lower for the WSF due to greater downstream heat loss, the unburned strained flame speed is not significantly altered (even when the flame is located within two flame thicknesses from the wall).

Effect of Nozzle Boundary Conditions

The strained flame speeds presented here were calculated using the CHEMKIN opposed flow code with plug flow boundary conditions at the nozzle exit. Since the experiments employed a high contraction ratio nozzle, the nozzle exit flow should be close to plug flow. However, due to nonideal behavior at the nozzle exit (wall boundary layer and pressure gradient induced by the stagnation condition), the exit velocity profile could slightly deviate from the plug flow boundary condition. This could potentially change the minimum axial velocity (identified as the strained flame speed) between the experiments and simulations for the same imposed strain rate (defined as the maximum gradient in the reactants). For large deviations from plug flow, one would expect the inflow boundary condition to approach a potential flow. Therefore, detailed numerical simulations were performed for plug and potential flow boundary conditions for the fuel mixtures and experimental conditions (Φ, L, and strain rates) reported here. Figure 12 shows the variation of the axial velocity for both boundary conditions at identical strain rates. While the flame location for the potential flow is closer to the nozzle than for the plug flow, the minimum velocity before the flame is not affected significantly by the change in boundary condition. The minimum velocity for the potential flow case is 351 cm/s, while it is 345 cm/s for the plug flow boundary condition (less than a 1.5% effect). Similar analyses were performed for a range of strain rates for mixtures of H_2 with N_2 diluted air at Φ=0.8 and 700 K preheat temperature (Fig. 13). The predicted flame speed with potential flow boundary conditions is less than that of the plug flow boundary conditions for all the strain rates, but the difference between the two is within 2%. This indicates that the minimum velocity axial velocity is not very sensitive to the boundary conditions (for the same applied strain rate defined by the maximum velocity gradient ahead of the flame). Hence the small deviations from plug flow that might be expected in the experimental nozzle boundary condition can be neglected (at least for the mixtures tested here).

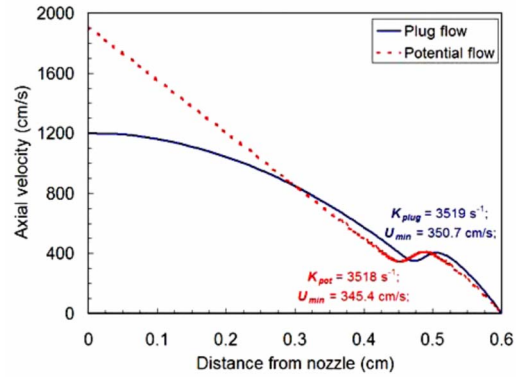

Fig. 12 Numerical simulation of stagnation flame with plug and potential flow boundary conditions for the same strain rates. The fuel mixture is H_2 with N_2 diluted air (O_2:N_2 1:9) at Φ=0.8 and 700 K preheat temperature.

References

[1] Moliere, M., 2002, "Benefiting From the Wide Fuel Capability of Gas Turbines: A Review of Application Opportunities," ASME Paper No. GT-2002-30017.

[2] Klimstra, J., 1986, "Interchangeability of Gaseous Fuels—The Importance of the Wobbe Index," SAE Paper No. 861578.

[3] Scholte, T. G., and Vaags, P. B., 1959, "Burning Velocities of Mixtures of Hydrogen, Carbon Monoxide, and Methane With Air," Combust. Flame, **3**, pp. 511–524.

[4] Günther, R., and Janisch, G., 1971, "Messwerte Der Flammegeschwindigkeit von Gasen Und Gasmischen," Chem.-Ing.-Tech., **43**, pp. 975–978.

[5] Strauss, W. A., and Edse, R., 1958, "Burning Velocity Measurements by the Constant-Pressure Bomb Method," Sym. (Int.) Combust., [Proc.], **7**, pp. 377–385.

[6] Yumlu, V. S., 1967, "Prediction of Burning Velocities of Carbon Monoxide-Hydrogen-Air Flames," Combust. Flame, **11**, pp. 190–194.

[7] Vagelopoulos, C. M., and Egolfopoulos, F. N., 1994, "Laminar Flame Speeds and Extinction Strain Rates of Mixtures of Carbon Monoxide With Hydrogen, Methane, and Air," Sym. (Int.) Combust., [Proc.], **25**, pp. 1317–1323.

[8] McLean, I. C., Smith, D. B., and Taylor, S. C., 1994, "The Use of Carbon Monoxide/Hydrogen Burning Velocities to Examine the Rate of the CO+OH Reaction," Sym. (Int.) Combust., [Proc.], **25**, pp. 749–757.

[9] Brown, M. J., McLean, I. C., Smith, D. B., and Taylor, S. C., 1996, "Markstein Lengths of CO/H_2/Air Flames, Using Expanding Spherical Flames," Sym. (Int.) Combust., [Proc.], **26**, pp. 875–881.

[10] Hassan, M. I., Aung, K. T., and Faeth, G. M., 1996, "Markstein Numbers and Unstretched Laminar Burning Velocities of Wet Carbon Monoxide Flames," 34th Aerospace Sciences Meeting and Exhibit, Reno, NV, Paper No. AIAA 96-0912.

[11] Hassan, M. I., Aung, K. T., and Faeth, G. M., 1997, "Properties of Laminar Premixed CO/H_2/Air Flames at Various Pressures," J. Propul. Power, **13**(2),

pp. 239–245.
[12] Sun, H. Y., Yang, S. I., Jomass, G., and Law, C. K., 2006, "High Pressure Laminar Flame Speeds and Kinetic Modeling of Carbon Monoxide/Hydrogen Combustion," Proc. Combust. Inst., **31**, pp. 439–446.
[13] Davis, S. G., Joshi, A. V., Wang, H., and Egolfopoulos, F. N., 2004, "An Optimized Kinetic Model of H_2/CO Combustion," Proc. Combust. Inst., **30**, pp. 1283–1292.
[14] Li, J., Zhao, Z., Kazakov, A., Chaos, M., Dryer, F. L., and Scire, J. J., Jr, 2007. "A Comprehensive Kinetic Mechanism for CO, CH_2O, and CH_3OH Combustion," Int. J. Chem. Kinet., **39**(3), pp. 109–136.
[15] Natarajan, J., Lieuwen, T., and Seitzman, J., 2007, "Laminar Flame Speeds of H_2/CO Mixtures, Effect of CO_2 Dilution, Preheat Temperature and Pressure," Combust. Flame, **151**, pp. 104–119.
[16] Smith, G. P., Golden, D. M., Frenklach, M., Moriarty, N. W., Eiteneer, B., Goldenberg, M., Bowman, C. T., Hanson, R. K., Song, S., Jr., Gardiner, W. C., Lissianski, V. V., and Qin, Z., http://www.me.berkeley.edu/gri_mech/
[17] Wu, C. K., and Law, C. K., 1984, "On the Determination of Laminar Flame Speeds From Stretched Flames," Sym. (Int.) Combust., [Proc.], **20**, pp. 1941–1949.
[18] Vagelopoulos, C. M., Egolfopoulos, F. N., and Law, C. K., 1994, "Further Considerations on the Determination of Laminar Flame Speeds With the Counterflow Twin-Flame Technique," Sym. (Int.) Combust., [Proc.], **25**, pp. 1341–1347.
[19] Egolfopoulos, F. N., Zhang, H., and Zhang, Z., 1997, "Wall Effects on the Propagation and Extinction of Steady, Strained, Laminar Premixed Flames," Combust. Flame, **109**, pp. 237–252.
[20] Andac, M. G., Egolfopoulos, F. N., and Campbell, C. S., 2002, "Premixed Flame Extinction by Inert Particles in Normal and Micro-Gravity," Combust. Flame, **129**, pp. 179–191.
[21] Li, J., Zhao, Z., Kazakov, A., and Dryer, F. L., 2004, "An Updated Comprehensive Kinetic Model of Hydrogen Combustion" Int. J. Chem. Kinet., **36**, pp. 566–575.
[22] Egolfopoulos, F. N., and Law, C. K., 1990, "An Experimental and Computational Study of the Burning Rates of Ultra-Lean to Moderately-Rich $H_2/O_2/N_2$ Laminar Flames With Pressure Variation" Sym. (Int.) Combust., [Proc.], **23**, pp. 333–340.
[23] Kalitan, D. M., and Peterson, E. L., 2005, "Ignition and Oxidation of Lean CO/H_2 Fuel Blends in Air," 41st AIAA/ASME/SAE/ASEE Joint Propulsion Conference and Exhibit, Tucson, AZ.

A Real-World Application of Fuzzy Logic and Influence Coefficients for Gas Turbine Performance Diagnostics

Richard W. Eustace
Defence Science and Technology Organisation,
506 Lorimer Street,
Fishermens Bend, Victoria 3207, Australia
e-mail: richard.eustace@dsto.defence.gov.au

This paper presents an example of the use of fuzzy logic combined with influence coefficients applied to engine test-cell data to diagnose gas-path related performance faults. The approach utilizes influence coefficients, which describe the changes in measurable parameters due to changes in component condition such as compressor efficiency. Such approaches usually have the disadvantages of attributing measurement noise or sensor errors to changes in engine condition and do not have the ability to diagnose more faults than the number of measurement parameters that exist. These disadvantages usually make such methods impractical for anything but simulated data without measurement noise or errors. However, in this example, the influence coefficients are used in an iterative approach, in combination with fuzzy logic, to overcome these obstacles. The method is demonstrated using eight examples from real-world test-cell data.
[DOI: 10.1115/1.2940989]

1 Introduction

The goal of gas-path diagnostics is to identify the health of the engine modules, such as the individual compressors and turbines, from the measurement of engine performance parameters. An accurate diagnosis enables the most time and cost effective maintenance to be performed. Well known historical methods for such an approach utilized weighted-least-squares concepts, based on Kalman filters [1–3]. While methods using these approaches have had some success 4, new methods are being sought to improve the state of the art. These new methods include the use of neural networks and empirical models either in isolation or as adjuncts to the Kalman filter [5–8]. Modifications of the Kalman approach itself are also offered as solutions [9].

These Kalman filter approaches rely on the use of influence coefficients that provide a relationship between changes in engine component health, such as efficiency, and corresponding changes in measured engine parameters, such as spool speed. In this paper, a modification to the use of influence coefficients is presented. The application described here involves the use of fuzzy logic to analyze solutions found using such influence coefficients. This linear method is not intended for modern engines that have features such as variable stator vanes or active clearance control, which make engine performance behavior nonlinear [10]. Instead, the method is presented as a practical approach to provide a beneficial diagnostic capability to the user for an in-service engine with relatively simple technology.

2 TF30 Engine Maintenance

The TF30 engine, for which the diagnostic method in this paper is applied to, is operated by the RAAF in the F-111 aircraft. The engine is a low bypass turbofan, with a mixed flow exhaust. The low pressure spool features a three stage fan and an LPC (Stages 4–9), both driven by the three stage LPT. The HPC is comprised of Stages 10–16 and is driven by a single stage turbine (Fig. 1).

Contributed by the International Gas Turbine Institute of ASME for publication in the JOURNAL OF ENGINEERING FOR GAS TURBINES AND POWER. Manuscript received May 2, 2007; final manuscript received January 6, 2008; published online August 26, 2008. Review conducted by Dilip R. Ballal. Paper presented at the ASME Turbo Expo 2007: Land, Sea and Air (GT2007), Montreal, QC, Canada, May 14–17, 2007.

In the early 1990s, personnels involved with the TF30 engine maintenance decided to move toward a condition based approach to reduce the costs and increase engine availability compared with a strict fixed interval approach. Figure 1 shows some of the costs associated with typical repairs to the various modules of the TF30 engine. The values in this figure represent either an opportunity to reduce costs and time if the diagnosis is correct or a penalty if the diagnosis is wrong. Such information can be very important when trying to measure the benefit of a diagnostic approach [11]. Since the engine predates modular design, the values for repair to the LPC and HPC modules are much higher than for the other modules.

3 TF30 Engine Performance Diagnostics

In general, decisions about engine maintenance are avoided on the basis of a single CM technique. Similarly, a number of engine performance diagnostic approaches are used in an attempt to improve the engine performance diagnosis reliability. Three diagnostic approaches have been developed by DSTO for the TF30 engine to make use of a wide variety of diagnostic information to improve the reliability of the final diagnosis.

The first of these three methods involves the use of an adaptive component-based thermodynamic cycle deck [12]. This method can identify 11 faults using 12 measurands. However, the adaptive model is slow to use with a simulation taking in the order of 5 min (using a Pentium 2.8 GHz Duo core). The second method [13] involves a probabilistic neural network that compares the performance loss observed in the engine that has been removed for repair to the performance loss observed in previous engines prior to their repair. This method is also used by a commercial diagnostic tool [14]. The approach attempts to capture and utilize a knowledge base that would exceed that which a human test-cell operator may gain over many years of engine testing. This paper describes a third method that utilizes influence coefficients provided by the OEM for the TF30 engine. Compared with the adaptive model, the method presented here obtains a diagnosis within the order of 10 seconds.

4 Influence Coefficients

Influence coefficients describe the change in a measurable engine parameter, such as N2 spool speed, due to a change in engine

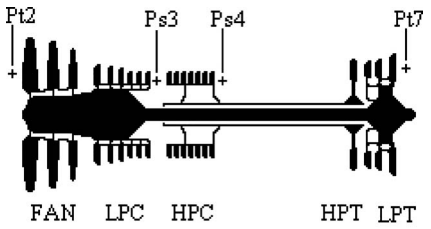

Module	Cost	Time
FAN	20 ~ 30 $k	2 weeks
LPT, HPT	50 ~ 100 $k	4 weeks
LPC, HPC	300 + $k	3 months

Fig. 1 Engine configuration and maintenance costs and times

Table 1 Example of influence coefficients

Fault	ΔN1 (rpm)	ΔN2 (rpm)	ΔTIT (°F)	ΔPs3/Pt2%	ΔPs4/Pt2%
Fault A	98	55	20	0.8	1.0
Fault B	−9	−121	−3	1.8	−0.1

Fault A: 1% reduction in efficiency of module *X*
Fault B: 1% reduction in mass flow of module *Y*

condition, such as a reduction in HPC efficiency. Influence coefficients for two nominal faults are presented in Table 1.

These coefficients indicate that a 1% reduction in the efficiency of a particular module, such as the fan, will increase N1 speed of 98 rpm, increase N2 speed of 55 rpm, etc. However, since multiple faults may exist at different severities to those tabulated for the influence coefficients, a mathematical method is required to enable such information to be efficiently utilized. Hence, a method is presented in this paper that utilizes the influence coefficients to identify the faults that will explain the performance change that have been observed in a specific engine that is about to undergo repair. The method is particularly suited to the situation where the number of possible faults exceeds the number of performance measurements.

5 Autostack Approach

The diagnostic program presented here is known as "AutoStack" since it automatically selects faults at particular severities so that when combined together (or "stacked") the total effect of all the faults is as close as possible to the measured performance degradation observed in the engine being diagnosed.

This section gives a brief overview of the AutoStack method, before the important features are described in more details later in this paper. The method uses an iterative approach, as indicated in Fig. 2 by the bold lines. Within each iteration, the method uses a least-squares algorithm to adjust the severity of many different combinations of faults in an attempt to explain the performance shift of five key engine parameters. Fuzzy logic is then used to examine the many solutions and identify trends across them,

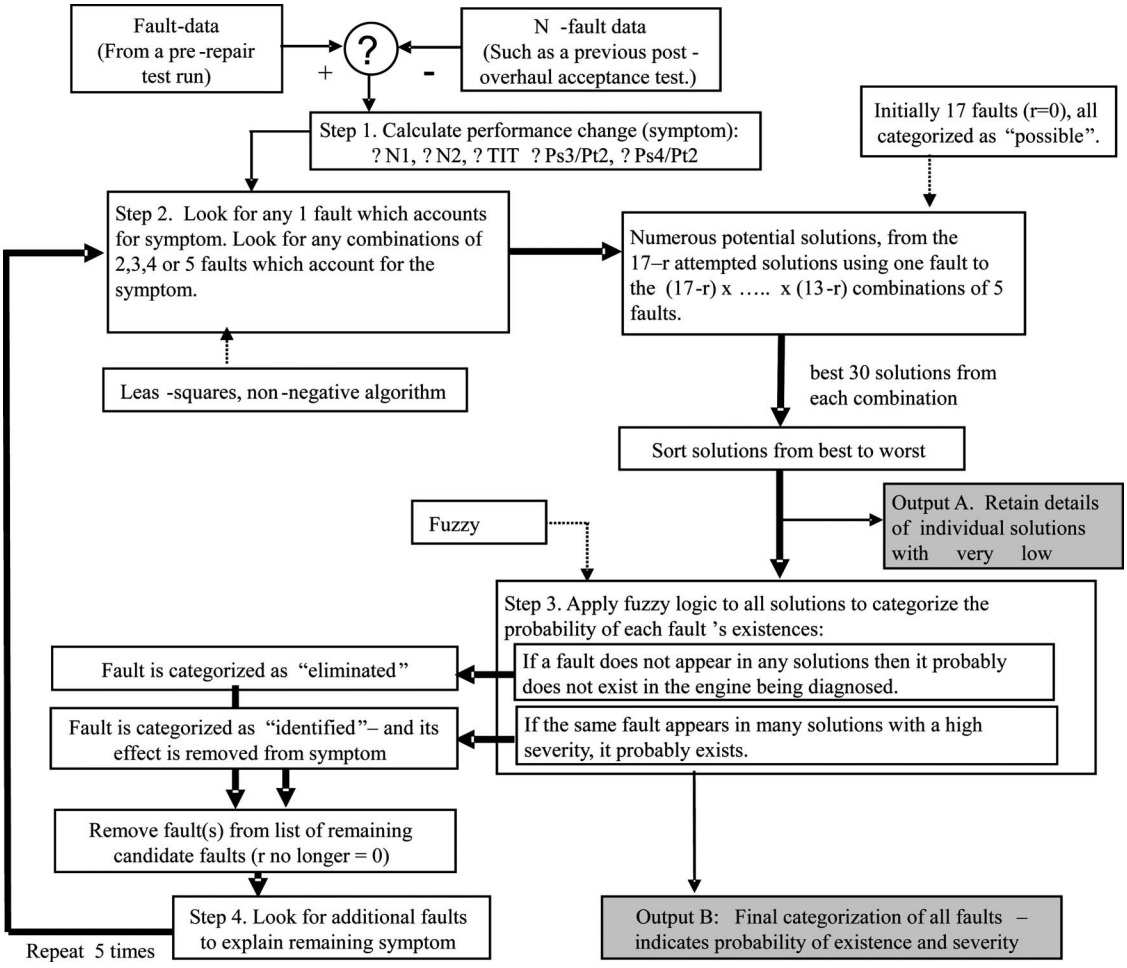

Fig. 2 Schematic of the AutoStack diagnostic process

rather than focusing on any individual solution. If a fault is used in many solutions, the fuzzy logic recognizes this fault as existing in the engine. The effects of these faults are then removed from the performance change or loss observed in the engine, and the subsequent loops of the iteration process attempt to identify the faults causing the remaining performance change.

6 Performance Symptom

The first step of the process is to calculate the change in engine performance, or symptom, that has occurred due to the degradation of the engine while it has been in service (Fig. 2, Step 1). When TF30 engines are removed from an aircraft for maintenance, the engines are run in the test cell prior to maintenance, unless their condition prevents this, such as due to excessive FOD. This increases the ability to identify multiple faults within the engine, in comparison to often a single known fault, which is the reason for engine removal, so that while the engine is stripped for repair other faults can be simultaneously repaired. This helps avoid the situation of faults being found during the postrepair acceptance test, which may either cause the engine to fail the test and require a second repair or shorten the time on wing that the engine is likely to achieve before requiring removal again. These prerepair fault data are compared with previous no-fault data from the same engine, such as data from an acceptance test conducted after a previous overhaul, or other data for which the gas-path condition was considered to be in a reasonable state of health.

The engine's performance symptom is calculated by subtracting the no-fault data from the fault data, such that an increase in a parameter with the passage of time, such as spool speed, will give a positive delta. The fault and no-fault data are recorded at Military PLA and corrected to standard day conditions. However, an additional adjustment is made to correct the data to a standard engine pressure ratio (EPR) value. The use of a standard EPR value gives the data a more consistent performance base line than data purely recorded at the same power lever setting.

For the AutoStack method, the symptom consists of changes in five parameters, these being N1, N2, TIT, Ps3/Pt2 (pressure ratio over the fan and LPC combination), and Ps4/Pt2 (pressure ratio over the fan, LPC and HPC combination). The choice of these parameters for the symptom is largely due to the fact that these are the parameters for which the influence coefficients were available. Fuel flow (WF) could have been utilized; however, while the test-cell WF meter is very accurate, the characteristics of the engine's operation are such that the WF value needs to be recorded over a long period of time (in the order of a minute or more) before a stable value is achieved. Since the diagnostic approach proposed here uses data recorded in normal day-to-day test-cell operation, as compared to during test-cell calibration or correlation exercises, such a long recording time is not practical.

The engine data are recorded by a PC-based data acquisition system that is standard fitment for the test cells [12].

7 Least-Squares Non-Negative Algorithm

The performance symptom, calculated above, is then used in a non-negative least-squares algorithm[1] (Fig. 2, Step 2) to identify which faults, and at what severities, can be combined to best account for the observed change in performance of the engine. The method has 17 faults that can be used to explain the performance change observed (Table 2). A non-negative form of the least-squares algorithm is used to restrict the fault severities to be one sided to match the expected practical behavior. For example, efficiencies and mass flows of the compressors and efficiencies of the turbines are only allowed to decrease, while turbine NGV areas and bleed leaks are only allowed to increase. Physical interference of the exhaust nozzle flaps effectively prevents decreases in the exhaust nozzle minimum area.

[1]This is implemented via the standard MATLAB "lsqnonneg" function.

Table 2 Fault list

No.	Fault
1	Fan—efficiency reduction
2	Fan—mass flow reduction
3	LPC—efficiency reduction
4	LPC—mass flow reduction
5	HPC—efficiency reduction
6	HPC—mass flow reduction
7	HPT—efficiency reduction
8	LPT—efficiency reduction
9	HPT NGV area increase
10	LPT NGV area increase
11	Exhaust nozzle area increase
12	Burner pressure loss
13	Anti-ice bleed leak
14	LPC seventh stage bleed leak
15	HPC 12th stage bleed leak
16	HPC 16th stage bleed leak to fan duct
17	HPC 16th stage bleed leak overboard

8 Parsimonious Approach

Within the inner loop of the process, the approach seeks to identify how well any single fault can account for the performance symptom, and how well any combination of two, three, four, or five faults can account for the symptom. The traditional approach to this problem would be to only seek combinations of five faults to explain the performance change that has occurred in the five engine parameters. This relies on the fact that if fewer than five faults can obtain a solution, the process should produce solutions where some faults have a zero level of severity. While this is true, trial and error has found that explicitly seeking solutions with fewer faults provides a larger number of solutions that have low error, and these extra solutions enable the fuzzy logic to make a better summary of the general diagnosis. In contrast, the traditional approach only identifies the solutions with zero error. The use of fewer than five faults is known as the parsimonious approach, which means that "no more faults than are necessary" to explain the performance change should be sought.

9 Fuzzy Logic

Fuzzy logic is used within each loop to analyze the solutions of the least-squares algorithm and use this information to sort the faults into heuristic categories describing the probability of their existence (Fig. 2, Step 3). The membership function for these categories is shown in Fig. 3, and their interpretation is given in Table 3.

In the first loop, all faults are initially classified as "possible," and the fuzzy logic then sorts them during each subsequent loop using the fault's current categorization, and two statistics calculated from the potential solutions to obtain the fault's new categorization. The fuzzy logic rules used to categorize the faults are shown in the Appendix. The first statistic these rules use is the number of potential solutions, which feature each fault known as

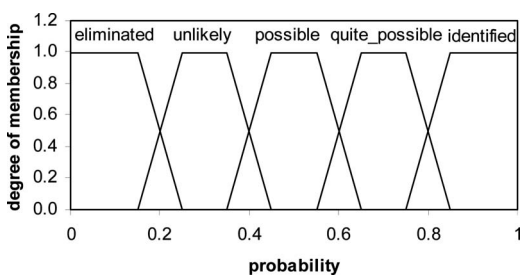

Fig. 3 Membership function for fault probability categories

Table 3 Fault categories and interpretation

Category	Interpretation
Identified	The diagnosis has a high confidence that this fault exists; the symptom cannot be explained without the presence of this fault.
Quite possible	The chance of this fault occurring is greater than 60%, but there is a small chance that it does not exist.
Possible	It is possible for this fault to exist in this engine, but there is an equal chance that it does not exist.
Unlikely	This fault is unlikely to be causing part of the given symptom; there is only a small chance of it occurring.
Eliminated	This fault is very unlikely to be part of the given symptom; it has been eliminated from occurring in this engine.

the "count." The second statistic is the average severity at which each fault occurs in these potential solutions, or the "fault severity." Both the count and fault severity can be low, medium, or high, and these classes are defined by their respective membership functions (Figs. 4 and 5).

If a fault is categorized as "eliminated," then it is removed from the list of faults available to explain the performance change. If a fault is categorized as "identified," it is also removed from the list of faults available to explain the performance change, but, in addition, its effect at its nominated severity is removed from the symptom, such that in the next iteration the process seeks the additional faults that account for the remaining portion of the symptom (Fig. 2, Step 4).

The benefit of the iterative nature of the process is to enable the faults to be categorized gradually. Since in the first loop, all faults are classified as possible, only the first nine rules (Appendix) will apply in the first loop. This small number of rules results in some faults initially being classified identically. However the subsequent iterations, which utilize all the rules, will apply a finer degree of categorization.

10 Validation Examples

The section below illustrates the AutoStack approach by using an example explained in detail. Final results are then provided for additional validation examples. These examples (Table 4) are engines in which a particular fault was clearly identified during the course of the repair. The performance data associated with these repairs have then been retained to form real-world validation cases for testing diagnostic processes.

Table 4 Validation cases for the diagnostic process

Case	Description of known fault
Case 1: Increased exhaust nozzle area Engine Serial No. 8841	One of the actuators on the exhaust nozzle was found to be limited in its travel, causing two nozzle segments to not close properly, thereby increasing the minimum nozzle area by approximately 1.5%.
Case 2: LPT untwist. Engine Serial No. 8946	During a hot-end repair of this engine, every turbine blade in the second and third stages of the LPT turbine blade failed a shroud rotation check due to untwisting of the blade. The level of untwist was considered excessive as the measured values were between four to five times greater than the allowed limits.
Case 3: HPC bleed leak Engine Serial No. 8945	During an engine run, one of the 12th stage bleed valves became unscrewed and was dislodged from the engine. There are eight bleed valves, hence 1/8th of the 12th stage bleed flow was lost.
Case 4: LPC bleed open Engine Serial No. 6627	This is an artificial example created by manually operating the bleed switch to fully open the seventh stage bleed system while the engine was at military power.
Case 5: LPT repair Engine Serial No. 9047	This engine underwent a LPT repair 680 h after being overhauled. The repair was 114 h early as an internal oil leak required repair. Hence, the LPT had accumulated a large portion of its expected service life and so would be likely to show some degradation.
Case 6: LPC Bleed leak	This engine featured an incorrect adjustment of the solenoid that activates the seventh stage (LPC) bleed system, resulting in a leak of mass flow from the LPC.
Case 7: HPT NGV erosion Engine Serial No. 6611	Borescope (RVI) inspection revealed a streaking fuel nozzle had caused total erosion of one HPT NGV, and partial erosion of the two adjacent vanes, out of the set of 40 NGVs. The other LPT and HPT parts should be in reasonable condition since a hot-end service had occurred 200 h prior.
Case 8: PCP/Ps4 ratio Engine Serial No. 4017	This engine featured a ratio between the turbine cooling air pressure (PCP) and the Ps4 pressure (its source), of 0.73, compared to the limits of 0.63–0.70. It was found that this was due to an assembly error in the turbine module involving components, which control the volume of the turbine cooling air.

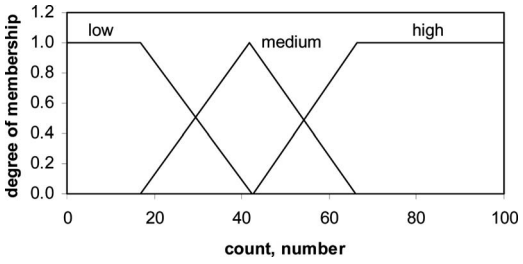

Fig. 4 Membership function for fault count

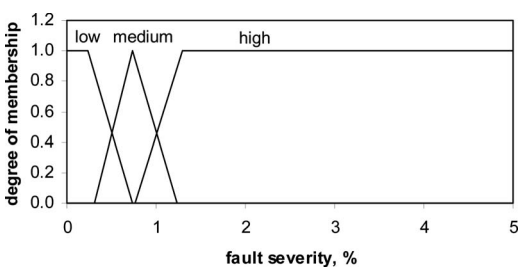

Fig. 5 Membership function for fault severity

However, prior to using these examples in the method and presenting the results, some analysis of these examples is required. In particular, it is useful to investigate how "large" the faults in these examples are expected to be since large faults should be easier to detect than much smaller faults.

The faults can only be observed via the engine's performance change or symptom. A useful metric against which to measure the size of this performance change, to identify how large or small it is, is the engine-to-engine performance variation that naturally occurs within the fleet of healthy in-service engines.

Figure 6 shows the engine-to-engine variation of the five parameters used in the AutoStack diagnostic method. The variation shown is the standard deviation of the parameter at a fixed value of EPR. (This variation is approximately half the variation that occurs at a specific PLA.) Since all parameters have different units, the standard deviations have been expressed as a percentage of their nominal value. These data have been calculated from 186 performance records from 56 individual TF30 engines.

Figure 6 also shows how the performance change for Case 1, an increased exhaust nozzle area, compares to the engine-to-engine variation. As can be seen, the symptom is larger than the engine-to-engine variation for every parameter. The performance change

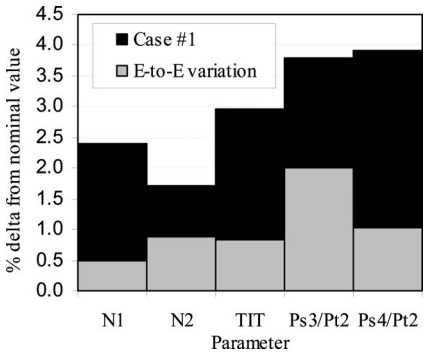

Fig. 6 Standard deviation of the engine-to-engine parameter variation compared to the performance change for Case 1

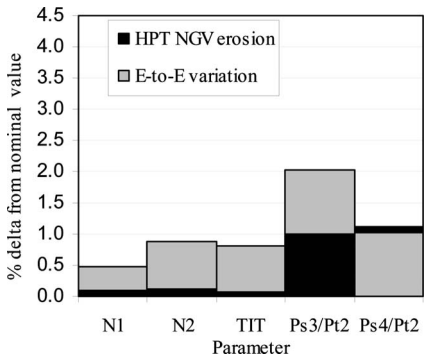

Fig. 8 Symptom of Case 7 (HPT NGV erosion) compared to engine-to-engine variation

due to the fault varies from almost four times larger than the engine-to-engine variation (for Ps4/Pt2), to just less than two times as large (for N2).

In order to classify the size of these performance changes, or symptoms, the guidelines in Table 5 have been developed. Using these criteria, the performance change for Case 1 is described as large.

As another example, Fig. 7 shows the symptom for Case 2 (LPT untwist) compared with the engine-to-engine variation. Only the change in TIT is greater than 1σ of the engine-to-engine variation. This performance change is considered medium, as the change in TIT is about twice the engine-to-engine variation.

Figure 8 shows the performance change in Case 7, which is described as small. The classification of all the cases is shown in Table 6. The validation examples contain a good range of faults, from those that are very large and should be clearly detected to those which are very small and will be a challenge to find.

11 Example 1: LPT Untwist (Case 2)

This example illustrates the method, giving insight into how the process obtains the final results. As previously stated, the fault for this example involved an excessive degree of untwist of the LPT turbine blades. For this engine, a test-cell file recorded almost two years prior was utilized as the no-fault data. Alternatively, average postoverhaul data could be utilized. The results vary little depending on which file is used for the no-fault data set.

The performance symptom (or change) calculated for this engine (Fig. 2 step 1) is as follows.

- N1 has decreased to 21 rpm.
- N2 has increased to 88 rpm.
- TIT has increased to 39°F.
- Ps3/Pt2 has decreased to 0.8%.
- Ps4/Pt2 has decreased to 0.1%.

When this symptom is inputted into the first iteration of the AutoStack process, with all 17 faults categorized as possible, three solutions are found that met the minimum remaining error tolerance. Each of these three solutions comes from using a different number of faults to explain the performance change. The three solutions found at this stage are solutions in Columns 9 (three faults), 4 (four faults), and 1 (five faults), as shown in Table 7.

When all the partial solutions using the 17 individual faults, and the 30 best solutions from using the combinations of two, three, four, and five faults are analyzed by the fuzzy logic, it eliminates three faults.

In the second iteration of the process, no additional solutions are found. However further sorting of faults into the various categories will occur in this second loop, since the fuzzy logic Rules 10–29 will be activated, as all the faults are no longer classified possible. In this example, the fuzzy logic now categorizes the LPT NGV area fault as identified at a severity of 0.958. Hence, the diagnostic process removes the effect of this fault at that severity, from the original symptom, by utilizing the influence coefficients. This results in a remaining unexplained symptom of the following:

- N1 decrease of 3 rpm
- N2 decrease of 15 rpm
- TIT increase of 32°F
- Ps3/Pt2 increase of 1.3%
- Ps4/Pt2 increase of 0.2%

Table 5 Criteria for describing the size of the performance changes

Description	Criteria
Very large	At least one parameter $\geq 5 \times e\text{-}e$
Large	At least one parameter $\geq 3.5 \times e\text{-}e$
Medium	At least one parameter $\geq 2 \times e\text{-}e$
Small	At least one parameter $\approx e\text{-}e$
Very small	All parameters $< e\text{-}e$

e-e: 1σ of the engine-to-engine parameter variation

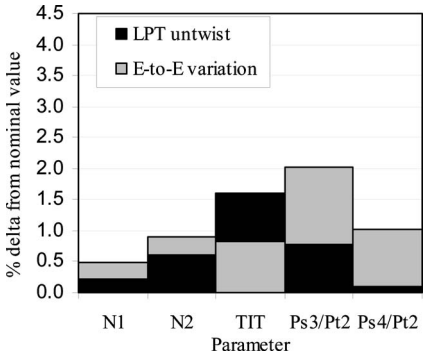

Fig. 7 Symptom of Case 2 (LPT untwist) compared to engine-to-engine variation

Table 6 Classification of validation examples

Description	For current examples
Very large	LPC bleed open (4)
Large	LPC bleed leak (6), Exhaust nozzle area (1)
Medium	LPT untwist (2)
Small	HPC bleed leak (3), LPT repair (5), HPT NGV erosion (7)
Very small	PCP/Ps4 ratio (8)

Table 7 Detailed results for Case 2, LPT untwist

	Fault	Probability	Severity	1	2	3	4	5	6	7	8	9
1	Fan η	0.25	0.41	0	0.442	0	0.787	0	0	0.793	0	0.940
2	Fan mf	0.29	0.33	0	0	0.265	0	0.377	0.294	0	0	0
3	LPC η	0.20	0.47	0	0	0.772	0	0.391	0	0	0	0
4	LPC mf	0.34	0.55	0	0.749	0.085	0	0	0	0	0	0
5	HPC η	0.62	0.30	0	0.317	0.492	0	0.593	0.406	0.594	0.204	0
6	HPC mf	0.49	0.27	0.363	0.275	0	0.292	0	0.278	0	0.144	0.288
7	HPT η	0.13	0.28	0	0	0	0	0	0	0	0	0
8	LPT η	0.70	0.97	0	0	0	1.255	0.646	0	0.692	0	1.390
9	HPT NGV area	0.49	0.56	0	0.067	0	0	0	0	0	0	0
10	LPT NGV area	0.89	0.96	0.646	0.958	0.958	0	0.958	0.958	0.958	0.958	0
11	Ex noz area inc.	0.32	0.43	0	0	0	0	0	0	0	0	0
12	Burner p loss	0.88	0.77	0.876	0.769	0.314	0	0	0.769	0	0.769	0
13	AI bleed leak	0.08	0.16	0	0	0	0	0	0	0	0	0
14	LPC bleed leak	0.34	0.54	0.403	0	0	0	0	0	0	0	0
15	12th bleed leak	0.32	0.78	0	0	0	0	0	0.996	0	0	0
16	16th bleed to FD	0.11	0.33	0	0	0	0	0	0	0	0	0
17	16th bleed to OB	0.40	0.77	1.108	0	0	0.244	0	0	0	1.211	0
			Error	0.000	0.000	0.000	0.002	0.003	0.003	0.037	0.064	0.070

This remaining symptom is now fed into the third iteration of the process, with 13 faults remaining available to explain this performance loss, since three faults were eliminated and one fault identified from the original 17 faults. In the third iteration of the process, a further three new solutions, which met the minimum error, are found. Since the LPT NGV area fault has been identified at the severity of 0.958, this fault is now part of every solution given, as it is required to explain a portion of the total symptom. The three additional solutions found in this second loop are 7, 5, and 3 (Table 7). For this example, no further faults are identified or eliminated in the third iteration.

In the fourth iteration, no new solutions are found but the fuzzy logic classifies a second fault as identified, being a burner pressure loss at a severity of 0.769. Again, the effect of this fault is removed from the remaining unexplained symptom, which is then fed into the fifth iteration.

In this last iteration, three new solutions are found (8, 6, and 2). The detailed results achieved after the last iteration are shown in Table 7, and are an accumulation of results from two parts of the process. The solutions numbered 1–9 have come from Output A, within Fig. 2, while the probability and fault severity columns have come from the fuzzy logic summarization, identified as Output B. While the user has access to the details of the individual solutions, the probabilities and severities are the key information that is presented to the user, as this is a summary of the diagnostic trends that have been found after examining all the solutions, rather than just selecting a single solution and providing that as the final or only answer to the user. The summary of this information, as presented to the user, is shown in Table 8, where the faults are in order of decreasing probability.

The diagnosis in Table 8 has identified the correct fault, although it has also identified a second fault, which on a black-and-white level is incorrect, but in reality is not unrelated to the primary fault.

This example demonstrates the benefits of the fuzzy logic approach. Solutions 1, 2, and 3 are three solutions with zero error, such as those obtained with traditional diagnostic approaches using influence coefficients. However, these three solutions all utilize a number of faults at significant severities. An examination of them does not easily lead the user to the conclusion that an increased LPT NGV area is the primary fault. In comparison, the fuzzy logic examines trends across a large range of solutions, and is able to summarize these in a deterministic and repeatable fashion.

12 Results for Additional Examples

Table 9 provides the final results for the additional validation cases itemized in Table 4 (with the exception of Case 6 for which the results have been presented in Table 8.). These results show, for each case, all the faults that achieved a category of possible or above. Hence, only the unlikely and eliminated faults are not shown.

As can be seen in virtually every example, the diagnostic method has correctly identified the known fault. Case 3 for the HPC bleed leak had a performance change that was "small" and is arguably the only example, which has returned a diagnosis that does not clearly and unambiguously identify the known fault.

The method could also not identify any fault with Case 8. However, this fault had a very small performance effect on the parameters used for diagnosis. In this example, one parameter (N2) had a performance change equal to only half the σ of the engine-to-engine variation for N2, and two parameters were in the order of one-fifth of the σ of the engine-to-engine variation for their respective parameters. The remaining two parameters displayed no change. Hence, this nonresult is understandable. The good news

Table 8 Summary of results for Case 2, LPT untwist

Fault	Severity	Probability	Category
LPT NGV area	+1.0%	89%	Identified
Burner p loss	+0.8%	88%	Identified
LPT η	−1.0%	70%	Quite possible
HPC η	−0.3%	62%	Quite possible
HPC mf	−0.3%	49%	Possible
HPT NGV area	+0.6%	49%	Possible
16th bleed to OB	+0.8%	40%	Possible
LPC mf	−0.6%	34%	Unlikely
LPC bleed leak	+0.5%	34%	Unlikely
Ex noz area inc.	+0.4%	32%	Unlikely
12th bleed leak	+0.8%	32%	Unlikely
Fan mf	−0.3%	29%	Unlikely
Fan η	−0.4%	25%	Unlikely
LPC η	−0.5%	20%	Unlikely
HPT η	−0.3%	13%	Eliminated
16th bleed to FD	+0.3%	11%	Eliminated
AI bleed leak	+0.2%	8%	Eliminated

Table 9 Diagnostic results for additional examples

Case 4: Seventh bleed open–very large			
Fault	Severity	Probability	Category
LPC bleed leak[a]	+6.3%	90%	Identified
Fan mf	−0.7%	86%	Identified
AI bleed leak	+0.2%	64%	Quite possible
12th bleed leak	+0.7%	51%	Possible
HPT NGV Area	+0.3%	49%	Possible
16th bleed to OB	+0.4%	42%	Possible
Ex. noz area inc.	+0.2%	41%	Possible
Case 1: Increased exhaust nozzle area—large			
Fault	Severity	Probability	Category
Ex. noz area inc.[a]	+2.8%	90%	Identified
HPC mf	−1.0%	89%	Identified
LPT NGV area	+0.7%	67%	Quite possible
LPT η	+0.6%	44%	Possible
Case 6: LPC bleed leak—large			
Fault	Severity	Probability	Category
LPC bleed leak[a]	+4.7%	90%	Identified
Burner p loss	+0.3%	70%	Quite possible
Fan mf	−0.1%	41%	Possible
Case 5: LPT repair—small			
Fault	Severity	Probability	Category
LPT NGV area[a]	+0.7%	87%	Identified
Case 3: HPC bleed leak—small			
Fault	Severity	Probability	Category
HPT NGV area	+0.4%	69%	Quite possible
HPC mf[a]	+0.3%	50%	Possible
LPT NGV area	+0.9%	41%	Possible
Case 7: HPT erosion—small			
Fault	Severity	Probability	Category
HPT NGV area[a]	+1.3%	89%	Identified
Case 8: PCP/Ps4 ratio—very small			
Fault	Severity	Probability	Category
All faults eliminated			

[a]Correct fault.

Table 10 Results for simulated faults

Actual faults[a]		Diagnostic results[b]		
Fault	Severity, %	Severity, %	Probability %	Category
Example 1: HPT only fault				
HPT η	−2.0	−2.0	90	Identified
HPT NGV area	+1.0	+0.9	89	Identified
Example 2: LPT only fault				
LPT η	−2.0	−2.0	90	Identified
LPT NGV area	+1.0	+1.4	90	Identified
HPT η	0	−0.3	49	Possible
Ex noz area inc[a]	+0.1	+0.3	49	Possible
Example 3: HPC only fault				
HPC η	−2.0	−2.0	90	Identified
HPC mf	−1.0	−1.2	90	Identified
Example 4: LPC & HPT double module fault				
LPC η	−2.0	−1.3	90	Identified
HPT η	−1.0	−0.9	81	Identified
Burner p loss	0	+0.6	81	Identified
HPT NGV area	0	+0.9	48	Possible
LPC bleed leak[a]	+0.1	+0.9	42	Possible
Example 5: HPC & HPT double module fault				
HPC mf	−1.0	−1.8	90	Identified
HPT η	−2.0	−4.7	90	Identified
HPT NGV area	+1.0	+0.5	76	Quite possible
HPC η	−2.0	−0.3	50	Possible

[a]For Examples 1, 2, 3, and 4, three additional faults of a small severity were also included in addition to the two faults listed in Table 10. These three small faults were nozzle area inc +0.1, fan η−0.2, and LPC bleed leak +0.1. For Example 5, only the small LPC bleed leak fault was used. The purpose of these small faults was to simulate measurement errors and additional faults due to the degradation of the entire engine to make the simulated examples more representative of real-world conditions. These additional small faults were not expected to be correctly diagnosed.
[b]The results only show the faults categorized as possible or higher. Hence, all undisplayed faults were categorized as unlikely or eliminated.

of the results for this case is that the method has returned a null finding rather than giving an erroneous diagnosis.

The approach has correctly identified the relative difference in the size of the seventh stage LPC bleed leak between Case 6, which was a partial leak, and Case 4 in which the bleed valve was fully open. These two related cases provide a useful guide between the size of bleed leak found in the field and the severity as diagnosed by the method. Thus, if a future diagnosis identifies a leak of 2%, it will be known that a leak less than half of what was found in Engine Serial No. 6622 is being sought. Conversely, if a future diagnosis predicts a severity well in excess of the 6.3% found when the bleed was fully open, the practical ability for a fault of that size to occur should be questioned.

Although the method has indicated the presence of two very different faults for Case 1, when only one is expected, this is not seen as a potentially misleading or ambiguous result in this example. This is because verifying the occurrence of faults should be investigated with some consideration of the cost or time that is required to perform this task, and not just investigated on the basis of the probability of their existence. Hence, when one considers the relative cost of inspecting the exhaust nozzle final area (virtually 0$), compared to refurbishing the HPC ($300,000), a sensible course of action would be to inspect the exhaust nozzle first, in which case the true fault will be found without wasted expenditure, irrespective of which of the two faults is actually in existence.

13 Results With Simulated Examples

This section includes some results of simulated examples to further demonstrate the method capability for fault combinations that are not illustrated by any of the real-world validation examples. While it is usually easy to identify LP spool problems from HP spool problems, it is usually more difficult to distinguish between the compressor and turbine faults on the same spool. However, Examples 1, 2, and 3 in Table 10 demonstrate that the AutoStack approach can distinguish HPT faults from LPT faults, and distinguish HPT faults from HPC faults. For Examples 1, 2, and 3, the method has identified the correct faults with a high probability and a severity very close to the actual severity. Only for Example 2 is there some incorrect attribution of the LPT fault to the HPT, but this is at a much lower probability and so is unlikely to be a misleading diagnosis.

Examples 4 and 5 demonstrate how well the method works when faults exist in two different modules. Example 4 contains one fault in each module, while Example 5 has two faults in each module. These examples demonstrate that the method will identify the faulty modules correctly, although for some combinations of faults it may also incorrectly identify other faults.

14 Practical Aspects of Real-World Fault Diagnosis

This section discusses three difficulties that are encountered when trying to apply diagnostics to real-world data. Despite some of the difficulties that occur when using real-world data, the great benefit is that a much more realistic indication of the method's true capability should be given than when using simulated data,

that even with noise added often produces unrealistically high success rates [15]. Very few papers demonstrate the ability of gas-path diagnostic methods using real-world data [4,16,17].

The first practical difficulty involves identifying, when the engine is stripped, if the predicted faults, or what other faults, did exist in the engine. It is difficult to identify what faults are in the engine for many reasons, some of which include a lack of suitable qualified staff to inspect parts and a lack of time to perform detailed inspections. For example, a study to identify the physical causes of increased fuel consumption in the CF6–50 engine [18] used four teams of five people—with each team consisting of a mechanical designer, an aerodynamicist, an airline service hardware engineer, a performance engineer, and a performance restoration specialist— to study each of the four major engine sections. Such a detailed study cannot occur for day-to-day diagnosis and validation. Thus, only significant defects, which will only occur in a few engines, are likely to be identified in a production engine repair facility.

Hence, while there was a single particular fault associated with each of the repairs of the eight validation cases (Table 4), in many of them the engine will also have had normal wear and tear on all the gas-path components. Hence, there will be additional faults within the engine, which have remained undiscovered due to their more insidious nature. Hence, while the diagnosis of these repairs is expected to identify a certain fault, it is not necessarily "wrong" if the diagnosis also identifies other additional faults (although these would be expected to have a lower severity).

A second practical difficulty involves identifying suitable data to represent the no-fault performance of the engine being investigated. This is particularly true for an approach using test-cell data, as the opportunities for obtaining data can be very limited. In many cases, it is often advisable to use the average performance of postoverhauled engines as the source of no-fault data, from which to calculate the performance change. The diagnosis obtained using the average postoverhaul performance as the no-fault data can be compared with a second diagnosis obtained using a file, which is from the actual engine being investigated and which is considered as possibly being suitable to represent the no-fault condition. If the diagnoses are similar, then one has more confidence. If the diagnoses are different, then one must consider if the no-fault data are reliable, or if this engine's normal operation is an outlier when compared with the average performance of a postoverhauled engine.

Measurement error is a third aspect of real-world fault diagnosis. For this aspect, the utilization of test-cell data is a benefit, for several reasons. First, some sensors have extra scrutiny that does not occur in-flight. For example, rather than recording a single exhaust gas temperature (EGT) value, the TF30 test-cell system displays the values of all seven thermocouples in the EGT harness. Hence, a failed sensor is much easier to detect. Second, multiple sensors also exist for fan inlet temperature and pressure, greatly reducing the chance of errors on these parameters. Hence, the number of sensors, which are likely to fail and not be detected when using test-cell data, is reduced compared to in-flight data.

15 Conclusions

A diagnostic process to identify module level engine performance faults has been presented and validated using eight examples from real-world test-cell data. The approach examines many combinations of faults in an attempt to explain the performance degradation observed in the engine undergoing repair. This aspect of the process enables the status of 17 faults to be determined, despite only five engine parameters being used. The method correctly identified the faults for all examples except for one fault, which had a very small degradation effect on the engine performance. Very small faults are defined as having an effect on the engine's performance that is less than half the standard deviation of the engine-to-engine variation of the engine fleet.

The primary feature of the process is the use of fuzzy logic to classify faults into categories describing the likelihood of the fault existing in the engine being diagnosed. The use of fuzzy logic has two benefits. First, it enables the diagnostic process to give a probability of the fault's existence, which is a unique feature. The vast majority of diagnostic processes indicate what the predicted faults are and their associated severity, but do not also indicate the confidence of the diagnosis. Second, the use of fuzzy logic enables a number of solutions to be summarized into a single solution, such that the dominant faults are identified, rather than faults whose existence is likely to occur only to create a solution with low mathematical error. This aspect of the process should reduce the effect of small measurement errors since the method seeks large faults that are consistently used in many solutions, rather than offering a single solution with zero or low error as the final diagnosis.

Two secondary features of the diagnostic process are the iterative nature of the method and the parsimonious approach, which explicitly seeks solutions with less than five faults to explain the performance change of five parameters. Both of these features increase the robustness of the summarization process by providing additional solutions with low error and enabling the fuzzy logic to utilize a richer (larger) set of fuzzy rules.

The use of the engine-to-engine variation that naturally occurs within a fleet of healthy engines is demonstrated as a practical basis against which to compare the size of the observed performance changes in a particular engine. This is important information as faults with large effects on the engine's performance should be easier to diagnose than faults with a small effect.

Acknowledgment

The author would like to acknowledge the assistance of Dr. Zhifeng Ye, who in collaboration with DSTO while on a posting at the University of Newcastle identified the parsimonious approach as a suitable diagnostic method to apply when seeking solutions using influence coefficients, and wrote the core mathematics of the diagnostic process, which utilizes the MATLAB non-negative least-squares algorithm.

The author would also like to acknowledge the continued assistance of numerous personnel within the TF30 Engine Business Unit, at RAAF Base Amberley, in particular, Greg Mason, Mick Donlan, and Evan Storey.

Nomenclature

CM = condition monitoring
EPR = engine pressure ratio (Pt7/Pt2)
FD = fan duct
FOD = foreign object damage
HPC = high pressure compressor
HPT = high pressure turbine
LPC = low pressure compressor
LPT = low pressure turbine
N1 = low pressure spool speed
N2 = high pressure spool speed
NGV = nozzle guide vane
OB = overboard
OEM = original equipment manufacturer
PLA = power lever angle
Ps3 = LPC exit static pressure
Ps4 = HPC exit static pressure
Pt2 = Fan inlet total pressure
Pt7 = LPT exit total pressure
RAAF = Royal Australian Air Force
RVI = remote visual inspection
SOA = spectrometric oil analysis
TIT = turbine inlet temperature
Tt2 = fan inlet total temperature
Wa = air mass flow
η = efficiency

σ = standard deviation

Appendix: Fuzzy Logic Rules

When old_category is "possible":

1. If (count is high) and (severity is low) and (old_category is possible) then (new_category is possible)
2. If (count is high) and (severity is medium) and (old_category is possible) then (new_category is quite_possible)
3. If (count is high) and (severity is high) and (old_category is possible) then (new_category is identified)
4. If (count is medium) and (severity is low) and (old_category is possible) then (new_category is unlikely)
5. If (count is medium) and (severity is medium) and (old_category is possible) then (new category is possible)
6. If (count is medium) and (severity is high) and (old_category is possible) then (new category is quite_possible)
7. If (count is low) and (severity is low) and (old_category is possible) then (new category is eliminated)
8. If (count is low) and (severity is medium) and (old_category is possible) then (new category is unlikely)
9. If (count is low) and (severity is high) and (old_category is possible) then (new category is possible)

When old_ category is "quite_ possible":

10. If (count is high) and (severity is low) and (old category is quite_possible) then (new category is quite_possible)
11. If (count is high) and (severity is medium) and (old category is quite_possible) then (new category is identified)
12. If (count is high) and (severity is high) and (old category is quite_possible) then (new category is identified)
13. If (count is medium) and (severity is low) and (old category is quite_possible) then (new category is quite_possible)
14. If (count is medium) and (severity is medium) and (old category is quite_possible) then (new category is quite_possible)
15. If (count is medium) and (severity is high) and (old category is quite_possible) then (new category is identified)
16. If (count is low) and (severity is low) and (old category is quite_possible) then (new category is unlikely)
17. If (count is low) and (severity is medium) and (old category is quite_ possible) then (new category is possible)
18. If (count is low) and (severity is high) and (old category is quite_possible) then (new category is quite_possible)

When old_category is "unlikely":

19. If (count is high) and (severity is low) and (old category is unlikely) then (new category is possible)
20. If (count is high) and (severity is medium) and (old category is unlikely) then (new category is possible)
21. If (count is high) and (severity is high) and (old category is unlikely) then (newcategory is quite_possible)
22. If (count is medium) and (severity is low) and (old category is unlikely) then (new category is unlikely)
23. If (count is medium) and (severity is medium) and (old category is unlikely) then (new category is possible)
24. If (count is medium) and (severity is high) and (old category is unlikely) then (new category is possible)
25. If (count is low) and (severity is low) and (old category is unlikely) then (new category is eliminated)
26. If (count is low) and (severity is medium) and (old category is unlikely) then (new category is unlikely)
27. If (count is low) and (severity is high) and (old category is unlikely) then (new category is possible)

When old_category is "eliminated" or "identified":

28. If (old category is eliminated) then (new category is eliminated)
29. If (old category is identified) then (new category is identified)

References

[1] Urban, L. A., and Volponi, A. J., 1992, "Mathematical Methods of Relative Engine Performance Diagnostics," SAE Paper No. 922048.
[2] Doel, D. L., 1994, "TEMPER—A Gas-Path Analysis Tool for Commercial Jet Engines," ASME Paper No. 92-GT-315.
[3] Barwell, M. J., 1987, "COMPASS—Ground Based Engine Monitoring Program for General Application," SAE Paper No. 871734.
[4] Danielsson, S.-G., 1977, "Gas Path Analysis Applied to Pre and Post Overhaul Testing of JT9D Turbofan Engine," SAE Paper No. 770993.
[5] Volponi, A. J., 2005, "Use of Hybrid Engine Modeling for an On-Board Module Performance Tracking," ASME Paper No. GT2005-68169.
[6] Brotherton, T., Volponi, A., Luppold, R., and Simon, D., 2003, "eSTORM: Enhanced Self Tuning On-Board Real-Time Engine Model," *Proceedings of the IEEE Aerospace Conference*, Big Sky, MT.
[7] Lu, P. J., Zhang, M. C., Hsu, T. C., and Zhang, J., 2001 "An Evaluation of Engine Faults Using Artifical Neural Networks," ASME Paper No. 00-GT-029.
[8] DePold, H. R., and Gass, F. D., 1999, "The Application of Expert Systems and Neural Networks to Gas Turbine Prognostics and Diagnostics," ASME Paper No. 98-GT-101.
[9] Simon, D., and Simon, D. L., 2006, "Kalman Filtering With Inequality Constraints for Turbofan Health Estimation," IEE Proc.: Control Theory Appl., **153**(3), pp. 371–378.
[10] Doel, D., 2003, "Development of Baselines, Influence Coefficients and Statistical Inputs for Gas Path Analysis," *Lecture Series 2003-01*, von Karman Institute.
[11] DePold, H. R., Rajamani, R., Morrison, W. H., and Pattipati, R. K., 2006, "A Unified Metric for Fault Detection and Isolation in Engines," ASME Paper No. 2006-GT-91095.
[12] Inan, S., Frith, P. C. W., and Eustace, R., 2001, "Gas-Path Diagnostics Using an Adaptive Model Modified to Accommodate Real-World Uncertainties," *Ninth Australian International Aerospace Congress*, Paper No. AIAC 2001-029.
[13] Eustace, R., and Frith, P. C. W., 2001, "Utilizing Repair and Overhaul Experience in a Probabilistic Neural Network for Diagnosing Gas-Path Faults," ISABE Paper No. 2001-1050.
[14] JenaNet.com, 1999, Aviation Week & Space Technology, May 10, p. 78.
[15] Doel, D., 2003, "Sample Analyses Including Interpretation of Residual Error," *Lecture Series 2003-01*, von Karman Institute.
[16] Herzog, J., Hanlin, J., Wegerich, S., and Wilks, A., 2005, "High Performance Condition Monitoring of Aircraft Engines," ASME Paper No. GT2005-68485.
[17] Visser, W. P. J., Pieters, H., Oostveen, M., and van Dorp, E., 2006, "Experience With GSP as a Gas Path Analysis Tool," ASME Paper No. GT2006-90904.
[18] Wulf, R. H., 1980, "Engine Diagnostics Program: CF6-50 Engine Performance Deterioration," Report No. NASA-CR-159867.

Influence of Force Field Direction on Pressure Sensors Calibrated at Up to 12,000 g

Wieland Uffrecht

Erwin Kaiser

Dresden Institute of Fluid Mechanics,
Technische Universität,
01062 Dresden, Germany

The measurement of pressure within both stationary and rotating frames of reference is a fundamental requirement when studying the flow field through turbomachinery blading. Measurement of pressure within the rotating frame presents a particular challenge, as centrifugal acceleration of the sensor can have a significant impact on sensor calibration, and therefore accuracy of the resulting measurements. In this paper the telemetric calibration of pressure sensors at up to 12,000 g is described, and the impact on calibration of membrane size, sensor body shape, and sensor mounting direction is discussed. The program of work reported in this paper focuses on experimental issues associated with rotating pressure measurement. The combined effect of centrifugal load and pressure on integrally temperature compensated silicon pressure sensors is presented. Experimental results are given that provide insight into the influence of acceleration on pressure readings. Implementation of acceleration into sensor calibration is presented. Supplementary finite element calculations enable impact of sensor body shape to be taken into account during the evaluation of sensor acceleration-to-pressure sensitivity ratio. Different sensors with varied membrane sizes and acceleration force directions are examined and compared. [DOI: 10.1115/1.2966390]

1 Introduction

Low cost silicon pressure sensors with integrated amplifier and temperature compensation became available within the past decade. These devices are used for consumer goods, medical devices, and all sorts of industrial applications including automotive. The sensors are small in size and weight. Furthermore the high degree of integration and the low power consumption make them interesting for applications with limited power supply and space. These are battery powered portable devices on the one hand and special applications on the other hand as, for instance, telemetric measurement systems.

Telemetric measurement systems (telemetry) are used when the range of interest is part of a moving object and wireless operation is needed. A modern digital telemetry consists of a wireless power supply, the measurement system, and at least one wireless data channel, which transfers the values from the moving to the stationary part of the apparatus. The measurement system can be separated into different sensors and their amplifiers. The wireless power supply usually uses high frequency generators connected to an antenna for energy transfer from the stationary to the moving system. The moving antenna receives the energy only partially. Due to the poor efficiency and the limited power of the high frequency system, which may affect other sensitive devices in the laboratory if using high power, the power consumption of the sensors is an important issue. The high centrifugal acceleration is an extra challenge for the use of telemetric measurement in the field of turbomachinery. The integrated pressure sensors are therefore ideal for telemetric application due to their low weight, size, and power consumption.

Sensor application and calibration are important issues for proper measurement under these circumstances. This paper presents the examination of integrated pressure sensor performance taking into consideration the parameter position, connection, direction, and high centrifugal acceleration as found in turbomachines.

Contributed by the International Gas Turbine Institute of ASME for publication in the JOURNAL OF ENGINEERING FOR GAS TURBINES AND POWER. Manuscript received March 28, 2008; final manuscript received March 28, 2008; published online August 27, 2008. Review conducted by Dilip R. Ballal. Paper presented at the ASME Turbo Expo 2008: Land, Sea and Air (GT2008), Berlin, Germany, June 9–13, 2008.

2 Air Column

Pressure measurements in the rotating system of turbomachines require different locations for sensor and measurement in most of the cases. The pressure sensor is located at a position that provides sufficient space and operating conditions. The pressure of interest leads to the sensor by a thin pipe usually. That means the pressure reading of the sensor is influenced by the centrifugal acceleration if the sensor is located at different radius compared with the pressure measurement hole. This pressure change caused by the fluid column in the force field can be calculated with the mass element dm in the cross section A of the pipe, the centrifugal acceleration a, and the radial pressure change dp:

$$\omega^2 r\, dm = A\, dp \quad \text{with} \quad dm = \rho A\, dr \tag{1}$$

$$\omega^2 r\, dr = RT\frac{dp}{p} \tag{2}$$

$$\frac{p_2}{p_1} = \pi_T = \exp\left[\frac{\omega^2}{2RT}(r_2^2 - r_1^2)\right] \tag{3}$$

See Fig. 1 for the details. A similar calculation can be found in Ref. [1]. The gas equation with gas constant R and temperature T in the pipe gives the density ρ and the following integration from radius r_1 to r_2 yields the ratio of pressures p_1 and p_2 corresponding to the radii mentioned before.

Figure 1 shows a typical pressure sensor instrumentation having the sensor at radius r_S and the pressure measurement hole at radius r_P. The connecting pipe path is designed according to the requirements of the machine. The path of the pipe can be divided into pieces with and without change of radius. The pressure transfer is unaffected by the pieces with no change of radius. The sections with radius change are fluid columns in a force field. Due to the fact that the centrifugal acceleration may exceed 100,000 g

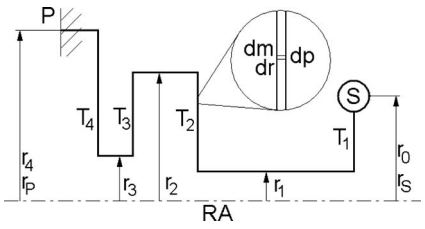

Fig. 1 Sensor (S) location and pressure measurement hole (P) with connecting pipe at different radii *r* and temperatures *T*, all rotating around the rotation axis (RA)

in turbomachines, the pressure change cannot be ignored. The temperature of the gas in the radial pipe influences the density, which affects the pressure change.

The pressure p at a measurement location can be calculated from sensor pressure p_S and the correction factor π_T from Eq. (3). An equivalent correction is presented in Ref. [1]. The correction for the more complicated pipe path shown in Fig. 1 with n radial pressure passages and one constant temperature each is calculated with

$$p = p_S \prod_{i=1}^{n} \exp\left[\frac{\omega^2}{2RT_i}(r_i^2 - r_{i-1}^2)\right] \tag{4}$$

$$p_S = p \prod_{i=1}^{n} \exp\left[\frac{\omega^2}{2RT_i}(r_{i-1}^2 - r_i^2)\right] \tag{5}$$

In the case of strong radial temperature changes along a radial passage a polynomial fit of the radial temperature distribution has to be used. This requires a modification of the integration from Eq. (2). The temperature T becomes dependent on the radius r with the coefficients k_j and with the degree j of the polynomial:

$$T = T_{r0}/(1 + k_1 r + \cdots + k_j r^j) \tag{6}$$

$$\frac{p_2}{p_1} = \pi = \exp\left[\frac{\omega^2}{2RT_{r0}}\left[r_2^2 - r_1^2 + \frac{2k_1}{3}(r_2^3 - r_1^3) + \cdots + \frac{2k_j}{j+2}(r_2^{j+2} - r_1^{j+2})\right]\right] \tag{7}$$

To examine the temperature influence in some detail, four test cases with two different temperature and radius spans have been calculated. Each test case consists of one radial step with radial temperature change.

The temperature distribution is assumed to be almost linear with only the coefficient k_1 used in Eqs. (6) and (7). The temperature distributions for the test cases are shown in Fig. 2.

Figure 3 shows the pressure change in a radial air column caused by the centrifugal acceleration for the four test cases. This diagram can also be understood as the error associated with no pressure correction. The error becomes huge at a few thousand rpm and depends mainly on the radius and its span. The radial temperature change turns out to be not significant.

A correction is needed for better accuracy, but additional telemetric temperature measurement for the radial pressure paths is costly. Figure 4 shows the remaining error for a pressure correction using a constant temperature of 10 K below the proper average (see Fig. 2, $T_A - 10$ K), which simulates an unknown value or an uncertainty in case no extra telemetric measurement is available for the pressure passage.

The error is reduced and the requirements in terms of accuracy and revolving speed are met for most of the measurement tasks. Estimated temperatures are applicable for the correction and no additional temperature measurement is needed for the pressure path.

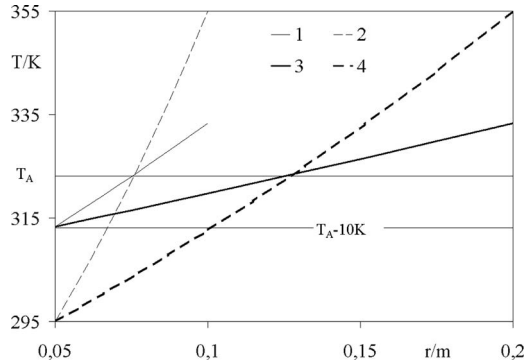

Fig. 2 Temperature *T* over radius *r* of pressure path, two different temperature and radius spans combined, Cases 1–4, average temperature T_A for all cases, and reduced average temperature $T_A - 10$ K simulating uncertainty in the known value

The influence of the neglected temperature distribution on the pressure correction becomes significant for very high accuracy requirements or for very high revolving speed only.

Figure 5 shows the difference between the pressure correction from Eq. (3) using one known or measured pressure passage average temperature and the correction from Eq. (7) using the known linear temperature distribution along the radial pressure passage.

The error of the constant temperature correction becomes noticeable. Thus the temperature distribution of radial pressure passages cannot be simplified by constant assumption and needs extra

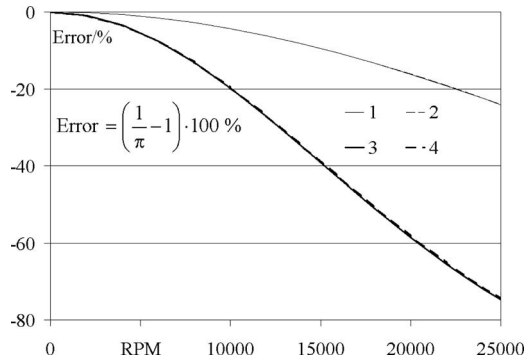

Fig. 3 Error over rpm caused by neglected correction for fluid column in force field for the four cases from Fig. 2 for pressure ratio π, see Eq. (7)

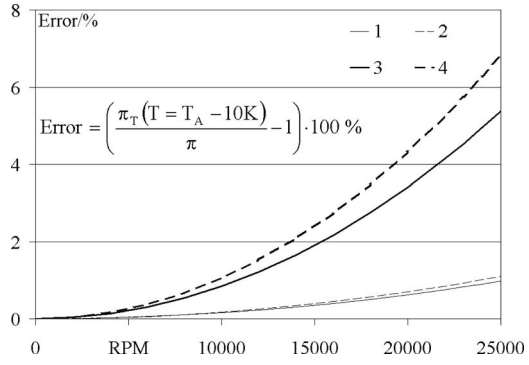

Fig. 4 Error over rpm caused by correction for the fluid column in the rotating system with constant 10 K to low temperature $T_A - 10$ K simulating uncertainty in the known temperature, see Fig. 2 for the four cases and see Eqs. (3) and (7) for the pressure ratios π_T and π

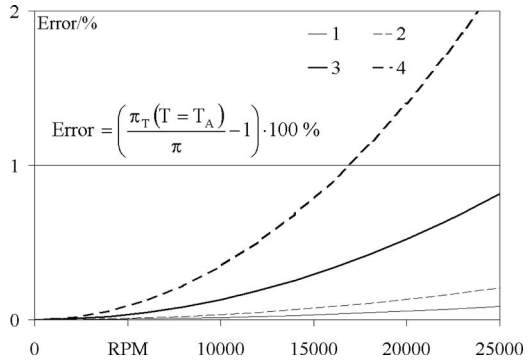

Fig. 5 Error over rpm caused by pressure correction for the fluid column in the rotating system with average temperature T_A instead of linear temperature distribution, four cases (see Fig. 2), for pressure ratios π_T and π, see Eqs. (3) and (7)

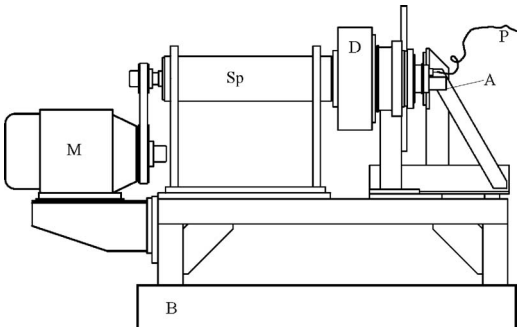

Fig. 7 Calibration test rig, motor M, spindle Sp, air supply A, measurement disk D with pressure sensors to be tested and the telemetry system, pressure measurement hose P, and basement B

measurement for applications with extreme centrifugal accelerations, high radial temperature gradients, and very high accuracy requirements.

3 Sensor Body

Normally the shape of the sensor body is of little interest from user point of view as long as the sensor works reliably. The sensor is a semiconductor device having a casing with pressure ports and pins for electrical connection. The outer dimensions are well documented. The parameters of the inner sensor body design are not part of the documentation.

The devices used are monolithic silicon piezoresistive transducers having a signal amplifier including temperature compensation on chip. The output signal is suitable for analog inputs of common microcontrollers. Furthermore the signal is proportional to the pressure applied.

The documentation contains a depiction, similar to Fig. 6, of the approximate not to scale cross section of the sensor element. It is not documented whether the element is a circular plate or a rectangular plate. Both shapes are common [2].

The documentation contains the pressure sensitivity of the transducer, but not the *sensitivity against acceleration*, which is required for telemetric measurement in the rotating system.

The membrane has the mass m_M, which causes extra pressure depending on the acceleration. The mass is low enough to prevent noticeable effects caused by gravity. That changes at several thousand g of centrifugal acceleration. The acceleration induced extra pressure p_A can be calculated as follows:

$$p_A = \frac{m_M r_S \omega^2}{A_M} = \frac{\rho_M h_M A_M r_S \omega^2}{A_M} = \rho_M h_M a \tag{8}$$

$$p = p_S + p_A \tag{9}$$

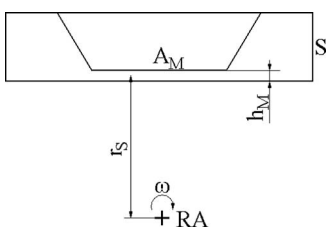

Fig. 6 Sensor element S schematically rotating around the axis RA with sensor radius r_S, membrane area A_M, and membrane thickness h_M

$$\frac{p-p_S}{r_S\omega^2} = \frac{p-p_S}{a} = \rho_M h_M \tag{10}$$

The centrifugal acceleration a, the pressure reading p of the sensor, and the pressure at the sensor p_S are known or measured. The product of the membrane density ρ_M and the membrane thickness h_M becomes the transducer parameter for the ratio of pressure sensitivity and acceleration sensitivity. It can also be seen as membrane mass m_M per membrane area A_M or as specific membrane mass. This parameter is usually unknown to the user. Due to the fact that the sensor is a real technical object with 3D dimensions, the specific mass represents a concentrated parameter.

4 Calibrator

The calibration system is expected to be capable of supplying known pressures and accelerations to the tested sensor with both parameters chosen independently. The common stationary calibration concept with test gas bottle, calibration transducer, and controlling valves for the pressure adjustment cannot fulfill these requirements.

Constant high accelerations can be found in rotating systems with high rotational frequencies, but the decision to place the sensors in a rotating system creates other difficulties. One of them is the necessity of a telemetry system, which survives the centrifugal accelerations needed for the calibration of the sensors. Another problem arises due to the missing airtight connection between the tested sensor and the calibration transducer.

One way to overcome this difficulty would be a pressure sensor with known acceleration sensitivity for full telemetric calibration. In case that kind of sensor is not available, the usage of labyrinth seals as common in turbomachines solves the problem.

It was decided to use stationary calibration sensor and labyrinth seal because the air supply with sufficient capacity was already available.

Central element of the mechanical part of the calibration test rig is a spindle, which is capable to run at up to 12,000 rpm. The one end of the shaft carries a belt drive pulley and the other end the measurement disk (Fig. 7). An asynchronous motor, which is controlled by frequency converter, drives the spindle by a synchronous belt. The rotational frequency of the motor is one-half of the one of the spindle.

The spindle and the motor support are fitted to a concrete basement of sufficient size. This precaution was taken due to the wide band excitement. The test rig actually runs at the whole range from 0 rpm to 11,600 rpm, which may cause excitement from 0 Hz up to 193 Hz base frequency. Proper balancing and high spindle rotation accuracy, better than 10 μm, keep the excitement low enough for full range operation.

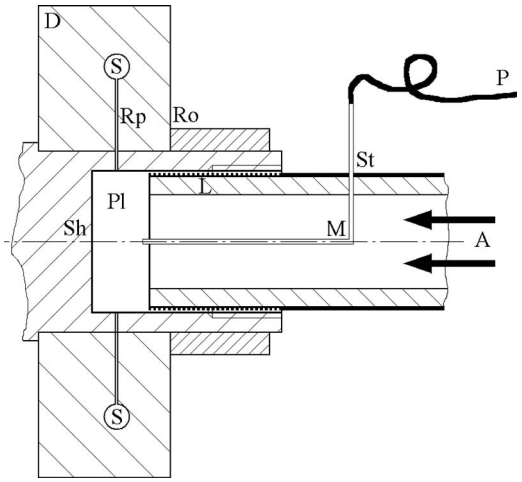

Fig. 8 Calibration test rig detail, rotating side Ro, rotating shaft Sh, measurement disk D with rotating radial pressure passage Rp and sensor S, plenum Pl, labyrinth seal L, stationary side St with air supply pipe A, pressure measurement pipe M, and pressure hose toward comparative sensor P

Vibration sensing equipment is attached to the spindle for balancing and for automated emergency stop. The balancing procedure has to be carried out each time when sensors are exchanged.

The labyrinth seal is built by the partially hollow shaft and the air supply pipe with a labyrinth structure on the outer diameter. The partially hollow shaft acts like pressure plenum for the sensors S, which are subject of calibration (see Fig. 8). These sensors are implemented in the measurement disk, which carries also the telemetry and the balancing masses.

The radial connection of the sensors to the plenum represents an air column in force field. The plenum pressure is measured by a stationary comparative sensor as usual for calibration.

The measurement disk carries the sensors, the radial pressure passage, and the telemetry system, which transmits the pressure values from rotor to stator directly toward the PC-RS232 interface. The telemetry works digitally and uses checksums for transmission. This prevents transmission caused measurement errors.

It was decided to align the sensor element for measurement usage as well as during calibration, as shown in Fig. 6. The pressure acts in the same direction as the centrifugal acceleration. Due to the fact that the sensors are not specified for high acceleration environment, it was assumed that the sensor survives acceleration force, which acts as the force caused by the pressure, better than differently orientated acceleration. The advantage of this tangential membrane alignment is the prevention of shear tension between the sensor element and the sensor casing.

5 Calibration

The first step of the preparation of a telemetric pressure measurement system for usage is a standard stationary calibration after the system passed the general functionality check.

All calibrations include the whole measurement chain from the sensor to the final discrete value. The analog to digital conversion is included. Due to the digital transmission, which is extended for a checksum as mentioned before, no errors caused by transmission influence the final result. In the case of transmission error the whole data set is ignored.

The hollow part of the shaft, Sh in Fig. 8, is closed by a lid, which is screwed in for stationary calibration instead of the air supply pipe, A in Fig. 8. The lid is connected to the stationary calibrator by a pressure hose. The stationary calibrator is a DPI 515 device, made by the company Druck, with an error of 0.01% from full scale. The ranges used are 7 bars and 0.7 bar full scale against atmosphere.

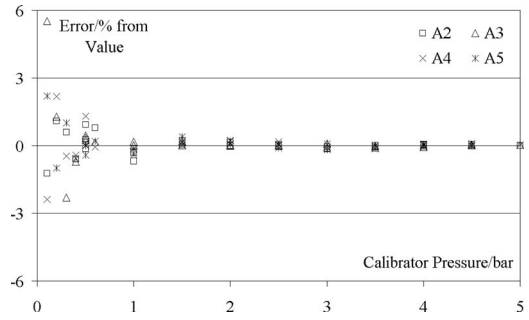

Fig. 9 Relative error of telemetric Sensors A2–A5 for stationary calibration using DPI 515 made by company Druck

Figure 9 shows the result of the stationary standard calibration. It is the relative pressure difference Δp_{rel} of the sensor pressure p and the calibrator pressure p_C, as shown in Eq. (12). The second order polynomial of Eq. (11) calculates the sensor pressure p from the original digital value p_D.

$$p = A\ p_D^2 + B\ p_D + C \tag{11}$$

$$\Delta p_{\text{rel}} = \frac{p - p_C}{p_C} \cdot 100 \tag{12}$$

The high error of one of the sensors for the very low pressure is attributable to the low noise 8 bit digitization and to the fact that the error is relative to the value and not to the measurement range.

Figure 10 shows the raw pressure readings p_D in digit from the 8 bit analog to digital converter of the telemetry system, as used in Eq. (11). The pressure readings are gained from the four telemetric sensors for different circular frequencies. The centrifugal acceleration acting at sensor radius is shown as well. Only atmospheric pressure is applied to the hollow shaft. The pressure values calculated using Eq. (11) are the sum of the acceleration caused part and of the air column induced portion, which is calculable by Eq. (3). Figure 11 shows the separated influences of acceleration and air column.

With respect to Eqs. (8)–(10) the acceleration induced part p_A and the pressure at the sensor p_S, which equals the air column induced part, are known. This yields the specific membrane mass $\rho_M h_M$, as discussed in Eq. (10) and shown in Fig. 12.

The error bars in Fig. 12 represent the assumed uncertainty of one digit in terms of specific membrane mass. Due to the low acceleration induced pressure values the uncertainty of the specific mass reaches very high values at low rotational speed. Only

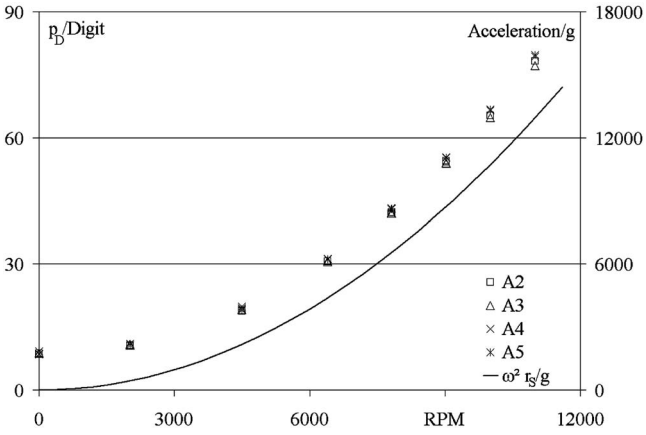

Fig. 10 Digital readings of Sensors A2–A5 in digit as supplied by the 8 bit analog to digital converter of the telemetry, centrifugal acceleration acting at sensor radius r_S

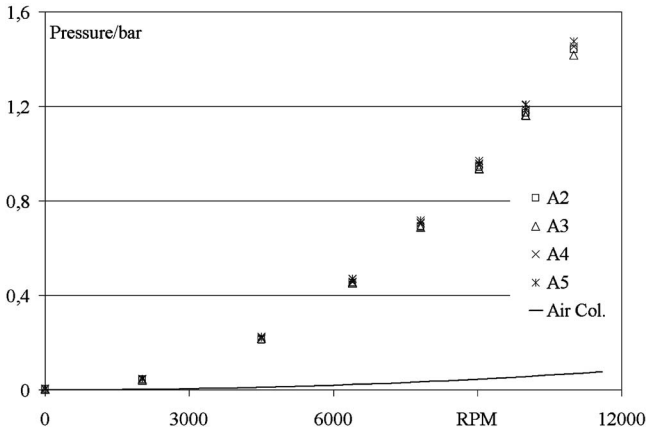

Fig. 11 Pressure readings p_A of Sensors A2–A5 caused by centrifugal acceleration and air column pressure

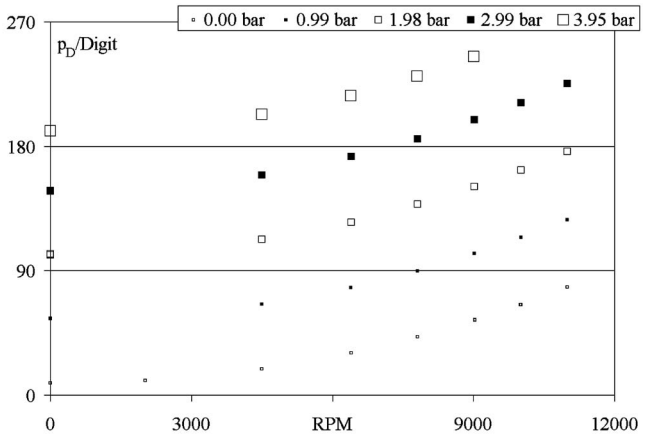

Fig. 13 Digital readings of Sensor A2 for different preset calibration pressures from the stationary system

the values for high rotational frequencies can be considered for the determination of the specific membrane mass, as shown in Fig. 12.

The specific membrane mass $\rho_M h_M$ should become a constant for the simplified usage of concentrated parameters, as stated in Eq. (10). Obviously this is not the case.

The application of extra pressure to the rotating system via the labyrinth sealed hollow shaft, as described in Sec. 4, yields the diagram shown in Fig. 13.

The values without extra pressure from Fig. 10 are also contained. Figure 13 gives reason for the assumption that the effect of the acceleration on the sensor is completely independent of the influence of the pressure on the measurement produced by the sensor.

Figure 14 supports this assumption. The diagram shows the characteristic calibration parameter for accelerated membrane pressure sensors here called specific membrane mass $\rho_M h_M$, as stated in Eq. (10). All different pressures yield the same dependency within the one digit uncertainty. The linear approximation is calculated from all measurements for more than 6000 rpm. The results for Sensors A3–A5, which are not shown in Fig. 14, are equivalent.

The acceleration caused pressure p_A is approximated, as shown in Eq. (13). The linear dependency shown in Fig. 14 is introduced into Eq. (8) using the calibration coefficients D and E with the rotational speed n (rpm). The pressure p_S arriving at the sensor is calculated using the full calibration equation (14).

$$p_A = \rho_M h_M r_S \omega^2 = r_S \omega^2 [D + n \cdot E] \tag{13}$$

$$p_S = A \; p_D^2 + B \; p_D + C - r_S \omega^2 [D + n \cdot E] \tag{14}$$

The calibration of the pressure sensors was successful; thus the dependency of the specific membrane mass on the acceleration or the rotational speed cannot be explained.

One reasonable speculation on this could be the fluorosilicone die coat, which prevents the contact between the silicon chip and the fluid. In case it has a jellylike behavior, which makes the silicone reversible elastically moving toward the center of the membrane, the specific membrane mass would change.

6 FEM Calculation

The finite element calculations are carried out for the examination of the influence of the sensor element orientation compared with the acceleration direction. The calculation requires the dimensions of the object of interest; thus the exact shape of the calibrated sensor element is not known. Therefore the dimensions of the KPY sensor elements made by Siemens and described in Ref. [2] are used.

The two elements considered are silicon square plates with an edge length of 4 mm having a thickness of 0.4 mm. The membrane of the elements is realized by a single sided thickness reduction, which represents a hole from one side. The membrane is a cirular plate with a diameter of 1 mm and a thickness of 0.02 mm for the 2 bar range sensor (KPY2) and with a thickness of

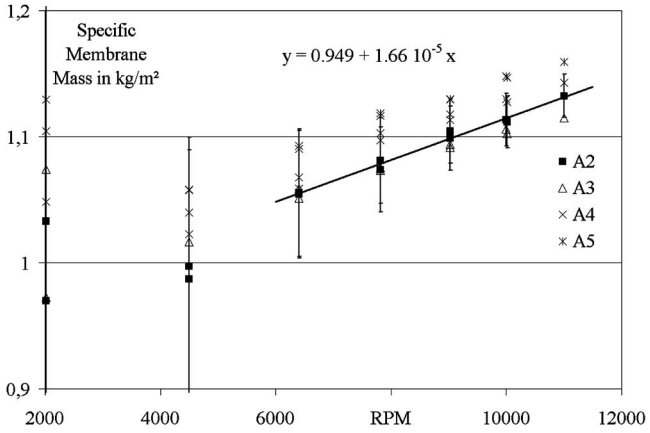

Fig. 12 Specific membrane mass $\rho_M h_M$ of Sensors A2–A5, linear fit shown for A2, error bars equal one digit uncertainty

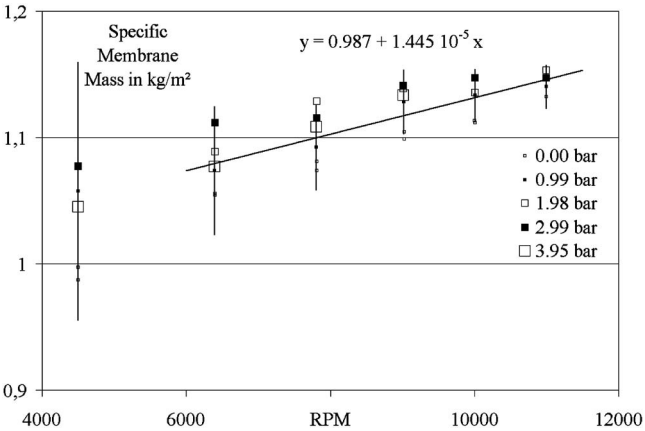

Fig. 14 Specific membrane mass $\rho_M h_M$ of Sensor A2 for different pressures, linear fit for all values >6000 rpm, error bars equal one digit uncertainty

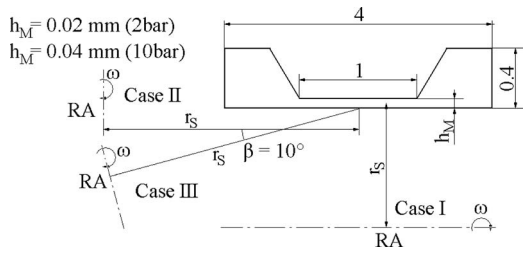

Fig. 15 KPY sensor elements schematically, rotation axis RA for Cases I–III along the dashed-dotted line in the picture plane, sensor radius r_S

0.04 mm for the 10 bar sensor (KPY10, see Fig. 15). The KPY sensors were not considered for the telemetric measurement due to its electrical incompatibility with the telemetry system.

The finite element method (FEM) calculations use the membrane dimensions of the KPY sensors whereas the model is a long rectangular membrane instead of the circular plate membrane of the original KPY sensor. The original membrane diameter (1 mm) is modeled as membrane width. Choosing the rotational axis as symmetry axis simplifies the modeling and saves calculation time.

Figure 15 shows the shape of the sensor element used for the calculation schematically. Three different cases of sensor direction relative to the rotational axis, as shown in Fig. 15, are examined. Further Si(111) material parameters, which are needed for the calculation, are listed below:

Young's modulus	170,000 MPa
Poisson's contraction number	0.068
Linear thermal expansion (300 K)	2.6×10^{-6} K^{-1}
Density	2330 kg/m^3

The above values are obtained from Refs. [2–4].

FEM calculations for pressure induced sensor element deformation have been done [3] using a volume element model for a quarter of an element with a circular plate membrane. The case of centrifugal acceleration and pressure was not considered.

The calculations presented here use a model, which is symmetric in the rotational axis (2D axial-symmetric element plane 42, ANSYS). Analytical equations as described below have been used for the plausibility check. The modified KPY2 sensor (rectangular instead of circular membrane) with a membrane thickness h_M of 0.02 mm and a membrane width of 1 mm has been implemented for plausibility. The pressure applied for test case is 2 bars. Literature provides different analytical approximations for the maximum displacement w_0 in the center of the membrane. The equations with the pressure p are similar as shown here:

$$w_0 \approx k \cdot \frac{b^4(1-\nu^2)}{h_M^3 E} \cdot p \tag{15}$$

The variation between the different equations is expressed by the coefficient k. The parameters elasticity E (Young's modulus), contraction number ν, and membrane width or diameter b are needed for the calculation. The coefficient k becomes 1/32 for a long rectangular membrane [2] with w_0=4.6 μm, 3/188 for a square membrane [3] with w_0=2.3 μm, and 3/256 for a circular membrane [3] with w_0=1.7 μm.

The FEM calculation yields w_0=5.2 μm. The lower stiffness of the FEM model can be explained by the fact that the analytical calculations are derived from plates clamped stiffly whereas the FEM model considers the whole sensor element.

The influence of the fix points of the FEM mesh on the results is studied prior to the examination of the effect of the acceleration. The results show no difference between the two fix point selections 2, 12, 13, 3 (bottom of the element only) and 1, 2, 12, 13, 3, 4 (bottom and side of the element, see Fig. 16). The pressure-membrane-displacement dependency and the temperature-membrane-displacement curve are not different for the two fix point selections, as shown in Figs. 17 and 18.

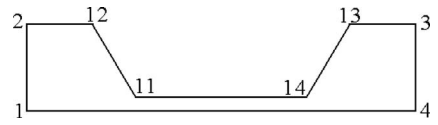

Fig. 16 Key points of the FEM model for the sensor element

For the calculation of the influence of the centrifugal acceleration on the deformation of the sensor element, which causes the strain of the bridge resistors on the membrane surface, three cases are examined (see Fig. 15).

Case I represents the situation examined experimentally as described in Secs. 4 and 5. The pressure acts in the same direction as the acceleration. Figure 19 shows the influence of the acceleration on the two examined sensor types KPY10 and KPY2. The acceleration induced pressure p_A, see also Eq. (8), and the membrane center displacement w_0 are linear functions of the acceleration. The gradient of the membrane displacement represents the sensitivity of the sensor for acceleration.

The pressure acts perpendicular to the acceleration for Case II (see Fig. 15), which reduces the effect of the acceleration on the membrane displacement. This advantage is accompanied by at least one technical difficulty. The base area used for the connection to the casing by adhesive sees shear tension, which may disintegrate the sensor; thus for the FEM calculation this is not of importance.

The calculation yields no significant acceleration sensitivity. The sensitivity for pressure is without any noticeable difference

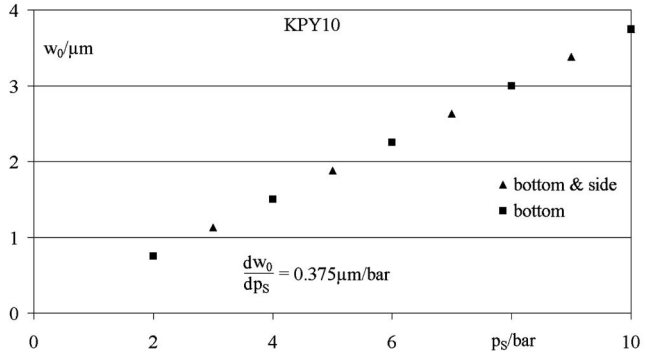

Fig. 17 Displacement at the membrane center over pressure; FEM results for the two fix point selections 2, 12, 13, 3 (bottom) and 1, 2, 12, 13, 3, 4 (bottom and side), see Fig. 16

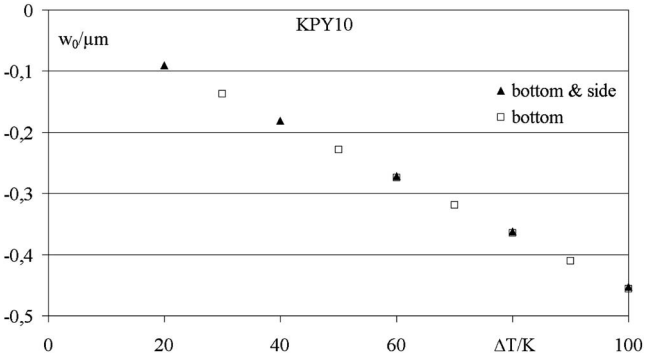

Fig. 18 Displacement at the membrane center over temperature; FEM results for the two fix point selections 2, 12, 13, 3 (bottom) and 1, 2, 12, 13, 3, 4 (bottom and side), see Fig. 16

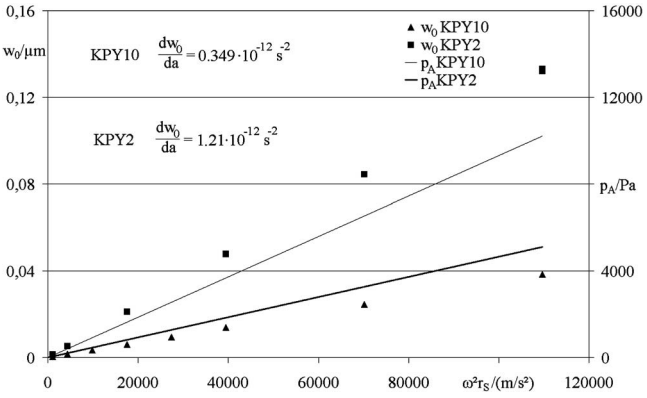

Fig. 19 Displacement w_0 at the membrane center and acceleration induced pressure p_A over acceleration for Case I; FEM results for sensors KPY10 for 10 bars with h_M=0.04 mm and KPY2 for 2 bars with h_M=0.02 mm

for the applied acceleration and is the same as shown in Fig. 17. The calculation shows minor influence on the membrane, which gets an S-shape in the case of acceleration. This effect is superimposed by the pressure sensitivity, which is stronger for almost four orders in magnitude.

The strain sensitive resistors are locally implemented in the membrane surface of the sensor element and the S-shape implies local tensions, which may therefore cause resistor readings to be influenced by the acceleration in an unpredictable manner.

The sensor is 10 deg inclined compared with Case II for Case III, as depicted in Fig. 15. The influence of the acceleration is diminished compared with Case I and increased compared with Case II, as shown in Fig. 20, which contains both FEM results from Cases I and III.

The inclination of the sensor from Case III compared with Case I amounts to 80 deg. The sensitivity against acceleration dw_0/da of the inclined sensor from Case III is approximately one-fifth of one of the not inclined sensors from Case I. This ratio is close to the cos(80 deg) for the force component. The remaining difference of 16% may be caused by the deformation of the sensor body, which sees mainly the shear force component calculated with sin(80 deg). This supports the assumption that the sensitivity against acceleration for not as much inclined sensors can be approximated with the cosine of the inclination angle and the sensitivity of the not inclined sensor.

7 Discussion

The steps gone in order to examine the problem have to be recapitulated for the comparison of the results of the experimental work and the FEM calculations.

First the pressure sensitivities of the real and the FEM-implemented sensors were obtained. The sensitivity is, from the system theoretical point of view, the output voltage change over the pressure change applied dV/dp. The stationary calibration provided the sensitivity of the real sensor, whereas the change of the membrane displacement over the pressure change dw_0/dp is chosen as pressure sensitivity (Fig. 17) for the FEM-sensor.

Second the acceleration sensitivities of the real and the FEM-sensor were found via the rotating calibration of the real pressure sensors using the calibration system described. The acceleration sensitivity is the output voltage change over the acceleration change dV/da and contained in the data of Figs. 10 and 11, whereas the membrane displacement change over the acceleration change dw_0/da (Fig. 19) is chosen as the acceleration sensitivity of the FEM-sensors.

Subsequently the effects were analyzed for the independency of each other. The rotating calibration for varied pressures and the FEM calculation for varied acceleration confirmed the validity of the superposition principle.

Finally the ratio of the sensitivities yields the parameter specific membrane mass dp/da from Eq. (8):

$$\frac{dV}{da}\Big/\frac{dV}{dp}=\frac{dp}{da} \quad \text{or} \quad \frac{dw_0}{da}\Big/\frac{dw_0}{dp}=\frac{dp}{da} \tag{16}$$

Figure 21 shows the specific membrane mass for the experimental and the FEM examination in one diagram. Despite the fact that the sensors examined by experiment and by FEM calculation are not the same, the parameter specific mass behavior is equivalent.

The sensors analyzed by experiment and the sensors examined by FEM calculations are made for pressures of the same order of magnitude. Therefore the differences of the parameter specific mass are expected to be not as big, as shown in Fig. 21. The fact that the real sensor has a membrane protection coating adding up to the membrane mass may explain the difference. The specific membrane mass is greater than the one gained from the FEM calculation, which does not consider any protection coating.

The validity of the specific mass as a general calibration parameter is useful for the description of a pressure sensor using concentrated parameters. The system modeling for complex apparatus becomes simplified dramatically due to the reduction in the model complexity from 2D or 3D to 1D.

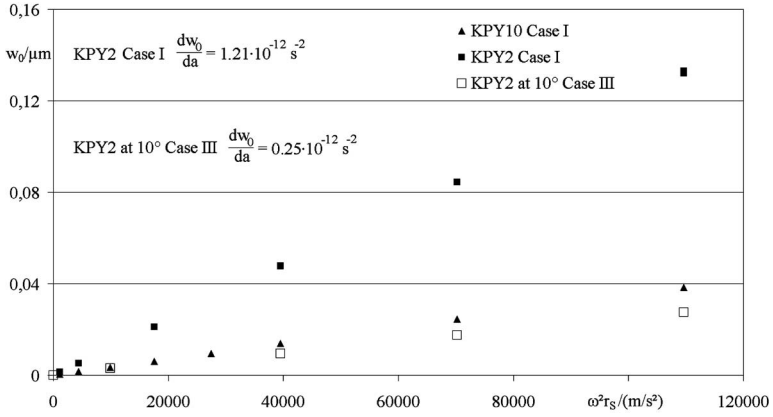

Fig. 20 Displacement at the membrane center over acceleration; FEM results from Case I, same as in Fig. 19, compared with the FEM results from Case III with KPY2 for a 10 deg inclination

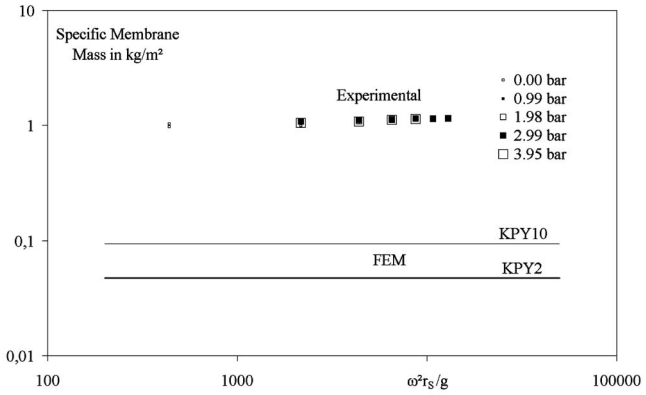

Fig. 21 Specific membrane mass over acceleration, experiment, and FEM results, different sensors, but valid as a general calibration parameter for acceleration sensitivity, see Fig. 14

8 Conclusion

The telemetric usage of pressure sensors in rotating systems requires the sensitivity of a sensor to acceleration to be established. The sensors evaluated during the program of work reported in this paper, with pressure and acceleration acting in the same direction, showed sensitivity great enough to invalidate measurement results if neglected.

The 90 deg inclination of the sensor membrane to the direction of the accelerating force reduces sensitivity to acceleration by more than an order of magnitude, a conclusion corroborated by finite element calculation. Finite element calculation is not, however, concluded to be enough to establish that a sensor is insensitive to acceleration. Sensor calibration is considered mandatory if data integrity is to be assured.

The calibration parameter "specific membrane mass" in kg/m^2 permits modeling of a sensor using concentrated parameters as usual within linear system theory. The parameter deviation of the sensor tested experimentally is low compared with the nonlinearity of some devices, which are modeled using linear system theory.

The pressure differences appearing along the radial pressure passages from the location of measurement toward the sensor cannot be neglected. These pressure passages are always present for telemetric measurement as soon as the sensor location deviates from the location of the measurement. The correction for the pressure difference over the radial passage takes the temperature distribution along the passage into consideration ideally. The simplified usage of the average temperature of the radial pressure passage yields good results up to high accelerations and radius spans.

Acknowledgment

Special thanks to Andrè Günther and Gunar Schroeder for their support of the experimental work.

Nomenclature

A, B, C, D, E = calibration coefficients
A = area
a = acceleration
b = membrane width or diameter
E = elasticity (Young's modulus)
h = thickness
k = coefficient
m = mass (kg)
n = revolutions per minute (rpm)
p = pressure
r = radius
R = gas constant (J/(kg K))
T = temperature (K)
V = voltage
w_0 = displacement at the center of the membrane
ν = Poisson contraction number
ω = circular frequency (rad/s)
π, π_T = pressure ratios
ρ = density (kg/m^3)

Subscripts

A = acceleration
C = calibrator, calibration
D = digital number (digit)
i, j = counter indices
M = membrane
S = sensor
$r0$ = radius=0

References

[1] Regnery, D., Hoeppner, U., Vortmeyer, N., and Nitsche, K., 1999, "Measurements of Complex Air Flow Phenomena Inside the Rotor of an Operating Industrial Gas Turbine," IMechE Conf. Trans., **1/A**, pp. 89–100.
[2] Pfeifer, G., and Werthschützky, R., 1989, *Drucksensoren*, Technik, Berlin.
[3] Stavroulis, S., and Werthschützky, R., 2003, "Analytical Formulations for the Design of Real Diaphragms of Silicon Pressure Transducers," *Proceedings of Sensor*, Nürnberg, May 13–15, Vol. 2.; Stavroulis, S., 2004, "Rechnergestützter Entwurf Piezoresistiver Si-Drucksensoren mit Realem Mechanischen Wandler," Ph.D. thesis, Darmstadt.
[4] Landolt, H., Börstein, R., and Hellwege, K.-H., *Numerical Data and Functional Relationships in Science and Technology*, Springer, New York; Schmidt, B., and Schubert, D., 1986, *Siliciumsensoren*, Akademie-Verlag, Berlin.

Biaxial Thermomechanical-Fatigue Life Property of a Directionally Solidified Ni-Base Superalloy

Takashi Ogata
Central Research Institute of Electric Power Industry,
2-11-1 Iwadokita,
Komae, Tokyo 201-8511, Japan
e-mail: togata@criepi.denken.or.jp

High-temperature components in thermal power plants are subjected to creep-fatigue loading where creep cavities initiate and grow on grain boundaries. Development of life assessment methods of high-temperature components in gas turbine for maintenance and operating cost reduction is strongly demanded by Japanese utilities. Especially, first row blades are subjected to complicated thermomechanical-fatigue (TMF) loading during start, steady state, stop cycles. Therefore it is important to clarify the TMF life property of blade materials to develop a life assessment procedure. In this study, tension-torsion biaxial TMF tests have been performed between 450°C and 870°C on a Ni-base directional solidified superalloy. Strain ratio ϕ was defined as shear strain range, $\Delta\gamma$, to normal strain range, $\Delta\varepsilon$, and ϕ varied from 0 to infinity. The "Blade wave form," which simulated temperature and strain condition of the blade surface, was employed. The biaxial TMF tests were also carried out on coated specimens with CoCrAlY. Fatigue life under the biaxial TMF loading showed strain ratio dependency giving shorter life with increasing ϕ. Considering biaxial stress effect on the failure life, an equivalent shear strain range was derived based on the Γ-plane theory, and the biaxial TMF life was well correlated with the equivalent shear strain range. The biaxial TMF life was reduced by introducing strain hold duration at the maximum temperature. The maximum stress increased by introducing the hold time due to increasing mean stress level in the Blade wave form. It was concluded that creep damage gradually accumulated during cycles resulting in reduction in the TMF life. The nonlinear creep-fatigue damage accumulation model was applied to predict failure life of the hold time tests. As a result, the failure lives were predicted within a factor of 1.5 on the observed life. It was found that the fatigue life of CoCrAlY coated material reduced 1/2 to 1/3 from that of the substrate. From observation of the longitudinal section of the coated specimens, many cracks started from the coating surface and penetrated into the substrate. It was concluded that the CoCrAlY coating reduced the biaxial TMF life due to acceleration of crack initiation period in the substrate. [DOI: 10.1115/1.2943158]

Keywords: gas turbine blade, directionally solidified Ni-base superalloy, biaxial thermomechanical fatigue, CoCrAlY coating

Introduction

For reliable maintenance of gas path components in high-temperature gas turbines, it is important to develop damage and life assessment methods of gas turbine blades, especially for first row blades subjected to thermomechanical-fatigue (TMF) during operation. The authors [1–3] conducted biaxial TMF tests on the polycrystal Ni-base superalloy of IN 738LC used in E class gas turbines considering actual blade operating condition, and found influence of strain hold time and corrosion resistance coating on failure life of the IN 738LC under the biaxial TMF loading. The TMF life prediction method was also proposed based on the test results and failure specimen observation. In addition, a gas turbine blade life assessment code, which includes the TMF life assessment method [2], based on finite element analysis was developed. Referring to temperature and stress analysis results of the first row blade of the E type gas turbine by the code, combined normal and shear stress cycled with temperature fluctuation on the surface of the blade resulted in crack initiation on the surface. It is presumed that similar biaxial TMF loading may occur at surface of row first blades in F type gas turbines, which are made of a Ni-base directionally solidified (DS) superalloy. It is necessary to understand life property of the DS superalloy under biaxial TMF loading and to develop a life prediction method of the DS blades. However, very limited studies of biaxial TMF life of DS superalloys has been conducted mainly due to difficulty of test procedure.

In this study, biaxial TMF tests were performed on a Ni-base DS superalloy to understand life property, and influence of the hold time and the corrosion resistance coating on biaxial TMF life was discussed based on the experimental results.

Experimental Procedure

Test Equipment. A biaxial TMF testing machine consists of a main frame, a digital controller, an induction heating device, an air compressor for cooling, temperature and strain measurement equipment, and a data acquisition system. The main frame has axial and torsional actuators, an induction heating coil, and hydropressure grips. The axial and torsional loading wave forms and temperature were controlled independently and arbitrarily by three different controllers, respectively. Temperature of a specimen is

Contributed by the International Gas Turbine Institute of ASME for publication in the JOURNAL OF ENGINEERING FOR GAS TURBINES AND POWER. Manuscript received January 14, 2008; final manuscript received February 18, 2008; published online August 21, 2008. Review conducted by Dilip R. Ballal. Paper presented at the ASME Turbo Expo 2006: Land, Sea and Air (GT2006), Barcelona, Spain, May 8–11, 2006.

Table 1 Chemical composition of used material

C	Al	B	Co	Cr	Mo	Ta	Ti	W	Zr	Ni
0.10	3.03	0.02	9.56	13.93	1.56	2.77	4.90	3.86	0.01	Bal

measured by a pyrometer without attaching to the specimen. It was confirmed that similar measurement accuracy to a thermocouple can be achieved by the pyrometer and that oxidation of the specimen surface during test did not affect measurement accuracy. By using the pyrometer, crack initiation from welding portion of the thermocouple on the specimen can be avoided resulting in obtaining more accurate life of the specimen. Correction of thermal strain in the TMF tests is carried out based on three dimensional approximation of temperature and strain relation described elsewhere [1]. The axial and the torsional strains were measured by a high-temperature extensometer, which can detect the axial and the torsional strains simultaneously and independently.

Tested Material. A material used in this study is a Ni-base DS superalloy, which is widely used as a first row blade material in the F type gas turbines. Chemical composition and mechanical property of solidified direction are shown in Tables 1 and 2. A specimen geometry used for the biaxial TMF tests is thin wall tube with outer diameter of 20 mm, inner diameter of 16 mm, and gage length of 25 mm, as shown in Fig. 1. The specimens were machined from 30 mm diameter and 300 mm length solid bars, and finished by horning for the inside surface and polishing by diamond past for the outside surface. The specimen axial direction is coincident with the solidified direction of the bar. In addition to the substrate specimens, CoCrAlY (Cr:30%, Al:8%, Y:0.35%) coating with aluminized pack applying to the substrate specimens was produced as coated specimens by low pressure plasma spray, which is used for actual blade treatment. After spraying, a solution treatment with 1120°C×2 h and an aging treatment with 845°C×24 h were made.

Test Condition. Temperature and strain condition of a biaxial TMF test, which simulated actual loading condition of a first row blade surface predicted by temperature and stress analyses of the blade [2], is shown in Fig. 2. This wave form condition is designated as a "Blade wave form" referring to the previous study [2]. The maximum temperature is 870°C and the minimum temperature is 450°C with temperature changing rate of 10°C/s. In the Blade wave form, the strain reaches the maximum compression strain when the temperature reaches the maximum value, and the strain reaches the maximum tensile strain at approximately 600°C during stop process. Strain ratio ϕ was defined as a ratio of torsional strain range, $\Delta\gamma$ to normal strain range, $\Delta\varepsilon$. The TMF tests

Table 2 Mechanical property of used material

	Proof Stress (MPa)	Tensile Stress (MPa)	Elonga -tion (%)	Reduction of area (%)
R.T.	835.7	1000.3	6.4	7.4
870°C	469.8	747.1	19.6	28.1

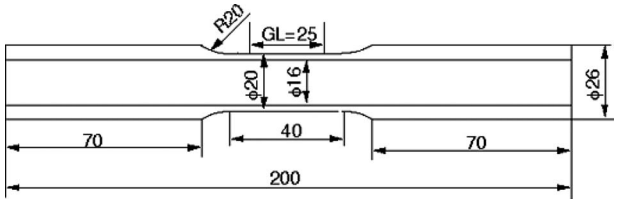

Fig. 1 Biaxial TMF test specimen geometry

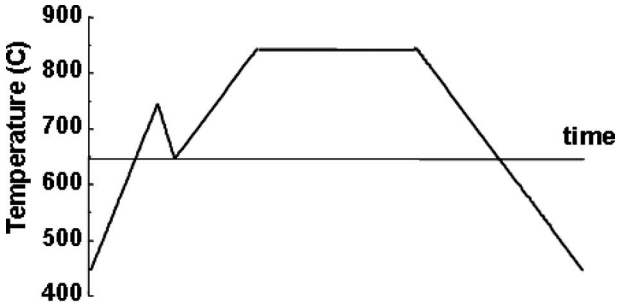

a) Temperature-Time

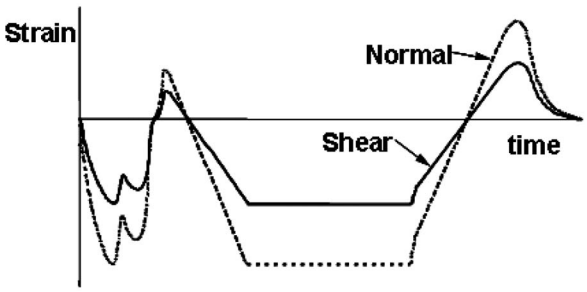

b) Strain-Time

Fig. 2 Blade wave form TMF test condition

were performed ranging from $\phi=0$ to ∞ and Mises equivalent strain range, $\Delta\varepsilon m=0.5-1.3\%$. The TMF tests were performed with and without hold times at the maximum temperature. 6 min and 60 min strain hold times were introduced in the TMF tests of $\phi=0$ and 0.5. In addition to the Blade wave form, the in-phase wave form of strain and temperature tests were conducted for comparison under $\phi=0.5$ and $\Delta\varepsilon m=0.7\%$ with and without strain hold time. In the in-phase test, the strain reaches the maximum tensile value at the maximum temperature. Failure life was defined as the number of cycles where either normal or torsional stress reduced to 75% of their maximum values.

Test Results and Discussion

Failure Appearance. The longitudinal section of the substrate specimens tested under $\phi=0.5$ with different strain hold times is shown in Fig. 3(*a*). It is seen that many cracks initiated from the outer surface in all test conditions, and oxidation layer of the surface and in the crack became thicker as the hold time increased. It suggests that cracking of the oxidation layer may accelerate crack initiation of the substrate. On the other hand, subcracks initiated from the surface were not seen in the longitudinal section of the failure specimen tested under the in-phase conditions. Typical longitudinal section of the specimen tested under the in-phase condition is shown in Fig. 4. Microvoids like creep voids observed in polycrystalline materials [4–6] were observed at dendrite boundaries indicating creep damage accumulated by introducing tensile strain hold even in the DS material. Similar small holes were observed at secondary dendrite boundaries normal to the loading direction in the DS specimens previously tested under the creep and creep-fatigue conditions [7].

The longitudinal section of the coated specimens tested under $\phi=0.5$ with different strain hold times is shown in Fig. 3(*b*). It is seen that many cracks initiated from the coating surface in all test conditions, and some of them arrested in the coating, some of them arrested at the boundary between the coating and the substrate, and some of them penetrated into the substrate. It suggests

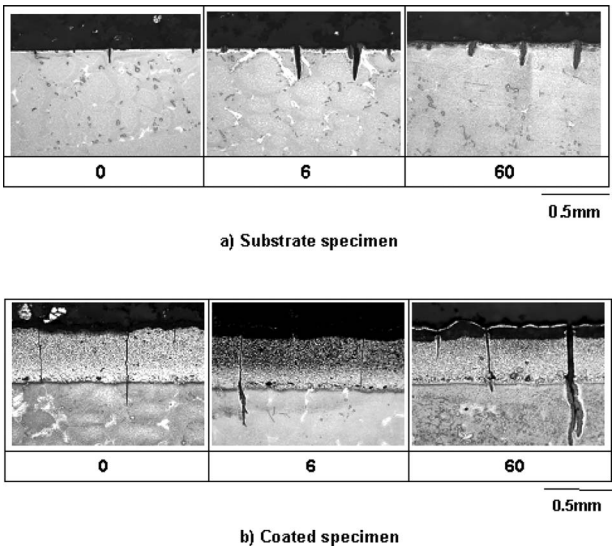

Fig. 3 Axial cross sections of failure specimens under the Blade wave form

that cracks initiated at the coating surface do not go through the coating immediately but gradually propagate in the coating by the crack tip sliding mechanism due to cyclic loading. The arrested cracks in the coating were also observed in the actual used gas turbine blade [8]. Oxidation layer yielded within the penetrated cracks into the substrate and thickness of the layer increases with increasing strain hold time. Contrary, less oxidation layer yielded within the cracks located in the coating, and β-phase depleted zone was observed around the crack resulted from the reaction between Al phase and oxygen. White lightening portion can be seen at the coating surface in the specimen tested with 60 min strain hold time. Similar lightening was observed in the actual used blade in which aluminized treatment was made on the CoCrAlY coating. This may be caused by reduction in Al contents due to yielding and spallation of oxidation layer by spending β-phase in surface Al layer resulted in transforming to the γ-phase from the β-phase.

From the failure surface observation of the Blade wave form tests by a scanning electron microscope, relatively flat surfaces having striation like trace marks were observed independent of the strain hold period indicating the main crack propagated by the fatigue loading. On the other hand, similar grain boundary surface having grain boundary facets and secondary cracks normally observed in the creep damaged failure surface of the polycrystalline materials was formed under the in-phase condition. It is presumed that the rough failure surfaces in the in-phase tests were yielded by crack propagation through the dendrite boundaries, which have microvoids due to creep damage accumulation. Failure surfaces of the coated materials tested under the Blade wave form showed the flat surfaces indicating that the crack propagated continuously

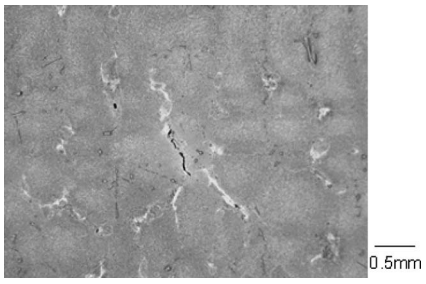

Fig. 4 Typical microvoids on dendrite boundaries

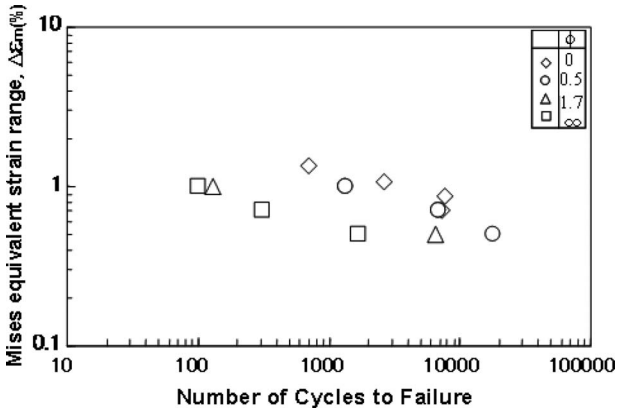

Fig. 5 Biaxial TMF life correlated with Mises equivalent strain range

from the coating to the substrate. A semielliptical shape crack was observed on the coating failure surface tested under the Blade wave form with 6 min hold time indicating the crack propagated by the fatigue mechanism.

TMF Life Property of Substrate. Figure 5 shows relationship between the failure life of the Blade wave form without hold time and Mises equivalent strain range. Although the TMF life of the polycrystalline IN738LC was well correlated with Mises equivalent strain range [1], the TMF life of the DS superalloy gives large scatter depending on ϕ. The TMF life under $\phi=\infty$ is the shortest and the TMF life under $\phi=0$ is the longest.

Based on the previous studies, it was suggested that reason why fatigue failure life under biaxial stress condition depends on the ϕ was that not only the maximum shear strain but also normal strain on the maximum shear strain contributes to crack initiation and propagation [9,10]. The TMF life increases with increasing normal strain on the maximum shear strain for the present DS material, which is a reverse tendency of the 304 stainless steel tested before [10]. This is mainly because crack initiation and propagation resistance becomes weaker as the maximum shear strain direction close to the solidified direction in the DS materials. In other words, contribution of the maximum shear strain to crack initiation and propagation is much larger than that of the normal strain on the maximum shear strain plane. In this study, the equivalent shear strain range, $\overline{\Delta\gamma}$, which is function of the maximum shear strain range, $\Delta\gamma_{\max}$, and normal strain range on the maximum shear plane, $\Delta\varepsilon_n$, was applied to correlate the biaxial TMF life. Generally, as the maximum shear strain yields in arbitrary direction against solidified direction under pure torsional condition in the DS material, difference of failure resistance depends on the relative location between the maximum shear and solidified directions. For the case of the blade, the maximum normal strain yields in solidified direction with superposition of small shear strain [2]. The axial and torsional strain conditions using DS material in this study correspond to normal strain in the radial direction and shear strain in the circumferential direction in actual blades.

The $\overline{\Delta\gamma}$ is derived from isolife curves on the Γ-plane, which consists of the $\Delta\gamma_{\max}$ and $\Delta\varepsilon_n$ on x and y axes, respectively. Isolife curves of the biaxial TMF of the DS material on the Γ-plane were obtained, as shown in Fig. 6. From the isolife curves, the $\overline{\Delta\gamma}$ was derived as Eq. (1).

$$\frac{\overline{\Delta\gamma}}{2} = ((\Delta\gamma_{\max}/2)^2 - 6.7\Delta\varepsilon_n{}^2)^{1/2} \quad (1)$$

The biaxial TMF life correlated with the $\overline{\Delta\gamma}$ is shown in Fig. 7. The biaxial TMF life is well correlated with $\overline{\Delta\gamma}$ without showing strain ratio dependency as observed in the relation between the

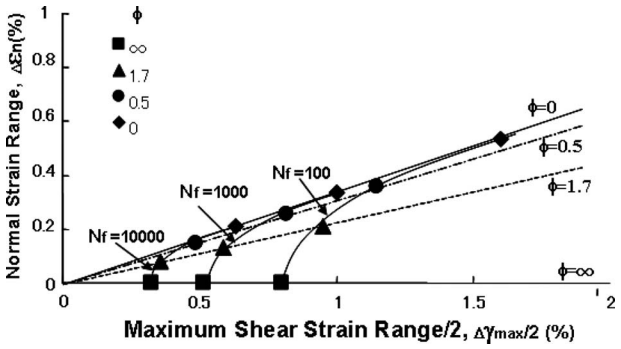

Fig. 6 Γ-plane obtained from TMF life of DS superalloy

life and the Mises equivalent strain range. The relation between the biaxial TMF life and $\overline{\Delta\gamma}$ is expressed as follows.

$$N_j = 2.83 \times 10^{-5} \overline{\Delta\gamma}^{-3.78} \tag{2}$$

The above equation was approximated by the straight line using present test results. Although the TMF life at lower strain ranges may be longer than that given by the equation, conservative prediction can be made.

Strain Hold Effect on Biaxial TMF Life. Figure 8 shows comparison of the biaxial TMF life at a strain range of 0.5% with and without hold time in the Blade wave form and the in-phase wave forms. Failure life in the Blade wave form reduced to 1/5 by introducing 6 min strain hold time. However, failure life reduction is only 3/4 from 6 min to 60 min hold time, indicating that significant life reduction does not occur by elongating the

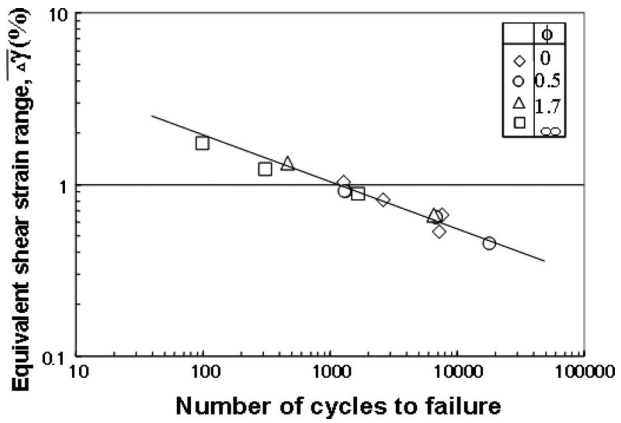

Fig. 7 Biaxial TMF life correlated with the equivalent shear strain range, $\overline{\Delta\gamma}$

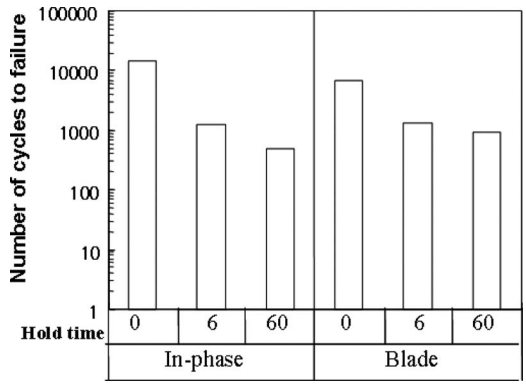

Fig. 8 Strain hold time effect on biaxial TMF life

hold time. Life reduction in the Blade wave form is considered to be caused by an increase in the maximum tensile stress due to relaxation during the compression hold, prompt crack initiation in the substrate induced by cracking of oxide film occurred during tensile process, and certain creep damage accumulated during compression hold period. Since the difference of the maximum tensile stress values between 6 min and 60 min hold time is not significant, the main cause of life reduction may be cracking of the oxide film. On the other hand, the biaxial TMF life in the in-phase wave form reduced to 1/10 by introducing 6 min hold time and the failure life of the 60 min hold time is 1/2 of the 6 min hold time, indicating that significant life reduction occurs by increasing strain hold time at the maximum temperature. As microvoids and cracks were observed on the dendrite boundaries in the longitudinal section of the failure specimens, life reduction may be caused by the creep damage during the hold time.

The nonlinear damage accumulation (NLDA) model [11] was applied to predict the biaxial TMF life under the strain hold condition. It has already been demonstrated that the biaxial TMF lives under strain hold condition of the IN 738LC were predicted by the NLDA model in the previous study [1]. Life prediction equations derived from the NLDA model are expressed by the following equations.

$$N_f = (-1 + \sqrt{1 + 2DcN_f})/Dc \tag{3}$$

$$Dc = \alpha_{sl} D_{sl} + \alpha_{gb} D_{gb} \tag{4}$$

$$D_{sl} = \frac{\Delta\varepsilon_{sl}}{\varepsilon_f}, \quad D_{gb} = \frac{\Delta\varepsilon_{gb}}{\varepsilon_f} \tag{5}$$

where D_{sl} and D_{gb} are so called "grain boundary sliding creep damage" and "grain boundary void creep damage," respectively, $\Delta\varepsilon_{sl}$ and $\Delta\varepsilon_{gb}$ are accumulated creep strains corresponding to grain boundary sliding and grain boundary diffusion, ε_f is the grain boundary creep ductility, and α_{sl} and α_{gb} are damage factors related to D_{sl} and D_{gb}. Definitions of parameters and factors are described elsewhere [11]. Although the DS material does not have any grain boundaries normal to the stress axis macroscopically, microvoids and cracks were observed on the dendrite boundaries. This means that the concept of grain boundary creep damage in the NLDA can be applied to the creep damage in the DS material. The transition of the creep strain rate from the grain boundary sliding damage to the grain boundary void damage during tensile strain hold was determined as 10^{-6} 1/s, which is the same as that of the IN 738LC. ε_f was determined as 0.065 from the uniaxial creep tests of the DS material. As the voids on the dendrite boundary were not observed in the Blade wave form, the entire creep strain accumulated during hold time was assumed to contribute to the grain boundary sliding creep damage. α_{sl} was determined as 1.0 from the strain hold test results in the Blade wave form and α_{gb} was determined as 25 from the in-phase wave form tests. The biaxial TMF life prediction result by the NLDA model is shown in Fig. 9. The biaxial TMF lives were predicted within a factor of 1.5 on observed lives, indicating that the NLDA model can be applied to life prediction of the biaxial TMF of the DS superalloy.

Influence of Coating on Biaxial TMF Life. Figure 10 shows comparison of the biaxial TMF life without hold time against $\overline{\Delta\gamma}$ between the substrates and the coated specimens. The biaxial TMF life of the coated material normalized by that of the substrate is shown in Fig. 11. The biaxial TMF life of the coated material is shorter than that of the substrate regardless of the hold time, indicating that the MCrAlY coating gives negative effect on the biaxial TMF life of the substrate. At the Mises strain range from 0.5% to 0.7%, the biaxial TMF life of the coated material reduced to 1/3 to 1/2 from that of the substrate. This should be taken into account for life prediction of actual blades having MCrAlY coating. As shown in Fig. 3(*b*), many cracks from the coating surface were observed in the coating. From the observa-

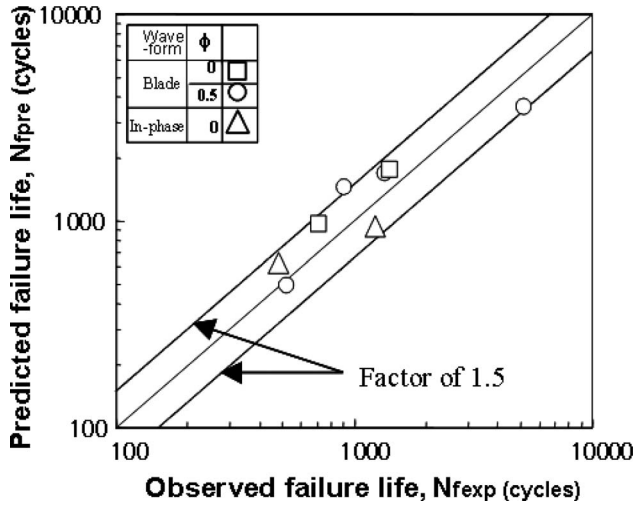

Fig. 9 TMF life prediction results based on the "NLDA model"

tion, life reduction in the coated material seems to be caused by acceleration of crack initiation at the substrate surface due to early penetration of the crack from the coating.

From Fig. 9, the relation between coated material and $\overline{\Delta\gamma}$ is represented by Eq. (6).

$$N_f = 1.94 \times 10^{-5} \overline{\Delta\gamma}^{-3.78} \tag{6}$$

It is seen that life reduction in the coated material decreases with increasing strain hold time from Fig. 10. This is due to reduction in the maximum tensile stress by the stress relaxation, resulting in

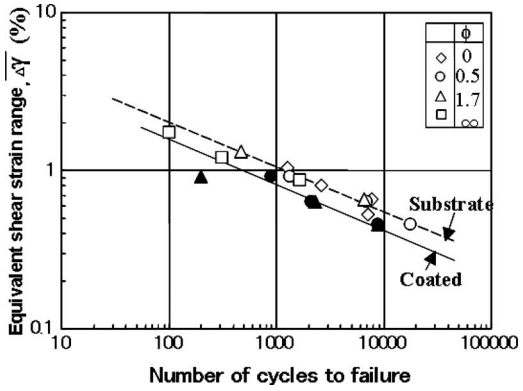

Fig. 10 Comparison of TMF life between substrate and coated material under Blade wave form

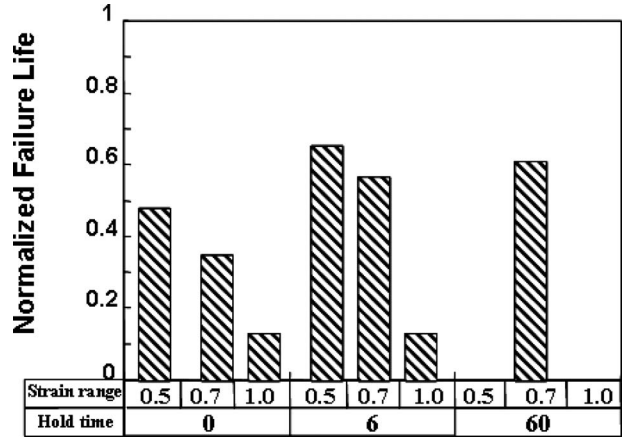

Fig. 11 Strain hold time effect on TMF life of coated material

reducing crack propagation rate in the coating and delaying crack initiation at the substrate. Life prediction of the coated material was made by using the NLDA model based on the failure life and $\overline{\Delta\gamma}$ relation represented by Eq. (6). As a result, the biaxial TMF life of the coated material was predicted within a factor of 1.5.

Conclusions

Biaxial (TMF) tests have been conducted on the DS material, which is used as first row blades in 1300°C class gas turbines. Failure appearance and life property are studied, and effects of strain hold time and MCrAlY coating on the TMF failure life were discussed based on the experimental results. The main results obtained in this study were as follows.

1. The biaxial TMF lives without strain hold time were not correlated with the Mises equivalent strain range, showing large scatter of the data. Equivalent shear strain range, $\overline{\Delta\gamma}$, was derived from the isolife curves of the biaxial TMF on the Γ-plane, and the biaxial TMF lives were well correlated with $\overline{\Delta\gamma}$.
2. The biaxial TMF life under the Blade wave form, which simulates actual blade surface condition, reduced by introducing only 6 min strain hold time at the maximum temperature. It was suggested that the life reduction was caused by an increase in mean tensile stress. On the other hand, life reduction increases with increasing strain hold time in the in-phase wave form. This is due to accumulation of creep damage during the hold time, resulting in initiation of creep voids and microcracks on the dendrite boundaries.
3. The biaxial TMF life of the MCrAlY coated material is shorter than that of the substrate regardless of with and without strain hold time. It was suggested from observation of the specimen cross section that life reduction in the coated material was caused by acceleration of crack initiation at the substrate surface due to early penetration of the cracks from the coating.

References

[1] Ogata, T., and Yamamoto, M., 2001, "Life Evaluation of IN738LC Under Biaxial Thermo-Mechanical Fatigue," *Proceedings of 6th International Conference on Biaxial and Multiaxial Fatigue and Fracture*, M. de Freitas, ed., ESIS, Lisbon, pp. 839–848.

[2] Ogata, T., Sakai, T., Yaguchi, M., Fukutomi, H., and Takahashi, T., 2002, "Analytical and Nondestructive Damage Assessment of Gas Turbine Blade," *Proceedings of International Conference on "Advances in Life Assessment and Optimization of Fossil Power Plants*," EPRI, Florida.

[3] Ogata, T., and Nomoto, A., 2002, "Effect of CoCrAlY Coating on Thermo-Mechanical Fatigue of Inconel 738LC," *Proceedings of International Conference on Fatigue 2002*, EMAS, Stockholm.

[4] Hales, R., 1980, "A Quantitative Metallographic Assessment of Structural Degradation of Type 316 Stainless Steel During Creep-Fatigue," Fatigue Fract. Eng. Mater. Struct., **3**, pp. 339–356.

[5] Ogata, T., and Arai, M., 1998, "Continuous Observations of Creep-Fatigue Damage Process," Fatigue Fract. Eng. Mater. Struct., **21**, pp. 873–884.

[6] Imamura, K., Ogata, T., and Yamamoto, M., 2002, "Evaluation of High Temperature Strength Properties of a Long-Term Service Exposed Rotor," *Proceedings of International Conference on "Advanced in Life Assessment and Optimization of Fossil Power Plants*," EPRI, Florida.

[7] Yamamoto, M., Yaguchi, M., and Ogata, T., 2000, "Development of High Temperature Strength Evaluation Method for Nickel-Based Directionally Solidified Superalloy," Denchuken Report No. T99024, in Japanese.

[8] Viswanathan, R., Schiebel, J., and Gandy, D. W., 2000, "Life Management System for Combustion Turbine Blades and Vanes," "Life Assessment of Hot Section Gas Turbine Components," IOM Communications, pp. 249–269.

[9] Brown, M. W., and Miller, K. J., 1973, "A Theory for Fatigue Failure Under Multiaxial Stress-Strain Conditions," Proc. Inst. Mech. Eng., **187**, pp. 745–755.

[10] Nitta, A., Ogata, T., and Kuwabara, K., 1989, "Fracture Mechanism and Life Assessment Under High-Strain Biaxial Cyclic Loading of Type 304 Stainless Steel," Fatigue Fract. Eng. Mater. Struct., **12**, pp. 77–92.

[11] Ogata, T., and Nitta, A., 1994, "Creep-Fatigue Damage Assessment Model for Boiler and Turbine Materials in Fossil Power Plant," ASME PVP-Vol. 276, pp. 97–105.

Parametric Studies on Dynamic Performance of Hybrid Airfoil Bearing

Manish Kumar

Daejong Kim[1]
e-mail: djkim@tamu.edu

Mechanical Engineering,
Texas A&M University,
College Station, TX 77843

Airfoil bearings offer many advantages over oil-lubricated bearings, but they have reliability issues during start/stops (wear) and limited heat dissipation capability. To address these issues, a hybrid airfoil bearing (HAFB) combining hydrodynamic airfoil bearing with hydrostatic lift was introduced previously by one of the authors of this paper. Their studies show that HAFB has superior performance compared to its hydrodynamic counterpart in load capacity and cooling performance. In this article, the bearing stiffness and damping coefficients of HAFB are calculated using a linear perturbation method developed for HAFB. Simulations showed that feed parameter and supply pressure affect the dynamic characteristics of HAFB. With an increase in either the supply pressure or the feed parameter, the rotor centers itself and hence one sees a decrease in direct stiffness. Simulations showed that the cross-coupled stiffness could be reduced by increasing either the supply pressure or the feed parameter. Direct damping showed increasing trend with the supply pressure and the feed parameter. Frequency-domain analysis of the bearing coefficients was also performed. The direct damping showed marginal changes with supply pressure but showed rapid increase with increasing excitation frequencies. The damping converged to null values for all the pressures for supersynchronous excitations. The loss in damping with high stiffness values for high frequency excitation is a typical hardening effect of gas bearings. In almost all the cases, there are rapid decreases in cross-coupled stiffness and damping and the values show converging trends in supersynchronous regime. [DOI: 10.1115/1.2940354]

Keywords: airfoil bearing, hydrostatic, hybrid, perturbation analysis, stability

Introduction

Airfoil bearings have been successfully used in high speed microturbomachinery such as turbocharger/generators, aircraft air cycle machines [1], and fuel cell microgas turbine (MGT) [2]. These bearings not only offer very low friction during operation but also circumvent the need of lubrication system and complex seals. The airfoil bearing consists of a top foil and compliant elastic foundation, which sustains the applied load and provides structural stiffness and damping. The compliant structure can also accommodate misalignments and distortions of the shaft. One of the most commonly used compliant structures is corrugated bump foil. Hydrodynamic pressure is generated when the shaft drags the air between the rotor and the top foil and pushes it against the bump foil creating a thin layer of high pressure gas, which elevates the rotor.

Due to the promising feature of airfoil bearings for oil-free microturbomachinery, extensive investigations have been performed for decades. In the analytical side, Ku and Heshmat [3] presented a theoretical model of bump foil deformation considering friction forces, local interaction forces, and variable load distribution. Dellacorte and Valco [4] introduced a simple "rule of thumb" design guideline for hydrodynamic airfoil bearings to calculate load capacities based on an empirical relation involving speed and bearing size. Peng and Carpino [5] calculated stiffness and damping coefficients of an elastically supported gas foil bearing from linearized dynamic coefficient equations. Peng and Khonsari [6] presented thermohydrodynamic analyses on temperature distribution of the air film and compared them with experimental results. San Andrés and Kim [7] presented 1D and 2D finite element (FE) models to calculate top foil deflections under hydrodynamic pressure. Carpino and Talmage [8,9] developed a fully coupled FE model that solves pressure field and bearing force coefficients considering top foil sagging effect and bump deflection along vertical and horizontal directions. Song and Kim [10] introduced a new elastic foundation consisted of compression springs and present analyticaled and experimental studies on their foil bearings. They also showed that, in general, airfoil bearing with elastic foundation can suppress the transcritical vibration but not the onset of hydrodynamic instability. Their computational model uses time-domain orbit simulation that can predict limit cycle behaviors encountered in many airfoil bearings. In subsequent studies, Kim [11] conducted parametric studies on two different types of air foil bearing (circular and three pads) and investigated the dependence of rotordynamic stability on the distribution of stiffness and damping of the compliant surface. The study shows that rotordynamic characteristics are more sensitive to the overall bearing geometry rather than stiffness and damping distribution within the elastic foundation. More recently, Le Lez et al. [12] presented parametric study on static and dynamic characteristics of the bump foil using FE method. They also presented an analytical model [13] of continuous bump using discrete nodes connected with spring elements to include bump interactions, and applied the model to investigate dynamic behaviors of continuous bumps [14]. Similar nonlinear bump dynamic analysis was also presented by Lee et al. [15] using FE method to model continuous bump foil and Coulomb friction. They also combined the model with prediction of rotor imbalance response.

Numerous experimental investigations were also performed. Dykas and Howard [16] presented thermal runaway phenomena of foil bearings even under lightly loaded cases upon undesirable rotor geometry and thermal gradient of the rotor. Radil et al. [17] showed that very small clearance without adequate cooling can lead to a thermal runway, i.e., film rupture, and reduce the bearing

[1]Corresponding author.

Manuscript received November 25, 2007; final manuscript received March 8, 2008; published online August 21, 2008. Review conducted by Patrick S. Keogh.

load capacity. Song and Kim [10] and Rubio and San Andrés [18] demonstrated in their experimental studies that elastic foundation can lose damping when excitation frequency is above natural frequency of the system defined with equivalent bearing stiffness and mass of a structure (bearing or rotor) under force excitations. Heshmat and co-worker [19–23] highlighted various applications of foil bearings and dampers in ambient-to-high temperature operations.

The extensive research on airfoil bearings for decades has provided valuable design guidelines for airfoil bearings and resulted in some successful industrial applications [1,24,25]. However, the foil bearings have a limited reliability issue that comes from dry rubbing during start/stops and limited heat dissipation capability. One may assume the air has very small viscosity compared to oil, and thus cooling is not as critically important as oil-lubricated hydrodynamic bearings. However, very small clearance and high speed operation can generate fairly good amount of heat that cannot be neglected. Regardless of lubricating media, the hydrodynamic pressure provides only load support but not dissipation of parasitic energy generated by viscous drag or heat input from other parts of the machine. It is well-known that the purpose of continuous oil circulation in oil-lubricated hydrodynamic bearings is to dissipate parasitic energy generated within/transferred to the bearing, and keep the oil temperature within a certain limit so that the oil can generate necessary hydrodynamic pressure.

Very often, critical advantages of airfoil bearing are claimed as no lubrication circuit and little friction (no heating), providing a "simple" environment-friendly solution. However, considering the two critical functions (load support and parasitic energy dissipation) of the bearings, the hydrodynamic airfoil bearing cannot be as simple as claimed. In fact, the success of bump foil bearings in industrial applications owes to continuous air cooling through the space behind the top foil and adequate surface coatings that can survive dry rubbings during start/stops. Especially when the hydrodynamic airfoil bearings are operated under large external loads, the importance of cooling and wear-resistant coating is more evident.

Kim and Park [26] introduced the first concept of hybrid airfoil bearing (HAFB) with hydrostatic orifices formed on the top foil. The HAFB combines benefits of airfoil bearings and hydrostatic air bearings, providing very little friction during start/stops and stable operation due to damping of the elastic foundations.

The motivation of the HAFB comes from the critical limitation of current cooling method of hydrodynamic airfoil bearings and dry rubbing issue. Firstly, the notorious thermal runaway of foil bearings comes from mainly rotor thermal expansion/distortion rather than the bearing itself. Because the cooling air passes through the space behind the top foil, the cooling efficiency is low and can consume a lot of air to achieve the required cooling performance. Furthermore, the current cooling method cannot be effective in controlling the rotor thermal distortion. However, in HAFB, the hydrostatic air line to the inside of the bearing clearance serves as an effective energy dissipation mechanism via forced convective cooling of both the bearing and rotor surfaces. Another major advantage of HAFB is that it can eliminate the chronic wears of the top foil and rotor during startups and stops. Their experimental works [26] show that because of the hybrid nature of HAFB, the hydrostatic air serves as a very effective cooling mechanism without any additional cooling air. They demonstrated higher load capacity of HAFB as compared to its hydrodynamic counterpart (with traditional cooling). They showed that the airflow rate used for hydrostatic operation is less than 10% of the cooling airflow used for hydrodynamic foil bearing. In addition, their predictions using orbit simulations showed increased stability of the rotor bearing system due to external pressurization.

The present study is a continuation of the work done by Kim and Park [26], where they adopted time-domain orbit method to investigate the rotordynamic performance of a rigid rotor in cylindrical mode. Ideally, airfoil bearings (and most air bearings) are best suited for high speed rigid rotors (with large shaft diameter) operating below their first bending critical speed. However, airfoil bearings are often considered with flexible rotors with locally large shaft diameter in regions where the bearings are located. Adoption of time-domain nonlinear orbit simulations to these flexible rotors supported on airfoil bearings require enormous computational time and thus is not practical. For general synchronous rotordynamic vibration analyses, stiffness and damping coefficients of the airfoil bearings can be used with commercial rotordynamic software.

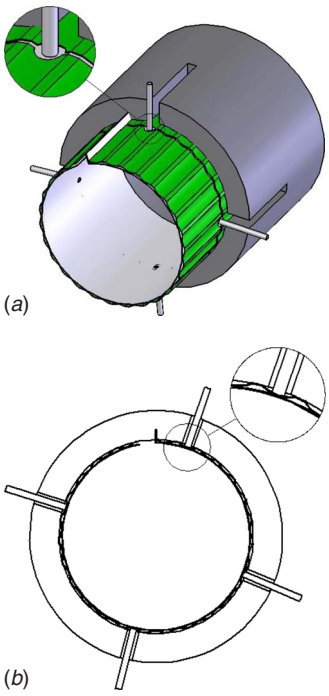

Fig. 1 Schematic description of circular HAFB and coordinate system for analysis (*a*) schematic description of HAFB (*b*) coordinate system for analysis

Scope of the Paper

As pointed out earlier, nonlinear time-domain rotordynamic analyses on a flexible rotor supported by airfoil bearings require intense computational effort. As a preliminary design step, usage of bearing stiffness and damping coefficients with commercial rotordynamic software can reduce the computational time and provide quick design guidelines of the whole rotor-bearing system.

In this article, the bearing stiffness and damping coefficients of HAFB are calculated using a linear perturbation method developed for HAFB. The initial study focuses on circular HAFB with a single continuous top foil supported by bump foils (Fig. 1), which are under manufacturing for experimental evaluations of load capacities and imbalance response. This article also includes a parametric study, which outlines the dependence of the stiffness and damping coefficients on various design parameters such as supply pressure (P_s), feed parameter (Γ_s), excitation frequency (ν), and bearing number (Λ).

Hybrid Airfoil Bearings (HAFBs)

The bearing shown in Fig. 1(*a*) has a single continuous top foil and a two bump foil strips. External pressurization is supplied through four feed tubes, which directly discharge air through the top foil to the bearing clearance. Circumferential arrangement of the feed tubes is shown in Fig. 1(*b*). The feed tubes are located at θ=72 deg, 166 deg, 247 deg, and 341 deg. The purpose of the

Table 1 Bearing parameters

Bearing diameter, $2R$	38.1 mm
Bearing axial length, L	38.1 mm
Nominal clearance, C	32 μm
Bump stiffness per unit area	4.7 GN/m^3
Top foil thickness	100 μm

unsymmetrical placement of the feed tubes is to put the orifices on top of the bumps, as described in Fig. 1. Table 1 shows the dimensions of the bearing, and the stiffness in the table was evaluated using the formula for free-free proposed in Ref. [27].

Solution Methodology

Figure 2 shows the grid scheme for the control volume and the dynamic mass balance.

In Fig. 2, $\dot{m}_s$ is the air mass flow rate through the orifice. Also, $\dot{m}_x$ and $\dot{m}_z$ from the classical formulation of Couette–Poiseuille flows are defined as

$$\dot{m}_x = \left(-\frac{1}{12\mu}\frac{p}{R_g T}h^3\frac{\partial p}{\partial x} + \frac{p}{R_g T}\frac{hR\omega}{2}\right)\Delta z \tag{1}$$

$$\dot{m}_z = \left(-\frac{1}{12\mu}\frac{p}{R_g T}h^3\frac{\partial p}{\partial z}\right)\Delta x \tag{2}$$

In the above equations, x is a local coordinate attached on the bearing surface along the circumferential direction, z is a coordinate in the axial direction, h is film thickness, p is pressure, μ is viscosity of air, R_g is the gas constant of air, and T is the temperature of supplied air. The dynamic mass balance of the control volume under transient condition gives

$$(\dot{m}_x + \dot{m}_z)_{\text{in}} + \dot{m}_s - (\dot{m}_x + \dot{m}_z)_{\text{out}} = \frac{d(\rho V)}{dt} = \frac{\Delta x \Delta z}{R_g T}\frac{d(ph)}{dt} \tag{3}$$

Substituting values from Eqs. (1) and (2) in the above equation, we get the Reynolds equation for compressible fluids with hydrostatic supply

$$\frac{\partial}{\partial x}\left(-\frac{1}{12\mu}ph^3\frac{\partial p}{\partial x} + \frac{R\omega}{2}ph\right) + \frac{\partial}{\partial z}\left(-\frac{1}{12\mu}ph^3\frac{\partial p}{\partial z}\right) + \frac{\partial (ph)}{\partial t} = \frac{R_g T \dot{m}_s}{\Delta x \Delta z} \tag{4}$$

Nondimensionalizing Eq. (4) yields

$$\frac{\dot{M}_s}{\Delta\theta\Delta Z} + \frac{\partial}{\partial\theta}\left(PH^3\frac{\partial P}{\partial\theta}\right) + \frac{\partial}{\partial Z}\left(PH^3\frac{\partial P}{\partial\theta}\right) = \Lambda\frac{\partial}{\partial\theta}(PH) + 2\Lambda\nu\frac{\partial}{\partial\tau}(PH) \tag{5}$$

where $P=p/P_a$, $\theta=x/R$, $Z=z/R$, $\tau=\omega_s t$, $H=h/C$, bearing number $\Lambda=6\mu\omega/p_a(R/C)^2$, excitation frequency ratio $\nu=\omega_s/\omega$, and $\dot{M}_s = 12\mu R_g T\dot{m}_s/p_a^2 C^3$. ω_s is the excitation frequency. See Fig. 1 for more details on the coordinate system used.

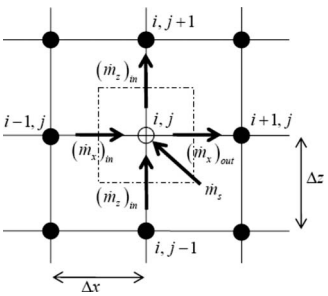

Fig. 2 Mesh defined for analysis

Assuming the flow through the orifice as an isentropic process, the mass flow rates of the compressible fluid for the choked and unchoked conditions are given by the following.

Unchoked: $P/P_s > (2/k+1)^{k/(k-1)} = 0.5283$.

$$\dot{M}_S = \Gamma_s P_s H\left[\frac{2k}{k-1}\left(\left(\frac{P}{P_s}\right)^{2/k} - \left(\frac{P}{P_s}\right)^{(k+1)/k}\right)\right]^{1/2} \tag{6}$$

Choked: $P/P_s < (2/k+1)^{k/(k-1)} = 0.5283$.

$$\dot{M}_S = \Gamma_s P_s H\left(2\frac{k}{k+1}\right)^{1/2}\left(\frac{2}{k+1}\right)^{1/(k-1)} \tag{7}$$

where $\Gamma_s = 12\mu C_d A_0\sqrt{R_g T}/p_a C^3$ is a feed parameter, P_s is the supply pressure, k is the ratio of specific heats for air, and C_d is a discharge coefficient. In the feed parameter, A_0 is the reference orifice curtain area defined as $A_0 = \pi d_0 C$, where d_0 is the orifice diameter.

For the perturbation analysis, equation of motion for the elastic foundation corresponding to the computational finite domain should be developed. For simplicity, the inertia of the elastic foundation is neglected and it is further assumed that each elastic foundation supports the corresponding top foil independently. Then, the equation of motion of elastic foundation becomes

$$pA_b = k_b u + c_b\frac{du}{dt} \tag{8}$$

where k_b and c_b are the effective stiffness and viscous damping coefficients of the elastic foundation, and A_b is the effective area for the elastic foundation. Note that the stiffness per unit area in Table 1 is k_b/A_b. Assuming the motion of elastic foundation is sinusoidal in normal operating conditions, the equivalent viscous damping coefficient can be found from structural damping model through structural loss factor, i.e., $\eta = c_b\omega_s/k_b$. For the present simulations, the structural loss coefficient of 0.25 is used for every elastic foundation. The chosen structural loss factor is from the empirical results of well-designed bump foil bearings [18,28,29]. Writing the bump dynamic equation in nondimensional form yields

$$P = K_b U + C_b\nu\frac{dU}{d\tau} \tag{9}$$

where $K_b = k_b C/p_a A_b$ and $C_b = c_b C\omega/p_a A_b$ are nondimensional bump stiffness and damping coefficients, respectively. Linearizing Eqs. (5) and (9), as illustrated in Refs. [5,11,30], yields the zeroth and first order equations.

Zeroth order:

$$\frac{\partial}{\partial\theta}\left(P_0 H_0^3\frac{\partial P_0}{\partial\theta}\right) + \frac{\partial}{\partial z}\left(P_0 H_0^3\frac{\partial P_0}{\partial z}\right) + \left(\frac{2k}{k-1}\right)^{1/2}\frac{\Gamma_s P_s}{\Delta\theta\Delta Z}f(H_0, P_0) = \Lambda\frac{\partial}{\partial\theta}[P_0 H_0] + 2\Lambda\nu\frac{\partial}{\partial\tau}[P_0 H_0] \tag{10}$$

First order:

$$\frac{\partial}{\partial\theta}\left[P_0 H_0^3\frac{\partial P_\alpha}{\partial\theta}\right] + \frac{\partial}{\partial Z}\left[P_0 H_0^3\frac{\partial P_\alpha}{\partial Z}\right] + \left(\frac{2k}{k-1}\right)^{1/2}\frac{\Gamma_s P_s}{\Delta Z\Delta\theta}\left[\left.\frac{\partial f(P,H)}{\partial P}\right|_{P_0,H_0} P_\alpha + \left.\frac{\partial f(P,H)}{\partial H}\right|_{P_0,H_0}\left(\frac{P_a}{K_b(1+\eta i)} + g_\alpha\right)\right] \times \frac{\partial}{\partial\theta}\left[\left(3H_0^2 P_0\left(\frac{P_a}{K_b(1+\eta i)} + g_\alpha\right) + H_0^3 P_\alpha\right)\left(\frac{\partial P_0}{\partial\theta}\right)\right] + \frac{\partial}{\partial Z}\left[\left(3H_0^2 P_0\left(\frac{P_a}{K_b(1+\eta i)} + g_\alpha\right) + H_0^3 P_\alpha\right)\left(\frac{\partial P_0}{\partial Z}\right)\right]$$

$$= \Lambda \frac{\partial}{\partial \theta}\left(P_0\left(\frac{P_a}{K_b(1+\eta i)} + g_\alpha \right) + P_\alpha H_0 \right)$$
$$+ 2\Lambda \nu i P_0\left(P_0\left(\frac{P_a}{K_b(1+\eta i)} + g_\alpha \right) + P_\alpha H_0 \right) \quad (11)$$

where $\alpha = X, Y$ and $g_X = \cos\theta$, $g_Y = \sin\theta$. Note that P_X and P_Y are complex number with real and imaginary parts. The values of $f(H_0, P_0)$, $\partial f(P,H)/\partial P|_{P_0,H_0}$, and $\partial f(P,H)/\partial H|_{P_0,H_0}$ for choked and unchoked conditions are given below.

Choked:

$$f(H_0, P_0) = H_0 \quad (12)$$

$$\left.\frac{\partial f(P,H)}{\partial P}\right|_{P_0,H_0} = 0 \quad (13)$$

$$\left.\frac{\partial f(P,H)}{\partial H}\right|_{P_0,H_0} = 1 \quad (14)$$

Unchoked:

$$f(H_0, P_0) = H_0\left(\left(\frac{P_0}{P_s}\right)^{2/k} - \left(\frac{P_0}{P_s}\right)^{(k+1)/k} \right)^{1/2} \quad (15)$$

$$\left.\frac{\partial f(P,H)}{\partial P}\right|_{P_0,H_0} = H_0 \frac{1}{2}\left(\left(\frac{P_0}{P_s}\right)^{2/k} - \left(\frac{P_0}{P_s}\right)^{(k+1)/k} \right)^{-1/2} \left(\frac{2}{k}\left(\frac{1}{P_s}\right)^{2/k} P_0^{((2/k)-1)} - \frac{k+1}{k}\left(\frac{1}{P_s}\right)^{(k+1)/k} P_0^{1/k} \right) \quad (16)$$

$$\left.\frac{\partial f(P,H)}{\partial H}\right|_{P_0,H_0} = \left(\left(\frac{P_0}{P_s}\right)^{2/k} - \left(\frac{P_0}{P_s}\right)^{(k+1)/k} \right)^{1/2} \quad (17)$$

Once the zeroth order equation is solved for equilibrium pressure profile and film thickness (P_0, H_0), the first order equation is solved to get the perturbed pressures. The perturbed pressure profile is then used to find the frequency-dependent stiffness and damping coefficients.

$$\begin{bmatrix} k_{xx} & k_{xy} \\ k_{yx} & k_{yy} \end{bmatrix} = \frac{W_0}{C}\begin{bmatrix} K_{xx} & K_{xy} \\ K_{yx} & K_{yy} \end{bmatrix} = -\frac{W_0}{C}\frac{R}{2L}\int\int \begin{bmatrix} \mathrm{Re}(P_x)\cos\theta & \mathrm{Re}(P_y)\cos\theta \\ \mathrm{Re}(P_x)\sin\theta & \mathrm{Re}(P_y)\sin\theta \end{bmatrix} \quad (18)$$

and

$$\begin{bmatrix} c_{xx} & c_{xy} \\ c_{yx} & c_{yy} \end{bmatrix} = \frac{W_0}{C\omega_s}\begin{bmatrix} C_{xx} & C_{xy} \\ C_{yx} & C_{yy} \end{bmatrix} = -\frac{W_0}{C\omega_s}\frac{R}{2L}\int\int \begin{bmatrix} \mathrm{Im}(P_x)\cos\theta & \mathrm{Im}(P_y)\cos\theta \\ \mathrm{Im}(P_x)\sin\theta & \mathrm{Im}(P_y)\sin\theta \end{bmatrix} \quad (19)$$

As mentioned earlier, both the zeroth order and first order equations were solved using finite volume methods with under relaxation. The grid size used for the numerical analysis was 104 in the circumferential direction and 14 in the axial. The grid independency study of the numerical method followed in the present article was done in Refs. [10,11]. The convergence criterion for the pressure was $\max(P_{i,j}^{n+1} - P_{i,j}^n / P_{i,j}^n) \le 5 \times 10^{-6}$, where n is the iteration index.

The equilibrium position of the rotor was found using orbit simulations, which are detailed in Ref. [11]. For the zeroth order solution, the 1D analytical beam model proposed by Kim and Park [26] was further advanced [31] to consider top foil sagging effect more accurately using three computational grid points between two bumps, as shown in Fig. 3. Figure 4 shows the pressure profile obtained by numerically solving the zeroth order equation. The peaks in the pressure profile are due to hydrostatic feed lines, the highest of which corresponds to the loaded region of the bearing.

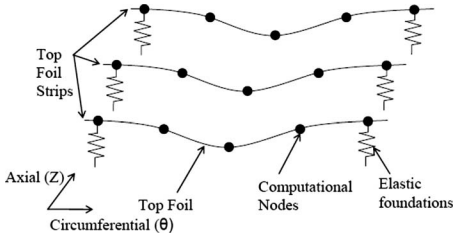

Fig. 3 Grid scheme

In the first order solution, the pressure and film thickness solved in the zeroth order solution are used as inputs. The first order solution uses the same computational grid, as shown in Fig. 3, but the stiffness per unit area (Table 1) and corresponding equivalent damping are assigned to each computational grid point. The perturbed pressure in X-direction obtained from the first order equation is shown in Fig. 5.

Results and Discussion

The bearing stiffness and damping coefficients of HAFB were calculated with various feed parameters (Γ_s), excitation frequencies (ν), supply pressures, and bearing numbers (Λ). Note that the feed parameter and bearing number are directly proportional to the orifice diameter and rotational speed, respectively.

First, the effect of various feed parameters on the bearing coefficients was investigated for different supply pressures at fixed bearing number of $\Lambda = 1.25$ (rotor speed of about 30,000 rpm). For all the simulations, the bearing is under a static load of 60 N in the X-direction (see Fig. 1).

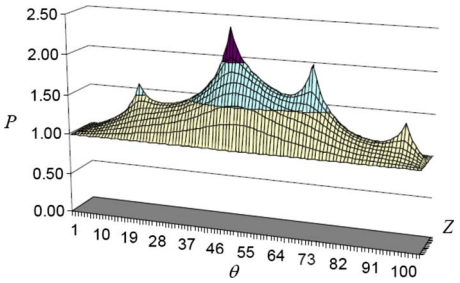

Fig. 4 Zeroth order pressure profile, $\Lambda = 1.25$, and static load 60 N

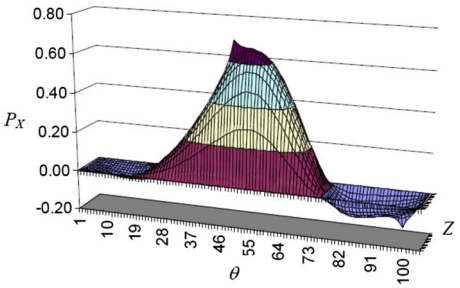

Fig. 5 First order perturbed pressure profile (P_X), $\Lambda = 1.25$, and static load 60 N

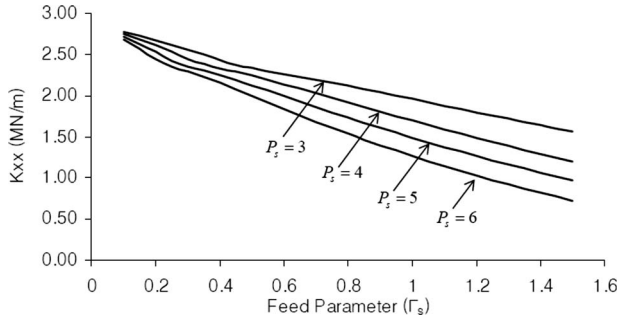

Fig. 6 Predicted direct stiffness coefficients versus feed parameter (Γ_s) with increasing supply pressure, $\Lambda = 1.25$

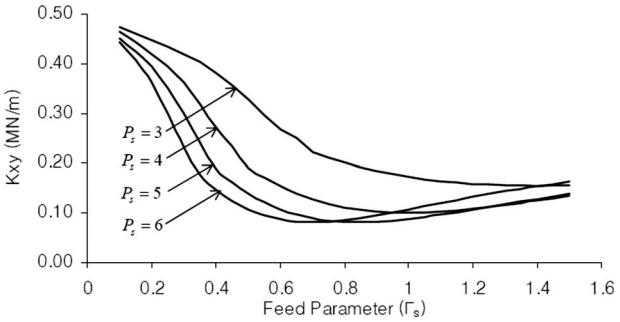

Fig. 9 Predicted cross-coupled stiffness coefficients versus feed parameter (Γ_s) with increasing supply pressure, $\Lambda = 1.25$

Figure 6 depicts the predicted synchronous direct stiffness coefficients versus the feed parameter. In general, the direct stiffness decreases with the increase in either the feed parameter or the supply pressure. At very low feed parameters, the stiffness value for all the pressures converge to a single value, which corresponds to the hydrodynamic case. The decrease in stiffness with supply pressure or feed parameter can be explained from journal eccentricity and attitude angles, as shown in Figs. 7 and 8.

Figure 7 shows the predicted journal eccentricity versus the feed parameter (Γ_s) for increasing supply pressures. Because of the fixed load, journal eccentricity decreases with an increase in either the feed parameter or the supply pressure. Since the feed parameter is directly proportional to the orifice size, one can conclude that the larger the orifices size, the smaller the eccentricity for a given pressure.

Figure 8 presents the trend in attitude angle versus the feed parameter for different supply pressures. Higher supply pressure or increase in feed parameter decreases the attitude angle. At relatively high values of the supply pressure and feed parameter, the attitude angle is negative. This can be attributed to the fact that with higher pressures more hydrostatic thrust is developed on the rotor. Now with more thrust and with the present arrangements of the feed tubes (Fig. 1), the rotor moves into the second quadrant corresponding to θ, yielding negative attitude angles. The small attitude angle in HAFB is very beneficial in terms of reducing cross-coupled stiffness and hydrodynamic instability.

Figure 9 shows predicted synchronous cross-coupled stiffness, which contributes to destabilizing forces in the gas bearings. In general, the cross-coupled stiffness decreases with supply pressure. For all pressures, stiffness values decrease for $\Gamma_s < 0.8$, after which they increase gradually.

Figures 10 and 11 show the direct and cross-coupled damping coefficients, respectively. Both damping coefficients increase slightly with an increase in feed parameter. The variation is not much for the direct damping coefficient, but significant for the cross-coupled damping for $\Gamma_s < 1$. The damping coefficients show a converging trend at higher feed parameters for all the supply pressures. The cross-coupled damping crosses over at $\Gamma_s = 1.2$, as shown in Fig. 11. This can be attributed to the fact that the higher the pressure, the earlier the cross-coupled damping becomes in-

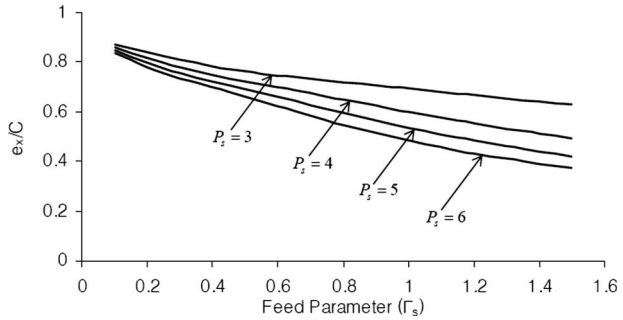

Fig. 7 Predicted journal eccentricities versus feed parameter (Γ_s) with increasing supply pressure, $\Lambda = 1.25$

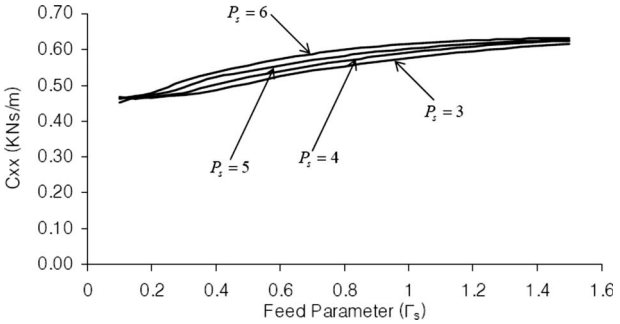

Fig. 10 Predicted direct damping coefficients versus feed parameter (Γ_s) with increasing supply pressure, $\Lambda = 1.25$

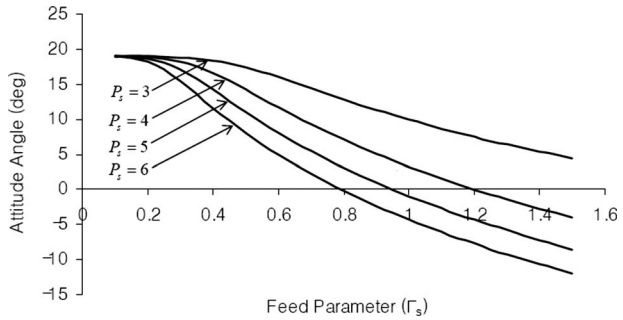

Fig. 8 Predicted attitude angle versus feed parameter (Γ_s) with increasing supply pressure, $\Lambda = 1.25$

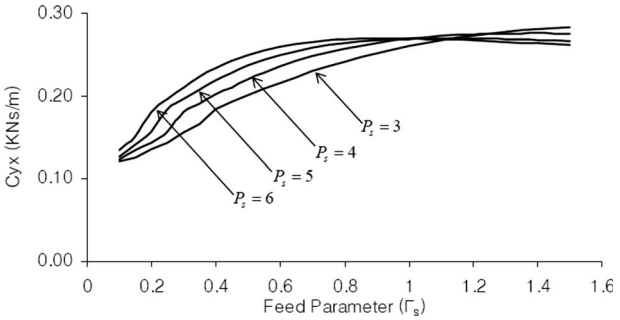

Fig. 11 Predicted cross-coupled damping coefficients versus feed parameter (Γ_s) with increasing supply pressure, $\Lambda = 1.25$

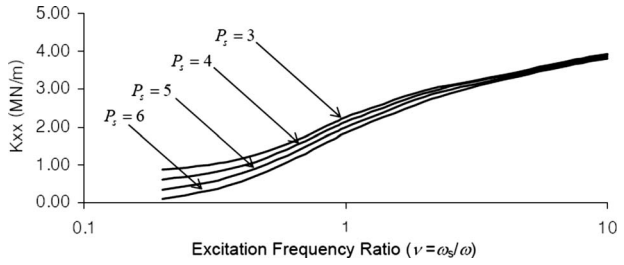

Fig. 12 Predicted direct stiffness coefficients versus excitation frequency ratio with increasing supply pressure, $\Lambda=1.25$

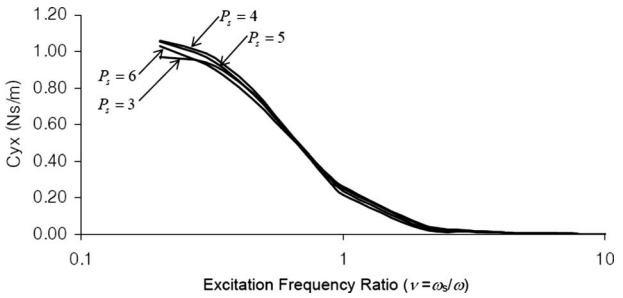

Fig. 15 Predicted direct stiffness versus excitation frequency ratio with increasing supply pressure, $\Lambda=1.25$

sensitive to increasing feed parameter. The crossover happens because damping, in the case of $P_S=6$, becomes insensitive to feed parameter much earlier as compared to $P_S=3$.

Figure 12 depicts the predicted direct stiffness coefficients versus the excitation frequency ratio (ν) at increasing supply pressures. Stiffness coefficients increase for $\nu<1$ but show converging trend at high excitation frequency ratios. In general, at low ν, lower pressures give higher stiffness values but the variation is not much with the supply pressure at higher frequencies. Cross-coupled stiffness versus ν is shown in Fig. 13. The cross-coupled stiffness is rather high at $\nu<1$ with rapid decrease with ν. However, the cross-coupled stiffness is almost independent of the ν for $\nu>1$.

Frequency-dependency characteristics of direct and cross-coupled damping coefficients are shown in Figs. 14 and 15, respectively. Both damping coefficients show a decreasing trend with an increase in ν at low ν and are almost frequency independent at higher excitation frequencies. The damping coefficients show a converging trend toward null value at high ν. The loss of damping is accompanied by large direct stiffness coefficients at high ν (Fig. 12) showing a typical hardening effect of gas bearings.

Figure 16 shows the predicted nondimensional journal eccentricity versus the bearing number (Λ) for increasing supply pressures at feed parameter $\Gamma_S=0.6$. In general, the nondimensional eccentricity decreases with an increase in either the bearing number or supply pressure. The variation in eccentricity with supply pressure is large at low bearing number (low rotational speeds). At high bearing numbers, the variation decreases and the nondimensional eccentricity shows a converging trend.

Figures 17 and 18 show the direct and cross-coupled stiffness coefficients, respectively. The direct stiffness coefficient increases rapidly at low bearing numbers but shows a converging trend at high bearing numbers. In general, lower supply pressures give higher stiffness values and this can be attributed to the fact that eccentricity increases with decreasing supply pressure (Fig. 16). Cross-coupled stiffness decreases rapidly with bearing number, and in general, higher pressures give lower cross-coupled stiffness values.

Figure 19 depicts the direct damping coefficient with increasing bearing number for various supply pressures. The direct damping coefficients decrease rapidly for $\Lambda<1$ after which a converging trend is observed. Direct damping values are almost independent

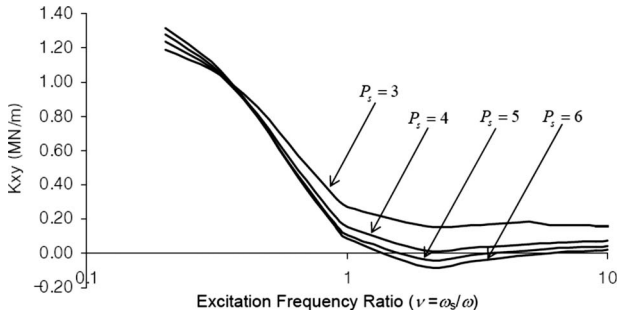

Fig. 13 Predicted cross-coupled stiffness coefficients versus excitation frequency ratio with increasing supply pressure, $\Lambda=1.25$

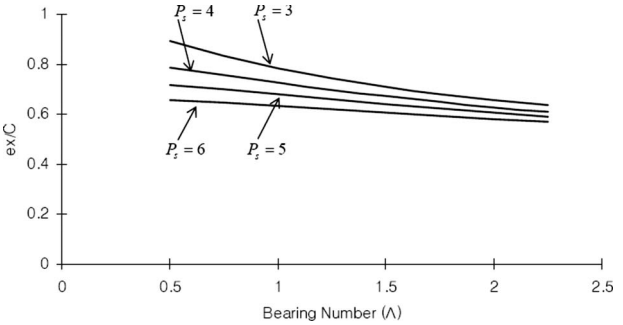

Fig. 16 Predicted journal eccentricities versus bearing number (Λ) with increasing supply pressure, $\Gamma_s=0.6$

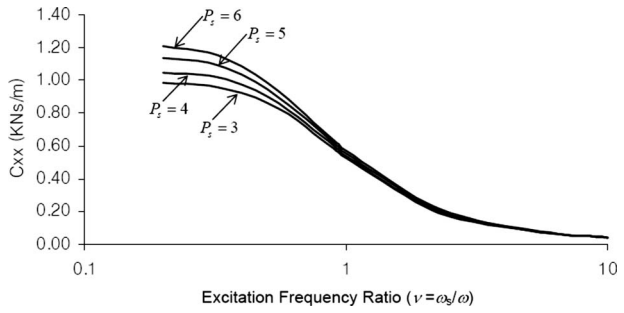

Fig. 14 Predicted direct damping versus excitation frequency ratio with increasing supply pressure, $\Lambda=1.25$

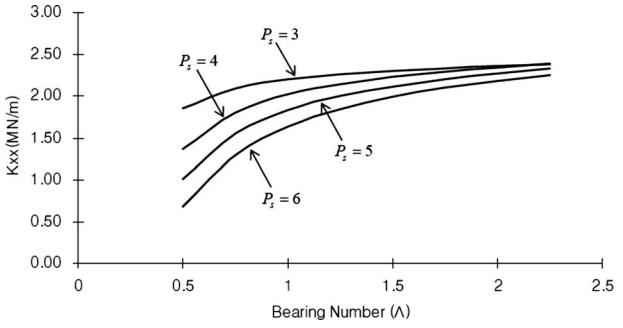

Fig. 17 Predicted direct stiffness versus bearing number (Λ) with increasing supply pressure, $\Gamma_s=0.6$

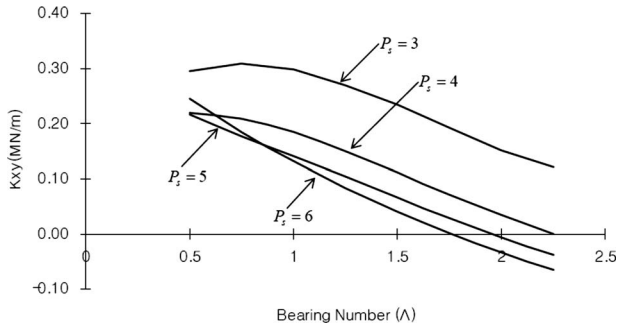

Fig. 18 Predicted cross-coupled stiffness versus bearing number (Λ) with increasing supply pressure, Γ_s=0.6

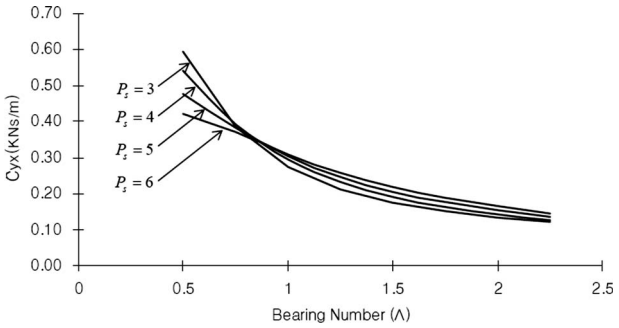

Fig. 20 Predicted cross-coupled damping versus bearing number (Λ) with increasing supply pressure, Γ_s=0.6

of variation in supply pressure. Cross-coupled damping (Fig. 20) shows a similar variation with bearing number, although in this case they change with the supply pressure.

Conclusions

Simulations show that feed parameter and supply pressure affect the dynamic characteristics of airfoil bearings. With the increase in either the supply pressure or the feed parameter, the rotor centers itself, and hence, one sees a decrease in direct stiffness. Simulations show that the cross-coupled stiffness, which contributes as a destabilizing force, could be reduced by increasing either the supply pressure or the feed parameter. There is a critical feed parameter (Γ_s) beyond which the cross-coupled stiffness is minimal. Direct damping, which dampens the vibrations in the bearing, showed increasing trend with the supply pressure and the feed parameter. The predictions demonstrate that the instabilities in air bearings can be attenuated by modulating the supply pressure.

Frequency-domain analysis of the bearing coefficients showed expected trends. The direct damping showed marginal changes with supply pressure but showed rapid increase with increasing excitation frequencies. The damping converged to null values for all the pressures for supersynchronous excitations. The loss in damping with high stiffness values for high frequency excitation is a typical hardening effect of gas bearings. In almost all the cases, there are rapid decreases in cross-coupled stiffness and damping and the values show converging trends in supersynchronous regime.

The trends one sees in bearing stiffness coefficients with increasing bearing number are basically the trends with increasing rotational speed. In general, direct stiffness increases rapidly at low bearing number but showed converging trends at high bearing number. It is interesting to note that the cross-coupled stiffness and direct damping decrease with increasing bearing number and cross-coupled stiffness are, in fact, negative for high pressures. Note that the destabilizing force is proportional to $K_{XY} - C_{XX}/\omega$ and with the trends in cross-coupled stiffness and direct damping, there is a possibility that backward whirl may be induced in the bearing. However, this backward whirl will always be dominated by forward whirl generated by the imbalance.

Nomenclature

A_b = effective area that one bump covers
A_{cont} = computational area surrounding the orifice
C = nominal clearance
C_b = nondimensional damping coefficient of elastic foundation
c_b = bump damping
H = nondimensional film thickness
h = film thickness
$H_{X,Y}$ = perturbed film thickness gradient in X and Y
k = ratio of specific heats for air
K_b = nondimensional stiffness coefficient of elastic foundation
k_b = bump stiffness
m_r = rotor mass
$\dot{M}_s$ = nondimensional mass flow rate
$\dot{m}_s$ = mass flow rate
P = nondimensional pressure
p_a = ambient pressure
P_0 = nondimensional zeroth order pressure
p_s = supply pressure

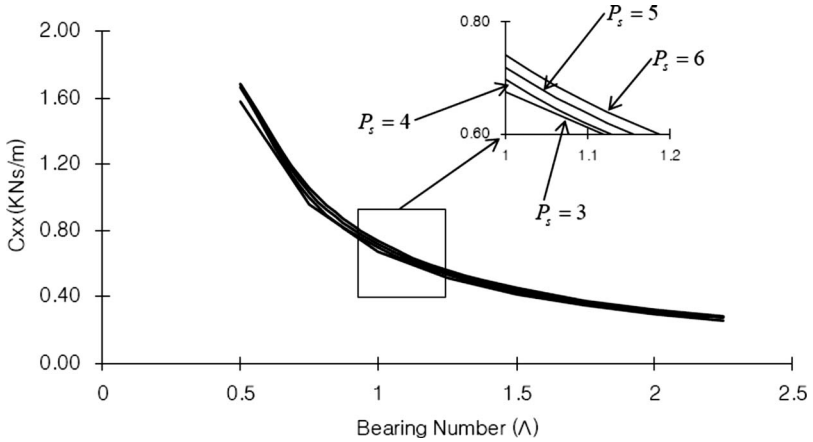

Fig. 19 Predicted direct damping versus bearing number (Λ) with increasing supply pressure, Γ_s=0.6

$P_{X,Y}$ = nondimensional perturbed pressure gradient in X and Y
R = bearing radius
R_g = gas constant of air
T = gas temperature
U = nondimensional bump deflection
u = bump deflection
Z = nondimensional axial coordinate
ΔH = nondimensional perturbed film thickness
ΔP = nondimensional perturbed pressure field
η = structural loss factor
Λ = bearing number
μ = air viscosity
ν = excitation frequency ratio (EFR)
θ = circumferential coordinate
τ = nondimensional time
ω = rotor speed
ω_s = excitation frequency

References

[1] Agrawal, G. L., 1997, "Foil Air/Gas Bearing Technology-An Overview," ASME Paper No. 97-GT-347.
[2] Costamagna, P., Magistri, L., and Massardo, A. F., 2001, "Design and Part-Load Performance of a Hybrid System Based on a Solid Oxide Fuel Cell Reactor and a Micro Gas Turbine," J. Power Sources, **96**, pp. 352–368.
[3] Ku, C.-P., and Heshmat, H., 1992, "Compliant Foil Bearing Structural Stiffness Analysis: Part I-Theoretical Model Including Strip and Variable Bump Foil Geometry," ASME J. Tribol., **114**, pp. 394–400.
[4] DellaCorte, C., and Valco, M. J., 2000, "Load Capacity Estimation of Foil Air Journal Bearings for Oil-Free Turbo-Machinery Applications," STLE Tribol. Trans., **43**(4), pp. 795–801.
[5] Peng, J. P., and Carpino, M., 1993, "Calculation of Stiffness and Damping Coefficients for Elastically Supported Gas Foil Bearings," ASME J. Tribol., **115**(1), pp. 20–27.
[6] Peng, Z.-C., and Khonsari, M., 2006, "A Thermohydrodynamic Analysis of Foil Journal Bearings," ASME J. Tribol., **128**, pp. 534–541.
[7] San Andrés, L., and Kim, T. H., 2006, "Computational Analysis of Gas Foil Bearings Integrating 1D and 2D Finite Element Models for Top Foil," Turbomachinery Laboratory, Texas A&M University, Technical Report No. TRC-B&C-1–06.
[8] Carpino, M., and Talmage, G., 2003, "A Fully Coupled Finite Element Formulation for Elastically Supported Foil Journal Bearings," STLE Tribol. Trans., **46**, pp. 560–565.
[9] Carpino, M., and Talmage, G., 2006, "Prediction of Rotor Dynamic Coefficients in Gas Lubricated Foil Journal Bearings With Corrugated Sub-Foils," STLE Tribol. Trans., **49**, pp. 400–409.
[10] Song, J., and Kim, D., 2007, "Foil Bearing With Compression Springs: Analyses and Experiments," ASME J. Tribol., **129**(3), pp. 628–639.
[11] Kim, D., 2007, "Parametric Studies on Static and Dynamic Performance of Air Foil Bearings With Different Top Foil Geometries and Bump Stiffness Distributions," ASME J. Tribol., **129**(2), pp. 354–364.
[12] Le Lez, S., Arghir, M., and Frene, J., 2007, "Static and Dynamic Characterization of a Bump-Type Foil Bearing Structure," ASME J. Tribol., **129**, pp. 75–83.
[13] Le Lez, S., Arghir, M., and Frene, J., 2007, "A New Bump-Type Foil Bearing Structure Analytical Model," ASME J. Eng. Gas Turbines Power, **129**(4), pp. 1047–1057.
[14] Le Lez, S., Arghir, M., and Frene, J., 2007, "A New Foil Bearing Dynamic Structural Model," *Proceedings of International Joint Tribology Conference*, Paper No. IJTC2007–44110.
[15] Lee, D. H., Kim, Y. C., and Kim, K. W., 2007, "The Dynamic Performance Analysis of Foil Journal Bearings Considering Coulomb Friction: Rotating Unbalance Response," *Proceedings of International Joint Tribology Conference*, Paper No. IJTC2007–44225.
[16] Dykas, B., and Howard, S. A., 2004, "Journal Design Considerations for Turbomachine Shafts Supported on Foil Air Bearings," STLE Tribol. Trans., **47**, pp. 508–516.
[17] Radil, K., Howard, S., and Dykas, B., 2002, "The Role of Radial Clearance on the Performance of Foil Air Bearings," STLE Tribol. Trans., **45**(4), pp. 485–490.
[18] Rubio, D., and San Andrés, L., 2005, "Structural Stiffness, Dry-Friction Coefficient and Equivalent Viscous Damping in a Bump-Type Foil Gas Bearing," ASME Paper No. GT 2005–68384.
[19] Heshmat, H., Walton, J. F., II, and Tomaszewski, M. J., 2005, "Demonstration of a Turbojet Engine Using an Air Foil Bearing," ASME Paper No. GT2005–68404.
[20] Heshmat, H., 2000, "Operation of Foil Bearings Beyond the Bending Critical Mode," ASME J. Tribol., **122**(1), pp. 192–198.
[21] Walton, J. F., and Heshmat, H., 1999, "Application of Foil Bearings to Turbomachinery Including Vertical Operation," ASME Paper No. 99-GT-391.
[22] Heshmat, H., Walton, J. F., DellaCorte, C., and Valco, M. J., 2000, "Oil Free Turbocharger Demonstration Paves Way to Gas Turbine Engine Applications," ASME Paper No. 2000-GT-0620.
[23] Walton, J. F., II, Heshmat, H., and Tomaszewski, M. J., 2004, "Testing of a Small Turbocharger/Turbojet Sized Simulator Rotor Supported on Foil Bearing," ASME Paper No. GT2004–53647.
[24] http://www.microturbine.com
[25] http://www.samsungtechwin.com
[26] Kim, D., and Park, S., 2006, "Hybrid Air Foil Bearings With External Pressurization," ASME Paper No. IMECE2006–16151.
[27] Iordanoff, I., 1999, "Analysis of an Aerodynamic Complaint Foil Thrust Bearing: Method for a Rapid Design," ASME J. Tribol., **121**, pp. 816–822.
[28] Ku, C.-P., and Heshmat, H., 1994, "Structural Stiffness and Coulomb Damping in Compliant Foil Journal Bearing: Parametric Studies," STLE Tribol. Trans., **37**(3), pp. 455–462.
[29] Salehi, M., Heshmat, H., and Walton, J. F., 2003, "On the Frictional Damping Characteristics of Compliant Bump Foils," ASME J. Tribol., **125**, pp. 804–813.
[30] Han, D. C., Park, S. S., Kim, W. J., and Kim, W. J., 1994, "A Study on the Characteristics of Externally Pressurized Gas Bearings," Precis. Eng., **16**(3), pp. 164–173.
[31] Kumar, M., 2008, "Analytical and Experimental Investigations of Hybrid Air Foil Bearing," MS thesis, Texas A&M University, College Station, TX.

Da-Ren Yu
Professor
e-mail: yudaren@hcms.hit.edu.cn

Wei Wang
e-mail: weiwanghit@126.com

Department of of Energy Science and Engineering,
Harbin Institute of Technology,
Harbin 150001, The People's Republic of China

Zhi-Qiang Zhang
Department of Mechanical and Vehicular Engineering,
Beijing Institute of Technology,
Beijing 100081, The People's Republic of China
e-mail: sunwithmoon@bit.edu.cn

Qing-Hua Hu
Department of Energy Science and Engineering,
Harbin Institute of Technology,
Harbin 150001, The People's Republic of China
e-mail: huqinghua@hcms.hit.edu.cn

Xiao-Min Zhao
Department of Mechanical Engineering,
University of Alberta,
Edmonton, Alberta, T6G 2G7, Canada
e-mail: xiaomin1@ualberta.ca

A Case Study for a Turbogenerator Accident Using Multiscale Association

This paper presents a novel method of multiscale association for analyzing a turbogenerator accident having strange behaviors and serious consequence. Wave index (WI) and credibility of sensor fault are proposed based on multiscale analysis of the recorded data, and then the associational degree of WI is used to detect sensor fault. In addition, mechanism models are built to verify that detection. Furthermore, maximum likelihood method and neural network are applied to estimate the confidence interval of the fault sensor and the true signal. The estimation has been used to clearly explain the cause of this accident. [DOI: 10.1115/1.2943149]

1 Introduction

The economic and secure operation of power stations directly affects the reliability of the whole power systems that play a fundamental role in the national economy. Serious accidents in power stations have highly negative impact on power systems. Two of the worst power station accidents, namely, Three Mile Island and Chernobyl Nuclear fuel leakage accidents, affected even the development of the power industries. Other recent major accidents, such as the broken rotor damage of the South China Sea, Japan, and Datong and Qinling, China, and the boiler furnace explosion of Beilun port, China, have resulted in huge economic loss. In power stations, the turbogenerator is one of the most important equipments. However it is so complex that it is impossible to conduct simulations concerning the large number of uncertain factors or to perform destructive tests. Therefore, one must carry out a detailed investigation diagnosis of every serious turbogenerator accident and should study various approaches to avoid similar accidents.

Now many methods of artificial intelligence are used in fault diagnosis (e.g., expert systems and fault trees causal model) [1,2]. An expert system is an accident diagnostic system based on rules [3–6]. Fault tree is a logic tree that propagates primary events or faults to a top level event or a hazard. This is a physical analytical method that is based on the understanding of the mechanism of the process [7,8]. Vibration diagnostic methods, commonly used in equipment accident analysis, detect faults with vibration signals [6,9]. Many other relevant methods, such as directed graph, observer, filters, qualitative simulation, neural network, and statistical estimations, are also used to handle different problems [10–12]. These methods have different characteristics and are usually used together in practice.

Fault diagnosis is hard to work on complex systems, especially those in which some important data are lost or unavailable. As a result, it is important to efficiently recover the process of an accident from incomplete history data. This recovery step is helpful not only to find the cause of the accident but also to design a strategy for preventing similar accidents.

Since a serious turbogenerator accident happened in China, where a rotor of a turbogenerator was broken into eleven segments, it is necessary to study the turbogenerator accident. In this paper, we discuss this turbogenerator accident and determine the key state of the accident with artificial intelligence methods. According to the multiscale features of the turbogenerator, we propose an approach to analyze the accident. In Sec. 2, we briefly describe the scene of the accident. In Secs. 3 and 4 we identify the sensor faults in the accident through multiscale association detection and physical mechanism analysis. Then we quantitatively estimate the key state of the turbogenerator using the maximum likelihood method and neural network technique based on the multiscale structure model of the turbogenerator in Sec. 5. Finally, the accident is well explained according to the state changing process estimated in Sec. 6.

2 Description of the Accident

One 200 MW turbogenerator of a power plant in Northeast China suffered a serious accident. This was a steam reheat unit with triple cylinders and two exhaust hoods, and the structure of

Manuscript received January 2, 2008; final manuscript received April 17, 2008; published online August 22, 2008. Review conducted by Jaroslaw Szwedowicz.

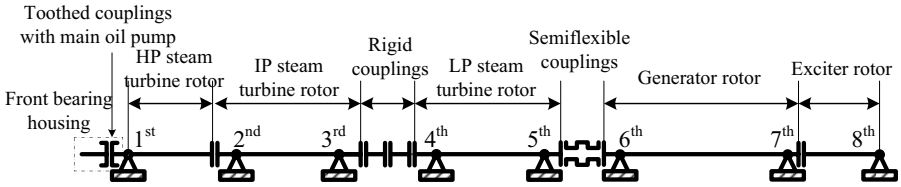

Fig. 1 Rotor shaft structure of the turbogenerator

the rotor shaft is shown in Fig. 1. The control system of the unit was electrohydraulic. Here, the load control was implemented either by the manual control system or by the automatic control system. In the manual control mode, operators manipulate a governor motor according to the output power meter. In the automatic control mode, the load is automatically controlled by an electrohydraulic governor.

The accident is described as follows. The turbogenerator was running normally with a load of 170 MW in the morning. The pressure, the temperature, and the mass flow rate of the main steam were 12.6 MPa, 535°C, and 536.9t/h, respectively. At 1:47:30 (1 h, 47 min, 30 s), the level of lubricants was lower than normal. Then the thermal protection of the power plant started up and caused the load of the power plant to be rejected from 170 MW. After the operators checked the equipments, they thought that there was no problem with the unit. So they set it up again and again, and then the turbogenerator was ruptured about 10 min later. The broken rotor segment at neck on the side close to generator is about 1.5 m. This segment flew away for 35 m. Figure 2 shows one surface of the fracture segments. The third and fourth bearings were damaged, and their upper bearing housings were broken. The fifth to seventh bearings and their housings were corrupted. The exciter bearing was also damaged. As to the turbine, the closures of the roof wear, steam separators, and rotor closures of high-pressure (HP) steam cylinder were seriously worn off. The 21st leaf shedding of cylinder pressure was partially ringed, and the 22nd full-leaf blade tips were worn off about 10 mm. The 27th leaves of the LP cylinder rotor were worn off about 200 mm from the leaf roof, and about 27 leaves in the 32nd level were broken at 15 mm from the leaf bottom. The broken leaves are shown in Fig. 3.

Fig. 2 Front section of the LP rotor

Fig. 3 Fractional leaves of the LP rotor

The process of this accident according to the recall of operators and process data can be described as follows. During the accident investigation process, the operators recalled the accident situation that they inspected the turbogenerator once its load was rejected. Moreover, they considered that the running state was normal. Then they set it up according to operation rules. The operators found the oil pressure of the velocity adjustment to be lower during the manual restarting process. So they suspended the setup. When the oil pressure of the velocity adjustment was recovered, they started the turbine again and found the main steam valves and the reheat valves closed as they were ready to switch from hydraulic control to digital electrohydraulic (DEH) control. Then the turbine was restarted using a hydraulic operation style, and the main steam valves were closed again. At that time, a huge explosion happened and the turbogenerator was damaged. The operators said that they were so tense that they could not memorize the details of the accident process clearly. Therefore the relevant details are not available.

This power plant had installed a recalling accident system (sequence of event (SOE)) to record operating information of switching equipments and a data acquisition system (DAS) to record the process data of the main parameters. The records can be viewed as the most reliable information for the accident analysis. As the

Table 1 Main stream valve recorded by SOE before the accident

Time	State
1:47:30:000	1 IP MSV closing
1:47:30:150	2 IP MSV closing
1:47:30:515	1 HP MSV closing
1:50:36:118	2 HP MSV closing
1:51:24:276	2 HP MSV opening
1:51:26:574	2 IP MSV opening
1:51:32:253	1 IP MSV opening
1:53:37:126	2 HP MSV closing
1:53:37:131	1 IP MSV closing
1:53:37:150	2 IP MSV closing
1:55:29:103	2 HP MSV opening
1:55:32:670	2 IP MSV opening
1:55:36:558	2 IP MSV closing
1:56:08:223	2 HP MSV closing
1:56:10:980	2 HP MSV opening
1:56:14:328	1 HP MSV opening
1:56:27:501	1 HP MSV closing
1:56:27:515	2 IP MSV opening
1:56:27:541	2 IP MSV closing
1:56:27:647	2 IP MSV opening
1:56:29:910	2 HP MSV closing

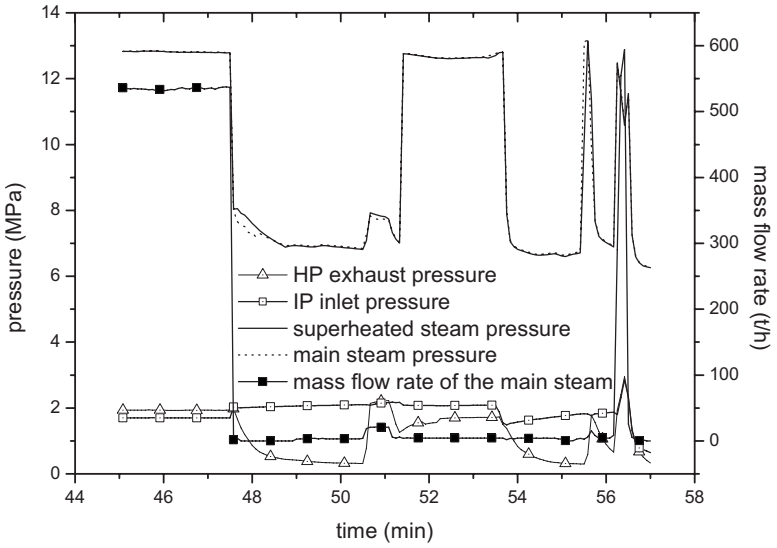

Fig. 4 Steam related parameters of DAS before the accident

turbogenerator is damaged, the parameters relevant to the turbogenerator should be focused on. The parameters in SOE record the switching states of main steam valves. Table 1 shows the data before the accident, where we can see that the valves are frequently switching before the accident. The facts indicate that the turbogenerator has been started up and stopped for many times. The parameters relevant to turbogenerator in DAS record running states of the main steam and rotor. To be more specific, the steam parameters include the mass flow rate and the pressure of the main steam, the outlet pressure of the main steam valve, the pressure of the HP cylinder exhaust steam, the pressure of the reheat valve, the axial displacement, etc. The rotor parameters include the rotor speed, the stator voltage, the excitation voltage, the relative expansions of HP, intermediate-pressure, and low-pressure cylinders, and the vibration of bearings. The values of the parameters before the accident are shown in Figs. 4–8. It can be seen from these figures that the parameters are stable before load rejection. Most of them fluctuate about 8 min after load rejection, and then turn into sudden and dramatic changes. We see that the main steam largely flowed into the turbine cylinders in an instant at 1:56:10, as shown in Fig. 4.

According to these records, we can get the following conclusions. First, from the viewpoint of investigators, the typical fracture interface is caused by tremendous local mechanical stress, and the mechanical stress is caused by the overspeeding of the turbogenerator. Second, according to the recorded data of SOE, the reheat valve started later than the main steam valve when the load was rejected, as shown in Table 1. This abnormality might generate powerful shock waves, which instantly produced the great pressure difference among diaphragms of the LP cylinder. This pressure difference crashed the diaphragms, and the crashed diaphragms gradually caused this accident during the repeat restarts. Third, in terms of records of DAS, as shown in Fig. 4, the main steam flow instantly surged into the turbine cylinders at 1:56:10, and Fig. 5 shows that the rotor speed was still zero before 1:56:10. Then, the rotor speed will normally not exceed 3000 rpm according to the energy equation of the rotor and the mass flow rate of the main steam. So the accident might have been caused by material defects of the rotor. Furthermore, according to the operators' recall, they had carefully examined the plant before they started up the turbogenerator, and they operated the turbogenerator on the operation rule until the accident occurred.

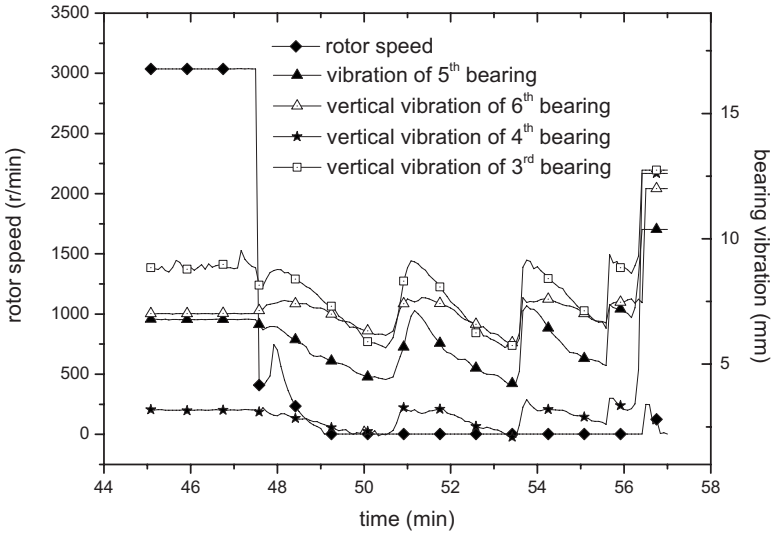

Fig. 5 Rotor related parameters of DAS before the accident: A

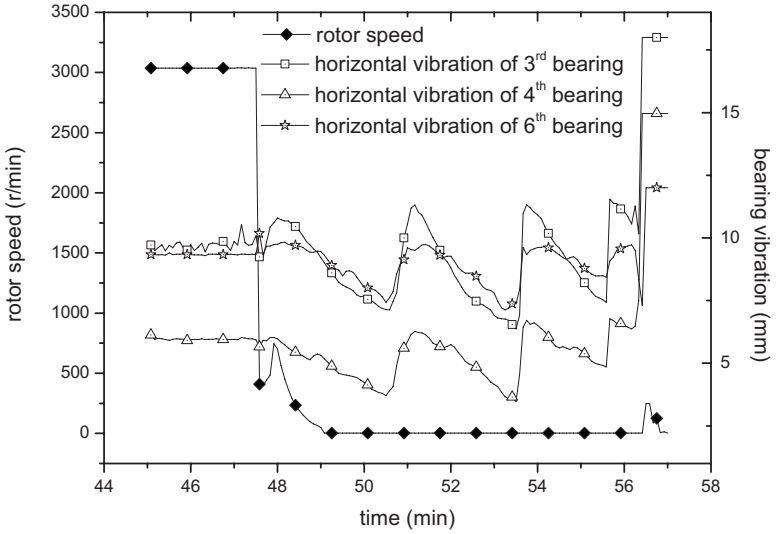

Fig. 6 Rotor related parameters of DAS before the accident: B

We get various judgments based on different sources of information. So the running process needs to be analyzed in detail to understand the relation between the judgments and the trip accident. During the trip accident, the records of DAS might be the most reliable information reflecting the running process, so a more careful analysis of records of DAS is required.

On the other hand, there was an inconsistent idea about whether the turbine was seriously overspeeding. The fracture interface of the rotor shows that the turbine was overspeeding, while the computation of the main steam flow and the rotor speed of DAS shows that it was not overspeeding. We can infer that some failure happened, which the operators did not notice and then the failure might have led to faults in the monitoring system. Therefore the records of DAS may be wrong due to sensor faults. We would analyze whether there are sensor faults just based on the records of DAS. So the most important work is to recover the main process based on the incomplete information in DAS.

3 Sensor Fault Detection

Figures 4–8 show that there are two abrupt points for most signals of DAS at 1:48:00 and 1:56:10. So we can divide the running process into three phases in the time domain. Phase I is before 1:48:00 (the process of the turbine before load rejection), in which all the parameters were normal. This phase can be named the load carrying state where the power plants were still in power supply mode. Phase II is after 1:56:00 (the instant when the process of the turbine at the accident occurred), in which most parameters sharply deviated from the normal operating state. This state consists of a period starting from 1:56:10 at which most signals started to jump until the accident happened. There, often, many other faults adjoint with big changes in the parameters happened. Phase III is the period from 1:48:00 to 1:56:10, that is, the period of transition from normal operation to the accident process between the above two phases. Compared with Phase II, all the signals were in the normal operating range in Phase III. So relations among equipments of the turbogenerator might be stable, and we can detect the fault sensors using these stable relations as redundant information. Phase III would be the key to analyze the evolution of the accident. Because this phase is close to the moment, the accident happened. Next we try to detect the fault sensors by the multiscale association characteristics of the turbogenerator records of DAS, and to verify the result of detection by analyzing the turbine mechanism.

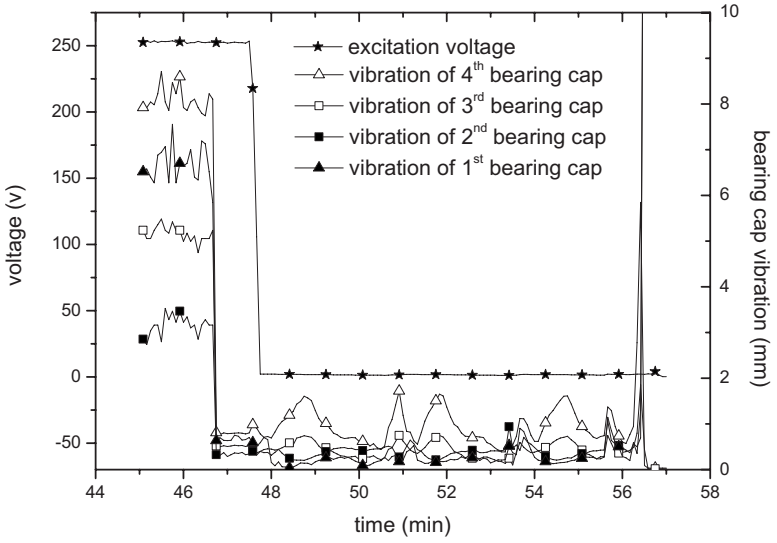

Fig. 7 Rotor related parameters of DAS before the accident: C

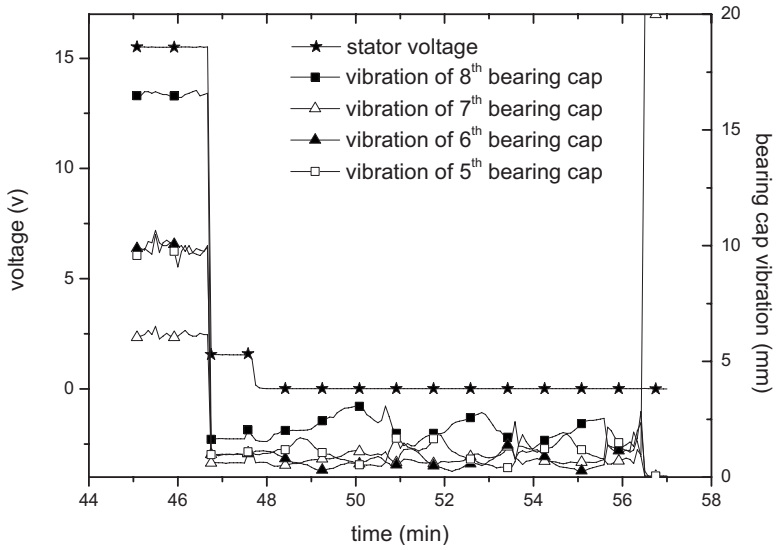

Fig. 8 Rotor related parameters of DAS before the accident: D

3.1 Multiscale Analysis of the Turbine. The operations of the turbogenerator were uncertain before the accident, and the records of DAS were inaccurate, so it is difficult to directly build the model for a diagnosis of sensor fault by the turbine mechanism or running records. However there exists a fact that the sensors are used to measure independent parameters of the turbine, and all the sensors are highly reliable. It is impossible for a large number of sensors to be broken at the same time. Even though there are some fault sensors, the number of fault sensors would be small. Further from the system point of view, the recorded signals contain the partial characteristic information of the measured object and the whole system. So all the signals should contain the system characteristic information. That is, if there are some signals not containing this system information, they may be considered as fault sensors. Based on the description above, if there is any feature that is present in most of the signals of the DAS records, then we can consider that as one of the system characteristic information. Any sensor not containing this feature might be broken.

Wave features are the main characteristics of systems. They reflect the variation of system states. As we know, the turbine system was restarted repeatedly. This leads to the wave of the system. Sensors should have reflected these wave features. We define the wave index (WI) as the ratio of signals containing wave feature in all the signals recorded. That is,

$$\mathrm{WI} = \frac{\text{number of signals with the wave feature}}{\text{number of all signals recorded}}. \tag{1}$$

When WI is close to zero, the wave feature cannot be viewed as system characteristic information. That is, this feature does not reflect the state of turbine system operation. On the contrary, when WI is close to 1 the wave feature can act as system characteristic information.

Multiscale analysis is not only an important method for detecting mutations, but is also good at analyzing the wave in different

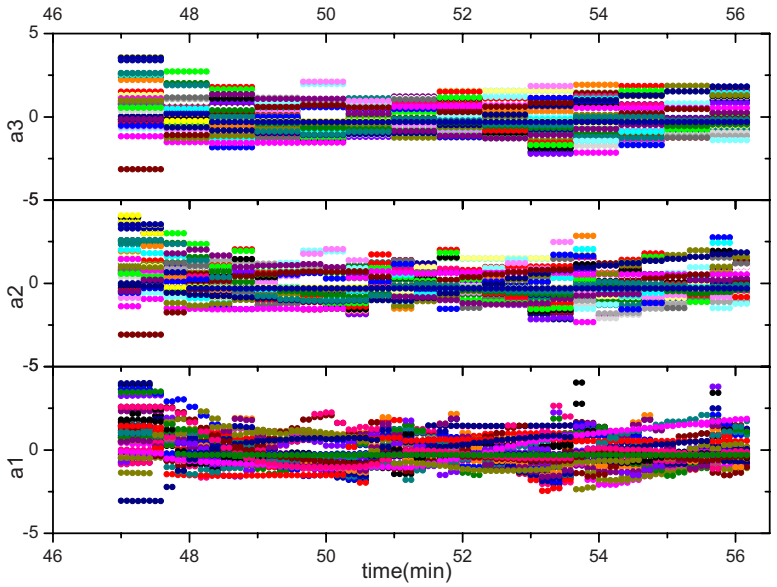

Fig. 9 Wave features of the turbine running process during phase III with multiscale decomposition

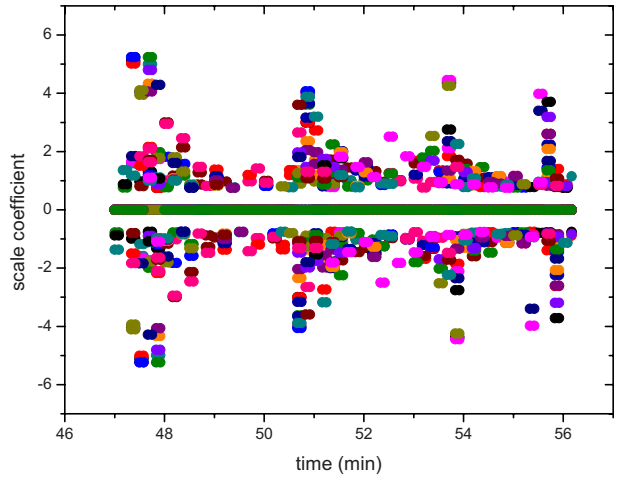

Fig. 10 Medial-scale wave feature of the turbine running process during Phase III

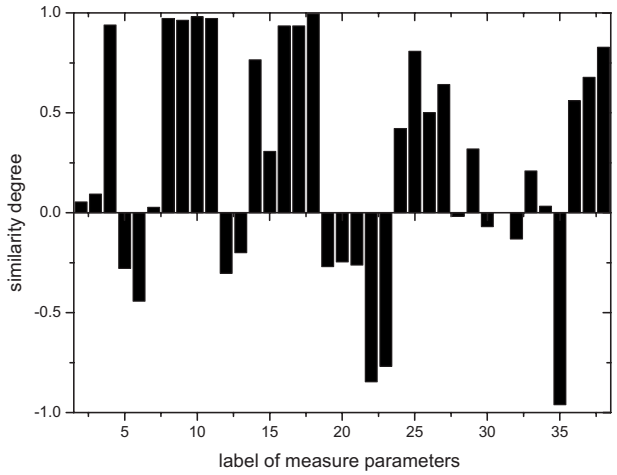

Fig. 11 Similarity distribution of measurement parameters

scales [13]. According to the multiscale analysis, on the small scales, signals mainly contain high-frequency dynamic information reflecting the local dynamic information of the measured object. On the medium and large scales, signals mainly contain low-frequency dynamic information. When analyzing WI for this accident data, we should focus on the system characteristic information. Therefore, we can study the data of DAS through the multiscale analysis method, and then study the WIs on the medium scales. After multiscale decomposition of the data, the wave features on the three scales are shown in Fig. 9. To study the wave features on the medium scale, we set the scale coefficients between two thresholds as zero for clearness and zoom out the medium-scale coefficients of Fig. 9 in Fig. 10. Figure 10 shows that there are four obvious wave features during Phase III.

3.2 Sensor Fault Detection Based on Multiscale Analysis. Four pieces of data wave features at different timings were found, and the WIs got close to 1 by selecting an appropriate threshold as shown in Table 2. So these wave features can be viewed as some of the turbogenerator characteristics. We select any of these wave features, denoted by J. We consider that the sensor is broken down if a sensor does not contain the wave feature J. The credibility of sensor fault (CSF) is equivalent to WI of the single wave feature J. If there are multiple wave features, the CSF should be a function of all the WIs. For example, if there are four wave features, the CSF is computed as

$$\mathrm{CSF} = 1 - \prod_{J=1}^{4} (1 - \mathrm{CSF}_J) = 1 - \prod_{J=1}^{4} (1 - \mathrm{WI}_J) \tag{2}$$

where WI_J denotes the WI for the wave feature J.

The records of DAS have been employed to compute the credibility for all the sensors using Eq. (2). The result is that the CSF of the rotor speed and the line pressure of speed control are equal to 1.000 and 0.9474, respectively, and the CSFs of other parameters are equal to zero. This shows that the sensors of rotor speed and line pressure of speed control possibly suffer malfunction. As rotor speed is one of the important parameters describing the turbogenerator states, the correctness of the DAS records of turbine speed will have greater effect on the analysis of this accident than other signals. The focus of conflict just lies in the rotor speed. Thus, we require to verify whether the rotor speed sensor was broken down before the accident. To confirm the correctness of the CSF analysis result, the judgment that the rotor speed sensor is broken down was to be further verified in the next section.

Table 2 WIs of the four wave features

Wave feature footnote J	1	2	3	4
Wave time	1:48:00	1:51:00	1:5:00	1:56:00
Wave index WI_J	1.0000	0.9737	0.9474	0.9737

4 Verification of the Sensor Fault With Mechanism Model

To make clear whether the rotor speed sensor is broken down, it is necessary to establish the corresponding mechanism model. As input parameters of the model directly impact the complexity of modeling, we first select the related parameters and then verify the fault of the rotor speed sensor.

4.1 Parameter Selection Based on Multiscale Analysis. To verify whether the rotor speed sensor is broken down, we need to construct a model using the rotor speed parameters as output. The complexity of modeling decreases with the increase in the quantity of output parameter information contained in the input parameters. Therefore, we choose the parameters containing a large amount of rotor speed information as input parameters of the model. The problem is that the rotor speed sensor may be broken down, so we cannot directly compare the rotor speed information. With the multiscale association analysis of the turbine, we can construct a benchmark signal that reflects rotor speed information and then compute the similarity degree between the benchmark signal and other measurements. According to the similarity degree, we select the input parameters with great similarity to build the model.

During load rejection, the rotor speed reflected the operational feature of the turbogenerator system. Accordingly, the operational feature of the turbogenerator contains a lot of information of the rotor speed. The medium-scale signals of most of the measurement parameters contain a lot of rotor speed information according to the multiscale analysis of the turbogenerator. Thus, the mathematical expectation with medium-scale signals would contain the turbogenerator feature. We standardize the different measure signals related to turbogenerator. Then we compute their average value at the same time as that of the benchmark signal.

Similarity search is used to find the signals that are most similar to the benchmark [14,15]. Using time-domain similarity algorithm, we can compute the similarity degree of the signals relative to the benchmark signal. The higher the similarity degree is, the more benchmark information this parameter contains. The parameter with great similarity to benchmark can be used as the input of models. Applying the time-domain similarity algorithm to the medium-scale records of DAS, we get the results as shown in Fig. 11. We see that there are many parameters with great similarity

Table 3 Classification of high similar parameters

Vibration signal of rotor	Fifth bearing vibration Vibration of eighth and fifth bearing caps Vertical vibration of third, fourth, and sixth bearings Horizontal vibration of third, fourth, and sixth bearings
Voltage signal of generator	Excitation voltage of generator Stator voltage of generator
Differential expansion signal	Differential expansion of the LP cylinder

degree to the rotor speed.

We select the sensors with great similarity degree and group them according to types and locations of the sensors. These sensors are grouped into three subsets: vibrations of rotor, voltages of generator, and differential expansion of turbine. The results are shown in Table 3. We now verify the fault of rotor speed sensor using the mechanism related to these parameters. Differential expansion parameters can be used to interpret rotor speed with the mechanism of rotor stress and voltage parameters with the mechanism of electric machinery. The mechanisms for rotor stress and electric machinery are clearer than that of vibration. So we verify the fault sensor according to these two mechanisms in the next section.

4.2 Verification With Mechanism of Rotor Stress. The differential expansion of the LP cylinder is the expansion of the LP rotor relative to that of the LP cylinder. According to the mechanism of electric machinery, the differential expansion is caused by the rotor thermal expansion, centrifugal force, axial displacement, and thermal expansion of LP cylinder. Because the exhaust pressure of the LP cylinder is constant after load rejection, the cylinder temperature and the rotor temperature have little change. So we neglect thermal expansions of the rotor and the LP cylinder.

According to the stress mechanism of rotor under the centrifugal force, the rotor deformation by centrifugal force is proportional to the square of rotor speed approximately, i.e.,

$$n^2 \propto 3000(Z_c - Z_{zv}) \tag{3}$$

where n represents rotor speed, and Z_c and Z_{zv} represent differential expansion of LP cylinder and axial displacement, respectively. Using Eq. (3), we can get the rotor speed according to the mechanism of rotor stress, denoted by S_{RS}, as shown in Fig. 12. S_{RS} can reflect the relative change although S_{RS} is only proportional to the actual rotor speed approximately. Figure 12 shows that the S_{RS} fluctuate significantly but the rotor speed of DAS records is still zero.

4.3 Verification With Mechanism of Electric Machinery. To establish the mechanism model of electric machinery for verifying the fault of rotor speed sensor through the excitation voltage, we firstly observe the changes in excitation voltage. Figure 7 shows that excitation voltage declined rapidly from 250 V to zero after load rejection. The fact is that de-excitation was started as the generator was disaggregated by electric power network, and after the transient process of electromagnetism (shorter than 10 s), a weak magnetic field remains in the generator. According to the electrical machinery theory, residual voltage can be induced when the rotor rotates in the remained magnetic field. The residual voltage is approximately proportional to the rotor speed [16] and is recorded as the excitation voltage in DAS. So we get the model electric machinery, as

$$U = Kn \tag{4}$$

where U and n are the excitation voltage and rotor speed, respectively, and K is the coefficient of proportionality. The coefficient K is the inherent characteristic of the turbine, and it is constant. This shows that excitation voltage was proportional to the rotor speed form 1:48:00 to 1:56:10. Because the flow rate of the main steam rapidly decreased to zero after load rejection, the process can be considered as the idle process affected only by frictional drag from the load rejection to the first manual restart. So the proportional coefficient can be determined by the load rejection test and the excitation voltage of the idle process. The variation of rotor speed can be computed by the excitation signal of DAS records and the proportion coefficient. Then the excitation voltage can

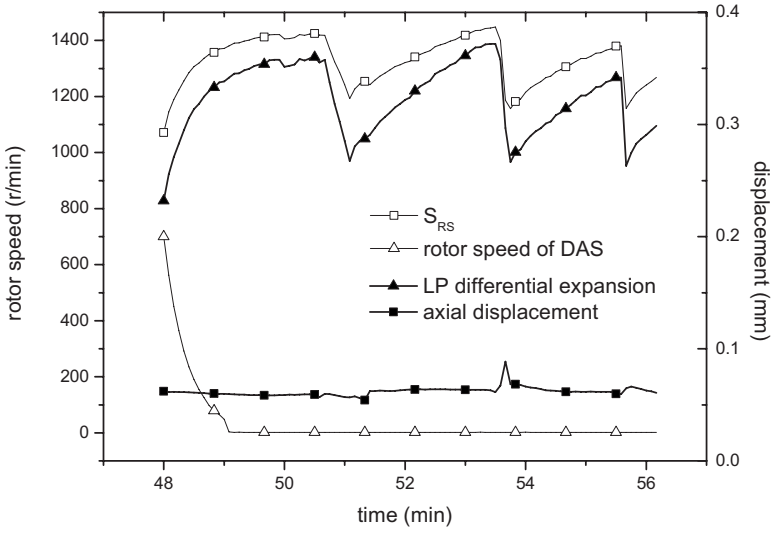

Fig. 12 Verification with mechanism of rotor stress

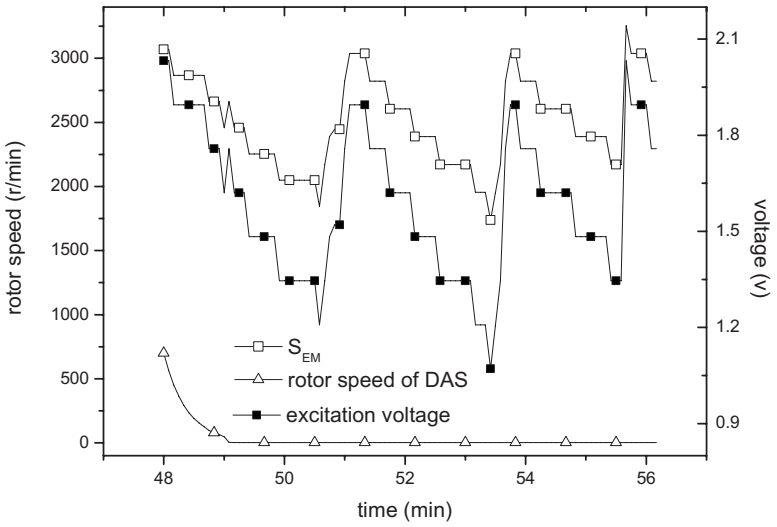

Fig. 13 Verification with mechanism of electric machine

roughly reflect the variation of rotor speed.

Figures 5 and 7 show that the rotor speed and excitation voltage are approximately zero after load rejection. From 1:48:00 to 1:56:10, the WIs of excitation voltage are almost 1. This can be explained by the residual voltage fluctuation. Therefore there is fluctuation in the rotor speed as the speed is proportional to the excitation voltage. A rotor speed is calculated through the mechanism model of electric machinery. We name it as rotor speed by mechanism of electric machinery, denoted by S_{EM}. Figure 13 shows the S_{EM} and the rotor speed of DAS.

After load rejection, the residual magnetic field of the generator was weak as compared with the magnetic field under normal running. The excitation voltage induced by the residual magnetic field was also weak. This will make the measurement accuracy of excitation voltage so poor that the S_{EM} just reflects varying trends of the rotor speed, although the speed cannot be derived precisely. Figure 13 shows the variation of speed computed with the mechanism of electric machinery. The results reflect that the rotor speed signal of DAS is different from S_{EM}.

We get the conclusion that the rotor speed sensor was broken down during the accident and the rotor speed data in the records of DAS were bad based on the above analysis.

5 Signal Estimation

Although we get the conclusion that the rotor speed sensor was broken down, the quantitative information of rotor speed is very important for identifying the dynamic process of turbine and for judging whether it is overspeed. Now we estimate the upper and lower bounds of the rotor speed using maximum likelihood method and the rotor speed with neural network.

5.1 Multiscale Association Structure of Signal Estimated. To quantitatively estimate the rotor speed, we need to analyze the relations between the rotor speed and the other parameters of the turbogenerator. We focus on the operating mechanism and the measurement accuracy. If there is a complex relation between the rotor speed and a parameter, the rotor speed estimated by this parameter may not be precise. If there are series of factors, the estimation certainty may be poor. For example, to estimate rotor speed based on the excitation voltage, we only use the principle of electromagnetic induction. However, based on the differential expansion of the LP cylinder, we need Poisson effect for the mechanical material, effect for the centrifugal force, and thermal expansion of the cylinder. The comprehensive factors in the former estimation are smaller than those in the latter. So the estimation

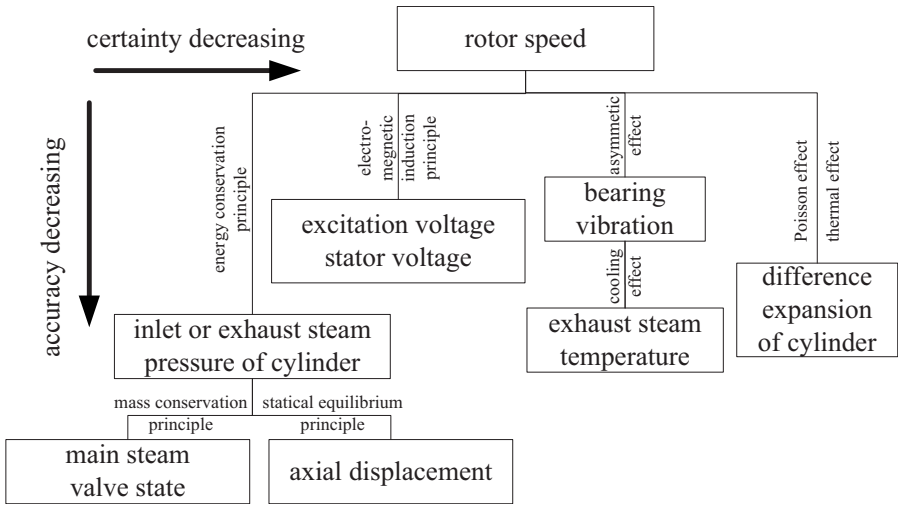

Fig. 14 Multiscale structure of rotor speed estimation

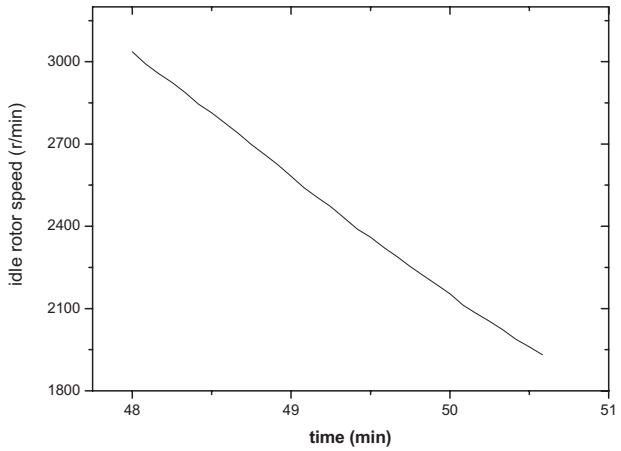

Fig. 15 Curve of the idle rotor speed

accuracy and certainty of rotor speed based on excitation voltage would be better than that those based on the differential expansion of the LP cylinder. The excitation voltage induced in residual magnetic field is so small that it is beyond the effective measurement range of excitation voltage sensor. So the measurement accuracy may be poor. However, the vibration signal is still in the effective measurement range of the vibration sensor. Thus, the measurement accuracy may be high in this case.

According to the above analysis, the multiscale association structure for rotor speed estimation, in terms of certainty and accuracy, can be built, as shown in Fig. 14. We should select the input parameters close to the upper-left corner so that the estimated performance is better. Considering the complexity of the modeling, we choose the signals of excitation voltage, stator voltage, and bearing vibration as the input parameters. They are excitation voltage, stator voltage, vertical vibration of the third bearing, horizontal vibration of the third bearing, vertical vibration of the fourth bearing, horizontal vibration of the fourth bearing, vibration of the fifth bearing vertical vibration of the sixth, bearing and horizontal vibration of the sixth bearing. We denote them as V_{ect}, V_{stt}, $V_3^{\perp}$, V_3^{-}, $V_4^{\perp}$, V_4^{-}, V_5, $V_6^{\perp}$, and V_6^{-}, respectively. The output of the estimated model is the rotor speed.

The specified parameters of the model structure are often determined by sample data. However, because of the test's harmfulness and high cost, the learning sample cannot be obtained by repeated tests. Since the process after load rejection has been considered as an idle process, we can set the signal of the rotor speed in the idle process of the turbogenerator as the output signal of rotor speed in load rejection. The period of the idle process is from 1:48:00 to 1:50:35, denoted by Δt_1, and the idle process during Δt_1 is shown in Fig. 15. Thus, we collect the sample data as shown in Table 4.

Now we view the recorded data in Δt_1 and the rotor speed in the idle process as the samples. The rotor speed from 1:48:00 to 1:56:10 needs to be estimated. We denoted this period by Δt.

5.2 Estimation of Rotor Speed Using the Maximum Likelihood Method. Now we estimate the rotor speed using the maximum likelihood method based on the nine parameters (V_{ect}, V_{stt}, $V_3^{\perp}$, V_3^{-}, $V_4^{\perp}$, V_4^{-}, V_5, $V_6^{\perp}$, and V_6^{-}). These fitting functions between the nine parameters and rotor speed, denoted by $f_i(x_i(t))$ $(i=1,2,\ldots,9)$ can be obtained through a fitting method based on the learning sample of Δt_1, where $x_i(t)$ is the input parameter. So the relation between the fitting speed and the rotor speed is

$$n(t) = f_i(x_i(t)) + \Delta n_i(t), \quad i = 1,2,\ldots,9 \tag{5}$$

where x_i is the records of the ith parameter by DAS; $\Delta n_i(t)$ de-

Table 4 Sample data

No.	V_{ect} (V)	V_{stt} (V)	V_3^{-} (mm)	V_4^{-} (mm)	V_5 (mm)	V_6^{-} (mm)	$V_3^{\perp}$ (mm)	$V_4^{\perp}$ (mm)	$V_6^{\perp}$ (mm)	Rotor speed (rpm)
1	2.0324	0.1269	10.8	5.979	6.4794	9.7509	8.7744	2.9394	7.456	3036.1
2	2.0324	0.1025	10.727	5.8447	6.3696	9.812	8.7622	3.0249	7.517	2992.5
3	1.8951	0.0964	10.678	5.7348	6.2719	9.8242	8.6401	3.0249	7.5415	2956.5
4	1.8951	0.0781	10.678	5.6005	6.1376	9.7387	8.6523	2.9516	7.517	2924.7
5	1.8951	0.0842	10.458	5.4418	5.979	9.7021	8.3969	2.8417	7.4072	2845.1
6	1.8951	0.072	10.288	5.3564	5.8335	9.6655	8.2983	2.8051	7.4194	2813.9
7	1.8951	0.072	10.08	5.2954	5.8081	9.6289	8.2128	2.8051	7.4072	2776.8
8	1.8951	0.0781	9.8608	5.1977	5.686	9.519	8.0908	2.8295	7.4072	2739
9	1.7578	0.0842	9.7265	5.1367	5.4174	9.4335	8.0297	2.7563	7.3095	2698.4
10	1.7578	0.0781	9.5678	5.2832	5.332	9.4213	7.8955	2.7075	7.2485	2661.8
11	1.6204	0.072	9.2138	5.3198	5.332	9.458	7.6147	2.6342	7.2363	2582.8
12	1.7578	0.0781	9.0063	5.1733	5.2587	9.3115	7.4682	2.5854	7.1875	2539.8
13	1.6204	0.0659	8.6035	4.8803	5.1245	8.9086	7.3096	2.4633	6.9921	2472
14	1.6204	0.0659	8.4204	4.7338	5.0634	8.7744	7.1508	2.4145	6.8579	2430.7
15	1.4831	0.0659	8.225	4.5996	5.039	8.7133	6.9189	2.3413	6.7602	2389.5
16	1.4831	0.0659	8.1152	4.5507	5.0024	8.4814	6.8212	2.3779	6.7236	2360
17	1.4831	0.072	7.9809	4.5019	4.8681	8.6889	6.4672	2.268	6.6748	2289.3
18	1.4837	0.072	7.7246	4.4287	4.6484	8.4326	6.4428	2.268	6.4672	2220.3
19	1.3458	0.0659	7.6513	4.331	4.5996	8.225	6.2231	2.2436	6.4062	2187.3
20	1.3458	0.0659	7.6879	4.2333	4.5385	8.0419	6.0034	2.5244	6.3452	2154.3
21	1.3458	0.0698	7.5537	4.1357	4.4897	8.0053	5.8935	2.3168	6.333	2112.4
22	1.3458	0.0659	7.4926	3.9648	4.4775	7.9687	5.8569	2.2314	6.2475	2081.8
23	1.3458	0.0598	7.395	3.9038	4.5019	7.9199	5.8447	2.3413	6.1865	2053.5
24	1.3458	0.0659	7.2729	3.8305	4.4531	7.7978	5.7836	2.1459	6.1987	2022.2
25	1.2084	0.0598	7.1264	3.9038	4.4409	7.6147	5.8325	2.2558	6.2231	1931.5
26	1.4837	0.0659	7.8833	4.4653	4.746	8.6279	6.4794	2.207	6.5771	2252.7
27	1.7578	0.072	9.4335	5.3686	5.3076	9.4702	7.7866	2.7075	7.2363	2624.1
28	1.8951	0.0781	10.544	5.5151	6.04	9.7021	8.5302	2.8906	7.5048	2887.6
29	1.3458	0.0598	7.1875	3.8061	4.4165	7.6513	5.7226	2.207	6.1987	1986.9
30	1.6204	0.0659	8.7744	5.0268	5.1855	9.104	7.3583	2.5366	7.0898	2504.4
31	1.3458	0.0598	7.1386	3.7084	4.392	7.4316	5.6494	2.1826	6.1499	1960.3
32	1.4831	0.0659	8.0419	4.5263	4.9414	8.6767	6.6503	2.3901	6.6992	2322.9

notes the ith fitting bias.

The estimation bias $\Delta n_i(t)$ satisfies a normal distribution. If the estimation functions are written as $\hat{n}_i(t)=f_i(x_i(t))$, then

$$\Delta\hat{n}_i(t) = \hat{n}_i(t) - n(t) \sim N(0,\sigma_i^2), \quad i = 1,2,\ldots 9 \tag{6}$$

where σ_i denotes the standard sample variance of the bias for parameter x_i.

We can improve the estimated accuracy of the rotor speed by fusing the nine fitting functions based on the maximum likelihood estimation. The maximum likelihood estimation function is

$$\hat{n}(t) = \sum_{i=1}^{9} k_i \hat{n}_i(t), \quad t \in \Delta t \tag{7}$$

where

$$k_i = \left(\frac{1}{\sigma_i}\right) \Bigg/ \left(\sum_{j=1}^{9} \frac{1}{\sigma_j}\right)$$

As each fitting bias of rotor speed follows a normal distribution, the estimation bias of the maximum likelihood estimation satisfies normal distribution, i.e.

$$\Delta\hat{n}(t) = \hat{n}(t) - n(t) \sim N(0,\sigma^2) \tag{8}$$

where

$$\sigma = \sqrt{\sum_{i=1}^{9} (k_i\sigma_i)^2}$$

According to the 3σ criteria of a normal random variable, the random variable is almost located in the range of $[\mu-3\sigma,\mu+3\sigma]$, where μ is the mean of the random variable, and σ is the standard deviation of the random variable. Then the upper-lower limits of rotor speed estimated with the maximum likelihood estimates are $n(t)=\hat{n}(t)\pm 3\sigma$.

Based on the records of DAS, including excitation voltage, stator voltage and bearings vibration, as shown in Figs. 5–8, we get the upper and lower limits of rotor speed, as shown in Fig. 18, where $\sigma=17.6$. From the figures we can see that the rotor speed exceeds 3000 rpm during all the three setup processes of the turbogenerator.

It is important to determine the speed at the last time of Δt, 1:56:10, for judging the cause of the accident. According to the maximum likelihood estimation, the rotor speed at 1:56:10 is 2985.8 rpm, and the confidence interval is [3038.5, 2933.1] rpm. This means that the rotor speed was close to the rated speed at that time.

5.3 Estimation of Rotor Speed Using Neural Network. Rotor speed estimated with the maximum likelihood method is an optimal linear combination of the single estimates. However, to estimate the rotor speed more accurately, we should use nonlinear methods because the relations between multiple parameters may be nonlinear. Neural network is a nonlinear modeling method. Now we use the radial basis function (RBF) neural network to estimate the rotor speed.

RBF neural network is a local approximation network, which has powerful capability of function approximation [17,18]. The network consists of three layers of nodes. The first layer connections implement a fan-out of the inputs to the hidden layer through a set of unweighted connections. The hidden layer implements a nonlinear transformation with Gaussian function as the basis function. The final output layer is the linear weighted sum of node outputs of the hidden layer.

We construct a RBF neural network using the orthogonal least squares learning algorithm proposed in Ref. [18]. The learning procedure consists of two steps. The first step is to select the centers, C, in the hidden layer for the samples. The second step is to learn the weights, W, connecting the hidden layer to the output layer.

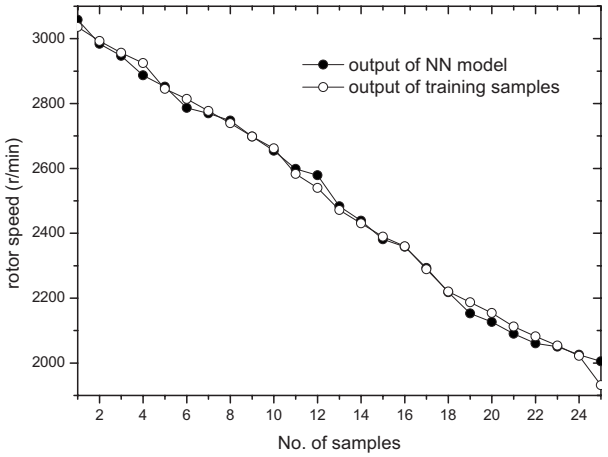

Fig. 16 Comparison of the measured and the estimated rotor speed for the training samples

The inputs of the neural network are the nine parameters (V_{ect}, V_{stt}, $V_3^{\perp}$, V_3^{-}, $V_4^{\perp}$, V_4^{-}, V_5, $V_6^{\perp}$, and V_6^{-}), and the output is the rotor speed of the idle process. There are 32 samples, out of which we select 25 samples as training samples and the other 7 samples as test samples. The data are given in Table 4.

We set the mean squared error goal and the spread of RBFs as 0.01 and 3, respectively. We use the technique of k-fold cross-validation to determine the best neural network. The training samples are partitioned into nine equally sized subsets. Each subset is used as a validation set for a RBF neural network trained on the remaining eight subsets. The empirical accuracy is given by the average of the accuracies of these nine RBF neural networks. Then we select the RBF neural network whose accuracy is the closest to the empirical accuracy as the final model. After being trained, the neural network has five hidden nodes. The training and test results are shown in Figs. 16 and 17. The results show that the trained network model can accurately predict the rotor speed.

The rotor speed estimated with the neural network is shown in Fig. 18. The estimate of the rotor speed at 1:56:10 is 3012.2 rpm.

6 Analysis of Accident Cause

Figure 18 shows that there are three manual startup processes, and the rotor speed of each startup had arrived to the rated speed. Then the turbogenerator went into an idle process. The involving process of this accident can be analyzed as follows: when the load

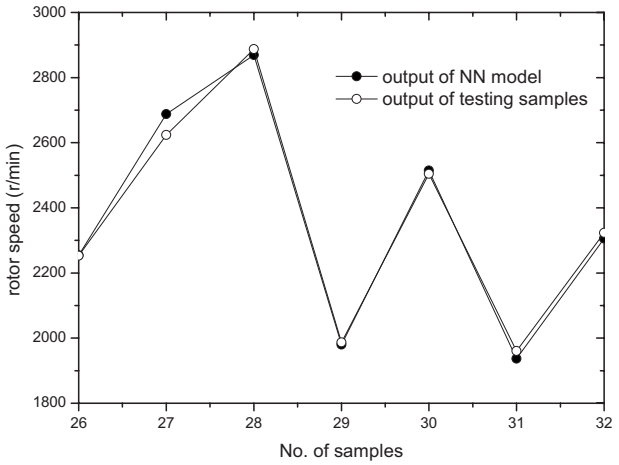

Fig. 17 Comparison of the measured and the estimated rotor speed for the testing samples

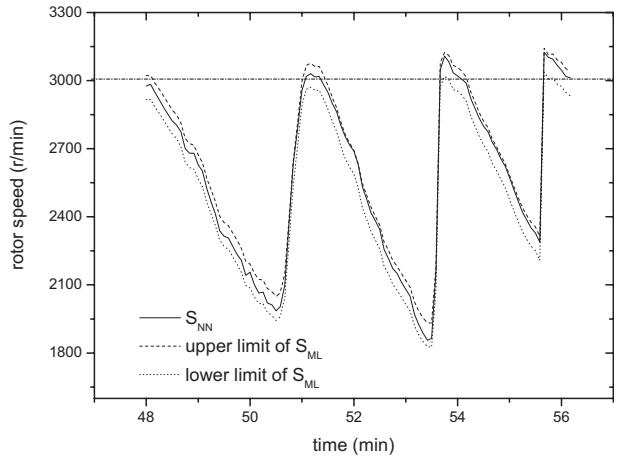

Fig. 18 Estimation of rotor speed

of the turbogenerator was rejected, the operators checked the turbogenerator and thought that the equipments were normal. Although the rotor speed sensor had been broken down, they did not find this event. So the operators started up the turbogenerator according to the tachometer of the rotor speed, which was bad. The value of the tachometer of the rotor speed was zero, far lower than the rated speed. To speed the turbogenerator up to the rated value, the operators kept the setup state until the mechanical overspeed protect controller automatically started to make the turbine trip. Then the turbogenerator began the idle process. As the operators thought that the turbogenerator was running normally, they started the turbogenerator repeatedly and the turbine tripped by the mechanical overspeed protect controller. At the third startup of the turbogenerator, the mechanical overspeed protect controller was destroyed, and the valves of the main steam could not be closed. Then large steam flowed into the cylinders. The rotor speed must be increasing because the energy of the steam was converted into the mechanical energy of the turbine, although the speed decreased after the final restart attempt.

Figure 4 shows that there was a large amount of main steam flowing into turbine suddenly after 1:56:10. The mass flow rate of the main steam was so large that the sensor can measure accurately, so the rotor dynamic model could be built based on the principle of thermodynamics and the recorded data of flow and pressure of the main steam. Setting the initial state of the rotor dynamic model as S_{NN} at 1:56:10, we can compute the rotor speed at the moment of the accident. The rotor speed is 4500 rpm at 1:56:30. As we know, the rated speed is 3000 rpm in China; the speed is far greater than the rated speed. The accident can be determined as a serious overspeed accident of turbine, which causes the turbogenerator to be destroyed.

According to the estimated speed, studying the cause of fault of the rotor speed sensor, investigators discovered that the direct cause of the sensor fault is the failure of teeth-shaft coupling in the main oil pump. Besides, the operators did not judge the state of the turbogenerator correctly. Their misjudgments cause the accident.

7 Conclusions

A method of multiscale association analysis has been proposed to investigate one serious accident in China. To analyze the cause of the accident, the rotor's overspeed before it is destroyed should be confirmed. However, the rotor speed sensor may be broken, and as a result it cannot reflect the real speed. We first use multiscale association to find the measurements relevant to the rotor speed and then use them to estimate speed signal based on the methods of maximum likelihood and neural network. Finally we get that the estimated speed is high, 4500 rpm.

In order to avoid similar accidents, we suggest that one additional tachometer must be located for facilitating the operators to compare and analyze the rotor speed during the process of startup and incident handling. Some rules preventing similar accidents should be added into operation regulations of 200 MW turbogenerators. The failure about the coexistence of such electrohydraulic system should be allocated to the operation regulations, so that the operators and maintenance personnel could judge and handle sudden events better with the rules.

The method of multiscale association analysis has been used to detect the fault sensor and estimate the fault signal under the limit data recorded for the system with multiscale characteristic. This method, making full use of the recorded data and having a clear mechanism principle, can also be applied to other cases of accidents.

Acknowledgment

The authors would like to thank Dr. Jaroslaw Szwedowicz and the three reviewers for their constructive and insightful suggestions for further improving the quality of this paper. This work is supported by the National Natural Science Foundation of China (No. 50606008).

Nomenclature

S_{RS} = rotor speed signal by mechanism of rotor stress
S_{EM} = rotor speed signal by mechanism of electric machinery
S_{ML} = rotor speed signal estimated with maximum likelihood
S_{NN} = rotor speed signal estimated with neural network
V_{ect} = excitation voltage
V_{stt} = stator voltage
$V_i^{\perp}$ = vertical vibration of the ith bearing
V_i^{-} = horizontal vibration of the ith bearing
n = rotor speed
Z_c = differential expansion of the LP cylinder
Z_{zy} = axial displacement
U = excitation voltage
σ = variance of sample or estimation

References

[1] Sehgal, R., Gandhi, O. P., and Angra, S., 2003, "Failure Cause Identification of Tribo-Mechanical Systems Using Fault—Tree a Digraph Approach," Tribol. Int., **36**(12), pp. 889–901.
[2] Yu, D., Hu, Q., and Bao, W., 2004, "Combining Rough Set Methodology and Fuzzy Clustering for Knowledge Discovery From Quantitative Data," Proc. Chin. Soc. Electr. Eng., **24**(6), pp. 205–210.
[3] H, B. R., 1986, "General Rotating Machinery Expert System," Proceedings of Expert System 1986 Bringhton, UK, pp. 79–83.
[4] Uraikula, V., Chan, C. W., and Tontiwachwuthikul, P., 2007, "Artificial Intelligence for Monitoring and Supervisory Control of Process Systems," Eng. Applic. Artif. Intell., **20**(2), pp. 115–131.
[5] Liao, S.-H., 2005, "Expert System Methodologies and Applications: A Decade Review From 1995 to 2004," Expert Systems With Applications, **28**(1), pp. 93–103.
[6] Yang, B.-S., Lim, D.-S., and Tan, A. C. C., 2005, "Vibex: An Expert System for Vibration Fault Diagnosis of Rotating Machinery Using Decision Tree and Decision Table," Expert Systems With Applications, **28**(4), pp. 735–742.
[7] Filippetti, F., Franceschini, G., Tassoni, C., and Vas, P., 2000, "Recent Developments of Induction Motor Drives Fault Diagnosis Using ai Techniques," IEEE Trans. Ind. Electron., **IE-47**(5), pp. 994–1005.
[8] Coudert, O., and Madre, J. C., 1994, "Metaprime: An Interactive Fault-Tree Analyzer," IEEE Trans. Reliab., **43**(1), pp. 121–127.
[9] C., T. T., and Z., W. Y., 1996, "Vibration Analysis and Diagnosis of a Cracked Shaft," J. Sound Vib., **192**(3), pp. 607–620.
[10] Venkatasubramanian, V., Rengaswamy, R., Yin, K., and Kavuri, S. N., 2003, "A Review of Process Fault Detection and Diagnosis Part I: Quantitative Model-Based Methods," Comput. Chem. Eng., **27**(3), pp. 293–311.
[11] Venkatasubramanian, V., Rengaswamy, R., and Kavuri, S. N., 2003, "A Review of Process Fault Detection and Diagnosis Part II: Qualitative Models and Search Strategies," Comput. Chem. Eng., **27**(3), pp. 313–326.
[12] Zhang, J.-X., Xu, M.-Q., Huang, W.-H., Zhang, J.-Y., and Zhang, G.-B., 2001, "Application of Black Box to Fault Diagnosis of Rotating Machine," J. Harbin

Inst. Technol., **8**(1), pp. 83–86.
[13] Bakshi, B. R., 1999, "Multiscale Analysis and Modeling Using Wavelets," J. Chemom., **13**(3–4), pp. 415–434.
[14] Agrawal, R., Faloutsos, C., and Swami, A., 1993, "Efficient Similarity Search in Sequence Databases," *Proceedings of the Fourth International Conference on Foundations of Data Organization and Algorithms*, pp. 69–84.
[15] Yi, B. K., and Roh, J. W., 2004, "Similarity Search for Interval Time Sequences," *Database Systems for Advances Applications, Ninth International Conference, DASFAA*, pp. 17–19.
[16] Fitzgerald, A. E., Umans, S. D., and Kingsley, C., Jr., 2002, *Electric Machinery*, McGraw-Hill, New York.
[17] Leonard, J. A., Kramer, M. A., and Ungar, L. H., 1992, "Using Radial Basis Functions to Approximate a Function and Its Error Bounds," IEEE Trans. Neural Netw., **3**(4), pp. 624–627.
[18] Chen, S., Cowan, C. F. N., and Grant, P. M., 1991, "Orthogonal Least Squares Learning Algorithm for Radial Basis Function Networks," IEEE Trans. Neural Netw., **2**(2), pp. 302–309.

K. Willenborg
e-mail: klaus.willenborg@rolls-royce.com

M. Klingsporn

Air and Oil Systems,
Rolls-Royce Deutschland Ltd & Co. KG,
Eschenweg 11, Dahlewitz
15827 Blankenfelde Mahlow, Germany

S. Tebby

T. Ratcliffe

Dunlop Equipment Ltd.,
Holbrook Lane,
Coventry, CV6 4QY, UK

P. Gorse

K. Dullenkopf

S. Wittig

Institut für Thermische Strömungsmaschinen,
Universität Karlsruhe,
Kaiserstrasse 12,
76128 Karlsruhe, Germany

Experimental Analysis of Air/Oil Separator Performance

Within the European research project (Advanced Transmission and Oil System Concepts), a systematic study of the separation efficiency of a typical aeroengine air/oil separator design was conducted. The main objectives were to obtain a basic understanding of the main separation mechanisms and to identify the relevant parameters affecting the separation efficiency. The results of the study contribute to an optimized separator technology. Nonintrusive optical measurement techniques like laser diffraction and multiple wavelength extinction were applied to analyze the separation efficiency and identify potential optimization parameters. Oil mist with defined oil droplet size distribution was supplied to the breather. By simultaneously measuring particle size and oil concentration upstream and downstream of the breather, the separation mechanism was analyzed and the separation efficiency was assessed. In addition, the pressure drop across the separator was measured. The pressure drop is an important design feature and has to be minimized for proper sealing of the engine bearing chambers. The experimental programe covered a variation of air flow, oil flow, shaft speed, and droplet size. The main emphasis of the investigations was on the separation of small droplets with a diameter of up to 10 μm. The following trends on separation efficiency of small droplets were observed: The separation efficiency increases with increasing rotational speed, with increasing particle size, and with decreasing air flow rate. In parallel, the pressure drop across the breather increases with increasing speed and increasing air flow. [DOI: 10.1115/1.2795785]

Introduction

Motivation. Aeroengine bearing chambers are often sealed by air-blown seals pressurized by compressor air. The sealing air mixes with the lubrication oil and forms a complex two-phase flow in the bearing chamber and in the components downstream.

In many designs, the sealing air is allowed to escape from the chamber through a dedicated vent line. The oil leaves the bearing chamber through an offtake at the bottom of the sump and is returned to the oil tank by a scavenge pump.

The bearing chamber vents combine with the vents from gearboxes and the oil tank. The air/oil mixture passing the combined vent cannot be directly exhausted overboard because of the unacceptably high oil content. Therefore, the air/oil mixture is separated in rotating separators, so called breathers, driven by the accessory gearbox. Many air/oil rotary separators for gas turbine engines contain metal foam, such as Dunlop Retimet®. The purpose of the metal foam is to improve the efficiency of the oil separation.

A typical design of a rotating air/oil separator for aeroengine applications to be placed in the accessory gear box is shown in Fig. 1. The air-oil mixture enters the breather through tangential inlets. Larger droplets are separated by the centrifugal forces in the swirling flow inside the breather housing. The flow passes the rotating metal foam and the exit air is exhausted overboard through the center of the rotating shaft.

Inside the rotating metal foam, most of the oil is extracted and centrifuged to the inner surface of the outer wall of the rotating housing. Peripheral drain holes in this outer wall allow the separated oil to be discharged radially outward the inner surface of the outer wall of the static breather housing. The swirling air flow inside the static breather housing forces the oil toward the exit port where it is scavenged from and returned to the engine oil tank.

A key component of the breather is the metal foam. The structure of such a metal foam, e.g., Retimet®, a patented material developed by Dunlop Equipment, is illustrated in Fig. 2. The three-dimensional structure of the metal foam provides a high particle retention capability at low pressure loss. The material shown in Fig. 2 is manufactured as a nickel chrome metal foam in a variety of grades (20 pores, 45 pores, and 80 pores per inch) and thicknesses, giving a complex three-dimensional material which can be tailored in size to meet specific design performance requirements. Air/oil separators equipped with such metal foam offer maintenance free operation and are used worldwide on many engines for both civil and military applications.

Although more than 99.8% of the oil carried within the vent flow is separated in the breather, the residual oil fraction in the overboard air is a source of oil consumption and contributes to environmental pollution. In addition, the residual oil fraction in the overboard air may be visible when it leaves the engine [1].

The pressure drop across the breather represents an important aspect in the breather design as it sets the backpressure of the vent system. Critical conditions are usually reached during low engine speeds (Idle) when the sealing air pressure provided by the compressor is low. A high pressure drop across the breather reduces the differential pressure across the bearing chamber oil seals compromising sealing integrity. Oil leakage from the bearing chambers could lead to cabin air contamination and could cause an oil fire risk and, therefore, has to be prevented during all operating conditions [2–4].

Contributed by the International Gas Turbine Institute of ASME for publication in the JOURNAL OF ENGINEERING FOR GAS TURBINES AND POWER. Manuscript received November 7, 2006; final manuscript received July 22, 2007; published online August 28, 2008. Review conducted by Dilip R. Ballal. Paper presented at the ASME Turbo Expo 2006: Land, Sea and Air (GT2006), Barcelona, Spain, May 8–11, 2006. Paper No. GT206-90708. Category: Gas Turbines: Structures and Dynamics.

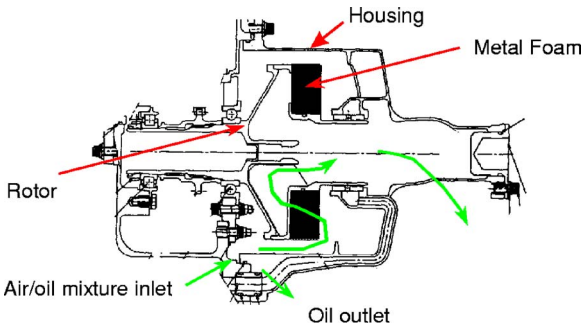

Fig. 1 Typical breather design

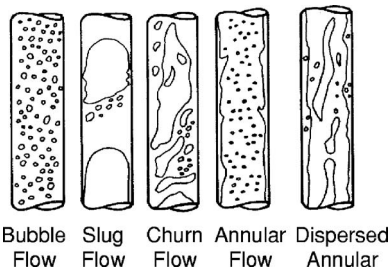

Fig. 4 Two-phase flow patterns for vertical upward flow

The target for a low pressure drop is usually contradictory to good separation efficiency due to physical mechanisms, i.e., an increase of separation efficiency may result in an increased pressure drop. Additionally, space and weight constraints of aeroengine applications have to be met and the breather has to be able to cope with the temperatures of the vent flow. Typically, the breather is exposed to temperatures up to 200°C [5,6].

The design of a breather represents a compromise between separation efficiency, pressure drop, dimensions, weight, and cost. Identifying the optimum design solution requires a trade-off between these different aspects.

An improvement of the separation efficiency offers several potential benefits such as reduced oil consumption, reduced maintenance effort, reduced oil tank size, weight reduction, and reduced environmental impact. All these topics contribute to an increased satisfaction of aircraft operators.

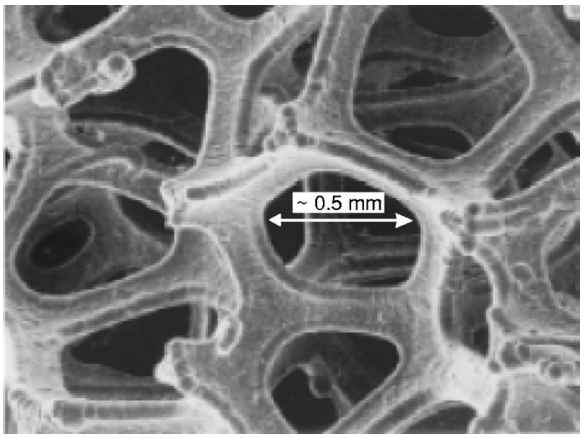

Fig. 2 Structure of Dunlop Retimet® metal foam, Grade 45

Characterization of Vent Flow. The two-phase flow in the vent line represents a boundary condition for the separation process in the breather. Two-phase flow maps [7–10] were prepared to characterize the flow situation in the vent. These flow maps are available for horizontal, vertical upward, and vertical downward flows and allow identifying the dominating flow patterns from the global air and oil flow rates and the physical properties like viscosity density and surface tension of air and oil.

Typical air and oil flow rates in the vent were analyzed for three different engine operating conditions. Three different pipe diameters were included in the analysis. As an example, the resulting flow map for vertical upward flow in the vent line is presented in Fig. 3. The corresponding flow patterns are illustrated in Fig. 4 [11,12].

As clearly visible in Fig. 3, for all conditions considered, an annular flow develops in the vent pipe. This flow pattern is characterized by a thin liquid film covering the wall and a central gas core loaded with smaller droplets (Fig. 4). This finding is confirmed by the results of a detailed experimental study on the air/oil two-phase flows in a vent pipe [13,14].

Hence, the total oil flow in the vent line splits into a wall film flow and a droplet flow in the center. The wall film enters the breather through the tangential inlets continuing as wall film on the inner surface of the breather housing. This film flow is rapidly

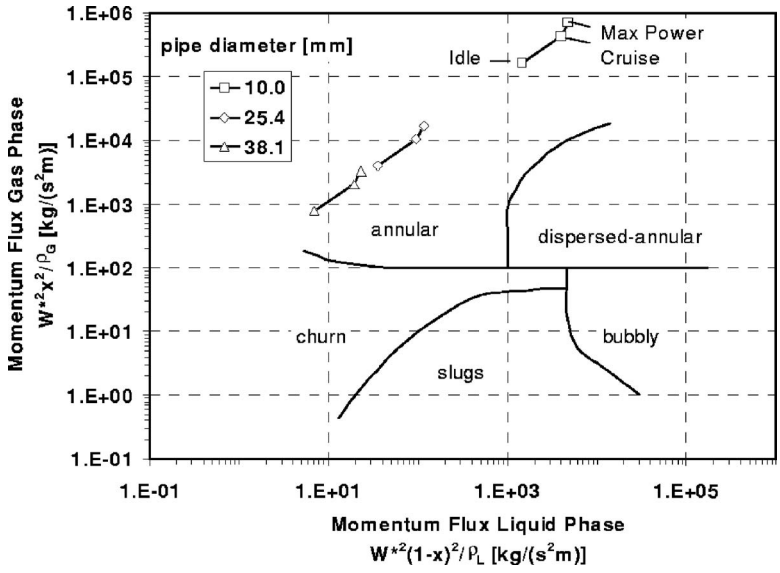

Fig. 3 Flow map for vent pipe flow, vertical upward

collected in the breather sump without moving radially inward. Only smaller droplets reach the rotating metal foam because their smaller inertia enables them to be carried by the air flow radially inward against the centrifugal field generated by the swirling flow.

Breather Flow. In a separate study within the earlier BriteEuram project INTRANS (Mechanical Integrity for Advanced Transmission Systems), numerical computations of the flow entering aeroengine air/oil separators were performed. The main results of the numerical study relevant for the current investigation are briefly summarized in the following. A more detailed description of the numerical work is available elsewhere [15–18].

The commercial computational fluid dynamics (CFD) package CFX was applied to first calculate the single-phase air flow in the breather. Here, the metal foam was modeled as an isotropic porous medium of uniform construction using Darcy's law.

Using the converged single-phase calculations, coupled Lagrangian tracking calculations were performed to obtain droplet trajectories in the breather. Particles with varying droplet sizes were released from positions near the inlet. The droplet tracking stopped when droplets reached a solid wall, i.e., particle sticks to the surface. The particles were not tracked through the metal foam.

A parametric study allowed resolving the effect of the air flow rate and the rotational speed on the breather pressure drop. From the Lagrangian particle tracking method, a critical droplet diameter was identified. This critical droplet diameter is defined as the maximum particle size for which the droplets will hit the face of the rotating metal foam.

The results of the CFD calculations indicated a strong and complex swirling motion inside the separator chamber. This swirling motion was primarily generated by the tangential inlets and was only very weakly affected by the shaft speed. The pressure drop across the breather chamber was predicted to be virtually independent of the rotational speed of the shaft. A critical droplet diameter of $3-4\ \mu$m was identified and was found to be not affected by the shaft speed.

Objectives. The main objective of the current study was to systematically investigate the separation mechanism in the breather to identify potential design optimizations for minimizing oil loss and improving the environmental friendliness of future engines.

As the analysis of the two-phase flow in the vent and inside the separation chamber has shown, most of the liquid oil is separated out before it can reach the rotating metal foam. Only droplets with a diameter below $3-4\ \mu$m follow the air flow radially inward and are drawn against the centrifugal forces in the swirling flow into the rotating metal foam.

Therefore, the main emphasis of the current investigation was on the separation of small droplets that may contribute to visible emissions. As the small droplets, which are carried in the central gas core of the vent flow, represent only a very small portion of the typical oil flow, the experiments were conducted with relatively small oil flows, i.e., low oil volume fraction compared to engine conditions.

A dedicated droplet generator was designed and manufactured by the Institut für Thermische Strömungsmaschinen (ITS), University of Karlsruhe, to provide a range of defined droplet size distributions. By simultaneously measuring the droplet sizes and droplet concentration entering the breather and leaving the breather, the separation efficiency was to be evaluated to understand the air/oil separation characteristics. Besides the droplet size distribution, the following parameters were regarded as relevant for the breather behavior and were to be investigated: air flow rate, oil flow rate, separator speed, and temperature. Parallel to the investigation of the separation efficiency, the pressure loss characteristic was to be obtained.

Experimental Setup

The experimental investigation of the current study represents a joint collaboration between the two industrial and the one academic partner. The test rig was built and operated by Dunlop Equipment. University of Karlsruhe provided the special measuring equipment, recorded the test data, and performed data analysis relating to oil droplet size distribution and oil mist flow rates. Rolls-Royce Deutschland defined boundary conditions and coordinated the tests.

Dunlop Breather Test Rig. The Dunlop Test Rig in Coventry, UK that was used in this study was initially developed with part funding from the European Union as part of the Brite Euram project INTRANS [1,19]. A schematic of the test rig is shown in Fig. 5.

The rig comprises an air-driven turbine, which is arranged to drive an air-oil separator contained within a housing rigidly mounted to the air turbine. The 120 hp turbine is operated from an adjoining control room by means of a digital electronic controller. The controller links to a drive solenoid, main control valve, and encoder mounted directly to the rear of the turbine. The turbine air is provided from one of two compressor sources. The turbine has a capability to run at 40,000 rpm and can operate in a variety of flight attitudes including negative g.

The rig air supply system has the capability to provide air at ambient temperature or via an existing furnace to the test room at temperatures up to 600°C.

The hot oil supply system for the rig comprises the following. A 300 l capacity oil reservoir is specially insulated and fitted with two thermostatically controlled 6 kW oil heaters. Two identical gear-type pumps driven by 0.75 kW four-pole electrical motors are used to pump the oil around the rig. One pump acts as the main supply pump and is controlled by an inverter drive and provides oil flow rates up to 25 l/min. The second pump acts as a constant speed scavenge pump and returns oil back to the reservoir. The maximum oil operating temperature is 200°C. The pumps can be remotely operated from the control room and the system has all the necessary safety and control equipment required for a unit of this type.

The oil separated in the breather is removed by the scavenge pump. The breather exit air is passed through a coalescer and then a flow meter before being exhausted to atmosphere outside the test area. During tests with engine representative oil flows, the coalescer is used as oil flow, rate measurement system.

The capabilities of the Dunlop breather test rig are summarized in Table 1.

Droplet Generator. In the current study, a droplet generator for providing a controlled air-oil mixture was designed and manufactured by the ITS. The air/oil mixture produced by this device was supplied to the inlet of the separator (Fig. 5).

The droplet generator design is illustrated in Fig. 6. The main air entering the droplet generator through two inlets is distributed in an annulus and discharged through ten nozzles such that air jets develop around the oil spray generated by three atomizers positioned in the center. Further downstream where the diameter of the flow path decreases, the air jets mix with the oil droplets and the air/oil mixture with the desired oil concentration and droplet size distribution forms.

Two different types of nozzles were selected for providing the desired droplet size distribution. Both nozzles are air-assist atomizers and use a high pressure air supply to atomize the oil. While the Schlick model 970S8 atomizer [20] mixes the oil and air externally, the Spraying Systems SU11 nozzle [21] employs internal mixing. The Schlick nozzle is equipped with an adjustable air cap and a control valve for the liquid flow. This allows adjusting the flow rate of air and oil for given air and oil pressures.

The adaptation of the droplet generator to the air/oil separator rig at Dunlop is included in Fig. 5. The air/oil mixture leaving the

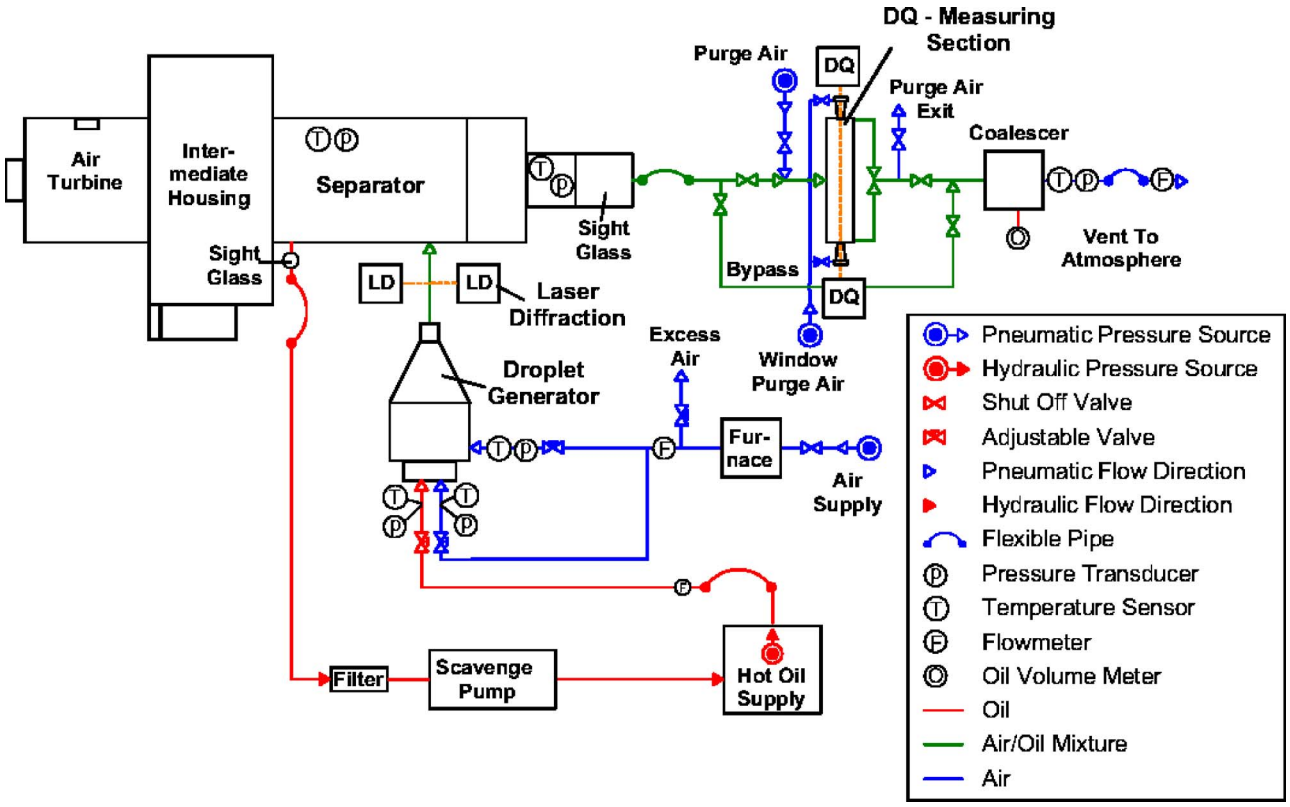

Fig. 5 Schematic of Dunlop breather test rig

droplet generator passes through a measuring section for droplet sizing. A glass tube viewing section then provides a direct visual impression of the air/oil mixture immediately upstream of the breather.

Table 1 Test rig capabilities

Maximum air flow	60 g/s (3 m^3/min)
Maximum air pressure	550 kPa
Maximum air temperature	600°C
Maximum oil flow	25 l/min (0.4 kg/s)
Maximum oil temperature	120°C
Maximum rotational speed	40,000 min^{-1}

Measurements of the droplet size distributions were performed at the ITS to obtain the atomization characteristics of the two nozzles. The cumulative volume distribution was obtained with the laser diffraction (Malvern) method. A substitute fluid with the same properties, i.e., density, viscosity, and surface tension, as engine oil at 70°C was used in the experiments.

Droplet size distributions for different operating conditions for the two different atomizers are given in Fig. 7. The chart plots the cumulative volume distribution of the spray against the droplet diameter. The value d_{30} represents the volume mean droplet

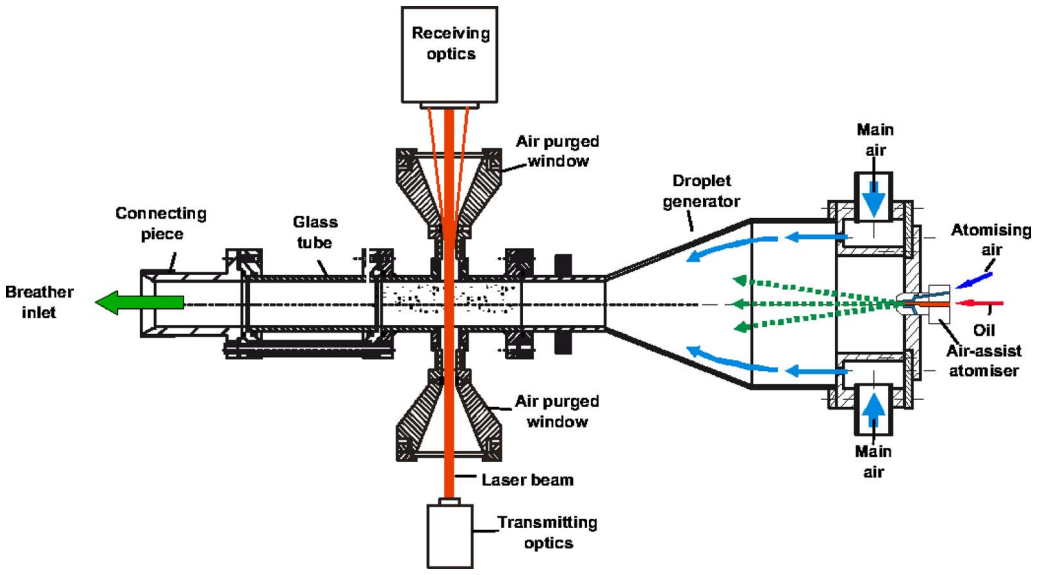

Fig. 6 Schematic of droplet generator design

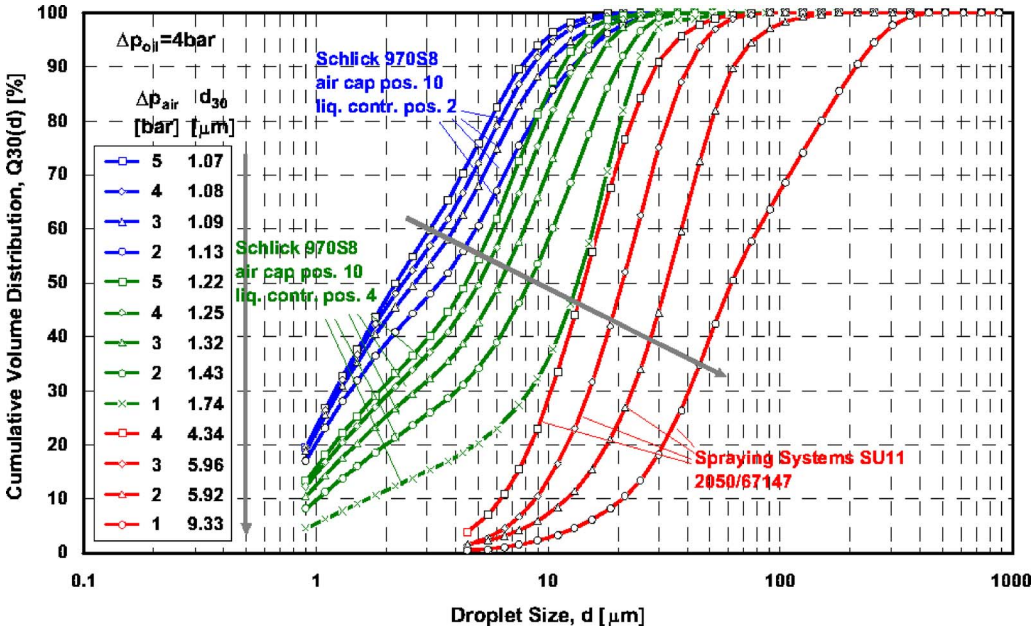

Fig. 7 Droplet size distribution

diameter.

The Schlick 970S8 nozzle (blue and green curves) produces the smallest oil droplets. For a given position of the oil control needle, a decrease of the pressure of the atomizing air results in an increase of the droplet diameters. For the droplet size distribution with the smallest mean droplet diameter (Schlick 970S8, air cap pos. 10, liq. contr. pos. 2, Δp_{air}=5 bars, d_{30}=1.07 μm), 20% of the liquid volume is carried by droplets smaller than 0.9 μm. This means that with respect to number, more than 80% of the droplets are smaller than 0.9 μm.

The Spraying Systems SU11 atomizer (red curve) produces a coarser oil spray compared to the Schlick nozzle. Also, for the Spraying Systems atomizer, the mean droplet diameter increases with decreasing atomizing air pressure.

As visible in Fig. 7, the two atomizers selected allow to adjust and control the droplet size distribution by varying the operating conditions of the nozzles. Discharge measurements, which were performed in parallel, showed that the two nozzles are well suited to reach the required oil volume concentrations.

Air/Oil Separator. A typical aeroengine air/oil separator design (see Fig. 1) configured to be placed into the gearbox vent system was tested in the study reported in this paper. The separator is the subject of RR patent EP1344559/US6893478. The separator was equipped with grade 45 metal foam as shown in Fig. 2 for all tests reported in this paper.

Rig Instrumentation and Data Acquisition. Platinum resistance thermometers were used for sensing temperatures. Absolute and differential pressures were measured by use of calibrated piezoresistive pressure sensors with an uncertainty of less than 0.1% full scale. A propeller-type flow meter was available for measuring the air flow rate exhausted from the breather. A positive displacement-type flow meter measured the oil flow supplied to the droplet generator. The flow meters had been calibrated at the manufacturer and allowed to measure the air and oil flow rate with an uncertainty of less than 5%.

The following parameters were acquired by the rig data acquisition system:

- air temperature and pressure upstream of droplet generator
- oil mass flow supplied to the droplet generator
- oil temperature and pressure upstream of droplet generator
- air flow rate downstream of breather overboard
- air temperature downstream of breather
- pressure at breather inlet
- pressure at breather outlet
- differential pressure between breather outlet and breather inlet

The analog output signals of the sensors were sampled and digitized at a frequency of 1 Hz by a National Instruments data acquisition board. For a data point, the readings were averaged over a period of 30 s. The data acquisition program uses the commercial code LABVIEW™ and operates on a personal computer (PC) platform. All readings from the instrumentation are recorded into spreadsheets on the PC readily available for further data analysis.

Droplet Sizing. For evaluating and resolving the separation characteristics, the droplet size distribution was simultaneously measured at the inlet and at the exit of the breather. Nonintrusive optical measurement techniques were applied to characterize the air/oil mixture upstream and downstream of the separator.

Breather Inlet and Laser Diffraction Technique. For obtaining the droplet size distribution of the air/oil mixture produced by the droplet generator and supplied to the breather, the laser diffraction technique (Malvern) was chosen. This technique represents a well established method for determining droplet size distributions of polydisperse sprays. The laser diffraction method utilizes the Fraunhofer diffraction of parallel laser light passing through a particle cloud. The commercially available Sympatec HELOS system [22,23] was used in the current study. The sensor offers a wide measuring range for particle sizes from 0.5 to several hundreds of micrometers. Transmitting and receiving optics are aligned in line. The droplet size distribution is derived from the radial light intensity distribution of the diffracted light measured by a photodetector. The detector unit was connected to a PC, which controlled the data acquisition and the data analysis such that the characterizing spray parameters like mean droplet size and volume distribution (see Fig. 7) were readily available.

The adaptation of the laser diffraction technique is illustrated in

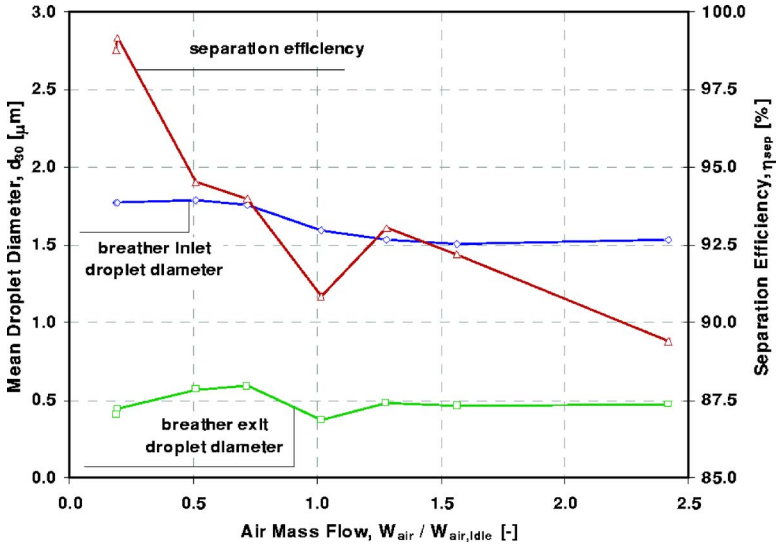

Fig. 8 Effect of air flow rate on separation of small droplets, $n/n_{Idle}=1.0$, $V_{oil,inlet}=0.2$ l/h

Fig. 5. The measuring section, which is positioned between droplet generator outlet and breather inlet, is equipped with special air-purged windows providing optical access to the two-phase flow.

For a given operating condition, three data points were acquired with the laser-diffraction technique and a mean value was derived from the three data points. The data points showed very good repeatability with deviations typically below 1%. In addition, good reproducibility was found between data obtained for identical operating conditions at different days.

Breather Exit and Dispersion Quotient Technique. The droplet size distribution and oil volume concentration of the oil mist leaving the breather were measured with the dispersion-quotient (DQ) technique developed at the University of Karlsruhe. This technique is capable of accurately measuring particle sizes in the micron and submicron diameter ranges, i.e., 0.1–3 μm [24–27].

The method accounts for the dependency of droplet light extinction on light frequency according to the Mie theory. Three different wavelengths (0.67 μm, 0.8 μm, and 1.3 μm) of laser light are applied. The relations of the extinction at different light frequencies are called DQs and depend only on droplet diameter and known droplet refractive index. Assuming a normal logarithmic droplet size distribution, the mean droplet diameter and the standard deviation can be determined. Additionally, the volume concentration of the particles in the two-phase flow is obtained. A suspension of latex particles of known size and water was used for calibration of the system [24].

As shown in Fig. 5, the DQ-measuring section was positioned downstream of the breather. It basically consists of a pipe with optical accesses at both sides and a bypass. The breather exit flow is directed through the pipe and a laser beam passes through the oil mist along the full length of the pipe. The air-purged windows for providing optical access were of the same type as used for the measuring section upstream of the breather. The bypass enabled to completely purge the measuring section with pure air and perform required offset measurements of the laser intensity without shutting down the test rig. In order to always obtain reliable measurements, i.e., sufficient extinction of the laser light intensity, the design of the DQ-measuring section allowed easy variation of the length. In this way, for a wide range of oil concentrations, an appropriate extinction rate could be achieved. The measurement system used is the one developed in-house by the ITS. It consists of a transmitter and control unit, transmitting optics, optical detectors, and a PC for data acquisition and analysis.

For a given operating condition, three measurements were acquired with the DQ system and a mean value was derived from the three single data points. The deviation between the single data points was typically below 5%. In addition, good reproducibility was found between data obtained for identical operating conditions at different days.

Experimental Program. A parametric variation of separator speed, air flow, and droplet size was conducted to systematically investigate and identify the separation characteristics of the breather tested. In addition to the separation efficiency, the differential pressure across the breather was measured. As the current study focused on small droplets, the oil flow rates are relatively small compared to typical engine conditions.

The results presented in the current paper were obtained for cold flow conditions, i.e., air and oil were at room temperature. Due to limitations by the rig in terms of a long heat-up period to achieve stabilized temperatures at the relatively low air flow rates tested and a limited duration of the test campaign, it was not possible to study the effect of temperature in detail. Limited test runs indicated no significant impact of temperature on separation efficiency.

Results

The effects of air mass flow, rotational speed, and particle size on the separation efficiency and breather pressure drop are presented in the following.

Separation Efficiency. The separation efficiency is defined as the ratio of separated oil to total oil flow supplied to the breather:

$$\eta_{sep} = (V_{oil,inlet} - V_{oil,exit})/V_{oil,inlet} \quad (1)$$

While the oil flow supplied to the breather ($V_{oil,inlet}$) was directly measured by a flow meter, the oil volume flow discharged from the breather ($V_{oil,exit}$) was derived from the oil volume concentration of the exhaust flow as measured with the DQ system. In addition to the separation efficiency, the mean droplet diameters at the inlet and at the outlet of the breather are shown in Figs. 8–10.

Air flow rate and separator speed have been normalized by typical values for engine operation at Idle.

Effect of Air Flow Rate. Figure 8 illustrates the effect of the air flow rate on the separation efficiency for inlet droplet sizes be-

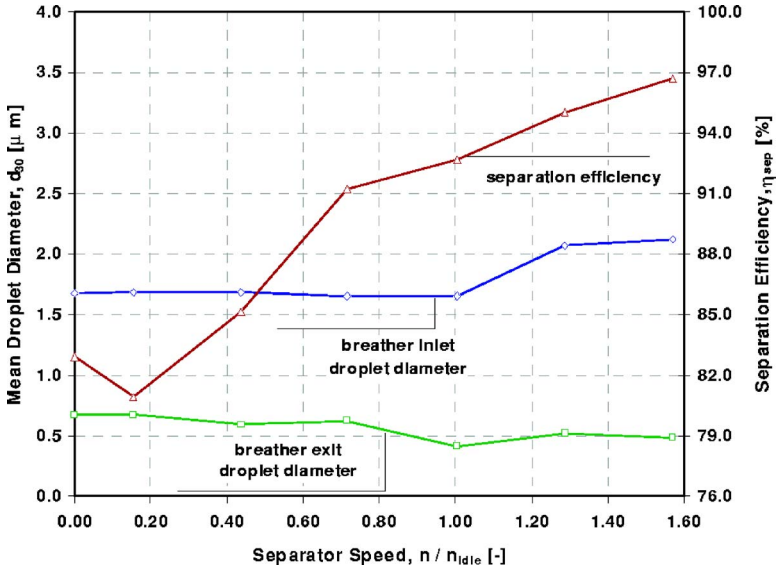

Fig. 9 Effect of separator speed on separation of small droplets, $V_{oil,inlet}$ =0.2 l/h, $W_{air}/W_{air,Idle}$=1.0

tween 1.5 μm and 2.0 μm. These small particles are considered not to be separated by the swirling flow in the breather housing and are considered to reach the rotating metal foam. The droplet generator was operated with the Schlick atomizers (see Fig. 7). The oil flow rate and the rotational speed are constant.

The settings of the atomizers, i.e., air pressure and oil pressure, were fixed and the air flow rate was varied by adjusting the main air flow (see Fig. 6). A slight decrease of the mean droplet diameter at the breather inlet for increasing air flow rate was observed (Fig. 8). This effect is attributed to an increased secondary atomization due to the higher air flow rate.

The mean particle diameter measured at the exit of the breather shows no definite dependence on the air flow rate and stays relatively constant around a value of 0.5 μm. The almost constant mean exit particle diameter suggests that only droplets below a certain size can pass the rotating metal foam.

A strong decrease of the separation efficiency with increasing air flow rate can be identified from Fig. 8. For typical Idle conditions, the data suggest a separation efficiency of about 92%. The separation efficiency drops from about 99% to less than 90% as the air flow rate is increased from 20% to 240% of typical Idle air flow rate.

These findings were supported by the visual impression of the breather exit flow. Typical breather emissions were observed and the intensity of the mist discharged from the breather noticeably decreased as the air flow was reduced.

It has to be highlighted that the separation efficiency stated above applies to the specific oil droplet size distribution, i.e., diameter smaller than 2 μm, supplied to the breather in the current tests. When the separator is operated at real engine conditions, the oil flow rates are significantly higher. For such typical engine oil flow rates, separation efficiencies greater than 99.8% are achieved.

Effect of Rotational Speed. The effect of the rotational speed of the breather is shown in Fig. 9. Again, a droplet size distribution with a mean particle size around 1.5–2.0 μm was supplied to the breather. For given air and oil flow rates, the breather speed was

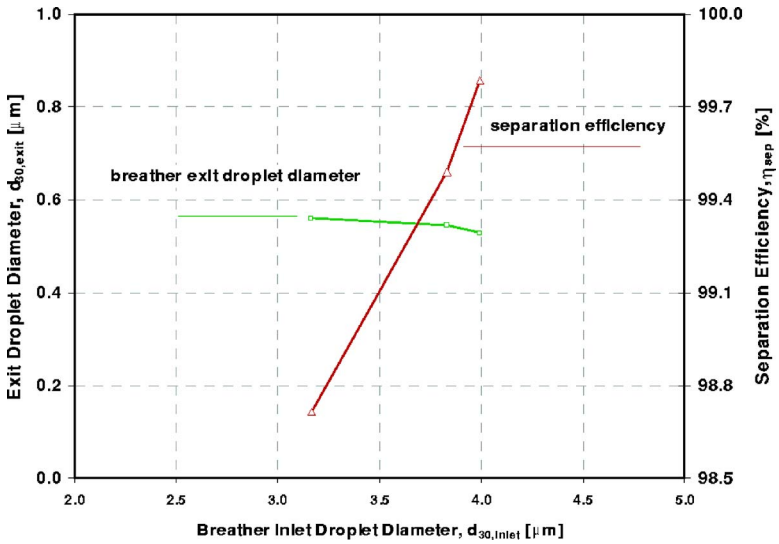

Fig. 10 Effect of droplet size on separation efficiency, $W_{air}/W_{air,Idle}$=1.0, n/n_{Idle}=0.5, $V_{oil,inlet}$=1.8–5.6 l/h

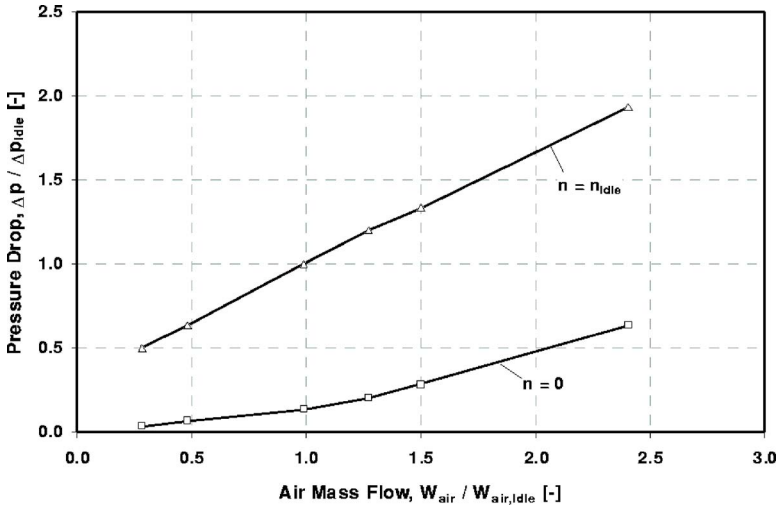

Fig. 11 Effect of air flow rate on breather pressure drop, $n/n_{Idle}=1.0$, $V_{oil,inlet}=2.0$ l/h

varied from 0% to 160% Idle speed.

Although the atomizer settings as well as the air and oil flow rates were fixed, a slight increase of the mean droplet size at the breather inlet occurred.

The results of the droplet size measurements at the breather exit indicate a decreasing mean particle size with increasing separator speed. For the speed range investigated, the mean droplet size at the breather exit decreases from 0.67 μm to 0.48 μm. The mean droplet size at the breather exit is always notably smaller than at the inlet of the breather.

A strong effect of the separator speed on the separation efficiency of small droplets is distinctly visible in Fig. 9. The separation efficiency increases from 82% at no rotation to 97% at 160% of Idle speed.

The small oil particles supplied to the breather can be considered not to be separated by centrifugal forces but to almost ideally follow the air flow in the breather. The significant reduction of the mean droplet size and the oil concentration across the breather is therefore attributed to the separation effect of the metal foam. As shown in Fig. 9, the separation effect of the metal foam is relevant already at no rotation and is enhanced with increasing rotational speed. This is reflected by the decreasing exit mean droplet diameter and the increasing separation efficiency with increasing speed.

Effect of Droplet Size. Varying the mean particle size of the air/oil mixture supplied to the breather was realized by operating the droplet generator with the Spraying Systems nozzles at varying air pressure and constant oil pressure (see Fig. 7). Continuously decreasing the differential air pressure across the atomizers resulted in a continuously increasing mean droplet size. Due to the discharge characteristics of the nozzle, decreasing the air pressure resulted in an increased oil flow rate, i.e., with increasing mean inlet droplet diameter, the oil flow supplied to the breather increased. The dependence of the separation efficiency of the breather on the droplet size is illustrated in Fig. 10. The data were obtained for a rotational speed of 50% Idle speed.

At the breather exit, a mean droplet diameter of about 0.55 μm was obtained. The data show a very slight decrease of the mean particle size at the breather exit with increasing inlet mean particle size.

A strong increase of the separation efficiency with increasing inlet mean droplet diameter can be identified from Fig. 10. Separation efficiencies of more than 98.5% up to close to 100% were obtained. For inlet mean droplet diameters larger than 4 μm, the high separation efficiency resulted in an insufficient extinction rate for the DQ system at the breather exit. This was in accordance to the visual observation of no mist blowing out of the breather exit if larger droplets were supplied to the breather. This also means that the breather itself did not produce mist at the conditions investigated.

As mentioned before, the discharge characteristics of the atomizer used for the data of Fig. 10 resulted in an increase of the oil flow rate with increasing mean droplet diameter. This means that the separation efficiency considerably increased while the inlet mean droplet diameter and hence the oil flow rate supplied to the breather increased.

This supports the result that only oil particles below a certain size can pass the breather. A certain fraction of these small droplets is removed from the air by the metal foam. The amount of these small particles that are separated in the breather increases with increasing rotational speed and increasing residence time, i.e., decreasing air flow rate.

Pressure Drop. The effects of air flow rate and rotational speed on the breather pressure drop are discussed in the following. As before, the data have been normalized by typical values for engine operation at Idle.

Effect of Air Flow Rate. Figure 11 shows the effect of the air flow rate on the differential pressure across the breather for zero rotation of the breather and for typical speed of the breather at Idle. The oil flow rate was fixed.

For zero rotation, the breather pressure drop increases approximately quadratically with increasing air flow. This behavior is typical for a single restrictor in incompressible flow.

As shown in Fig. 11, the differential pressure increases significantly with rotation. Interestingly, at Idle speed, the breather pressure drop increases only linearly with air flow rate. Doubling the air flow rate at this speed results in an increase of the differential pressure across the breather by 70%.

Effect of Rotational Speed. The effect of the separator speed on the breather pressure drop is further illustrated in Fig. 12. A strong nonlinear dependence can be identified. The differential pressure across the breather progressively increases with increasing rotational speed. The effect of the rotational speed on the breather pressure drop is considerably stronger than the effect of the air flow rate. Relative to Idle conditions, an increase of the rotational speed by 40% results in doubling the breather pressure drop.

Summary of Results. The following main results have been obtained.

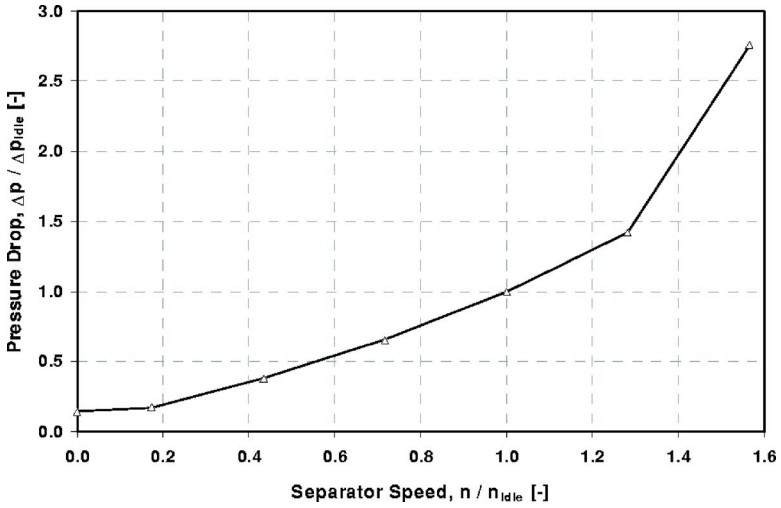

Fig. 12 Effect of rotational speed on breather pressure drop, $W_{air}/W_{air,Idle}=1.0$, $V_{oil,inlet}=2.0$ l/h

- The separation efficiency of the breather increased with decreasing air flow rate, i.e., increasing residence time of oil particles in the breather.
- The separation efficiency increased with increasing rotational speed.
- The separation efficiency increased with increasing particle size.
- Only droplets below a certain size ($\sim$0.5 μm) can pass the breather.
- The separator itself did not produce mist in the tests.
- The breather pressure drop increased with increasing air flow rate and with increasing rotational speed.
- The effect of the rotational speed on the breather pressure drop is stronger than the effect of the air flow rate.

As can be seen from the results, the target for low pressure drop is contradictory to good separation efficiency. An increase of the rotational speed improves separation efficiency but at the expense of an increased pressure drop across the breather. Increasing the length of the breather is expected to increase separation efficiency as the residence time in the breather is increased. But, an increase in length is accompanied by a larger size, weight, and pressure drop. An increased mean breather radius may improve separation efficiency as the centrifugal forces are increased but implies larger weight and size.

Optimisation Strategy

The contradictory effects as described before need to be traded against each other to meet the limiting requirement and obtain the optimum design for a specific application. The following strategy was developed as a guideline for optimum breather design.

For good separation efficiency,

- maximize rotational speed to increase centrifugal separation
- maximize separator diameter, which assists centrifugal separation, maximizes flow area, and reduces pressure drop
- maximize path length (particularly if high rpm and generous diameter are not available), which increases separation and pressure drop

For low pressure drop across separator,

- maximize air flow area
- reduce speed consistent with the required separation efficiency

For light weight,

- maximize rotational speed

Conclusions

A systematic study of the separation efficiency of a typical aeroengine air/oil separator design was conducted. The main emphasis of the investigations was on the separation of small droplets with a diameter of up to 10 μm. Oil mist with defined oil droplet size distribution was supplied to the breather.

By simultaneously measuring particle size and oil concentration upstream and downstream of the breather, the separation mechanism was analyzed and the separation efficiency was assessed. In addition, the pressure drop across the separator was measured. The experimental program covered a variation of air flow, oil flow, shaft speed, and droplet size.

The experimental investigation identified relevant parameters and quantified their effect on separation efficiency and pressure drop. As shown by the results, the target for low pressure is contradictory to good separation efficiency. These effects need to be traded against each other according to the limiting requirements of a specific application. Therefore, based on the experimental results, guidelines for an optimum breather design have been established.

The application of advanced seals such as carbon or brush seals instead of labyrinth seals offers potential for better separation efficiency and reduced oil consumption. Due to the significant reduction of the sealing air flow by the tight seals, the breather flow and hence the oil loss through the breather exhaust flow are significantly reduced.

As the current study has shown, the breather itself did not produce mist. Only small droplets below a certain size can pass the breather and contribute to the oil loss through the breather discharge. Therefore, the generation of small oil particles in the engine oil system, e.g., at fast rotating surfaces or bearings [28–31] or in valves, upstream of the breather should be avoided.

Acknowledgment

These investigations were supported by the European Commission within the GROWTH Programme, Research Project "Advanced Transmission and Oil System Concepts (ATOS)." Contract No. G4RD-CT-2000-00391. This financial support is gratefully acknowledged.

Special thanks are due to Bob Cooper, Dunlop Equipment, for his dedicated support during the experimental phase of the study.

Nomenclature

A = area (m^2)
$c_{vol,exit}$ = oil volume concentration in breather exhaust flow, $c_{vol,exit} = V_{oil,exit}/V_{air}$
d = droplet diameter (m)
d_{30} = mean volumetric diameter (m)
n = separator speed (min^{-1})
n_{Idle} = separator speed at Idle (min^{-1})
$Q30(d)$ = cumulative volume distribution
V_{air} = air volume flow (m^3/s)
$V_{oil,inlet}$ = oil volume flow at breather inlet (m^3/s)
$V_{oil,exit}$ = oil volume flow at breather exit (m^3/s)
W_{air} = air mass flow (kg/s)
$W_{air,Idle}$ = air mass flow at Idle (kg/s)
W^* = mass flux, $W^* = (W_{air} + W_{oil})/A (kg/(m^2\,s))$
x = mass flow ratio, $x = W_{air}/(W_{air} + W_{oil})$
Δp = breather pressure drop (Pa)
Δp_{Idle} = breather pressure drop at Idle (Pa)
Δp_{air} = differential air pressure across atomizer (Pa)
Δp_{oil} = differential oil pressure across atomizer (Pa)
η_{sep} = separation efficiency, $\eta_{sep} = (V_{oil,inlet} - V_{oil,exit})/V_{oil,inlet}$
ρ_G = density of gas phase (kg/m^3)
ρ_L = density of liquid phase (kg/m^3)
σ_g = geometric standard deviation of droplet size distribution (m)

References

[1] Klingsporn, M., 2004, "Advanced Transmission and Oil System Concepts for Modern Jet Engines," ASME Paper No. GT-2004-53578.
[2] Schmidt, J., Hank, W. K., Klein, A., and Maier, K., 1982, "The Oil/Air System of a Modern Fighter Aircraft Engine," AGARD-CP-329, pp. 7_1–7_{20}.
[3] Willenborg, K., Au, J., Dullenkopf, K., and Wittig, S., 2005, "Experimental Investigation of the Two-Phase Flow Through a Leaking Bearing Chamber Seal," *Proceedings of the XVII Symposium on Air Breathing Engines (ISABE 2005)*, Munich, Germany, Sep. 4–9, AIAA Paper No. 2005_1207.
[4] Willenborg, K., Busam, S., Roßkamp, H., and Wittig, S., 2002, "Experimental Studies of the Boundary Conditions Leading to Oil Fire in the Bearing Chamber and in the Secondary Air System of Aeroengines," ASME Paper No. GT-2002-30241.
[5] Zimmermann, H., Kammerer, A., Fischer, R., and Rebhan, D., 1991, "Two-Phase Flow Correlations in Air/oil Systems of Aero Engines," ASME Paper No. 91-GT-51.
[6] Fischer, R., 1998, "Zweiphasenströmung in Triebwerksleitungen—Theoretische und Experimentelle Untersuchungen von Luft/Öl Strömungen durch Blenden," dissertation, Universität Karlsruhe, Karlsruhe, Germany.
[7] Baker, O., 1954, "Simultaneous Flow of Oil and Gas," Oil Gas J., **23**, pp. 185–195.
[8] Hewitt, G. F., and Roberts, D. N., 1969, "Studies of Two-Phase Flow Patterns by Simultaneous X-Ray and Flash Photography," AERE Report No. M 2159.
[9] Oshinowo, T., and Charles, M. E., 1974, "Vertical Two-Phase Flow, Part 1: Flow Pattern Correlation," Can. J. Chem. Eng., **52**, pp. 25–35.
[10] Mayinger, F., 1982, *Strömung und Wärmeübergang in Gas-Flüssigkeits-Gemischen*, Springer, Wien.
[11] Wallis, G. B., 1968, *Two-Phase Flow and Heat Transfer*, McGraw-Hill, New York.
[12] Brauer, H., 1971, *Grundlagen der Einphasen-und Mehrphasenströmung*, Verlag Sauerländer, Arau und Frankfurt am Main.
[13] Busam, S., Ebner, J., and Wittig, S., 2001, "An Experimental Study of Liquid Film Thickness in Annular Air/Oil Flow in a Vertical Pipe Using a Laser Focus Displacement Meter," ASME Paper No. 2001-GT-0116.
[14] Busam, S., 2004, "Druckverlust und Wärmeübergang im Entlüftungssystem von Triebwerkslagerkammern," dissertation, Universität Karlsruhe, Karlsruhe, Germany.
[15] Wang, Y., Care, I., Eastwick, C. N., Hibberd, S., and Simmons, K., 1999, "CFD Study of Droplet Motion in a Simplified Breather Chamber Geometry at High Shaft Rotating Speeds," *Proceedings of the Fourth International Symposium of Multiphase Flow and Heat Transfer*, X'ian, China, Aug. 22–24.
[16] Care, I., Hibberd, S., Simmons, K., and Wang, Y., 1999, "CFD Computation of Oil-Air Separation in an Engine Breather," I Mech E Seminar: CFD Technical Developments And Future Trends, Dec. 13–14.
[17] Hossain, M., Wang, Y., Eastwick, C. N., Simmons, K., and Hibberd, S., 2000, "A Comparison of Flow Characteristics for Two Aero-Engine Air/Oil Separators," NAFEMS, Industrial CFD and the Move Towards Multiphase Analysis, Warwick University, Nov. 8.
[18] Eastwick, C., Hibberd, S., Simmons, K., Wang, Y., Care, I., and Aroussi, A., 2001, "Using CFD to Improve Aero-Engine Air/Oil Separator Design," Computational Technologies for Fluid/Thermal/Structural/Chemical Systems With Industrial Application, PVP (Am. Soc. Mech. Eng.), **448-1**.
[19] 1997, "Dunlop Equipment Retimet Deoilers for Aeroengines," Aircraft Engineering and Aerospace Technology, **69**, pp. 64–66.
[20] Düsen-Schlick GmbH, Company web site: www.duesen-schlick.de.
[21] Spraying Systems Co., Company web site: www.spray.com.
[22] Sympatec GmbH, Company web site: www.sympatec.com.
[23] Röthele, S., and Witt, W., 1999, "Laser Diffraction: Millenium Link for Particle Size Analysis," Cah. Groupe Fr. Rheol., **11**, pp. 91–95.
[24] Wittig, S. L. K., Zahoransky, R. A., and Sakbani, Kh., 1981, "The Dispersion Quotient Technique in Submicron Particle Size Analysis," J. Aerosol Sci., **12**, pp. 183–184.
[25] Schneider, W., Kausch, E., Wittig, S., and Feld, H.-J., 1988, "The Mean Particle Size in Fresh Undiluted Cigarette Smoke Determined by Means of the Dispersion Quotient Method," J. Aerosol Sci., **19**, pp. 995–898.
[26] Wittig, S., Feld, H.-J., Müller, A., Samenfink, W., and Tremmel, A., 1990, "Application of the Dispersion-Quotient Method Under Technical System Conditions," *Proceedings of the Second International Congress on Optical Particle Sizing*, Tempe, AZ, Mar. 5–9.
[27] Dittmann, R., Feld, H.-J., Samenfink, W., and Wittig, S., 1994, "Multiple Wavelength Extinction Technique for Particle Characterization in Dense Particle Clouds," Part. Part. Syst. Charact., **11**, pp. 379–384.
[28] Glahn, S., Busam, S., Blair, M. F., Allard, K. L., and Wittig, S., 2002, "Droplet Generation by Disintegration of Oil Films at the Rim of a Rotating Disk," ASME J. Eng. Gas Turbines Power, **124**, pp. 117–124.
[29] Glahn, S., Blair, M. F., Allard, K. L., Busam, S., Schäfer, O., and Wittig, S., 2003, "Disintegration of Oil Jets Emerging From Axial Passages at the Face of a Rotating Cylinder," ASME J. Eng. Gas Turbines Power, **125**, pp. 1003–1010.
[30] Glahn, S., Blair, M. F., Allard, K. L., Busam, S., Schäfer, O., and Wittig, S., 2003, "Disintegration of Oil Films Emerging From Radial Holes in a Rotating Cylinder," ASME J. Eng. Gas Turbines Power, **125**, pp. 1011–1020.
[31] Gorse, P., Dullenkopf, K., and Bauer, H.-J., 2005, "The Effect of Airflow Across Aero-Engine Roller Bearing on Oil Droplet Generation," *Proceedings of the XVII Symposium on Air Breathing Engines (ISABE 2005)*, Munich, Germany, Sept. 4–9, AIAA Paper No. 2005_1208.

An Energy-Based Uniaxial Fatigue Life Prediction Method for Commonly Used Gas Turbine Engine Materials

Onome E. Scott-Emuakpor

Herman Shen[1]
Professor
e-mail: shen.1@osu.edu

Department of Mechanical Engineering,
The Ohio State University,
206 West, 18th Avenue,
Columbus, OH 43210

Tommy George

Charles Cross
e-mail: shen.1@osu.edu

Air Force Research Laboratory,
Propulsion Directorate,
1950 Fifth Street, Bldg. 18,
Wright Patterson Air Force Base, OH 45433

A new energy-based life prediction framework for calculation of axial and bending fatigue results at various stress ratios has been developed. The purpose of the life prediction framework is to assess the behavior of materials used in gas turbine engines, such as Titanium 6Al-4V (Ti 6Al-4V) and Aluminum 6061-T6 (Al 6061-T6). The work conducted to develop this energy-based framework consists of the following entities: (1) a new life prediction criterion for axial and bending fatigue at various stress ratios for Al 6061-T6, (2) the use of the previously developed improved uniaxial energy-based method to acquire fatigue life prior to endurance limit region (Scott-Emuakpor et al., 2007, "Development of an Improved High Cycle Fatigue Criterion," ASME J. Eng. Gas Turbines Power, ***129****, pp. 162–169), (3) and the incorporation of a probabilistic energy-based fatigue life calculation scheme to the general uniaxial life criterion (the first entity of the framework), which is capable of constructing prediction intervals based on a specified percent confidence level. The precision of this work was verified by comparison between theoretical approximations and experimental results from recently acquired Al 606-T6 and Ti 6Al-4V data. The comparison shows very good agreement, thus validating the capability of the framework to produce accurate uniaxial fatigue life predictions for commonly used gas turbine engine materials.* [DOI: 10.1115/1.2943152]

1 Introduction

In an effort to reduce the possibilities of gas turbine engine damage, which is mostly caused by high cycle fatigue (HCF) [2], the search for more sufficient fatigue assessment tools and instrumentation is currently in overdrive; thus, there is a parallel advancement in fatigue and fracture analysis. Through the progression of fatigue analysis, tools such as a stress versus cycles plot, or *S-N* curve, have been used to observe fatigue strength due to the respective cycles to failure. The *S-N* curve is a plot of alternating stress (amplitude, max, min, etc.) versus number of cycles to failure, which is generally plotted on a semilogarithmic scale. Other tools for assessing fatigue properties are the Goodman diagram and the modified Goodman diagram [3], which are the popular choices for a failure-free aircraft engine design criterion. The Goodman diagram is a plot of alternating stress versus mean stress and represents the fatigue properties of a given material for a specified number of cycles. The Goodman diagram and the *S-N* curve are often constructed with uniaxial fatigue data that are acquired, conventionally, via servohydraulic machinery operating in tension/compression (axial) at a frequency of approximately 40 Hz. HCF of turbine engine blades, however, often occurs under high order bending or combined bending and twist modes [4]. Therefore, the uniaxial fatigue results from the Goodman diagram and the *S-N* curve are insufficient means for characterizing the fatigue that occurs in gas turbine engine components. Adding to this insufficiency, conventional uniaxial fatigue testing (tension/compression) requires significant amounts of time to obtain sufficient HCF results. For example, at the operating frequency of 40 Hz, nearly 70 h are required to accumulate 10^7 cycles. Therefore, long time periods are needed to acquire the desired fatigue properties of a material.

In an effort to achieve a realistic experimental comparison to turbine engine blade fatigue results, a vibration-based uniaxial testing methodology was developed to acquire bending fatigue data [4–6]. The thought behind the methodology is supplying a dynamic base excitation to a specimen at a specified high resonant frequency, between 1200 and 1600 Hz, showing bending behavior. Using this method, roughly 1.5–2.5 h are required to accumulate 10^7 cycles, which is a significant reduction in time as opposed to the conventional method.

Along with the vibration-based fatigue methodology, a prestraining procedure is used as a preliminary step to generating bending fatigue results at stress ratios other than −1 (fully reversed) [7,8]. The prestraining procedure is executed by applying a localized tensile load on a bending test specimen until the specimen undergoes a specific localized yielding: Once the localized yielding occurs, the applied load is released. Upon returning the applied load to zero, a maximum residual stress is present at the fatigue zone. This residual stress can be observed as the applied mean stress during vibration-based bending fatigue [9]. Further details for determining the location where yielding should occur on the bending specimen during the prestraining procedure can be found in Refs. [7,8].

The recent development of the vibration-based methodology, combined with the prestraining procedure, is a preliminary step that leads to development of a fatigue assessment method, which is sufficient in characterizing biaxial and multiaxial fatigue properties. The efforts to accommodate the set forth task have led to the examination of the association between strain energy and failure. Curiosity of this correlation can be dated back as early as the 1920s [10]. However, in the 1940s and 1950s, a number of well-publicized attempts to relate strain energy per cycle to the number of cycles for failure were considered and initially resulted in minimal success [11]. However, success in this area was later achieved

[1]Corresponding author.

Contributed by the International Gas Turbine Institute of ASME for publication in the JOURNAL OF ENGINEERING FOR GAS TURBINES AND POWER. Manuscript received January 5, 2008; final manuscript received February 19, 2008; published online August 28, 2008. Review conducted by Dilip R. Ballal. Paper presented at the ASME Turbo Expo 2007: Land, Sea and Air (GT2007), Montreal, QC, Canada, May 14–17, 2007.

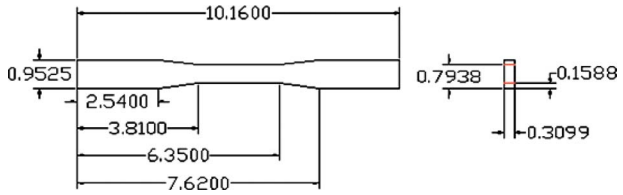

Fig. 1 Dimensions (cm) of the ASTM fatigue dog-bone specimen [14]

by introducing the hypothesis implied; under cyclic loading, there exists a critical energy value for which failure occurs [12]. This hypothesis was later justified by displaying agreement between the theoretical and the experimental results on an *S-N* curve. Further investigation of the assumption made in Ref. [12] led to the introduction of a more sufficient correlation between the fatigue life of a material and the strain energy dissipation during the fatigue process. It has been suggested that the strain energy required to fracture a material monotonically is the same as the strain energy accumulated during a cyclic fatigue procedure [11,13]. Thus, the critical energy value for each material is the monotonic strain energy. Based on this understanding, an improved energy-based criterion has been developed to allow one to systematically determine uniaxial fatigue life based on the amount of energy loss per fatigue cycle [1]. This previously developed energy-based theory shows the capability of accurately predicting the uniaxial fatigue life of Al 6061-T6 specimens [1]. Although the results from this prediction are promising, progress towards a more realistic application was needed. In other words, prediction for the cases of fully reversed cyclic bending and uniaxial fatigue at various stress ratios was essential. Moreover, since Al 6061-T6 is not in heavy use in gas turbine engines, an important progressive step was changing the experimental testing material. This led to experimental analysis on the more commonly used Ti 6Al-4V material. This material, however, experiences a phenomenon known as an endurance limit; which is essentially the minimum stress level that fatigue occurs at. In other words, the *S-N* behavior of a material with an endurance limit asymptotically approaches a specific stress level as fatigue cycles increase to the 10^9 cycle region. Based on this phenomenon, a statistical approach along with the energy-based method developed in Ref. [1] is required to determine HCF in Ti 6Al-4V.

In this study, the development of a new uniaxial energy-based prediction criterion for fatigue life of gas turbine engine materials is discussed. First the mentioned prediction method, summarizes the capabilities for uniaxial fatigue assessment at various stress ratios. Thereafter, the method incorporates a probabilistic energy-based fatigue life calculation scheme to the uniaxial life criterion of Ref. [1]; resulting in the capability to construct prediction intervals for stresses near the endurance limit based on a specified percent confidence level. The summarization of the uniaxial criterion with mean stress effect and the probabilistic method for endurance limit observation were executed and compared with Al 6061-T6 and Ti 6Al-4V experimental results, respectively, on *S-N* curves. The results show that the criterion provides good fatigue life estimation for a component undergoing tension/compression or bending cyclic loading.

2 Experimental Procedures

2.1 Conventional Axial Testing Procedures for Tension/Compression Fatigue. Axial (tension/compression) loading fatigue data were acquired from the ASTM standard fatigue dog-bone (coupon) specimen in Fig. 1 [14]. All the tests were conducted at room temperature using an MTS Systems Corporation servohydraulic load frame (Fig. 2) located in the Turbine

Fig. 2 TEFF laboratory's 22,000 lb uniaxial MTS system corporation

Engine Fatigue Facility (TEFF) of the Air Force Research Laboratory (AFRL) in the Propulsion Directorate (AFRL/RZ) at Wright-Patterson Air Force Base (WPAFB) [1]. To conduct each tension/compression fatigue test, an axial load was applied on the dog bone, at an operational frequency of 40 Hz, until complete fracture occurred [1]. Though the fundamental nature of the uniaxial energy-based prediction method focuses on crack initiation, the number of cycles between initiation and complete fracture during tension/compression HCF is negligible [7]. Therefore, an extraneous method for distinguishing crack initiation from complete fracture was not developed; resulting in crack initiation cycle and complete fracture cycles being equal for tension/compression fatigue test data. The test results were acquired with a strain gage, an extensometer (Fig. 3), and the MTS TestStarIIs control system.

2.2 Vibration-Based Testing Procedures for Bending Fatigue. Bending fatigue tests, which were carried out via the vibration-based fatigue methodology [4–6], were conducted on the uniaxial fatigue specimen in Fig. 4 with a Ling 18,000 lb or an Unholtz Dickie 6000 lb electrodynamic shaker (Fig. 5) located at the TEFF. As shown in Fig. 5, the test specimen is a cantilever plate mounted to the shaker head and a base excitation is applied to the specimen, generating a two-stripe resonant frequency of 1200–1600 Hz for the geometry shown in Fig. 4 [4–6]. Applied stress for this geometry is determined by a linear correlation between the strain gage of Fig. 4 and the laser vibrometer of Fig. 5, where the laser is located at a region of minimal displacement [7]. The optimal location for the laser is determined by analyzing a

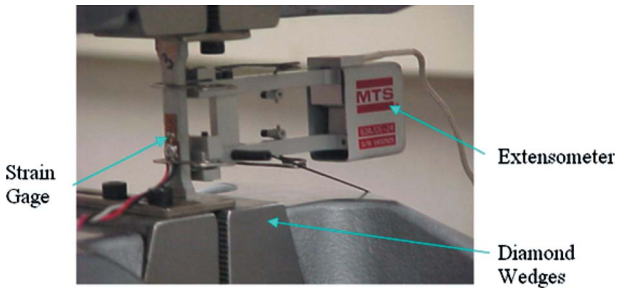

Fig. 3 MTS clamping and measurement devices [1]

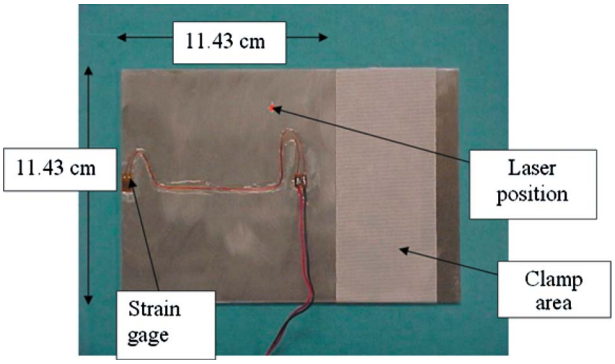

Fig. 4 Bending fatigue specimen [1]

Table 1 Al 6061-T6 fatigue test data for bending specimen

Step Test Method: Plate No. 22					
Step No.	Freq (Hz)	Time (s)	Laser (mm/s)	% Response drop	Response drop rate (mm/s^2)
1	1568	0	634	2.05	0.0289
1	1566	450	628	n/a	n/a
2	1566	0	710	2.25	0.0593
2	1566	270	719	n/a	n/a
3	1565	0	795	2.26	0.0571
3	1565	315	795	n/a	n/a
4	1564	0	870	2.64	0.329
4	1564	**70**	873	2.63	0.371
4	1563	132	875	n/a	n/a

displacement contour plot of a two-striped mode. The displacement plot is generated by computational finite element methods (FEMs) [4–6].

In Sec. 2.1, it is understood that the fundamental nature of the uniaxial energy-based prediction method focuses on crack initiation. Therefore, the fatigue limits for all the bending tests are defined at the instance corresponding to a sudden change in the dynamic response (laser vibrometer) of the plate; which is associated with the initial stage of fatigue crack development. The sudden change in the dynamic response of the specimen during fatigue testing is shown in Table 1. Using the step testing fatigue method [15], each step shown in Table 1 is approximately 638 s long. The "Time" column shows the instance of the respective laser reading and the "% response drop" column represents the corresponding decrease in the laser output. Represented in boldface numbering, the table shows the testing time related to the instance of failure. At the instance of failure, a series of 0.5 –1 mm long microcracks had developed. Identification of these cracks was due to the change in the stiffness of the specimen, which directly resulted in the change of the resonant frequency and dynamic response as well. This observational technique was developed and has been used in previous studies [1,4–7].

3 Previous Research Scope

3.1 Improved Energy-Based Prediction Method for Tension/Compression (Axial). Though several energy-based methods for predicting tension/compression fatigue life have been developed [11,13], an improved energy-based criterion for tension/compression with the capability to easily incorporate the effects of stress gradient on fatigue life was essential for the future possibility of developing a general prediction criterion to address fatigue in the bending case. This improved energy-based criterion was developed from the stress-strain representation of the monotonic (Eqs. (1) and (2)) and cyclic (Eq. (3)) loading behaviors shown in the following equations, where Eqs. (1) and (2) represent the stress-strain relation prior to and after the necking phenomenon, respectively [1,13].

$$\varepsilon = \frac{\sigma}{E} + \varepsilon_0 \sinh\left(\frac{\sigma}{\sigma_0}\right) \tag{1}$$

$$\sigma = \beta_1 \varepsilon + \beta_0 \tag{2}$$

$$\varepsilon_{\text{cycle}} = \frac{\sigma_{\text{P.P.}}}{E} + \frac{1}{C} \sinh\left(\frac{\sigma_{\text{P.P.}}}{\sigma_c}\right) \tag{3}$$

The parameters displayed are defined as follows: σ is the value for stress at the surface of the specimen (in the bending case, max stress), ε is the strain corresponding to the stress σ, β_1 and β_0 are the respective slope and intercept of the stress-strain relationship in the necking region (from ultimate tensile to point of fracture), $\sigma_{\text{p.p.}}$ is the generalized stress value corresponding to the generalized cyclic strain $\varepsilon_{\text{cycle}}$ (i.e., the minimum fully reversed point is observed as the origin), E is the modulus of elasticity, and the variables σ_c, σ_0, ε_0, and C are curve fit parameters [1]. These curve fit parameters for the cyclic and monotonic representations (Eqs. (1)–(3)) are statistically acquired by comparison between low cycle (LC) experimental results and experimental monotonic results, respectively [1].

Fatigue life is systematically determined for the improved energy-based prediction criterion by taking the total monotonic strain energy density and dividing it by the strain energy density for one cycle. The total strain energy density dissipated during a monotonic process is determined as the area underneath the curve constructed by Eqs. (1) and (2) and the strain energy density for one cycle is represented by the area within the hysteresis loop formed by Eq. (3). Though finding the monotonic strain energy density was a straightforward task, the cyclic strain energy density was determined by assuming that the tensile stress-strain behavior of the hysteresis loop was identical to the compressive behavior. Therefore, the cyclic strain energy density is determined by Eq.

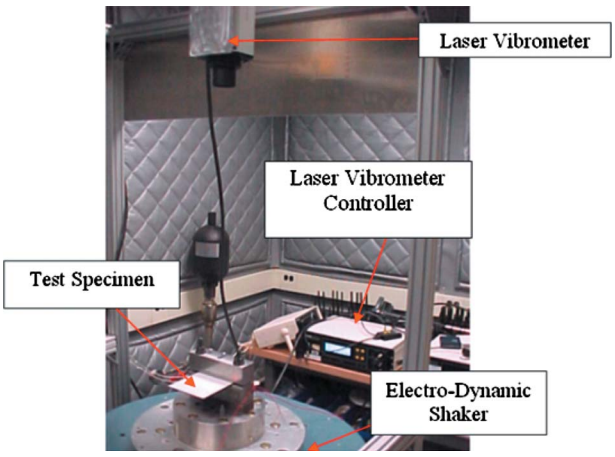

Fig. 5 Vibration-based fatigue experiment setup [1]

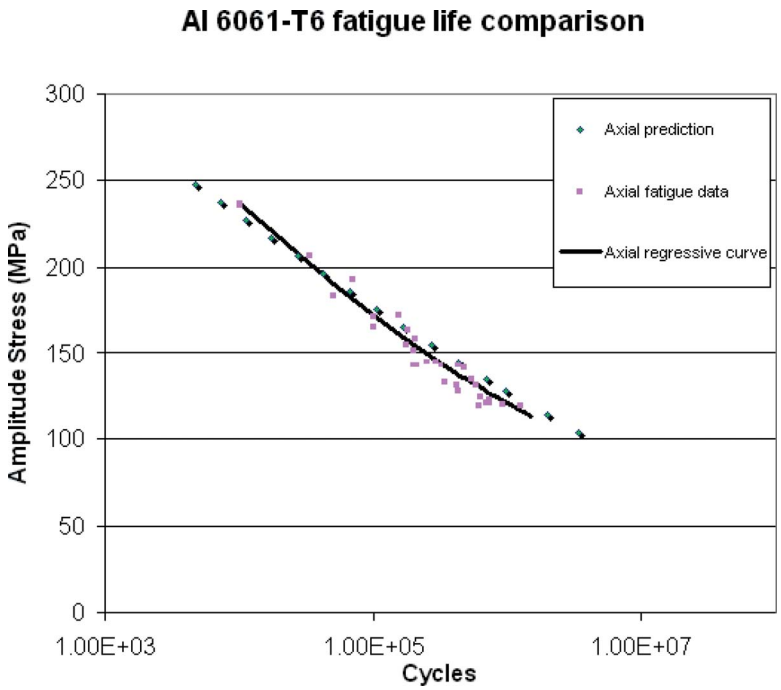

Fig. 6 Fully reversed tension/compression fatigue life comparison for Al 6061-T6 [1]

(4) and the expression of the improved energy-based criterion for systematically determining fatigue life at a specified stress amplitude level (σ) is given by Eq. (5) [1];

$$W_{\text{cycle}} = \sigma_{\text{P.P.}}\varepsilon_{\text{cycle}} - 2\int_0^{\sigma_{\text{P.P.}}} \varepsilon_{\text{cycle}} d\sigma_{\text{P.P.}} \tag{4}$$

$$N = C\frac{\sigma_n\left(\varepsilon_n - \frac{\sigma_n}{2E}\right) - \varepsilon_0\sigma_0\left[\cosh\left(\frac{\sigma_n}{\sigma_0}\right) - 1\right] + \frac{\beta_1}{2}(\varepsilon_f^2 - \varepsilon_n^2) + \beta_0(\varepsilon_f - \varepsilon_n)}{2\sigma_c\left\{\frac{\sigma}{\sigma_c}\sinh\left(\frac{2\sigma}{\sigma_c}\right) - \left[\cosh\left(\frac{2\sigma}{\sigma_c}\right) - 1\right]\right\}} \tag{5}$$

where σ_n is the necking stress, ε_f is the facture strain, and ε_n is the necking strain. Using Al 6061-T6 as the material of choice, the results from Eq. (5) are compared to the previously acquired fully reversed tension/compression test results [1] and the corresponding linear regression curve on the *S-N* plot of Fig. 6. The comparison shows that the criterion provides good life estimations for tension/compression fatigue results. To further validate the accuracy of the comparison, strain energy density per cycle is calculated from LC experimental results and matched with the experimental linear regression cycles to failure: These results are then compared with the energy-based predicted cyclic strain energy density and the related cycles to failure, which are all displayed in Fig. 7. It has been previously presented that the logarithmic slope of this comparison is roughly −0.6 [16]. Though the experimental results of Fig. 7 concur with this belief, further analysis of the cyclic strain energy density calculation method is conducted to provide reasoning for this agreement. Conclusion of this analysis shows that the variation between experimental and analytical results is more obvious in test data with a higher standard deviation of the hysteresis loop curve fit constructed by Eq. (3) [1]. Due to a more sensitive stress-strain comparison, minor changes in the standard deviation of the curve fit causes a major variation in strain energy density calculation [1]. Based on this sensitivity issue, the cyclic curve fit parameters that provided minimal standard deviation were used in Eq. (5) for the comparison between the energy-based prediction method and experimental results (Fig. 6). This comparison, as previously stated, validates that the improved uniaxial energy-based method provides encouraging fatigue life prediction outputs.

3.2 Improved Energy-Based Prediction Method With Stress Gradient Effect (Bending). In order to extend the improved energy-based criterion to the bending case, the difference between stress gradient effect through the thickness of the bending and tension/compression specimen was evaluated. This difference is illustrated in Fig. 8. Since the distribution of the applied stress in the bending specimen shown in Fig. 8 varies with respect to the distance from the neutral axis, the strain energy through the thickness of each specimen (effective-strain energy) differs from tension/compression. In order to determine the total effective-strain energy in the bending case (strain energy per surface area), the alternating stress from the monotonic and cyclic strain equations was written as a function of the distance from the neutral axis. After determining the respective effective-strain energy from the monotonic and cyclic procedures, the energy-based fatigue life prediction understanding (mentioned in Sec. 1) was used to de-

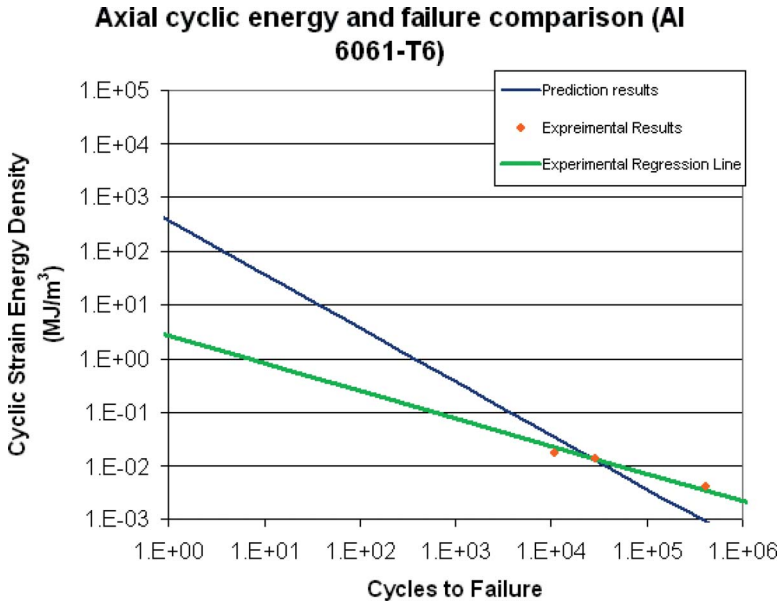

Fig. 7 Fully reversed tension/compression cyclic strain energy comparison for Al 6061-T6

velop the improved energy-based method with stress gradient effect (Eq. (6))[17]. Fatigue life prediction results were calculated from Eq. (6) and another encouraging uniaxial comparison is made on Fig. 9 with the bending experimental data, tension/compression test data, and the improved energy-based prediction results for tension/compression (Eq. (5))

$$N = C\frac{\sigma_n\left(\varepsilon_n - \frac{\sigma_n}{2E}\right) - \varepsilon_0\sigma_0\left[\cosh\left(\frac{\sigma_n}{\sigma_0}\right) - 1\right] + \frac{\beta_1}{2}(\varepsilon_f^2 - \varepsilon_n^2) + \beta_0(\varepsilon_f - \varepsilon_n)}{\sigma_c\left[\cosh\left(\frac{2\sigma}{\sigma_c}\right) - \frac{3\sigma_c}{2\sigma}\sinh\left(\frac{2\sigma}{\sigma_c}\right) + 2\right]} \tag{6}$$

4 Mean Stress Effect on Uniaxial Fatigue Life

4.1 Axial Fatigue at Various Stress Ratios. The effect of an applied mean stress on fatigue life can be observed in two sections. The first section implies that strain energy is dissipated by the constant applied static load; second, the plastic deformation in the hysteresis loop with positive mean stress effect is greater than the deformation in fully reversed cyclic loading. These two occurrences simultaneously result in the reduction of the amount of cycles required to fatigue a specimen under positive mean stress influence.

Energy due to constant static mean loading is described as follows: When conducting a cyclic test at stress ratios ($R = \sigma_{\min}/\sigma_{\max}$) greater than -1.0, a constant mean stress is applied. Therefore, some of the strain energy required for monotonic fracture has already been dissipated, thus reducing the total strain energy required for fatigue. An illustration of this is shown on the stress-strain curve in Fig. 10. To further elaborate on this figure, the area underneath the stress-strain curve between zero and mean stress represents a monotonic mean strain energy density based on the constant load; this is expressed by Eq. (7) for mean stresses less than necking and Eq. (8) for mean stresses between the necking and fracture point. The total monotonic strain energy density

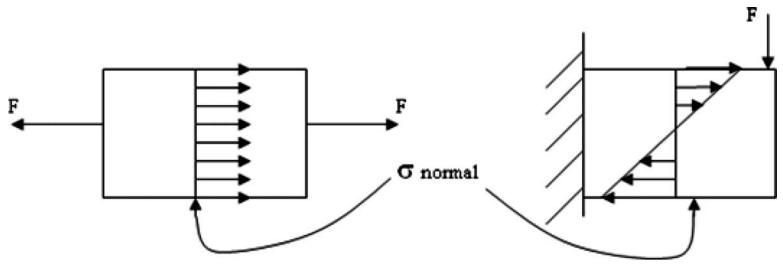

Fig. 8 Stress distribution as a result of the respective uniaxial loading application [17]

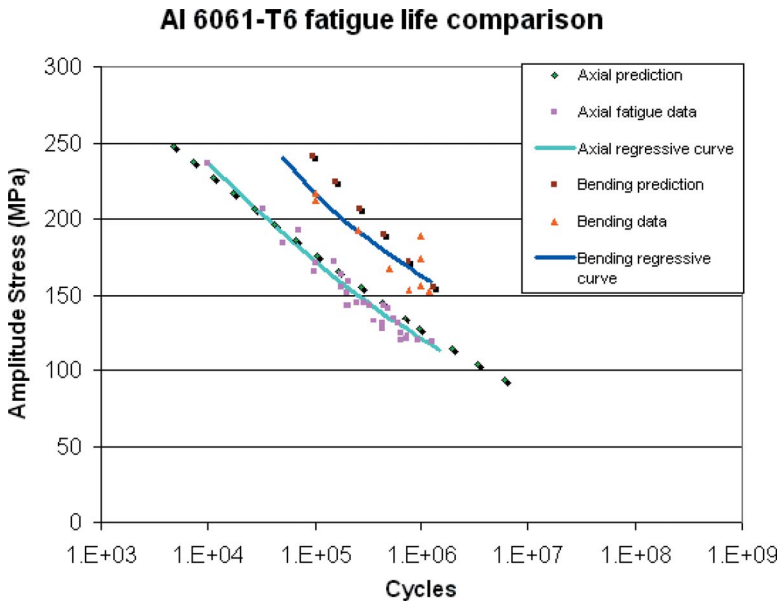

Fig. 9 *S-N* fully reversed tension/compression and bending fatigue life comparison (Al 6061-T6)[17]

is defined by the area underneath the entire stress-strain curve of Fig. 10 and is represented by Eq. (9). Therefore, the remaining strain energy density required for fatigue is expressed by subtracting the mean strain energy density from the total strain energy density (Eq. (10)).

$$W_{\text{mean}} = \sigma_{\text{mean}}\left(\varepsilon_{\text{mean}} - \frac{\sigma_{\text{mean}}}{2E}\right) - \varepsilon_0\sigma_0\left(\cosh\left(\frac{\sigma_{\text{mean}}}{\sigma_0}\right) - 1\right) \quad (7)$$

$$W_{\text{mean}} = \sigma_n\left(\varepsilon_n - \frac{\sigma_n}{2E}\right) + \varepsilon_0\sigma_0\left[\cosh\left(\frac{\sigma_n}{\sigma_0}\right) - 1\right] + \frac{\beta_1}{2}(\varepsilon_{\text{mean}}^2 - \varepsilon_n^2) + \beta_0(\varepsilon_{\text{mean}} - \varepsilon_n) \quad (8)$$

$$W_f = \sigma_n\left(\varepsilon_n - \frac{\sigma_n}{2E}\right) + \varepsilon_0\sigma_0\left[\cosh\left(\frac{\sigma_n}{\sigma_0}\right) - 1\right] + \frac{\beta_1}{2}(\varepsilon_f^2 - \varepsilon_n^2) + \beta_0(\varepsilon_f - \varepsilon_n) \quad (9)$$

$$W_N = W_f - W_{\text{mean}} \quad (10)$$

When evaluating the fully reversed tension/compression cyclic behavior, two assumptions were set in place: The strain equation is determined from a generalized coordinate system, and the compressive behavior of the cyclic stress-strain relation is the same as the tensile [1]. Both of these statements are also assumed for cyclic loading with mean stress effect: Therefore Eq. (3), and all of the curve fit parameter values from Ref. [1], can still be used to characterize the stress-strain behavior. However, unlike the fully reversed stress-strain loop formed in Ref. [1], the loop formed with mean stress effect is much different. This assertion is proven by the experimental results in Fig. 11, which shows that the effect of a positive mean stress on cyclic stress-strain behavior results in an open hysteresis loop.

The assumption for this particular behavior can be fully explained in Figs. 12 and 13. These figures show an extreme exaggeration of the cyclic stress-strain relation on a generalized coordinate system, which has shifted the minimum alternating stress-strain point of a fully reversed analysis to the origin (0, 0); thus; the corresponding maximum alternating stress and strain are twice the original alternating value (i.e., 2σ and 2ε, or $\sigma_{\text{p.p.}}$ and $\varepsilon_{\text{p.p.}}$ where p.p.=peak to peak). In Fig. 12, the fully reversed stress-strain loop can be developed using the cyclic strain equation (Eq. (3)) from zero to peak to peak for both the tensile and compressive relations. Developing the hysteresis loop with the mean stress

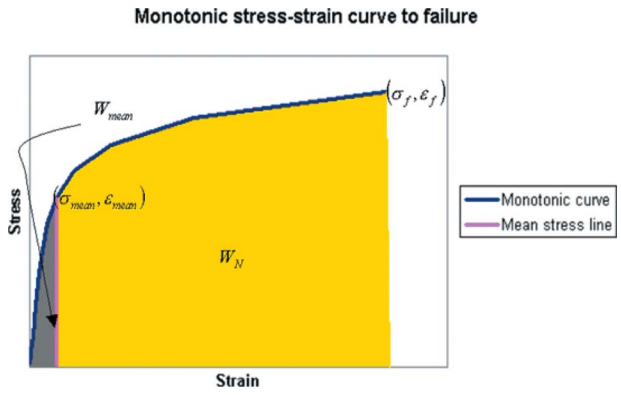

Fig. 10 Simulated monotonic stress-strain curve

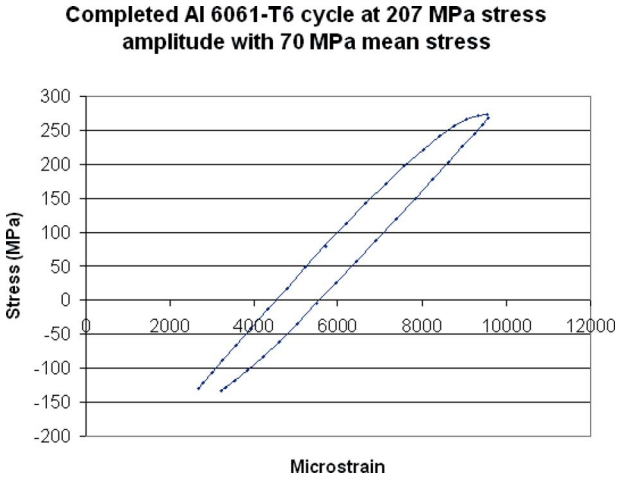

Fig. 11 Hysteresis loop for one cycle with mean stress effect (Al 6061-T6)

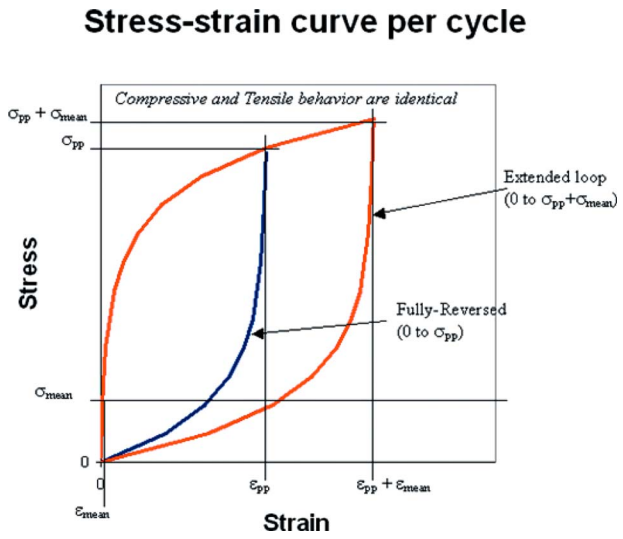

Fig. 12 Simulated hysteresis loop comparison

effect, however, is more complicated. The first observation made is that the tensile stress-strain behavior does not start from the generalized origin. Further observation of Fig. 12 shows that the hysteresis loop with mean stress effect begins and ends at the horizontal line indicating the applied mean stress level and the maximum point of the loop is at the horizontal line indicating peak-to-peak stress plus mean stress. Next, it is shown in Fig. 13 that if the compressive curve were to go back to the origin, it would have the same stress-strain behavior as the tensile curve from zero to peak-to-peak plus mean. Based on this observation, the tensile behavior of the hysteresis loop with mean stress effect is characterized as Eq. (3) from mean to peak-to-peak plus mean stress and the compressive behavior is characterized as Eq. (3) from zero to peak-to-peak stress.

From the in-depth mean-stress-effect analysis on cyclic behavior shown in Fig. 13, the cyclic strain energy density can be determined by the generalized expression

$$W_c = \sigma_{\text{p.p.}}(\varepsilon_{\text{p.p.}} + \varepsilon_{\text{mean}}) - \int_{\sigma_{\text{mean}}}^{\sigma_{\text{p.p.}}+\sigma_{\text{mean}}} \varepsilon d\sigma - \int_{0}^{\sigma_{\text{p.p.}}} \varepsilon d\sigma \quad (11)$$

where $\sigma_{\text{p.p.}}$ is peak-to-peak stress, $\varepsilon_{\text{p.p.}}$ is peak-to-peak strain, σ_{mean} is the mean stress, and $\varepsilon_{\text{mean}}$ is the mean strain. The general expression of Eq. (11) is made up of three sections. Each of these sections is individually solved and written as

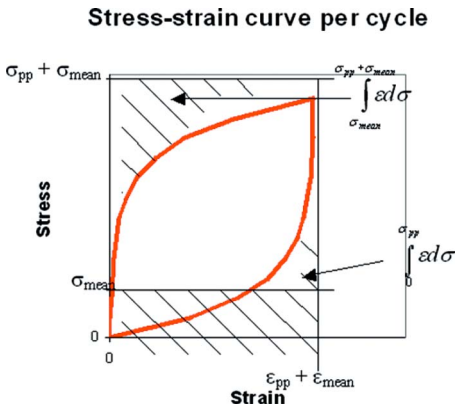

Fig. 13 Simulated hysteresis loop with mean stress effect (non shaded area)

$$\sigma_{\text{p.p.}}(\varepsilon_{\text{p.p.}} + \varepsilon_{\text{mean}}) = 2\sigma\left[\frac{2\sigma + \sigma_{\text{mean}}}{E} + \frac{\sinh\left(\frac{2\sigma + \sigma_{\text{mean}}}{\sigma_c}\right)}{C}\right] \quad (12)$$

$$\int_{\sigma_{\text{mean}}}^{\sigma_{\text{p.p.}}+\sigma_{\text{mean}}} \varepsilon d\sigma = \frac{1}{2EC}\left[(2\sigma + \sigma_{\text{mean}})^2 C + 2\sigma_c \cosh\left(\frac{2\sigma + \sigma_{\text{mean}}}{\sigma_c}\right)E - \sigma_{\text{mean}}^2 C - 2\sigma_c \cosh\left(\frac{\sigma_{\text{mean}}}{\sigma_c}\right)E\right] \quad (13)$$

$$\int_{0}^{\sigma_{\text{p.p.}}} \varepsilon d\sigma = \frac{-\sigma_c E + 2\sigma^2 C + \sigma_c \cosh\left(\frac{2\sigma}{\sigma_c}\right)E}{EC} \quad (14)$$

Observation of these equations combined (i.e., Eq. (11) solved) shows that if σ_{mean} is zero, the summed up expression reverts to the strain energy density calculation for fully reverse loading [1], which is shown as

$$W_{\text{cycle}} = \frac{2\sigma_c}{C}\left\{\frac{\sigma}{\sigma_c}\sinh\left(\frac{2\sigma}{\sigma_c}\right) - \left[\cosh\left(\frac{2\sigma}{\sigma_c}\right) - 1\right]\right\} \quad (15)$$

Based on the understanding of the strain energy relation between monotonic and cyclic failures, Eqs. (10) and (15) can be used to determine the number of cycles required to fatigue a specimen with $R>$ or $=-1.0$ (Eq. (16)).

$$N = \frac{W_N}{W_c} \quad (16)$$

Tension/compression experimental results were acquired from several Al 6061-T6 dog-bone specimens using the MTS servohydraulic machine. Tests were conducted at mean stresses of 70 MPa and 138 MPa, with R ranging from −0.5 to 0.3. The results were compared to the mean energy-based fatigue life prediction criterion (Eq. (16)) and plotted in Figs. 14 and 15. The comparison shows commendable accuracy at higher fatigue life cycles. The minimal variations at lower cycles may be associated with factors such as the load control issue of the MTS actuators at large tensile loads, slipping between the wedges of the hydraulic grips and the dog bone at high tensile loads, or excess applied pressure by the hydraulic grips on the dog bone that causes supplementary axial loading at lower applied loads. Nevertheless, the strain energy density analysis of axially loaded specimens under mean stress effect provides a valid method for fatigue life prediction and estimation.

4.2 Bending Fatigue at Various Stress Ratios: The Effect of Mean Stress and Stress Gradient. Due to present time limitations on advanced bending specimen fixtures, mean stresses cannot be superimposed on vibration-based bending test specimens. Therefore, the prestraining procedure and the vibration-based method are used to generate fatigue results at R values other than the fully reversed case ($R=-1$) [7,8]. Using this two-step experimental testing method, bending fatigue data with R values ranging from −0.1 and −1.0 were acquired from Al 6061-T6 specimens. The fatigue results are displayed on the Goodman diagram of Fig. 16 [7].

In order to construct a Goodman diagram with the theoretical energy-based prediction approach [1], mean stress and stress gradient effect were simultaneously analyzed. The combined analysis of the mean stress and stress gradient effect is conducted by incorporating the analysis of stress through the neutral axis (stress gradient effect) to the mean-stress-effect analysis. Equations (17)

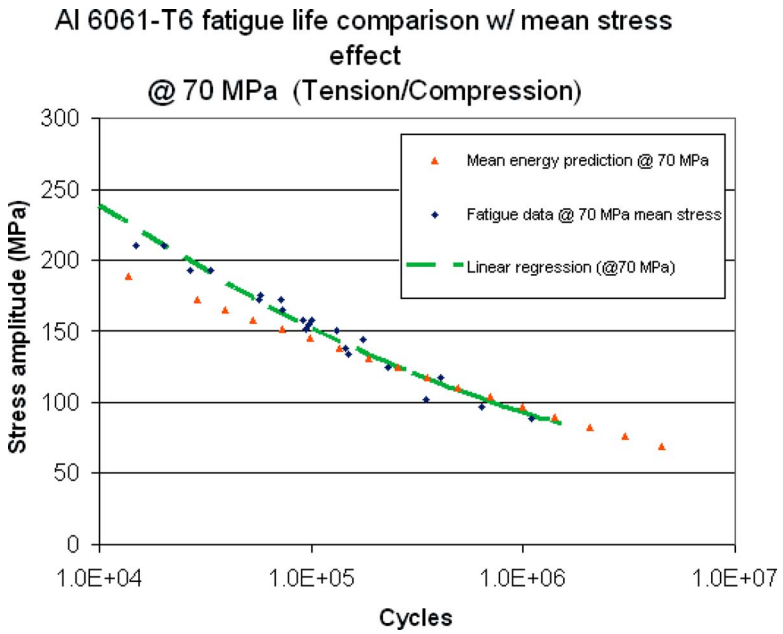

Fig. 14 Tension/compression fatigue life comparison with mean stress effect of 70 MPa (Al 6061-T6)

and (18) show the generalized incorporation of the two analyses, where $W_{N,\mathrm{ev}}$ is the required effective volume (ev) strain energy for fatigue and $W_{\mathrm{mean,ev}}$ is the monotonic mean strain energy for an ev, which is expressed by Eq. (19) for mean stresses less than necking and Eq. (20) for mean stresses between necking and fracture.

$$W_{\mathrm{cycle,mean,ev}} = \int_{-R_y}^{R_y} W_{\mathrm{cycle,mean}} dy_t \tag{17}$$

$$W_{N,\mathrm{ev}} = 2R_y(W_f - W_{\mathrm{mean,ev}}) \tag{18}$$

$$W_{\mathrm{mean,ev}} = \frac{\sigma_{\mathrm{mean}}^2 R}{3E} + 2\varepsilon_0\sigma_0 R\left[\cosh\left(\frac{\sigma_{\mathrm{mean}}}{\sigma_0}\right) - 1\right] \tag{19}$$

$$W_{\mathrm{mean,ev}} = \frac{\sigma_n^2 R}{3E} + 2\varepsilon_0\sigma_0 R\left[\cosh\left(\frac{\sigma_n}{\sigma_0}\right) - 1\right] + \frac{\beta_1}{2}\left\{\left[\frac{\varepsilon_0\sigma_0 R\cosh\left(\frac{\sigma_{\mathrm{mean}}}{\sigma_0}\right)}{\sigma_{\mathrm{mean}}}\right]^2 - [2\varepsilon_n R]^2\right\} + \beta_0\left[\frac{\varepsilon_0\sigma_0 R\cosh\left(\frac{\sigma_{\mathrm{mean}}}{\sigma_0}\right)}{\sigma_{\mathrm{mean}}} - 2\varepsilon_n R\right] \tag{20}$$

Acquiring the fully solved cyclic strain energy expression from the incorporation of the mean stress and stress gradient effect (Eq.

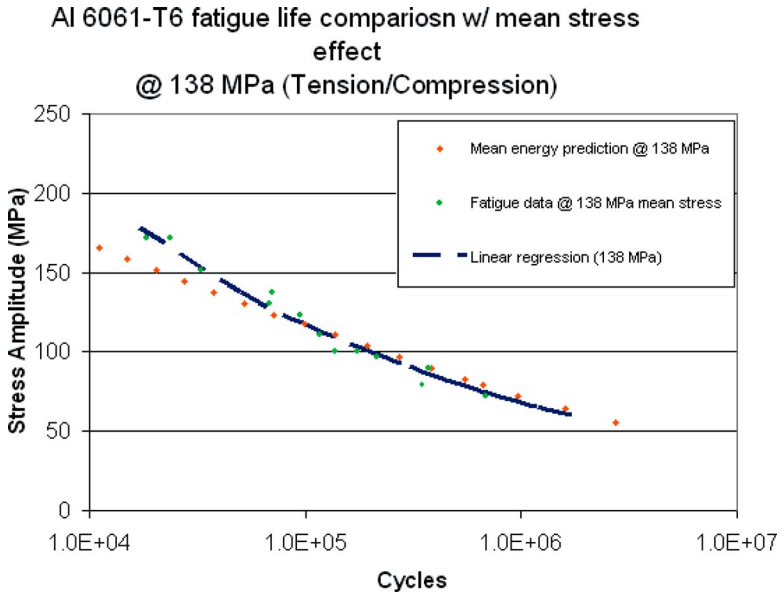

Fig. 15 Tension/compression fatigue life comparison with mean stress effect of 138 MPa (Al 6061-T6)

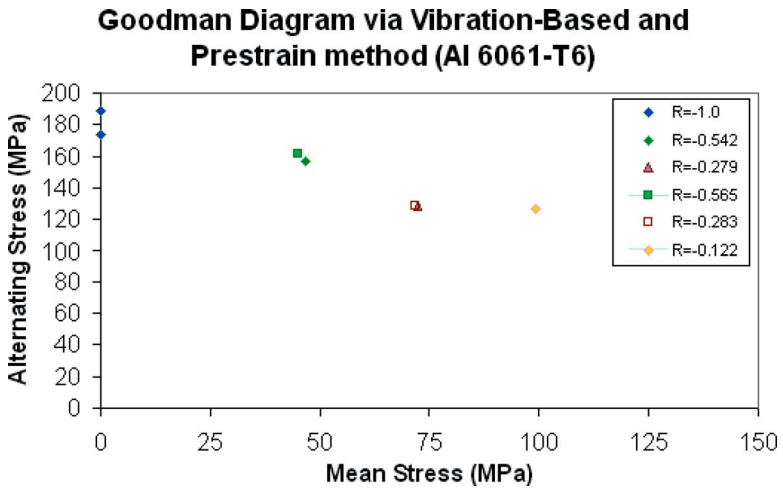

Fig. 16 Bending fatigue data at various *R* values for Al 6061-T6 [7,8]

(17)) can be explained as follows: Stress values used in the strain approximation equations for mean stress effect are multiplied by y_t/R_y (similar to stress gradient analysis from Sec. 3), where y_t is any the distance from the neutral axis and R_y is the maximum distance from the neutral axis, then the equations are integrated with respect to the neutral axis. This analysis leads to the following equations for effective cyclic strain energy with mean stress effects:

$$W_1 = \frac{4\sigma(2\sigma+\sigma_{\text{mean}})R}{3E} + \frac{4\sigma\sigma_c R}{C(2\sigma+\sigma_{\text{mean}})}\left[\cosh\left(\frac{2\sigma+\sigma_{\text{mean}}}{\sigma_c}\right) - \frac{\sigma_c}{(2\sigma+\sigma_{\text{mean}})}\sinh\left(\frac{2\sigma+\sigma_{\text{mean}}}{\sigma_c}\right)\right] \tag{21}$$

$$W_2 = \frac{2\sigma_c^2 R}{C}\left[\frac{1}{2\sigma+\sigma_{\text{mean}}}\sinh\left(\frac{2\sigma+\sigma_{\text{mean}}}{\sigma_c}\right) - \frac{1}{\sigma_{\text{mean}}}\sinh\left(\frac{\sigma_{\text{mean}}}{\sigma_c}\right)\right] + \frac{R}{3E}[(2\sigma+\sigma_{\text{mean}})^2 - \sigma_{\text{mean}}^2] \tag{22}$$

$$W_3 = \frac{-2\sigma_c R}{C} + \frac{4\sigma^2 R}{3E} + \frac{\sigma_c^2 R}{\sigma C}\sinh\left(\frac{2\sigma}{\sigma_c}\right) \tag{23}$$

$$W_{\text{cycle\_mean,ev}} = W_1 - W_2 - W_3 \tag{24}$$

Therefore, using the understanding of the strain energy relationship between monotonic and cyclic failures, Eqs. (17) and (24) can be used to determine the number of cycles required to fatigue a specimen under bending load conditions at $R>$or$=-1.0$ (Eq. (25)).

$$N = \frac{W_{N,\text{ev}}}{W_{\text{cycle,mean,ev}}} \tag{25}$$

Experimental bending results, which where acquired from seven Al 6061-T6 specimens at 10^6 cycles for R between the range of -0.1 and -1.0 [7,8] were compared to the energy-based prediction method (Eq. (25)) on the Goodman diagram of Fig. 17. The comparison shows good agreement between the experimental and predicted results. Minor variations between the two results may rest on the computational FEM procedure for determining the values

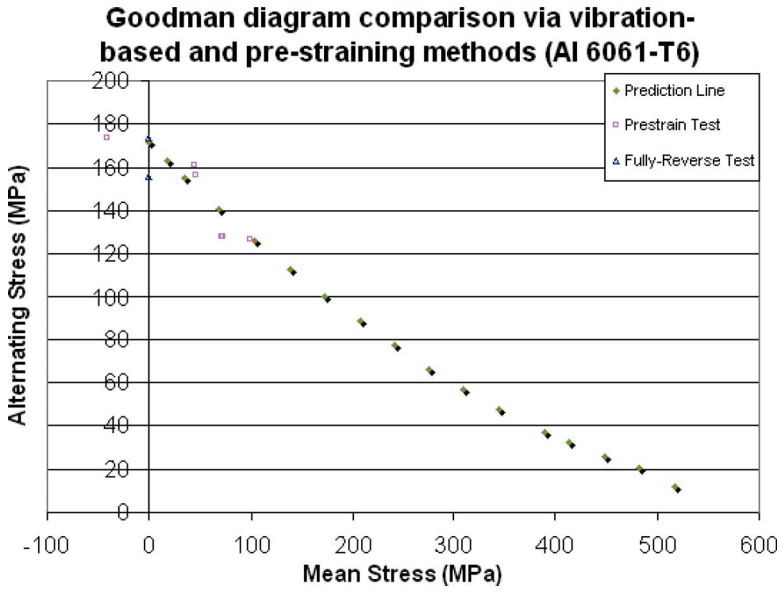

Fig. 17 Bending fatigue comparison at various *R* values for Al 6061-T6

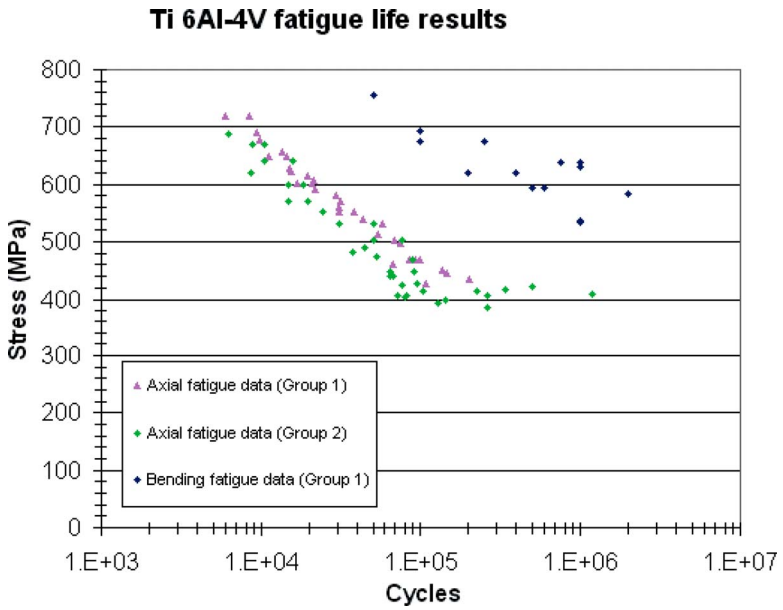

Fig. 18 Fully reversed tension/compression fatigue life results for Ti 6Al-4V

of the localized strains and stresses as needed for the prestraining procedure [7,8]. Improvements to the FEM, via a more realistic model for representing the actual prestraining process, would reduce the minor difference between the comparison, thus making the agreement between the results more accurate [8].

5 Ti 6Al-4V Experimental Results

Fully reversed fatigue and tensile (monotonic) results from two different raw plate stocks of Ti 6Al-4V have been acquired for each respective uniaxial case and are shown on Figs. 18 and 19, where each of the respective specimens was created with a water-jet process from two 3.175 mm thick low stress polished Ti 6Al-4V square plates (0.607 m^2). Observing the fatigue data in Fig. 18 shows that there is an obvious difference between the fatigue limits of the two Ti 6Al-4V stocks (groups). There is also a difference between the behaviors of the respective monotonic curves for each stock (group) in Fig. 19. The difference between the two monotonic curves in Fig. 19 is that the yielding stress of the first titanium material is roughly 5% larger than the second one. It is believed that this difference is the reason for the shorter fatigue life of specimens from Stock 2 in comparison to Stock 1 at a particular stress level. For the purpose of generating accurate tension/compression and bending fatigue prediction analysis, a method that provided a reasonable correction factor for the difference between the two stocks was needed. Therefore, due to the lack of microstructure information and based on the available material property (i.e., the difference in yield stress), a yielding correction factor was developed. This factor was developed based on the calculation showing that the percent difference of Stock 2 yielding stress is 4.6% lower than Stock 1, thus providing the correction value of 1.046. This value is then multiplied to the fatigue results of stock for acceptable comparison to Stock 1.

After using the yielding correction factor, a comparison is made between bending and tension/compression fatigue results in Fig. 20. From this comparison, the fatigue results also show a significant difference between the fatigue stresses of the respective procedures at a specified fatigue life. The difference seen in the com-

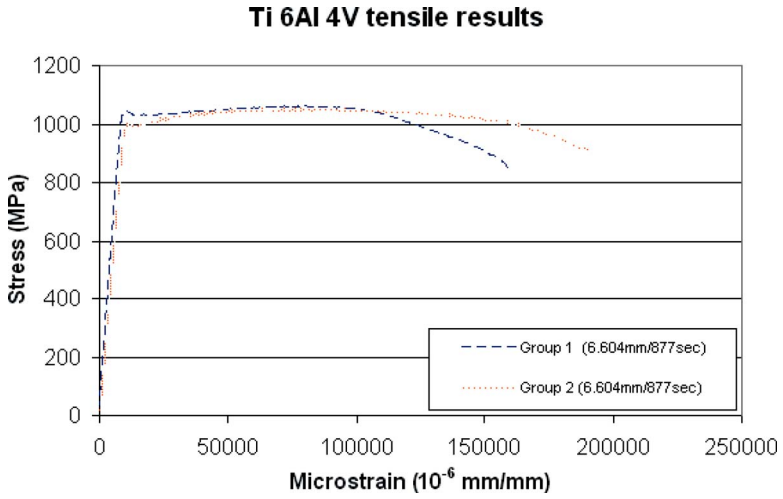

Fig. 19 Monotonic results for Ti 6Al-4V

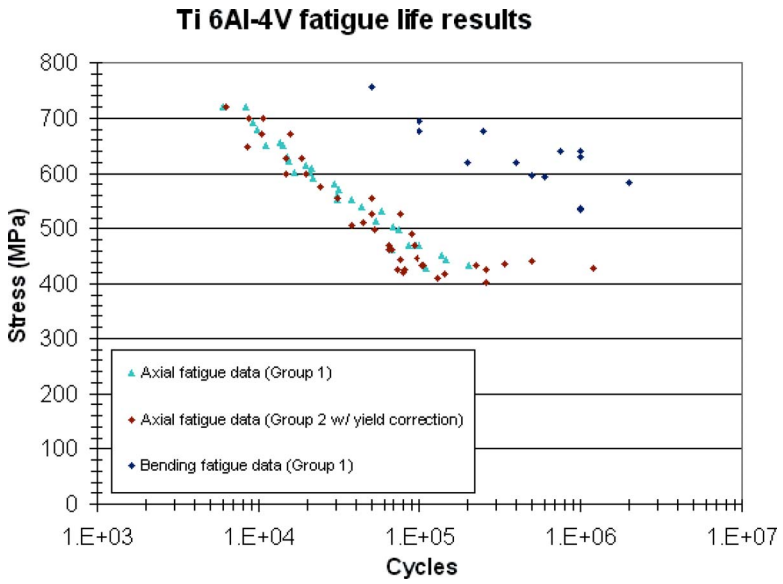

Fig. 20 Fully reversed tension/compression and bending fatigue life results for Ti 6Al-4V

parison of Fig. 20 is similar to the difference observed in the Al 6061-T6 fatigue results from Sec. 3 [1]. Therefore, the stress gradient implication is valid here as well.

6 New Energy-Based Fatigue Prediction Method

6.1 Axial Prediction Method for Fatigue Prior to the Endurance Limit. It is rationally understood that once an object operates at a stress level near the endurance limit (approximately 400 MPa for the available Ti 6A1-4V data), it is considered in a danger zone for conventional HCF of materials (i.e., evaluated at 10^7 cycles with the assumption of similar behavior up to 10^9 cycles). Therefore, using the uniaxial energy-based prediction criterion to acquire fatigue estimation up to the endurance limit is a sufficient contribution to understanding the fatigue behavior of materials similar to Ti 6Al-4V.

Following the energy-based procedures from tension/compression fatigue analysis of Al 6061-T6 (Sec. 3.1), the parameters in Table 2 were acquired from the average of several monotonic stress-strain results [1]. Furthermore, following the procedures mentioned in Ref. [1], a number of low cycle (LC) test were conducted at stress levels between 380 MPa and 1100 MPa, where the parameters C and σ_c were acquired for each stress level. LC results at stresses near the endurance limit were discarded due to the uncertainties of the energy dissipation mechanism. From the observed LC results at stresses much higher than the endurance limit (Table 3), however, the optimal curve fit is determined based on the minimal standard deviation technique used for the fatigue life prediction criterion in Sec. 3.1 [1].

Using the axial energy-based method (Eq. (5)) with the corresponding boldface C and σ_c values from Table 3, a comparison between the prediction and experimental data is shown in Fig. 21. The comparison shows that the axial energy-based method can be used to estimate tension/compression fatigue life prior to the endurance limit, where the value of the endurance limit can be acquired from a number of material property sources as the stress level at 10^7 cycles and beyond (approximately 10^9). Therefore, the axial energy-based method is capable of accurately predicting the lower fatigue limit of the danger zone.

6.2 Incorporation of a Statistical Estimation Scheme to the Energy-Based Prediction Method. For Ti 6AL-4V, the affirmation that stress is the dominant factor of strain energy calculation is not valid for stress levels approaching the endurance limit. However, the major influences to irreversible deformation of Ti 6Al-4V at relatively low stress levels are currently unknown. These uncertainties have led to the introduction of a probabilistic approach, which is an alternative method that provides the capability to systematically determine fatigue life of materials experiencing the endurance limit phenomenon.

The initial energy-based assumption, which states that the strain energy required to fracture a material monotonically is the same as the strain energy accumulated during a cyclic fatigue procedure [11,13], is not discarded for the probabilistic approach. Therefore, the probability approach used for life cycle prediction will be based on the likelihood of generating a certain amount of strain energy, which is ultimately determined by the curve fit parameters C and σ_c of the cyclic strain equation previously shown in Sec. 3 (Eq. (3)).

In order to develop an accurate probability approach, C and σ_c

Table 2 Monotonic strain equation curve fit results for Ti 6Al-4V

E (MPa)	$1.17E+05$
ε_0	$1.53E-22$
ε_n	0.13419
σ_0 (MPa)	23.34
σ_y (MPa)	1037
σ_n (MPa)	1155
β_1 (MPa)	541.0
β_0 (MPa)	1083

Table 3 Cyclic strain equation curve fit results for Ti 6Al-4V

σ (MPa)	C	σ_c (MPa)	Standard deviation
827	**$1.67E+06$**	**$3.50E+04$**	**1.1101**
1103	$1.07E+04$	$6.14E+04$	4.8157
827	$4.00E+05$	$4.43E+04$	1.1252
1034	$1.69E+04$	$5.98E+04$	4.865
655	$1.00E+07$	$2.13E+04$	1.334
793	$4.76E+05$	$4.01E+04$	1.3499
862	$2.27E+05$	$4.84E+04$	1.376

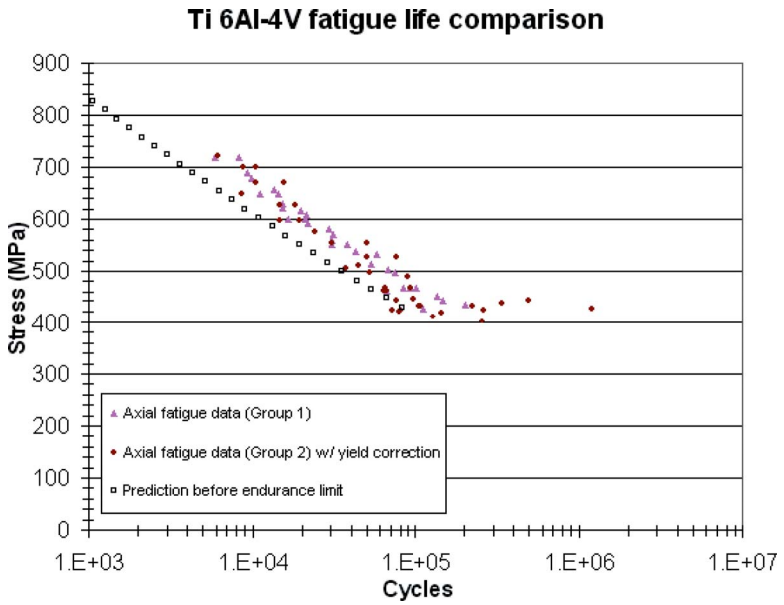

Fig. 21 Tension/compression fatigue comparison prior to the endurance limit for Ti 6Al-4V

results from the previously mentioned LC experimental tests were analyzed. Observation of the LC results showed that the optimized parameters C and σ_c change simultaneously based on the stress amplitude under analysis. However, this change follows a specific pattern with respect to the applied alternating stress: As stress decreases, C increases infinitely and σ_c decreases to an asymptotic value. Therefore, to characterize the probabilistic prediction approach, a clear understanding of the relationship between the curve fit parameters (C and σ_c) and alternating stress was essential. To understand this relationship, a regression analysis is conducted. Since a linear regression analysis is preferred, the relationship between the parameters and the alternating stress is adjusted to a linear form. To define the linear relationship for C-σ, the y-axis (C) is converted to a logarithmic scale, and the relationship for σ_0-σ at lower stresses is defined as a linear band. Each of the linear relationships can be seen in Figs. 22 and 23.

The simple linear regression analysis of the C-σ (with transformation) and σ_c-σ relationship can be expressed by

$$\log_e(C) = \beta_{01} + \sigma\beta_{11} \tag{26}$$

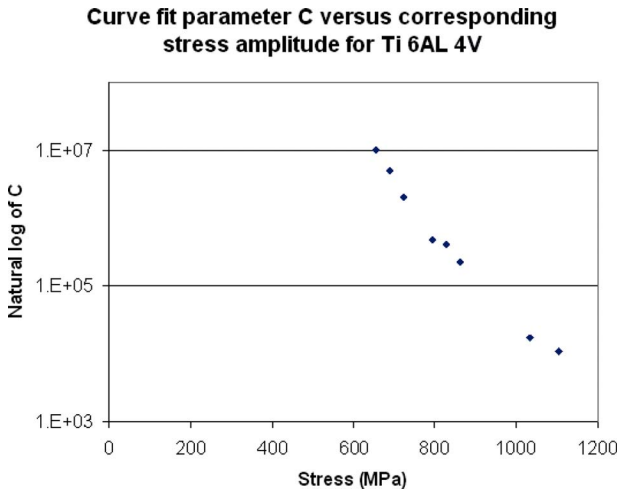

Fig. 22 Semilog plot of C versus alternating σ for Ti 6Al 4V

$$\sigma_c = \beta_{02} + \sigma\beta_{12} \tag{27}$$

The estimators β_{0j} and β_{1j} (for $j=1,2$) are acquired using least squared approximation and based on LC experimental results. The least squared approximation as well as other numerous statistical manipulations were conducted using the MINITAB software. Results from the linear-log scale of C-σ are shown in Table 4, where the coefficient of determination (R-Sq) shows reasonably good linear dependence.

It was assumed previously in this section that the relationship

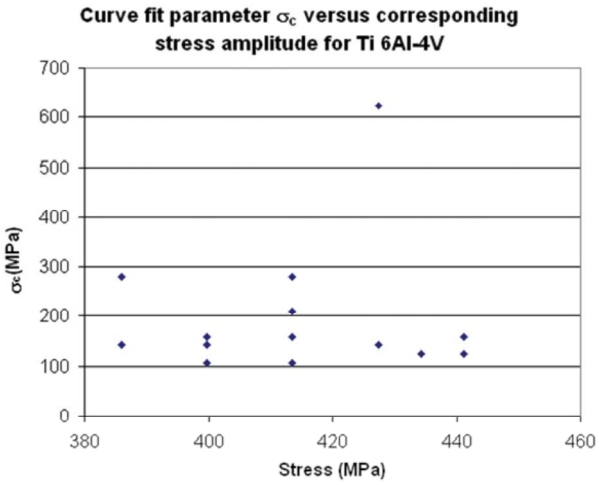

Fig. 23 Plot of σ_c versus alternating stress σ for Ti 6Al 4V

Table 4 MINITAB results for regression analysis of C and σ (English units). S=0.351306, R-Sq=98.2%, and R-Sq(adj) =98.0%.

The regression equation ($\ln(C)=25.9-0.000106\sigma$)				
Predictor	Coef	SE_Coef	T	P
Constant	25.8611	0.6559	39.43	0.00
σ	−0.0001	5.4E−06	−19.6	0.00

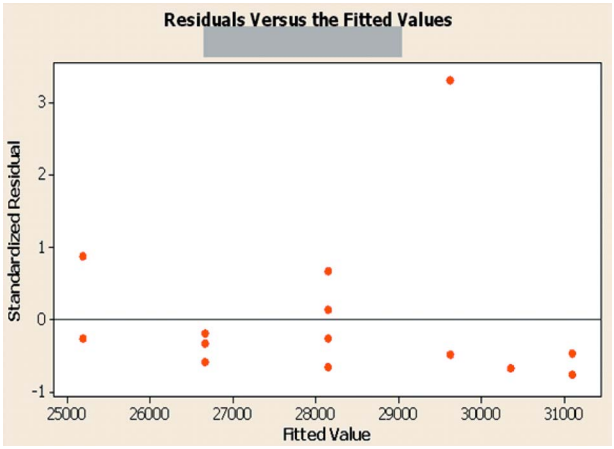

Fig. 24 Standardized residual versus fitted values of σ-σ_c analysis (Ti 6Al-4V)

between σ_c and σ is a linear band. In order to observe this, a linear regression of the existing data is conducted and the standardized residuals are plotted against the corresponding fitted values from the analysis in Fig. 24. It is possible that the lack of regression fit may be caused by the outlier data point in Fig. 24, which sits outside the range $[-1,1]$ recommended by Ref. [18]. By removing the outlier, a regression analysis for the linear relationship between σ_c and σ was conducted and the results are shown in Table 5. Furthermore, by conducting a hypothesis test to check the linearity of the regression result, it is fair to say that σ_c for lower alternating stress levels ($\sigma < 482.5$ MPa) is a constant value; where the chosen value is defined as the median from the data in Fig. 23 minus the outlier.

Table 5 MINITAB results for regression analysis of σ_c and σ. S =8207.32, R−Sq=5.2% and R−Sq(adj)=0.0%.

The regression equation (σ_c=62438−0.652σ)				
Predictor	Coef	SE_Coef	T	P
Constant	62438	48232	1.29	0.22
σ	−0.6522	0.8079	−0.81	0.435

Based on the results acquired, the probabilistic approach is a method for providing a fatigue life prediction range of a specified alternating stress due to a given confidence level. The method used here is a well-known linear regression means of observation called a prediction interval for unknown regression parameters [18]. A prediction interval for estimated results of $\log_e(C)$ that are based on a specified stress value can be obtained with the following equation:

$$\log_e(C)_h \pm t(1-\alpha/2;n-2)S\{\log_e(C)_h\} \tag{28}$$

where $\log_e(C)_h$ is the estimated value from Eq. (26), α is 1− confidence level (i.e., for 95% confidence, α=1−0.95), n is the number of samples used in the regression construction, $t(1-\alpha/2;n-2)$ is the t-distribution number corresponding to the specified confidence level, and $S\{\log_e(C)_h\}$ is the square root of the estimated variance for the estimated value of $\log_e(C)_h$.

Due to the previously stated understanding that the estimation of strain energy is ultimately decided by the estimated values of the curve fit parameters, transformation of the prediction intervals from $\log_e(C)_h$ to C_h (where C_h is the transformation of the estimated $\log_e(C)_h$ value to a linear scale) provides the direct capability to construct prediction intervals for fatigue life at the respective stress. This is accomplished by using the bounding C values from the transformed prediction interval to solve for two different fatigue cycles. Therefore, these calculated upper and lower fatigue values define the prediction interval of the alternating stress and the confidence limit corresponding to the C parameter interval. Figures 25 and 26 show the fatigue prediction intervals for low stresses with a 95% and a 99% confidence limit, respectively.

Though the tension/compression comparison looks promising, a sufficient amount of fatigue test results from the two available stocks of Ti 6Al-4V was not acquired beyond 10^5 cycles (where the endurance limit begins) to determine the accuracy of the prediction. The uniaxial bending case, however, poses the exact opposite problem. Though there are sufficient HCF data (10^5–10^7), there are not enough experimental data prior to the endurance limit. Therefore, to observe the validity of the probabilistic approach, the stress gradient analysis from Sec. 3 was used to de-

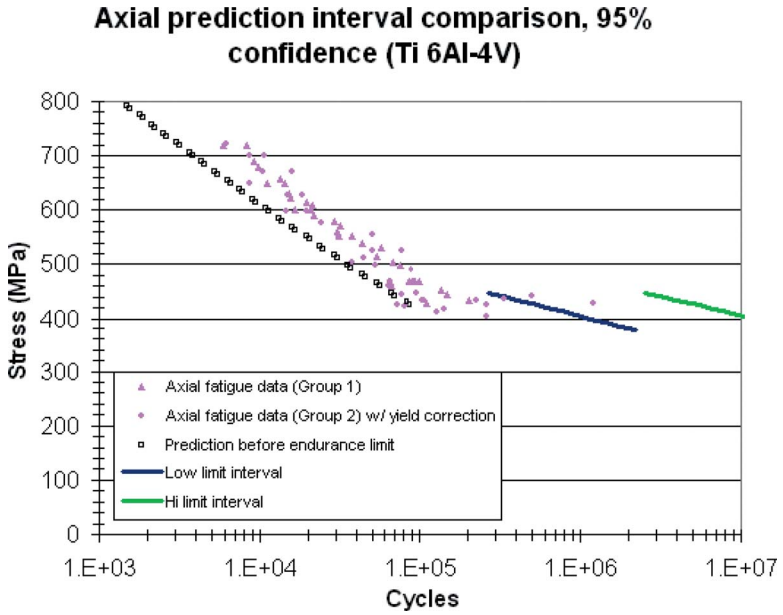

Fig. 25 Fully reversed tension/compression fatigue life comparison at 95% confidence (Ti 6Al-4V)

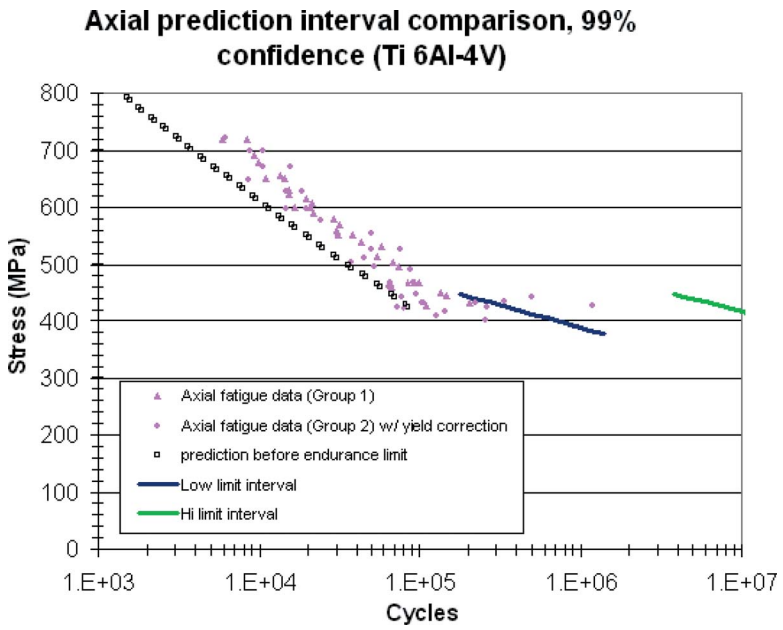

Fig. 26 Fully reversed tension/compression fatigue life comparison at 99% confidence (Ti 6Al-4V)

velop the prediction intervals for the bending fatigue case. The bending fatigue prediction intervals are compared with the experimental results in Figs. 27 and 28 for 95% and 99% confidence limits, respectively. This comparison sufficiently validates the probabilistic approach for the bending case, therefore indirectly validating it for the axial case as well.

7 Conclusion

There were a number of worthwhile findings in the presented manuscript. First, the energy-based understanding for fatigue life prediction was extended to determine bending and tension/compression fatigue results for $R>$ or $=-1$; the comparison between each respective mean-stress-effect life prediction process and corresponding uniaxial experimental results for Al 6061-T6 indicates that the energy-based method is an encouraging fatigue estimation tool for cyclic loading at various stress ratios. Also, a procedure for comparing the *S-N* behavior of Ti 6Al-4V materials with slightly different yielding stresses is presented with encouraging success.

It has also been validated in this manuscript that the uniaxial energy-based fatigue life prediction method with the incorporated probabilistic approach is capable of sufficiently creating an upper and a lower bound for fatigue results near the endurance limit. An example of this prediction application was clearly confirmed with an experimental versus analytical comparison for the bending case. The stress gradient theory, however, can make a correlation between tension/compression and bending fatigue by estimating bending fatigue limits based on tension/compression test results

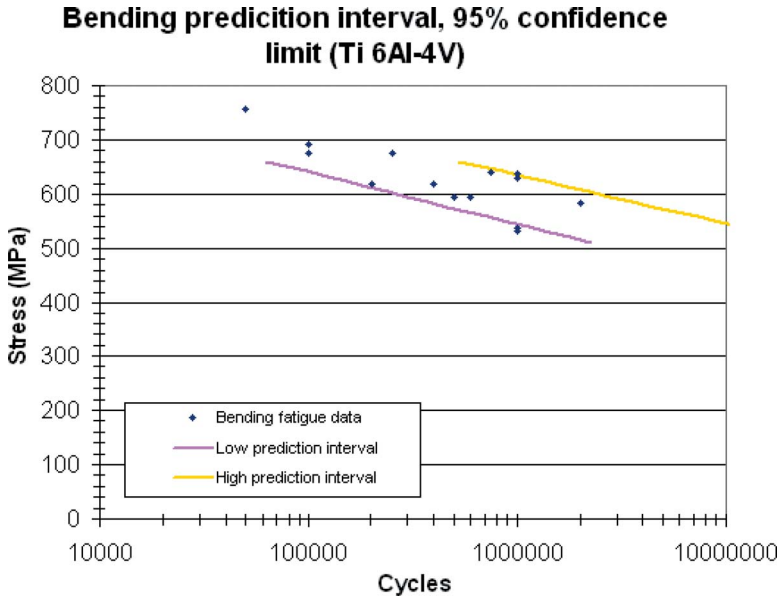

Fig. 27 Fully reversed bending fatigue life comparison at 95% confidence (Ti 6Al-4V)

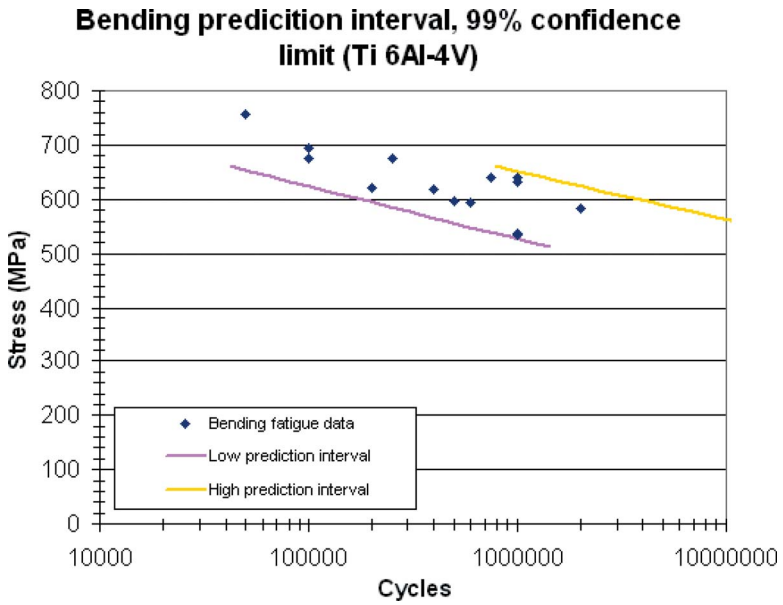

Fig. 28 Fully reversed bending fatigue life comparison at 99% confidence (Ti 6Al-4V)

[17]. Based on this correlation, the probabilistic method is also valid for tension/compression fatigue near the endurance limit. Therefore, this indicates that the energy-based prediction method with probabilistic intervals is capable of providing a good assessment for the range of fatigue life corresponding to a specified stress and confidence level.

The contribution of the energy-based prediction method to gas turbine engine design is the emergence of another simplified method (like the Goodman diagram) to determine fatigue results of components based on the stresses acting on the part. Like the Goodman diagram, the energy-based method can also be implemented into FEM software and computational analysis as an equation. However, the energy-based prediction method can also be implemented into FEM software by way of the minimum potential energy equation; this ability is what makes the energy-based fatigue life prediction method a more useful gas turbine engine design tool than the Goodman diagram.

Acknowledgment

The authors would like to thank the Air Force Research Laboratories (AFRL), specifically the Turbine Engine Fatigue Facility (TEFF) laboratory, for their financial support, facility and equipment access, and encouragement of this research.

References

[1] Scott-Emuakpor, O., Shen, M.-H. H., Cross, C., Calcaterra, J., and George, T., 2007, "Development of an Improved High Cycle Fatigue Criterion," ASME J. Eng. Gas Turbines Power, **129**(1), pp. 162–169.
[2] Nicholas, T., 1999, "Critical Issues in High Cycle Fatigue," Int. J. Fatigue, **21**, pp. S221–S231.
[3] Goodman, J., 1899, *Mechanics Applied to Engineering*, Longmans, Green and Co., London.
[4] George, T., Seidt, J., Shen, M.-H. H., Cross, C., and Nicholas, T., 2004, "Development of a Novel Vibration-Based Fatigue Testing Methodology," Int. J. Fatigue, **26**, pp. 477–486.
[5] Shen, M.-H. H., Seidt, J., George, T., Cross, C., Whaley, P. W., and Nicholas, T., 2001, "Development of a Novel Method for Evaluating Material Behavior Under Turbine Engine Operating Conditions, Part I: Design of Accelerated HCF Testing Procedures," Sixth National Turbine Engine High Cycle Fatigue Conference.
[6] Shen, M.-H. H., Seidt, J., George, T., Cross, C., Whaley, P. W., and Nicholas, T., 2001, "Development of a Novel Method for Evaluating Material Behavior Under Turbine Engine Operating Conditions, Part II: An Empirical Vibration-Based Fatigue Assessment Framework," Sixth National Turbine Engine High Cycle Fatigue Conference.
[7] George, T., Shen, M.-H. H., Scott-Emuakpor, O., Nicholas, T., Cross, C., and Calcaterra, J., 2005, "Goodman Diagram Via Vibration-Based Fatigue Testing," ASME J. Eng. Mater. Technol., **127**(1), pp. 58–64.
[8] Scott-Emuakpor, O., 2004, "Development of an Improved Energy-Based Criterion for Fatigue Life Assessment," MS thesis, The Ohio State University, Columbus, OH.
[9] Lanning, D., Nicholas, T., and Haritos, G., 2002, "Effect of Plastic Prestrain on High Cycle Fatigue of Ti-6Al-4V," Int. J. Fatigue, **34**, pp. 127–134.
[10] Jasper, T. M., 1923, "The Value of the Energy Relation in the Testing of Ferrous Metals at Varying Ranges of Stress and at Intermediate and High Temperatures," Philos. Mag., **46**, pp. 609–627.
[11] Feltner, C. E., and Morrow, J. D., 1960, "Microplastic Strain Hysteresis Energy as a Criterion for Fatigue Facture," ASME Paper No. 60-MET-2.
[12] Enomoto, N., 1955, "On Fatigue Tests Under Progressive Stress," Proc. ASTM, **55**, pp. 903–917.
[13] Stowell, E., 1966, "A Study of the Energy Criterion for Fatigue," Nucl. Eng. Des., **3**, pp. 32–40.
[14] American Society for Testing and Materials, 2002, "E466–96: Standard Practice for Conducting Force Controlled Constant Amplitude Axial Fatigue Tests on Metallic Materials," *ASTM Book of Standards*, ASTM International, West Conshohocken, PA, Vol. 03.01.
[15] Nicholas, T., and Maxwell, D., 2003, "Mean Stress Effects on the High Cycle Fatigue Limit Stress in Ti-6Al-4V," *Fatigue and Fracture Mechanics*, 33rd ed., W. G. Reuter and R. S. Piascik, eds., American Society for Testing and Materials, West Conshohocken, PA, pp. 476–492, Paper No. ASTM STP 1417.
[16] Garud, Y. S., 1979, "A New Approach to the Evaluation of Fatigue Under Multiaxial Loading," *Proceedings of Symposium on Methods for Predicting Material Life in Fatigue*, ASME, New York, pp. 247–264.
[17] Scott-Emuakpor, O., Shen, M.-H. H., Cross, C., Calcaterra, J., and George, T., 2005, "A Promising New Energy-Based Fatigue Life Prediction Framework," ASME Paper No. GT2005–68423.
[18] Kutner, M., Nachtsheim, C., and Neter, J., 2004, *Applied Linear Regression Models*, McGraw-Hill, New York.

Hybrid Gas Bearings With Controlled Supply Pressure to Eliminate Rotor Vibrations While Crossing System Critical Speeds

Luis San Andrés
Mast-Childs Professor
Fellow ASME
e-mail: lsanandres@mengr.tamu.edu

Keun Ryu
Research Assistant
e-mail: keun@tamu.edu

Mechanical Engineering Department,
Texas A&M University,
College Station, TX 77843-3123

Microturbomachinery implements gas bearings in compact units of enhanced mechanical reliability. Gas bearings, however, have little damping and wear quickly during transient rub events. Flexure pivot tilting pad bearings offer little or no cross-coupled stiffnesses with enhanced rotordynamic stability; and when modified for hydrostatic pressurization, demonstrate superior rotordynamic performance over other bearing types. External pressurization stiffens gas bearings thus increasing system critical speeds, albeit reducing system damping. Most importantly, measurements demonstrate that external pressurization is not needed for rotor supercritical speed operation. In practice, the supply pressure could be shut off at high rotor speeds with substantial gains in efficiency. This paper introduces a simple strategy, employing an inexpensive air pressure regulator to control the supply pressure into the hybrid bearings, to reduce or even eliminate high amplitudes of rotor motion while crossing the system critical speeds. Rotor speed coast-down tests with the pressure controller demonstrate the effectiveness of the proposed approach. A simple on-off supply pressure control, i.e., a sudden increase in pressure while approaching a critical speed, is the best since it changes abruptly the bearing stiffness coefficients and moves the system critical speed to a higher speed. A rotordynamic analysis integrating predicted bearing force coefficients forwards critical speeds in agreement with the test results. Predicted rotor responses for the controlled supply conditions show an excellent correlation with measured data. The experiments validate the predictive tools and demonstrate the controllable rotordynamic characteristics of flexure pivot hybrid gas bearings. [DOI: 10.1115/1.2966391]

1 Introduction

Microturbomachinery (MTM) with output power below 400 kW operates at high speeds and extreme temperatures, and delivers reliable power in compact, low count part units of reduced weight. MTM implements gas bearings that offer low friction, less heat generation, and power losses than oil-lubricated bearings [1,2]. Gas bearings in MTM aid to satisfy environmental restrictions and even add value for those concerned with global warming.

Gas bearings, however, have low damping and load-carrying capacity due to the inherently small gas viscosity [3]. Consequently, gas film bearings do not generate a large enough hydrodynamic pressure field to support static and dynamic loads during rotor start-up or shutdown events. Externally pressurized gas bearings, however, prevent transient rotor-bearing contact and reduce wear while at start-up and shutdown conditions [4].

Gas foil bearings are customarily used in air cycle machines, auxiliary power units, and commercial MTM because of their distinct advantages including tolerance to shaft misalignment and centrifugal/thermal growth, and large load capacity compared with rigid surface gas bearings [5]. However, the expensive development cost and lack of reliable analytical tools have limited universal application of foil bearings into larger TM.

Tilting pad bearings are widely used in high performance turbomachinery because of their inherent stability characteristics resulting from no generation of cross-coupled stiffness coefficients [6]. Flexure pivot tilting pad bearings, machined as a single piece using wire electrical discharge machining (EDM), provide the same rotordynamic advantages as tilting pad bearings. Flexure pivot tilting pad bearings eliminate pivot wear, contact stresses, and pad flutter, and minimize the manufacturing tolerance stack-up [7]. Integrally machined pads with the bearing shell offer a compact unit, easier to install and maintain. This bearing type can be designed and manufactured not only with a low rotational web stiffness allowing for pad tilting and hence promoting rotordynamic stability but also with a radial stiffness giving a margin of tolerance for shaft growth, centrifugal and thermal, and also permitting shaft excursions beyond its nominal clearance.

Zhu and San Andrés [8] describe rotordynamic measurements of a high speed rotor supported on flexure pivot tilting pad gas hydrostatic bearings. Tests without supply pressure show the rotor becomes unstable at ~81 krpm with a whirl frequency ratio of ~20%. With external pressurization, the rotor-bearing system is stable to the top speed of the drive motor, 99 krpm. San Andrés and Ryu [9] present further rotordynamic measurements of a test rotor supported on flexure pivot tilting pad gas hydrostatic bearings for various mass imbalances, increasing supply pressures, and load-on-pad (LOP) and load-between-pad (LBP) configurations. In particular, rotor deceleration tests with a manual control of the supply pressure into the hybrid gas bearings are conducted to eliminate high amplitudes of rotor vibration while crossing the system critical speeds.

The present research advances the technology of hybrid gas bearings for application into oil-free high performance MTM by demonstrating experimentally their rotordynamic performance, reliability, and durability. To accomplish the desired objective, the current work focuses on suppressing excessive levels of rotor vibration while traversing critical speeds of a rotor-bearing system.

Contributed by the International Gas Turbine Institute of ASME for publication in the JOURNAL OF ENGINEERING FOR GAS TURBINES AND POWER. Manuscript received March 28, 2008; final manuscript received April 1, 2008; published online August 28, 2008. Review conducted by Dilip R. Ballal. Paper presented at the ASME Turbo Expo 2008: Land, Sea and Air (GT2008), Berlin, Germany, June 9–13, 2008.

Vibration limits in a rotor-bearing system are essential to improve its reliability, performance, and life. In industrial practice, API specifications require tight vibration restrictions. API 610 [10] and API 617 [11] standards determine the vibration limit of a rotating shaft, i.e., $A_u < (5.2 \times 10^6/N)^{0.5}$ and $A_u < 25.4 \times (12,000/N)^{0.5}$, where A_u is the peak-to-peak amplitude of unfiltered rotor vibration in μm and N is the rotational speed in rpm, respectively. These standards also restrict the maximum A_u to 50 μm peak-to-peak and 25 μm peak-to-peak, respectively. In petroleum, chemical, and gas industries, API 610 and API 617 standards cover the requirements for centrifugal pumps and axial/centrifugal compressors, respectively. The accepted API specifications are clearly too stringent for high speed MTM, and hence difficult to achieve in practice.

Prior exhaustive research, analytical and experimental [8,9,12,13], demonstrates that external pressurization increases the gas bearings' direct stiffnesses albeit with a notable reduction in damping. The drop in damping makes a rotor-gas bearing system more sensitive to imbalance, and considerable efforts must be spent in tightening manufacturing tolerances for rotors and bearings; for example, as well as by enlarging tip clearances in turbines or compressors to allow for the larger rotor excursions and hence reducing overall system efficiency.

The present work presents additional rotordynamic tests using a control system of the supply pressure into the bearings to eliminate rotor motion peaks while passing through the critical speed of the rotor-bearing system. Open and closed loop control systems relate the supply pressure to the rotor speed and regulate the supply pressure into the test bearings. A simple and inexpensive electro-pneumatic air regulator controls the air supply pressure, whose magnitude is set inversely proportional to the rotor speed. Comprehensive rotor speed coast-down tests are performed to characterize the rotor response for various pressure supply control methods over certain rotor speed regions. The measured rotor responses for controlled supply air pressures are compared with predictions from computational models.

The literature on active control of shaft motions in rotor and oil-lubricated bearing systems is quite extensive. Actively controlled bearing systems offer advantages over passive devices such as versatility in adjusting to the load condition and machinery configuration. However, active vibration control systems typically require an external power source to operate actuators supplying controlled forces for ready delivery to the rotating structure. Most force actuators are limited in load amplitude and frequency span; and thus cannot readily compensate for imbalance-induced forces which can be large at high rotor speeds.

As applied to oil-lubricated tilting pad bearings, Santos [14] uses hydraulic actuators to push bearing pads, thus controlling bearing clearances to modify the bearing force coefficients. Later, Santos et al. [15] detail measurements and analysis conducted on a rigid rotor supported on tilting pad bearings with active oil injection, i.e., controlled pressurized lubricant delivery. A complex system integrates hydraulic servovalves, rotor displacement/velocity transducers, and proportional-derivative (PD) feedback controllers. The servovalves are controlled by the rotor dynamic displacements and velocity components. A displacement feedback control reduces the rotor vibration amplitude at low frequencies. On the other hand, rotor velocity feedback control lessens the amplitude of rotor motion at high frequencies. Combination of displacement and velocity signals with proper control gains provides the lowest rotor amplitude over extended rotor speed regions.

Bently et al. [16] apply active lubrication into hydrostatic bearings and report the rotordynamic performance of turbocompressor supported on oil hydrostatic bearings. The four pocket bearings integrate high-speed electrohydraulic valves and a closed-loop feedback control system. The controller sets the desired pocket supply pressure and anti-swirl of the oil injected into the bearings. External pressurization increases the stiffnesses of the test bearings, thereby raising the system critical speed above the operating speed range.

Qiu et al. [17] describe rotordynamic measurements in actively controlled tilting pad gas bearings for vibration control in a turboexpander. Embedded piezoelectric actuators support the bearings and with a feedback control system integrating a proportional-integral-derivative (PID) controller, actuators, and displacement sensors. The tests show that subsynchronous motions of a test rotor-bearing system are suppressed with feedback control if the gains of the controllers are appropriately chosen. However, synchronous vibration amplitudes remain almost unchanged.

Ryu [18] presents a comprehensive review of the relevant literature on passive and active controls of vibrations in rotating machinery. The few publications referred above show that active control systems can be rather complex and costly, while still delivering mixed results. The proposed supply pressure control described below is simple and inexpensive; and most importantly, it achieves its intended action; i.e., reduction of rotor amplitudes of motion while traversing critical speeds.

2 Experimental Facility

Figure 1 depicts a schematic view of the gas bearing test rig and the supply air system into the test bearings. The test rig has a steel casing integrating a brushless AC motor armature, with a maximum speed of 99 krpm. The motor controller offers 0.9 kW of continuous power. A K-type thermocouple monitors the temperature of the motor armature. Three alignment bolts position the test bearings 120 deg apart within their housings. Piezoelectric load cells installed between the bearing housing and each alignment bolt measure the dynamic forces transmitted to the rig casing. The airflow into the bearings is controlled by on/off valves and an adjustable air pressure regulator connected to the main shop line. Calibrated turbine flow meters measure the mass flow rate into each bearing with an uncertainty of 0.05 l/min.

Two pairs of eddy current sensors, orthogonally positioned and facing the rotor ends, measure the rotor vibration amplitudes along the X-(vertical) and Y-(horizontal) planes. Rotor displacement voltage signals from the eddy current sensors are routed through a signal conditioner to bias their DC offset levels. The conditioned signals are inputted into PC DAQ systems. Two analog oscilloscopes display the unfiltered real time rotor orbits for the left and right sides of the rotor. An infrared tachometer mounted at the right end of the rotor is a keyphasor signal for data acquisition. References [8,9,12,13] also detail the components of the test rig.

The test rotor consists of a steel shaft, 15 mm in diameter and 190 mm in length, and integrates brushless AC motor armature. Thrust pins with a spring hold the rotor axially. Two cylindrical steel sleeves are press-fit on the left and right sides of the shaft. The surface of the sleeves at the bearing locations is hard-chrome coated with a 0.25 mm thickness. The right journal sleeve has a smaller diameter than the left journal sleeve due to the extensive wear during prior rotor coast-down tests [9]. Eight holes, 1 mm in diameter and 12 mm in a radial distance from the rotor center, are equally spaced on each rotor end face. Balancing and added masses are inserted in these holes.

Figure 2 details the dimensions of the test flexure pivot hydrostatic gas bearing with four 72° pads and 60% pivot offset. Prior extensive testing with the bearings [8,9] left the pads' surfaces with uneven wear. The present condition of the bearings shows quite dissimilar clearances along the circumference and axial lengths of each pad. The original bearing nominal clearance and dimensionless pad preload, as reported in Ref. [8], are 40 ± 4.5 μm and 40%, respectively. Presently, the estimated radial clearances vary from $40 \sim 80$ μm for the left bearing and $30 \sim 60$ μm for the right bearing. Reference [18] details currently measured bearing radial clearances on the test bearings and a

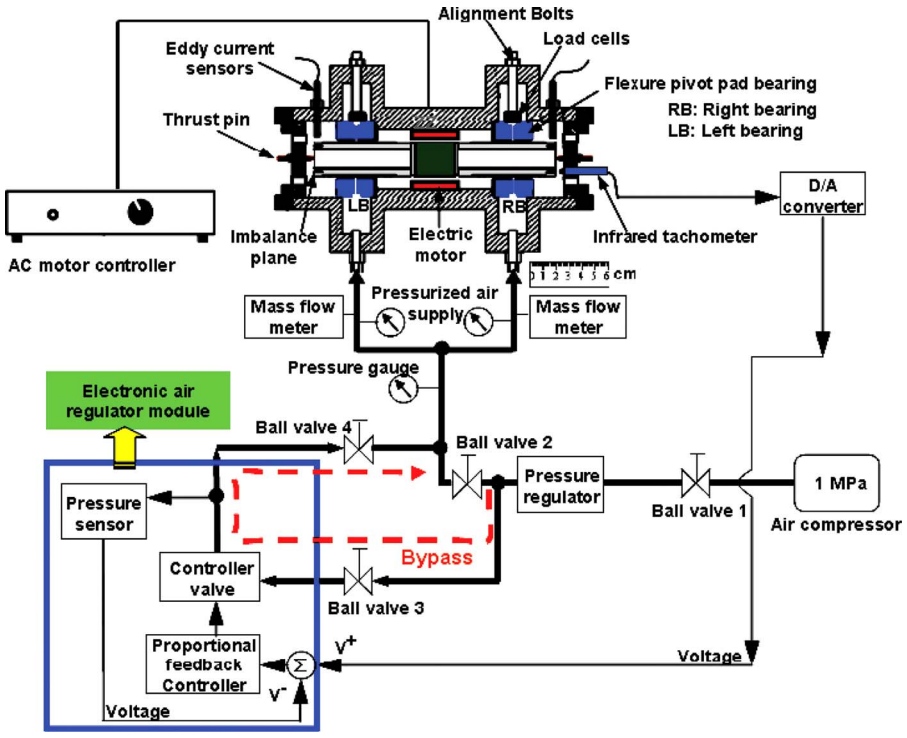

Fig. 1 Layout of gas bearing test rig and air supply system with controller

comparison with prior measurements in Ref. [9]. Table 1 lists the main parameters of the test rotor and the bearings. Pressurized air flows through the orifices into the middle plane of each pad. The bearings are installed in the LOP configuration.

The electro-pneumatic air regulator controls the air supply pressure in proportion to the rotational speed of the test rotor. The tachometer integrates a digital to analog converter which provides a voltage output according to a customized rotor speed range. The analog output from the tachometer is an input to the electronic air regulator. The analog output changes in step-wise form, 4096 steps, throughout the specified voltage range. The step size is ~0.0244% (1/4096 step) of the total controlled speed range. Note that the tachometer acquires data and updates the analog output at ~25 times/s, i.e., every 40 ms. The sensitivity (voltage/rpm) of the tachometer output depends on the user-defined speed range for control. A narrow speed range leads to an abrupt increase of the voltage output as the speed changes. The air regulator offers a proportional pressure in compliance with an input signal, i.e., rotor speed. As the rotor speed decelerates, the supply pressure increases steadily from a low pressure to a high pressure. Note that the controller has approximately 0.3–0.4 s of time delay. A detailed description on the control loop follows later.

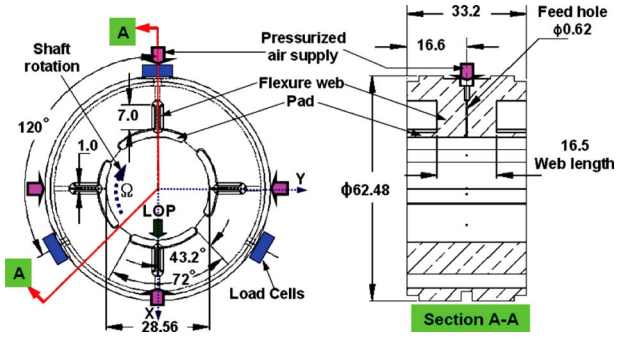

Fig. 2 Dimensions of flexure pivot pad hydrostatic gas bearing (units: mm)

3 Experimental Procedure

Table 2 lists the eight test operating conditions based on various pressure supply control methods and preset rotor speed regions. Operating conditions #1–#4 represent an open control loop, with a manual setup of supply pressure using an adjustable pressure regulator. Pressure gauges monitor the supply pressure into each test bearing. Note that operating condition #1 is a coast-down rotor speed demonstration without any pressure control, i.e., with a constant supply pressure over the whole coast-down speed range.

Closed loop control of the supply pressure governed by rotor speed, using the electro-pneumatic air regulator, is established for operating conditions #5–#8. The electro-pneumatic air regulator automatically adjusts the supply pressure as per the control desired. This device consists of controller, control valve, and pres-

Table 1 Main parameters of test rig and flexure pivot bearings

Parameter		Value	Unit
Rotor mass, M		0.825	kg
Rotor diameter, D_j	Left side	28.555 ± 0.001	mm
	Right side	28.551 ± 0.001	mm
Bearing axial length, L		33.2	mm
Pads number and arc length		4(72°)	
Pad pivot offset		60%	
Pad mass moment of inertia, I_p		0.253	g mm^2
Web rotational stiffness, $K_{\delta\delta}$		20	N m/rad
Number of feed orifices		4	
Feed orifice diameter, d_o		0.62	mm
Bearing diameter, D_b	Left side	28.63–28.71	mm
	Right side	28.61–28.67	mm
Bearing clearance, C_b	Left side	40–80	μm
	Right side	30–60	μm

Table 2 Summary of rotor speed and feed pressure conditions

Operating condition #	Speed control method	Control strategy: Preset rotor speed region for pressure control	Control strategy: Method of controlling supply pressure	Control strategy: Step # of supply pressure control over preset speed region
1	Coast down	None	None	—-
2	Operator set speed	14.2 krpm	Manual	1 step, Figs. 3(*a*) and 4(*a*)
3	Operator set speed	14.2 krpm	Manual	4 steps, Figs. 3(*a*) and 4(*b*)
4	Operator set speed	13.9–13.0 krpm	Manual	4 steps, Fig. 3(*b*)
5	Coast down	14.2 krpm	Controlled	1 step, Fig. 3(*a*)
6	Coast down	14.2–13.0 krpm	Controlled	Continuous, Fig. 3(*c*)
7	Operator set speed	14.2 krpm	Controlled	1 step, Fig. 3(*a*)
8	Operator set speed	14.2–13.0 krpm	Controlled	Continuous, Fig. 3(*c*)

sure sensor as shown in Fig. 1. When the voltage of the input signal raises, the controller valve opens, thereby supply pressure passes through it. This pressure feeds back to the controller via a pressure sensor. The controller compares the supply pressure with the customized reference value based on the rotor speed range, and determines the final output pressure. The manipulated pressure, the output of the controller, is the supply pressure into the test bearings.

For coast-down rotor speed tests (operating conditions #1, #5, and #6), the power to the motor controller is turned off allowing the rotor to freely coast down from 40 krpm. For operator set speed demonstrations (operating conditions #2, #3, #4, #7, and #8), the rotor speed is set manually, starting at 40 krpm and ending at 11.5 krpm; and then, the motor power is turned off. Note that the operator set speed demonstration obviously provides a longer deceleration time over the controlled feed pressure versus rotor speed region.

For operating conditions #2 and #3, the rotor speed is decreased manually, i.e., starting at 40 krpm. When reaching ~14.2 krpm, the supply pressure is manually increased from 2.36 bar to 5.08 bar (absolute) using an adjustable pressure control valve, as shown in Fig. 3(*a*). Figure 4 displays the air pressure supply variation for operating conditions #2 and #3. Operating condition #2 provides an instantaneous one-step pressure increase of 2.72 bar from 2.36 bar to 5.08 bar (absolute). Operating condition #3 implements a four-step supply pressure increase, 0.68 bar each step from 2.36 bar to 5.08 bar (absolute) with a 10 s time lag. For operating condition #4, the supply pressure varies as in operating condition #3, increasing from 2.36 bar to 5.08 bar (absolute) over a narrow speed range (13.9~13.0 krpm) as depicted in Fig. 3(*b*).

Operating conditions #5–#8 utilize the electro-pneumatic air regulator for active control of the supply pressure. Figure 3(*c*) depicts the supply pressure versus rotor speed for operating conditions #6 and #8. The supply pressure increases continuously from 2.36 bar to 5.08 bar (absolute) over the speed range 14.2–13.0 krpm.

4 Experimental Results

4.1 Determination of Control Speed Regime for Air Regulator. In Ref. [9], rotor deceleration tests with manual changes in supply pressure are performed to reduce rotor motion amplitudes while passing through a critical speed. Current demonstrations include controlled changes of supply pressure using the electro-pneumatic air regulator and also manual changes in external pressurization.

Figure 5 depicts the amplitudes of rotor synchronous motions along the right horizontal (RH) direction for operating condition #1 at supply pressures from 2.36 bar to 5.08 bar (absolute). External pressurization into the gas bearings increases their direct stiffnesses, thereby raising the system critical speeds. The critical speed increases linearly with supply pressure. The supply pressure into the test bearings will be manipulated within the rotor speed range between 14.2 krpm (an intersection of the rotor synchronous motions for 2.36 bar and 5.08 bar) and 13.0 krpm (the critical speed for 2.36 bar).

While coasting down from the top speed of 40 krpm to 14.2 krpm, the supply pressure is maintained at the lowest pressure of 2.36 bar (absolute). The supply pressure will be increased from 2.36 bar to 5.08 bar (absolute) while the rotor traverses the speed region between 14.2 krpm and 13.0 krpm, as shown later.

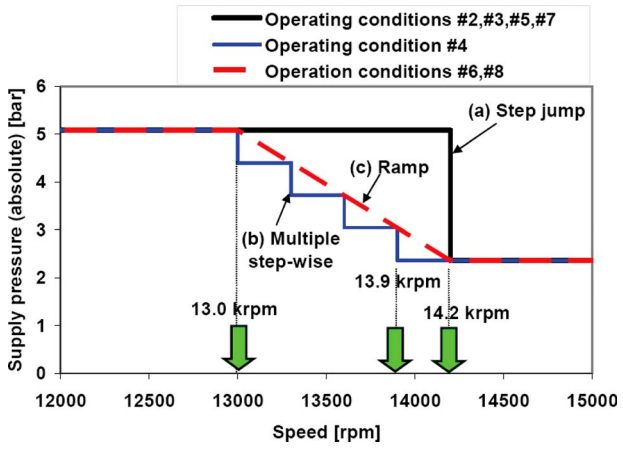

Fig. 3 Controlled supply pressure versus rotor speed for operating conditions #2–#8

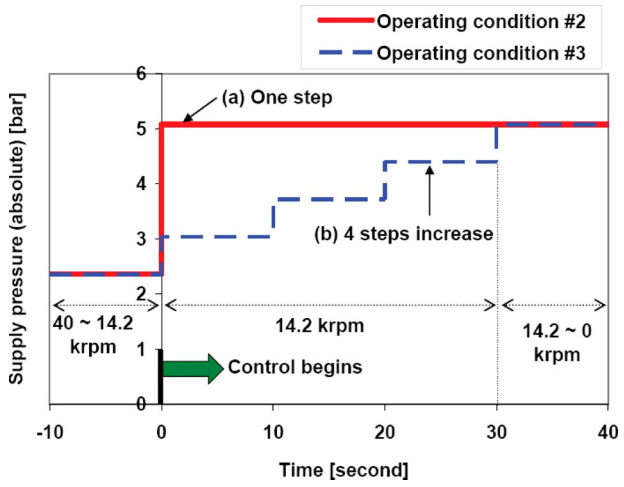

Fig. 4 Increase of controlled supply pressure over selected time span. Operating conditions #2 and #3.

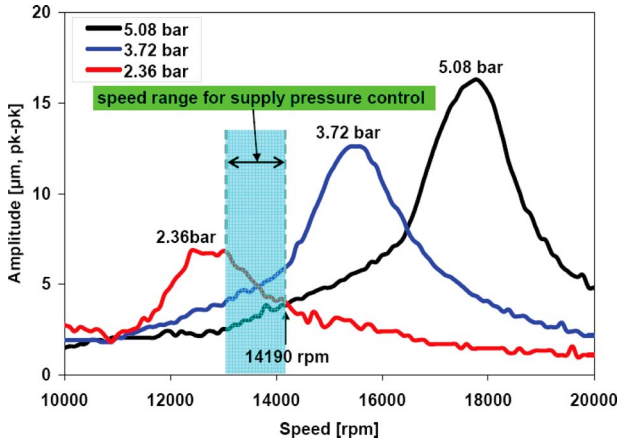

Fig. 5 Determination of speed range for control of supply pressure. Right bearing horizontal direction (RH). Operating condition #1 (constant pressure supply, rotor speed coast down).

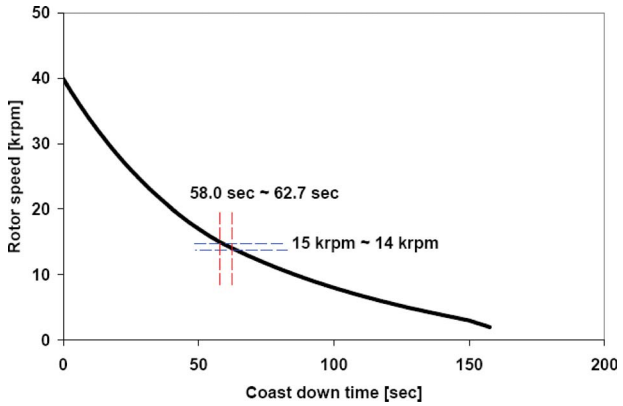

Fig. 6 Estimation of shaft speed change rate based on recorded coast-down rotor speed versus time. 2.36 bar feed pressure. Operating condition #1 (constant pressure supply, rotor speed coast down).

4.2 Estimation of Air Pressure Regulator Response Delay for Test System. Figure 6 depicts the recorded coast-down speed of the test rotor versus time for bearings supplied with a 2.36 bar (absolute) feed pressure. Note that the controller in the air pressure regulator has a response time lag of approximately 0.3–0.4 s (manufacturer provided). Over the speed range from 15 krpm to 14 krpm, the deceleration rate of the shaft is approximately 210 rpm/s. Therefore, the time lag of the air regulator will cause a response delay of approximately 60~85 rpm. Thus, the regular has an increasing supply pressure rate equal to $[(5.08\ \text{bar}-2.36\ \text{bar})/(60\sim85\ \text{rpm})]\times(210\ \text{rpm/s})=9.45\sim6.72\ \text{bar/s}$. Recall that the air pressure regulator is operated according to the output voltages of the tachometer which is proportional to the rotor speed.

4.3 Measured Rotor Response Amplitudes for Each Operating Configuration. Figures 7 through 10 depict the amplitudes of rotor synchronous motion for each operating configuration. The graphical inserts in the figures recall the supply air feeding methods for each operating configuration. In all figures, tests results with a fixed supply pressure maintained throughout the whole rotor speed range are shown.

Figure 7 shows that the peak amplitude of rotor response is completely eliminated by the sudden increase in supply pressure for both operating conditions #2 and #3.

For operating condition #4, the supply pressure into the test bearings is increased in a similar fashion as in prior measurements [9]. The rotor motion amplitude abruptly decreases while varying the supply pressure over a narrow speed region from 13.9 krpm to 13.0 krpm, as shown in Fig. 8. Deceleration fixed rotor speed tests demonstrate that manual step-control of the supply pressure can effectively reduce the rotor synchronous response amplitudes while crossing the system critical speed.

Based on the test results depicted in Fig. 7, the electropneumatic air regulator is used with a closed loop to control the supply pressure. Figure 9 shows that the rotor responses for operating configurations #5 and #7 have a similar behavior over the entire rotor speed range.

Figure 10 shows the rotor synchronous responses for a continuous (ramp) increase in supply pressure to the bearings. Over the

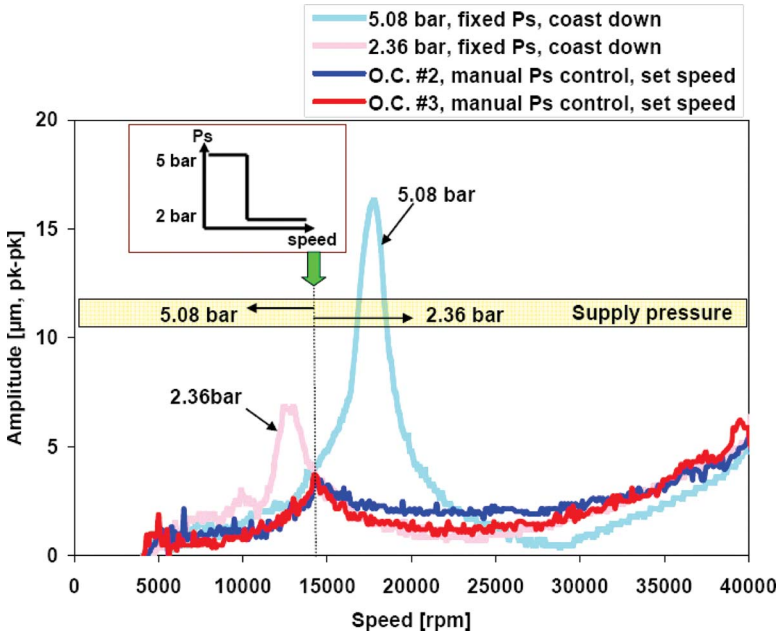

Fig. 7 Rotor synchronous response versus shaft speed. Right bearing horizontal direction (RH). Operating conditions #2 and #3. Manual pressure supply setting.

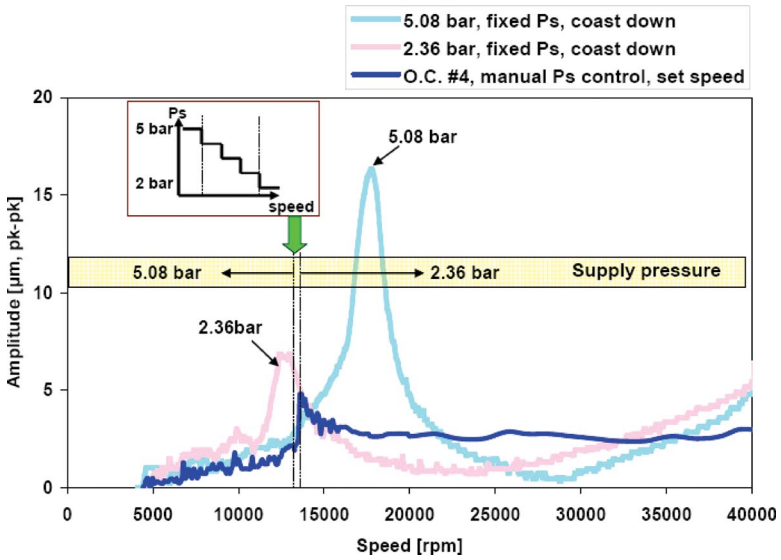

Fig. 8 Rotor synchronous response versus shaft speed. Right bearing horizontal direction (RH). Operating condition #4. step-wise manual pressure supply setting.

narrowly selected speed region, the rotor response evidences a distinct peak over the controlled pressure regime. The rotor-bearing system experiences a sudden critical speed when the pressure supply is increased continuously from 2.36 bar to 5.08 bar within 14.2–13.0 krpm.

Both the fixed speed rotor deceleration and speed coast-down operation render similar rotor synchronous motions for each method of supplying the feed pressure. A step change in supply pressure is more effective than a ramp increase for reducing high vibration amplitudes of the rotor while crossing the system critical speeds.

5 Prediction of Rotordynamic Response and Comparison to Test Results

The rotordynamic analysis includes modeling the rotor structure and predicting the gas bearing force coefficients using the computational model described by San Andrés in Ref. [19]. Details on the finite element (FE) structural model for the test rotor and a comparison of measured and predicted free-free mode shapes and natural frequencies can be found in Ref. [20]. Table 1 details the bearing dimensions; and in the predictive model, the representative radial clearance $(C_p=R_p-R_j)$ and preload are

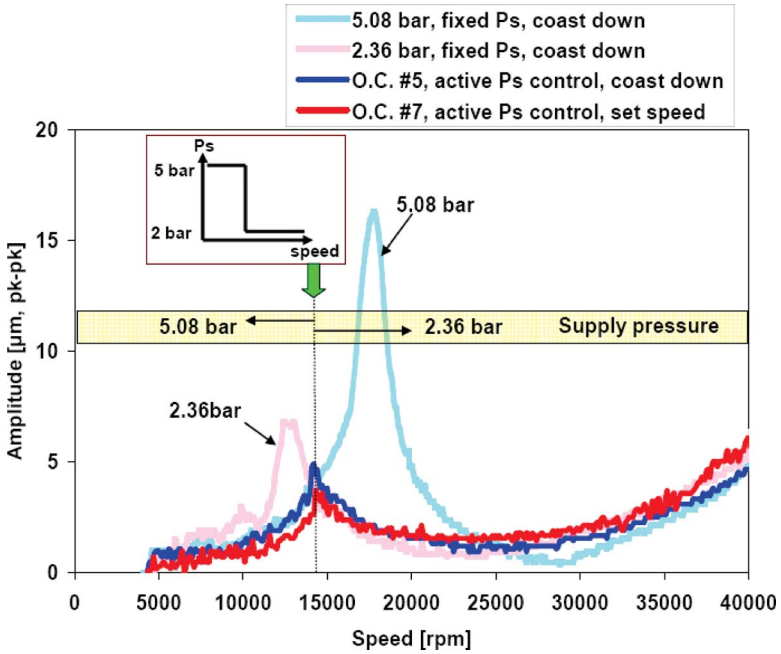

Fig. 9 Rotor synchronous response versus shaft speed. Right bearing horizontal direction (RH). Operating conditions #5 and #7. Controller activated system.

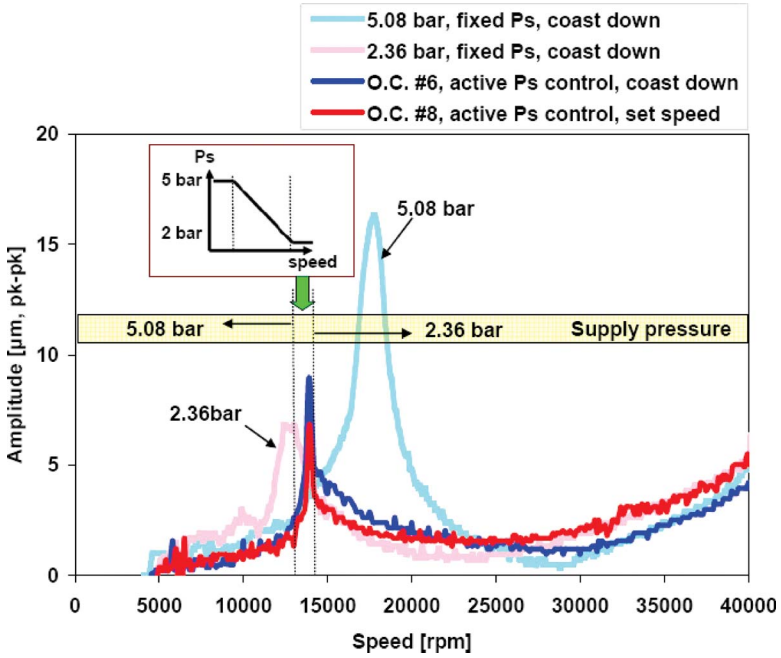

Fig. 10 Rotor synchronous response versus shaft speed. Right bearing horizontal direction (RH). Operating conditions #6 and #8. Controller activated system.

38 μm and 8.4 μm for the right bearing and 44.5 μm and 6.7 μm for the left bearing, respectively. As compared with prior reported measurements and predictions given in Ref. [9], exhaustive rotor speed coast-down tests with intermittent rubbing at low rotational speeds have deteriorated the bearings pads' surfaces, thereby reducing their original preload.

Predicted (synchronous) force coefficients for each supply pressure condition are incorporated into the rotor structural model for prediction of the rotor imbalance response. Appendix includes the predicted (synchronous speed) rotordynamic force coefficients for the gas bearings with controlled supply pressures. The eigenvalue analysis of the rotor-bearing system renders the natural frequencies and modal damping ratios, see Ref. [18].

5.1 Comparison Between Predictions and Measured Imbalance Responses. From the rotordynamic measurements, estimated imbalance masses are 0.028 g mm and 0.565 g mm at the left and right ends of the rotor, respectively, and 180° out of phase. Figure 11 compares the predicted and measured imbalance responses of the test rotor for increasing feed pressures. For P_s (supply pressure) >3.5 bar (absolute), the correlation of predictions to measurements is remarkable. However, as the supply pressure decreases, the test data show higher critical speeds with smaller rotor motion amplitudes. This implies that the stiffness and damping coefficients of the test bearings are larger than the predicted values for low supply pressure conditions (P_s <3.5 bar).

Figures 12 through 14 depict the predicted synchronous response to rotor imbalance for three different control methods of supply pressure into the bearings and comparisons to the test data. The predictions show a remarkable agreement within the rotor speed region of controlled supply pressure. Note that the rotor motion for operating condition #4 shows much smaller peak amplitude while passing through the manually controlled supply pressure region.

6 Conclusions

Earlier test results with hybrid flexure pivot gas bearings detailed in Ref. [9] show that external pressurization stiffens the bearings thereby increasing the rotor-bearing system critical speeds. However, the system damping ratio decreased considerably thus making the system more sensitive to imbalance with large amplitude responses while crossing the critical speed regions. Furthermore, the measurements evidence that external pressurization into the test gas bearings is not necessary for operation beyond the critical speed of the rotor-bearing system.

In particular, the measurements of rotor motion during rotor speed coast downs while manually controlling the feed pressure show elimination of critical speeds with smooth operation over an extended operating speed range. The present work continues prior art [9] and provides further rotordynamic demonstrations using an inexpensive electro-pneumatic air regulator to control the supply pressure into the hybrid gas bearings.

The feed pressure needs to increase as the rotor speed decreases

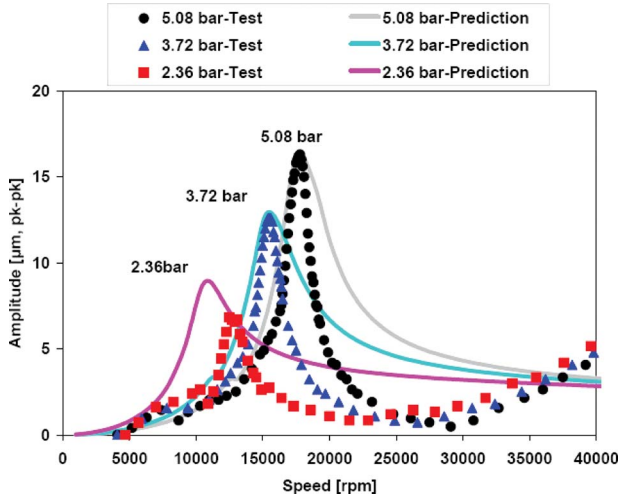

Fig. 11 Comparison of predicted and measured imbalance response of test rotor for increasing supply pressures. Right bearing horizontal direction (RH).

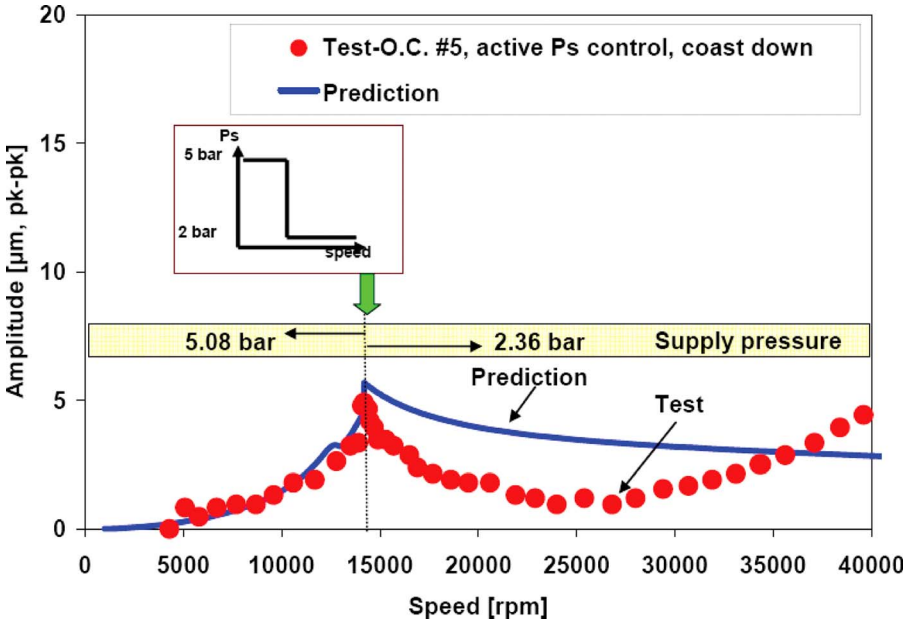

Fig. 12 Comparison of predicted and measured imbalance responses. Measurement for operating condition #5 and prediction for one-step increase in supply pressure (2.36 bar) at 14.2 krpm. Right bearing horizontal direction (RH).

over a relatively narrow speed region. Open and closed loop control systems of supply pressure into the test bearings are set up to relate the rotor speed to the supply pressure. Rotordynamic response measurements are conducted for eight test operating conditions based on various feeding pressure control methods and preset rotor speed regions. The demonstrations show that step and multiple step-wise increases in supply pressure noticeably lessen the rotor synchronous response amplitudes while crossing the system critical speed. However, for a uniformly increasing (ramp) supply pressure condition, the rotor-bearing system encounters a sudden critical speed over the narrow preset speed region, thus showing a notable peak in the rotor synchronous response.

A FE rotordynamic analysis models the test rotor and integrates predicted synchronous speed bearing force coefficients. Predicted response amplitude to imbalance for cases with controlled supply pressures correlate very well with the measurements. The computational model predicts reliable bearing force coefficients even when the bearings are severely worn.

Low or virtually nil amplitudes of rotor motion while crossing a system critical speed enables MTM supported on hybrid gas bearings to operate more efficiently (tighter tip clearances) with less power losses and ensuring longer bearing structure life. Presently, the accurate control of bearings' centering stiffnesses with gas feed pressure allows to increase the system natural frequency, thus

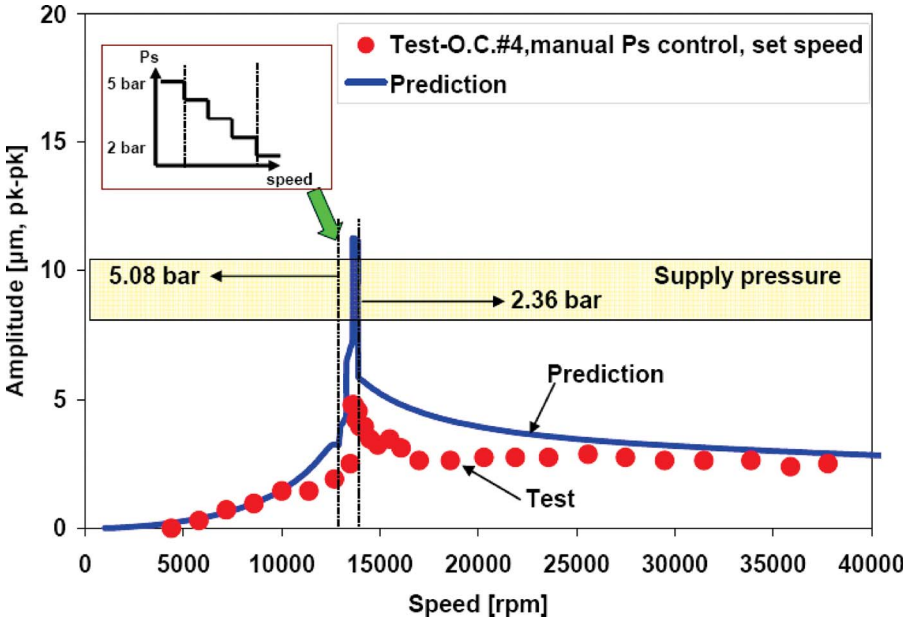

Fig. 13 Comparison of predicted and measured imbalance responses. Measurement for operating condition #4 and prediction for four-step increase in supply pressure (2.36 bar) from 13.9 krpm to 13.0 krpm. Right bearing horizontal direction (RH).

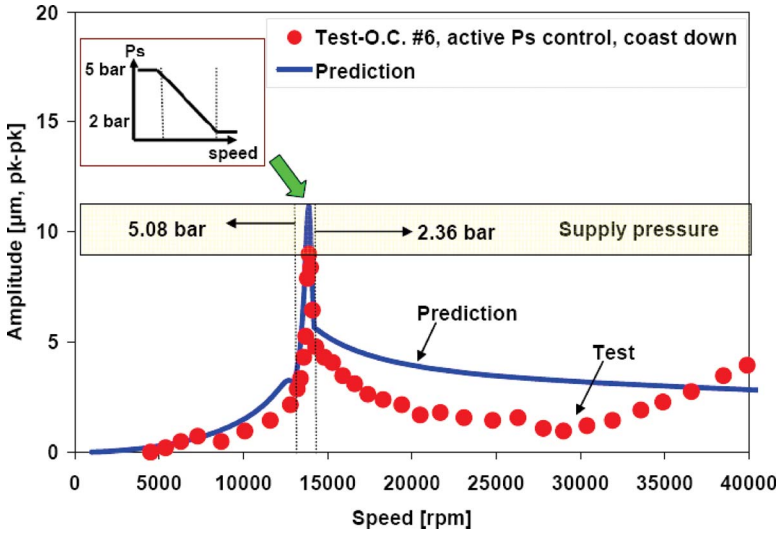

Fig. 14 Comparison of predicted and measured imbalance responses. Measurement for operating condition #6 and prediction for ramp increase in supply pressure (2.36 bar) from 14.2 krpm to 13.0 krpm. Right bearing horizontal direction (RH).

raising the margin for stable rotordynamic performance should aerodynamic forces from other rotating components appear at high speeds, for example. The current research advances reliable and predictable flexure pivot gas bearing technology with improved rotordynamic performance for ready application in oil-free high-speed MTM, even when operating with worn pad surfaces.

Acknowledgment

The continued support of the TAMU Turbomachinery Research Consortium is gratefully acknowledged. Thanks to KMC, Inc. for manufacturing the test bearings.

Nomenclature

A_u = peak-to-peak amplitude of unfiltered rotor motion (m)
C_b = radial bearing clearance (m)
$C_{i,j}$ = bearing damping coefficients, $i,j=X,Y$(N s/m)
C_p = radial pad clearance (m)
d_o = feed orifice diameter (m)
D_b = bearing diameter (m)
D_j = rotor diameter (m)
e = journal eccentricity (m)
I_p = pad mass moment of inertia (kg m^2)
$K_{i,j}$ = bearing stiffness coefficients, $i,j=X,Y$(N/m)
$K_{\delta\delta}$ = flexure web rotational stiffness (N m/rad)
L = bearing axial length (m)
M = rotor mass (kg)
N = rotor speed (rpm)
P_s = supply pressure (absolute) (bar)
R_p = pad radius (m)
R_j = rotor radius (m)
W = external load acting on bearing (N)
X,Y = inertial coordinate system
Ω = rotor speed (rad/s)

Appendix: Predicted Bearing Stiffness and Damping Force Coefficients

Reference [9] discusses the effect of supply pressure on the static load performance and dynamic force coefficients of hybrid gas bearings. For step, multiple step-wise, and ramp increases in supply pressure, Figs. 15 and 16 depict the predicted static journal

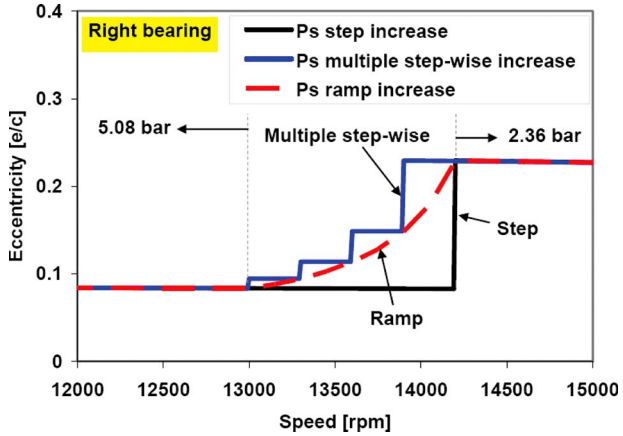

Fig. 15 Predicted gas bearing static journal eccentricity for step, multiple step-wise, and ramp increase in supply pressure. Static load W=4 N.

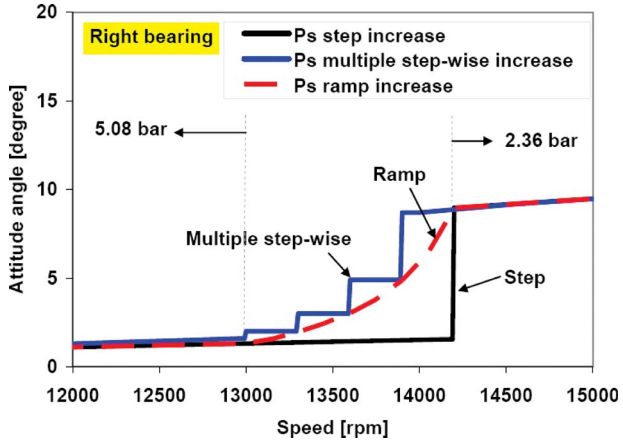

Fig. 16 Predicted gas bearing attitude angle for step, multiple step-wise, and ramp increase in supply pressure. Static load W=4 N.

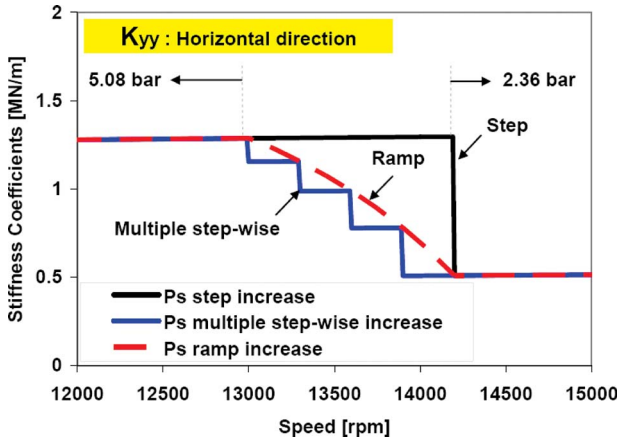

Fig. 17 Comparison of gas bearing direct stiffnesses for step, multiple step-wise, and ramp increase in supply pressure. Right bearing horizontal direction.

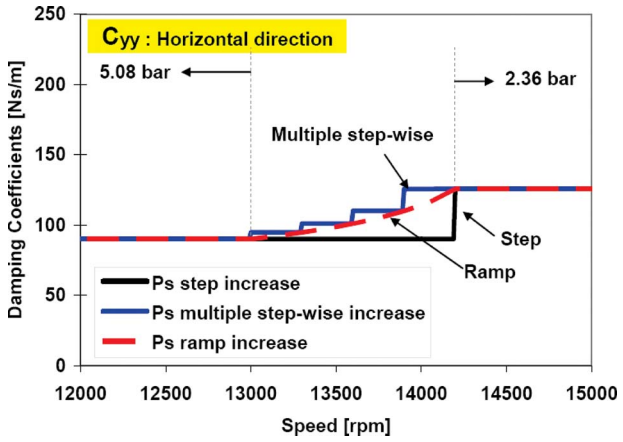

Fig. 18 Comparison of gas bearing direct damping coefficients for step, multiple step-wise, and ramp increase in supply pressure. Right bearing horizontal direction.

eccentricity and attitude angle for the right gas bearing as rotor speed decreases. The static load on each bearing is 4 N. Note that the maximum dimensionless journal eccentricity is 0.78 for hydrodynamic operation and low rotor speed conditions. High supply pressures into the bearings lead to smaller journal eccentricities and attitude angles.

Figures 17 and 18 compare the direct stiffness and damping coefficients for step, multiple step-wise, and ramp increase in supply pressure. The direct stiffnesses increase in proportion to the supply pressure, as depicted in Fig. 5; whereas the damping coefficients show a decrease with supply pressure.

References

[1] Sternlicht, B., 1968, "Gas Bearing Turbomachinery," ASME J. Lubr. Technol., **90**, pp. 665–679.

[2] Kolanowski, B. F., 2004, *Guide to Microturbines*, Fairmont, Lilburn.

[3] Hamrock, B. J., 1994, *Fundamentals of Fluid Film Lubrication*, McGraw-Hill, New York.

[4] Fleming D. P., Cunningham, R. E., and Anderson, W. J., 1968, "Stability Analysis for Unloaded Externally Pressurized Gas-Lubricated Bearings With Journal Rotation," NASA, Report No. NASA TN D-4934.

[5] Lucero, J. M., and DellaCorte, C., 2004, "Oil-Free Rotor Support Technologies for Long Life, Closed Cycle Brayton Turbines," *Proceedings of the 2nd International Energy Conversion Engineering Conference*, Providence, RI, Aug. 16–19, Paper No. AIAA 2004-5720.

[6] Zeidan, F. Y., and Herbage, B. S., 1991, "Fluid Film Bearings Fundamentals and Failure Analysis," *Proceedings of the 20th Turbomachinery Symposium*, Dallas, TX, Sep. 17–19, pp. 161–186.

[7] Zeidan, F., 1992, "Developments in Fluid Film Bearing Technology," Turbomach. Int., **9**, pp. 24–31.

[8] Zhu, X., and San Andrés, L., 2007, "Rotordynamic Performance of Flexure Pivot Hydrostatic Gas Bearings for Oil-Free Turbomachinery," ASME J. Eng. Gas Turbines Power, **129**, pp. 1020–1027.

[9] San Andrés, L., and Ryu, K., 2008, "Flexure Pivot Tilting Pad Hybrid Gas Bearings: Operation With Worn Clearances and Two Load-Pad Configurations," ASME J. Eng. Gas Turbines Power, **130**, p. 042506.

[10] American Petroleum Institute, 2004, *API 610: Centrifugal Pumps for Petroleum, Petrochemical and Natural Gas Industries*, Washington, DC.

[11] American Petroleum Institute, 2002, *API 617: Axial and Centrifugal Compressors and Turboexpanders for Petroleum, Chemical and Gas Industry Services*, Washington, DC.

[12] Osborne, D. A., and San Andrés, L., 2006, "Experimental Response of Simple Gas Hybrid Bearings for Oil-Free Turbomachinery," ASME J. Eng. Gas Turbines Power, **128**, pp. 626–633.

[13] Zhu, X., and San Andrés, L., 2005, "Experimental Response of a Rotor Supported on Rayleigh Step Gas Bearings," ASME Paper No. GT 2005–68296.

[14] Santos, I. F., 1995, "On the Adjusting of the Dynamic Coefficients of Tilting-Pad Journal Bearings," STLE Tribol. Trans., **38**, pp. 700–706.

[15] Santos, I. F., and Scalabrin, A., 2003, "Control System Design for Active Lubrication With Theoretical and Experimental Examples," ASME J. Eng. Gas Turbines Power, **125**, pp. 75–80.

[16] Bently, D. E., Grant, J. W., and Hanifan, P. C., 2000, "Active Controlled Hydrostatic Bearings for a New Generation of Machines," ASME Paper No. 2000-GT-354.

[17] Qiu, J., Tani, J., and Kwon, T., 2003, "Control of Self-Excited Vibration of a Rotor System With Active Gas Bearings," ASME J. Vibr. Acoust., **125**, pp. 328–334.

[18] Ryu, K., 2007, "Hybrid Gas Bearings With Controlled Supply Pressure to Eliminate Rotor Vibrations While Crossing System Critical Speeds," M.S. thesis, Texas A&M University, College Station, TX.

[19] San Andrés, L., 2006, "Hybrid Flexure Pivot-Tilting Pad Gas Bearings: Analysis and Experimental Validation," ASME J. Tribol., **128**, pp. 551–558.

[20] San Andrés, L., and Ryu, K., 2006, "Test Results for Load-On-Pad and Load-Between-Pad Hybrid Flexure Pivot Tilting Pad Gas Bearings," Turbomachinery Laboratory, Texas A&M University, Research Report No. TL-B&C-1-06.

Ali Mohammadi
Toyota Motor Europe,
Hoge Wei 33B-1930 Zaventem,
Belgium
e-mail: ali.mohammadi@toyota-europe.com

Masahiro Shioji
e-mail: shioji@energy.kyoto-u.ac.jp

Yuki Matsui

Rintaro Kajiwara

Graduate School of Energy Science,
Kyoto University,
Sakyo-ku, Kyoto 606-8501, Japan

Spark-Ignition and Combustion Characteristics of High-Pressure Hydrogen and Natural-Gas Intermittent Jets

Recently, an in-cylinder injection method has been considered for the improvement of thermal efficiency in natural-gas and hydrogen spark-ignition (SI) engines. However, the SI and combustion processes of gaseous jets are not well understood. The present study aims to provide fundamental data for the development of direct-injection SI gas engines. The ignition, combustion, and flame behavior of high-pressure and intermittent hydrogen and natural-gas jets in a constant volume combustion chamber were investigated. The effects of injection pressure, nozzle size, ambient pressure, and spark location were also investigated for various spark timings and equivalence ratios.
[DOI: 10.1115/1.2938271]

Introduction

Consideration of the current environmental issues and energy security has led to the examination of hydrogen and natural gas as alternative fuels for internal combustion engines. The use of hydrogen can provide CO_2, smoke, and hydrocarbon (HC)-free combustion. Although there are still several barriers to the utilization of hydrogen as a fuel in internal combustion engines, the results of recent work on hydrogen production, distribution, and storage have been promising [1]. Hydrogen fuel exhibits desirable characteristics for the combustion in spark-ignition (SI) engines. A wide range of flammability limits in hydrogen engines enables smooth engine operation for a very lean mixture with low NO_x levels, and throttle control is unnecessary, even at idle. The high burning velocity of hydrogen may contribute to a relatively high thermal efficiency with a shorter combustion period for an ignition timing close to top dead center (TDC). Additionally, the low-spark energy requirement can prevent cyclic combustion fluctuations. These preferable features have encouraged a number of studies to establish a high-performance hydrogen engine with various designs and operating conditions [2–10]. Nevertheless, the extremely rapid combustion of hydrogen causes abnormal burning, such as knock, preignition, and backfires at higher loads, which prevents reliable operations and restricts the maximum power output for the engine [11–14]. Furthermore, a significantly higher burn velocity leads to a lower thermal efficiency compared to other gaseous fuels because of the increase in heat loss due to knocklike explosive combustion. To overcome such problems with hydrogen engines, internal mixing of hydrogen has been examined by some researchers [15–17]. Generally, internal mixing of hydrogen is achieved by high-pressure injection systems. This technique is very effective for the prevention of backfire and knock, particularly under high engine loads. However, high heat loss due to the high burning velocity of hydrogen is still a major barrier to achieving thermal efficiency as high as that seen in recently advanced direct-injection diesel engines.

Natural-gas engines, with less smoke combustion and low CO_2 emission per output power, are also an attractive solution with regard to the factors already mentioned. Natural-gas engines are widely utilized in passenger cars, buses, and trucks. Most of these engines are operated under SI stoichiometric conditions with three-way catalysts [18,19]. Although these engines have clean exhaust emissions, the occurrence of a knock under high engine loads limits the compression ratio, and therefore lowers the thermal efficiency. In addition, pumping loss under low engine loads is also a limiting factor affecting thermal efficiency. In heavy-duty stationary natural-gas engines, utilization of lean-burn combustion with prechamber technology offers high thermal efficiency and output power with low NO_x emission [20,21]. However, such engines are designed to ensure lean-burn operation only under limited engine loads and speeds. Unfortunately, lean-burn combustion in light/medium duty natural-gas engines is not easily achieved. Use of the prechamber in such engines is subject to space limitations and the demand for a wide range of engine operation.

Recently, direct-injection, spark/glow plug ignition natural-gas engines have been investigated because of their potential for high thermal efficiency and power output [22,23]. However, these engines require well controlled mixing, especially for low engine loads.

The utilization of direct-injection technology, for both hydrogen and natural-gas engines, is a very effective way to achieve efficient and clean combustion for a wide range of engine operation. However, to achieve these goals, a better understanding of the spark ignition of transient gaseous jets (hydrogen and natural gas) is necessary. Although combustion of premixed gaseous fuel (beside other fuels) has received intensive fundamental investigation for many decades [24], the ignition and combustion of transient and high-pressure gaseous jets are still not well understood [25,26]. This is due to two major reasons: (1) In the past, there has not been a strong demand for direct-injection technology in gas engines, and (2) there has been a lack of research on high-pressure gas injection technology. However, recently, thermal efficiency and emission potential for direct gas injection have attracted much attention.

The aim of the present study is to obtain fundamental data required for the development of direct-injection gas engines. The effects of ambient conditions, injection parameters, and spark conditions on the ignition and combustion of transient/high-pressure natural-gas and hydrogen jets were extensively investigated under various ignition timings and equivalence ratios, using a constant volume combustion chamber. The results indicate that optimiza-

Contributed by the Internal Combustion Engine Division of ASME for publication in the JOURNAL OF ENGINEERING FOR GAS TURBINES AND POWER. Manuscript received January 25, 2006; final manuscript received March 6, 2008; published online August 21, 2008. Review conducted by Margaret Wooldridge.

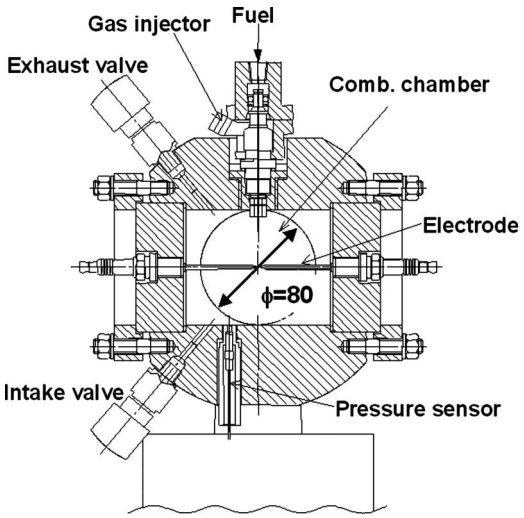

Fig. 1 Constant volume combustion vessel

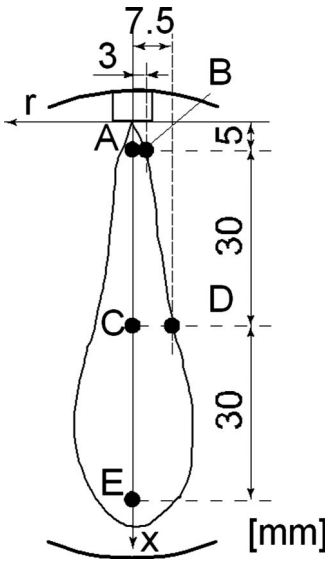

Fig. 2 Ignition locations

tion of these parameters is very important to achieve stable ignition and efficient combustion for a wide range of equivalence ratios.

Experimental Apparatus and Procedure

Investigation of the ignition and combustion characteristics of transient natural-gas and hydrogen jets was performed using a constant volume combustion vessel, which is schematically shown in Fig. 1. The vessel has a combustion chamber with a volume of 300 cm^3 (100 mm wide, 25 mm deep, and 80 mm high). The chamber consists of intake and exhaust valves, which were used to charge the chamber with air or the fuel premixture, and discharge the burned gases, respectively. A high-pressure solenoid type single-hole gas injector, installed at the top part of the chamber, was used to inject hydrogen and natural gas toward the center of the combustion chamber. A maximum injection pressure of 15 MPa could be achieved using this injector. The timing and quantity of injected fuel were varied by adjusting the timing and duration of the trigger signal sent to the injector driver. Optical access to reacting gaseous jets was provided using two quartz windows with diameters of 80 mm. Reacting gas jets were visualized by shadowgraphy methods, using a high-speed digital video camera (Vision Research, Phantom 7.0). Photography was conducted with a speed of 8200 fps and an exposure of 30 μs. The gas pressure inside the combustion chamber was measured with a piezoelectric pressure transducer (Kistler 6052A), and it was used to calculate the heat release rate. The heat release rate was calculated based on the first law of thermodynamics, and consideration of heat loss to the chamber wall.

Table 1 indicates the experimental conditions for the present study. All experiments were carried out at a room temperature of 298 K. The ambient pressure p_a, injection pressure p_j, and nozzle hole size d_N were varied in the range of 0.5–1.5 MPa, 5–10 MPa, and 0.56–0.8 mm, respectively. The underlined numbers in the table correspond to the base conditions. The effects of ignition position on combustion were investigated using five ignition locations, as shown in Fig. 2. The coordinates of these points are shown in Table 1. Here, x and r correspond to the axial and radial distances from the nozzle exit. The ignition Points A, C, and E are located on the central axis of the gas jets, while Points B and D are located on the jet boundary.

Table 1 Experimental conditions

Fuel	H_2, natural gas
Equivalence ratio ϕ (Inj. duration Δt_i (ms)	Variable
Ignition timing t_i (ms)	Variable
Ambient pressure p_a (MPa)	*0.5*, 1.0, 1.5
Injection pressure p_i (MPa)	5, *8*, 10
Ign. position (x,r) (mm)	(10.0), (10.3), (*40.0*), (40.7.5), (70.0)
Nozzle diameter d_N (mm)	0.56, *0.8*

Prior to the main experiment, the effects of ambient pressure p_a and injection pressure p_j on the penetration of nonreacting hydrogen and natural-gas jets were investigated, and the results are presented in Fig. 3. The graph reveals the penetration length of the hydrogen and natural-gas jets, x_t, against the time from the start of

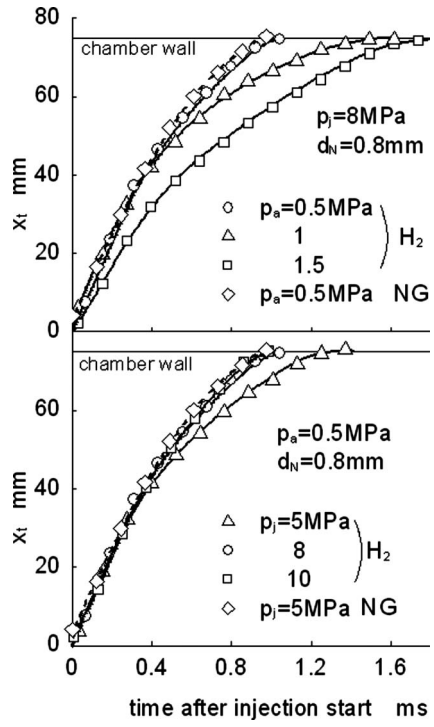

Fig. 3 Penetration lengths of natural-gas and hydrogen jets for different ambient pressures p_a, and injection pressures p_j

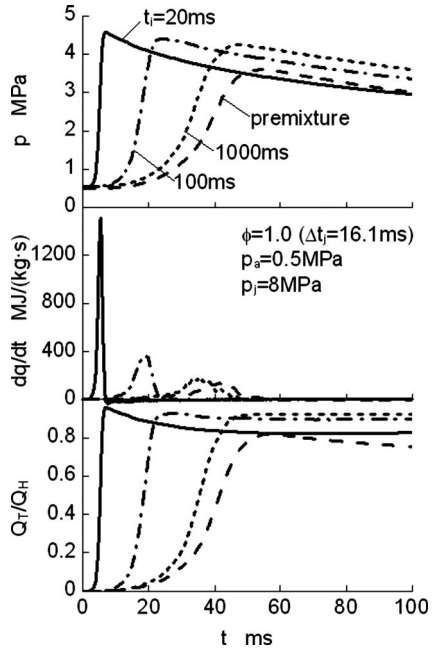

Fig. 4 History of pressure *p*, and heat release rate *dq/dt*, for natural-gas combustion at an equivalence ratio of ϕ=1.0

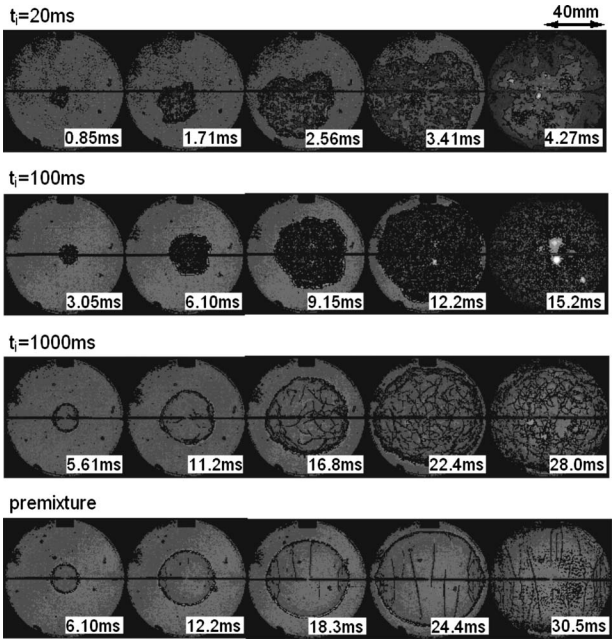

Fig. 5 Shadowgraph images of natural-gas combustion with an equivalence ratio of 1.0

injection. For the hydrogen jets, increasing the ambient pressure p_a, for an injection pressure of p_j=8 MPa and nozzle size of d_N =0.8 mm, results in a decrease in jet penetration. However, for p_a=0.5 MPa, increasing the injection pressure above p_j=8 MPa results in small changes in the jet penetration, x_t. Under the experimental conditions used in this study, small differences were observed in the penetration length x_t, for natural-gas and hydrogen jets, before their interaction with the wall of the combustion chamber. The results shown in this figure were used later to estimate the time when the gas jets reach the spark positions.

Results and Discussion

In the present study, ignition and combustion of natural-gas jets, under various equivalence ratios and spark timings, were first carried out under the base experimental conditions. Next, the effects of ambient pressure, injection pressure, spark location, and nozzle hole size on the ignition of hydrogen jets were investigated for various spark timings and equivalence ratios.

Spark Ignition of Natural-Gas Jets

At first, the spark ignition of natural-gas jets was investigated for an overall equivalence ratio of ϕ=1.0 (injection duration of Δt_j=16.1 ms), ambient pressure of p_a=0.5 MPa, and an injection pressure of p_j=8 MPa, while the time from injection start to spark t_i was varied in the range of 20–1000 ms. Figure 4 shows the pressure p, heat release rate dq/dt, and amount of heat released for combustion Q_T, normalized by the amount of heat energy for the injected fuel Q_H, against the time from the spark t. Here, the maximum value of Q_T/Q_H corresponds to the apparent combustion efficiency η_c with the inclusion of heat loss. In order to estimate the heat loss, the heat transfer coefficient was adjusted to obtain a flat Q_T/Q_H curve at the end of combustion, using the average temperature and internal area of the combustion chamber. As shown in the graph, SI of the natural-gas premixture gives a low rate of pressure rise, a low peak combustion pressure, a weak heat release rate, a long combustion duration, and a low Q_T/Q_H. However, natural-gas injection with the same overall equivalence ratio for various t_i gives better results. Advancing t_i promotes jet combustion by an increase in p, dq/dt, and Q_T/Q_H, and the decrease in the duration of combustion. For t_i=20 ms, the maximum value of Q_T/Q_H was very close to that which corresponds to a very high combustion efficiency.

To describe the effects of t_i on the combustion of natural-gas jets, high-speed shadowgraphy of the reacting jets was performed under the same experimental conditions as given in Fig. 4, and the results are presented in Fig. 5. For the premixture, a wrinkleless flame propagates spherically around the spark gap and takes a relatively long time (approximately 30.5 ms) to fully cover the observation window. t_i values of 1000 ms and 100 ms result in wrinkly spherical flame propagation with a much shorter time (28.0 ms and 15.2 ms, respectively) for the flame to cover the window. These results indicate that natural-gas combustion is enhanced by the turbulence from injection, even after a relatively long time from the injection end. Jet ignition at t_i=20 ms (4 ms after injection end) results in flame propagation toward the downstream area of the combustion chamber. This is due to the momentum of the gas jet, even after the end of injection. In this case, the strong turbulence of the jets results in very short combustion duration. The time required for the flame to cover the observation window is approximately three times shorter than that for t_i =100 ms.

Summarizing the above results, it can be suggested that utilization of fuel injection is very effective for the promotion of natural-gas combustion.

The effect of t_i on the combustion characteristics of natural-gas jets was investigated for various equivalence ratios, and the results are shown in Fig. 6. This figure shows the combustion efficiency η_c, combustion duration Δt_{comb}, maximum heat release rate $dq/dt_{\max}$, and the maximum combustion pressure $p_{\max}$ against t_i for various equivalence ratios ϕ in the range of 0.6–1.0. The graph also presents results for combustion of the premixture. In the case of a premixture, fuel-air mixtures were first prepared in a mixture tank and then introduced to the combustion chamber through the intake valve. Here, the combustion efficiency of η_c is measured by the maximum value of Q_T/Q_H shown in Fig. 4.

For every equivalence ratio ϕ, an increase in t_i results in the lowering of $p_{\max}$ and $dq/dt_{\max}$, and longer combustion duration Δt_{comb}, which corresponds to a weaker combustion. A larger increase in t_i results in combustion characteristics very similar to

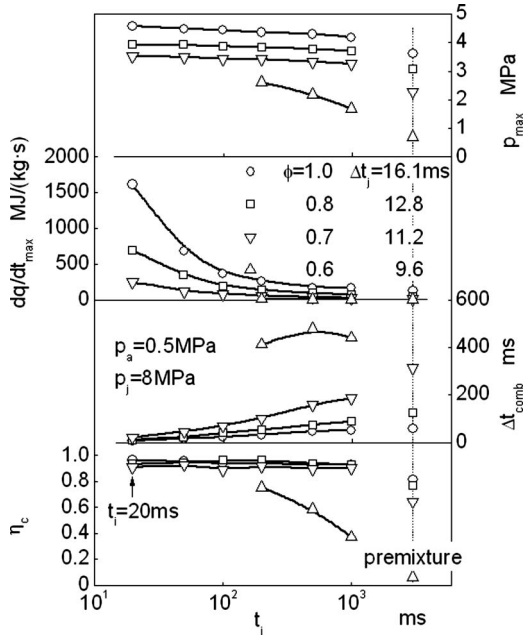

Fig. 6 Combustion characteristics of natural-gas jets for various equivalence ratios

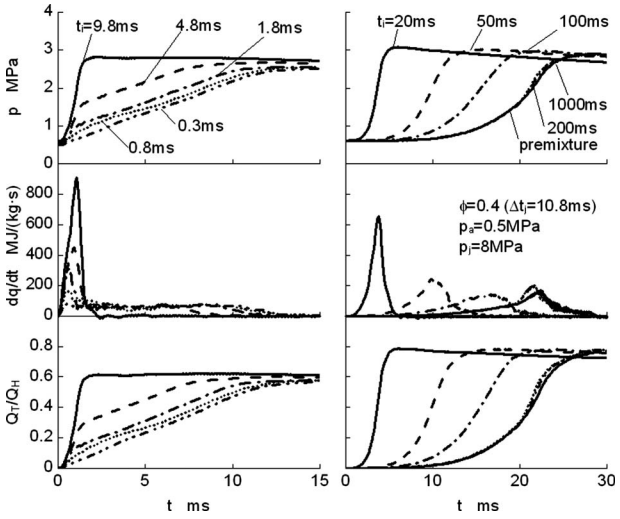

Fig. 7 Combustion characteristics of hydrogen jets for various injection timings with ϕ=0.4: (*a*) $t_i<\Delta t_j$; (*b*) $t_i>\Delta t_j$

those observed for the premixture condition. For every condition, at $t_i<20$ ms, the strong gas flow extinguished the flame kernel, resulting in misfire. For $\phi=0.6$, with very weak combustion characteristics for the premixture, injection was very effective for improvement of the combustion. For example, a combustion efficiency η_c, as high as 80% was achieved at $t_i=200$ ms. However, further advancement of the spark timing results in misfire. This suggests that for lean combustion, the utilization of heterogeneous mixtures and turbulence is effective for the stabilization of ignition and enhancement of the combustion of natural-gas jets under proper ignition timing.

Spark Ignition of Hydrogen Jets

Ignition and Combustion Characteristics Under the Base Experimental Conditions. The ignition and combustion characteristics of transient hydrogen jets with an equivalence ratio of $\phi=0.4$ ($\Delta t_j=10.8$ ms) were investigated under the base experimental conditions and the results are presented in Fig. 7. Results are presented for (a) ignition during the injection ($t_i<m\Delta t_j$) and (b) ignition after the end of injection ($t_i\Delta t_j$). The figure shows that an increase in t_i results in combustion enhancement for (a) and weakens the combustion for (b). Moreover, for the conditions of (a), ignition delay was not observed and an increase in pressure was observed just after the ignition. However, for the conditions of (b), an increase in t_i results in a delay in combustion. For (a) at $t_i=0.3$ ms, which corresponds to ignition at the jet tip, the maximum heat release rate could be lowered, and the combustion is well controlled with the fuel injection rate. The results suggest that the combustion of hydrogen jets can be controlled by fuel injection.

For further clarification of the effects of t_i on the combustion of hydrogen jets, high-speed shadowgraphy of burning hydrogen jets was carried out under the same conditions as given for Fig. 7, and the results are presented in Fig. 8. For $t_i=0.3$ ms, the spark kernel moves toward the downstream end of the chamber, which is due to the jet flow. In addition, the flame propagates against the jet flow, toward the nozzle tip, and the fuel burns as soon as it is injected into the chamber. However, for $t_i=9.8$ ms, when the spark occurs at the end of injection, the flame propagates at a small distance from the spark plug and combustion is completed very quickly due to the strong turbulence of the jet. In this case, a luminous flame was observed at the final stage of combustion. Finally, at $t_i=50-100$ ms, a decay in turbulence is observed, and for $t_i=100$ ms, the flame propagation behavior is very similar to

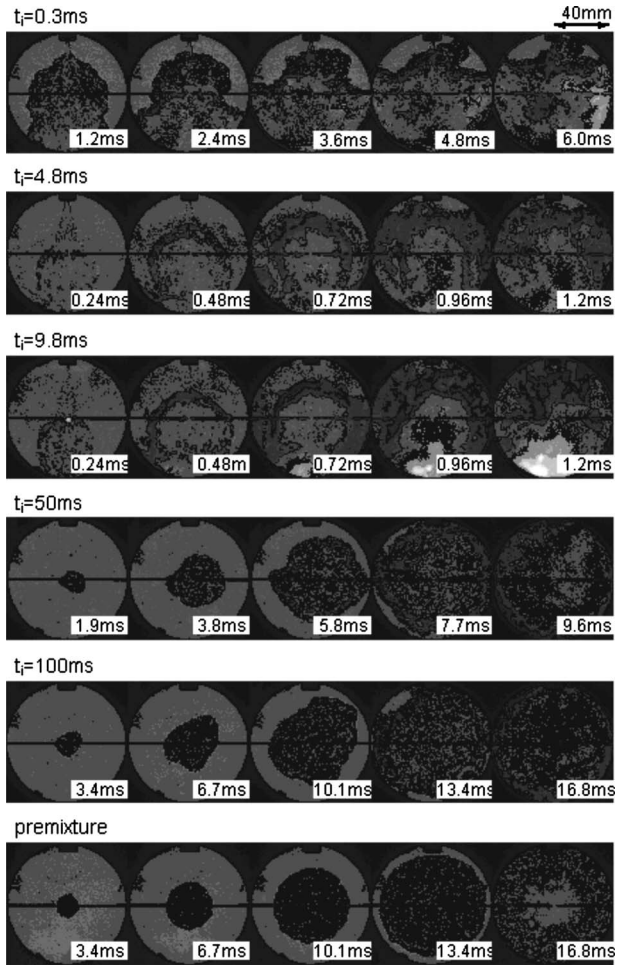

Fig. 8 Shadowgraph images for hydrogen jet combustion with an equivalence ratio of ϕ=0.4

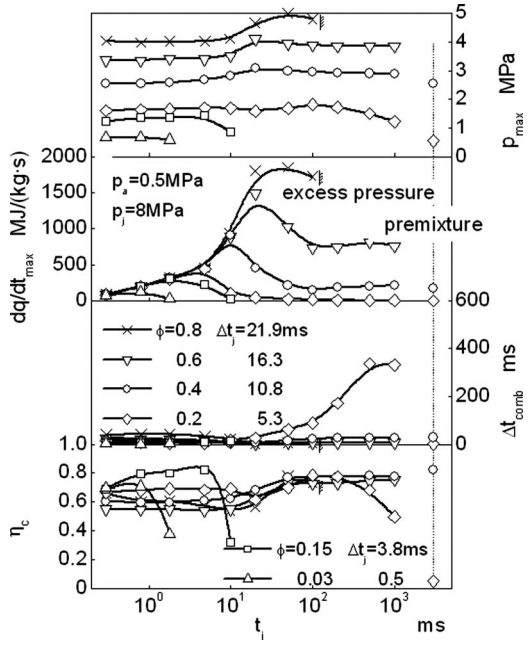

Fig. 9 Combustion characteristics of hydrogen jets, for various equivalence ratios

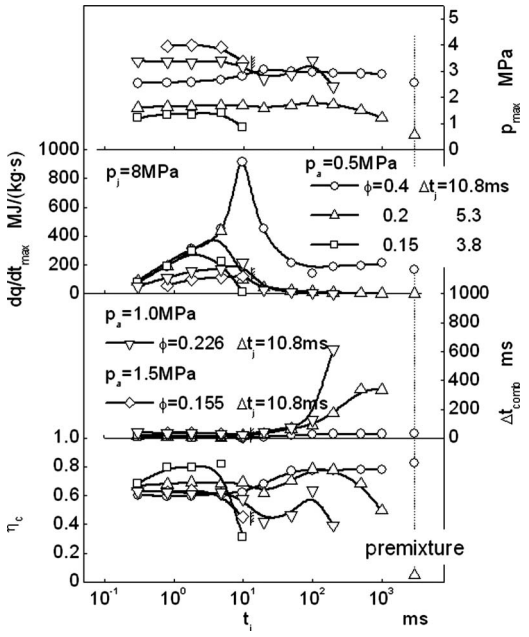

Fig. 10 Effect of ambient pressure p_a, on the combustion of hydrogen jets

that seen for the premixture condition.

Figure 9 shows the combustion characteristics against t_i when the equivalence ratio ϕ was varied in the range of 0.03–0.8. For $t_i < \Delta t_j$, when the spark occurs during the injection, a decrease in t_i lowers the amount of mixture prepared before the spark; therefore, $p_{\max}$ and $dq/dt_{\max}$ are decayed. However, for $t_i > \Delta t_j$, an increase in t_i results in a delay in the progress of combustion, which is due to the decay in the jet turbulence with time. Therefore, for every ϕ, a spark at the injection end ($t_i \cong \Delta t_j$) gives the most enhanced combustion with the highest maximum heat release rate $dq/dt_{\max}$.

As shown in Fig. 9, $p_{\max}$ and $dq/dt_{\max}$ increase with the increase in the equivalence ratio. For $\phi=0.8$, a very intense increase in pressure resulted in the rupture of the diaphragm in the safety valve attached to the chamber for safety purposes. For the premixture condition with $\phi=0.2$, stable ignition was almost impossible, due to an overlean condition. However, for the same equivalence ratio and lower ($\phi=0.03$, 0.15), the utilization of gas injection with advanced spark timing (smaller t_i) not only stabilized the ignition but also resulted in a higher combustion efficiency η_c. It should be noted that in the present study, η_c is not the real combustion efficiency directly measured from unburned fuel but the apparent one estimated by the maximum value of Q_T/Q_H with the inclusion of heat loss. Actually, in most cases of experiments in Fig. 9, unburned hydrogen was scarcely detected even at the ambient temperature of 298 K. This indicates that a lower value of η_c in Fig. 9 may be caused by a greater amount of heat loss due to the extremely rapid combustion of hydrogen jets. Also, for the present results, the spark was carried out at Location C, which is the center of the chamber. For this spark location, $t_i > \Delta t_j$ results in flame propagation around the spark position, while $t_i < \Delta t_j$ results in flame propagation near the chamber wall, with higher heat loss to the wall. Therefore, for $t_i > \Delta t_j$, $p_{\max}$ and η_c are slightly lower than that seen for $t_i < \Delta t_j$.

Effects of Ambient Pressure. Increase in ambient pressure at the same temperature results in a higher ambient density and this accelerates the mixing of jets, due to the increase in the amount of air entrainment. Figure 10 shows the combustion characteristics of hydrogen jets against t_i for various ambient pressure in the range of $p_a=0.5-1.5$ MPa. The change in ambient pressure under the same injection duration ($\Delta t_j=10.8$ ms) results in a change of the overall equivalence ratio. For every p_a, ignition at the end of injection ($\Delta t_j \cong 10.8$ ms) gives the maximum $dq/dt_{\max}$. However, the peak value decreases with the increase in the ambient pressure p_a. This could be due to the accelerated mixing of the jets, because of the high ambient density. For a retarded spark condition ($\Delta t_j > 10.8$ ms), the combustion characteristics show a direct relation to the equivalence ratio. For $p_a=1.5$ MPa, with the highest ambient density, mixing is significantly promoted, and therefore, very late ignition ($t_i > 10.8$ ms) results in misfire.

Effects of Injection Pressure. For the direct-injection hydrogen engine, a high injection pressure is required to achieve high power output, particularly for operation with late injection. In addition, increase in the injection pressure significantly promotes fuel-air mixing. The effect of the injection pressure on the combustion of hydrogen jets was studied under an ambient pressure of $p_a=0.5$ MPa, an injection duration of $\Delta t_j \cong 10.8$ ms, and nozzle hole diameter of $d_N=0.8$ mm, for various injection pressures p_j in the range of 5–10 MPa, and the results are shown in Fig. 11. For all injection pressures, the maximum $dq/dt_{\max}$ is obtained at $t_i \cong 10.8$ ms when injection ends. Elevating the injection pressure increases $dq/dt_{\max}$. This is due to the increase in the amount of fuel injected before the spark and the enhancement in fuel-air mixing. The injection rate for a p_j of 5 MPa is smaller than that for $p_j=8$ MPa; therefore, it results in lower $dq/dt_{\max}$. However, within this range of injection pressures, the combustion efficiency η_c is not significantly affected. For $p_j=10$ MPa, ignition of the hydrogen jet at the jet tip was possible. Nevertheless, at $t_i=0.8-4.8$ ms, the very high momentum of the gas jet resulted in misfire.

Effects of Spark Position. For transient gas jets, the fuel concentration and gas flow velocity have wide temporal and spatial distributions. This has a significant effect on the ignitability of the jet. To clarify the effect, the spark location was changed from that near the nozzle tip to downstream, and from the jet axis to the jet boundary, as shown in Fig. 2. Figure 12 shows the effect of the spark position on the combustion characteristics for $p_a=0.5$ MPa, $p_j=8$ MPa, $\Delta t_j=10.8$ ms, and $d_N=0.8$ mm. This experiment was

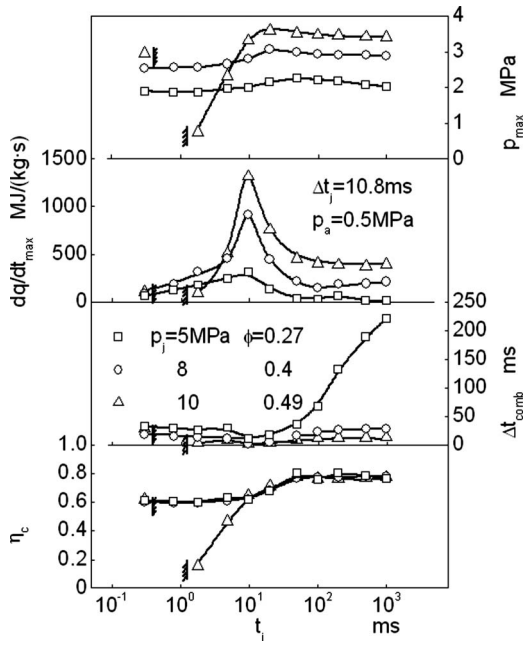

Fig. 11 Effect of injection pressure p_j, on the combustion of hydrogen jets

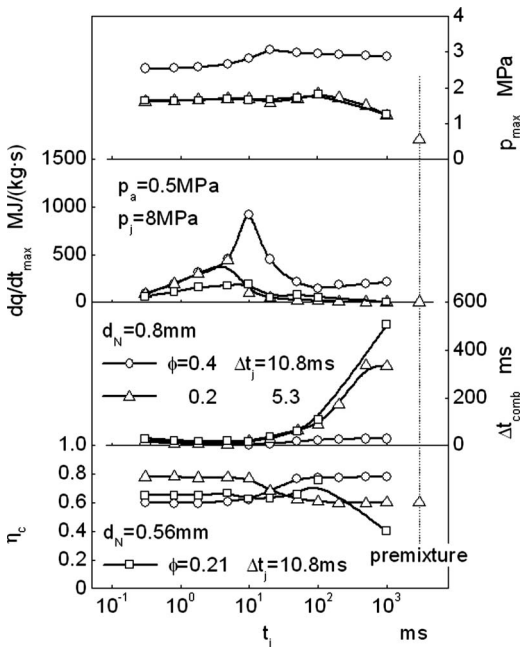

Fig. 13 Effect of nozzle hole diameter d_N, on the combustion of hydrogen jets

mainly conducted to determine the spark timing during fuel injection. Changing the spark position from the center of the combustion chamber (C) to near the nozzle tip (A) resulted in misfire due to a very high jet velocity. A spark located near the bottom wall of the chamber (E) results in a small difference in the combustion characteristics when compared to that for Location C. However, since the flame propagates near the chamber wall, the combustion duration Δt_{comb} is prolonged and a slight decay in dq/dt_{max} can be observed. In the case of ignition at the jet boundary, a spark located at B and D provides almost the same result as that for Position E. For a spark Position at B, stable ignition was achieved even though it is only 3 mm away from Location A, which produced unstable ignition characteristics. For a spark at Position B, combustion can be controlled when the spark occurs just after the start of fuel injection.

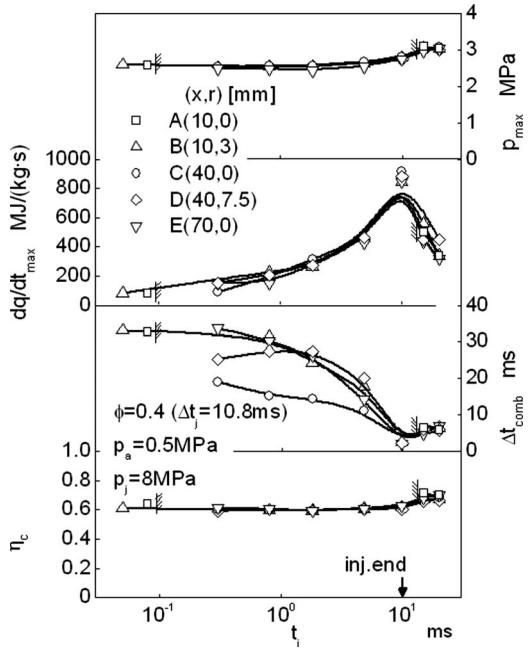

Fig. 12 Effect of spark location on the combustion of hydrogen jets, for an equivalence ratio of 0.4

Based on these results, it can be suggested that for direct-injection hydrogen engines, stable ignition and mild combustion can be achieved if the spark gap is located in the jet periphery and near the nozzle exit.

Effects of Nozzle Hole Size. In transient gas jets, microscopic fuel-air mixing is greatly improved when a small nozzle hole is utilized. Therefore, in this study, the effects of nozzle hole size on ignition and combustion of hydrogen jets were studied by changing the nozzle hole size from a base size of d_N=0.8 mm to d_N =0.56 mm, and the results are presented in Fig. 13. The hole area of the new nozzle is half that of the original one. In this figure, the major combustion characteristics for both nozzles are shown for the same injection duration of Δt_j=10.8 ms (different equivalence ratios) and for the same equivalence ratio of ϕ=0.2 (different injection durations). A smaller hole size results in a lower injection rate; therefore, p_{max} and dq/dt_{max} decay, although the combustion efficiency η_c is slightly improved. For spark after the injection end ($t_i > \Delta t_j$), the effect of nozzle size on the combustion characteristics is very small and mostly varies with the equivalence ratio. This result reveals that for stable ignition and mild combustion, it is better to utilize the minimum available nozzle hole size.

Conclusion

SI and combustion of transient/high-pressure hydrogen and natural-gas jets were investigated under room temperature and high ambient pressure using a constant volume combustion chamber. Jet combustion experiments were conducted for a wide range of ambient pressures, injection parameters, and ignition timing and locations. The following conclusions may be drawn from the results.

1. For natural-gas jets, ignition of the jets during injection was very difficult under high-pressure injection conditions. However, late ignition after the end of injection results in stable

combustion. Optimization of the ignition timing provides stable ignition with high combustion efficiency, even for low equivalence ratios.
2. For hydrogen jets, stable ignition can be achieved even during injection. Ignition of hydrogen jets at the end of injection offers the shortest combustion duration, while combustion control is much easier when the jet is ignited just at the time when the jet tips reaches the spark gap.
3. Under high ambient pressure, the jet leans very quickly. Therefore, under low equivalence ratio conditions, advancing spark timing is required to achieve stable ignition and high combustion efficiency.
4. Increase in the injection pressure significantly enhances the combustion of hydrogen jets. However, for very high injection pressure, the high jet momentum results in unstable ignition.
5. Ignition of hydrogen jets at the boundary of the jet is very effective for stabilizing the ignition, and in combination with advanced spark timing, the intense combustion of hydrogen can be controlled.
6. It is possible to control the intense combustion of a hydrogen jet using a small hole nozzle with a lower injection rate.

In this study, the effects of several important parameters on the ignition and combustion of natural-gas and hydrogen jets were extensively investigated. Nevertheless, several phenomena such as local mixture concentration, wall/in-cylinder flow interactions with gaseous jets, fuel injection strategies, such as pilot injection, etc., are very important; therefore, detailed understanding requires further investigation.

Acknowledgment

The authors would like to thank graduate students Mr. Akira Kato and Mr. Hiroyuki Suganuma for their valuable assistance with the experimental work. Toyota Motor Corporation is acknowledged for providing the gas injection system. This study was partially supported by a Grant-in-Aid for the 21st Century COE Program "Establishment of COE on Sustainable-Energy System" from Japanese Ministry of Education, Culture, Sports, Science and Technology, and by the Industrial Technology Research Grant Program in 2003 from New Energy and Industrial Development Organization NEDO of Japan.

Nomenclature

d_N = nozzle hole diameter, mm
dq/dt = heat release rate, MJ/(kg s)
$dq/dt_{\max}$ = maximum heat release rate, MJ/(kg s)
NG = natural gas
p = pressure, MPa
p_a = initial ambient pressure, MPa
p_j = injection pressure, MPa
$p_{\max}$ = maximum combustion pressure, MPa
Q_T = total heat released form combustion, J
Q_H = total heat energy of injected fuel, J
r = radial distance from nozzle exit, mm
t = time from the spark, ms
t_i = time gap between injection start and spark occurrence, ms
x = axial distance from nozzle exit, mm
x_t = penetration length of gas jets, mm
ϕ = overall equivalence ratio
Δt_j = injection period, ms
Δt_{comb} = combustion duration, ms
η_c = apparent combustion efficiency estimated by the amount of heat release with the inclusion of heat loss

References

[1] Mizuno, M., et al., 2005, "High Pressure Hydrogen Tank for FCHV," *JSAE Proceedings*, 84-05, 20055157, pp. 13–16, in Japanese.
[2] Varde, K. S., and Lucas, G. G., 1974, "Hydrogen as a Fuel for Vehicle Propulsion," Proc. Inst. Mech. Eng., **26**, pp. 365–372.
[3] Saga, K., and Furuhama, S., 1976, "Performance and Emission Control in Stratified Charge Hydrogen Fueled Engines," I Mech E Conf. Publ., **C244/6**, pp. 29–36.
[4] Wallace, J. S., and Ward, C. A., 1983, "Hydrogen as a Fuel," Int. J. Hydrogen Energy, **8**(4), pp. 255–268.
[5] Knecht, W., Hakimifard, D., and Carletta, M., 1989, "A Hydrogen Engine for Heavy Duty Vehicles," 93, pp. 205–211, SAE Paper No. 845138.
[6] Kukkonen, C. A., and Shelef, M., 1994 "Hydrogen as an Alternative Automotive Fuel," SAE Paper No. 940766.
[7] Shioji, M., Houki, Y., and Ishiyama, T., 2000, "Feasibility of the High-Speed Hydrogen Engine," *Hydrogen Engine Progress XIII*, 1, pp. 641–647.
[8] Tang, X. et al., 2002, "Ford P2000 Hydrogen Engine Dynamometer Development," SAE Paper No. 2002-01-0242.
[9] Natkin, R. J. et al., 2003, "Hydrogen IC Engine Boosting Performance and NO_x Study," SAE Paper No. 2003-01-0631.
[10] Lee, S. T., Yi, H. S., and Kim, E. S., 1995, "Combustion Characteristics of Intake Port Injection Type Hydrogen Fueled Engine," Int. J. Hydrogen Energy, **20**(4), pp. 317–322.
[11] Kondo, T. et al., 1996, "A Study on the Mechanism of Backfire in External Mixture Formation Hydrogen Engines," *Proceedings of the 11th World Hydrogen Energy Conference*, Vol. 2, pp. 1547–1556.
[12] Sierens, R. et al., 1998, "Backfire Mechanism in a Carbureted Hydrogen Fuelled Engine," *Proceedings of the 12th World Hydrogen Energy Conference*, Vol. 2, pp. 1537–1546.
[13] Shioji, M. et al., 2004 "Knock Characteristics and Performance in an SI Engine With Hydrogen and Natural-Gas Blended Fuels," SAE Paper No. 2004-01-1929, SAE Int. F & L, pp. 1–8.
[14] Shioji, M., and Inoue, N., 1998, "Performance and NO_x Formation in a Hydrogen Premixed-Charge Engine," *Proceedings of the 12th World Hydrogen Energy Conference*, Vol. 2, pp. 1469–1478.
[15] Rottengruber, H. et al., 2004, "A High-Efficient Combustion Concept for Direct Injection Hydrogen Internal Combustion Engines," *Proceedings of the 15th World Hydrogen Energy Conference*, 28J-01, pp. 1–13.
[16] Kim, Y. Y. et al., 2005, "An Investigation on the Causes of Cycle Variation in Direct Injection Hydrogen Fueled Engines," Int. J. Hydrogen Energy **30**(1), pp. 69–76.
[17] Shioji, M., Mohammadi, A., and Nakai, Y., 2005, "Performance and Combustion Characteristics of a Direct Injection SI Hydrogen Engine," *Proceedings of 18th Internal Combustion Engine Symposium*, Korea.
[18] Toda, T. et al., 2002, "Development of a 1.7 Liter CNG Engine for the 2001 Honda Civic CX," *Proceedings of NGV2002*.
[19] Suematsu, T., 1999, "Toyota 5S-FNE Engine for Natural Gas," Engine Technology, **1**(3), pp. 99.44–99.49.
[20] Nylund, I., 2004, "Status and Potentials of the Gas Engines," *Proceedings of International Congress CIMAC2004*, Paper No. 163.
[21] Tsunoda, A. et al., 2004, "Further Development of Advanced Gas Engine KU30GA (MACH-30G)," *Proceedings of International Congress CIMAC2004*, Paper No. 120.
[22] Okada, M. et al., 2004, "Development of CNG Direct Injection Diesel-Cycle Engine," NGV2004 Buenos Aires Conference.
[23] Honjo, F. et al., 2002, "Development of Stratified Charged Combustion CNG Engine," NGV2002.
[24] Glassman, I., 1996, *Combustion*, 3rd ed., Academic, San Diego, CA.
[25] Kidoguchi, Y., Ikeda, D., Miwa, K., and Mohammadi, A., 2005, "Control of Rapid Combustion of Hydrogen Jet Ignited by Spark Plug," JSME Int. J., Ser. B **70–299**, pp. 2922–2927.
[26] Kitakawa, T. et al., 2005, "Flame Inertia Into Lean Region in Stratified Hydrogen Mixture," Int. J. Hydrogen Energy, **30**, pp. 1457–1464.

Nonlinear Versus Linear Stress-Strain Relations in Engine Turbulence Modeling Under Swirl and Squish Flow Conditions

Mirko Baratta

Andrea E. Catania

Stefano d'Ambrosio

IC Engines Advanced Laboratory,
Politecnico di Torino, c.so Duca degli Abruzzi,
24-10129 Torino, Italy

*A general form of the stress-strain constitutive relation was introduced for the application of two nonlinear k-ε turbulence models, namely, the algebraic Reynolds stress model of Gatski and Speziale (1993, "On Explicit Algebraic Stress Models for Complex Turbulent Flows," J. Fluid Mech., **254**, pp. 59–78) and the cubic model of Lien et al. (1996, "Low Reynolds Number Eddy-Viscosity Modeling Based on Non-Linear Stress-Strain/Vorticity Relations," Proceedings of Third Symposium on Engineering Turbulence Modeling and Measurements, Crete, Greece), to the numerical analysis of flow fields in a test engine with flat-piston and bowl-in-piston arrangements, under swirling and no-swirling flow motored conditions. The model capabilities in capturing turbulent flow features were compared to those of the upgraded linear RNG k-ε model, which was previously indicated as a good compromise between accuracy and computational cost. Evaluations were made on the basis of the predicted flow evolution throughout the whole engine cycle, as well as of the comparison between the numerical and experimental results. Furthermore, the effect of the stress-strain relationship on the predicted averaged turbulence quantities and anisotropy-invariant values were examined, in addition to the sensitivity of the nonlinear models to the mesh quality. Finally, prospects concerning possible improvements of turbulence eddy-viscosity models were presented. The predictions were made by a newly developed CFD code embedding various accuracy-order finite-volume discretization schemes. Modified wall boundary conditions with respect to the conventional logarithmic-function approach were used, so as to make the local equilibrium hypothesis virtually ineffective.* [DOI: 10.1115/1.2938274]

Keywords: turbulence modeling, in-cylinder flow numerical simulation, stress-strain relation, anisotropy

Introduction

The rapid development of CFD codes, allowing researchers to numerically simulate fluid flows in almost arbitrarily complex geometries and conditions, has increased the demand of physical accuracy in the characterization of turbulent phenomena.

With specific reference to internal combustion engines (ICEs), it is important to properly account for the various physical aspects concerning in-cylinder flow fields, in order to better predict air-fuel mixing and reaction processes, so as to carry out a more efficient engine combustion-system design. Because of the wide dynamic range of scales of motion at characteristic Reynolds numbers of in-cylinder flows, direct numerical simulation (DNS) by the Navier–Stokes equations is not proposable for the current generation of computer, especially in the presence of turbulent reacting flows. Therefore, turbulence modeling of some nature remains an essential element of multidimensional computations of ICE flows. A survey of the various turbulence-model groups that have long and more recently been applied to engine flows can be found in Refs. [1–3].

The most widely used approach in turbulent flow modeling involves the Reynolds averaged Navier–Stokes (RANS) equations and two-equation linear turbulence models, i.e., simply eddy-viscosity models (EVMs). These models imply that the principal axes of the stress tensor are coincident with those of the strain rate tensor. Thus, linear models offer a good compromise between accuracy and computational effort when applied to relatively simple flows, but can present limitations in complex flows, such as those occurring in ICE combustion chambers, when stress and strain tensors evolve at different rates and cannot be parallel.

One approach to achieve a more appropriate description of the Reynolds stress tensor, without introducing any additional differential equations or correction terms, is to assume that the Boussinesq approximation is simply the first-order term in a series expansion of functionals leading to nonlinear EVM. These models are supposed to capture flow features, such as streamline curvatures, stress anisotropy, and body force effects, better than linear models do, although such a capability needs to be further assessed in nonstationary flows. However, an apparent merit of nonlinear EVM in comparison to linear ones is their ability to reproduce some kind of secondary motion in noncircular ducts and corners, as is underlined in Ref. [4]. Such a merit is mainly due to a more accurate prediction for the normal Reynolds stresses, with respect to linear models [5]. Recent examples of application of nonlinear EVM to the flow simulation in IC engines can be found in Refs. [3,6,7].

The explicit version of algebraic Reynolds stress (ARS) models has the same framework of nonlinear EVM, but it is characterized by strain-dependent coefficients [8–10]. Furthermore, unlike classical nonlinear EVM, these models are not derived from an em-

Contributed by the Internal Combustion Division of ASME for publication in the JOURNAL OF ENGINEERING FOR GAS TURBINES AND POWER. Manuscript received July 28, 2006; final manuscript received March 12, 2008; published online August 21, 2008. Review conducted by Margaret Wooldridge. Paper presented at the ASME Internal Combustion Engine Division 2004 Fall Technical Conference (ICEF2004) Long Beach, CA, October 24–27, 2004.

Table 1 Additional tensor τ_{ij}^* for the various models

	C_μ	τ_{ij}^*
Linear RNG model [1]	0.09	0
Cubic model [14]	$\frac{0.667}{1.25+\sqrt{2}\eta+0.9\sqrt{2}\xi}$	$-4B_1\rho C_\mu\frac{k^3}{\varepsilon^2}\left(S_{ik}S_{kj}-\frac{1}{3}S_{kl}S_{kl}\delta_{ij}\right)-4B_2\rho C_\mu\frac{k^3}{\varepsilon^2}(\Omega_{ik}S_{kj}+\Omega_{jk}S_{ki})$ $-4B_3\rho C_\mu\frac{k^3}{\varepsilon^2}\left(\Omega_{ik}\Omega_{jk}-\frac{1}{3}\Omega_{kl}\Omega_{kl}\delta_{ij}\right)-8B_4\rho C_\mu\frac{k^4}{\varepsilon^3}(S_{ki}\Omega_{lj}$ $+S_{kj}\Omega_{li})S_{kl}-8B_5\rho C_\mu\frac{k^4}{\varepsilon^3}(S_{kl}S_{kl}-\Omega_{kl}\Omega_{kl})S_{ij}$
ARS model [8,9]	$-\frac{1}{2}f_1\alpha_1$	$-f_2\rho\frac{k^3}{\varepsilon^2}\alpha_2(S_{ik}\Omega_{kj}+S_{jk}\Omega_{ki})+f_3\rho\frac{k^3}{\varepsilon^2}\alpha_3\left(S_{ik}S_{kj}-\frac{1}{3}S_{kl}S_{kl}\delta_{ij}\right)$

pirical generalization of the Boussinesq stress-strain relationship but from the differential transport equations of the Reynolds stress components [8].

Another turbulence modeling approach, that is, large eddy simulation (LES), requiring subgrid scale modeling (SSM), has recently been applied for turbulence prediction in engine combustion-chamber flows [11–13]. Such an approach is said to be more accurate than the RANS equation one [12]. However, it still requires some approximation in the near-wall region [3], and is currently faced with some issues regarding SSM closure [3,12]. Besides, LES should be applied to very fine grids, so that the resultant computational effort would be very high, particularly for engine flow application. LES has been compared to the RNG k-ε model in the simulation of different sized diesel engines [13], showing the capability of giving a more structured flow field, despite the limitations of the currently available version, which is intended for incompressible and isothermal flows. For this application, LES provided virtually the same degree of accuracy in the cylinder pressure prediction, but gave rise to some problems in a reliable maximum temperature evaluation, with respect to the RNG k-ε model.

In the present work, the explicit version [9] of the ARS model [8] and the cubic EVM [14] were applied to the charge-flow simulation in a test engine with either a flat piston or an axisymmetric bowl-in-piston combustion chamber, for both swirl and no-swirl motored operating conditions. The numerical results were analyzed by their comparison to experimental data [15] and to predictions made by using the RNG k-ε model with a modified approach to the wall-function conditions [1,16]. The influence of the stress-strain constitutive relation on predictions of the averaged turbulence variables and anisotropy-invariant values was also investigated. Furthermore, the sensitivity of nonlinear models to the mesh quality was examined.

The calculations were carried out by means of a previously developed homemade CFD code using finite-volume implicit schemes of various orders and solving the discretized form of the conservation laws by means of an iterative procedure [1] based on a modified version of the SIMPLER algorithm [17].

Flow Model and Numerical Method

Generalized Stress-Strain Relation. The noncommercial CFD code NUMAC-T [1] was applied for calculations. It is based on the RANS equations of a compressible flow, which are written in terms of mass-weighted ensemble-averaged velocities.

The RANS form of the momentum conservation equation, in Cartesian tensor notation, writes as follows:

$$\frac{\partial(\rho U_i)}{\partial t}+\frac{\partial}{\partial x_j}(\rho U_jU_i)=-\frac{\partial}{\partial x_i}\left(p+\frac{2}{3}\mu D\right)+\frac{\partial}{\partial x_j}(2\mu S_{ij})+\frac{\partial\tau_{ij}}{\partial x_j} \tag{1}$$

The mean-motion and fluctuating-component interaction is accounted for through the Reynolds stress tensor τ_{ij}. In the linear EVM approach, the Reynolds stresses are modeled by means of the Boussinesq approximation, that is,

$$\tau_{ij}=2\mu_T\left(S_{ij}-\frac{1}{3}S_{ll}\delta_{ij}\right)-\frac{2}{3}\rho k\delta_{ij} \tag{2}$$

where

$$S_{ij}=\frac{1}{2}\left(\frac{\partial U_i}{\partial x_j}+\frac{\partial U_j}{\partial x_i}\right) \tag{3}$$

Consistent with the modeling strategy of the linear k-ε model, the turbulent viscosity in Eq. (2) is defined as

$$\mu_T=C_\mu\rho\frac{k^2}{\varepsilon} \tag{4}$$

In this paper, a generalized form of the stress-strain relation is proposed and applied. This is obtained by observing that all two-equation models present a leading first-order term, which is similar to the right side of Eq. (2). In particular, in the linear term of all the models, there is a scalar quantity having viscosity dimensions. Therefore, from an operating point of view, one can assign the same role of the turbulent viscosity to such a scalar quantity [18]. Consistently with this idea, Eq. (2) can be put into the following general form:

$$\tau_{ij}=2\mu_T\left(S_{ij}-\frac{1}{3}S_{ll}\delta_{ij}\right)-\frac{2}{3}\rho k\delta_{ij}+\tau_{ij}^* \tag{5}$$

in which τ_{ij}^* includes the nonlinear terms of the constitutive relation. Equation (5) is an effective formulation to implement different modeling approaches into the same code. The expressions of τ_{ij}^* for the considered turbulence models, along with those of C_μ (Eq. (4)), are given in Table 1.

The introduction of Eq. (5) into Eq. (1) leads to

$$\frac{\partial(\rho U_i)}{\partial t}+\frac{\partial}{\partial x_j}(\rho U_jU_i)=-\frac{\partial}{\partial x_i}\left(p+\frac{2}{3}\rho k\right)+\frac{\partial}{\partial x_j}[2(\mu+\mu_T)S_{ij}]+\frac{2}{3}\frac{\partial}{\partial x_i}[(\mu+\mu_T)D]+\frac{\partial\tau_{ij}^*}{\partial x_j} \tag{6}$$

Equation (6) shows that the generalized form of the turbulent stress tensor, Eq. (5), yields an increase in the effective pressure and viscosity values, due to the turbulence terms. It is worth pointing out that, for a nonlinear constitutive relation, the "turbulent viscosity" locution for μ_T is not appropriate. The novelty in Eq. (6) is given by the gradient of the tensor τ_{ij}^*. It should also be noted that, if the generalization of the Boussinesq relation by a

series expansion of functionals is removed, so that the whole turbulent stress is embedded in τ_{ij}^*, Eq. (5) reduces to $\tau_{ij}=\tau_{ij}^*$ and the general form of the momentum balance, Eq. (6), with k and μ_T set to zero, can be coupled to a Reynolds stress model (RSM) of turbulence.

Governing Equations. The complete set of flow-model equations is made up of Eq. (6) and the following:

(a) continuity equation,

$$\frac{\partial \rho}{\partial t} + \frac{\partial}{\partial x_j}(\rho U_j) = 0 \tag{7}$$

(b) energy equation,

$$\frac{\partial(\rho h)}{\partial t} + \frac{\partial}{\partial x_j}(\rho U_j h) = \frac{\partial p}{\partial t} + \frac{\partial}{\partial x_j}\left[\left(\mu + \frac{\mu_T}{\sigma_h}\right)\frac{\partial h}{\partial x_j}\right] \tag{8}$$

(c) turbulent kinetic energy equation,

$$\frac{\partial(\rho k)}{\partial t} + \frac{\partial}{\partial x_j}(\rho U_j k) = \frac{\partial}{\partial x_j}\left[\left(\mu + \frac{\mu_T}{\sigma_k}\right)\frac{\partial k}{\partial x_j}\right] + 2\mu_T S_{ij} S_{ij} - \frac{2}{3}(\mu_T D^2 + \rho k D) + \tau_{ij}^* \frac{\partial U_i}{\partial x_j} - \rho\varepsilon \tag{9}$$

(d) turbulent dissipation rate equation,

$$\frac{\partial(\rho\varepsilon)}{\partial t} + \frac{\partial}{\partial x_j}(\rho U_j \varepsilon) = \frac{\partial}{\partial x_j}\left[\left(\mu + \frac{\mu_T}{\sigma_\varepsilon}\right)\frac{\partial \varepsilon}{\partial x_j}\right] + C_1 \frac{\varepsilon}{k}\left[2\mu_T S_{ij} S_{ij} - \frac{2}{3}(\mu_T D^2 + \rho k D) + \tau_{ij}^* \frac{\partial U_i}{\partial x_j}\right] - C_2 \rho \frac{\varepsilon^2}{k} + C_3 \rho \varepsilon D - C_4 R \tag{10}$$

Solution Algorithm. A complete description of the solution method used to carry out the numerical simulations in the present paper is given in Ref. [1]. The integral counterpart of the conservation laws (6)–(10) is discretized with reference to a staggered grid and the resultant nonlinear algebraic equation system is solved by means of an iterative procedure, in which pressure-velocity decoupling is carried out, based on a modified version of the SIMPLER algorithm [1,17,18]. This latter was modified so as to take fluid compressibility into account and to make the convergence criterion application more efficient.

Turbulence Models

Linear RNG k-ε Model. The RNG-based k-ε model is set within the same framework as the traditional two-equation models, but uses renormalization group methods. The stress-strain relation is the Boussinesq one and the anisotropy effects on the turbulence behavior are accounted for by the function R:

$$R = \rho C_\mu \frac{\eta^3\left(1 - \frac{\eta}{\eta_0}\right)}{1 + \beta\eta^3}\frac{\varepsilon^2}{k} \tag{11}$$

The RNG model details and the related reference papers are reported in Ref. [1], along with the upgraded boundary conditions that were also applied to the nonlinear models, instead of the so-called "wall function," for the present study. The following constant values were introduced in the RNG model: $C_1=1.42$; $C_2=1.75$; $C_3=-0.373$; $C_4=1.0$; $\sigma_k=1.0$; $\sigma_\varepsilon=1.22$; $\beta=0.012$; $\eta_0=4.38$.

Cubic k-ε Model. The cubic version of Lien et al. [14] was considered. Craft et al. [19] pointed out that with a quadratic constitutive relation only a slightly greater generality is achievable than that given by linear EVMs. In particular, the various effects of streamline curvature on the turbulent stresses cannot be adequately modeled at this level. As a consequence, efforts had to be focused on providing a suitable cubic stress-strain relation. Retaining terms up to the cubic level, an expression satisfying the required symmetry and contraction properties can be written as follows [14]:

$$\tau_{ij} = -\frac{2}{3}(\rho k + \mu_T D)\delta_{ij} + 2\mu_T S_{ij} - 4B_1\rho C_\mu \frac{k^3}{\varepsilon^2}\left(S_{ik}S_{kj} - \frac{1}{3}S_{kl}S_{kl}\delta_{ij}\right) - 4B_2\rho C_\mu \frac{k^3}{\varepsilon^2}(\Omega_{ik}S_{kj} + \Omega_{jk}S_{ki}) - 4B_3\rho C_\mu \frac{k^3}{\varepsilon^2}\left(\Omega_{ik}\Omega_{jk} - \frac{1}{3}\Omega_{kl}\Omega_{kl}\delta_{ij}\right) - 8B_4\rho C_\mu \frac{k^4}{\varepsilon^3}(S_{ki}\Omega_{lj} + S_{kj}\Omega_{li})S_{kl} - 8B_5\rho C_\mu \frac{k^4}{\varepsilon^3}(S_{kl}S_{kl} - \Omega_{kl}\Omega_{kl})S_{ij} \tag{12}$$

where

$$\Omega_{ij} = \frac{1}{2}\left(\frac{\partial U_i}{\partial x_j} - \frac{\partial U_j}{\partial x_i}\right) \tag{13}$$

$B_1, B_2, \ldots, B_5$ are stress-dependent closure coefficients that are given in Table 2. As is done, for example, in Ref. [20], Eq. (12) can be considered as an extension of the correspondent quadratic model [21]. Equation (12) is used to compute the turbulent Reynolds stresses. The model closure was completed by Eqs. (9) and (10) with the following constant values: $C_1=1.44$; $C_2=1.92$; $C_3=-0.373$; $C_4=0.0$; $\sigma_k=1.0$; $\sigma_\varepsilon=1.22$.

Table 2 Coefficients for the cubic model

B_1	B_2	B_3	B_4	B_5
$\frac{0.75}{(1000+2\sqrt{2}\eta^3)C_\mu}$	$\frac{3.75}{(1000+2\sqrt{2}\eta^3)C_\mu}$	$\frac{4.75}{(1000+2\sqrt{2}\eta^3)C_\mu}$	$-10C_\mu^2$	$-2C_\mu^2$

Algebraic Reynolds Stress Model. ARS models were derived from second-order closures, by means of an equilibrium hypothesis, in which the Reynolds stress convection, diffusion, and unsteady terms were approximately given by

$$\frac{D\tau_{ij}}{Dt} - \frac{\partial}{\partial x_k}\left[\nu\frac{\partial \tau_{ij}}{\partial x_k} + C_{ijk}\right] \approx \frac{\tau_{ij}}{k}\left\{\frac{Dk}{Dt} - \frac{\partial}{\partial x_k}\left[\nu\frac{\partial k}{\partial x_k} - \frac{C_{jik}}{2\rho}\right]\right\} \tag{14}$$

where C_{ijk} represents the Reynolds-stress turbulent transport, as is defined in Ref. [22].

The introduction of Eq. (14) into the transport equation of the Reynolds stress τ_{ij} yields the following equilibrium form of this equation:

$$(P_k - \rho\varepsilon)\frac{\tau_{ij}}{\rho k} = -\tau_{ik}\frac{\partial U_j}{\partial x_k} - \tau_{jk}\frac{\partial U_i}{\partial x_k} + \varepsilon_{ij} - \Pi_{ij} \tag{15}$$

The Reynolds stresses are thus implicitly related to the mean velocity gradients. Based on a higher-order closure, such a link provided the first formal justification of the Boussinesq hypothesis extension, for incorporating nonlinearities into mean velocity gradients [22]. Equation (15) turns to an implicit version of ARS model if the tensors $\boldsymbol{\varepsilon}_{ij}$ and $\boldsymbol{\Pi}_{ij}$ are modeled in an appropriate way [4]. However, this type of model is cumbersome to implement in complex flows, because the stress-strain relation is not explicit. Numerical stiffness problems can arise from the need for successive matrix inversions at each iteration [8].

Table 3 Coefficients for the explicit ARS model

f_1	$\dfrac{(1+2\xi_C^2)(1+6\eta_C^5)+\frac{5}{3}\eta_C^2}{(1+2\xi_C^2)(1+2\xi_C^2+\eta_C^2+42\eta_C^6)}$	ξ_C	$\frac{1}{2}g\frac{k}{\varepsilon}(2-A_4)\sqrt{\Omega_{ij}\Omega_{ij}}$
f_2	$\dfrac{(1+2\xi_C^2)(1+\eta_C^4)+\frac{2}{3}\eta_C^2}{(1+2\xi_C^2)(1+2\xi_C^2+6.3\eta_C^6)}$	η_C	$\frac{1}{2}g\frac{k}{\varepsilon}(2-A_3)\sqrt{S_{ij}S_{ij}}$
f_3	$\dfrac{(1+2\xi_C^2)(1+\eta_C^4)+\frac{2}{3}\eta_C^2}{(1+2\xi_C^2)(1+2\xi_C^2+4\eta_C^6)}$	g	0.214
α_1	$g(A_2-4/3)$	A_2	0.36
α_2	$1/2g^2(A_2-4/3)(2-A_4)$	A_3	1.25
α_3	$g^2(A_2-4/3)(2-A_3)$	A_4	0.40

In Ref. [8], an explicit ARS model is developed by generalizing an innovative procedure due to Pope [23], on the grounds of an integrity-basis analysis for functions of symmetric and antisymmetric tensors. The explicit solution for τ_{ij} expressed by this model formally constitutes an anisotropic EVM with strain-dependent coefficients. The algebraic relation between stress and strain was subsequently reguralized in order to make the model well behaved in far-from-equilibrium flows [9]. Further model improvement was achieved by a modification based on the comparison between the actual and the desired model behavior in an homogeneous shear flow, within the rapid distortion theory (RDT) limit [9,10].

The definitive constitutive relation of the ARS model of Gatski and Speziale can thus be written in the following way:

$$\tau_{ij} = -\frac{2}{3}\rho k\delta_{ij} - f_1\alpha_1\rho\frac{k^2}{\varepsilon}\left(S_{ij}-\frac{1}{3}S_{ll}\delta_{ij}\right) - f_2\rho\frac{k^3}{\varepsilon^2}\alpha_2(S_{ik}\Omega_{kj}+S_{jk}\Omega_{ki}) + f_3\rho\frac{k^3}{\varepsilon^2}\alpha_3\left(S_{ik}S_{kj}-\frac{1}{3}S_{kl}S_{kl}\delta_{ij}\right) \quad (16)$$

All the closure constants and functions that define this ARS model can be found in Table 3. Conservation equations of the turbulent quantities and the associated closure coefficients used in this work were the same as those applied for the cubic model.

Test Engine

The model engine with its central valve and bowl-in-piston arrangement is schematically shown in Fig. 1. In Ref. [15], a detailed experimental analysis of the flow in such an engine is reported. It was carried out by means of laser doppler velocimetry (LDV) under motored conditions at the crankshaft engine speed of 200 rpm. The results in Ref. [15] were used for assessment of the nonlinear constitutive relations presented in the previous section and for comparison to the results of the linear RNG model.

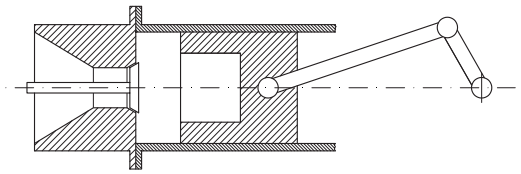

Fig. 1

Test engine Characteristics	Cylinder bore:	75.4 mm
	Stroke:	94 mm
	Bumping clearance:	0.6 mm (bowl-in-piston) 16.49 mm (flat piston)
	Bowl diameter:	23.5 mm
	Bowl depth:	41 mm
	Compression ratio:	6.7
	Valve diameter:	34 mm
	Maximum valve lift:	8 mm
	Valve seat angle:	60 deg

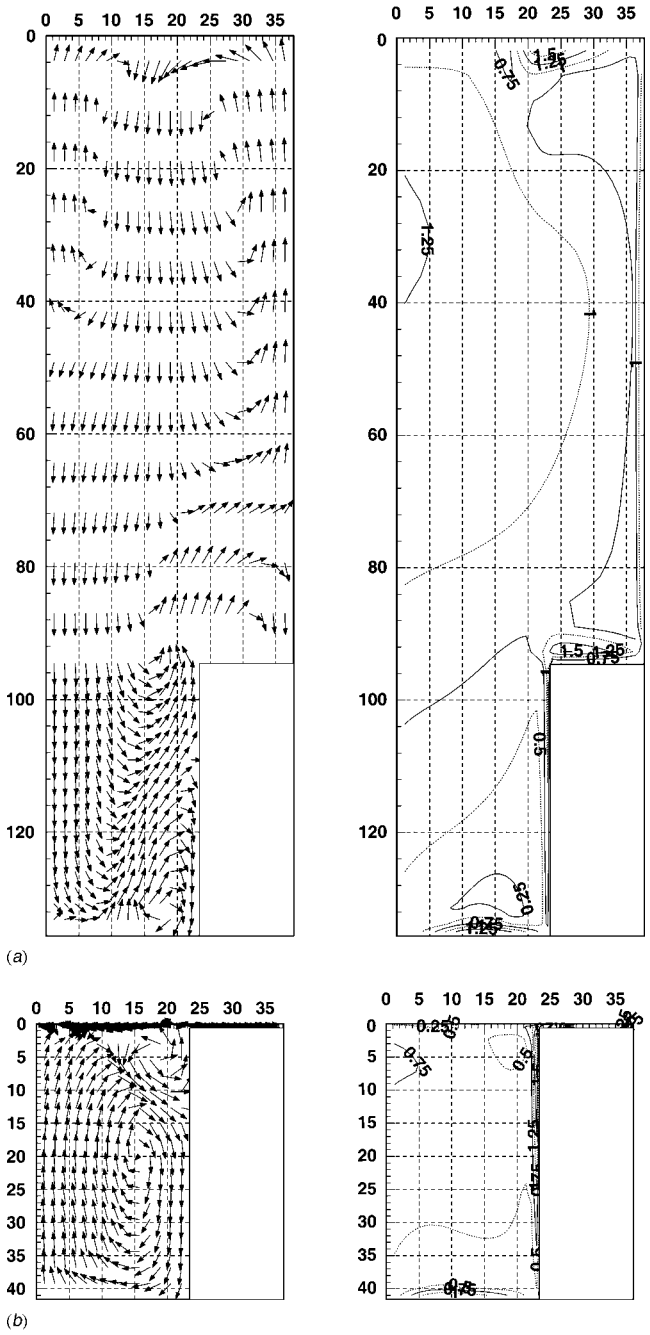

Fig. 2 Velocity fields (left side) and TI distributions (right side) for the RNG k-ε model—bowl-in-piston—swirl: (*a*) θ=180 deg; (*b*) θ=360 deg

Stress-Strain Relation Assessment

Flow Evolution Throughout the Engine Cycle. The flow evolution during the engine cycle will be described with reference to the bowl-in-piston configuration in the presence of swirl. In-cylinder velocity fields and adimensional turbulence intensity (TI)

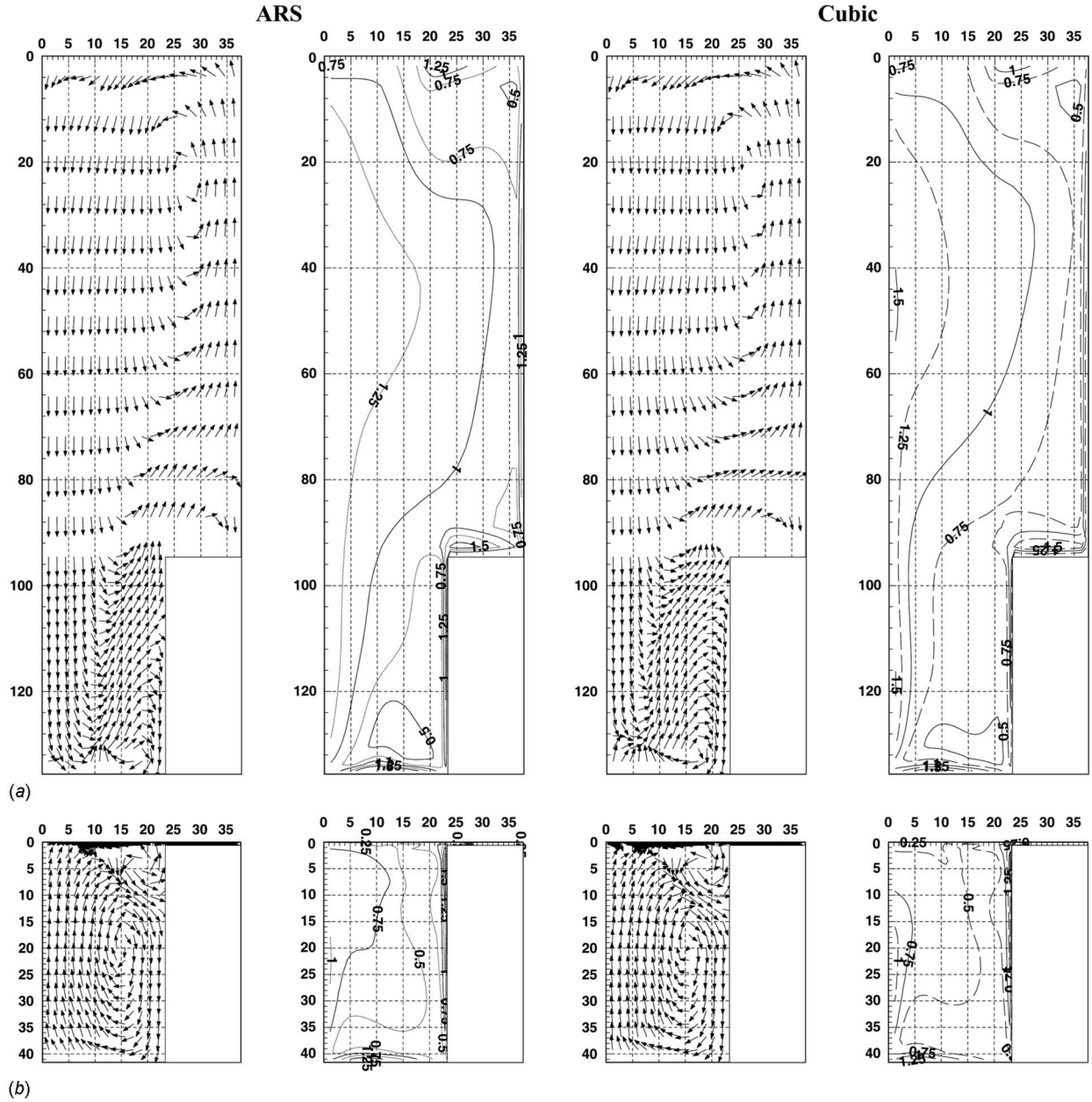

Fig. 3 Velocity fields and TI distributions for nonlinear two-equation models—bowl-in-piston—swirl: (*a*) θ=180 deg; (*b*) θ =360 deg

distributions, obtained with the linear RNG k-ε model, at the end of induction (θ=180 deg) and of the compression (θ=360 deg) strokes are shown in a longitudinal plane in Fig. 2. By comparing the results in Fig. 2(*a*) to those presented in Ref. [1] under the no-swirl conditions, it can be concluded that even during the induction stroke there is a significant effect of the swirl on the overall streamline configuration, particularly within the bowl. Figure 3 shows the velocity and TI distributions in the longitudinal plane obtained with the ARS and cubic models. From Fig. 3(*a*), it can be inferred that at the end of the induction stroke there is a dominant anticlockwise vortex, which is located out of the bowl and presents approximately the same size for both nonlinear models. The relative size of the clockwise vortex with respect to the anticlockwise one is different when either linear or nonlinear models are considered (compare Figs. 2(*a*) and 3(*a*)). With reference to the TI results, Fig. 4 shows the comparison between the evolutions of the mass-averaged TI and of its dissipation rate for "bowl-in-piston—swirl" (Fig. 4(*a*)) and "flat-piston—no swirl" (Fig. 4(*b*)) configurations, during the last part of the compression stroke and the early expansion stroke. For the first of these configurations, although during induction the highest TI values were given by the RNG model, the ARS model gives rise to a higher turbulence than RNG and cubic models from about θ=170 deg onward (Fig. 4(*a*)). These two latter models give almost the same mass-averaged k value at BDC. However, the nonlinear models tend to predict a sensible growth in TI as the distance from axis reduces, as is shown by the isolines in Fig. 3(*a*). This tendency is more evident for the cubic model than for the ARS model. With reference to the flat-piston arrangement in the absence of swirl (Fig. 4(*b*)), the RNG model provides higher values of TI than nonlinear models, as was also found in Ref. [3].

During the compression stroke of the bowl-in-piston engine, the squish effect, which is shown in Figs. 2(*b*) and 3(*b*) at the compression end, is qualitatively well reproduced by both linear and

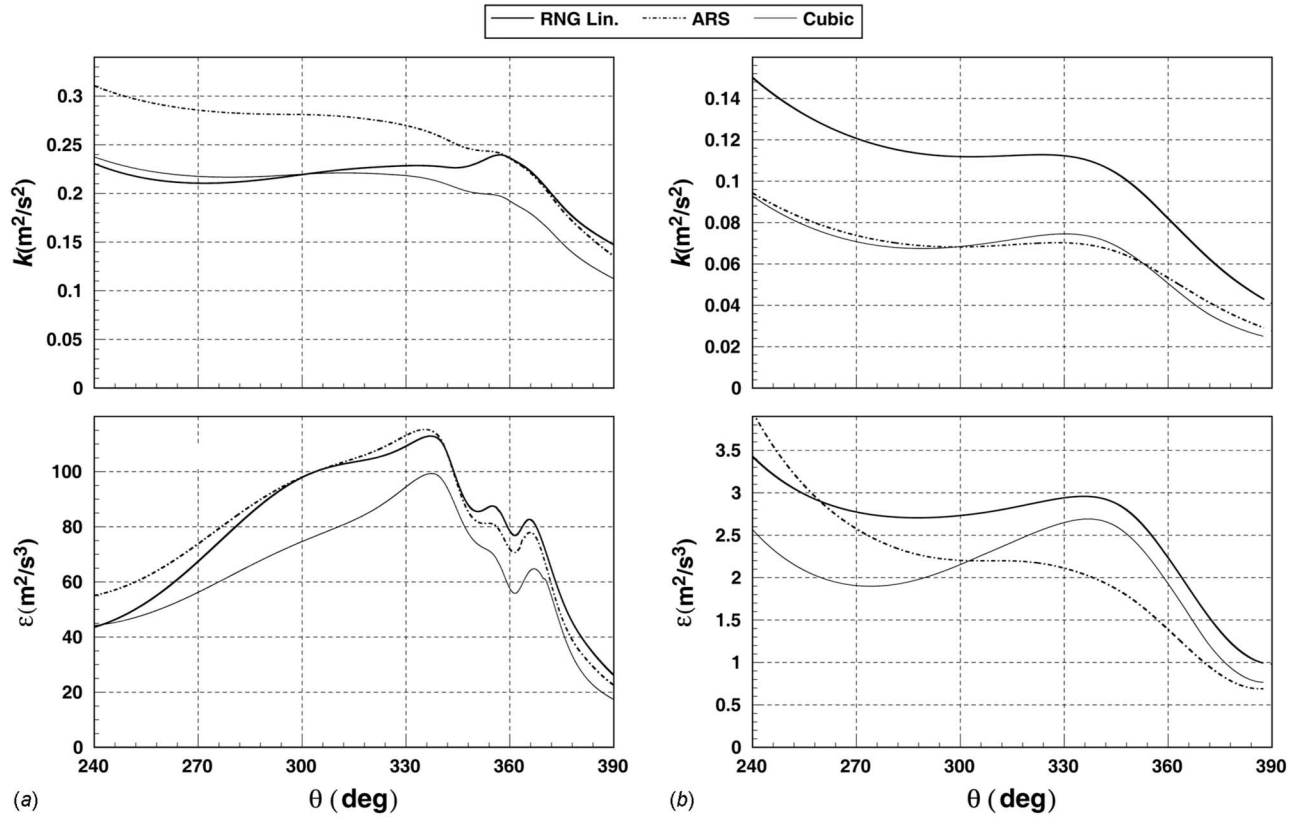

Fig. 4 Mass-averaged turbulence quantities: (*a*) bowl-in-piston—swirl; (*b*) flat-piston—no swirl

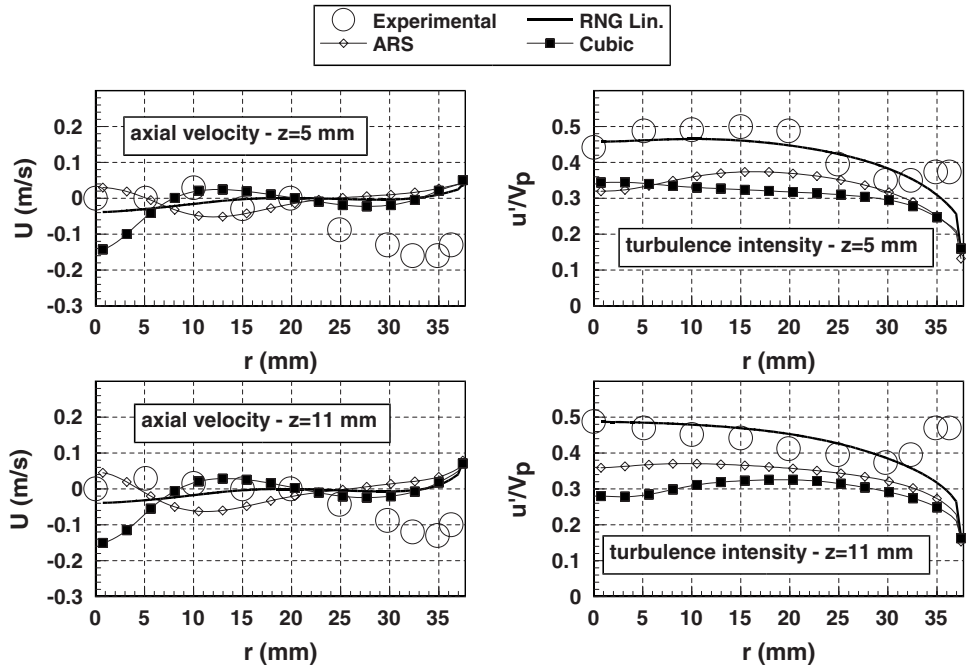

Fig. 5 Radial profiles of axial mean velocity and TI at compression TDC—flat-piston—no swirl

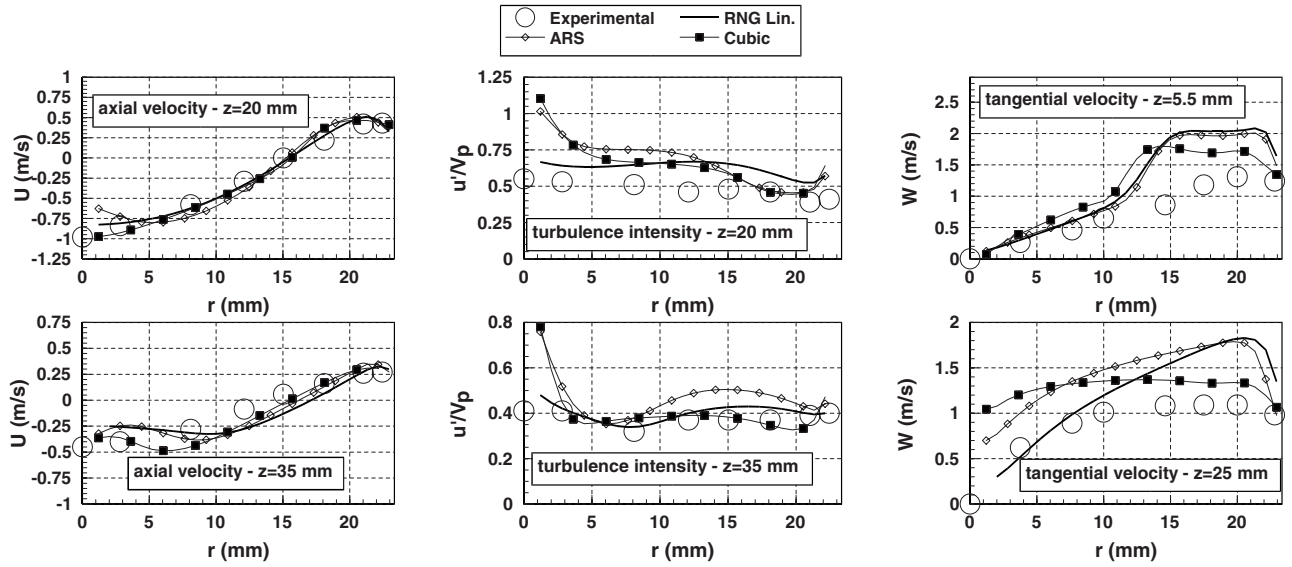

Fig. 6 Radial profiles of axial mean velocity and TI at compression TDC—bowl-in-piston—swirl

nonlinear stress-strain relations. All the models predict higher TI within the bowl, and the highest mass-averaged values are given by the ARS model (Fig. 4(*a*)). Furthermore, the RNG model shows a maximum of TI close to $\theta=360$ deg, while the ARS and the cubic models only predict an inflexion point there. This indicates a lower influence of piston-induced motions on the turbulence level. At compression TDC (Figs. 2(*b*) and 3(*b*)), the considered models predict similar flow field configurations, as a result of the interaction between swirl and squish flows [16,18]. Furthermore, the increasing rate of TI, obtained with the nonlinear models when the distance from the cylinder axis decreases, is higher at compression TDC than at the end of the induction stroke (Figs. 3(*a*) and 3(*b*)).

Comparison With Experimental Data. The comparison between numerical and experimental results at compression TDC is reported in Fig. 5, for the flat-piston case in the absence of swirl, and in Fig. 6, for the bowl-in-piston arrangement in the presence of swirl.

With reference to the flat-piston configuration results (Fig. 5), nonlinear constitutive relations produced more fluctuating radial distributions of axial velocity with respect to the RNG model, even though the numerical values are close to each other. As is pointed out in the previous section, ARS and cubic models predict lower turbulence intensities than the linear RNG model. It can be inferred from Fig. 5 that this difference does not improve the agreement with experimental data.

With reference to the bowl-in-piston—swirl configuration, the radial distributions reported in Fig. 6 show that the axial velocity is particularly well predicted by the RNG and cubic models at a distance from the cylinder head $z=20$ mm, whereas at $z=35$ mm, the behavior of the models is almost the same on an average. However, the nonlinear models show a worse agreement of the turbulence data with experiments, in comparison to the RNG model. Besides, the previously mentioned tendency of ARS and cubic models to predict higher values of TI close to the cylinder

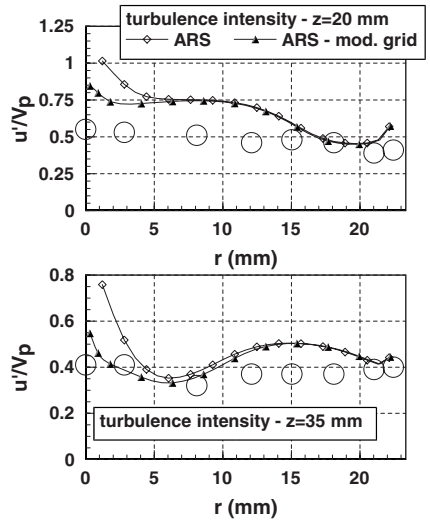

Fig. 7 Influence of the radial mesh distribution on results for the ARS model—bowl-in-piston—swirl

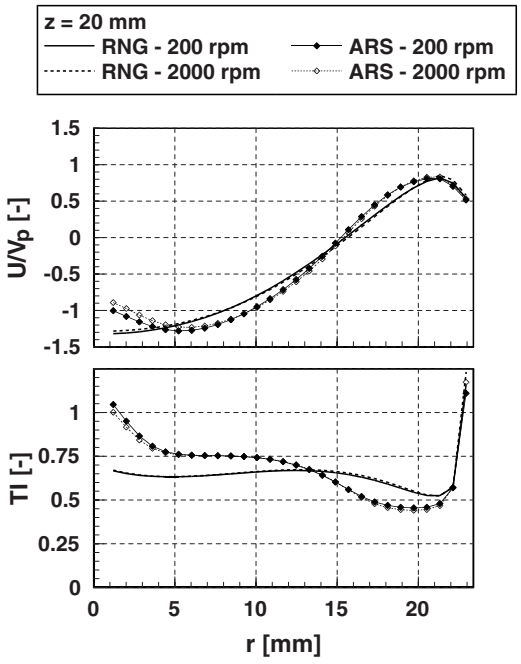

Fig. 8 Comparison between linear RNG and ARS models at different engine speeds, bowl-in-piston—swirl

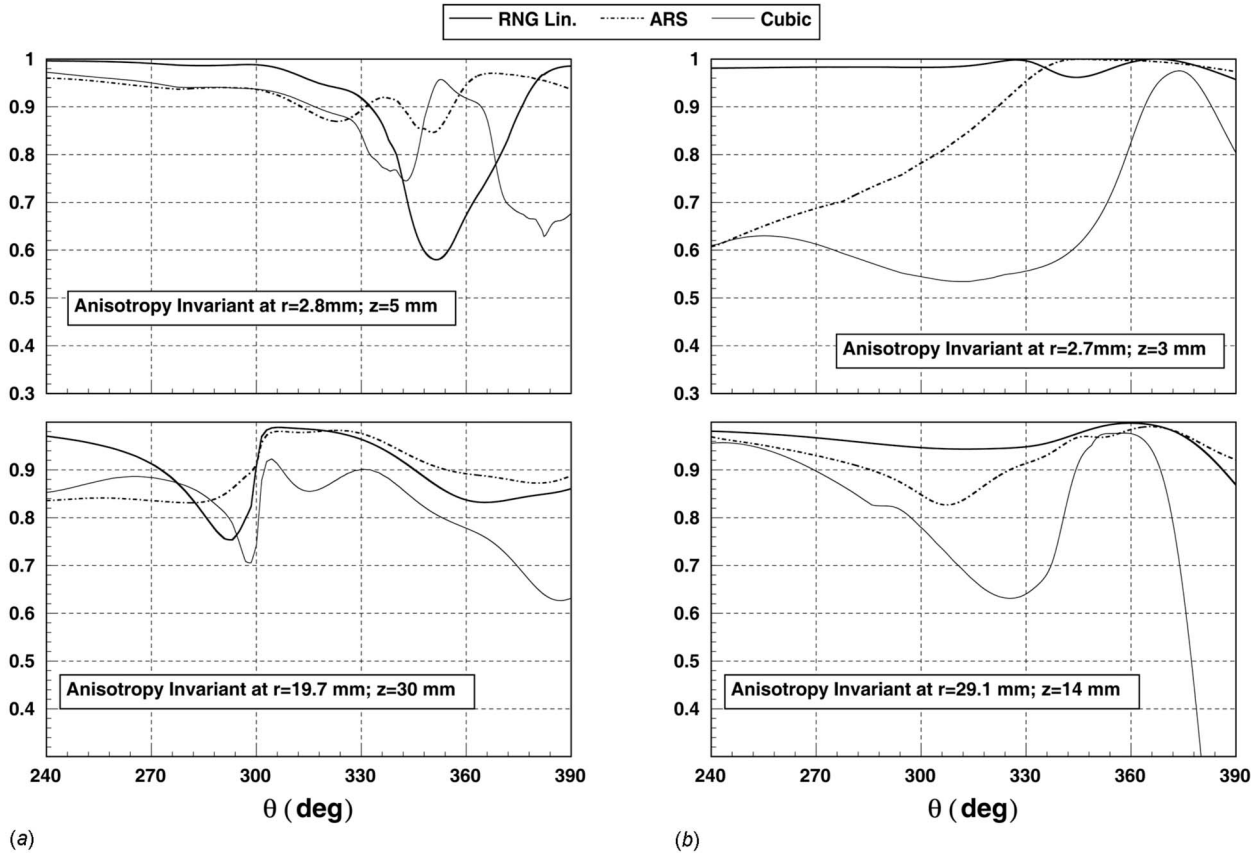

Fig. 9 Anisotropy-invariant evolution: (*a*) bowl-in-piston—swirl; (*b*) flat-piston—no swirl

axis is not supported by the experimental results and hence constitutes a weakness of nonlinear models in the turbulence prediction for bowl-in-piston engine configurations.

Figure 7 shows the dependence of the TI results on the mesh quality, for the ARS model. The base case, that corresponds to no additional indications in the legend, refers to a uniform radial grid size along the radial direction, whereas the curve labeled by "mod. grid" was obtained with a radial mesh, which was refined in the vicinity of the axis. While the radially uniform grid can be suitable when applied for a linear model, it gives rise to physically inconsistent numerical results when used for a nonlinear stress-strain relation. Nevertheless, a radial mesh refinement in the region close to cylinder axis can address this shortcoming. On the contrary, the overprediction between the radial coordinates of 10 mm and 15 mm in Fig. 7 can be considered as independent of the mesh characteristics. With reference to the right column in Fig. 6, nonlinear models may yield a better agreement of the predicted swirl velocity component with the experimental values far from the cylinder axis and a more or less worse agreement close to the axis, with respect to the RNG model. After all, based on a global evaluation, the nonlinear models cannot be considered to be more satisfactory than the linear RNG model, at least for the considered in-cylinder experimental data.

Experimental data for the axisymmetric model engine under study were available only at the crankshaft engine speed of 200 rpm. Therefore, in order to give an insight into the model performance at engine-relevant speeds, numerical investigations were carried out at higher engine speeds, and the results were compared to those at 200 rpm. Figure 8 shows a comparison between the results of the linear RNG and ARS models at both 200 rpm and 2000 rpm. As can be seen, the behavior of such models is virtually independent of the engine speed. This result is in agreement with the common knowledge that for many engine configurations swirl and turbulence scale with the engine speed. In particular, it is in agreement with both numerical and experimental results previously obtained by the authors [16,24], consistent with a virtually negligible dependence of volumetric efficiency on engine speed. Hence, the relative merits of linear and nonlinear approaches will be almost the same at different engine crankshaft speeds.

Influence of Constitutive Relation on Results. The influence of the stress-strain relation on the mass-averaged turbulence energy and dissipation rate was analyzed in the "Flow Evolution Throughout the Engine Cycle" section. If the flat piston is considered (Fig. 4(*b*)), higher mean values of turbulence are obtained with a linear model than with higher order closures. From around 260 crank-angle degrees on, the linear model predicts also a higher mass-averaged turbulence dissipation rate. For the bowl-in-piston arrangement (Fig. 4(*a*)), the interaction between stress tensor and mean velocity field acts so as to modify the relative turbulence levels predicted by the nonlinear models with respect to the RNG one, so that the TI given by the ARS model becomes the highest one from about the end of induction to the end of compression. In addition, the extent of the predicted effects of the swirl amplification and squish formation on the mean turbulence level is different for the various models, as can be inferred from the k curves in Fig. 4(*a*).

The differences in model behavior can be ascribed to the distinct sets of values for the closure coefficients C_1, C_2, C_3, and C_4, and to the constitutive relation. In fact, this latter modifies the stress tensor corresponding to a given velocity field. Such a modified stress tensor will subsequently cause a different flow evolution. In order to gain insight into the stress-strain mutual dependence for each model, it is worth introducing the anisotropy invariant [25,26], which is given by

$$A = 1 - \frac{9}{8}(\mathrm{II}_a - \mathrm{III}_a) \tag{17}$$

It can be shown [26] that $A=0$ for two-component turbulence (i.e., a turbulent flow in which the rms value of one fluctuating velocity component is much smaller than the others) and $A=1$ for isotropic turbulence.

In Fig. 9, the evolution of the anisotropy invariant at two different locations of the computational domain is reported for both the bowl-in-piston—swirl and the flat-piston—no swirl cases. The differences in A values between different points are only marginally relevant, because these reflect dissimilarities in the flow field. On the contrary, the disparities in A among the results of various constitutive relations at the same location are significant, because these provide a dimensionless measure of the aforementioned differences in the stress-strain tensor relationship. As can be observed from Fig. 9, nonlinear models generally present lower values of the invariant A with respect to the RNG model, indicating a higher anisotropy level. Exceptions are present in some crank-angle intervals for the bowl-in-piston arrangement, because the positions of the anisotropy-invariant maxima and minima are different. Moreover, in most cases, the higher the order of the stress-strain relation is, the higher the predicted anisotropy is. The distinct model invariant evolutions can be ascribed to the various stress-strain relationships, reflecting in different flow evolutions during the compression stroke. The constitutive relation effect on the predicted anisotropy level is particularly significant in the flat-piston—no swirl configuration. In fact, while the anisotropy invariant provided by the linear RNG model keeps almost equal to 1, the ARS and the cubic models predict a strong anisotropy in the middle part of compression, due to the high piston velocity, and subsequently approach the values predicted by the linear model in the TDC neighborhood. Thus, in the flat-piston configuration and in the absence of swirl, a nonlinear constitutive relation behaves in a way that the calculated stress-tensor anisotropy is much higher than that resulting from the linear model application. On the other hand, the bowl-in-piston flow presents anisotropy features that can be captured even by a linear EVM.

The comparison between the values of A shown in Fig. 9(a) and those in Fig. 9(b) reveals that the anisotropy level predicted by a nonlinear EVM under the flat-piston—no swirl condition is even higher than that associated to the bowl-in-piston—swirl configuration. As a matter of fact, an axisymmetric swirling flow determines a decrease in the stress anisotropy, because some components of the stress tensor, such as τ_{12} and τ_{23}, which are zero in the absence of swirl, take nonzero values in the presence of swirl motion.

Directions for Model Improvement

The analysis of numerical and experimental results indicates that the choice and implementation of a nonlinear model does not improve the agreement of mean-flow and TI predictions with the experimental data, in comparison to the linear RNG model. The main reason for this resides in the fact that for ICE confined nonstationary flows, in which the scales of mean motion and turbulence overlap each other and rapid distortion can take place, the unsteadiness causes the adjustment of the various turbulence length scales to flow changes to occur at different rates. Therefore, on the one hand, nonlinear models allow a better prediction of the Reynolds stress-tensor components in various cases of practical interest, namely, flows in rectangular ducts or turbulent separated flows over backward-facing steps [4,5]. On the other hand, in Ref. [4] it is pointed out that, like their linear predecessors, also nonlinear models violate the principle of physical coherence, since they express turbulence properties (the Reynolds stresses) as being proportional to the mean-flow properties (the mean rate of strain) ([27]). In other words, from a theoretical point of view, both linear and nonlinear two-equation models are only valid for equilibrium flows, in which there is a separation of scales between turbulence and mean motion, and the turbulent components are able to immediately follow the changes in mean strain rate. This means that all length scales of turbulence adjust to mean-flow changes at the same rate, thus preserving the energy spectrum shape. Hence, the description of the turbulence wave-number spectrum with only one length scale and, similarly, of the turbulence frequency spectrum with only one time scale, constitutes a limit in both linear and nonlinear two-equation EVM [28].

Another consideration can be made, in order to better understand both the potentialities and the limits of nonlinear two-equation models. Due to the inclusion of higher-order terms in the series expansion defining the stress-strain relationship, nonlinear constitutive relations extend the range of applicability of two-equation approaches to flows with a moderate departure from equilibrium [4,5]. Thus, larger ratios between turbulent and mean-flow scales are allowed. In spite of this, in far-from-equilibrium flows, as those occurring in IC engines, such ratios are usually too high, giving rise to a poor accuracy of the series expansion up to second or third order. Furthermore, the separation of scales is postulated also in the formulation of turbulent-related quantity transport equations, namely, in the dissipation production modeling and in the diffusion term approximation by means of a gradient hypothesis [29]. This confirms that all two-equation models can hardly provide accurate predictions in far-from-equilibrium flows, because the dissipation production and diffusion terms are not correctly estimated and, hence, turbulence quantities are not accurately calculated.

In order to overcome such limitations, multiple time scale turbulence models were developed [30,31]. In Ref. [1], a two-scale linear k-ε model was applied to the same engine flow conditions as those of the present investigation, but in the absence of swirl. The turbulence spectrum was split in two parts and two independent length scales were introduced. Owing to the presence of four model equations instead of two, a larger computational effort was required and this was not supported by a significant improvement in results, particularly for the bowl-in-piston case. A higher number of scales can be chosen [30], with the addition of two equations for each scale and thus a rapidly increasing CPU. A nonlinear multiple-scale turbulence model may be a more effective refined approach but at a quite high computational cost.

In order to surmount the aforementioned shortcoming of both linear and nonlinear two-equation EVMs, a semiempirical approach was proposed in Refs. [32,33], based on a homogeneous, isotropic, pure shear-flow hypothesis [34] and on a correction of the turbulent characteristic combustion time, in order to match experimental cylinder pressure data. A relation was introduced between the dissipation rate functions under equilibrium and nonequilibrium conditions, respectively. Such a relation, with the conservation equations of turbulent kinetic energy production and dissipation rates, was asserted to simulate turbulence inertia. Alternatively, nonequilibrium ARS closures by means of a relaxation time approximation were proposed [9,10], based on the following relation for homogeneous turbulence:

$$\dot{a}_{ij} = -C_R \frac{\varepsilon}{k}(a_{ij} - a_{ij}^E) \tag{18}$$

where $\mathbf{a}_{ij}$ is the anisotropy tensor and $\mathbf{a}_{ij}^E$ corresponds to the stress tensor given by Eq. (16) and C_R is a strain-dependent closure coefficient.

Another aspect that affects the overall model performance is the capability of predicting anisotropy effects, for example, wall proximity and local strain-rate effects, paying attention not so much to the stress-strain relation as to the transport equation of the dissipation rate ε. With reference to the wall effects, it is sometimes proposed [19] to use the low-Re versions of the k-ε model, in which specific exponential damping functions are introduced and the equation of the so-called "isotropic dissipation rate" is solved [35]. However, low-Re k-ε model versions require very fine grids within the boundary layer, whose thickness is not a priori known

and is also variable, so that the moving mesh strategy becomes cumbersome for engine flow application (in addition, the boundary layer concept in the narrow clearance at TDC is open to question). Such a version is rarely applied to engine flows and in Ref. [36] it was taken to be advantageous when RSM are applied to enginelike flows. On the other hand, in Ref. [1] as well as in the present work, the high-Re logarithmic wall-function approach, which is widely used for engine flow simulation, was replaced by a novel approach in which the hypothesis of local equilibrium between turbulence production and dissipation in the logarithmic region was given a negligible weight.

Finally, the dissipation rate equation, partially including local strain-rate effects by means of the R function in the linear RNG model, can be combined with a nonlinear stress-strain constitutive relation, as is proposed in [37]. Even though this choice may look arbitrary, because the R function is derived from a series expansion in powers of S_{ij}, it should be pointed out that the anisotropy effects, which the R function includes in the ε balance, are virtually not correlated to those of the stress-strain constitutive relation. Therefore, both the R function and the nonlinear stress-strain relation can be embedded in the same model.

Conclusion

Two nonlinear turbulence EVMs, namely, the ARS model of Gatski and Speziale [8–10] and the cubic model of Lien et al. [14] were assessed for their capability in properly simulating ICE turbulent flows. The models were embedded in a previously developed homemade CFD code and this was applied to the flow-field numerical analysis in a test engine combustion chamber featuring either a flat-piston or an axisymmetric bowl-in-piston arrangements, throughout the whole engine cycle under motored conditions. The investigation was carried out in both the presence and the absence of a swirling flow. The simulation results obtained for the flat-piston—no swirl and the bowl-in-piston—swirl operating conditions were reported and compared to those of the upgraded linear RNG k-ε model, which was indicated in Ref. [1] as a good compromise between accuracy and computational cost. The RNG model included a modified wall boundary condition approach with respect to the conventional logarithmic function, so as to make the local equilibrium hypothesis virtually ineffective. This approach was also used in the application of nonlinear models. A general form of the stress-strain constitutive relation was introduced for the implementation of both linear and nonlinear EVMs.

The model capabilities in capturing turbulent flow features were evaluated by the analysis of the physical consistency of the predicted-flow evolution and by the comparison between numerical and experimental results.

From a theoretical point of view, the nonlinear constitutive relations are appealing, because they are supposed to allow two-equation EVM to take account of anisotropy and flow curvature better than the linear models do. This statement particularly suits ARS model types, which are derived from complete Reynolds-stress closures. The computational results indicated that the form of the stress-strain constitutive relation significantly affects the turbulence quantity values as well as the resultant stress-tensor anisotropy. However, in effect, the implementation of nonlinear EVM does not improve the agreement between numerical and experimental results with respect to the linear RNG model, at least for the considered engine flow conditions. Moreover, the increased model sensitivity to the mesh quality is a drawback with respect to the Boussinesq relation.

The description of turbulence spectra with only one length or time scale constitutes a limit in both linear and nonlinear two equation EVMs for their application to ICE nonstationary flows, as a consequence of the hypothesis of scale separation between turbulence and mean motion, which is common to both approaches. This has led to the development of multiple time scale models, which can be implemented also in the nonlinear form, and may be a more effective refined approach but at a higher computational cost. Another means of improving both linear and nonlinear EVMs is the modification of the turbulent dissipation equation by including anisotropy effects through R-like functions as in the RNG model or through low-Re formulations. However, low-Re k-ε models require very fine grids within the boundary layer, whose variable thickness is not generally known, so that the moving mesh strategy becomes cumbersome for engine flow application. Such a version is rarely applied to engine flows and was taken to be advantageous when RSM are applied to enginelike flows [36].

Acknowledgment

Financial support to this research was provided by CRF (Centro Ricerche Fiat) and by MUR (Ministry of University and Research) under COFIN04-06 Research Projects of National Relevant Interest.

Nomenclature

A = anisotropy invariant

$A_1, A_2, A_3, A_4, g, \alpha_1, \alpha_2, \alpha_3$ = constants in the ARS model

$a_{ij} = -(\tau_{ij}/\rho k) - (2/3)\delta_{ij}$ = anisotropy tensor

$B_1, B_2, \ldots, B_5$ = cubic model closure coefficients

BDC = bottom dead center

C_1, C_2, C_3, C_4 = empirical constants for ε equation

C_{ijk} = Reynolds-stress turbulent transport

C_μ = empirical constant for μ_T

C_R = closure coefficient for the relaxation time approximation of a_{ij}

$D = S_{ll}$ = velocity divergence

h = stagnation enthalpy

k = turbulence kinetic energy

$\mathrm{II}_a = a_{ij}a_{ji}$ = second anisotropy tensor invariant

$\mathrm{III}_a = a_{ij}a_{jk}a_{ki}$ = third anisotropy tensor invariant

P_k = turbulence kinetic energy production term

p = pressure

R = anisotropy function in the RNG k-ε model

S_{ij} = mean-flow strain tensor

TDC = top dead center

$\mathrm{TI} = u'/V_p$ = adimensional turbulence intensity

U_i = absolute mean velocity in the i direction

u_i = turbulence velocity in the i direction

u' = turbulence intensity

V_p = mean piston velocity

β, η_0 = constants in the RNG k-ε model

Δt = time step size

ΔV = mesh control volume

Δx, Δy = grid sizes

δ_{ij} = Kronecker delta

ε = turbulence energy dissipation rate

ε_{ij} = dissipation rate tensor in the Reynolds-stress equations

$\eta = \|\eta_{ij}\|$ = dimensionless strain rate

$\eta_{ij} = S_{ij}k/\varepsilon$ = dimensionless mean-flow strain tensor

θ = crank angle

μ, μ_T = molecular viscosity, turbulent viscosity

$\xi = k/\varepsilon\|\Omega_{ij}\|$ = dimensionless rotation rate

ξ_C, η_C = "corrected" dimensionless rates in Table 3

Π_{ij} = pressure-strain correlation tensor

ρ = density

$\sigma_h, \sigma_k, \sigma_\varepsilon$ = Prandtl numbers

$\tau_{ij} = -\overline{\rho u_i u_j}$ = Reynolds stress tensor

Ω_{ij} = mean-flow rotation tensor

References

[1] Baratta, M., Catania, A. E., Spessa, E., and Liu, R. L., 2005, "Multidimensional Predictions of In-Cylinder Turbulent Flows: Contribution to the Assessment of k-ε Turbulence Model Variants for Bowl-In-Piston Engines," Trans. ASME: J. Eng. Gas Turbines Power, **127**, pp. 883–896.

[2] El Tahry, S. H., and Haworth, D. C., 1992, "Directions in Turbulence Modeling for In-Cylinder Flows in Reciprocating Engines," J. Propul. Power, **8**(5), pp. 1040–1048.

[3] Bianchi, G. M., Cantore, G., Parmeggiani, P., and Michelassi, V., 2002, "On Application of Nonlinear k-ε Models for Internal Combustion Engine Flows," Trans. ASME: J. Eng. Gas Turbines Power, **124**, pp. 668–677.

[4] Hanjalic, K., 1994, "Advanced Turbulence Closure Models: A View of Current Status and Future Prospects," Int. J. Heat Fluid Flow, **15**(3), pp. 178–203.

[5] Speziale, C. G., 1987, "On Nonlinear k-l and k-ε Models of Turbulence," J. Fluid Mech., **178**, pp. 459–475.

[6] Yavuz, I., Celik, I., and McMillian, M. H., 2002, "Knock Prediction in Reciprocating Gas-Engines Using Detailed Chemical Kinetics," SAE 2001 Trans., **110**(3), pp. 981–987.

[7] Hayashida, T., Okamoto, M., and Shima, N., 2004, "Implementation of Both a Second-Moment Closure and a Third-Order Nonlinear Eddy-Viscosity Turbulence Models to KIVA-3V Code," SAE 2003 Trans., **112**(3), pp. 2010–2017.

[8] Gatski, T. B., and Speziale, C. G., 1993, "On Explicit Algebraic Stress Models for Complex Turbulent Flows," J. Fluid Mech., **254**, pp. 59–78.

[9] Speziale, C. G., and Xu, X. H., 1996, "Towards the Development of Second-Order Closure Models for Nonequilibrium Turbulent Flows," Int. J. Heat Fluid Flow, **17**, pp. 238–244.

[10] Speziale C. G., 1998, "Turbulence Modeling for Time-Dependent RANS and VLES: A Review," AIAA J., **36**, pp. 173–184.

[11] Celik, I., Yavuz, I., Smirnov, A., Smith, J., Amin, E., and Gel, A., 2000, "Prediction of In-Cylinder Turbulence for IC Engines," Combust. Sci. Technol., **153**, pp. 339–368.

[12] Sone, K., and Menon, S., 2003, "Effect of Subgrid Modeling on the In-Cylinder Unsteady Mixing Process in a Direct Injection Engine," Trans. ASME: J. Eng. Gas Turbines Power, **125**, pp. 435–443.

[13] Kaario, O., Pokela, H., Kjäldman, L., Tiainen, J., and Larmi, M., 2003, "LES and RNG Turbulence Modelling in DI Diesel Engines," SAE Paper No. 2003-01-1069.

[14] Lien, F. S., Chen, W. L., and Leschziner, M. A., 1996, "Low Reynolds Number Eddy-Viscosity Modeling Based on Non-Linear Stress-Strain/Vorticity Relations," *Proceedings of Third Symposium on Engineering Turbulence Modeling and Measurements*, Crete, Greece.

[15] Arcoumanis, C., Bicen, A. F., and Whitelaw, J. H., 1982, "Squish and Swirl-Squish Interaction in Motored Model Engines," Flows in Internal Combustion Engines, ASME H00245, pp. 45–52.

[16] Baratta, M., and d'Ambrosio, S., 2004, "Further Investigation of RNG k-ε Model Capabilities in the Simulation of In-Cylinder Turbulent Flows" *Proceedings of the Sixth Intern. Symposium on Diagnostic and Modeling of Combustion in Internal Combustion Engines*, COMODIA 2004, Yokohama, Japan.

[17] Patankar, S. V., 1980, "Numerical Heat Transfer and Fluid Flow," McGraw-Hill, New York.

[18] Baratta, M., 2004, "Multidimensional CFD Methods, Turbulence Models and Their Application to the Analysis of Charge Motion in an IC Engine Cylinder" Ph.D. thesis, Politecnico di Torino.

[19] Craft, T. J., Launder, B. E., and Suga, K., 1996, "Development and Application of a Cubic Eddy Viscosity Model of Turbulence," Int. J. Heat Fluid Flow, **17**, pp. 108–115.

[20] Star-CD v. 3.26 Methodology Manual, 2005, Computational Dynamics Ltd.

[21] Shih, T. H., Zhu, J., and Lumley, J. L., 1993, "A Realizable Reynolds Stress Algebraic Equation Model," NASA Tech. Memo. 105993.

[22] Rodi, W., 1976, "A New Algebraic Relation for Calculating Reynolds Stresses," Z. Angew. Math. Mech., **56**, pp. 219–221.

[23] Pope, S. B., 1975, "A More General Effective Viscosity Hypothesis," J. Fluid Mech., **72**, pp. 331–340.

[24] Catania, A. E., 1985, "Induction System Effects on the Fluid Dynamics of a DI Automotive Diesel Engine," *ASME Diesel & Gas Engines Symposium*, ETCE, Paper No. 85-DGP-11.

[25] Johannsson, A., 2002, "Engineering Turbulence Models and Their Development, with Emphasis on Explicit Algebraic Reynolds Stress Models," in *Theories of Turbulence*, Springer, New York, pp. 253–300.

[26] Lumley, J. L., 1978, "Computational Modeling of Turbulent Flows," Adv. Appl. Mech., **18**, pp. 123–176.

[27] Wilcox, D. C., 1994, "Turbulence Modeling for CFD," DCW Industries Inc.

[28] Catania, A. E., and Spessa, E., 1997, "Speed Dependence of Turbulence Properties in a High-Squish Automotive Engine Combustion System," SAE 1996 Trans., **105**(3), pp. 313–334.

[29] Speziale, C. G., 1991, "Analytical Methods for the Development of Reynolds-Stress Closures in Turbulence," Annu. Rev. Fluid Mech., **23**, pp. 107–157.

[30] Kim, S. W., and Chen, C. P., 1989, "A Multiple Time Scale Turbulence Model Based on Variable Partitioning of the Turbulence Kinetic Energy Spectrum," Numer. Heat Transfer, Part B, **16**, pp. 193–211.

[31] Kim, S. W., 1991, "Calculation of Divergent Channel Flows with a Multiple Time Scale Turbulence Model," AIAA J., **29**(4), pp. 547–554.

[32] Tanner, F. X., Zhu, G. S., and Reitz, R. D., 2001, "Non-Equilibrium Turbulence Considerations for Combustion Processes in the Simulation of DI Diesel Engines," SAE 2000 Trans., **109**(3), pp. 707–717.

[33] Tanner, F. X., Zhu, G. S., and Reitz, R. D., 2003, "A Nonequilibrium Turbulence Dissipation Correction and Its Influence on Pollution Predictions for DI Diesel Engines," Trans. ASME: J. Eng. Gas Turbines Power, **125**, pp. 534–443.

[34] Tennekes, H., and Lumley, J. L., 1972, A First Course in Turbulence, MIT, Cambridge, MA.

[35] Jones, W. P., and Launder, B. E., 1972, "The Prediction of Laminarization with a Two-Equation Model of Turbulence," Int. J. Heat Mass Transfer, **15**, pp. 301–314.

[36] Jakirlic, S., Tropea, C., Hadzic, I., Pascal, H., and Hanjalic, K., 2002, "Computational Study of Joint Effects of Shear, Compression and Swirl on Flow and Turbulence in a Valveless Piston-Cylinder Assembly," SAE 2001 Trans., **110**(3), pp. 1402–1439.

[37] Lien, F. S., and Leschziner, M. A., 1994, "Assessment of Turbulence-Transport Models Including Non-Linear RNG Eddy Viscosity Formulation and Second-Moment Closure for Flow Over a Backward-Facing Step," Comput. Fluids, **23**(8), pp. 983–1004.

Analysis of the Interactions Between Indicated and Reciprocating Torques for the Development of a Torsional Behavior Model of the Powertrain

Fabrizio Ponti

Luca Solieri

DIEM,
University of Bologna,
Via, Fontanelle 40,
Forlí 47100, Italy

Torque-based engine control systems usually employ a produced torque estimation feedback in order to verify that the strategy target torque has been met. Torque estimation can be performed using static maps describing the engine behavior or using models describing the existing relationships between signals measured on the engine and the indicated torque produced. Signals containing information on the combustion development, suitable for this purpose, are, among others, the ion-current signal, the vibration signals obtained from accelerometers mounted on the engine block, or the instantaneous engine speed fluctuations. This paper presents the development and the identification process of an engine-driveline torsional behavior model that enables indicated torque estimation from instantaneous engine speed measurement. Particular attention has been devoted to the interactions between indicated and reciprocating torques, and their effects over instantaneous engine speed fluctuations. Indicated and reciprocating torques produce, in fact, opposite excitations on the driveline that show opposite effects on the engine speed wave form: For low engine speed, usually indicated torque prevails, while the opposite applies for higher engine speed. In order to correctly estimate indicated torque from engine speed measurement, it is therefore necessary to correctly evaluate the reciprocating torque contribution. Reciprocating torque is usually described using a wave form as a function of crank angle, while its amplitude depends on the value of the reciprocating masses. As mentioned before, knowledge of the reciprocating masses is fundamental in order to obtain correct estimation of the indicated torque. The identification process that has been set up for the engine-driveline torsional model enables to evaluate the relationship between torques applied to the engine and the corresponding engine speed wave form even without knowing the value of the reciprocating masses. In addition, once this model has been set up, it is possible to estimate with high precision the value of the reciprocating masses. Particular attention has also been devoted to the feasibility of the application of the identified model onboard for torque estimation; for this reason, the model has been developed in a very simple form. The approach proved to be effective both on gasoline and diesel engines, both for engine mounted on a test cell and onboard, with different engine configurations. Examples of application are given for some of the configurations investigated. [DOI: 10.1115/1.2939010]

Introduction

Most engine control systems nowadays are torque based, meaning that ignition, injection, and all the control parameters are set in such a way to produce a desired torque level, while respecting other goals, for example, emissions or drivability. Information on the real torque produced is very much useful in order to check if the control action gave the desired result.

Torque measurement is still challenging on board production vehicles due to reliability issues. For this reason, torque estimation is one option followed to obtain information on the real torque produced by the engine [1–16]. Many studies have been performed in order to obtain an accurate and reliable over time torque estimation. Some of them determine the mean indicated torque through signals from additional sensors mounted on the engine: pressure sensors [13], accelerometers [5], and ignition coil for ionization current. Nevertheless, at this time, only indicated torque evaluation from measuring in-cylinder pressure gives good results, even if these sensors are not so reliable in time and, anyway, they represent an additional cost. In some cases, engine speed information is used to reduce the amount of additional pressure sensors required [10], but still their reliability could be an issue. Other works try to estimate mean indicated torque from engine speed measurement, basing their evaluation on statistical [6] or stochastic [3] correlations with many engine parameters. They require a lot of experimental tests and, in some cases, have good accuracy only for steady-state engine operating conditions. Some authors [7,11,14] developed procedures based on state observers (linear, nonlinear, and Kalman filters) that require as inputs one or more engine parameters. Another work [8] uses a methodology named support vector machine, that is, a supervised learning method used for linear classification and regression. Hence, in these cases, the accuracy is related to the number of the input parameters, and if it increases a lot, the algorithm may not be well suitable for real time applications. Others try to estimate

Contributed by the Internal Combustion Division of ASME for publication in the JOURNAL OF ENGINEERING FOR GAS TURBINES AND POWER. Manuscript received September 16, 2007; final manuscript received April 8, 2008; published online August 21, 2008. Review conducted by Jim Cowart. Paper presented at the 2007 Fall Conference of the ASME Internal Combustion Engine Division (ICEF2007), Charleston, SC, October 14–17, 2007.

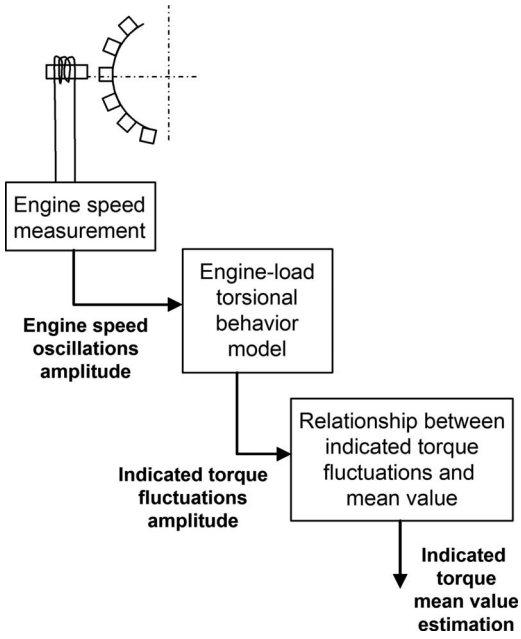

Fig. 1 Flowchart of the methodology employed for indicated torque estimation

mean indicated torque analyzing the instantaneous engine speed fluctuations, directly from the sensor facing the toothed wheel already present onboard for control purposes [1,2,4,9,12]. In fact, as many works demonstrated, some of them of the same authors of this paper [17,18], the engine speed fluctuation is strictly connected to the generated torque.

The torque estimation approach used in this paper makes use of the information contained in the engine speed fluctuation signal. Many studies, some of them from the same authors of this work, demonstrated the feasibility of estimating mean indicated torque starting from engine speed fluctuation measurement. In particular, fluctuation measurement is needed at an order characteristic of the engine (mainly related to its number of cylinders and its firing order); at this order, the speed wave form over an engine cycle shows fluctuation of the highest amplitude. In this study, engine speed has been measured using the same magnetic pickup and the same 60-2 teeth wheel already present for control purposes. In this way, no additional sensors or mechanical components are required.

Measurement of the speed fluctuation at the engine order of interest allows for estimating the corresponding indicated torque fluctuations at the same engine order. This can be done if an accurate torsional behavior model of the engine-driveline-load system has been developed.

Knowledge of the relationship between the amplitude of the indicated torque frequency component at the order of interest and its mean value enables finally to evaluate the indicated torque mean value from the estimated torque fluctuations. A scheme of the entire procedure is presented in Fig. 1.

This paper will focus on the first step of this torque estimation procedure, i.e., the identification of the system torsional behavior model. The main goal is to develop a standard process that enables model identification quickly and even if some or all the geometric information of the engine are not known (usually, this information is used to determine inertias and stiffness of the connections between the different parts of the powertrain system).

The next section will present the development of the torsional behavior model, the experimental tests used to identify and validate the model, and finally some results.

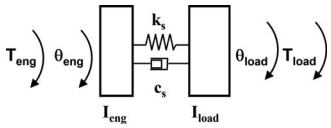

Fig. 2 Scheme of the inertia-stiffness equivalent representation to describe the system dynamic behavior

Torsional Vibration Model

Several engines have been used throughout this work. Some of them have been mounted on a test bench; some other onboard a vehicle. Both diesel and gasoline engines with different architecture have been considered.

As already mentioned, the main goal of the developed model is its use within a torque estimation procedure. For indicated torque mean value estimation, as already recalled also in the Introduction, engine speed fluctuations at an engine order characteristic of the engine under study have to be considered. The engine order to be considered depends on the number of cylinders and on the firing order, and is the one at which the engine speed fluctuations show the higher amplitude. Recalling that a vibration's order is the number of times it occurs per crankshaft revolution, for a Z cylinder engine with evenly spaced combustions, the order to be taken into account is $Z/2$. If the combustions are not evenly spaced, the choice of the order could be more difficult, but still it is possible to determine the one at which the response in terms of engine speed fluctuations is expected to be higher.

Once the engine order of interest has been selected, it is possible to determine the frequency range in which the torsional model has to correctly describe the dynamic behavior of the system. For a six cylinder engine with evenly spaced combustions (Order 3 is selected), running from 900 rpm to 6000 rpm, the frequency range to be investigated goes from 45 Hz to 300 Hz. The evaluation of the interesting frequency range is important for the correct definition of the dynamic model, since all the natural frequencies of the system out of this range can be neglected. Neglecting natural frequencies out of the frequency range of interest yields the development of a reduced model: This model will be fully representative of the system behavior inside the frequency range considered, while out of this range, it will give an approximate response. Following the example of the six cylinder engine, if the lowest natural frequency on the crankshaft is higher than 300 Hz, it can be neglected.

Either if the engine is mounted onboard a vehicle or it is mounted on a test bench, the lowest resonance frequencies associated with the driveline are usually within the frequency range of interest. These conditions (crankshaft eigenfrequencies out of the frequency range of interest, and one or more driveline natural frequencies within this range) have been verified for all the powertrain configurations investigated and is the main hypothesis of this study. If this condition is not verified, restrictions to application of the proposed approach have to be considered, as it will be explained in the following.

Based on the previous considerations, only the natural frequencies on the driveline will be taken into account. The system torsional behavior can be described by means of an equivalent model with two or more inertias, one of them representing the engine, the number of inertias to be employed depending on the number of natural frequencies of the driveline, up to the frequency of interest. Figure 2 shows the simplest case with two inertias.

Considering for the sake of simplicity the model with two inertias, dynamic equations of the system can be obtained as

$$I_{\text{eng}}\ddot{\theta}_{\text{eng}} = T_{\text{eng}} - k_s(\theta_{\text{eng}} - \theta_{\text{load}}) - c_s(\dot{\theta}_{\text{eng}} - \dot{\theta}_{\text{load}})$$

$$I_{\text{load}}\ddot{\theta}_{\text{load}} = T_{\text{load}} - k_s(\theta_{\text{load}} - \theta_{\text{eng}}) - c_s(\dot{\theta}_{\text{load}} - \dot{\theta}_{\text{eng}}) \qquad (1)$$

Fourier expansion can be applied to the signals in Eq. (1) in order to obtain a relationship between the corresponding terms in the Fourier expansion series. For signals that can be considered periodic with period equal to an engine cycle (as it is for the torques and the angular positions of the inertias of the system of Fig. 2), the frequency associated with the ith term of the Fourier expansion series is equal to $\omega = i\Omega/2$ (i is the number of the harmonic over the engine cycle). For the ith terms of the torques and angular positions ($\mathbf{T}_{\text{eng}i}$, $\mathbf{T}_{\text{load}i}$, $\boldsymbol{\theta}_{\text{eng}i}$ and $\boldsymbol{\theta}_{\text{load}i}$), it is therefore possible to write

$$\begin{bmatrix} I_{\text{eng}}\omega^2 - j\omega c_s - k_s & j\omega c_s + k_s \\ j\omega c_s + k_s & I_{\text{load}}\omega^2 - j\omega c_s - k_s \end{bmatrix} \begin{bmatrix} \boldsymbol{\theta}_{\text{eng}i} \\ \boldsymbol{\theta}_{\text{load}i} \end{bmatrix} = \begin{bmatrix} -\mathbf{T}_{\text{eng}i} \\ -\mathbf{T}_{\text{load}i} \end{bmatrix} \tag{2}$$

Equation (2) could be seen as the relationship between the corresponding oscillations of torques and angular positions at frequencies $\omega = i\Omega/2$ for $i > 0$. The engine order associated with these oscillations is $\text{ord} = i/2$. The oscillations, in fact, occur i times per engine cycle and therefore $i/2$ times per crankshaft revolution.

Since the harmonic content of the load torque T_{load} is usually negligible (its dynamic is very slow), the terms $\mathbf{T}_{\text{load}i}$ have been set equal to 0.

$$\begin{bmatrix} I_{\text{eng}}\omega^2 - j\omega c_s - k_s & j\omega c_s + k_s \\ j\omega c_s + k_s & I_{\text{load}}\omega^2 - j\omega c_s - k_s \end{bmatrix} \begin{bmatrix} \boldsymbol{\theta}_{\text{eng}i} \\ \boldsymbol{\theta}_{\text{load}i} \end{bmatrix} = \begin{bmatrix} -\mathbf{T}_{\text{eng}i} \\ 0 \end{bmatrix} \tag{3}$$

Focusing the attention on the relationship between the corresponding Fourier expansion coefficients (i.e., between the corresponding oscillation) of the crank angle position and the torque applied to the engine, it is possible to obtain

$$\boldsymbol{\theta}_{\text{eng}i} = -\frac{1}{\omega^2} \frac{I_{\text{load}}\omega^2 - j\omega c_s - k_s}{I_{\text{eng}} I_{\text{load}}\omega^2 - (I_{\text{eng}} + I_{\text{load}})(j\omega c_s + k_s)} \mathbf{T}_{\text{eng}i} \tag{4}$$

Rewriting Eq. (4) in terms of torque and speed, it yields

$$\dot{\boldsymbol{\theta}}_{\text{eng}i} = \frac{1}{\omega} \frac{I_{\text{load}}\omega^2 - j\omega c_s - k_s}{j(I_{\text{eng}} I_{\text{load}}\omega^2 - (I_{\text{eng}} + I_{\text{load}})(j\omega c_s + k_s))} \mathbf{T}_{\text{eng}i} \tag{5}$$

Equation (5) has been obtained for the simplest two inertias model case. Similar equations can be obtained if more complex torsional models have to be designed to correctly describe the system. The obtained equation will present in the case of a more complex system a higher number of parameters (inertias, stiffness, and dampings). In any case, it will be possible to describe the relationship between the corresponding Fourier expansion coefficients of torque and speed using a frequency response function (FRF), reported in the following as $F(j\omega)$.

$$\dot{\boldsymbol{\theta}}_{\text{eng}i} = \frac{1}{\omega F(j\omega)} \mathbf{T}_{\text{eng}i} \tag{6}$$

The FRF $F(j\omega)$ represents the dynamic behavior of the system and depends on the inertia-stiffness configuration of the system itself. Inertias and stiffness values can be determined starting from a CAD representation of the system, even if this approach is quite time consuming and requires full access to component CAD representation. In addition, once FRF has been obtained, usually it has to be verified and validated through specific experimental tests.

The approach presented in this study allows evaluating the FRF as a whole, without any information needed on the inertia-stiffness representation of the system. FRF identification is made directly on an experimental basis, using engine speed and in-cylinder pressure measurements (that allow determining indicated torque) during specifically designed tests. Rearranging Eq. (6), it is, in fact, possible to see that FRF can be obtained as

$$F(j\omega) = \frac{\mathbf{T}_{\text{eng}i}}{\omega \dot{\boldsymbol{\theta}}_{\text{eng}i}} \tag{7}$$

Amplitude and phase of the engine speed oscillation can be directly measured and, for the engine order of interest, it results in

$$\dot{\boldsymbol{\theta}}_{\text{eng}i} = \Omega_{\text{ord}} e^{j\phi_{\text{ord}}} \tag{8}$$

Engine torque T_{eng} is the result of all the torques applied to the cylinders, i.e., the difference between indicated and reciprocating torques. The same will also apply to the ith harmonic component of the indicated and reciprocating torques that can be seen as the sum of the ith harmonic components for all the cylinders. Considering indicated and reciprocating torque wave forms similar for all the cylinders, the Fourier representation of the torque harmonic components will differ only for the phase, whose value can be determined knowing the number of cylinders and the firing order (Eq. (9) reports as an example what can be obtained for a Z cylinder engine with evenly spaced combustions).

$$\mathbf{T}_{\text{ind}mi} = \mathbf{T}_{\text{ind}1i} \cdot e^{jim2\pi/Z}$$

$$\mathbf{T}_{rmi} = \mathbf{T}_{r1i} \cdot e^{jim2\pi/Z} \tag{9}$$

$\mathbf{T}_{\text{ind}1i}$ is the ith indicated torque harmonic component for Cylinder 1; indicated torque can be evaluated from the indicated pressure measurement for the same cylinder through Eq. (10) [19]:

$$T_{\text{ind}1}(\theta_1) = A_p r p_1(\theta_1) f(\theta_1) \tag{10}$$

Reciprocating torque can be expressed using the well known geometric expression [20]

$$T_{rm}(\theta_m) = M_{\text{eq}} r^2 f(\theta_m) \left[f(\theta_m)\ddot{\theta}_m + \frac{df(\theta_m)}{d\theta_m} \dot{\theta}_m^2 \right] = M_{\text{eq}} \hat{T}_{rm}(\theta_m) \tag{11}$$

where M_{eq} is the value of the reciprocating masses and $\hat{T}_{rm}(\theta_m)$ represents the normalized reciprocating torque with respect to the reciprocating masses that do not depend on M_{eq}. Even if all the necessary drawings are available, the evaluation of M_{eq} presents some difficulties, since its value is the sum of two contributions: The first one due to the mass of the piston assembly, the second one associated with the reciprocating motion of the connecting rod. While the first contribution can be easily determined, the second one is usually more difficult to be evaluated. The approach presented in this work enables to identify the value of M_{eq}, together with the system FRF, without any additional information needed, and is therefore useful to verify M_{eq} value coming from calculations.

Amplitude and phase of indicated and normalized reciprocating torques for the order of interest ($\mathbf{T}_{\text{ind}mi}$ and $\hat{\mathbf{T}}_{rmi}$) are reported as a function of engine speed in Figs. 3 and 4 for a four cylinder multijet diesel engine with evenly spaced combustions (Order 2 selected), and in Figs. 5 and 6 for a six cylinder gasoline engine with evenly spaced combustions (Order 3 selected). The phase is always evaluated taking as a reference within a cycle the TDC position of Cylinder 1 at the beginning of its intake stroke. The values reported are calculated using measurements on the engine.

As it is possible to observe, while indicated torque components are obviously dependent both on engine speed and load, reciprocating torque components depends only on the engine speed. This is essentially due to the fact that reciprocating torque is an inertial effect on the crankshaft, caused by the presence of reciprocating masses (mainly piston assembly and connecting rod) [19,20]. In addition, reciprocating and indicated torque components show similar phases. Since the torque applied to the engine is the difference between these two contributions, they will be applied to the crankshaft with opposite phases.

These observations are quite important for the setup of the FRF estimation scheme, as it will be explained in the next paragraphs.

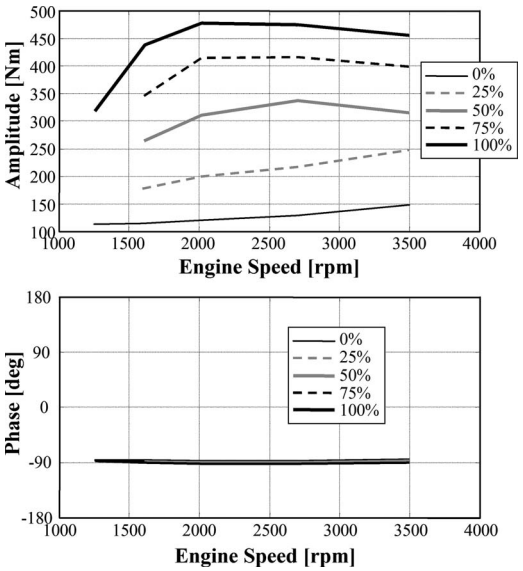

Fig. 3 Amplitude and phase of the indicated torque Order 2 component for an L4 multijet diesel engine at different percentages of full load

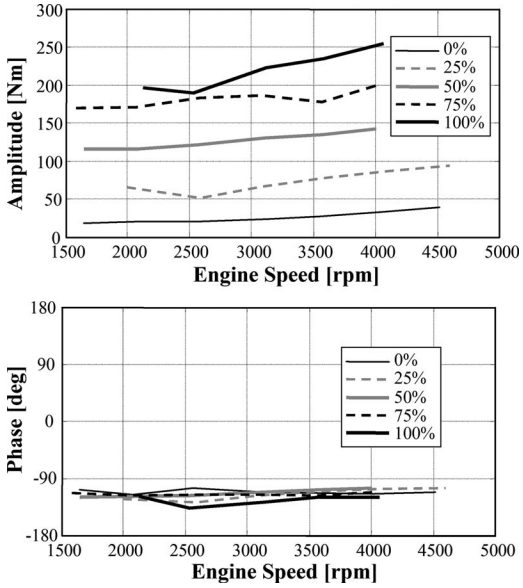

Fig. 5 Amplitude and phase of the indicated torque Order 3 component for a V6 gasoline engine at different percentages of full load

Rearranging Eq. (7), it is possible to obtain

$$F(j\omega) = \frac{\sum_m (\mathbf{T}_{\text{ind}mi} - M_{\text{eq}}\hat{\mathbf{T}}_{rmi})}{\omega\dot{\boldsymbol{\theta}}_{\text{eng}i}} \tag{12}$$

All the terms in Eq. (12) are either known or can be measured with the exception of M_{eq}. Therefore, under the hypothesis made, the FRF appears not to be directly estimable. In order to overcome this conclusion and contemporarily estimate the value of M_{eq}, the observation that the reciprocating torque frequency components depend only on the engine speed value has been used. Running, in fact, two tests (A and B) at the same engine speed but different loads, Eq. (12) can be rewritten for these tests, obtaining

$$\omega_{\text{A}}\dot{\boldsymbol{\theta}}_{\text{engA}i}F(j\omega_{\text{A}}) = \sum_m (\mathbf{T}_{\text{indA}mi} - M_{\text{eq}}\hat{\mathbf{T}}_{r\text{A}mi})$$

$$\omega_{\text{B}}\dot{\boldsymbol{\theta}}_{\text{engB}i}F(j\omega_{\text{B}}) = \sum_m (\mathbf{T}_{\text{indB}mi} - M_{\text{eq}}\hat{\mathbf{T}}_{r\text{B}mi}) \tag{13}$$

Due to the observation that the reciprocating torque frequency components depend only on the engine speed value, since Tests A and B have been run at the same engine speed, it can be concluded that $\omega_{\text{A}} = \omega_{\text{B}}$ and $\hat{\mathbf{T}}_{r\text{A}mi} = \hat{\mathbf{T}}_{r\text{B}mi}$.

The difference between Eq. (13) is now considered, yielding

$$\omega(\dot{\boldsymbol{\theta}}_{\text{engA}i} - \dot{\boldsymbol{\theta}}_{\text{engB}i})F(j\omega) = \sum_m (\mathbf{T}_{\text{indA}mi} - \mathbf{T}_{\text{indB}mi}) \tag{14}$$

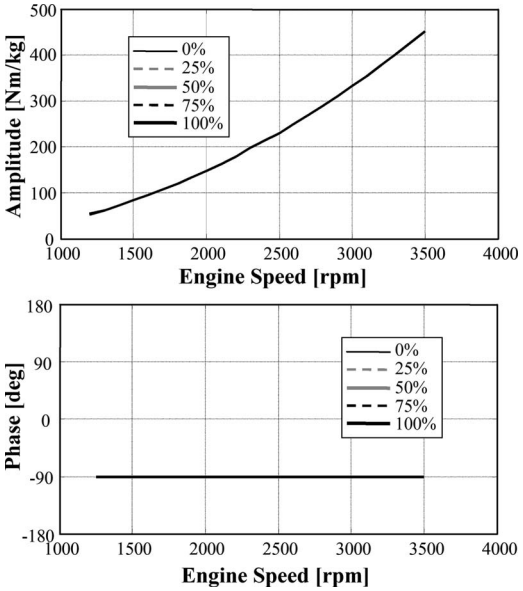

Fig. 4 Amplitude and phase of the reciprocating torque Order 2 component for an L4 multijet diesel engine at different percentages of full load

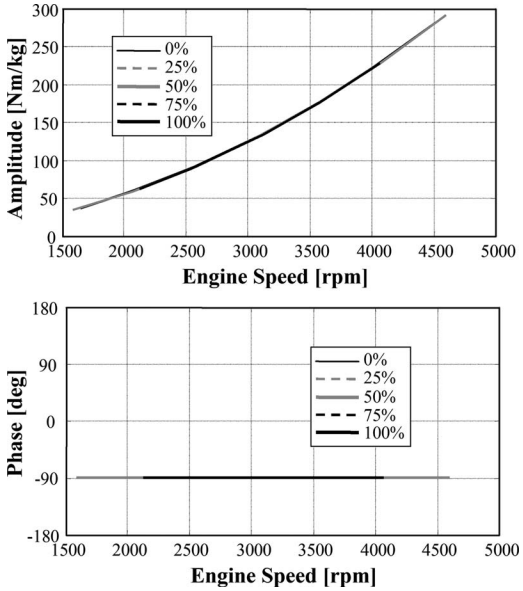

Fig. 6 Amplitude and phase of the reciprocating torque Order 3 component for a V6 gasoline engine at different percentages of full load

Rearranging Eq. (14), it is possible to obtain

$$F(j\omega) = \frac{[\sum_m (\mathbf{T}_{\text{indA}m} - \mathbf{T}_{\text{indB}m})]_i}{\omega[\dot{\boldsymbol{\theta}}_{\text{engA}} - \dot{\boldsymbol{\theta}}_{\text{engB}}]_i} \tag{15}$$

Equation (15) shows that the FRF can be determined using only engine speed and in-cylinder pressure measurements, performed during two tests at the same engine speed and different loads. Using this approach, FRF can be therefore estimated independently from the knowledge of M_{eq} at the engine speed, and therefore at the associated frequency, at which the tests have been performed. Running couples of tests each at a different engine speed, it is possible to identify $F(j\omega)$ over the whole interesting range of frequency.

Once $F(j\omega)$ has been evaluated, M_{eq} can be estimated as well, since from a suitable rearrangement of Eq. (13), it is possible to obtain for Test A:

$$M_{\text{eq}} = \frac{\omega_{\text{A}} \dot{\boldsymbol{\theta}}_{\text{engA}i} F(j\omega_{\text{A}}) - \Sigma_m(\mathbf{T}_{\text{indA}mi})}{\Sigma_m(\hat{\mathbf{T}}_{\text{rA}mi})} \tag{16}$$

The developed approach allows identifying both the FRF of the dynamic system under study and the reciprocating mass value. This is obviously useful if geometric and CAD information are not available for the engine under study, but it represents a quick validation procedure useful even when those information are available.

The presented procedure has been applied to several different engine-load configurations, comprising both gasoline and diesel engines, test bench and in vehicle tests, and different engine architectures. Examples of the application of the proposed approach to some of these configurations will be presented in the next section together with some validation results.

Once the model identification process has been concluded, estimation of the indicated torque components is possible from the measured engine speed at the engine order characteristic of the engine. As already mentioned, this is the first step of a complete algorithm that enables mean indicated torque estimation. The second step is the identification of the relationship between the estimated component of the indicated torque and its mean value. This second step is not the main topic of this work and is not developed and presented here. Information on this topic can be found in literature [17,18].

Results

Experimental tests have been run on several powertrain configurations. In order to report the most meaningful ones, it has been chosen to present, in particular, the results obtained for a V6 turbocharged gasoline engine coupled to an eddy-current brake and for an L4 turbocharged diesel engine mounted onboard a vehicle. All the other engine-driveline configurations gave similar results.

Measurements needed for the setup of the identification process are instantaneous engine speed, measured through a magnetic pickup facing a wheel with 60-2 teeth, and in-cylinder pressure for all the cylinders, measured using piezoelectric sensors integrated in the spark plug for gasoline engines and in the glow plug for diesel engines. The choice of this easy to be mounted in-cylinder pressure sensors is compatible with the application of the proposed procedure to a high number of engine-driveline configurations, as it is the case for an engine mounted on different vehicles or on vehicle with different gearbox equipment, and so on. A higher accuracy could be obtained with cooled sensors, but they have not been considered for this work, since they require a specific machining of the engine block.

In order to estimate the FRF of the engine-driveline system, tests at the same engine speed and different load levels are needed (at least two). This enables the evaluation of the FRF value at that engine speed (or at the corresponding frequency) through Eq. (15). For the purpose of identifying the FRF over the whole engine speed (frequency) range, many couples of steady-state tests have to be performed. In order to overcome the need of a high number of steady-state tests, the possibility of using two ramps performed at different loads has been investigated: In this case, Eq. (15) has to be applied to engine cycles within the two ramps that present close engine speed values. Both steady-state and ramp tests have been run, and the obtained results have been compared: If the result accuracy is similar, the ramp option is preferable for its ease and quickness.

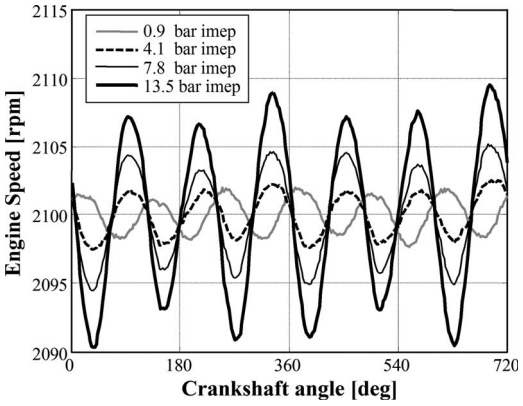

Fig. 7 Engine speed wave forms for a V6 gasoline engine running at 2100 rpm and different loads

Engine speed and indicated torque measurements for steady-state tests conducted at the same engine speed and different loads are reported in Figs. 7 and 8 for the V6 turbocharged gasoline engine coupled to an eddy-current brake.

The tests conducted on the V6 engine clearly show that as the torque produced increases, the amplitude of the engine oscillations becomes higher. The only test that apparently seems to have a different behavior is the one conducted at 0.9 bar IMEP. In this case, the phase of the oscillation is opposite with respect to all the other tests. In addition, the amplitude is not decreased with respect to the test at 4.1 bar IMEP.

This behavior is due to the presence of the reciprocating torque that acts on the crankshaft together with the indicated torque. The amplitude of the reciprocating torque depends on the engine speed. At lower loads, its amplitude can be higher than that of the indicated torque, and therefore it prevails, while at high load, indicated torque prevails. Since indicated and reciprocating

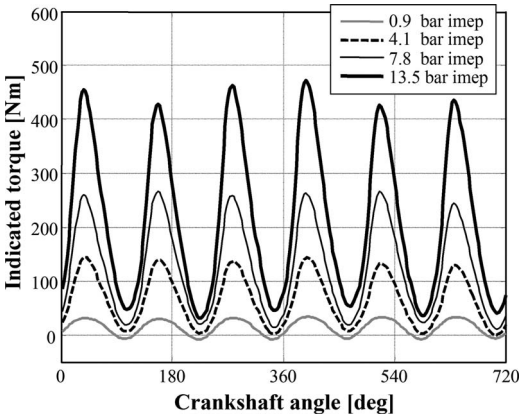

Fig. 8 Indicated torque wave forms for a V6 gasoline engine running at 2100 rpm and different loads

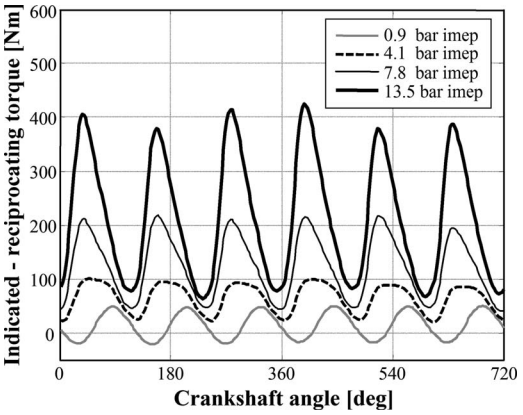

Fig. 9 Indicated and reciprocating torque difference for a V6 gasoline engine running at 2100 rpm and different loads

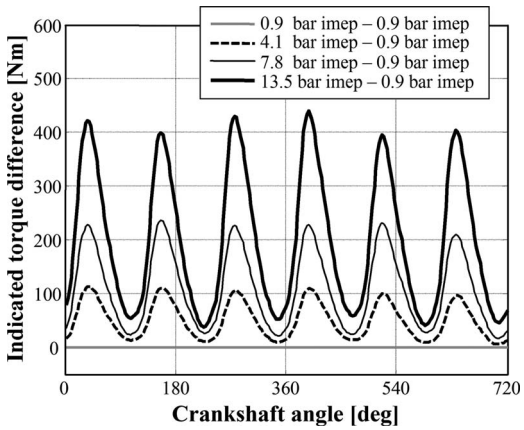

Fig. 11 Indicated torque difference for a V6 gasoline engine running at 2100 rpm and different loads

torques present opposite phases (as shown in Figs. 3–6), the corresponding phase of the engine speed oscillation will be different, depending on which torque component prevails.

Figure 9 shows the difference between indicated and reciprocating torques for the same tests reported in Figs. 7 and 8. Phase inversion is similar to what has been observed in the engine speed wave forms.

Following Eq. (15), the difference between each of the wave forms in Figs. 7 and 8 and the wave form obtained at 0.9 bar IMEP is performed. The results are reported in Figs. 10 and 11.

As is possible to observe, the wave forms reported in Fig. 10 do not show any influence by the reciprocating torque, as desired, and as expected following the approach presented in this study.

Amplitude and phase of the oscillations at Order 3 are finally evaluated, and the FRF value at 2100 rpm (105 Hz) can be determined. Repeating this process for other engine speeds, it is possible to obtain an estimation of the dynamic system FRF over the whole engine speed operating range.

Equation (16) allows finally estimating the reciprocating mass, giving a 0.820 kg value. Once M_{eq} and $F(j\omega)$ have been identified, it is possible to estimate the indicated torque frequency component from the corresponding engine speed oscillations, as it will be shown in the following.

The shape of the FRF suggests the presence of a resonance at a frequency lower than 80 Hz, since the ratio between the amplitude of the oscillation on the engine speed and the corresponding oscillation on the indicated torque (the inverse of the FRF amplitude reported in Fig. 12) increases as the frequency lowers.

The same path has been also followed for the L4 diesel engine mounted onboard the vehicle. In this case, the reciprocating torque components are much higher (Order 2 is considered instead of Order 3) and the interactions with the indicated torque are less trivial, as is possible to observe in Figs. 13 and 14.

It is possible to see that the phase of the engine speed oscillations at the engine order of interest (Order 2 for this engine) for the test at a lower load is opposite to the phase of the test at higher load. This is due again to the interaction between indicated and reciprocating torques, with reciprocating torque prevailing at low load and indicated torque prevailing at high load.

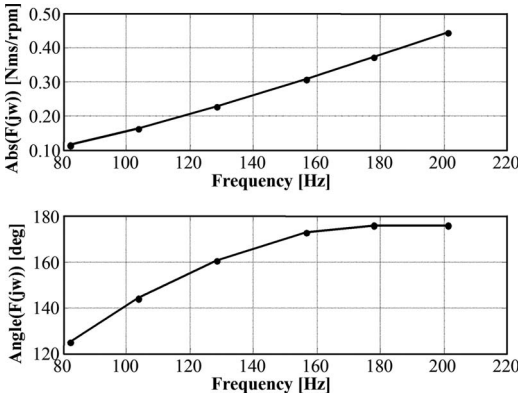

Fig. 12 Amplitude and phase of the identified FRF

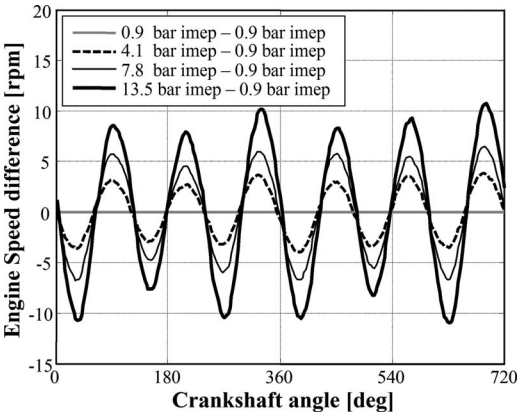

Fig. 10 Engine speed difference for a V6 gasoline engine running at 2100 rpm and different loads

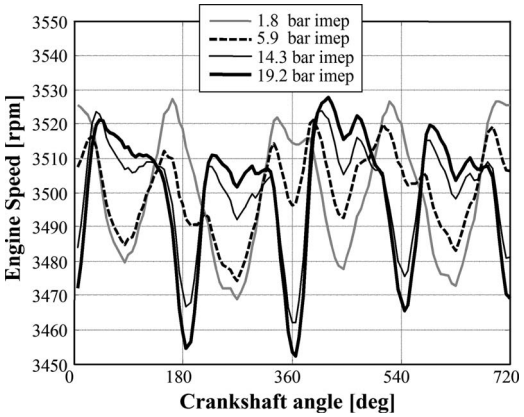

Fig. 13 Engine speed wave forms for an L4 diesel engine running at 3500 rpm and different loads (third gear)

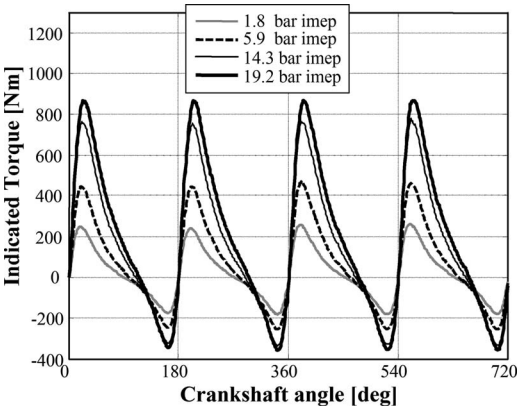

Fig. 14 Indicated torque wave forms for an L4 diesel engine running at 3500 rpm and different loads (third gear)

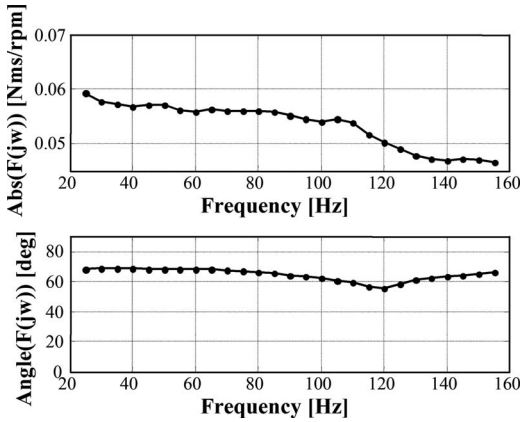

Fig. 17 Amplitude and phase of the identified FRF (third gear)

Considering the difference between the engine speed and the indicated torque wave forms for the tests in Figs. 13 and 14 and the corresponding wave form for the test at lower load, it is possible to eliminate the reciprocating torque influence, as suggested by Eq. (14) and confirmed by Figs. 15 and 16, where the results of the difference are reported.

Applying Eqs. (15) and (16), the FRF of the dynamic system has been identified (see Fig. 17), and the value of M_{eq} has been obtained (0.637 kg).

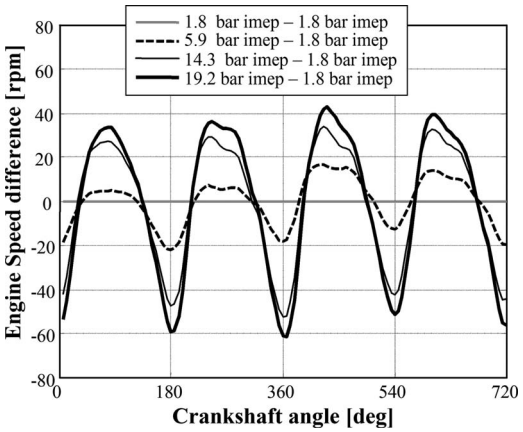

Fig. 15 Engine speed difference for an L4 diesel engine running at 3500 rpm and different loads (third gear)

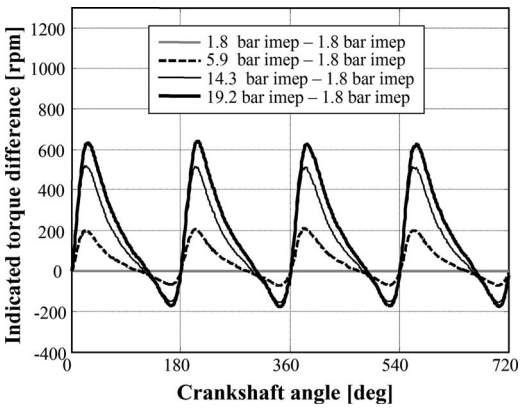

Fig. 16 Indicated torque difference for an L4 diesel engine running at 3500 rpm and different loads (third gear)

Ramp tests have been run on the same system in order to check the possibility of identifying the FRF in a quicker way. As already mentioned, Eq. (15) can be employed if at least two engine operating conditions at the same engine speed but at different loads are available. The tests have therefore been designed running the engine full load while increasing its speed, followed by a cutoff phase where the engine speed is decreased; the whole procedure has been repeated twice. Figure 18 shows the engine speed trace during the test run for FRF identification in the third gear.

The FRF identification gave results very similar to those presented in Fig. 17, and has therefore been repeated also for all the other gears, giving the results reported in Fig. 19. Differences on the FRF identified with the two methods employed in the third gear (steady-state tests and ramp tests) are lower than 1%. This confirmed the possibility to correctly identify the torsional model of the engine-driveline system even using the faster ramp tests, which are for this reason the preferred choice.

Figure 19 shows that changing the gear inserted the system behavior changes since the FRF depends on the inserted gear. This means that when the torque estimation algorithm will be employed onboard, the FRF will be gear dependent.

Identification of the torsional model of the system enables the estimation of the indicated torque frequency component at the engine order considered, from the corresponding engine speed frequency component. As already mentioned, this information will be used for mean indicated torque estimation. Figure 20 shows an example of the comparison between measured and estimated Order 2 indicated torque frequency component for the L4 diesel engine.

The transient tests considered have been conducted with the third gear inserted; torque estimation has been obtained using the FRF identified with the ramp tests. The RMSE obtained is equal to 4.8 N m, which is approximately 1% of the full scale value. This result is compatible with the accuracy required for onboard applications.

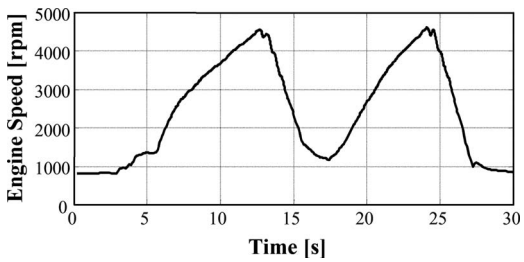

Fig. 18 Engine speed trace during the ramp tests run for FRF identification purposes

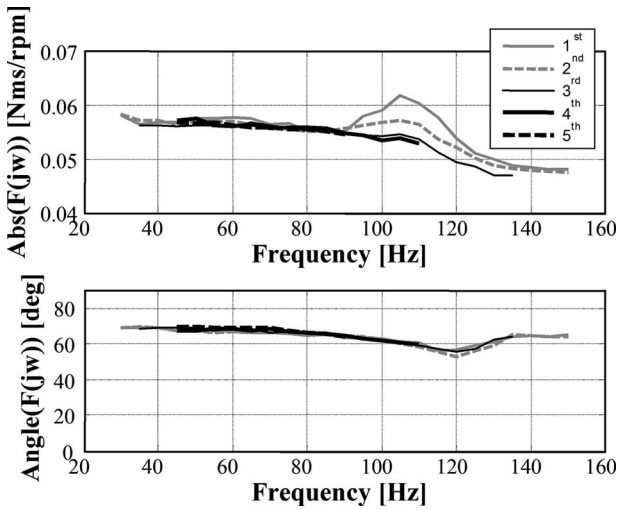

Fig. 19 Amplitude and phase of the identified FRF for different gears inserted

Similar results have also been obtained for the other engine-driveline configurations investigated. The accuracy obtained showed also to be compatible with the application of the model describing the relationship between indicated torque frequency component amplitude and its mean value.

Conclusions

This work presented the development of a torsional vibration model suitable for indicated torque estimation. The relationship between indicated and reciprocating torques applied to the crankshaft has been investigated, showing the effect of the two contributions over the engine speed oscillations. The proposed approach enables to identify the torsional model even if no information on the geometric characteristics of the system is available. Model identification, in fact, is on an experimental basis, and specific experimental tests have been designed to enable model identification.

Particular attention has been devoted to the applicability of the proposed procedure to different engine-driveline configurations and to the quick and simple execution of the required experimental tests. Different types of engines and different mountings have been studied, some of which have been presented in the paper. The results obtained always showed a good agreement with experimental data, and the overall accuracy seems to be compatible with the use of the model onboard.

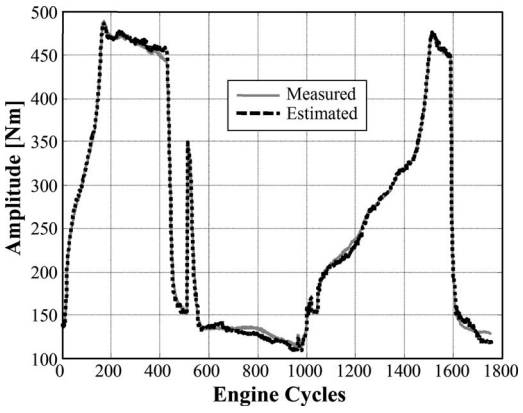

Fig. 20 Measured and estimated Order 2 indicated torque frequency component for the L4 diesel engine (third gear)

Nomenclature

ord = Engine order: the number of times a phenomenon occurs per crankshaft revolution
Z = number of cylinders
m = index identifying the mth cylinder
Ω = engine speed
Ω_{ord} = amplitude of the engine speed oscillation at engine order ord
ϕ_{ord} = phase of the engine speed oscillation at engine order ord
θ = crank angle
$\theta_{\text{TDC}m}$ = mth cylinder TDC crank angle position
θ_m = mth cylinder crank angle position
r = crank-slider mechanism radius
l = connecting rod length
A_p = piston area
$\lambda = r/l$ = crank-slider radius/connecting rod length ratio
$p_m(\theta_m)$ = relative pressure inside the mth cylinder

$$f(\theta_m) = \sin(\theta - \theta_{\text{TDC}m}) + \frac{\lambda \sin(2(\theta - \theta_{\text{TDC}m}))}{2\sqrt{1 - \lambda^2 \sin^2(\theta - \theta_{\text{TDC}m})}}$$

= crank-slider mechanism function for the mth cylinder
$T_{\text{ind}m}$ = indicated torque for the mth cylinder
M_{eq} = equivalent mass of the reciprocating masses
T_{rm} = reciprocating torque for the mth cylinder
ω = frequency
θ_{eng} = engine angular position
θ_{load} = load angular position
I_{eng} = engine inertia
I_{load} = load inertia
k_s = engine-load connection stiffness
c_s = engine-load connection damping
T_{load} = load torque
T_{eng} = torque applied to the engine
$F(j\omega)$ = engine-driveline system transfer function
$\hat{T}_{rm}$ = normalized reciprocating torque for mth cylinder
TDC = top dead center
CAD = computer aided design
MAP = manifold absolute pressure
ECU = electronic control unit
RMSE = root mean square error
IMEP = indicated mean effective pressure

References

[1] Iida, K., Akishino, K., and Kido, K., 1990, "IMEP Estimation From Instantaneous Crankshaft Torque Variation," SAE Technical Paper No. 900617.
[2] Moskwa, J. J., Wang, W., and Bucheger, D. J., 1998, "A New Methodology for Engine Diagnostics and Control Utilizing "Synthetic" Engine Variables: Theoretical and Experimental Results," *Proceedings of the ASME, Dynamic Systems and Control Division*, ASME, DSC-Vol. 64.
[3] Guezenec, Y. G., and Gyan, Ph., 1999, "A Novel Approach to Real-Time Estimation of the Individual Cylinder Combustion Pressure for S.I. Engine Control," SAE Paper No. 1999-01-0209.
[4] Citron, S. J., O'Higgins, J. E., and Chen, L. Y., 1989, "Cylinder by Cylinder Engine Pressure and Pressure Torque Waveform Determination Utilizing Speed Fluctuation," SAE Paper No. 890486.
[5] Ball, J. K., Bowe, M. J., Stone, C. R., and McFadden, P. D., 2000, "Torque Estimation and Misfire Detection Using Block Angular Acceleration," SAE Technical Paper No. 2000-01-0560.
[6] Taraza, D., 2001, "Statistical Correlation Between the Crankshaft's Speed Variation and Engine Performance—Part I: Theoretical Model," ASME J. Eng. Gas Turbines Power, **123**, pp. 428–432.
[7] Chauvin, J., Corde, G., Moulin, P., Castagné, M., Petit, N., and Rouchon, P., 2004, "Real-Time Combustion Torque Estimation on a Diesel Engine Test Bench Using Time-Varying Kalman Filtering," 43rd IEEE Conference on Decision and Control, Paradise Island, Bahamas, Dec. 14–17.
[8] Gani, E., and Manzie, C., 2005, "Indicated Torque Reconstruction From Instantaneous Engine Speed in a Six-Cylinder SI Engine Using Support Vector Machines," SAE Paper No. 2005-01-0030.
[9] Tong, Y., Li, J.-Q., and Zhang, J., 2004, "Coordinating Control-Oriented Re-

search on Algorithm of Engine Torque Estimation for Parallel Hybrid Electric Powertrain System," SAE Paper No. 2004-01-0424.
[10] Hamedovic, H., Raichle, F., Breuninger, J., Fischer, W., Dieterle, W., Klenk, M., and Böhme, J. F., 2005, "IMEP-Estimation and In-Cylinder Pressure Reconstruction for Multicylinder SI-Engine by Combined Processing of Engine Speed and One Cylinder Pressure," SAE Paper No. 2005-01-0053.
[11] Grunbacher, E., Kefer, P., and Del Re, L., 2005, "Estimation of the Mean Value Engine Torque Using an Extended Kalman Filter," SAE Paper No. 2005-01-0063.
[12] Li, J., Minggao, Y., Ming, Z., and Xihao, L., 2002, "Advanced Torque Estimation and Control Algorithm of Diesel Engines," SAE Paper No. 2002-01-0198.
[13] Jaine, T., Chamaillard, Y., Charlet, A., and Higelin, P., 2002, "High-Frequency Imep Estimation and Filtering for Torque- Based SI Engine Control," SAE Paper No. 2002-01-1276.
[14] Drakunov, S., Rizzoni, G., and Wang, Y.-Y., 1995, "On-Line Estimation of Indicated Torque in Ic Engines Using Nonlinear Observers," SAE Paper No. 950840.
[15] Maloney, P. J., 2004, "Embedded Torque Estimator for Diesel Engine Control Application," SAE Paper No. 2004-01-1371.
[16] Fam, M., and Hendriks, E., 2004, "A Load Torque Estimator," SAE Paper No. 2004-01-1372.
[17] Ponti, F., 2005, "Development of a Torsional Behavior Powertrain Model for Multiple Misfire Detection," ASME ICE 2005 Spring Technical Conference, Chicago, Apr., Paper No. ICES2005-1035.
[18] Ponti, F., 2005, "Indicated Torque Estimation Using a Torsional Behavior Model of the Engine," SAE Powertrain and Fuel Systems Conference and Exhibition, San Antonio, TX, Oct., Paper No. 2005-01-3761.
[19] Heywood, J. B., 1989, *Internal Combustion Engine Fundamentals*, McGraw-Hill, New York.
[20] Ligier, J. L., and Baron, E., 2002, *Acyclisme et Vibrations: Applications aux Moteurs Thermiques et aux Transmissions*, Publications de l'Institut Francais du Petrole, Ecole du Petrole et des Moteurs, Editions Technip, Paris.

Controlling Backfire for a Hydrogen-Fueled Engine Using External Mixture Injection

T. C. Huynh
J. K. Kang
K. C. Noh
Jong T. Lee

School of Mechanical Engineering,
Sungkyunkwan University,
Jangan-gu, Suwon 440-746, Korea

J. A. Caton
Department of Mechanical Engineering,
Texas A&M University,
College Station, TX 77843-3123

The development of a hydrogen-fueled engine using external mixture injection (e.g., using port or manifold fuel injection) with high efficiency and high power is dependent on the control of backfire. This work has developed a method to control backfire by reducing the valve overlap period while maintaining or improving engine performance. For this goal, a single-cylinder hydrogen-fueled research engine with a mechanical continuous variable valve timing system was developed. This facility provides a wide range of valve overlap periods that can be continuously and independently varied during firing operation. By using this research engine, the behavior of backfire occurrence and engine performance are determined as functions of the valve overlap period for fuel-air equivalence ratios between 0.3 and 1.2. The results showed that the developed hydrogen-fueled research engine with the mechanical continuous variable valve timing system has similar performance to a conventional engine with fixed valve timings, and is especially effective in controlling the valve overlap period. Backfire occurrence is reduced with a decrease in the valve overlap period, and is also significantly decreased even under operating conditions with the same volumetric efficiency. These results demonstrate that decreasing the valve overlap period may be one of the methods for controlling backfire in a hydrogen-fueled engine while maintaining or improving performance. [DOI: 10.1115/1.2940353]

Introduction

The combustion characteristics of hydrogen (such as wide flammability limits, fast burning velocities, and low ignition energy) enable engine operation, which results in high thermal efficiencies and low NO_x emission levels. Hydrogen-fueled engines may be divided according to the fuel supply method: (1) external mixture injection (e.g., using port or manifold fuel injection) and (2) direct-cylinder fuel injection [1–3]. A direct-cylinder fuel injection hydrogen engine is not typically subjected to backfire occurrence and typically has the potential for the highest power. Problems with a direct-cylinder fuel injection hydrogen engine, however, include a decrease in the thermal efficiency due to nonhomogeneity of the inlet mixture and the development of the high-pressure fuel injection system.

The advantages of a hydrogen engine with external mixture injection include potentially high thermal efficiency because of a more homogeneous inlet mixture, simplicity, and a lower-pressure fuel injection system. For a hydrogen engine with external mixture injection, however, backfire under higher load conditions may be a problem. If backfire can be eliminated, the hydrogen-fueled engine with external mixture injection will be a near-term possibility with high efficiency and high power [4–13].

The backfire phenomena of H_2-air mixtures in the intake system are often a result of backflow during the valve overlap period (VOP). During this overlap period, the H_2-air mixture may be preignited due to an ignition source in the combustion chamber. The flame due to this ignition is able to propagate backward into the intake system and causes the well-known backfire. Many researchers [4–8] have tried to prevent this backfire by using a number of methods. These methods have included (1) a decrease in the ignition source's temperature, (2) a decrease in the burning velocity, (3) lean burn techniques, and (4) a reduction in crevice volume and elimination of abnormal discharges. In general, these methods have not been universally successful for preventing backfire. Most of this previous work has described the difficulty of controlling the unknown ignition source and the rapid burning velocity.

As mentioned above, the causes of backfire may be divided into an unknown ignition source, fast combustion velocity and VOP. When the VOP is short enough, however, backfire may not occur even under high load operating conditions due to the fact that the preignited flame cannot flow backward into the inlet system. Consequently, backfire may be controlled with a decrease in the VOP, but this has not been clearly demonstrated yet. In addition, the trade-offs with respect to the engine performance are not known and need to be documented for reduced overlap periods.

The major objective of this investigation is to examine the feasibility of backfire control while maintaining or improving overall engine performance. To accomplish this objective, a single-cylinder research engine with a mechanical continuous variable valve timing (MCVVT) system (which permits a wide range of VOP to be continuously varied during engine operation) was developed and its basic performance was determined. Existence or nonexistence of backfire and overall engine performance were investigated as functions of the VOP by using the MCVVT hydrogen-fueled research engine. Experiments using the same amount of supplied energy for arbitrary fuel-air equivalence ratio were also completed to compensate for the fact that volumetric efficiency decreases for decreases in the VOP. Methods to obtain both high power and high efficiency for a hydrogen engine with external mixture injection were examined with respect to engine performance for different VOPs.

Experimental Apparatus and Method

Hydrogen-Fueled Engine and the MCVVT System. *Hydrogen-fueled engine with external mixture injection*. Figure 1 shows a photograph of the hydrogen-fueled research engine using external mixture injection with the MCVVT system. The crank mechanism and combustion chamber are modified from conven-

Contributed by the Internal Combustion Division of ASME for publication in the JOURNAL OF ENGINEERING FOR GAS TURBINES AND POWER. Manuscript received November 19, 2007; final manuscript received December 17, 2007; published online August 21, 2008. Review conducted by Dilip R. Ballal. Paper presented at the 2007 Fall Conference of the ASME Internal Combustion Engine Division (ICEF2007), Charleston, SC, October 14–17, 2007.

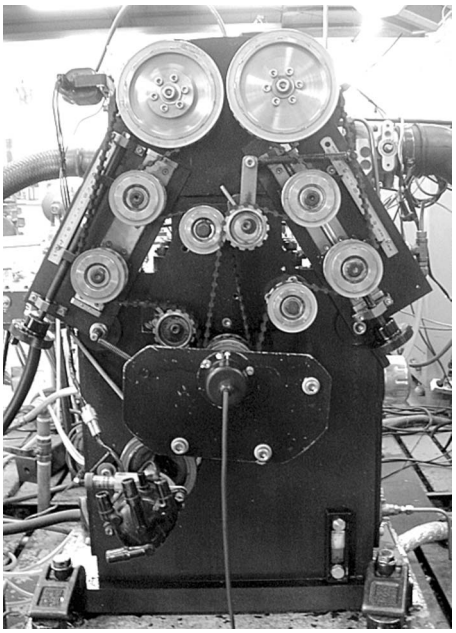

Fig. 1 Single-cylinder hydrogen-fueled engine with the MCVVT system

tional engine parts and their specifications are determined to allow for variable compression ratios for later work. Table 1 lists the main specifications of the MCVVT engine.

Characteristics of the MCVVT system. The operating principle of the MCVV is based on the fact that the phase angle of the fixed two pulleys (cam gears) is changed by the length of the belt contacted. To obtain the above effect in the structure using a fixed length of timing belt, a pair of pulleys are mechanically moved between the fixed two pulleys. The relation of the phasing angle and the displacement, and the detailed structure of the MCVVT system are presented in the Appendix.

Figure 2 shows the relation between the phasing angle of the camshafts and the displacement of the VVT gear. The valve timing can be controlled by the handle during engine operation, because the phasing angle of the camshaft is varied linearly as the timing gear moves.

Figure 3 shows the engine power with the MCVVT system compared with that under conventional operation for a range of engine speeds. The lower power for the case with the MCVVT system is noted at all engine speeds and is a reflection of the mechanical loss associated with the additional timing and idle gears, and other items of the MCVVT system. As the engine speed increases, the mechanical loss increases. The results of this investigation, however, are still considered to be relevant and will be able to demonstrate the feasibility of using changes of VOP to control backfire.

Experimental Setup. Figure 4 is a schematic of the experimental setup, which consists of the MCVVT hydrogen-fueled engine, the ac dynamometer, the hydrogen gas supply system, the cooling

Table 1 Specifications of the MCVVT engine

Engine	Four-cycle single cylinder
Bore × stroke	86 mm × 86 mm
Displacement volume	500 cc
Combustion chamber	Pent-roof type
Compression ratio	10.5:1
Valve timing control	MCVVT system
Cooling type	Water cooling

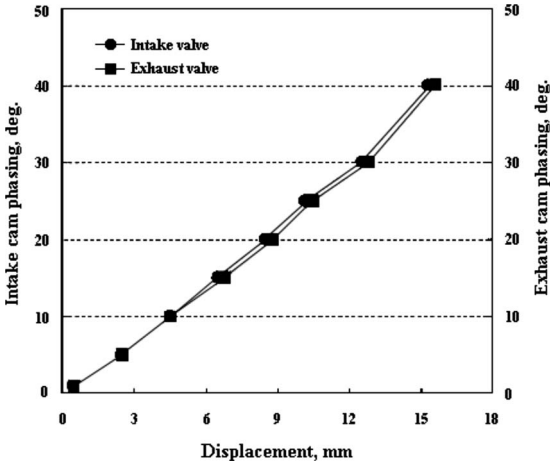

Fig. 2 Variation of intake/exhaust cam phasing with displacement of timing gears

system, the lubricant system, the injector control system, and the data acquisition system. Hydrogen gas (12–15 MPa) in the commercial high-pressure cylinder is decompressed to 1.5 MPa by a pressure regulator and is controlled to 0.3 MPa by a secondary precise regulator installed in front of a hydrogen mass flow meter. Hydrogen gas is then injected into the intake port by using a compressed natural gas (CNG) injector. Injection timing and injection duration can be adjusted by the injector control system. Airflow rate and hydrogen flow rate are measured by an orifice and a hydrogen mass flow controller (MFC/MFM Manager, FM-30V4), respectively. An electrical blower (supercharger) operated with external power is installed at the front of the inlet pipe to compensate for the decrease in the intake airflow mass due to the change in VOP. Two surge tanks of 200 l in volume are added in the front and rear of the airflow meter, respectively, to eliminate measurement error due to any pulsation of the air stream. In-cylinder pressure is monitored using a piezoelectric transducer (Kistler 6061-B) inserted in the cylinder head. For detecting inlet and exhaust pipe pressures, two piezoresistive transducers (Kistler 4045A-1.0 MPa and 0.5 MPa) are utilized, respectively. Coolant water is supplied to the modified cylinder head, the block, and the

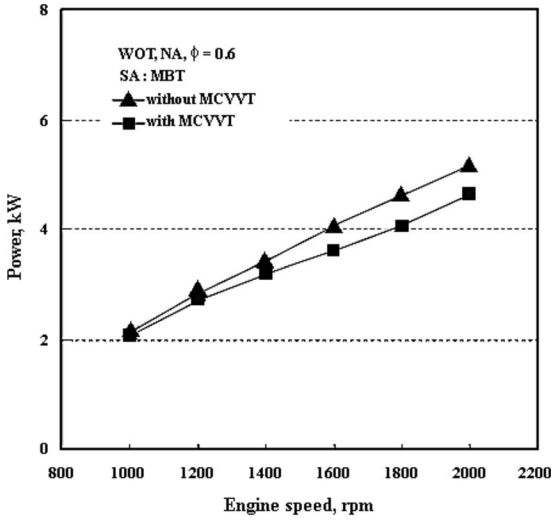

Fig. 3 Comparison of engine power with and without the MCVVT system as engine speed increases

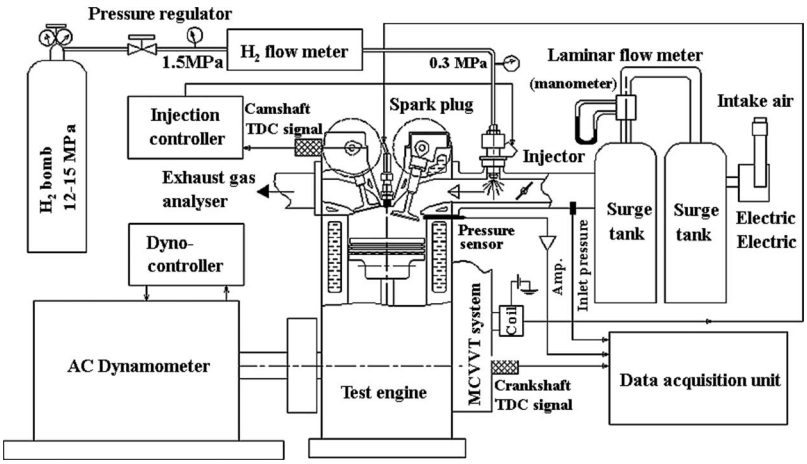

Fig. 4 Schematic of complete experimental system

oil cooler separately. The coolant temperature is controlled by coolant flow valve at the outlet and fixed at 70°C. The measured data were stored in a data acquisition unit.

Experimental Methods. The major experimental variable is the VOP. VOP is varied from 0 deg crank angle (CA) to 50 deg CA by 10 deg CA increments by changing the intake valve opening timing while keeping the exhaust valve closure timing fixed at 10 deg after top dead center (aTDC). Two major cases were examined: (1) unequal energy input and (2) equal energy input. The naturally aspirated cases resulted in unequal energy input due to changes in volumetric efficiency. To conduct experiments with the same supplied energy, the supplied energy was adjusted to compensate for the decrease in the volumetric efficiency as the VOP decreases. For each VOP, the fuel-air equivalence ratio is varied from the lean limit of $\phi=0.3$ (step=0.1) at which stable operation is ensured to a rich limit just before backfire occurs. The major objective is to determine how backfire is controlled and to determine the behavior of overall engine performance with the change in VOP. Most of the experiments are conducted at a fixed engine speed of 1600 rpm for wide-open throttle (WOT), and using minimum spark advance for the best torque (MBT). The test matrix is summarized in Table 2.

Table 2 Test matrix

Experimental cases	-Naturally aspirated -Equal energy input
Fuel-air equivalence ratio	0.3–1.2/step=0.1
Valve overlap period	0, 10, 20, 30, 40, 50
Engine speed	1600 rpm
Spark timing	MBT

Figure 5 shows examples of the pressure curves of in-cylinder and inlet pipe when backfire occurs. In the figure, the trace in Channel 2 displays the in-cylinder pressure curves for normal combustion, for backfire occurrence, and for misfiring cycles due to backfires. The trace in Channel 3 displays the pressure curve

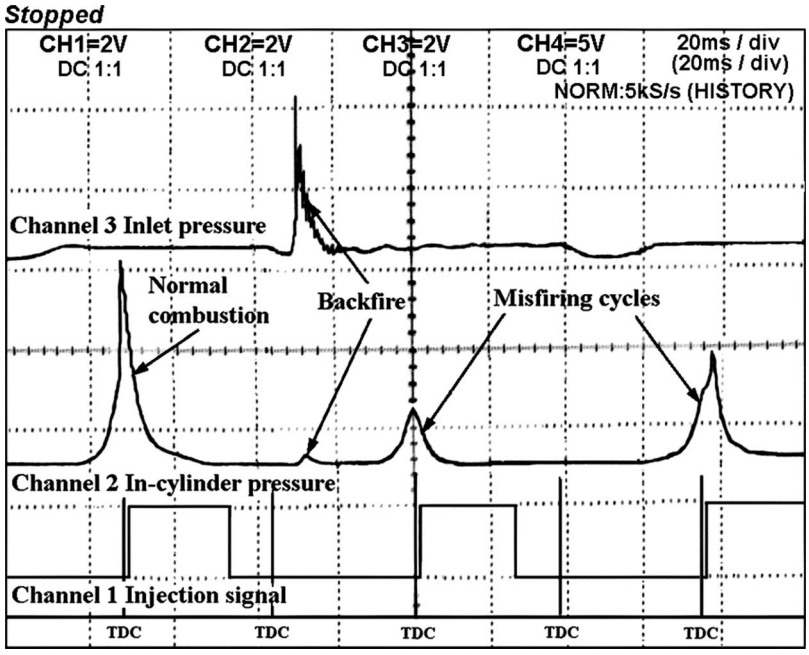

Fig. 5 Histories of cylinder pressure and inlet pressure once backfire occurs

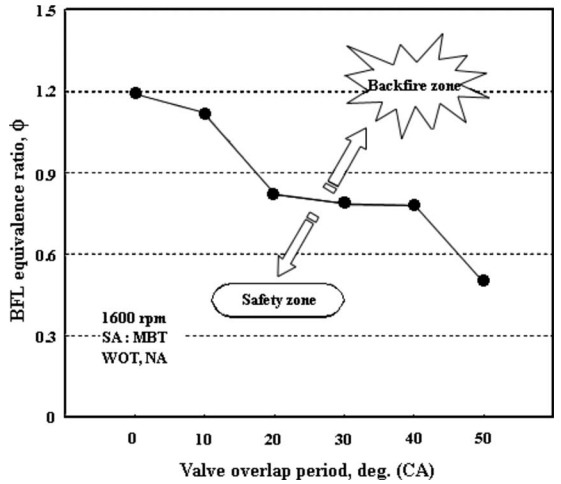

Fig. 6 The BFL equivalence ratio as a function of the VOP at 1600 rpm for naturally aspirated cases (energy input not equal)

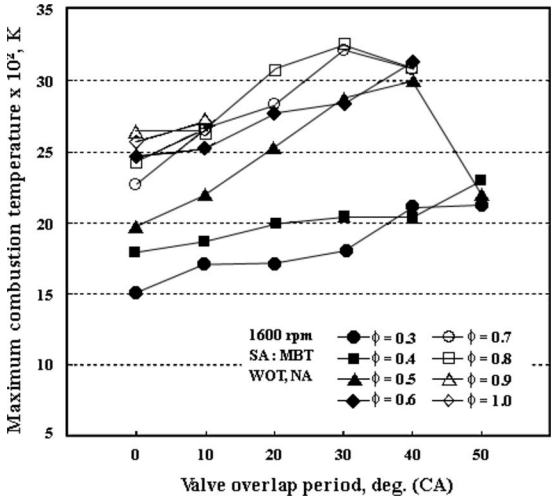

Fig. 8 Maximum combustion temperatures as functions of the VOP for each fuel-air equivalence ratio for naturally aspirated cases (energy input not equal)

for the inlet pipe as backfire occurs. This pressure information and the detection of backfire noise are used to estimate whether backfire occurs or not [2,3,5–8].

Results and Discussion

Cases of Unequal Energy Input. Figure 6 shows the backfire limit (BFL) equivalence ratio as a function of VOP for the hydrogen-fueled engine with external mixture injection. Here, the BFL equivalence ratio is defined as the maximum equivalence before backfire occurs (i.e., backfire occurs in the region above the curve). In the figure, as the VOP is reduced the BFL equivalence ratio increases continuously. Backfire could be controlled by limiting operation to equivalence ratios below the BFL value for each VOP. For the case of a VOP of 0 deg CA (where the VOP is zero), the BFL equivalence ratio is about 53% higher than for the case of a VOP of 30 deg CA where the maximum torque is obtained (maximum torque is shown below in Fig. 7). As mentioned above, the fact that the BFL equivalence ratio is higher for smaller VOP is caused by the decrease in the possibility of backflow of a preignited flame. As is generally known, however, the volumetric efficiency will be reduced for nonoptimum VOP values. So, the control of backfire by changing the VOP may reduce engine torque.

Figure 7 shows the brake torque as a function of VOP for a range of equivalence ratios. The maximum torque for the hydrogen-fueled engine with external mixture injection occurs for specific values of the VOP, which is similar to a conventional engine using gasoline. The torque decreases from the maximum value due to the decrease in intake duration or the backflow of fresh mixture. For these conditions, a VOP of 30 deg CA resulted in the maximum torque. The torque decreased most for decreasing the VOP compared with increasing the VOP based on the maximum torque for a VOP of 30 deg CA. This means that the volumetric efficiency is affected more by the reduction in the intake duration than by the backflow of new mixture.

The above results are for naturally aspirated conditions with unequal energy input. The overall gas and surface temperatures are expected to vary for these conditions. Figure 8 shows the maximum in-cylinder gas temperature as a function of the VOP for a range of equivalence ratios. Here, the gas temperature in the combustion chamber is determined by using the measured pressure and the thermodynamic equation of state. In this figure, the maximum temperature of the burned gas for the various VOP

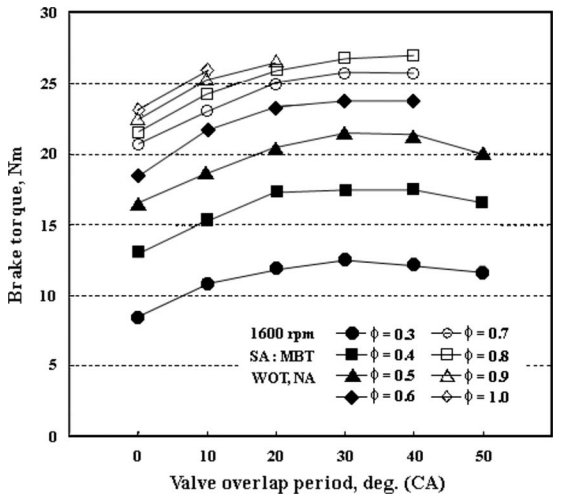

Fig. 7 Brake torque with respect to VOP for each fuel-air equivalence ratio for naturally aspirated cases (not equal energy input)

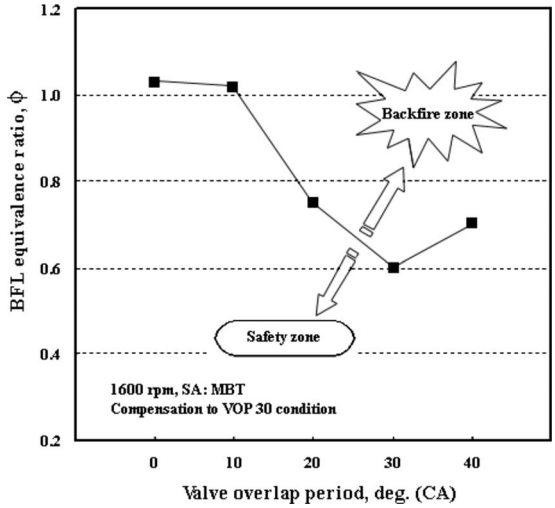

Fig. 9 The BFL equivalence ratio as a function of VOP for the case where the energy input is equal to the case for a VOP of 30 deg CA

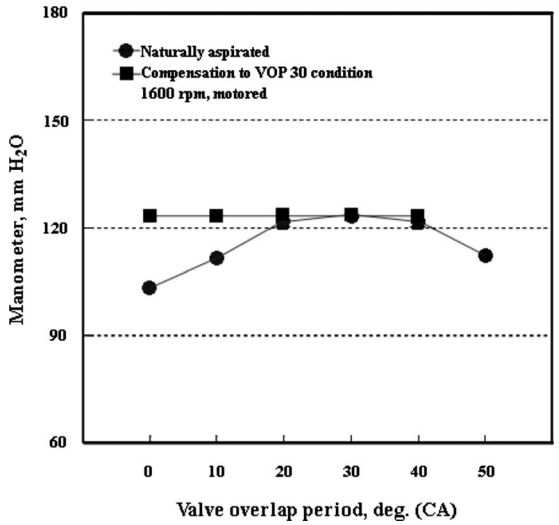

Fig. 10 Manometer reading for inlet mass flow rate as functions of VOP for naturally aspirated case (different supplied energy) and supercharged case (compensated case; i.e., supplied energy equal to the VOP of 30 deg CA case)

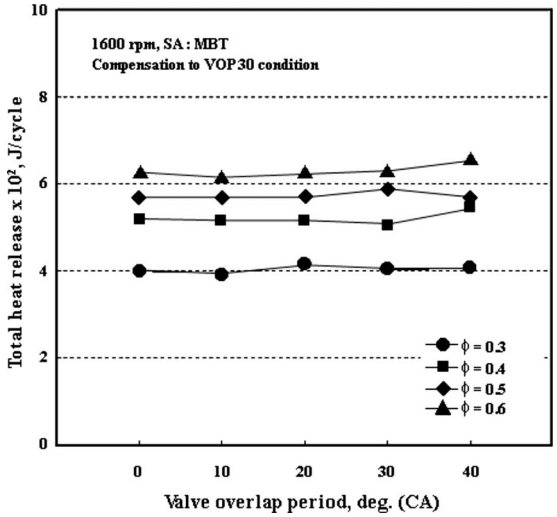

Fig. 12 Total heat release as a function of VOP for four equivalence ratios for supplied energy equal to the VOP of 30 deg CA

varies as the equivalence ratio is changed. The maximum difference of temperature between a VOP of 30 deg CA (which represents the maximum torque) and a VOP of 0 deg CA (whose BFL equivalence ratio is over ϕ=1.0) is about 1000 K. This implies that the higher BFL equivalence ratio for the smaller VOP may be caused by the reduction in volumetric efficiency due to the decreased intake period.

In Fig. 6, the fact that the BFL equivalence ratio is reduced in spite of a decrease in supplied energy when VOP is increased more than VOP 30 deg CA demonstrates that the period to flow backward is increased. The above results indicate that backfire occurrence may be understood and controlled for cases where the supply energy is kept constant.

Cases of Equal Energy Input. Figure 9 shows the BFL equivalence ratio as a function of VOP for equal energy input (energy input was equal to the case of VOP of 30 deg CA where the maximum torque appears). As shown, the BFL equivalence ratio increases as the VOP is decreased from 30 deg CA. This is similar to the results in Fig. 6 (for unequal energy input), which show that the volumetric efficiency changes as the VOP changes. For the case of increasing VOP from 30 deg CA to 40 deg CA, however, the BFL equivalence ratio has the opposite tendency and the BFL equivalence ratio increases. These results may be due to the fact that the counterflow possibility is decreased by the VOP decrease. Details of this observation follow.

Figure 10 shows the intake flow rate pressure differential for the laminar flow meter as functions of the VOP for the naturally aspirated cases and for the supercharged (equal energy input) cases. The intake flow rate pressure differential is represented by the difference of the water height of the airflow meter for full load with a speed of 1600 rpm. In the figure, similar to conventional engines, for the naturally aspirated cases, the intake air flow rate increases, reaches a maximum, and then decreases as the VOP increases. For these conditions, the intake air pressure differential is decreased by about 18% as the VOP is changed from 30 deg CA to 0 deg CA. As a result of this intake air flow rate decrease, the supplied energy is not constant. For the equal energy input cases, on the other hand, the intake air pressure differential could be kept at a constant value for all VOP values. In addition, the combustion stability seemed little changed for all cases—probably due to near constant mixture-mixing rate, flows in the cylinder, and turbulence intensities.

Figure 11 shows the combustion duration for five VOP values for the case of equal energy input (based on a VOP of 30 deg CA).

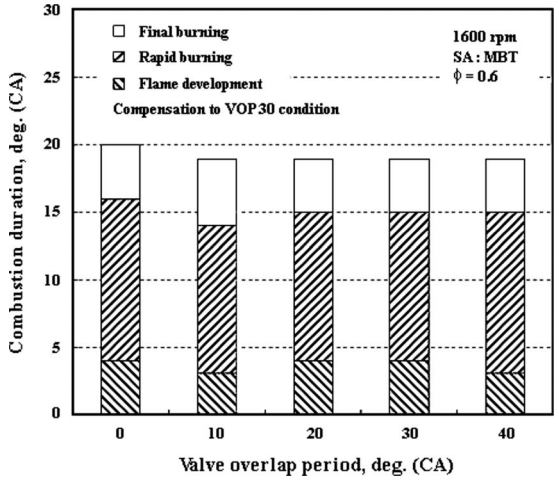

Fig. 11 Combustion duration as a function of VOP for supplied energy equal to the VOP of 30 deg CA

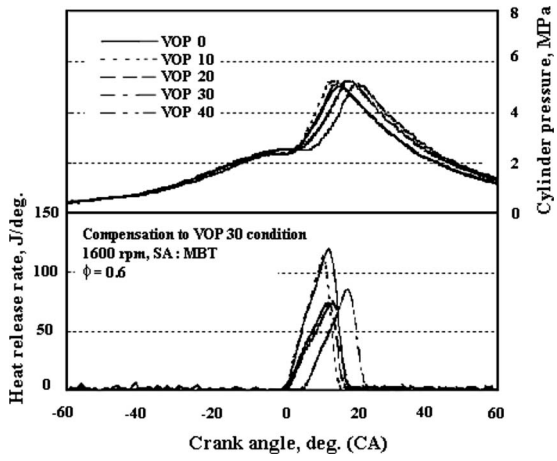

Fig. 13 In-cylinder pressure and heat release versus crank angle for each VOP with compensation to a VOP of 30 deg CA

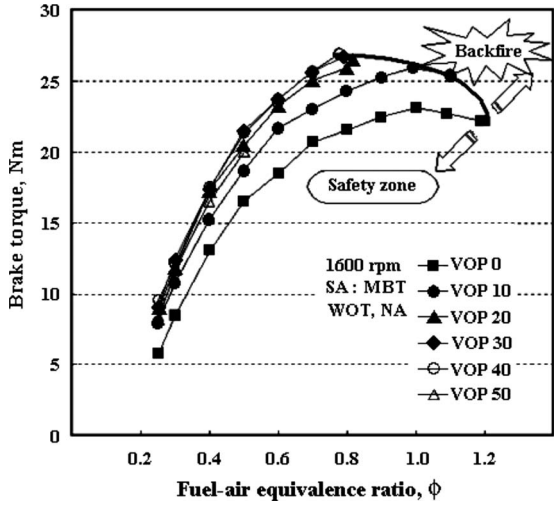

Fig. 14 Brake torque with increase in fuel-air equivalence ratio and limitation of backfire occurrence ratio for naturally aspirated cases (energy input not equal)

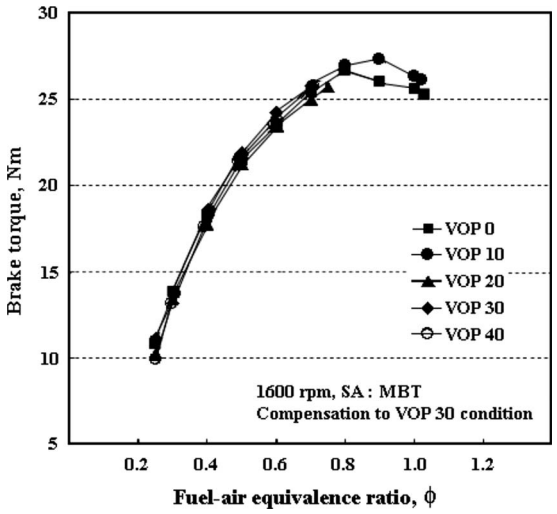

Fig. 15 Brake torque with increase in fuel-air equivalence ratio for equal energy compensation to a VOP of 30 deg CA

Here, the flame development angle is between 0% and 5% of the mass fraction burned and the rapid burning is between 5% and 95% of the mass fraction burned. In general, the combustion duration depends on the mixing rate, in-cylinder flow, turbulent intensity, and other items. For the same equivalence ratio, the combustion duration with VOP change shows little difference. This is because the change in VOP resulted in minimal variations of the mixing duration, inertial forces, and flow patterns. Although the combustion duration is nearly constant as the VOP changes, the tendency of increasing BFL equivalence ratio as the VOP decreases (see Fig. 9) means that decreasing backfire is caused by a reduction in the possibility of backflow of the flame into the intake system. Changes of the VOP, however, may change the ignition ability of the fuel-air mixture, and the combustion speed, because it changes the intake period, the inertia force of the gases, and the flow patterns [14,15,18,19]. For example, for a VOP of 0 deg CA, an increase in the BFL equivalence ratio is possible. Therefore, reducing the VOP has a high possibility for backfire control. More studies are needed, however, to examine the fundamental mechanisms of backfire for a wide range of operating conditions.

Figure 12 shows the total heat release as a function of VOP for four equivalence ratios for cases with equal energy input. The total heat release is nearly constant for the different VOP cases even in spite of the same amount of supplied energy. The VOP changes not only the intake duration but also the gas inertia force and the flow pattern of the inlet mixture, which changes the ignitability of the mixture and the combustion process. Recall (Fig. 9) that the BFL equivalence ratio increased as VOP increased from 30 deg CA to 40 deg CA. Hence, the possibility to control the backfire occurrence by decreasing VOP is complex, and more detailed studies are necessary to understand how to control the backfire mechanism for a variety of conditions.

Figure 13 shows the instantaneous in-cylinder pressure and heat release rate as functions of crank angle for the cases with energy compensation to the VOP of 30 deg CA. For the same experimental conditions of 1600 rpm, ϕ=0.6, and MBT, the variation of VOP affected the cylinder pressures and the heat release rates. It is suspected that the fluctuation of the flow patterns and the energy of flow charges that was caused by the change in VOP is the major reason for these tendencies. Also, it is found that the rate of heat release is higher at a VOP of 0 deg CA and a VOP of 10 deg CA than that with the other VOP values because of the significant increase in intake pressure due to supercharging.

Increase in Power by the Control of the Valve Overlap Period. Although the heating value of hydrogen is about 2.7 times higher than that of gasoline, the actual supplied energy of hydrogen is only about 85% compared to a gasoline engine due to the displacement of air by the hydrogen gas (which has a high specific volume). Furthermore, maximum engine power is further reduced by using lean mixtures for backfire control. So, research about BFL extension of hydrogen-fueled engines with external mixture injection has a secondary purpose: in addition to avoiding backfire, the possibility of increasing power. Figure 14 shows the brake torque as functions of equivalence ratio for six VOP values. By operating at specific VOP values according to each equivalence ratio, the possibility of increasing power by extension of the BFL equivalence ratio is demonstrated.

For the conditions of Fig. 14, the energy input is not equal. The figure shows the increasing tendency of brake torque for each VOP value with the increase in fuel-air equivalence ratio up to stoichiometric. For an increase in the equivalence ratio from stoichiometric to rich conditions, the brake torque decreases (refer to the curves of VOP of 0 deg CA and 10 deg CA). This result is suspected to be due to the incomplete combustion of the H_2-air mixture for the rich mixtures. At these VOP values, though the

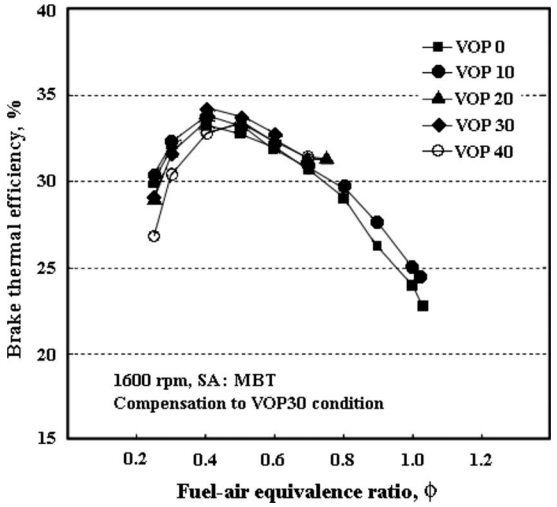

Fig. 16 BTE as a function of fuel-air equivalence ratio for equal energy compensation to a VOP of 30 deg CA

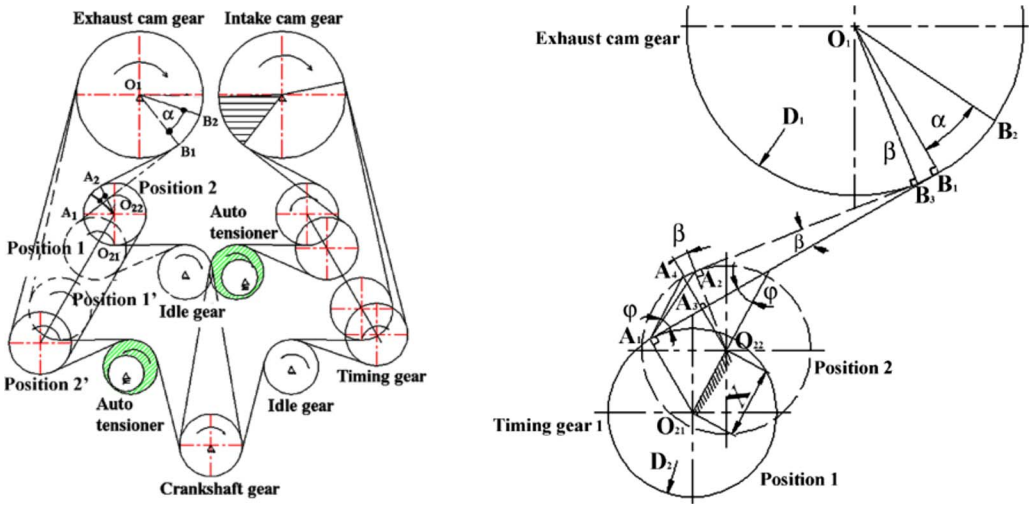

Fig. 17 Schematic of the MCVVT system

BFL equivalence ratio increases significantly, the engine power is found to be reduced by the decrease in the energy input or intake air quantity. At the BFL equivalence ratio of each VOP value, in fact, the power for the case of a VOP of 0 deg CA was about 13.1% less than that for the case of a VOP of 30 deg CA. The tendency of these results may be explained that, for naturally aspirated methods, the increase in the BFL equivalence ratio by the decrease in VOP has had an indirect effect on the diminution of the engine power. Thus, it seems to be difficult to improve the power in hydrogen-fueled engine with external mixture injection by the effect of expanding backfire suppression according to VOP change.

As a result of these findings, a supercharging method [16,17,20] is suggested to improve the power of hydrogen-fueled engine with external mixture injection at the above mentioned VOP values. Normally, backfire still occurs as the supercharging approach is employed. To avoid backfire, therefore, selecting the proper operating conditions with supercharging is important. In the next case, the authors tried to estimate whether the engine power can be increased by supercharging with the changes of VOP value in the same energy input with the specific VOP that gives the maximum power.

Figure 15 shows the brake torque as a function of fuel-air equivalence ratio for five VOP values. In this case, the same energy input as used for the VOP case of 30 deg CA was used for all VOP conditions. For cases such as this where the electric blower as a supercharger was used, the reported torque is the gross value (no subtraction for the supercharger). This effect was estimated to be insignificant. As shown, the torque is nearly independent of the VOP for these conditions (also, see Fig. 10).

As discussed above, the brake torque increases as the fuel-air equivalence ratio increases toward stoichiometric, and then decreases as the fuel-air equivalence ratio becomes greater than about 0.9. The same explanation as was used above for Fig. 16 applies here. Also, operating at a VOP of 10 deg CA gives the maximum brake torque at around ϕ=0.9. The maximum brake torque at a VOP of 0 deg CA is slightly less than that of VOP 10 deg CA due to the change in flow pattern with the change in VOP. The results show that both backfire control (which is obtained from the VOP change) and maximizing power output (by supercharging) can be obtained at the same time.

Figure 16 shows the brake thermal efficiency (BTE) as functions of the fuel-air equivalence ratio for five values of the VOP for the above conditions. As is well known, the thermal efficiency for hydrogen engines is highest in the lean burn region where the fuel-air equivalence ratio is between 0.4 and 0.5. This is because the hydrogen gas has good lean burn combustibility and the low burned gas temperatures reduce the relative importance of the cylinder heat transfer [21]. The thermal efficiency for the fuel-air equivalence ratio range of 0.4-0.5 is increased by around 39% compared to the stoichiometric case. The thermal efficiency decreases slightly due to the VOP decrease for the equivalence ratios associated with the maximum thermal efficiency. The amount of this decrease, however, is much smaller than that due to the equivalence ratio change.

Considering the above results, the power output improvement of a hydrogen-fueled engine with external mixture injection is enabled as the lean mixture raises the thermal efficiency and due to the supercharging for the cases of reduced VOP.

Summary and Conclusions

To evaluate the possibility of controlling backfire by changing the VOP, a hydrogen-fueled research engine with external mixture injection and a MCVVT system has been developed. This engine was used to determine the (BFL) equivalence ratio and basic engine performance as functions of the VOP. The results of this investigation may be summarized as follows:

- The hydrogen-fueled research engine with external mixture injection using the MCVVT system was shown to have similar performance to a conventional (fixed valve timing) engine, and it was shown to be an effective mechanism for changing the VOP during firing operation. This makes the quantitative experimental results reliable and forms the basis of the current study.
- Experiments were completed both for naturally aspirated cases and for supercharged cases. The latter cases permitted experiments with the same energy input for a range of VOPs. These cases were necessary for equal energy input since the mass of the intake charge decreased due to the change in VOP.
- For the naturally aspirated (not equal energy input) cases, the BFL equivalence ratio increased as the VOP shortened. For the experimental conditions studied, the maximum BFL equivalence ratio increased from 0.5 to 1.2 as the VOP decreased from 50 deg CA to 0 deg CA. These results show that the change in VOP enables the control of backfire occurrence.
- Although the BFL equivalence ratio was increased due to the decrease in VOP, the power decreased because the intake air decreased. The power can be restored, however, with the use of supercharging.
- For the cases of equal energy input, the BEL equivalence ratio increased from 0.6 to 1.03 as the VOP decreased from

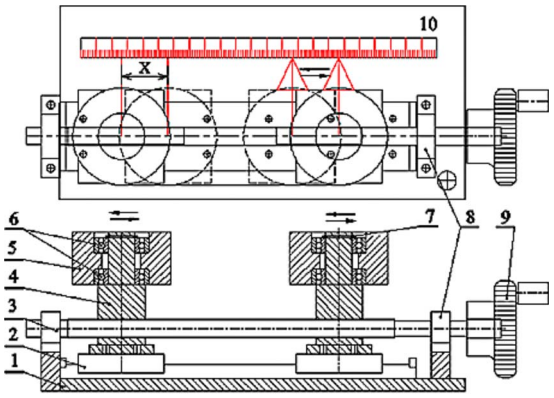

Fig. 18 The main components of the MCVVT system

30 deg CA to 0 deg CA. These results show that the change in VOP for equal energy input provides backfire control and maintains or improves engine performance.

- A method of controlling backfire by decreasing the VOP while maintaining power was demonstrated. Only a limited set of operating conditions was examined at this time. Future work will consider other combinations of the operating conditions to better define this approach, and will consider the important aspect of nitric oxide emissions.

Appendix: The Operating Concept and Detail Structure of the MCVVT System

Figure 17 shows the schematic of the MCVVT system. Valve timing is adjusted by the change in the angle of camshaft (α) as the VVT gear moves from Position 1 to Position 2 in the figure. The belt length between tangential points of belt and timing gear is not changed because when Timing Gear 1 moves from Position 1 to Position 2, the Timing Gear 2, which is installed on the opposite side, moves from Position 1′ to Position 2′. Based on this principle, the relation between the rotating angle of the camshaft and the displacement of the VVT gear is as follows:

$$\overline{A_1B_1} \approx \overline{A_2B_2} \tag{A1}$$

$$\overline{A_1B_1} = \overline{A_1A_3} + \overline{A_3B_1} = X\cos\varphi + \overline{A_3B_1} \tag{A2}$$

$$\overline{A_2B_2} = \overline{A_4B_1} + \frac{\pi}{360}(\alpha D_1 - \beta D_2) \tag{A3}$$

where X is the displacement of the timing gear and φ is the actual attached angle of the MCVVT system. α and β are the phasing angle of the camshaft and the phasing angle of the timing gear, respectively. D_1 and D_2 are the diameters of the camshaft gear and the timing gear, respectively.

From the above, the relation between the two angles is

$$X \approx 1.29\alpha - 0.63\beta \tag{A4}$$

The MCVVT is installed at the front of the two camshafts, and possesses the ability to control valve timing continuously and independently. Figure 18 shows the main components of the MCVVT system. The MCVVT system is composed of the driving shaft that consists of right-hand thread and left-hand thread, two timing gears (which can move in opposite directions), one idle gear, autotensioner, and the traverse device to move the timing gear straight. By setting off the change in the timing belt tension, the autotensioner maintains the tension of the timing belt due to the moving of Timing Gear 1.

References

[1] Lee, J. T., 1996, "Current Status and Characteristics of Hydrogen-Fueled Engine," J. Korea Soc. Automotive Engineers, **18**, pp. 29–52.

[2] Sierens, R., Verhelst, S., and Verstraeten, S., 2005, "An Overview of Hydrogen Fuelled Internal Combustion Engines," *Proceedings of International Hydrogen Energy Congress and Exhibition IHEC 2005*, Istanbul, Turkey, pp. 1–12.

[3] Kondo, T., Hiruma, M., and Furuhama, S., 1996, "A Study on the Mechanism of Backfire in External Mixture Formation Hydrogen Engine," *Proceedings of WHEC*, Stuttgart, Vol. 3, pp. 1547–1556.

[4] Yi, H., Min, K., and Kim, E. S., 1995, "Combustion Characteristics of Intake Port Injection Type Hydrogen Fueled Engine," Int. J. Hydrogen Energy, **20**, pp. 317–322.

[5] Lee, J. T., Kim, Y. Y., and Caton, J. A., 2006, "The Development of a Dual-Injection Hydrogen-Fueled Engine With High Power and High Efficiency," ASME J. Eng. Gas Turbines Power, **128**, pp. 203–212.

[6] Lee, J. T., Kim, Y. Y., Lee, C. W., and Caton, J. A., 2001, "An Investigation of a Cause of Backfire and Its Control Due to Crevice Volumes in a Hydrogen Fueled Engine," ASME J. Eng. Gas Turbines Power, **123**, pp. 204–210.

[7] Choi, H. K., Ahn, J. Y., Kim, Y. Y., and Lee, J. T., 1999, "A Basic Study on the Hydrogen Fueled Engine With Dual Injection," *Proceedings of Fifth KHES-HESS (Korean Hydrogen Energy Society–Hydrogen Energy System Society of Japan) Joint Symposium*, Taejon, pp. 237–248.

[8] Kim, Y. Y., Ryu, T. H., and Lee, J. T., 1998, "Backfire Occurrence by Abnormal Electric Discharge in Hydrogen Fueled Engine," *Proceedings of KHES Autumn Annual Meeting*, Jinju, May 29, pp. 105–115.

[9] Eichlseder, H., Wallner, T., Freymann, R., and Ringler, J., 2003, "The Potential of Hydrogen Internal Combustion Engines in a Future Mobility Scenario," SAE Technical Paper No. 2003-01-2267.

[10] Yamin, J. J., and Gupta, H. N., 2000, "Effect of Combustion Duration on the Performance and Emission Characteristics of a Spark Ignition Engine Using Hydrogen as a Fuel," Int. J. Hydrogen Energy, **25**, pp. 581–589.

[11] Lee, J. T., and Kim, Y. Y., 2002, "A Study on Development of a Dual Injection Hydrogen-Fueled Engine," *The Fifth International Symposium on Next Generation Vehicle Technology*, pp. 6–18.

[12] Wei, S. H., Kim, Y. Y., Kim, H. J., and Lee, J. T., 2001, "A Study on Transient Heat Transfer Coefficient of In-Cylinder Gas in the Hydrogen Fueled Engine," *KHES and HESS, The Sixth Korea-Japan Joint Symposium '01 on Hydrogen Energy*, pp. 85–104.

[13] Lee, J. T., Lee, S. Y., Kim, K. H., and Lee, J. C., 1988, "A Basic Study on the Development of Hydrogen Fueled Engine," *Proceedings of KSAE Spring Conference*, pp. 59–63.

[14] Sher, E., and Bar-Kohany, T., 2002, "Optimization of Variable Valve Timing for Maximizing Performance of an Unthrottled SI Engine—A Theoretical Study," Int. J. Hydrogen Energy, **27**, pp. 757–775.

[15] Nagumo, S., and Hara, S., 1994, "Study of Fuel Economy Improvement Through Control of Intake Valve Closing Timing: Cause of Combustion Deterioration and Improvement," JSAE Rev., **16**, pp. 13–19.

[16] Kesgin, U., 2004, "Effect of Turbocharging System on the Performance of a Natural Gas Engine," Energy Convers. Manage., **46**, pp. 11–32.

[17] Clarke, D. P., Such, C. H., Overington, M. T., and Das, P. K., 1992, "A Lean Burn Turbocharged, Natural Gas Engine for the US Medium Duty Automotive Market," SAE Paper No. 921552.

[18] Soderberg, F., and Johansson, B., 1997, "Fluid Flow, Combustion and Efficiency With Early or Lately Inlet Valve Closing," SAE Paper No. 972937.

[19] Tuttle, H. J., 1982, "Controlling Engine Load by Means of Early Intake-Valve Closing," SAE Paper No. 820408.

[20] Leonard, H. J., and Stone, C. R., 1991, "Parameter Investigation of Variable Valve Timing Applied to a Turbocharged Diesel Engine," SAE Paper No. 910453.

[21] Caton, J. A., 2006, "First and Second Law Analyses of a Spark-Ignition Engine Using Either Isooctane or Hydrogen," *Proceedings of the 2006 Fall Conference of the ASME Internal Combustion Engine Division*, Sacramento, CA, Nov. 5–8.

Prediction of Combustion Parameters, Performance, and Emissions in Compressed Natural Gas and Gasoline SI Engines

Mirko Baratta
Andrea E. Catania
Stefano d'Ambrosio
Ezio Spessa

IC Engines Advanced Laboratory,
Dipartimento di Energetica,
Politecnico di Torino,
C.so Duca degli Abruzzi,
24 10129 Torino, Italy

The simulation of heat release, flame propagation speeds, and pollutant formation was carried out in both a turbocharged compressed natural gas (CNG) engine and a multivalve naturally aspirated bifuel engine running on either CNG or gasoline. The predictive tool used for investigation is based on an enhanced fractal geometry concept of the flame front, which is able to capture the modulation of turbulent to laminar burning speed ratio throughout the overall combustion phase without introducing flame kernel growth or burnout submodels. The prediction model was applied to a wide range of engine speeds, loads, relative air-fuel ratios, and spark advances, and the obtained results were compared to experimental data. These latter were extracted from measured in-cylinder pressure by an advanced diagnostics technique that was previously developed by the authors. The results confirmed a quite accurate prediction of burning speed even without any kind of tuning, with respect to different currently available fractal as well as nonfractal approaches for the simulation of flame-turbulence interaction. Furthermore, the computational code proved to be capable of capturing the effects of fuel composition, different combustion-chamber concepts, and operating conditions on engine performance and emissions. [DOI: 10.1115/1.2943193]

Introduction

Renewed interest in SI engine combustion optimization and model-based control strategies has been aroused by the need of pollutant emission reduction and conversion efficiency increase over the last years, thus stimulating considerable research and development activities [1,2]. To achieve these objectives and also to reduce the dependence of the transportation sector on oil supplies, a broader use of alternative fuels, such as compressed natural gas (CNG), hydrogen-CNG blends as well as biofuels, is forecasted in the short and medium term, particularly for urban transportation [3–5].

The development and optimization of advanced engine concepts that are capable of simultaneously reducing pollutant emissions and fuel consumption, as well as the need of fully exploiting natural gas potential, require a better knowledge of basic combustion processes taking place in IC engine chambers.

Accurate and fast computational tools for the simulation of indicated-cycle performance parameters [6–17] are essential to engine design and control, especially when the development of advanced combustion systems is the main objective, involving a significant number of variables to be optimized.

For achieving satisfactory predictive capability, simulation codes require an accurate heat-release prediction, which, in turn, involves the evaluation of in-cylinder turbulence generation and flame-turbulence interaction. To that end, a major role is played by the use of reliable flame propagation models in conjunction with semiempirical correlations involving readily obtainable geometrical and thermodynamical quantities.

With reference to operating conditions that are relevant to SI engines fueled by conventional or alternative fuels, the task of critically comparing in-cylinder flame propagation speeds as obtained by different correlations and from experimental results has recently been undertaken in Ref. [18].

Present Work

Combustion modeling is a fundamental feature of engine simulation codes. Its primary objective is to predict the rate of heat release and hence the in-cylinder pressure evolution, which will be employed for subsequent calculations. The key point of such a design characteristic is the evaluation of the mass that is instantaneously entrained across the flame front. Basically, two approaches have been applied up to now in order to determine the combustion evolution in SI engines. The first one consists in imposing a burn profile that approximates the almost S shape of experimentally observed burn rates, i.e., the Wiebe function. The main attractiveness of this is its completely straightforward application, which does not require either any information about combustion-chamber geometry or any evaluation of in-cylinder turbulence intensity levels and flame-turbulence interaction. The second approach, which was first proposed in Ref. [7], determines the rate of mixture burning through the calculation of both turbulent flame speed and flame front area, according to the following expression:

$$dx_b = \frac{1}{m}\rho_u A_{bf} S_b \frac{d\theta}{\omega} \tag{1}$$

where m is the in-cylinder trapped mass, ρ_u is the unburned-gas density, A_{bf} is the flame front area, S_b is the turbulent flame speed, and ω is the engine speed. The attractiveness of this latter procedure is that the model is based on physical principles and can take changes of combustion-chamber geometry, in-cylinder flow, mixture properties, and spark timing into account. Besides, it can provide spatial resolution about the instantaneous flame location required for heat-transfer calculation. The approach in Ref. [7] was further extended and refined in Refs. [8–12], and was applied for different studies in the SI engine field [13–17].

Contributed by the Internal Combustion Division for publication in the JOURNAL OF ENGINEERING FOR GAS TURBINES AND POWER. Manuscript received January 28, 2008; final manuscript received February 8, 2008; published online August 21, 2008. Review conducted by Dilip R. Ballal.

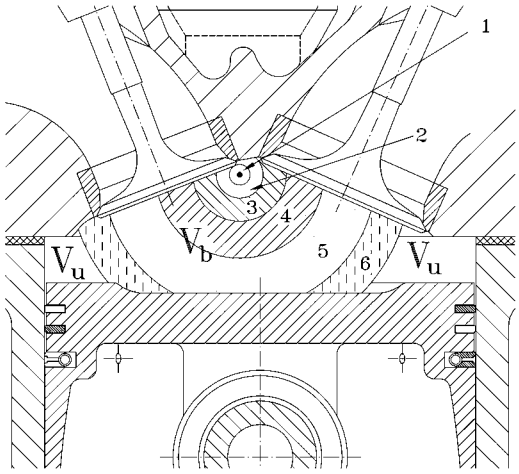

Fig. 1 Burned (V_b) and unburned (V_u) region volumes in the 2000 cc 16 V engine combustion chamber

The present paper is concerned with the refinement and application of the quasidimensional simulation model that was previously developed in Ref. [16]. The original burning speed model, based on a fractal geometry concept [18], was generalized and embedded in the prediction code. It is capable of capturing the modulation of turbulent- to laminar-flame speed ratio throughout the overall combustion phase without introducing flame kernel growth or burnout submodels.

The simulation of heat release, burning velocity, indicated-cycle pressure in the closed-valve phase, and pollutant formation was carried out both for a 1200 cc 8 V turbocharged (TC) CNG engine and for a 2000 cc 16 V naturally aspirated (NA) bifuel engine running on either gasoline or natural gas.

An insight is also given into the problem of modeling in-cylinder turbulence, as the proper evaluation of the turbulence level is required for an accurate computation of the turbulent burning speed. The advantages and drawbacks of the widely used *K-k* model of Poulos and Heywood [9] are discussed, when the model is either coupled with the angular-momentum conservation hypothesis [9,13] or includes a rather equivalent compression-related source term [15,17].

The predictive model was used for a wide range of engine speeds (N=2000–5500 rpm), loads (bmep=200–790 kPa for the NA engine, and bmep=200–1400 kPa for the TC one), relative air-fuel ratios (RAFR=0.80–1.60), spark advances (SA ranging from an advance of 8 deg to a retard of 8 deg with respect to MBT) and the related results were compared to experimental based data. These latter were extracted from the measured in-cylinder pressure through a previously developed advanced diagnostics technique [19].

Combustion Simulation Model

The quasidimensional, multizone, predictive program was extensively discussed in Ref. [16]. The engine charge is split into the unburned zone and the burned region, which in turn is divided into additional zones. Each of these burned zones is generated at a specified crank angle during combustion and no mixing is allowed to occur between them, so that temperature gradients take place across the chamber. As an example, Fig. 1 shows a schematic of the 2000 cc 16 V NA engine, where the combustion-chamber volume is divided into the unburned-gas zone (V_u) and the burned-gas region (V_b), which is split in six zones. A number of burned zones up to 10 were required for an accurate prediction of NO, i.e., the most sensitive quantity to such parameter [19].

Turbulent Flame Speed Submodel. As is well known, the fractal approach to model turbulence-flame interaction is based on both fractal and laminar flamelet concepts [18,20–22], to represent turbulent premixed flames.

In this work, the following generalized form of the relation to calculate the S_b/S_L ratio is proposed:

$$\frac{S_b}{S_L}=\left(\frac{\rho}{\rho 0}\right)^n\left(\frac{C_L\sqrt{A_{\mathrm{bf}}}}{C_L(h_{\min}+S_p)\left[\dfrac{u'C_L(h_{\min}+S_p)}{\nu}\right]^{-3/4}}\right)^{D-2} \tag{2}$$

where A_{bf} is the surface area of the burning front, D is the flame front fractal dimension, $h_{\min}$ is the chamber clearance at TDC, n is a modulation exponent, S_p is the instantaneous distance of the piston crown from its TDC position, u' is the turbulence intensity, and ν is the kinematic viscosity of the unburned-mixture. C_L is expressed as a function of the engine speed in [16,18] and can be considered of general application for the mentioned fuels.

As pointed out in Ref. [18], an improved modulation of S_b/S_L is obtained by estimating the so-called outer cutoff length scale of turbulence through the square root of the burning front area, and a further improvement is given by the multiplier ρ/ρ_0, which is replaced by $(\rho/\rho_0)^n$ in Eq. (2). In Refs. [16,18], the average charge density ρ_0 was evaluated at the end of the flame-development interval $\Delta\theta_{0-1\%}$. However, in the present work, it was established that ρ_0 has to be evaluated at a fixed crank angle, which changes from one engine to another but, for a given engine, keeps the same value at all the operating conditions. In particular, such a selection has a sensibly positive effect on the variation of S_b/S_L modulation whenever a change in any engine operating variable is introduced. The criteria to select the reference crank angle for the evaluation of ρ_0 will be discussed later on. It can be stated that, in general, the advance of this crank angle with respect to the combustion TDC decreases as the engine compression ratio increases.

The exponent n was introduced in Eq. (2) in order to further improve the S_b/S_L modulation. As a matter of fact, although the modulation given by $\sqrt{A_{\mathrm{bf}}}$ and ρ/ρ_0 is noticeable, an extensive comparison between the experimental and numerical data showed that a better fit can be obtained with n=1.25, for both engines. Such a value of n is virtually independent of engine operating conditions and most likely can be considered as a fixed quantity for different engines.

Hence, different from other models [14,15], Eq. (2) has virtually only one parameter that needs to be fitted for a specific engine, i.e., the crank angle at which ρ_0 should be evaluated.

In addition to the turbulence-flame interaction modeling, the computation of S_b involves also the in-cylinder turbulence evaluation. In the developed prediction tool, a turbulence model based on the zero dimensional energy cascade from mean flow to viscous eddy dissipation has been applied [9]. The ordinary differential equations for the temporal evolution of the mean flow kinetic energy K($K=1/2mU^2$) and of the turbulence kinetic energy k($k=3/2mu'^2$) can be written as follows:

$$\frac{dK}{dt}=\frac{1}{2}\dot{m}_i\nu_i^2-P-K\frac{\dot{m}_o}{m} \tag{3}$$

$$\frac{dk}{dt}=P-m\varepsilon-k\frac{\dot{m}_o}{m} \tag{4}$$

where $\varepsilon\cong u'^3/L_i$ is the dissipation rate of the turbulent kinetic energy per unit mass, $L_i=V/\pi B^2/4$ being the characteristic size of large-scale eddies, subject to the restriction $L_i\leqslant B/2$; m is the in-cylinder mass; $\dot{m}_i$ the mass-flow rate entering the cylinder with a jet velocity ν_i, $\dot{m}_o$ the mass-flow rate out of the cylinder, and P the rate of turbulent kinetic energy production. This latter is provided by the following empirical relation:

$$P = 0.3307 c_\beta \frac{K}{L_i}\left(\frac{k}{m}\right)^{1/2} \tag{5}$$

The turbulent dissipation constant c_β is adjusted to give the expected profiles of u' and U throughout the whole cycle [18].

The numerical integration of Eqs. (3)–(5) is carried out from IVO to SA. As soon as the combustion starts, the evolution of the turbulence intensity and of its spatial integral scale is calculated by assuming conservation of angular momentum for large-scale eddies. This assumption requires that the following relations hold after ignition:

$$\frac{L_i}{L_{i0}} = \left(\frac{\rho_{u0}}{\rho_u}\right)^{1/3} \tag{6}$$

$$\frac{u'}{u'_0} = \left(\frac{\rho_u}{\rho_{u0}}\right)^{1/3} \tag{7}$$

In particular, it is worth pointing out that the accuracy of a turbulent burning-speed model is considerably dependent on the unburned-gas turbulence evolution during combustion, which is normally thought to present a maximum near firing TDC [6,9,13]. Although the magnitude of such a maximum is dependent on the configurations of the combustion chamber and, to a lesser extent, of the intake system, among other factors, its presence is generally modeled by means of heuristic approaches that add turbulence during compression and combustion. An example of such approaches is given by the conservation assumption of angular momentum, i.e., by Eqs. (6) and (7). Recently, Eqs. (3) and (4) have been modified as follows [15]:

$$\frac{dK}{dt} = \frac{1}{2}\dot{m}_i \nu_i^2 - P - K\frac{\dot{m}_o}{m} + K\frac{\dot{\rho}}{\rho} \tag{8}$$

$$\frac{dk}{dt} = P - m\varepsilon - k\frac{\dot{m}_o}{m} + k\frac{\dot{\rho}}{\rho} \tag{9}$$

The last terms in Eqs. (8) and (9) are compression-related terms, which take the density variation in the cylinder throughout the compression and expansion strokes into account. If such terms are introduced in the *K-k* model equations, these have to be integrated also through the combustion phase [15]. During the discussion of the simulation results, a comparative insight will be provided into these two almost equivalent approaches.

Laminar-Flame Speed Submodel. The above described turbulent flame speed model is applied for evaluating the burning speed increase due to the turbulent motion conditions that occur in the engine combustion chamber. Therefore, a laminar-flame speed model is required in order to calculate the absolute value of S_b starting from the values of S_L and S_b/S_L ratio.

In the developed combustion simulation code, the laminar burning velocity is evaluated by means of the following power law correlation [6,22,23]:

$$S_L = S_{L,0}\left(\frac{T_u}{T_0}\right)^\alpha \left(\frac{p}{p_0}\right)^\beta (1 - 1.5x_{\text{res}}) \tag{10}$$

in which T_0=298 K and p_0=1 atm are reference temperature and pressure; $S_{L,0}$, α, and β are constant values for a given fuel and RAFR. The reduction of S_L that is caused by the presence of residual burned gas in the unburned cylinder charge is taken by the factor $(1-1.5x_{\text{res}})$ into account. In reality, α and β are independent of the fuel type within the estimated experimental error and can be expressed by [6,22]

$$\alpha = 2.18 - 0.8\left(\frac{1}{\text{RAFR}} - 1\right) \tag{11}$$

$$\beta = -0.16 + 0.22\left(\frac{1}{\text{RAFR}} - 1\right) \tag{12}$$

The reference velocity $S_{L,0}$ is a function of the fuel type. For gasoline, it can be fitted by a second-order polynomial of the form [6]

$$S_{L,0} = 0.305 - 0.549\left(\frac{1}{\text{RAFR}} - 1.21\right)^2 \tag{13}$$

where $S_{L,0}$ is given in m/s. With reference to CNG operations, this equation is not adequate [6] and therefore the following correlation was used [23,24]:

$$S_{L,0} = 0.369 - 2.10\left(\frac{1}{\text{RAFR}} - 1.12\right)^2 - 3.35\left(\frac{1}{\text{RAFR}} - 1.13\right)^3 \tag{14}$$

Initial Conditions. For starting the combustion calculation, the model requires pressure, temperature, and chemical composition of the charge at spark timing, as well as the x_b value of the first ignited mass.

The charge is taken to be a homogeneous mixture of air, fuel, and residual gas. For the given fuel, the air-fuel ratio is set to its measured value and the residual-fuel ratio is estimated by the procedure referred to in Ref. [6]. Hence, from experimental or thermodynamically evaluated conditions at IVC, the simulation program applies the energy conservation equation for the whole unburned-gas charge and calculates pressure and temperature at each crank angle until spark discharge occurs [16].

The flame kernel growth following spark discharge, i.e., the process during which the energy release is so small that the combustion effect on pressure rise is negligible, depends on several random variables whose prediction is a very challenging task. Hence, the flame kernel growth was not modeled in the code, but global effects were considered by means of a lumped parameter, i.e., the crank-angle interval $\Delta\theta_{0-1\%}$ between SA and the angle at which 1% of the cylinder mass has burned. More specifically, $\Delta\theta_{0-1\%}$ was determined according to the following quite general correlation [25]:

$$\Delta\theta_{0-1\%} = a[1 + b(\text{RAFR} - \text{RAFR}_0)^2] p_{\text{SA}}^{-c} \exp(d/T_{u,\text{SA}}) \tag{15}$$

in which the coefficients a, b, c, and d were experimentally evaluated for each fuel as is detailed in Ref. [25], resulting almost the same for the two considered engines, RAFR_0 is the relative air-fuel ratio at which S_L has a peak, p_{SA} and $T_{u,\text{SA}}$ are the pressure and unburned-gas temperature, respectively, at spark timing.

In order to correctly initialize the calculation, it is necessary to have not only information about the interval $\Delta\theta_{0-1\%}$, but also a reliable estimation of the related burned-gas temperature and volume. For this reason, the energy conservation equation has to be applied also during the flame-development interval, in which an appropriate osculating polynomial of the actual burned-gas mass fraction evolution is postulated.

From a theoretical point of view, the proposed fractal model is capable of capturing physical phenomena in the early phase of flame propagation, because it can extrapolate an S_b/S_L value of nearly unity as the burning flame-front radius r_{bf} approaches 0, according to the flame propagation theory [16,18]. Therefore, it is possible to apply the fractal model starting before the $\theta_{1\%}$ crank angle. In particular, one can start the model application when, say, x_b=0.1%. However, as will be examined further on, better results can generally be obtained if such x_b threshold is set to 1%.

Test Engines and Experimental Setup

As already mentioned, the model prediction capability was evaluated with reference to two different engines, for which the experimental data on performance and emissions were available. The first engine was a NA, multivalve (i.e., 16 V), variable intake system (VIS), bifuel (gasoline—CNG) engine, with a pent-roof type combustion chamber and tumble inducing inlet ports [26].

Table 1 Main engine specifications

	2000 cc 16 V NA	1200 cc 8 V TC
Cycle	Otto, four stroke	Otto, four stroke
Cylinder number	4, in-line	4, in-line
Bore	84 mm	70.4 mm
Stroke	90 mm	78.8 mm
Compression ratio	10.35	10.1
Displacement	1995 cm^3	1242 cm^3
Distribution	two OHC, four valves per cylinder	one OHC, two valves per cylinder
Air induction	NA, VIS	Turbocharger controlled by waste-gate valve, intercooler

The second engine was a prototype downsized TC CNG engine ([27]). Main engine specifications are reported in Table 1.

The engines were operated on a test bench that had been previously installed and instrumented in a soundproof hall for typical engine dynamometric measurements. More specifically, the test rig was equipped with a "Borghi and Saveri" eddy-current dynamometer, a "Degussa-Hartmann and Braun" hot-film air-mass sensor within the induction system, two "MicroMotion" Coriolis mass-flow meters installed in the fuel distribution pipes for measurements of gasoline and CNG consumption, and a "Fisher-Rosemount" exhaust-gas analyzer, which can measure the levels of THC, MHC, NO_x, CO, CO_2, and O_2 in the exhaust gases of engines running on gasoline, diesel, or alternative fuel (such as LPG and CNG). All measurement instruments were connected to a PC based "National Instruments" data-acquisition system, which allowed simultaneous measurement of the major engine working parameters. These included torque, crankshaft angular speed, flow rates, pressures, temperatures as well as exhaust emissions. A high-frequency acquisition card enabled measurements of in-cylinder pressure time histories to be recorded over the whole engine cycle.

Results and Discussion

The generalized combustion simulation model was applied to the prediction of combustion related quantities in the specified engines, within a wide range of loads (bmep=200–790 kPa, for the NA engine, and 200–1400 kPa for the TC engine), crankshaft speeds (N=2000–4600 rpm), relative air-fuel ratios (RAFR =0.80–1.60), and spark advances (SA in the range from 8 deg of retard to 8 deg of advance with reference to MBT), under gasoline and CNG operations. The prediction model results were then compared to the experimental data [23,27,28] drawn from in-cylinder pressure time histories through the diagnostic tool developed in Ref. [19]. The pressure data, which were acquired by a high precision cooled piezoelectric transducer, presented an uncertainty of $\pm 0.5\%$.

The distributions of U and u', as average values throughout the cylinder volume, were calculated by Eqs. (3)–(7). The bell-like trend of the average turbulence intensity after the combustion onset [16] is mainly due to tumble or to squish effect [29], although it is obtained by a phenomenological approach in the K-k model. With regard to the value of c_β in Eq. (5), experimental turbulence data close to TDC (θ=360 deg), taken in a motored engine [29], were in fair agreement with calculated levels if the value c_β =3.0 was employed. Therefore, in the following results, such a value of c_β was used to calculate the turbulence intensity distributions. Concerning the K-k model implementation through Eqs. (8) and (9), the determined turbulence intensity profiles are quite similar to those provided by Eqs. (3)–(7), because the term $\dot{\rho}/\rho$ plays an important role only in the last compression and early expansion stages, where it has a similar effect to the application of the angular-momentum conservation hypothesis.

The comparison of theoretical and experimental results that follows is aimed at showing the performance and assessing the capability of the quasidimensional multizone combustion simulation code [16] in predicting burning speeds, indicated-cycle pressure in the closed-valve phase, and operation variable effects on performance and emissions of CNG and gasoline SI engines under a wide range of working conditions. More specifically, it was intended to show the robustness and the generality of the S_b/S_L fractal formulation given by Eq. (2). In this expression, the numerical value of n is 1.25, and C_L is given in Ref. [16] for each fuel as a function of engine speed, independent of engine configuration, while the reference crank angle θ_0 for the evaluation of ρ_0 takes the values of 345 deg, in the case of the 2000 cc 16 V NA engine and 338 deg for the 1200 cc 8 V TC engine. Each of these θ_0 values kept constant for the corresponding engine at all of the operating conditions. As stated above, ρ_0 is a model parameters, which has to be tuned in order to obtain the best measurement-prediction data fit, because it exerts the main influence on the S_b/S_L modulation.[1]

Figure 2 shows the experimental (diamond symbols) and the predicted (lines) distributions of S_b/S_L for the 2000 cc 16 V NA engine, as functions of crank angle, at different engine loads, for gasoline (left column) and CNG (right column) fueling. It is worth pointing out that, for the medium range of speeds and loads, the model outcome did not show any sensible dependence on ρ_0 and n. The generally good agreement between the predicted and experimental results in Fig. 2 clearly shows the capability of the model, Eq. (2), to describe the flame-turbulence interaction in the overall flame propagation interval, from the development to the extinction of the flame. Furthermore, as can be inferred from this figure, Eq. (2) can extrapolate a value of S_b/S_L that is nearly equal to 1 as r_{bf} approaches zero, in agreement with the flame propagation theory [16,18].

Figures 3 and 4 show an extensive overview of the model performance, when applied to both of the considered engines, by means of the comparison between the experimental (solid dots) and the computed (lines) maximum values of the in-cylinder pressure (p_{max}), heat-release rate (HRR_{max}) as well as turbulent combustion velocity ($S_{b,max}$). Each value of the abscissa in the graphs corresponds to a different engine condition and the roman numbers designate specific experiment sets, in which a sweep of a single engine relevant operating variable is carried out. The sweep specifications are reported in Table 2, for the 2000 cc 16 V NA engine and in Table 3, for the 2000 cc 8 V TC engine. In both figures, the simulation results are reported for two calibrations of the model: "Baseline calibration" (dotted line), in which all of the model constants were set to the same unfitted values for both engines, and "Refined calibration" (solid line), featuring specific constant values which can differ from one engine to the other.

The comparison of "Baseline calibration" to "Experimental" results in Figs. 3 and 4 shows that the model has an acceptable degree of accuracy even without any sort of tuning. This further substantiate the physical consistency of the model, in particular, of the characteristic length $\sqrt{A_{bf}}$ in the definition of turbulence outer

[1]The modulation of S_b/S_L is defined as $(S_b/S_{L,max}/S_b/S_{L,min}-1)\times 100\%$.

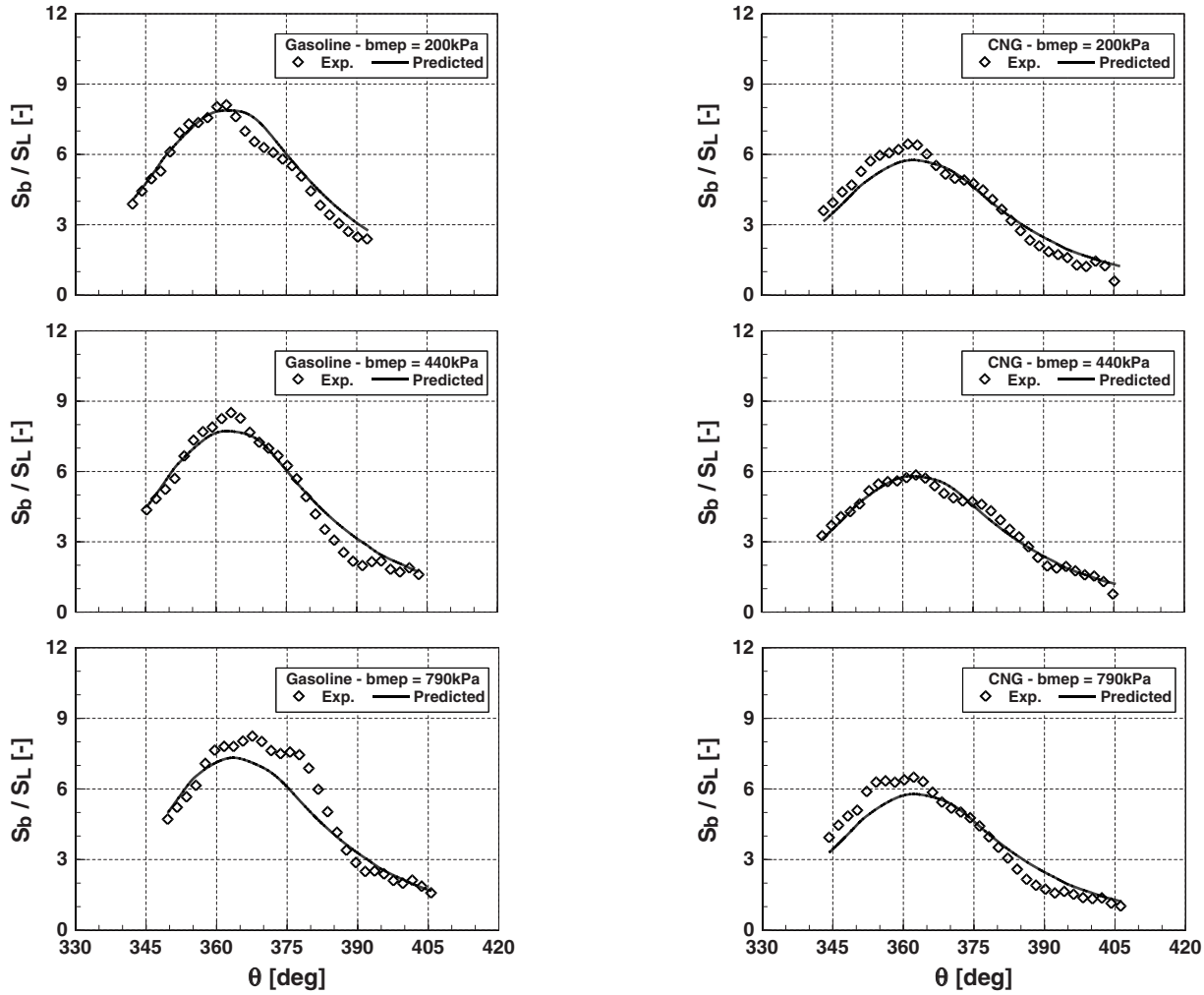

Fig. 2 Distributions of experimental and predicted S_b/S_L, for gasoline (left column) and CNG (right column) fueling under different engine loads, at the indicated operating conditions

cutoff length scale ε_o [18], to consider the reduction of the flame front wrinkling when its dimensions are comparable to those of turbulence eddies, and also of the term ρ/ρ_0 to take the reduced species and heat transfer across the flame front into account, at low in-cylinder densities. However, the accuracy of the model can be improved if a careful calibration is made, based on experimental data, as the "Refined calibration" results show.

Figures 5–8 report a sample of distributions of experimental (diamond symbols) and predicted (lines) pressure (upper rows), turbulent burning velocity (middle rows), and heat-release rate (lower rows). These distributions are extracted from the related sweeps in Table 2 (2000 cc 16 V NA engine) and in Table 3 (1200 cc 8 V TC engine) by means of the refined calibration, further substantiating the accuracy of the model. Actually, not only the predicted $p_{\max}$, $S_{b,\max}$, and $\mathrm{HRR}_{\max}$ values (taken as indices of the combustion sensitivity to changes in engine operation variables) are in generally good agreement with the experimental results, but also the distributions of p, S_b, and HRR versus crank angle show a strong similarity to experimental data. In particular, the crank-angle positions of the selected quantity maximum values are in close agreement with these data.

Finally, Fig. 9 reports the exhaust amounts of NO (upper row) and of CO (lower row), as functions of the relative air-fuel ratio for the indicated engine working conditions under gasoline (left column) and CNG (right column) operations. The engine operation with natural gas was extended to leaner mixtures with respect to those considered for gasoline, owing to the practically greater interest for lean-burn combustion in CNG engines. The measured (empty squares) emission levels are compared to the concentrations that were determined through the diagnostic tool (empty triangles) and to those predicted by the simulation code (empty diamonds). Trend lines are reported for each distribution in the graphs. Basically, a good agreement among the measured, diagnosed, and predicted NO and CO distributions was found for both fuels at all RAFR values, denoting a good estimation of the in-chamber thermodynamic conditions and the pollutant submodel capability of correctly capturing NO and CO formation mechanisms. With regard to the exhaust NO concentration, the small discrepancies that may occur between predicted/diagnosed and measured distributions are consistent with minor uncertainties ($\approx$10 K) in the predicted peak burned-gas temperatures. As far as CO exhaust levels are concerned (Figs. 9(*c*) and 9(*d*)), the predictive and diagnostic models slightly underestimate the measured CO levels. This can be ascribed to the fact that CO deriving from HC oxidation and local air-fuel ratio inhomogeneities, which can be present in the real engine, were not taken into account, CO emissions being sensibly dependent on local RAFR.

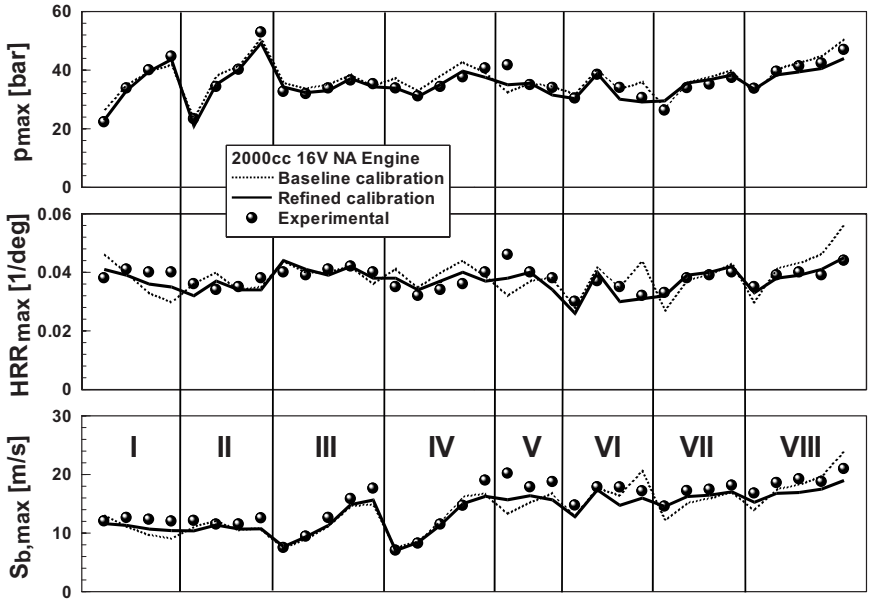

Fig. 3 Overview of model performance when applied to the 2000 cc 16 V NA engine (test cases in Table 2)

Model Calibration Settings. As stated above, the baseline calibration and the refined calibration results were obtained by means of distinct settings for different aspects of the model. The influence of these settings will be discussed one by one in what follows.

The first aspect to be considered concerns the crank angle of the switch from the imposed flame-kernel-growth profile to the application of the turbulent burning speed model. As mentioned, the development of the early flame kernel following the spark discharge was not modeled, because of the numerous random variables involved, but an osculating polynomial was applied for the evolution profile of the burned mass fraction over the flame development interval $\Delta\theta_{0-1\%}$ given by Eq. (15). For the physical consistency of Eq. (2) outcomes up to tiny flame sizes, one may expect to apply this equation from the early stage of the flame-development interval. In effect, correlations similar to Eq. (15) can be derived for different intervals. However, no correlation was developed for a small interval such as $\Delta\theta_{0-0.1\%}$, because this is very sensitive to cycle-by-cycle variations. Hence, the interval $\Delta\theta_{0-1\%}$ was selected, also because it is the widely used "flame-development angle" in the literature. Therefore, in the refined calibration approach, the switch from the polyinomial x_b profile to the use of Eq. (2) was made at the crank angle $\theta_{1\%}$ for which $x_b = 1\%$. In the baseline calibration, such a shift was set at the crank angle $\theta_{0.1\%}$ for which the polynomial distribution of x_b in $\Delta\theta_{0-1\%}$ gave $x_b = 0.1\%$. The acceptable results that were obtained showed the small influence of this setting.

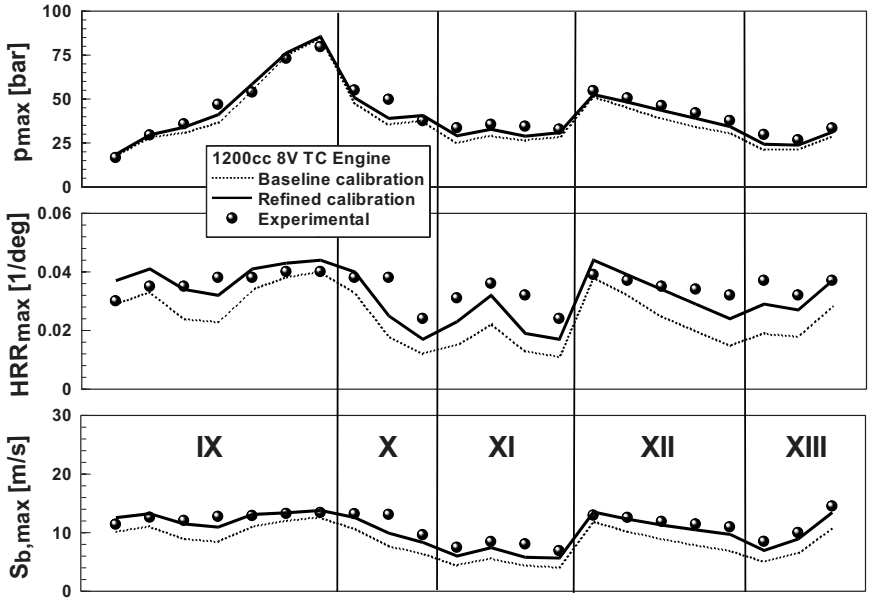

Fig. 4 Overview of model performance when applied to the 1200 cc 8 V TC engine (test cases in Table 3)

Table 2 Summary of test cases for the 2000 cc 16 V NA engine

Sweep No.	Fuel	bmep (kPa)	N (rpm)	RAFR	SA (CA deg ± MBT)
I (bmep)	Gasoline	200, 440, 620, 790	3300	1.0	0
II (bmep)	CNG	200, 440, 620, 790	3300	1.0	0
III (N)	Gasoline	440	2000, 2500, 3300, 4000, 4600	1.0	0
IV (N)	CNG	440	2000, 2500, 3300, 4000, 4600	1.0	0
V (RAFR)	Gasoline	440	4600	0.8, 1.0, 1.3	0
VI (RAFR)	CNG	440	4600	0.8, 1.0, 1.3, 1.6	0
VII (SA)	Gasoline	440	4600	1.0	−8,−2, 0, 2
VIII (SA)	CNG	440	4600	1.0	−8,−2, 0, 2, 8

The coefficient C_L, taking the wrinkling effect of turbulence on flame front in Eq. (2), is expressed for each fuel as a function of the engine speed in Ref. [16], consistent with the dependence of turbulence on N, and can be considered of general application, as it was found to be almost independent of the engine.

The crank angle at which ρ_0 in Eq. (2) should be evaluated is a key point in the model tuning process. Actually, this crank angle, together with the exponent n of ρ/ρ_0 in Eq. (2), influences the predicted S_b/S_L modulation, and can generally improve it in a wide range of working conditions. The crank angle to evaluate ρ_0 in the baseline calibration was the $\theta_{1\%}$ angle, whereas in the refined calibration approach, it was a fixed crank angle for a specific engine, being different from one engine to the other. An effective way of choosing the crank angle to evaluate ρ_0 can be the following. At fixed engine speed and RAFR values, and at MBT timing, a sweep of bmep should be taken as a reference set of experiments. More precisely, for the 2000 cc 16 V NA engine the Sweep I was selected (Table 2, Fig. 3), whereas the Sweep IX was taken for the 1200 cc 8 V TC engine (Table 3, Fig. 4). The crank angle for ρ_0 is the one giving the best agreement between the experimental and numerical $p_{\max}$, $\mathrm{HRR}_{\max}$, and $S_{b,\max}$ values and the best trend reproduction from one test case to the other. In

Table 3 Summary of test cases for the 1200 cc 8 V TC engine

Sweep No.	Fuel	bmep (kPa)	N (rpm)	RAFR	SA (CA deg ± MBT)
IX (bmep)	Methane	200, 400, 600, 800, 1000, 1200, 1400	3000	1.0	0
X (RAFR)	Methane	800	3000	1.0, 1.1, 1.25	0
XI (RAFR)	CNG	600	2000	0.8, 1.0, 1.3, 1.5	0
XII (SA)	Methane	800	3000	1.0	6, 3, 0, −3, −6
XIII (N)	CNG	440	2000, 2600, 3300	1.0	0

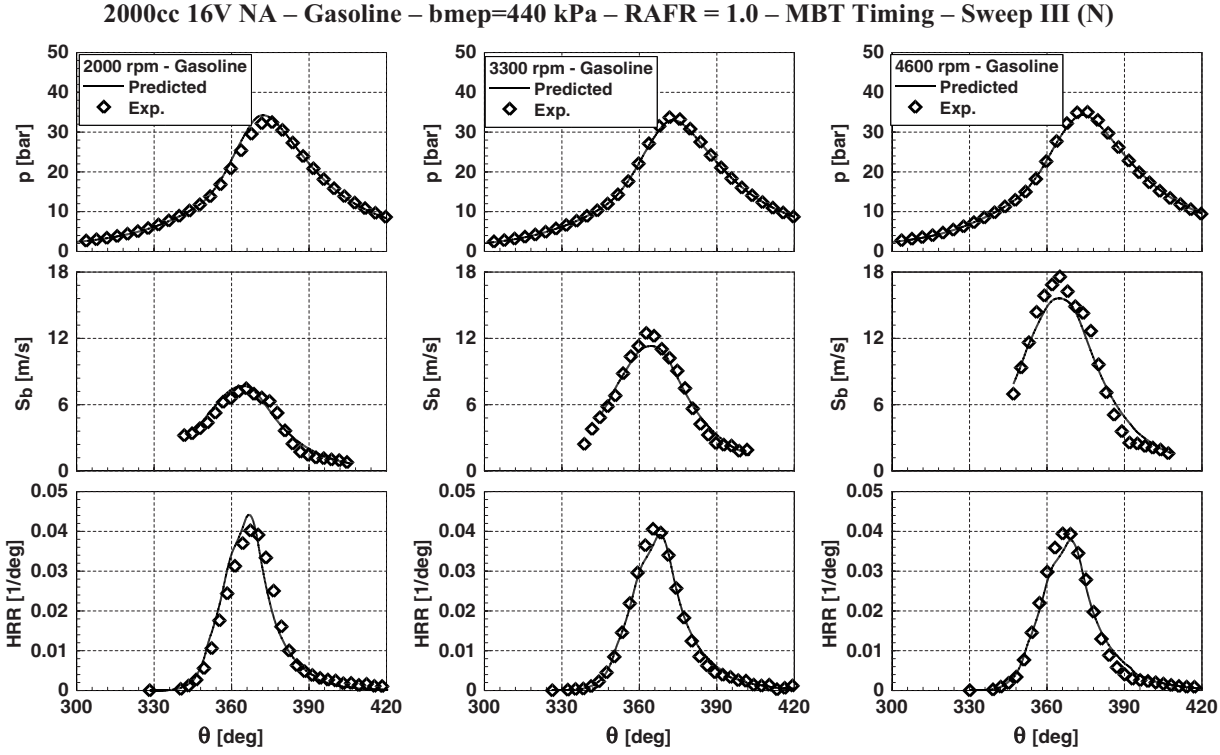

Fig. 5 Distributions of experimental and predicted combustion-related quantities for different engine speeds

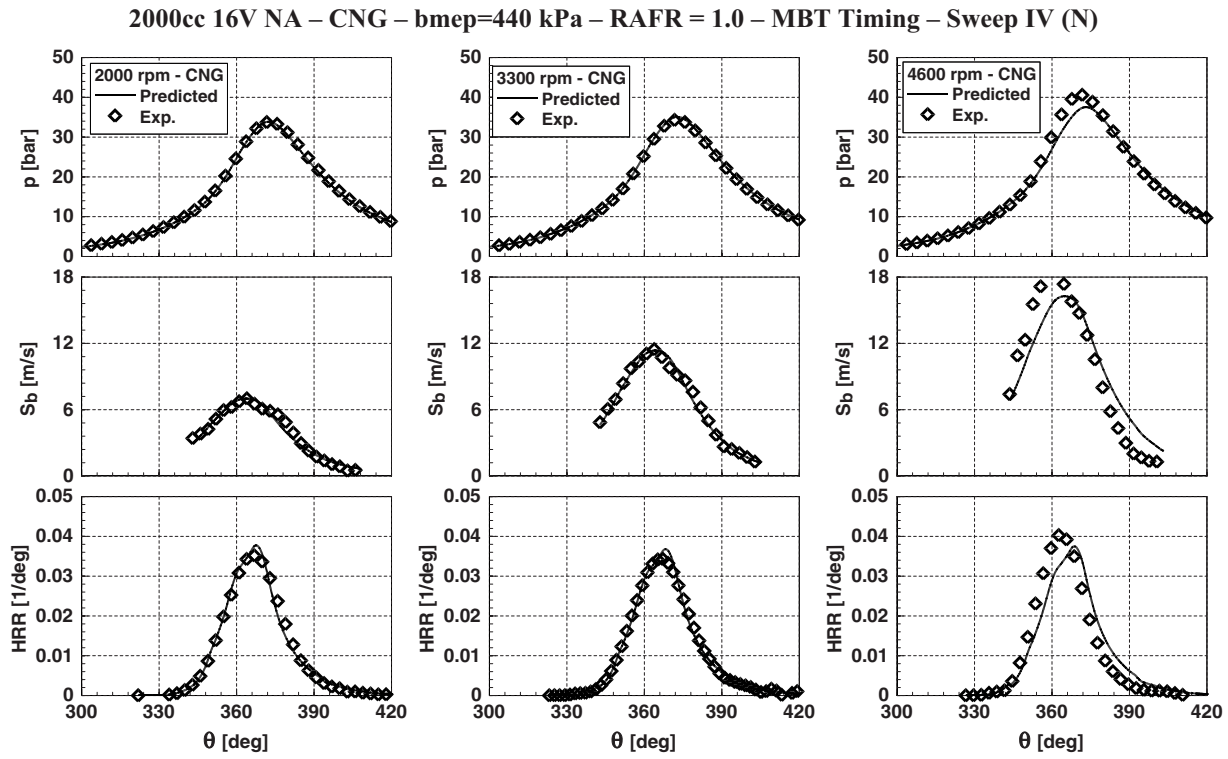

Fig. 6 Distributions of experimental and predicted combustion-related quantities for different engine speeds

particular, the experimental HRR_{max} trend in Sweeps I and IX is better reproduced, on average, by refined calibration settings rather than by those of the baseline calibration.

The reference angle that is chosen in this way can be kept constant for all the engine working conditions, and a generally good agreement between the numerical and experimental quanti-

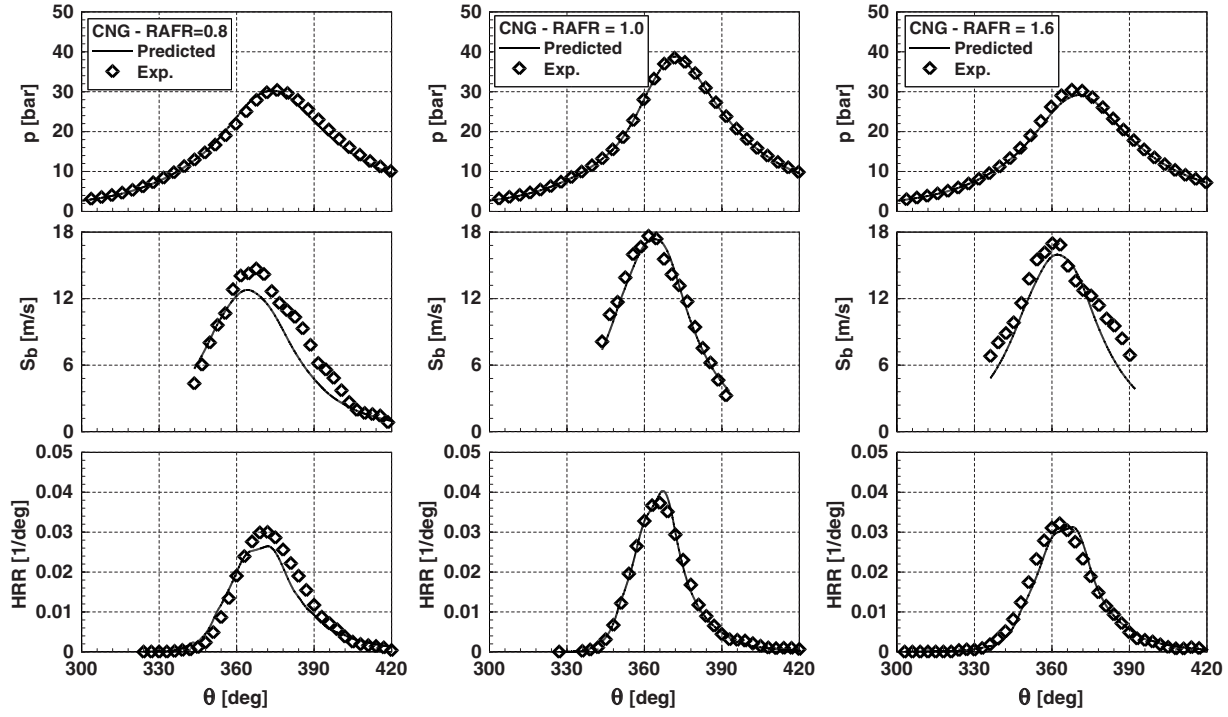

Fig. 7 Distributions of experimental and predicted combustion-related quantities for different *A*/*F* ratios

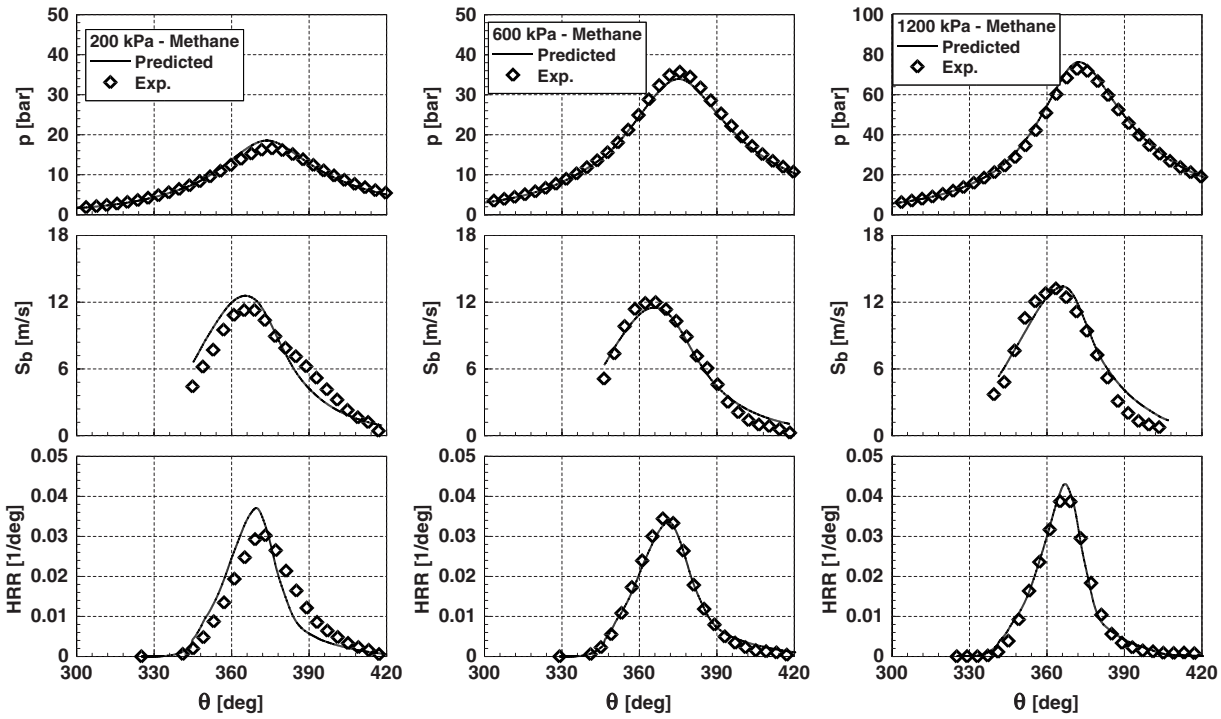

Fig. 8 Distributions of experimental and predicted combustion-related quantities for different bmep values

ties will be obtained, as can be seen in Figs. 3 and 4.

The exponent n further influences the modulation of S_b/S_L, although it is less important than the examined reference angle for ρ_0 evaluation. Based on the comparison between the prediction and measurement data, over the large number of test cases in Tables 2 and 3, it was ascertained that the value $n=1.25$ works well for both engines. Hence, the exponent n can most likely be considered as a fixed parameter for different engines and fuels.

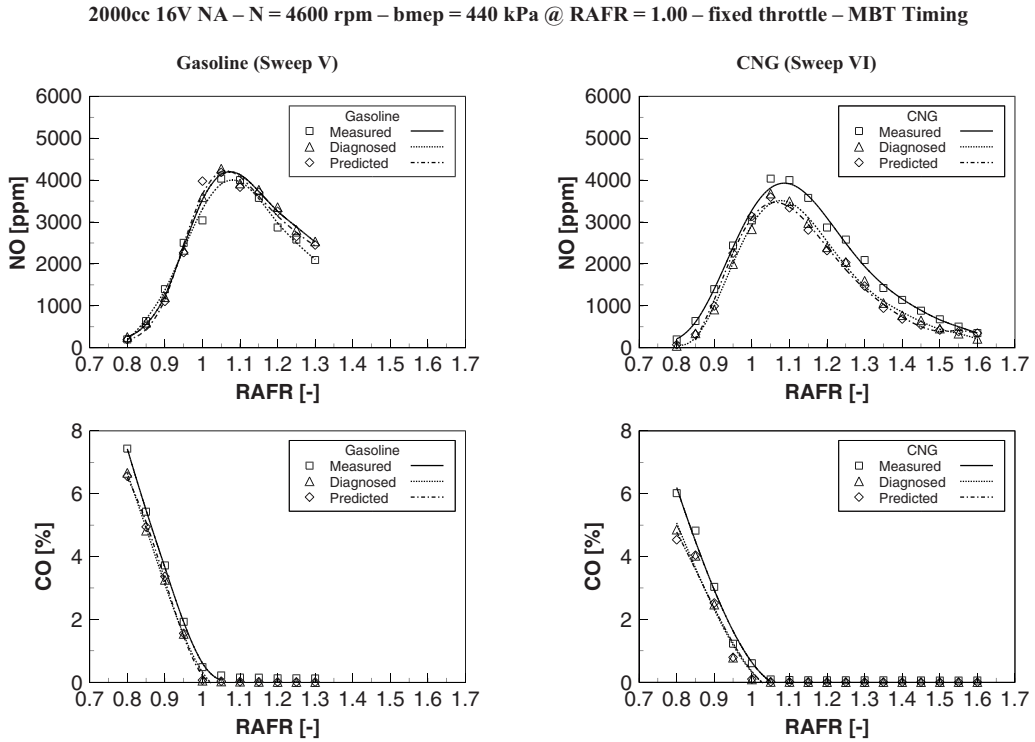

Fig. 9 Measured, diagnosed, and predicted exhaust NO (upper row) and CO (lower row) concentrations at the indicated operating conditions for gasoline (left column) and CNG (right column) fueling

Conclusion

A generalized turbulent burning-speed equation, based on a novel fractal formulation, was applied to the predictive study of an NA bifuel (gasoline and CNG) and a downsized TC CNG SI engines in a significant range of operating conditions.

The prediction and experimental results showed a generally good agreement in the study of the effect of operation variables on engine performance and emissions, with specific reference to indicated-cycle pressure, combustion quantities, and NO as well as CO emissions, substantiating the effective model applicability for SI engine design and combustion control.

Two sets of numerical results were presented to assess the robustness of the proposed analytical relation for the combustion speed. These are the baseline calibration results, in which all the model parameters to set were given untuned values for both engines, and the refined calibration results, presenting some specific choices for each test engine.

Main conclusions of the present assessment can be summarized as follows:

- The simulation tool showed a good accuracy level even without any sort of tuning. This supports the physical consistency of the model, in particular, the correctness of both length $\sqrt{A_{\mathrm{bf}}}$ introduction in the definition of the turbulence outer cutoff length scale ε_o to account for the decreased wrinkling of flame front when its dimensions are comparable to those of turbulence eddies and of the term $(\rho/\rho_0)^n$ to account for the reduced species and heat transfer across the flame front when the in-cylinder gas density is low.
- The crank angle θ_0 at which the ρ_0 term is evaluated in the S_b/S_L analytical expression is the only parameter that should be set for a specific engine, virtually independent of fueling and operating conditions. Such a crank angle influences the predicted modulation of S_b/S_L, and can sensibly improve this. An effective way of choosing the angle for ρ_0 evaluation was proposed, based on a bmep sweep as a starting set of experiments.
- Finally, the NO and CO results from both the diagnostic and the predictive models showed an accurate estimation of the in-chamber gas thermodynamic state and also their capability of correctly capturing the pollutant formation mechanisms. Nevertheless, the slight underestimation of CO exhaust concentration levels that is shown by both diagnosed and predicted distributions with respect to the measured data can be ascribed to the disregard of local air-fuel ratio inhomogeneities, which can be found in real engine operation instead.

Acknowledgment

This research was financially supported by CRF (Fiat Research Center) and by MUR (Ministry of University and Research) under COFIN2004 and COFIN2006 Programs.

Nomenclature

A = surface area
B = bore
bmep = brake mean effective pressure
C_L = coefficient for tuning the turbulence outer cutoff length scale
c_β = turbulent dissipation constant
$h_{\min}$ = clearance height at TDC
HRR = heat-release rate
IVO = intake valve opening
k = turbulent kinetic energy
K = mean flow kinetic energy
L_i = turbulence integral length scale
m = mass
MBT = maximum brake torque
N = engine angular speed
p = in-cylinder pressure
P = rate of turbulent kinetic energy production
r = radius
rpm = revolutions per minute
S_b = turbulent burning speed
S_L = laminar burning speed
S_p = piston shift from TDC position
SFF = spherical flame front
t = time
T = temperature
u' = average charge turbulent intensity
U = average charge velocity
U_P = mean piston speed
V = volume
x = mass fraction
$\Delta\theta_{0-0.1\%}$ = crank-angle interval from SA to $x_b=0.1\%$
$\Delta\theta_{0-1\%}$ = crank-angle interval from SA to $x_b=1\%$
ε = rate of turbulent kinetic energy dissipation
ε_o = turbulence outer cutoff length scale
ν = velocity, kinematic viscosity
θ = crank angle
ρ = density
ω = engine angular speed

Subscripts and Superscripts

0 = reference
b = burned, burning
bf = burning front
i = inlet jet flow
L = laminar
max = maximum
n = modulation exponent
o = out, outer
res = residual burned gas
SA = spark advance or spark timing
u = unburned

References

[1] Morikawa, K., Kaneko, M., Moriyoshi, Y., and Sano, M., 2005, "A Study on New Combustion Method of High Compression Ratio Spark Ignition Engine," SAE Paper No. 2005-01-0240.

[2] Habermann, K., Lang, O., Geiger, J., and Wittler, M., 2005, "Boosting and Direct Injection—Synergies for Future Gasoline Engines," SAE Paper No. 2005-01-1144.

[3] Kato, K., Igarashi, K., Masuda, M., Otsubo, K., Yasuda, A., Takeda, K., and Sato, T., 1999, "Development of Engine for Natural Gas Vehicle," SAE SP-1436 Combustion in SI Engines, pp. 52–60.

[4] Anand, G., Ravi, M. R., and Subrahmanyam, J. P., 2005, "Performance and Emissions of Natural Gas and Hydrogen/Natural Gas Blended Fuels in Spark Ignition Engine," ASME Paper ICES2005-1086.

[5] Zhang, F. R., Okamoto, K., Morimoto, S., and Shoji, F., 1998, "Methods of Increasing the BMEP (Power Output) for Natural Gas Spark Ignition Engines," SAE SP-1371 Combustion Processes in Engines Utilizing Gaseous Fuels, pp. 11–19.

[6] Heywood, J. B., 1988, *Internal Combustion Engine Fundamentals*, McGraw-Hill, New York.

[7] Blizzard, N. C., and Keck, J. C., 1974, "Experimental and Theoretical Investigation of Turbulent Burning Model for Internal Combustion Engines," SAE Paper No. 740191.

[8] Heikal, M. R., Benson, R. S., and Annand, W. J. D., 1976, "A Model for Turbulent Burning Speed in Spark Ignition Engines," SAE Paper No. 760160.

[9] Poulos, S. G., and Heywood, J. B., 1983, "The Effect of Chamber Geometry on Spark-Ignition Engine Combustion," SAE Paper No. 830334.

[10] Wahiduzzaman, S., Morel, T., and Sheard, S., 1993, "Comparison of Measured and Predicted Combustion Characteristics of a Four-Valve SI Engine," SAE Paper No. 930613.

[11] De Petris, C., Diana, S., Giglio, V., Golini, S., and Police, G., 1995, "Numerical Simulation of Combustion in Premixed SI Engines Using Fractal Flame Models," SAE Paper No. 952383.

[12] Matthews, R. D., Hall, M. J., Dai, W., and Davis, G. C., 1996, "Combustion Modeling in SI Engines With a Peninsula-Fractal Combustion Model," SAE Paper No. 960072.

[13] Yoshiyama, S., Tomita, E., Zhang, Z., and Hamamoto, Y., 2001, "Measurement and Simulation of Turbulent Flame Propagation in a Spark Ignition Engine by Using Fractal Burning Model," SAE Paper No. 2001-01-3603.

[14] D'Errico, G., Ferrari, G., Onorati, A., and Cerri, T., 2002, "Modeling the Pollutant Emissions From a SI Engine," SAE Paper No. 2002-01-0006.
[15] Bozza, F., Gimelli, A., Merola, S. S., and Vaglieco, B. M., 2005, "Validation of a Fractal Combustion Model Through Flame Imaging," SAE Paper No. 2005-01-1120.
[16] Baratta, M., Catania, A. E., Spessa, E., and Vassallo, A., 2006, "Development and Assessment of a Multizone Combustion Simulation Code for SI Engines Based on a Novel Fractal Model," SAE Paper No. 2006-01-0048.
[17] Bozza, F., Gimelli, A., Strazzullo, L., Torella, E., and Cascone, C., 2007, "Steady-State and Transient Operation Simulation of a "Downsized," Turbocharged SI Engine," SAE Paper No. 2007-01-0381.
[18] Baratta, M., Catania, A. E., Spessa, E., and Vassallo, A., 2005, "Flame Propagation Speed in SI Engines: Modeling and Experimental Assessment," ASME Paper ICEF2005-1216.
[19] Catania, A. E., Misul, D., Spessa, E., and Vassallo, A., 2004, "A Diagnostic Tool for the Analysis of Heat Release, Flame Propagation Parameters and NO Formation in SI Engines," *COMODIA 04*, Yokohama, Japan, Aug. 2–5, JSME No. 04-202, pp. 471–486.
[20] Gülder, Ö. L., and Smallwood, G. J., 1995, "Inner Cutoff Scale of Flame Surface Wrinkling in Turbulent Premixed Flames," Combust. Flame, **103**, pp. 107–114.
[21] Lee, T. W., and Lee, S. J., 2003 "Direct Comparison of Turbulent Burning Velocity and Flame Surface Properties in Turbulent Premixed Flames," Combust. Flame, **132**, pp. 492–502.
[22] Metghalchi, M., and Keck, J. C., 1982, "Burning Velocities of Mixtures of Air With Methanol, Isooctane and Indolene at High Pressure and Temperature," Combust. Flame, **48**, pp. 191–210.
[23] Catania, A. E., Misul, D., Spessa, E., and Vassallo, A., 2005, "Analysis of Combustion Parameters and Their Relation to Operating Variables and Exhaust Emissions in an Upgraded Multivalve Bi-Fuel CNG SI Engine," SAE 2004 Trans., Journal of Engines, **113**, SAE International, pp. 682–703.
[24] Iljima, T., and Takeno, T., 1986, "Effects of Temperature and Pressure on Burning Velocity," Combust. Flame, **65**, pp. 456–468.
[25] Baratta, M., d'Ambrosio, S., Spessa, E., and Vassallo, A., 2006, "Cycle-Resolved Detection of Combustion Start in SI Engines by Means of Different In-Cylinder Pressure Data-Reduction Techniques," ASME Paper No. ICES2006-1367.
[26] Catania, A. E., Misul, D., Spessa, E., and Martorana, G., 2001, "Conversion of a Multivalve Gasoline Engine to Run on CNG," SAE 2000 Trans., Journal of Engines, **109**, SAE International, pp. 809–817.
[27] d'Ambrosio, S., Misul, D., Spessa, E., and Vassallo, A., 2006, "Evaluation of Combustion Velocities in Bi-Fuel Engines by Means of an Enhanced Diagnostic Tool Based on a Quasi-Dimensional Multizone Model," SAE 2005 Trans., Journal of Engines, **114**, SAE International, pp. 975–993.
[28] d'Ambrosio, S., Spessa, E., Vassallo, A., Ferrera, M., and Peletto, C., 2006, "Experimental Investigation of Fuel Consumption, Exhaust Emissions and Heat Release of a Small-Displacement Turbocharged CNG Engine," SAE Paper No. 2006-01-0049.
[29] Catania, A. E., and Spessa, E., 1997, "Speed Dependence of Turbulence Properties in a High-Squish Automotive Engine Combustion System," SAE 1996 Trans., Journal of Engines, **105**, SAE International, pp. 186–196.

Junseok Chang
General Motors Research and Development,
30500 Mound Road,
Warren, MI 48090
e-mail: junseok.chang@gm.com

Zoran S. Filipi
University of Michigan,
2031 W.E. Lay Automotive Laboratory,
1231 Beal Avenue,
Ann Arbor, MI 48109
e-mail: filipi@umich.edu

Tang-Wei Kuo
General Motors Research and Development,
30500 Mound Road,
Warren, MI 48090
e-mail: tang-wei.kuo@gm.com

Dennis N. Assanis
University of Michigan,
2236 G.G. Brown,
2350 Hayward Street,
Arbor, MI 48109
e-mail: assanis@umich.edu

Paul M. Najt
e-mail: paul.m.najt@gm.com

Rodney B. Rask
e-mail: raskrl@aol.com

General Motors Research and Development,
30500 Mound Road,
Warren, MI 48090

Investigation of Mixture Preparation Effects on Gasoline HCCI Combustion Aided by Measurements of Wall Heat Flux

Expanding the range of HCCI operation will be critical for maximizing the fuel economy benefits in future vehicle applications. The mixture stratification, both thermal and compositional, can have very tangible impact on HCCI combustion, and gaining a deeper insight into these effects is critical for expanding the HCCI range of operation. This paper presents results of the comprehensive experimental investigation of the mixture preparation effects on a single-cylinder gasoline HCCI engine with exhaust reinduction. The effects include the type of mixture preparation (external mixing versus direct injection), charge motion, and injection timing. A combination of pressure-based combustion diagnostics, emission analysis, and heat flux measurements on the combustion chamber wall quantifies the effects on combustion and provides insight into reasons for observed engine behavior. As an example, the instantaneous temperature and heat flux measurements show the fuel impingement locations and allow assessing the fuel film dynamics and their effect on mixture stratification. The effects of direct injection and partial closing of the swirl control valve are relatively small compared with extending the injection timing late into the intake process or completely closing the swirl control valve and allowing charge storage in the intake port. [DOI: 10.1115/1.2943194]

Keywords: HCCI, mixture preparation, surface heat flux

Introduction

The main advantage of gasoline-fueled HCCI is improving the part load thermal efficiency while keeping the NO_x and soot emissions at negligible levels. The primary mechanisms for improving part load fuel efficiency are relatively high compression ratio (CR) and lean and unthrottled operation. The load is adjusted by changing the fueling rate rather than the mass of premixed charge. The challenges are related to the difficulty in controlling combustion without a direct trigger for ignition and a limited range of HCCI operation. The load range is limited by the misfire limit at the low end and knock limit at the high end. Therefore, the future practical implementation will likely be a dual-mode engine, operating in the HCCI mode at part load and switching to SI at higher loads. Insight into possible mechanisms for controlling HCCI burn rates is critical for expanding the HCCI range and improving vehicle fuel economy. As an example, several recent publications demonstrated utilizing charge stratification in the cylinder to control the HCCI burn rate [1–5]. Charge stratification includes thermal (charge gas temperature) and chemical (local equivalence ratio) inhomogeneity.

In the case of direct injection (DI), the timing of injection can have a strong impact through variations of impingement patterns and time scales for mixing. The freedom of fuel mixing offers very rapid adjustments of fueling and helps manage load/speed transients and combustion mode switching. Homogeneous environment in the cylinder can be achieved by injecting fuel very early in the intake process. A previous study in the literature [6] shows that iso-octane injection directly into the cylinder very early can generate engine behavior that matches premixed operation with port fuel injection. The variations of injection timing can provide optimized fuel stratification if so desired in a "pure" HCCI engine with high CR. On the other hand, in-cylinder environment in the engine with reinduction of the residual and a swirl-generating port is more complex, hence part of the motivation for this study.

Another important parameter in mixture preparation is the flow motion in the cylinder. Any means of intensifying and/or organizing charge motion in the cylinder will have an effect on mixture preparation. In fact, the effect differs significantly from the conventional SI combustion where turbulence has a very direct impact on flame propagation. The macroeffect is the consequence of

Contributed by the Internal Combustion Engine Division of ASME for publication in the JOURNAL OF ENGINEERING FOR GAS TURBINES AND POWER. Manuscript received February 4, 2008; final manuscript received February 22, 2008; published online August 21, 2008. Review conducted by Dilip R. Ballal. Paper presented at the 2007 Fall Conference of the ASME Internal Combustion Engine Division (ICEF2007), Charleston, SC, October 14–17, 2007.

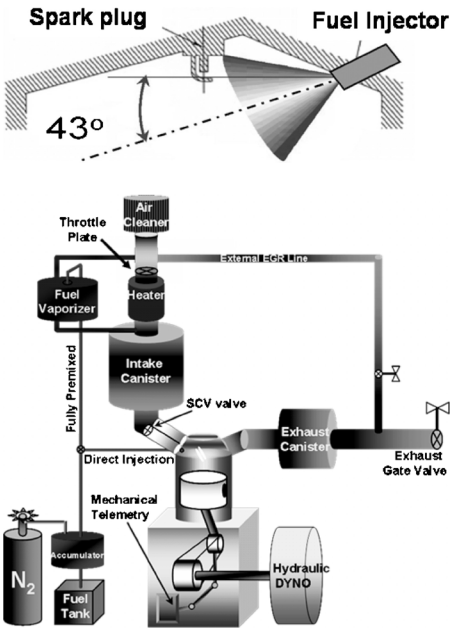

Fig. 1 Schematic of the HCCI engine setup

flow-spray interactions, while the turbulence intensity has the potential to impact heat and mass transfer. The magnitude of the charge motion effect on the HCCI combustion is still an open question due to conflicting reports in published literature [7–12]. Since the HCCI combustion is governed by chemical kinetics rather than flame propagation, Najt and Foster argued that there is no sufficient time for the effect of turbulence [7]. Aceves et al. suggested that in the case of a truly homogeneous CI engine there can be only an indirect effect on combustion through the temperature distribution in the boundary layer [8,9]. A very different point of view is that reactions could be partly controlled by the breakup of turbulent eddies [11,12]. We intend to quantify this effect in a single-cylinder engine with a tangential port and a swirl control valve (SCV) that allows adjustments of the flow restriction in the secondary intake port. The heat flux measurements will help with assessments of the spray-charge flow interactions and evaluation of the possible impact of flow intensity on heat transfer.

The paper is organized as follows. The experimental engine setup is described in the next section. This is followed by a description of the methodology for local surface temperature and heat flux measurements and error analysis. The analysis of results starts with the comparison of the external mixture preparation method (i.e., a fully premixed (FP) case) and DI. Subsequent study addresses the effect of injection timing in a DI case and discusses the level of stratification and its impact on combustion and emissions. In both cases the local heat flux measurements shed light on wall impingement and spatial variations in the combustion chamber. Finally, the effect of intake charge motion is explored via testing the engine with different SCV setting. The paper ends with conclusions.

Experimental Engine Setup

Figure 1 shows schematics of single-cylinder test setup. A GM prototype, pent-roof shape cylinder head is designed specially for this experiment. The basic shape of the combustion chamber is similar to a typical modern four-valve cylinder head, but the head has a machined sleeve for installation of the fuel injector on the side and specially shaped intake ports (Fig. 1(*a*)). An exhaust rebreathing strategy is applied to provide the necessary internal residual fraction for HCCI combustion control. This involves the exhaust valves opening for a second time during the intake stroke via an additional lobe on the exhaust cam. During this period, hot exhaust residual gas is drawn back into the cylinder to help with ignition during HCCI operation. The hot residual affects autoignition and combustion via a thermal and chemical effect. The exhaust back pressure is maintained at the level close to ambient pressure by controlling the gate valve shown in Fig. 1(*b*). Table 1 summarizes engine specifications.

Table 1 Engine specifications

Engine type	Four valves, single cylinder
Bore/stroke	86.0/94.6 mm
Displacement	0.549 l
Connecting rod length	152.2 mm
Compression ratio	12.5
IVO/IVC[a]	346 deg/592 deg[b]
Main EVO/EVC[c]	130 deg/368 deg[b]
Second EVO/EVC	394 deg/531 deg[b]
Fuel type	Gasoline ($H/C=1.898$)
RON/MON[d]	90.8/83.4
Specific gravity	0.7373
Low heat value	44.37 MJ/kg

[a]Intake valve open/intake valve close.
[b]0 deg CA is assigned to TDC combustion.
[c]Exhaust valve open/exhaust valve close.
[d]Research octane number/motor octane number.

One of the intake ports has a tangential orientation and is intended to produce organized swirling motion, while the other contains a SCV installed ~180 mm upstream from the valve seat. Exhaust gas is sampled at the exhaust plenum and gaseous analyzers measure concentrations of HC, NO_x, CO, CO_2, and O_2, thus allowing calculation of engine-out air/fuel ratio and combustion efficiency. The high-pressure fuel delivery system is based on a bladder-type accumulator. A bladder containing fuel is in a vessel pressurized by nitrogen. Regulating the pressure of N_2 allows control of the fuel injection pressure. The fuel delivery line is split so that fuel can be introduced in an injector in the cylinder head for DI or the injector in the vaporizer for a FP operation. Both injectors are identical designs, the typical swirl spray type. In case of DI, the fuel rail pressure is set at 10 MPa.

The fuel vaporizer consists of a 320 cm^3 aluminum chamber surrounded by a 750 W electric band heater to maintain the inner surface temperature at ~220°C, sufficiently high to fully boil gasoline at 100 kPa. The vaporizer air intake is positioned above the main throttle valve (see Fig. 1), thus ensuring the pressure drop required for the desired air flow. The air flow is large enough to prevent condensation in cold spots and stable operation, and yet small enough to keep the mixture well outside of the flammable limit. The residence time of fuel in the vaporizer has been estimated at five engine cycles. Vaporized fuel and air are routed to the intake runner upstream of the plenum to ensure complete mixing. Mixture temperature is controlled by the electric heater located upstream of the intake plenum.

A piezoelectric pressure transducer measures the pressure trace in the cylinder with a 0.5 deg crank-angle (CA) resolution. A flame shield is installed in front of the transducer tip to avoid thermal shock, and 200 consecutive cycles are recorded and averaged at any given condition. The heat release analysis is performed based on the average in-cylinder pressure trace. In-house developed single-zone heat release model described in Chang et al. [13] is used for the analysis. The results of heat release analysis provide the crank-angle resolved net energy release rate, as well as the cumulative energy release.

Local Wall Temperature and Heat Flux Measurement

As shown in Fig. 2(*a*), a total of nine heat flux probes, including two probes in the cylinder head and seven probes in the piston (four inside the piston bowl and three at the periphery), are installed to measure local instantaneous temperature and heat flux

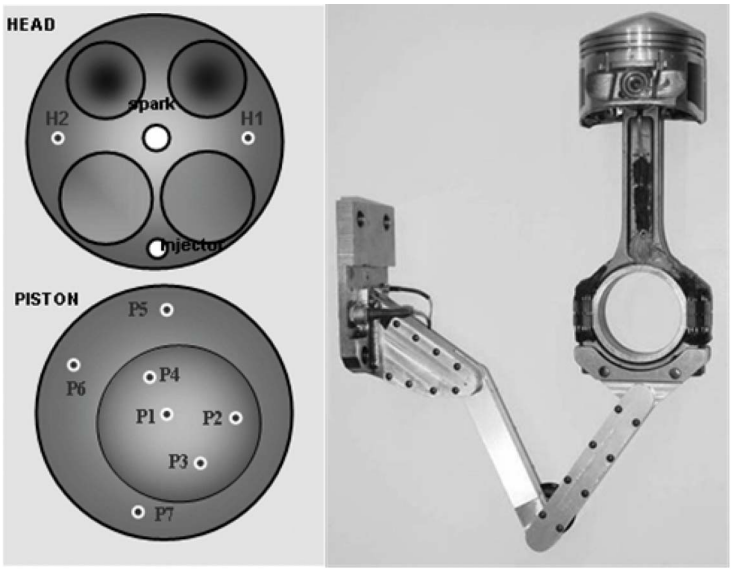

(*a*) (*b*)

Fig. 2 Heat flux measurement instrumentation: (*a*) locations of heat flux probes and (*b*) mechanical linkage telemetry system

variations. Measurement locations on the cylinder head are dictated by available space for installing special sleeves for mounting fast-response thermocouple probes. However, locations on the piston top are strategically chosen to provide complete insight into spatial variation of instantaneous heat flux due to local combustion difference or possible thermal stratification. A mechanical telemetry system is used for conveying signals from the moving piston and connecting rod. Figure 2(*b*) shows a picture of the in-house designed grasshopper linkage, made of aluminum, prior to installation. Special electrical connectors with a total of 28 pins are custom built for the big end of the connecting rod to allow easy installation and disassembly while ensuring reliable transmission of signals. From the fast-response surface thermocouple, local surface temperature can be measured at each 0.5 deg CA resolution. Temperature at 4 mm backside from the surface junction is also measured to calculate steady heat flux even though it is very much smaller than the transient portion. With the surface and backside temperature result, total heat flux can be obtained by applying transient heat conduction equation and using the fast Fourier transform to solve it. Detailed methodology and validation are mentioned in author's previous papers [13–15].

Results: Mixture Preparation Effects Related to Fuel Injection

Analysis is based on three types of measurement, such as CA resolved cylinder pressure for combustion diagnostics, CA resolved surface temperature and heat flux for near-wall heat transfer diagnostics, and slow response steady-state measurements of performance, emissions, etc. CA resolved profiles represent an average of 200 cycles measured with 0.5 deg resolution. Measurement accuracy of heat flux probe is very important, and it is assessed by considering manufacturing tolerance, bias error, and precision error of surface temperature. Uncertainty analysis is covered by authors' previous paper [16].

Fully Premixed Charge Versus Direct Injection. This section is focused on comparing the two different charge preparation methods. Table 2 shows details of operating conditions. Both FP and DI fuel charge preparation methods are evaluated with the same operating condition: 2000 rpm, 11 mg fuel/cycle. About 40% of residual is recirculated via rebreathing of exhaust to obtain enough thermal energy for autoignition. Four different SCV settings are compared for each fuel charge preparation method. The intention is to monitor possible spray-charge motion interactions that could be a factor in the DI case, while a separate section is devoted to an in-depth discussion of the effects of SCV and charge motion. In the case of direct fuel injection into the cylinder, the start of injection (SOI) occurs at 333 deg $BTDC_{firing}$, i.e., 27 deg after top dead center (TDC) intake stroke. It is expected that such early injection, only 27 deg after TDC intake, allows sufficient time for mixing and generates a nearly homogeneous charge in the cylinder.

Figure 3(*a*) shows net indicated mean effective pressure (NMEP) as a function of SCV position. Both the FP and DI results are included and compared. The SCV position has minimal effect on the variations of NMEP, except for the fully closed case. The SCV-closed operation obviously creates very different conditions in the cylinder, and this will be discussed further in the section on intake charge motion effect. The DI charge preparation results in a slight reduction of NMEP for any SCV setting. This indicated efficiency loss is the consequence of retarded combustion and slower burn duration for a DI case. Charge cooling due to injection and subsequent evaporation in the cylinder delays autoignition by 2 deg CA compared to the FP case, as indicated by the location of the 10% mass fraction burned. The combustion phasing, indicated by the location of 50% mass burned is retarded, too (see Fig. 3(*b*)). In Fig. 4(*a*), NO_x emissions with DI charge preparation is slightly higher than in the FP case, especially for the SCV open case. A locally fuel-rich zone due to the stratification result-

Table 2 Operating conditions for the study of fuel injection effects

Speed	(rpm)	2000
Fueling rate	(mg/cycle)	11.0
Air-fuel ratio		20
Internal EGR	(%)	39
External EGR	(%)	0
Intake charge	Temperature	365
Oil-in	(K)	370
Coolant-in		371
Intake manifold	Pressure	93.6
Exhaust manifold	(kPa)	101.0

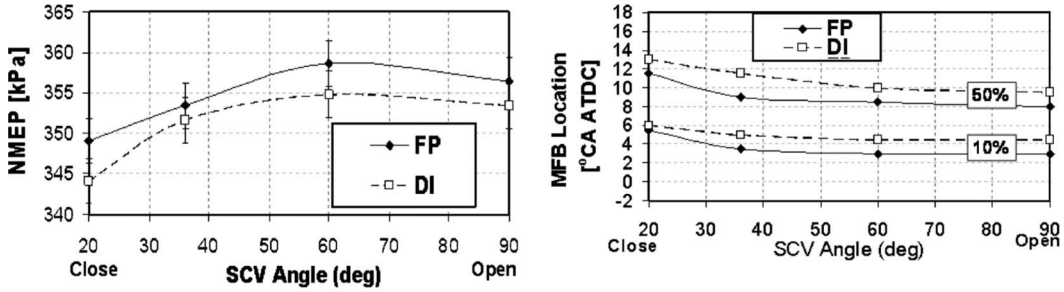

(*a*) (*b*)

Fig. 3 FP versus DI fuel charge comparisons with respect to varying SCV: Performance and mass fraction burn locations

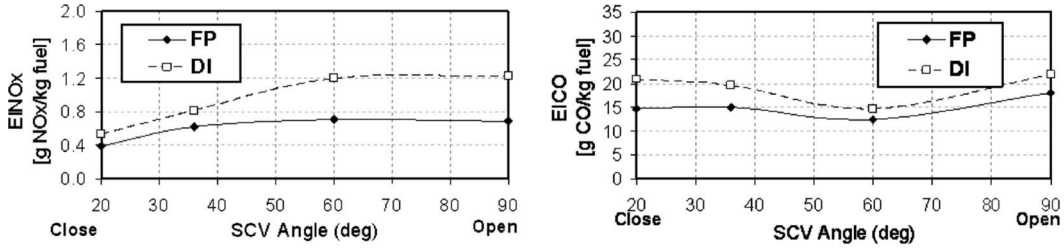

(*a*) (*b*)

Fig. 4 FP versus DI fuel charge comparisons with respect to varying SCV: engine-out emissions

ing from DI produces high peak temperature and high NO_x emission. The CO emissions with DI are higher than in the FP case as well, indicating that the fuel mixing in the cylinder is less uniform with DI.

Instantaneous Surface Temperature and Local Heat Flux Comparisons. Figure 5 includes instantaneous surface temperature measurements obtained for FP and DI cases. The graphs in individual figures are produced for discrete SCV positions. In terms of head surface, temperatures of $h2$ are consistently lower than $h1$ regardless of the FP or DI case because the coolant enters the cooling jackets near $h2$ and flows through transversally. The surface temperature at the $h1$ location is higher for the DI than the FP case, irrespective of the SCV setting. The vicinity of $h1$ is the region with strong squish flow caused by a small minimum piston-to-head clearance. Witze and Green [17] and Ohyama et al. [18] showed the presence of liquid fuel film in the squish area at the PFI engine. As the increased amount of fuel is trapped in this zone due to reverse squish after TDC, this leads to locally richer fuel concentration and increased local heat release.

In terms of piston surface, temperature is much more directly affected by the mixture preparation method, as it is consistently lower in the case of DI. The fuel impinging on the wall cools the surface due to the heat required to heat up the liquid fuel and vaporize it. As a result, the overall surface temperature level with DI charge preparation is about 4 °C below than those recorded with premixed charge, with $T_{\text{surface},p6}$ as the only exception showing higher values with DI charge. It is located directly under the head location $h1$, and this confirms the presence of the richer zone in the vicinity of $h1$-$p6$. The highest surface temperature is always observed at the center of the piston ($p1$), and lowest surface temperature occurs at $p4$ in the corner of the bowl where the thermal boundary layer is largest. The piston bowl area is affected by fuel spray hitting; i.e., temperature profiles of the $p1$, $p3$, and, in some cases, $p2$ show negative fluctuations due to the forced cooling by liquid fuel impingement.

Temperature swings due to the combustion excitation differ between the FP and DI cases. In the FP case the temperature swings at all locations show very similar features. In contrast, DI and impingement diminish a swing of the $T_{\text{surface},p2}$ signal (see Fig. 5, SCV closed) and retard its phasing (see Fig. 5, SCV=36 deg). The $T_{\text{surface},p1}$ signal is also delayed (see Fig. 5). Surprisingly, the $T_{\text{surface},p3}$ swing is as intense as the fluctuations observed in the FP case, despite the fuel impingement at this location early in the intake process. The fuel film obviously splashes away and moves swiftly toward locations $p1$ and $p2$ and leaves location $p3$ exposed to hot gases. The cooling of the surface by the evaporating liquid fuel film at locations $p1$ and $p2$ is accompanied by slower reaction rates in their vicinity, and this reduces the local surface temperature swings.

Local heat flux profiles during combustion excitation indicates a better picture in terms of spatial uniformity. Figure 6 show a local heat flux behavior for the FP and DI cases. As expected, the FP case demonstrates minimal spatial variations of local heat flux. All head and piston side heat flux profiles during combustion are similar, thus confirming that reactions occur simultaneously across the combustion chamber. This is the main distinction between the HCCI combustion and the flame propagation in the SI engine that was shown in authors' previous work [13].

However, noticeable spatial variations occur in the case of DI when SCV is fully closed or just partially open (36 deg). The nonuniformity is mainly driven by the fuel impingement on the piston, fuel film dynamics, and resulting stratification of mixture. In particular, location $p3$ shows a huge negative heat flux when the SCV is fully closed, which indicates that air jet coming from the tangential port pushes the fuel spray toward the piston and forces surface cooling. The profile of the heat flux signal at $p2$ shown in Fig. 6(*e*) and 6(*f*) indicates slower local burning due to the cooling effect of the fuel film and remnants of the fuel film at the time of ignition. Drake et al. [19] performed fuel film measurements on a quartz piston window of an optically accessible DI engine and concluded that vaporization of thin fuel films on the piston is slow and the fuel film persists past 60 deg ATDC, with late injection timing. Although the injection in the HCCI engine occurs very early, the large quantity of fuel impinges on the pis-

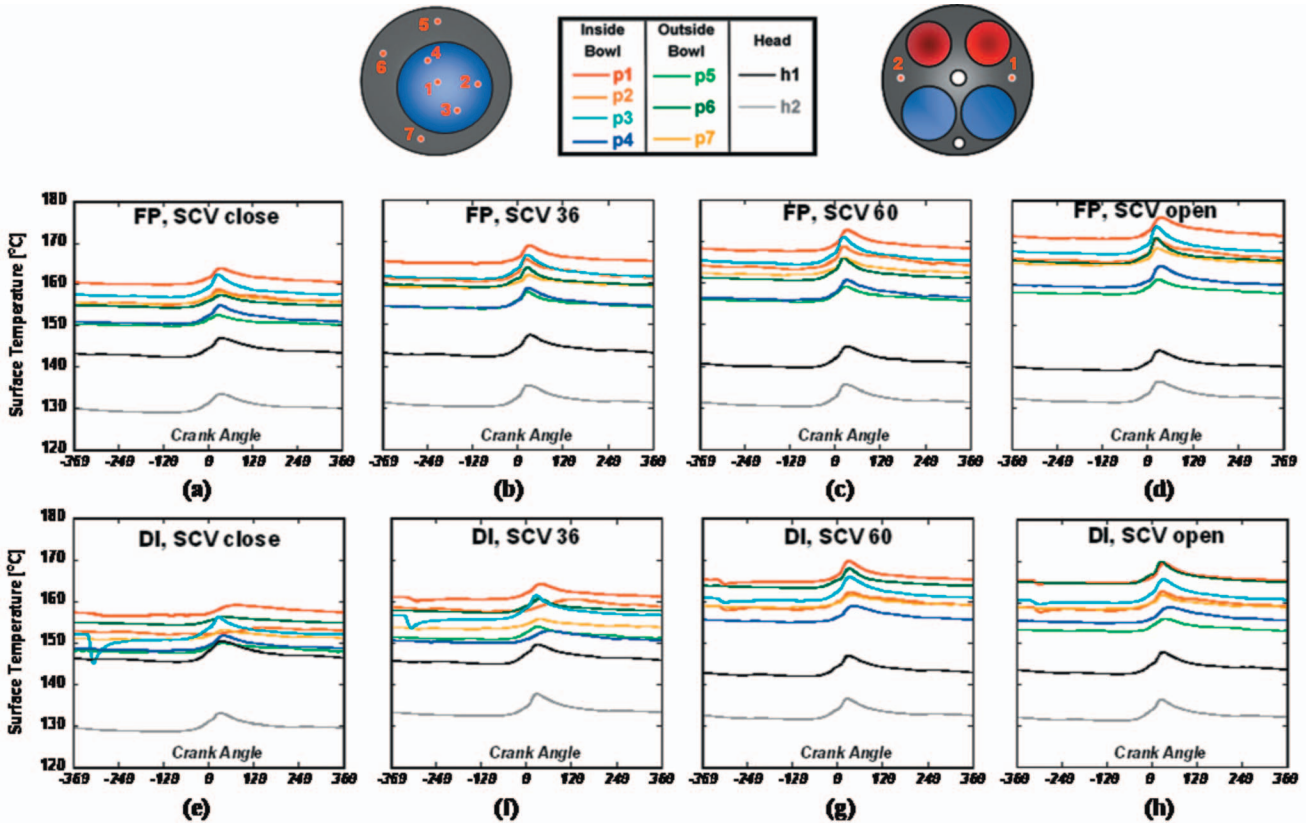

Fig. 5 Instantaneous local surface temperature (100 cycle ensemble average) comparison with different SCV settings: FP versus DI charge preparation

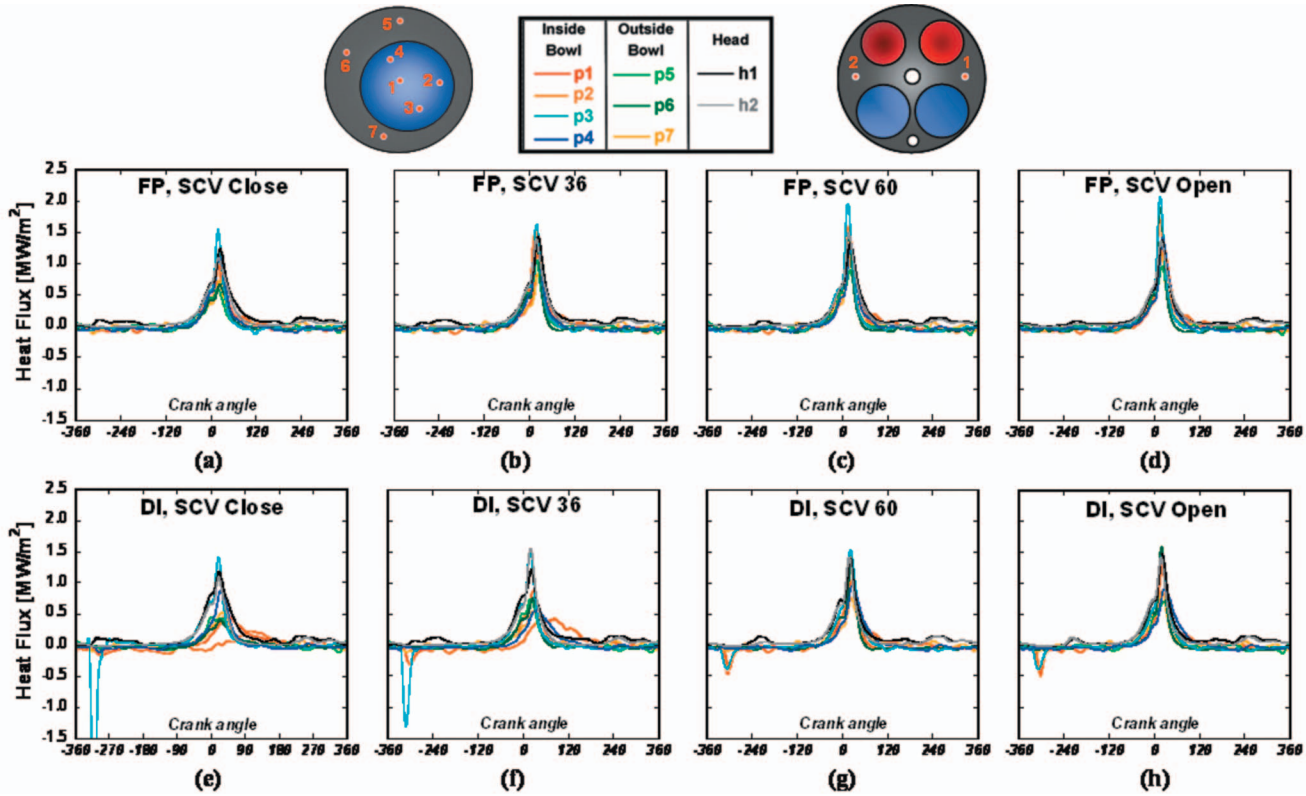

Fig. 6 Instantaneous local heat flux (100 cycle ensemble average) comparison with different SCV settings: FP versus DI charge preparation

Table 3 Operating conditions for injection timing sweep

Speed	(rpm)	2000
Fueling rate	(mg/cycle)	11.0
Air-fuel ratio		20
Internal EGR	(%)	40
External EGR	(%)	0
Intake charge	Temperature	366
Oil-in	(K)	370
Coolant-in		371
Intake manifold	Pressure	93.7
Exhaust manifold	(kPa)	101.0
SCV setting	(deg)	36

ton, and it is possible that small fuel film lingers even after ignition. When the fuel impingement on the piston bowl decreases with the SCV fully open (Fig. 6(*h*)), spatial variation of local heat flux during the combustion is reduced. The negative swing at location *p*3 disappears when the SCV is fully open and instead appears at locations *p*1 and *p*2 with smaller magnitudes.

In summary, two different fuel preparation methods are compared to assess the effect on HCCI burning. The higher heat loss in a DI case, due to fuel evaporation in the cylinder, leads to charge cooling, slower HCCI burn rates, and higher CO emission. Mixture is also more stratified, as higher spatial variation of heat flux in a DI case indicates locally heterogeneous burning. Locally richer burning results in higher NO_x emission with DI charge. It has to be pointed out that the trends might change in the case of higher accumulation of deposits since deposit growth on the piston affects dynamic fuel film behavior through the interaction between the spray and the surface, including the absorption/desorption processes.

Stratification by Varying Injection Timing. The injector axis is 43 deg down from the horizontal plane, and the spray is targeted toward the cylinder axis (refer to the schematic at Ref. [16]). A swirl injector with a 70 deg cone angle is installed on the side of the cylinder head. Note that real spray cone angle and penetration length change at different injection timings depending on the chamber pressure and temperature condition. Spray targeting is also affected by intake charge motion. In this test, SCV sets at partially open (36 deg) since it was found to give the best compromise between performance and emissions with DI charge case. Injection timing sweep is then performed without spark for any of the operating points. Table 3 provides a description of operating conditions for the injection timing sweep.

As can be seen in Fig. 7(*a*), COV of IMEP increases and combustion efficiency decreases when the SOI is retarded beyond 270 deg BTDC. As SOI is retarded very late (for example, 55 deg CA BTDC), time for mixing becomes insufficient to prepare homogeneous charge by the time of ignition. High degree of stratification leads to pockets of excessively lean mixture beyond the lean combustion limit. These pockets result in incomplete burning that reduces combustion efficiency.

Interestingly, burn locations shown in Fig. 7(*b*) are not affected much by the injection timing until it becomes very retarded. Once SOI is retarded beyond 220 deg BTDC, 90% mass fraction burned point (mass fraction burned is normalized by combustion inefficiency number) occurs much later, which indicates a long tail of combustion. For the extreme case of SOI=55 deg BTDC (late in compression), combustion possibly includes a diffusion flame due to the fuel film on the piston top. Such late injection timing with nonoptimized fuel cloud generates a high degree of stratification and leads to pockets of excessively lean mixture characterized by slow and incomplete burning. High amounts of CO and smoke are measured in the exhaust port due to the excessive stratification and liquid fuel film on the piston surface (see Fig. 7(*c*)). NO_x emission at early injection timing is low, thanks to the low-temperature burning and large amount of exhaust dilution. The NO_x emission does not increase with late injection timing because of lower peak gas temperature from a very unstable and retarded burn.

Instantaneous local heat flux results in Fig. 8 illustrate well how the impingement and fuel film formation processes change with variations of injection timing. A huge negative heat flux swing is observed at location *p*3 when injection starts at TDC. It indicates direct impingement at high velocity. The negative peak is smaller at SOI=33 deg BTDC, but there is evidence of impingement at location *p*1. The nature of the process changes as the SOI is retarded to 300 deg BTDC or more, and piston moves further away from TDC. The large negative swing disappears, and instead the fuel film forms gradually over location *p*2. The fuel does not "wash" the surface at high velocity, but a tangible quantity is still deposited in the piston bowl. There is less time for evaporation

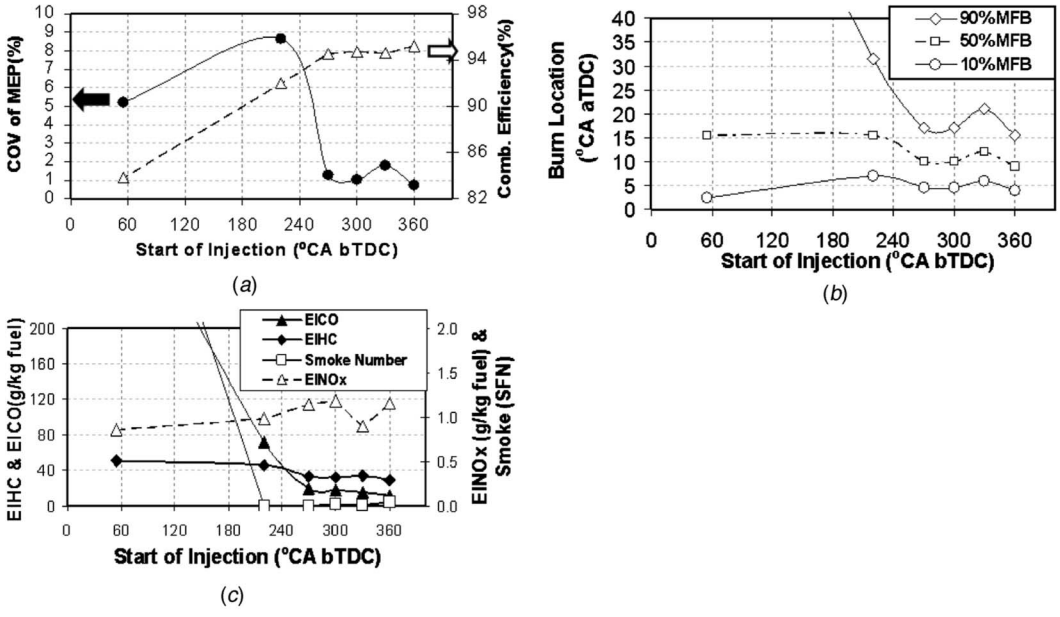

Fig. 7 Effect of injection timing on HCCI combustion stability, burn locations, and emissions

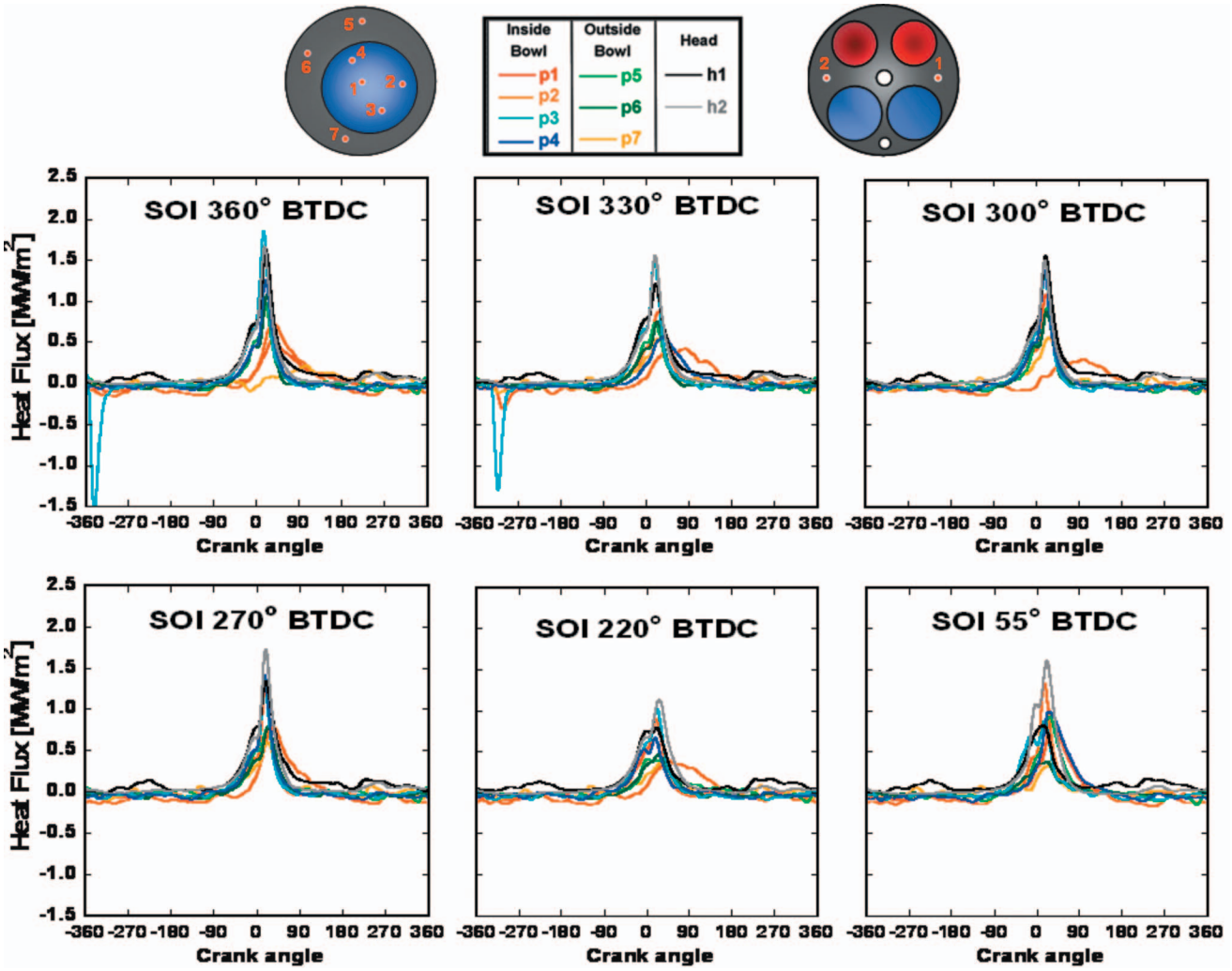

Fig. 8 Instantaneous local heat flux (100 cycle ensemble average) comparison with varying injection timing

and mixing; hence some fuel seems to linger close to $p2$ during combustion. This causes compositional stratification and leads to incomplete reactions. When fuel is injected late during the compression stroke, e.g., SOI=55 deg BTDC, spatial variations of heat flux paint a different picture. Few signals are retarded, including $p1$, $p6$, $p7$, and $h1$, thus suggesting fuel wetting in these zones. The spray is narrower and less affected by intake charge motion, and the penetration length is shorter at high pressures, while high temperatures speed up evaporation. In contrast, the gradient of the heat flux and its peak at $p3$ are higher. This is due to a locally rich zone and the locally increased reaction rates.

In summary, varying the injection timing during intake, between 360 deg TDC and 270 deg BTDC, has little impact on performance, combustion stability, burn duration, and emissions. The local heat flux profiles show spatial variation mainly due to different impingement patterns and the effect of stratification on local reaction rates. When fuel is injected very late during compression, the burn rate decreases and burn duration increases dramatically. There is a possibility of diffusion burning in the late stage of combustion, and both combustion efficiency and combustion stability deteriorate.

Results: Intake Charge Motion Effect

A secondary throttle in one intake port is adopted in this study to alter the in-cylinder charge motion pattern and intensity. The cylinder head was originally designed to provide swirl motion when the SCV valve is closed, thus blocking the straight port (refer to the schematic in Ref. [16]). In that case, the entire intake air flow goes through the tangential port and creates clockwise (bottom-view) swirl. If SCV is open, the counterflow reduces the organized swirl flow. The swirl intensity as a function of SCV setting is evaluated by measurements on the steady flow rig. Swirl index increases systematically from 0.6 to 3.7 as the SCV position changes from fully open (90 deg) to close (20 deg). However, in the case of the HCCI engine with *reinduction*, the exhaust valves open one more time during the intake stroke and the *flow of residual into the cylinder* disturbs the organized motion of the fresh charge. Estimated exhaust mass coming into the cylinder during the rebreathing event is around 40% of the total trapped mass. As a result, both the SCV fully closed (20 deg) and partially open (36 deg) cases show reduced levels of swirl when exhaust valves are fully open, down to only 25% of the value obtained with only intake valves operating [16]. This explains the trends observed in the first section of the paper (see Fig. 3). The trends as a function of SCV setting are mostly flat since (i) swirl levels in the engine with reinduction are low and (ii) changes in the charge motion intensity as a function of SCV setting are not large.

Nevertheless, fully closed SCV was the only exception. Closed SCV does slow down burning, with expected implications related to performance, efficiency, and emissions (Figs. 3 and 4). The heat release rate response to varying SCV angles is shown in Fig. 9. While there is a temptation to attribute the changes to the in-

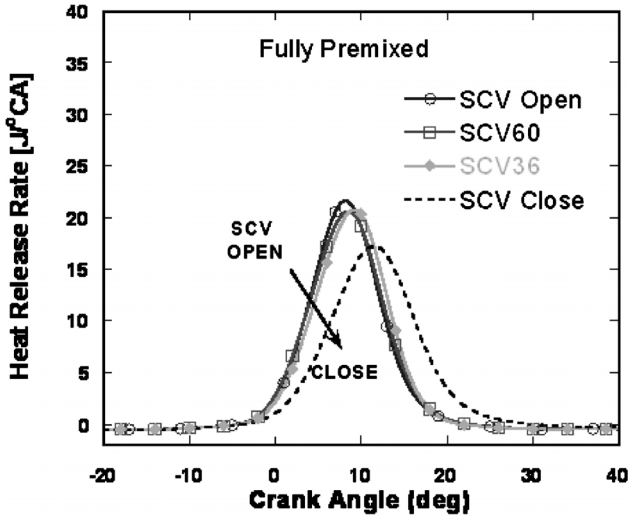

Fig. 9 Heat release rate comparison with respect to varying SCV setting

creased intensity of intake charge motion, the change of swirl intensity between the SCV=36 deg and SCV closed is negligible and cannot explain the "digital" change of burn rates. Therefore, the relatively small changes in the turbulence level with variations of SCV setting do not have a significant impact on HCCI burning; rather, the thermal environment is the primary driver of chemistry. The effect of flow variations on heat transfer is apparently very small, again due to the relatively small impact of the SCV setting on the charge motion intensity in the engine with rebreathing. The other possible reasons for observed behavior are discussed below.

Burn Rate Reduction in Case of SCV Fully Closed Setting. When SCV is fully closed, burning slows down significantly in both FP and DI cases. The discussion in the previous section rules out the impact of increased heat loss due to intensified charge motion since rebreathing diminishes the level of swirl in the chamber. Therefore, it can be hypothesized that the charge storage in the intake port and subsequent effect on the charge thermal state bear responsibility for the reduced burn rate with SCV closed. Namely, while the SCV valve is closed, the engine intake valve continues to operate as usual and enables some portion of the reinducted hot exhaust gas to enter the intake port. This hot charge is trapped in the port once the intake valve is closed. Hot charge then resides in the port until the intake valve opens in next cycle. Heat flux variations shown in Fig. 10 support this hypothesis. Local heat flux at $h1$ in Fig. 10 changes significantly during the intake event when SCV is closed. There is a sudden increase at the beginning of intake valve opening, which is due to the flow of previously trapped hot gas out of the SCV port. If this portion of the charge suffered some heat loss during the period between two consecutive cycles, this could definitely explain the changes of burn rate since the authors' previous investigations uncovered a very high sensitivity of the HCCI engine to intake charge and wall temperatures [15]. The complete verification of the hypothesis requires additional work, including a detailed simulation of flow through the intake ports for different SCV settings and will be addressed in a follow-up paper.

Conclusions

This paper investigated the impact of mixture preparation methods on combustion, performance, and emission of a gasoline HCCI engine with reinduction. The experimental work was performed on a single-cylinder, four-valve engine with an exhaust rebreathing cam. The mixture preparation included the choice of external mixing in a vaporizer or DI. A SCV in one of the intake ports allowed adjustments of the intake charge motion intensity. Heat flux measurement at seven locations on the piston top surface and two locations on the cylinder head of the HCCI engine aided more traditional engine diagnostics and enabled assessment of spatial variations due to stratification and/or fuel impingement. The findings can be summarized as follows:

1. The spatial variation of heat flux is very small in the case of the FP gasoline-air mixture prepared externally, thus confirming very uniform conditions in the HCCI combustion chamber. DI fuel mixture is more stratified as indicated by larger spatial variations in heat flux. The fuel impingement is clearly detectable at piston bowl locations when the fuel injection timing is close to TDC_{intake}. The bulk burn rate with DI charge is slightly slower, primarily due to charge cooling. Nevertheless, stratification and locally rich zones in a DI case result in higher NO_x emission than that in the FP case. Overall, the effects of DI are moderate under optimized early injection timing.

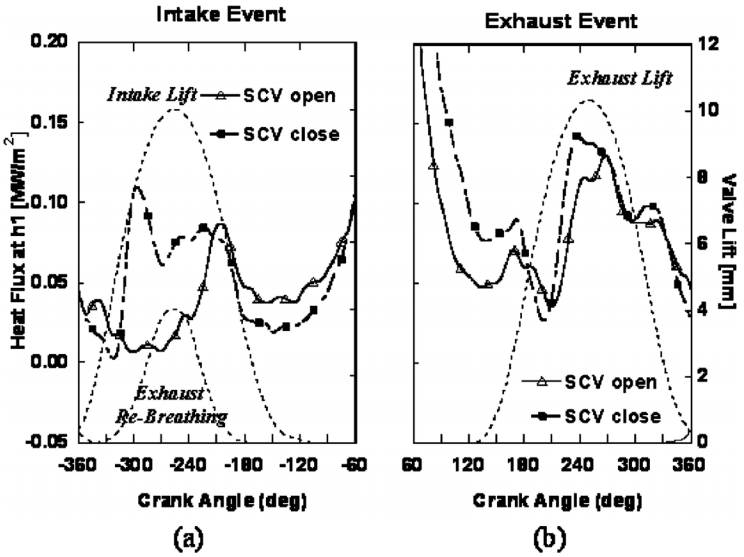

Fig. 10 Effect of SCV setting on the head surface heat flux at location $h1$ during (*a*) intake and (*b*) exhaust event

2. Even though changing the SOI causes clear variations of impingement patterns in the piston bowl, the overall performance, burn rates, and emissions do not change much as SOI is varied from TDC_{intake} to mid 90 deg CA after TDC_{intake}. Burning in the core zone is apparently not affected much, as long as the bulk of fuel evaporates on time. However, when the injection timing is further retarded to the late phase of the compression, burn rate decreases due to excessive fuel stratification and diffusion burning close to the piston surface wetted by fuel.
3. Neither the burn rates nor the heat loss change much with varying SCV from fully open to partially closed case. While partial closing of SCV increases velocities through a tangential intake port, reinduction of residual during the intake stroke diminishes the swirl levels due to the simultaneous flow into the cylinder through straight exhaust ports.
4. Autoignition timing and burn durations slow down for the SCV fully closed case, regardless of either FP or DI charge preparation. The intensity of swirl motion does not change much as SCV fully closed to partially closed, and yet there is a digital reduction of the burn rate. It is hypothesized that the charge storage in the port when the SCV (located upstream of the engine valve) is fully closed and its recycling in the subsequent cycle provide a strong impact on the thermal state of the charge and combustion. This phenomenon could provide a useful way of controlling the peak burn rates [20], and will be investigated further in a follow-up paper.

Acknowledgment

This research has been supported by the GM/UM Collaborative Research Laboratory in Engine System Research at the University of Michigan.

Nomenclature

ATDC = after top dead center
BTDC = before top dead center
COV of IMEP = covariant of IMEP
DI = direct injection
FP = fully premixed
h = temperature location at the head surface
MFB% = percentage of mass fraction burned
p = temperature location at the piston surface
SCV = swirl control valve

References

[1] Grenda, J., 2004, "Numerical Modeling of Charge Stratification for the Combustion Control of HCCI Engines," unpublished; Aroonsrisopon, T., Werner, P., Waldman, J., Sohm, V., Forester, D., Morikawa, T., and Iida, M., "Expanding the HCCI Operation With the Charge Stratification," SAE Paper No. 2004-01-1756.
[2] Sjoberg, M., and Dec, J. E., 2005, "Effects of Engine Speed, Fueling Rate, and Combustion Phasing on the Thermal Stratification Required to Limit HCCI Knocking Intensity," SAE Paper No. 2005-01-2125.
[3] Sjoberg, M., Edling, L., Eliassen, T., Magnusson, L., and Angstrom, H., 2002, "GDI HCCI: Effects of Injection Timing and Air Swirl on Fuel Stratification, Combustion and Emissions Formation," SAE Paper No. 2002-01-0106.
[4] Aleiferis, P. G., Charalambides, A. G., Hardalupas, Y., Taylor, A. M. K. P., and Urata, Y., 2005, "Modeling and Experiments of HCCI Engine Combustion Charge Stratification and Internal EGR," SAE Paper No. 2005-01-3725.
[5] Reuss, D. L., and Sick, V., 2005, "Inhomogeneities in HCCI Combustion: An Imaging Study," SAE Paper No. 2005-01-2122.
[6] Dec, J. E., and Sjoberg, M., 2004, "Isolating the Effects of Fuel Chemistry on Combustion Phasing in an HCCI Engine and the Potential of Fuel Stratification for Ignition Control," SAE Paper No. 2004-01-0557.
[7] Najt, P. M., and Foster, D. E., 1983, "Compression-Ignited Homogeneous Charge Combustion," SAE Paper No. 830264.
[8] Aceves, S. M., 2001, "A Sequential Fluid-Mechanic Chemical-Kinetic Model of Propane HCCI Combustion," SAE Paper No. 2001-01-1027.
[9] Aceves, S., Flowers, D., Martinez-Frias, J., Espiosa-Loza, F., Christensen, M., Johansson, B., and Hessel, R., 2005, "Analysis of the Effect of Geometry Generated Turbulence on HCCI Combustion by Multi-Zone Modeling," SAE Paper No. 2005-01-2134.
[10] Sun, Y., Shuai, S., Wang, J., and Wang, Y., 2003, "Numerical Simulation of Mixture Formation and Combustion of Gasoline Engines With Multi-Stage Direct Injection Compression Ignition (DICI)," SAE Paper No. 2003-01-1091.
[11] Christensen, M., and Johansson, B., 2002, "The Effect of In-Cylinder Flow and Turbulence on HCCI Operation," SAE Paper No. 2002-01-2864.
[12] Kong, S., Marriott, C. D., Rutland, C. J., and Reitz, R. D., 2002, "Experiments and CFD Modeling of Direct Injection Gasoline HCCI Engine Combustion," SAE Paper No. 2002-01-1925.
[13] Chang, J., Guralp, O., Filipi, Z., Assanis, D., Kuo, T., Najt, P., and Rask, R., 2004, "New Heat Transfer Correlation for an HCCI Engine Derived From Measurements of Instantaneous Surface Heat Flux," SAE Paper No. 2004-01-2996.
[14] Chang, J., 2004, "Thermal Characterization and Heat Transfer Study of a Gasoline Homogeneous Charge Compression Ignition Engine Via Measurements of Instantaneous Wall Temperature and Heat Flux in the Combustion Chamber," Ph.D. thesis, Department of Mechanical Engineering, University of Michigan.
[15] Chang, J., Filipi, Z., Assanis, D., Kuo, T., Najt, P., and Rask, R., 2005, "Characterizing The Thermal Sensitivity of a Gasoline HCCI Engine With Measurements of Instantaneous Wall Temperature and Heat Flux," Int. J. Engine Res., 6, Special Issue Paper No. 289.
[16] Chang, J., Filipi, Z., Assanis, D., Kuo, T., Najt, P., and Rask, R., 2007, "Investigation of Mixture Preparation Effects on Gasoline HCCI Combustion Aided by Measurements of Wall Heat Flux," Charleston, SC, ASME Paper No. ICEF2007–1698.
[17] Witze, P. O., and Green, R. M., 2005, "Comparison of Single and Dual Spray Fuel Injectors During Cold Start of a PF I Spark Ignition Engine Using Visualization of Liquid Fuel Films and Pool Fires," SAE Paper No. 2005-01-3863.
[18] Ohyama, Y., Nogi, T., and Ohsuga, M., 1992, "Effects of Fuel/Air Mixture Preparation on Fuel Consumption and Exhaust Emission in a Spark Ignition Engine," IMechE Paper No. C389/232, p. 59.
[19] Drake, M. C., Fansler, T. D., Solomon, A. S., and Szekely, G. A., 2003, "Piston Fuel Films as a Source of Smoke and Hydrocarbon Emissions From a Wall-Controlled Spark-Ignited Direct—Injection Engine," SAE Paper No. 2003-01-0547.
[20] Chang, J., Guralp, O., Filipi, Z., Assanis, D., Kuo, T., Najt, P., and Rask, R., 2006, "Method for Mid Load Operation of Auto-Ignition Combustion," U.S. Patent No. 7128,062.

Simulating Area Conservation and the Gas-Wall Interface for One-Dimensional Based Diesel Particulate Filter Models

Christopher Depcik[1]
Department of Mechanical Engineering,
The University of Kansas,
3120 Learned Hall,
1530 West 15th Street,
Lawrence, KS 66045-7609
e-mail: depcik@ku.edu

Dennis Assanis
Department of Mechanical Engineering,
The University of Michigan,
2045 W.E. Lay Automotive Laboratory,
1231 Beal Avenue,
Ann Arbor, MI 48109

Researchers have been using one-dimensional based models of diesel particulate filters (DPFs) for over two decades with good success in comparison to measured experimental data. Recent efforts in literature have expanded the classical model to account for the effects of varying soot layer thickness on the flow area of the gases. However, some discrepancies exist with respect to this formulation and the physical phenomena modeled in the channel equations. In addition, there is still some discussion regarding the calculation of the gas temperature within the soot and wall layers. As a result, this paper presents a model to discuss these different phenomena to remove or validate previous assumptions. In specific, formulation of the flow equations in area-conserved format (or quasi-one-dimensional) allows the model to account for the changes in the gaseous area as a function of soot loading. In addition, imposing thermodynamic equilibrium at the interface of the channels and wall layers allows the model to capture the thermal entrance lengths. These tasks were undertaken to illustrate whether or not the results justify the effort is worthwhile and this additional complexity needs to be incorporated within the model. By utilizing linear density interpolation in the wall to increase the computational efficiency of the code, it was determined that the classical model assumptions of neglecting soot thickness and gas temperature in the wall are valid within the range of typical DPF applications. [DOI: 10.1115/1.2939002]

Keywords: catalysis, combustion, environment, filtration, fluid mechanics, aftertreatment, particulates

1 Introduction

Diesel particulate filters (DPFs) have been researched for close to three decades based on their ability to capture particulate or soot matter with near 100% efficiency [1–4]. In the early market introduction, a fibrous type of DPF was used which trapped the soot according to the classical theory of aerosol filtration [5–7]. While the collection efficiency of such a device is initially high, eventually the tendency of the soot to adhere to the fibers decreases, lowering its trapping efficiency [8]. Hence, most researchers abandoned this type of device and instead moved onto the porous wall type.

The porous wall DPF consists of a honeycomb of long channels similar to the traditional catalytic converter [1]. Unlike the catalytic converter, the manufacturer now blocks alternating open channels of the honeycomb so all of the flow entering the device must pass through a porous wall, as illustrated in Fig. 1. The sizes of the pores in the wall are small enough to capture the soot by interception. During operation, the soot deposit builds up on one side of the monolith walls, increasing the flow resistance and pressure drop. Eventually, regeneration is required in order to reduce the pressure drop to a more reasonable value. Similar to the fibrous DPF, this regeneration occurs through a temperature excursion with the proper amount of oxidant available. The energy released by this oxidation conducts along the monolith and convects to the exhaust flow that passes through the deposited soot layer and the porous wall. The structure of the DPF offers the advantage of a large potential filter area in a reasonably compact volume. In addition, another benefit of this type of DPF is that as the soot builds up on the inlet channel, its trapping efficiency will *increase* instead of decrease.

Flow through a DPF is inherently three dimensional (3D) with a different soot loading, oxidation, and temperature for each flow channel. Furthermore, when the DPF is located close to the exhaust manifold, the pulsating flow leaving the engine along with the 3D geometry of the manifold creates flow maldistribution within the DPF that can lead to partial regeneration events and incomplete utilization. Nonetheless, there are many applications in the exhaust where the flow profile has time to develop and provide relatively uniform inlet conditions. For those types of problems, a one-dimensional (1D) based treatment of the DPF will often yield satisfactory results [9–11]. In addition, when studying catalyzed DPFs, these 1D based models incorporating chemical kinetics have a significant computational edge over their 3D counterparts. 1D models are also attractive for engine-aftertreatment system configuration studies where the placement and size of a number of aftertreatment devices need to be optimized. Lastly, if multidimensional models of DPFs are needed, the 1D model can be readily adapted [12–15].

As discussed in a previous paper [16], a monolithic type of device can be reduced from 3D to 1D by making a number of reasonable assumptions. The first step in simplifying the modeling effort is to reduce the 3D device in Cartesian coordinates into two-dimensional (2D) cylindrical coordinates: axial and radial. Keeping these radial components allows for a 2D DPF model; however, assuming that all axial and radial cells are identical results in the traditional 1D model. While a catalyst only needs one channel to describe the proper flow profile, a DPF will need an

[1]Corresponding author.

Manuscript received April 20, 2007; final manuscript received April 23, 2008; published online August 22, 2008. Review conducted by Christopher J. Rutland.

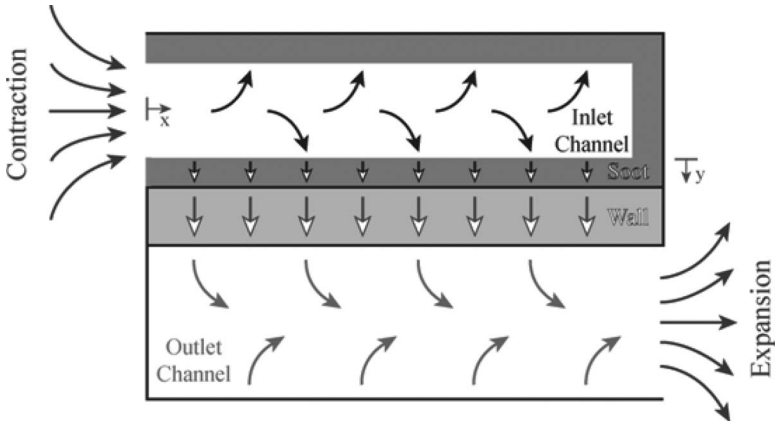

Fig. 1 Flow schematic of a DPF

inlet and outlet channel to obtain the correct profile. Most of the 1D DPF modeling efforts of today stem from the papers by Bissett [9,17] and Bissett and Shadman [18].

There are a number of empirical assumptions embedded in these models with respect to area conservation and gas temperature within the filter for computational efficiency. This paper presents a model based on the governing equations of flow to discuss these assumptions. In specific, the flow equations are formulated in the area-conserved format often used for converging-diverging nozzles [19,20] and the intake and exhaust of internal combustion engines [21,22], often called quasi one-dimensional flow. The use of area conservation for a DPF model is not a new technique as described in Refs. [23–27]; however, these papers simplify the velocity through the soot and wall layers into just one or two values. As a result, the convective terms for mass flow into the wall may not accurately account for the actual surface area in the channels.

In addition, these previous efforts simplify the computational task by setting the gas temperature in the soot and wall layers equal to the filter temperature. However, the small distance scales associated with these layers make the diffusion component of the Navier–Stokes equations important for the species equations. In this paper, the conduction component in the energy equation is included along with heat transfer between the filter and the gas in order to calculate the actual gas temperature profile in the wall. Including conduction allows the simulation to check previous model assumptions.

The following sections present the governing equations for the channels, soot, and wall layers including a brief historical summary of the assumptions and models to date. This brief summary helps illustrate where this paper enhances literature. To account for transient soot loading and oxidation, the model contains a surface particulate mass equation that adapts to the changing soot levels. The formulation also includes the effects of a changing surface area on the filter energy equation through the proper physics. To capture the thermal entrance length and the gas-wall interactions, this paper describes the boundary conditions at the interface according to local thermal equilibrium. This paper also contains disclosure of the numerical methods utilized in the model solution. Finally, the results are presented and a number of conclusions are reached regarding whether or not this increase in model complexity is worth the numerical effort.

2 Governing Equations

In 1984, Bissett [9] created a model for the transport of nearly all thermodynamic variables through a wall-flow DPF while trying to avoid the complexities of multidimensional compressible fluid flow. He accomplished this by representing the flow at each axial position in one dimension and incorporating the proper physics for the flow to and from the wall system. In his paper, Bissett makes the following assumptions.

1. The properties of the gas entering the front face of the monolith are spatially uniform; however, they can be time dependent.
2. The model assumes perfect insulation for the circumferential walls of the monolith.
3. A single inlet and outlet channel represents the behavior of all inlet and outlet channels.
4. He neglects radiative heat transport in the channels since the long thin channel walls have similar view factors and should have similar temperatures.
5. The thickness of the soot layer is so thin compared to the channel thickness during the initial period of operation; the change in the channel geometry due to the presence of the soot layer can be neglected: $t_d \ll d_m$.
6. The emitted particles do not interfere with the flow due to their low mass fraction within the bulk gas.
7. While not explicitly stated in his paper, Bissett omits the time derivatives of the bulk gas flow variables effectively stating that there is not any energy storage in the gas: $\partial\rho/\partial t = \partial(\rho u)/\partial t = \partial T/\partial t \rightarrow 0$.
8. He also neglects the thin heat transfer layer in the wall requiring all heat transfer to take place in the channels. As a result, the filter temperature is the equal temperature of both phases in the filter and independent of the radial direction; it can still vary in the axial direction.

In this paper, the authors target Assumptions 5 and 8 from the list above to illustrate how to properly incorporate them in the model and determine whether or not this computational effort is worthwhile. To simplify the computational task, this paper neglects all radial multidimensional effects. In addition, omission of the species governing equations allows for a reduction in the complexity of the model. The following sections describe the governing equations of motion through the channels, the soot, and wall layers, incorporating the latest literature results along with new adaptations.

2.1 Mass Equations. The assumption of changes in channel geometry due to the soot layer was revisited by Peters et al. [23,24] and Haralampous et al. [25–27] through the incorporation of varying soot mass levels in the inlet channel and their effect on flow through area conservation in the governing equations. In the papers of Peters et al., the mass equations for the inlet and outlet channels utilize different velocities to represent the lateral components through the soot layer and the porous filter wall, respectively; i.e., one velocity for the soot layer and one velocity for the

wall layer. However, in their formulation, the convective term for the mass flows entering or exiting the wall utilizes the densities of the channels; i.e., they use the inlet density leaving the inlet channel and for the outlet channel, they use the outlet channel density entering from the wall. According to the classical model, this does not correspond correctly to the system since the density at the interface of the wall can have a different value than the channels. Discussion of this concept occurs later in Sec. 3, illustrating how the density at the interface is a function of a local thermodynamic equilibrium.

In the papers of Peters et al., the wall flow surface areas in the inlet and outlet channels are different because of the soot layer in the inlet channel; i.e., equates to a smaller control volume for the gas in the inlet channel when the soot is present. However, while the papers of Haralampous et al. include the proper density; their model makes no distinction between the two channels with the same surface area used in the inlet and outlet channels. This is because a physical property met by models is that there should not be any mass storage in the soot or wall layers during steady-state conditions: $\partial\rho_s/\partial t=0$ and $\partial\rho_w/\partial t=0$. Since the mass flux terms cancel each other for both models, they do not violate any mass conservation laws. When utilizing different surface areas for the inlet and outlet channels when the soot is present, to balance the mass fluxes the density, velocity, or density times velocity must change in the soot and wall layers. This allows different mass flux values for the inlet and outlet channels to account for the dissimilar surface areas while not causing mass accumulation within the wall. These terms in the mass equations then use boundary conditions for the density and velocity variables instead of constant values; i.e., $\rho_s u_s|_{y=0}$ and $\rho_w u_w|_{y=t_m+t_d}$. While Peters et al. did not utilize boundary conditions per se, they did utilize different wall velocities for the soot and wall layers to account for the different surface areas. In the papers of Haralampous et al., since they only use one value for the density and velocity to describe the properties in the wall, they use the same surface area to prevent mass accumulation.

In this paper, the thermodynamic properties through the soot and wall layers are allowed to change and will be calculated according to the Navier–Stokes equations of motion. As a result, the equations of mass for the channels incorporating different surface areas are

$$\frac{\partial(\rho_{\mathrm{I}} u_{\mathrm{I}} A_{\mathrm{I}})}{\partial z} = -\rho_s u_s S_{\mathrm{I}} \tag{1}$$

$$\frac{\partial(\rho_{\mathrm{II}} u_{\mathrm{II}} A_{\mathrm{II}})}{\partial z} = \rho_w u_w S_{\mathrm{II}} \tag{2}$$

where the cross-sectional area and surface area on a per length basis are represented as

$$A_{\mathrm{I}} = (d_m - 2t_d)^2, \quad S_{\mathrm{I}} = 4(d_m - 2t_d), \quad A_{\mathrm{II}} = d_m^2 \text{ and } S_{\mathrm{II}} = 4d_m \tag{3}$$

for the inlet and outlet channels, respectively, similar to the model equations presented by Haralampous and Koltsakis [26]. In this case, for the inlet channel equations, the density and velocity of the gas in the soot layer used in the flux term are evaluated at $y=0$. For the outlet channel equations, the density and velocity of the gas in the wall layer used in the flux term are evaluated at $y=t_m+t_d$.

While the area-conserved formulation is not necessary for the outlet channel, writing the equations in this manner allows for different geometries to be utilized similar to the work previously accomplished by Konstandopoulos et al. [28,29]; i.e., writing the numerical method using A and S allows those to be easily changed based on geometry. Area-conserved format is often used for converging-diverging nozzles [19,20] and the intake and exhaust of internal combustion engines [21,22] in order to better account for mass conservation in varying geometry situations. In this situation, the different sizes of the control volumes and surface areas encountered require this version of the governing equations.

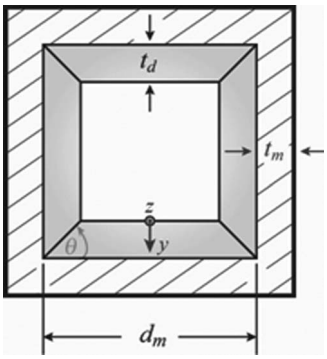

Fig. 2 Square channel schematic illustrating the important geometric and soot parameters

In the soot layer, the flow is no longer 1D due to the varying cross-sectional area through the layer. Since area conservation is a methodology for incorporating multidimensional effects without having to include the other dimensions in the solution algorithm, the soot layer equation becomes

$$\frac{\partial(\rho_s u_s A_s)}{\partial y} = A_s \dot{S}_{\mathrm{mass}} \tag{4}$$

where the right-hand side equates to a gain in mass due to soot oxidation reactions; i.e., as the solid soot burns, it converts into partial and complete products of combustion in gaseous form. This term in the soot mass equation has been discussed previously in literature in models of soot oxidation [30] and will be explored later in this paper as to its impact on the mass flow rate exiting the DPF.

For square channels, the change in cross-sectional area per unit length through the soot layer can be determined as in Fig. 2:

$$A_s = 4\left[d_m - 2\left(t_d - \frac{y}{\tan\theta}\right)\right] \quad \text{where } \tan\theta = 1 \tag{5}$$

and the instantaneous change in the cross-sectional area can then be determined by taking the derivative of this value with respect to the distance through the soot layer; i.e., $dA_s/dy=8$.

Even though the cross-sectional area that the flow sees is constant in the wall layer, writing the mass equation in area-conserved format allows for continuity with the other equations:

$$\frac{d(\rho_w u_w A_w)}{dy} = 0 \tag{6}$$

where

$$A_w = 4d_m \tag{7}$$

Upon inspection of the mass equations in the channel, the mass flux terms do cancel each other out similar to the before mentioned references. While the properties in the soot and wall layers change, they must remain consistent with the governing equations of mass in each respective layer. In all cases, time derivatives of the variables are neglected, which is a reasonable assumption as long as the time scales in the problem are a function of the filter and not the bulk gas [16].

By modeling the velocity profile through the soot and wall layers instead of utilizing average velocities, the model allows for proper utilization of surface areas for the channel mass equations. In addition, the resonance time of the gas in the soot and wall layers is more accurately modeled in the situation where there might be a large change of velocity through the wall. This may become important when simulating catalyzed walls to get a better

indication of the conversion rate through the device. This comparison is noted as future work as constant mass fractions are assumed for reduced complexity in this paper.

2.2 Momentum Equations. For the momentum equations in the channels, all DPF models assume that the gas flows only in the z-direction as it enters or exits the channel. As a result, there is no transport of the y-component of momentum in the wall. However, because the no slip condition holds at the walls in the z-direction, friction will occur. Bissett states that this variation should be very close to that observed when the walls are solid since only a very small fraction of the flow at each axial position passes through the wall. As a result, the 1D model for the bulk gas momentum equations looks exactly like those used in traditional, area-conserved 1D flow [21,22,31]:

$$\frac{\partial(\rho_{\mathrm{I}} u_{\mathrm{I}}^2 A_{\mathrm{I}})}{\partial z} + \frac{\partial(p_{\mathrm{I}} A_{\mathrm{I}})}{\partial z} = -\frac{F\mu|u_{\mathrm{I}}|}{d_m - 2t_d} S_{\mathrm{I}} + p_{\mathrm{I}} \frac{dA_{\mathrm{I}}}{dz} \tag{8}$$

$$\frac{\partial(\rho_{\mathrm{II}} u_{\mathrm{II}}^2 A_{\mathrm{II}})}{\partial z} + \frac{\partial(p_{\mathrm{II}} A_{\mathrm{II}})}{\partial z} = -\frac{F\mu|u_{\mathrm{II}}|}{d_m} S_{\mathrm{II}} + p_{\mathrm{II}} \frac{dA_{\mathrm{II}}}{dz} \tag{9}$$

Writing the above equations in area-conserved format results in an additional term on the right-hand side to balance the forces. It is important to note that the derivatives can be expanded and the more traditional DPF momentum equations can be recovered; i.e., the last term on the right-hand side will be eliminated when the derivative involving the pressure is expanded on the left-hand side. However, keeping the area terms in the derivatives and solving the governing equations as indicated is more accurate with respect to mass conservation [20–22]. This is also illustrated later in this paper in Sec. 4 when the non-area-conserved formulation is compared to the area-conserved formulation with respect to the pressure drop through the soot layer.

Following Wooding [32] and Brinkman [33,34], a theorized extension of the Navier–Stokes momentum equation to porous media involves the use of an effective viscosity to account for the diffusion of velocity. However, for many practical purposes, there is no need to include this viscous term [35]. In addition, Beck [36] found that the inclusion of the convective term, $\partial(\rho u^2)/\partial y$, is erroneous when Darcy's law is employed. Including these concepts results in the following equation for momentum in the soot and wall layers:

$$\frac{d(p_s A_s)}{dy} = p_s \frac{dA_s}{dy} - \frac{\mu u_s A_s}{K_d} - \beta_d \rho_s A_s u_s^2 \tag{10}$$

$$\frac{d(p_w A_w)}{dy} = p_w \frac{dA_w}{dy} - \frac{\mu u_w A_w}{K_m} - \beta_m \rho_w A_w u_w^2 \tag{11}$$

Again, it is important to note that the area change term on the right-hand side allows a balance in the pressure forces when writing in area-conserved format. By expanding the derivative of the pressure force, the traditional equation for wall pressure written by Bissett will be recovered.

2.3 Energy Equations. For the bulk gas energy equations, there is some discrepancy in literature on how to write the governing equations. Because there is mass flowing through the walls, there will be a transport of energy from (to) the inlet (outlet) channel to (from) the porous wall in addition to convective heat transfer. In Bissett's paper, he neglects the thin heat transfer layer in the wall requiring all heat transfer to take place in the channels. As a result, the filter temperature is the equal temperature of both phases in the wall and independent of the radial direction; it can still vary in the axial direction. Note that in this paper, there is a distinction between the temperature of the filter wall and the temperature of the gas within the soot and wall layers. Using Bissett's assumption and the notation in this paper, the gas in the soot (T_s) and wall layers (T_w) is equal to the filter solid temperature (T_f); i.e., $T_s = T_w = T_f$.

In 1997, Bissett's original energy equations were modified by Koltsakis and Stamatelos, illustrating the inclusion of an additional term in the outlet bulk gas energy equation [10]. However, no discussion is noted regarding this discrepancy and in the same year, the original equation of Bissett is published by the same authors [37]. This inconsistency is again seen in a paper by Konstandopoulos et al. in 2001 [14] through a derivation of these equations using a continuum description of the filter formulated from a multidimensional model of a DPF. A later multidimensional paper by Kostoglou et al. [15] referencing this 2001 paper discusses this discrepancy. In this paper, for a perimeter-averaged 1D approach for the temperature field in the channel, the cross-sectional temperature distribution of the channel no longer enters the problem and the gas entering the porous medium assumes a temperature equal to T_{I}. This gas quickly goes to thermal equilibrium with the porous wall and exits into the outlet channel with the filter temperature T_f. They note that the difference between the models is small for most practical cases; however, the older model can lead to some unphysical behavior in some circumstances. Recent efforts by Konstandopoulos et al. [28] revisit this difference but no definitive conclusion is reached.

The full formulation of the area-conserved Euler equation of energy includes the effects of kinetic energy in the internal energy and enthalpy terms. However, these kinetic energy terms are small in comparison and can be eliminated; $u^2 \ll h$. Writing the energy equation must take this historical discussion regarding this equation into account. Papers by Kostoglou et al. [15] and Konstandopoulos et al. [28] illustrate that the gas entering the porous medium is assumed to have a temperature equal to T_{I}. However, instead of using this assumption, this paper solves the gas temperature in the soot and wall equations as a function of the governing equations of flow accordingly; i.e., T_s at $y=0$, the inlet channel and soot interface is computed in deference to T_{I} assumed as the value. This will then solve for the thermal heat transfer layer in the wall, allowing for continuity between the channel gas temperature and the gas in the soot and wall layers. In other words, this model imposes thermal equilibrium at the surface according to the first law of thermodynamics as illustrated later in Sec. 3. As a result, the channel equations are

$$\frac{\partial(\rho_{\mathrm{I}} u_{\mathrm{I}} h_{\mathrm{I}} A_{\mathrm{I}})}{\partial z} = -S_{\mathrm{I}}[h_g(T_{\mathrm{I}} - T_s) + \rho_s u_s h_{\mathrm{I}}] \tag{12}$$

$$\frac{\partial(\rho_{\mathrm{II}} u_{\mathrm{II}} h_{\mathrm{II}} A_{\mathrm{II}})}{\partial z} = -S_{\mathrm{II}}[h_g(T_{\mathrm{II}} - T_w) - \rho_w u_w h_w] \tag{13}$$

Note that these equations write the heat transfer term as a function of the local temperature of the soot and wall layers; this is analogous to the use of mass transfer in the papers of Haralampous et al.

By expanding the derivatives, using the definition of constant pressure specific heats, $\partial h/\partial z = c_p(\partial T/\partial z)$, and incorporating mass Eq. (1), the model produces the same result for the energy equations as the recent papers by Kostoglou et al. and Konstandopoulos et al. for the inlet channel:

$$\rho_{\mathrm{I}} u_{\mathrm{I}} c_p \frac{dT_{\mathrm{I}}}{dz} = -\frac{S_{\mathrm{I}}}{A_{\mathrm{I}}} h_g(T_{\mathrm{I}} - T_s) \tag{14}$$

For the outlet channel, performing the same analysis with Eq. (2) results in a similar equation as the previously mentioned papers with the main difference in the use of enthalpy terms in the second term on the right-hand side:

$$\rho_{\mathrm{II}} u_{\mathrm{II}} c_p \frac{dT_{\mathrm{II}}}{dz} = -\frac{S_{\mathrm{II}}}{A_{\mathrm{II}}}[h_g(T_{\mathrm{II}} - T_w) - \rho_w u_w (h_w - h_{\mathrm{II}})] \tag{15}$$

Often, researchers write this second term as the constant pressure specific heat times a temperature difference: $\rho_w u_w c_p (T_w - T_{\mathrm{II}})$. However, derivation from the governing equations indicates that

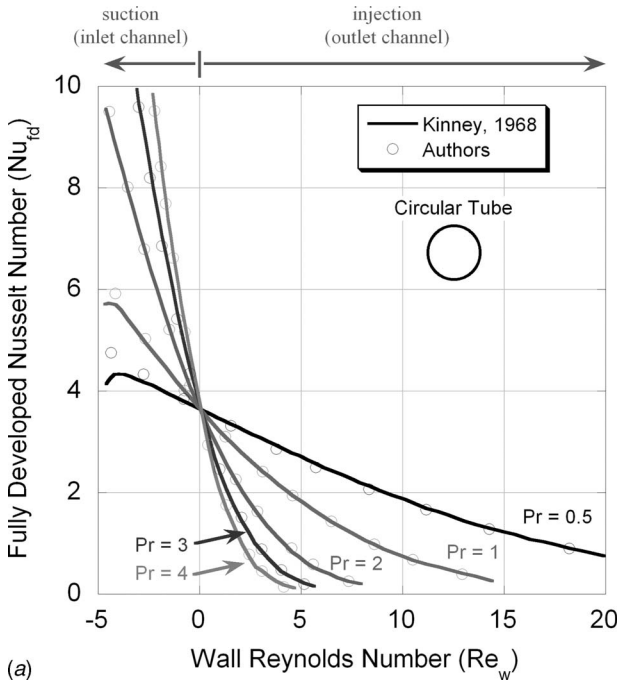

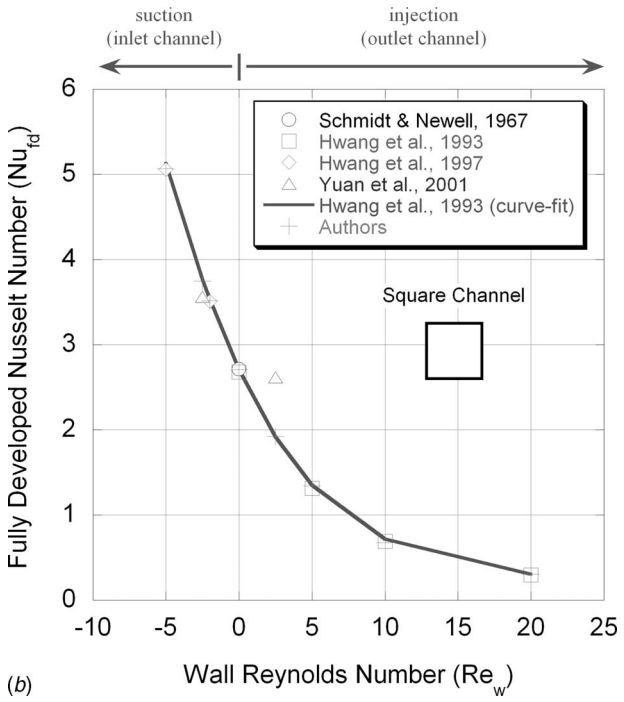

Fig. 3 Fully developed Nusselt number correlations based on suction and injection values of the wall Reynolds number for (*a*) circular tube and (*b*) square channel

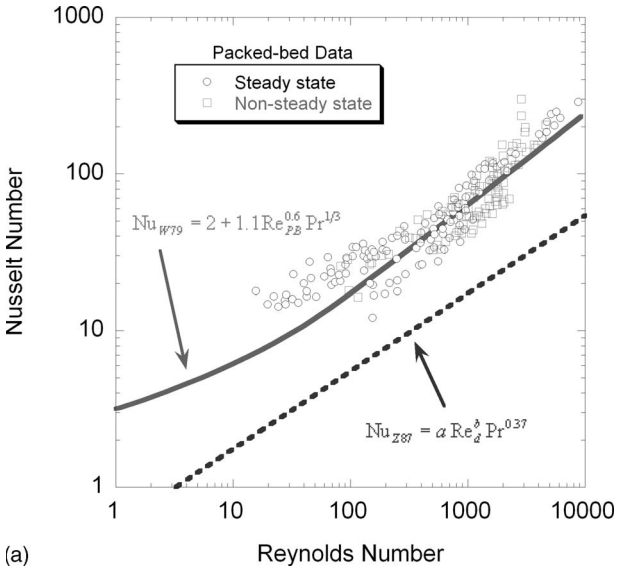

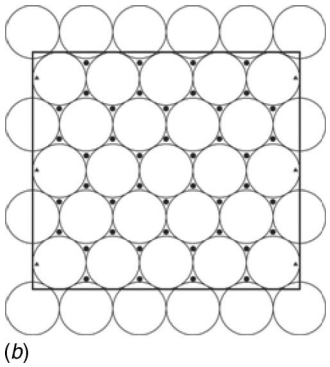

Fig. 4 (*a*) Packed bed and staggered cylinder correlations as a function of Reynolds and Prandtl numbers and (*b*) 2D illustration of particles and voids used in adapting packed-bed heat transfer correlation

an enthalpy difference should be used. When using chemical species and their associated heats of formation, the use of the constant pressure specific heats will result in a dissimilar value. However, since the composition change is typically small in the normal direction, this difference may be negligible. Future work is targeted at determining this change when the species equations are included in the formulation.

Recent work by Konstandopoulos et al. [28] looks into the effects of suction and injection on the heat transfer coefficients in these channels. A fundamental analysis is presented in that paper; however, using Refs. [38–46], a fully developed Nusselt number correlation based on the flow Peclet number through the wall was determined:

$$\mathrm{Nu_{fd}} = \frac{h_g d}{k_g} = 3.6568 - 0.459\mathrm{Pe}_w + 0.0198\mathrm{Pe}_w^2 - 0.000296\mathrm{Pe}_w^3 \quad \text{(circular)} \tag{16}$$

$$\mathrm{Nu_{fd}} = \frac{h_g d}{k_g} = 2.71 - 0.504\mathrm{Pe}_w + 0.0381\mathrm{Pe}_w^2 - 0.00102\mathrm{Pe}_w^3 \quad \text{(square)} \tag{17}$$

where $\mathrm{Pe}_w = u_w d/\alpha_g$. The form of the above correlations resembles the paper of Hwang et al. that includes a curve fit based on Re_w number only. It is important to note that the square channel model based on Peclet number is currently only valid for a Pr=0.72 (approximately air) as that was all of the data found in those papers. Figure 3 presents the results of the curve fits for the circular and square correlations, respectively.

As mentioned in the Introduction, diffusion within the soot and wall layers is important because of the small distance scales. Because of these small scales, in the energy equations for the soot and wall layers, conduction might also be important. Again, since

the kinetic energy of the gas in the wall is much smaller than the enthalpy of the gas $h_w \gg u_w^2$, the following equations for the energy of the gas in the soot and wall layers can be written [47–50]:

$$\frac{\partial(\rho_s u_s h_s A_s)}{\partial y} - \frac{\partial}{\partial y}\left(k_g^* A_s \frac{\partial T_s}{\partial y}\right) = h_c A_s \tilde{a}(T_f - T_s) \tag{18}$$

$$\frac{\partial(\rho_w u_w h_w A_w)}{\partial y} - \frac{\partial}{\partial y}\left(k_g^* A_w \frac{\partial T_w}{\partial y}\right) = h_c A_w \tilde{a}(T_f - T_w) \tag{19}$$

In these equations, the close proximity of the filter affects the thermal conductivity of the fluid in the porous layers and, as a result, requires an effective thermal conductivity calculation. The calculation of which is described for metal foams by Boomsma and Poulikakos [51]. Since no fundamental models of effective conductivity exist for DPF purposes, the metal foam formulation is utilized here (see also Ref. [49] for more information on its application).

The first term on the right-hand side accounts for the heat transfer between the filter and the gas in each respective layer. It has been stated that the calculation of the heat transfer coefficient (h_c) is difficult to measure [48]; however, two correlations exist in literature that will serve as an approximate upper and lower bounds. In the situation where the filter wall is packed full of soot and a cake layer exists in the inlet channel, it is theorized here that the heat transfer will be analogous to a packed-bed reactor as proposed by Wakao et al. [52]:

$$\mathrm{Nu}_{\mathrm{W79}} = 2 + 1.1\,\mathrm{Re}_{\mathrm{PB}}^{0.6}\,\mathrm{Pr}^{1/3} \tag{20}$$

When the filter is empty, a correlation developed by Zukauskas [53] for staggered cylinders used in heat transfer studies for metal foams can be utilized:

$$\mathrm{Nu}_{\mathrm{Z87}} = a\,\mathrm{Re}_d^b\,\mathrm{Pr}^{0.37} \tag{21}$$

where a and b are function of the Reynolds number. This correlation should give a heat transfer coefficient smaller than the actual due to the high porosity of the metal foams comparative to a DPF wall. However, contrasting the two models will give an idea whether to accomplish a more fundamental study of heat transfer in the filter wall. Figure 4(*a*) illustrates these correlations to demonstrate the upper and lower bounds.

Since the correlation of Wakao et al. models a packed-bed structure where the Reynolds number is a function of the diameter of a particle, use in a porous wall structure requires conversion. The metal foam papers utilize an effective diameter for the Zukauskas correlation as a function of the pore diameter (d_p) and the porosity (ε_p):

$$d = 1.18 d_p \sqrt{\frac{1-\varepsilon_p}{3\pi}} \tag{22}$$

In addition, these variables describe the surface area density used in the energy equation:

$$\tilde{a} = \frac{6.14\sqrt{1-\varepsilon_p}}{d_p} \tag{23}$$

In a packed bed, the porosity is equal to the pore volume divided by the total volume of the wall and the particle volume is equal to 1 minus the porosity. Hence, calculation of the total pore volume using the effective diameter is equal to

$$\text{pore volume} = N_{\text{pore}} \frac{\pi d^3}{6} \tag{24}$$

and the calculation of the particle volume uses the particle size:

$$\text{particle volume} = N_{\text{part}} \frac{\pi D_p^3}{6} \tag{25}$$

where N_{pore} is the total number of pores and N_{part} is the total number of particles. Equating these two terms using the porosity, we find

$$\frac{\varepsilon_p}{1-\varepsilon_p} = \frac{d^3 N_{\text{pore}}}{D_p^3 N_{\text{part}}} \tag{26}$$

Using a simple 2D approximation of particles within a box, as illustrated in Fig. 4(*b*), a correlation between the number of pores and the number of particles is equal to

$$N_{\text{pore}} = 2N_{\text{part}} \tag{27}$$

As a result, the pore diameter and the particle diameter relationship is

$$d = D_p \left[\frac{\varepsilon_p}{2(1-\varepsilon_p)}\right]^{1/3} \tag{28}$$

Hence, the Reynolds number of the gas and the Reynolds number of the packed-bed formation are

$$\mathrm{Re}_d = \frac{\rho u_w d}{\mu} = \mathrm{Re}_{\mathrm{PB}} \left[\frac{\varepsilon_p}{2(1-\varepsilon_p)}\right]^{1/3} \tag{29}$$

2.4 Surface Particulate Mass Equation. When particulates flow into a DPF, they first load within the wall layer where the pores are small enough to capture the soot by interception (deep bed filtration). After the wall has filled with soot, the particulate then loads upon the surface in a growing cake layer. Previous efforts in DPF modeling have described these two phases of storage [28,54–57]; however, for simplicity, only the cake layer is modeled here with the deep bed filtration inclusion noted as future work.

In the efforts of Peters et al., a model for particulate propagation throughout the channels is included to simulate the loading as a function of transient input conditions. In this paper, the authors revise this formulation slightly for simplification purposes and notation consistency. Based on the input flow rate of the soot, the mass fraction of the soot in the flow can be determined:

$$Y_d = \frac{\dot{m}_{\text{soot}}}{\dot{m}_{\text{in}}} \tag{30}$$

where $\dot{m}_{\text{soot}}$ is the mass flow rate of the soot and $\dot{m}_{\text{in}}$ is the total flow rate of gas into the DPF, respectively. Similar to Bissett, this paper assumes that the emitted soot particles from the engine have a negligible impact on the fluid mechanics of the flow (Assumption 6); stated mathematically as $Y_d \ll Y_{\mathrm{N}_2}, Y_{\mathrm{O}_2}$, etc.

In Bissett's original efforts, he assumes that the mass fraction of O_2 is constant throughout the inlet channel. Following this methodology, a constant mass fraction of the soot in the gas occurs along the inlet channel:

$$\frac{dY_d}{dz} = 0 \tag{31}$$

A revisit of this assumption will occur in future efforts when the effects of species diffusion in the channels are included in the formulation.

From inlet channel mass equation (Eq. (1)), the total amount of mass per unit length flowing to the surface comes from the term $\rho_s u_s S_{\mathrm{I}}$. Incorporating the mass fraction of the soot, a soot mass flow rate per mesh interval to the surface of the inlet channel is determined as a function of the changing surface area:

$$\varsigma = \rho_s u_s S_{\mathrm{I}} Y_d \tag{32}$$

Once the temperature gets large enough and a proper amount of oxidant is available, this particulate mass on the surface will combust raising the temperature of the surface while adding additional

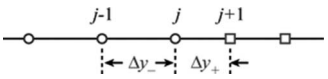

Fig. 5 Variable differentiation utilized in soot and wall layer energy equations

mass to the gas in the wall layers via Eq. (4). In Bissett and Shadman's original efforts [9,18], along with a number of other researchers [15,54,56,58–61], this gas source term within the surface layers was not included and the soot oxidation was written as a function of soot thickness (t_d). Recent work in this area involves writing the soot mass equation on a mass basis instead of thickness to account for this component in the soot mass equation [13,25–27,30,62]. However, the foundation of this model is still Bissett and Shadman's early work.

The molar combustion reactions are often written including partial oxidation factors [63–65]:

$$C_{(s)} + \alpha_{O_2} O_2 \rightarrow 2(\alpha_{O_2} - 0.5)CO_2 + 2(1 - \alpha_{O_2})CO \quad (0.55 \leq \alpha_{O_2} \leq 0.90) \tag{33}$$

$$C_{(s)} + \alpha_{NO_2} NO_2 \rightarrow \alpha_{NO_2} NO + (2 - \alpha_{NO_2})CO + (\alpha_{NO_2} - 1)CO_2 \quad (1.2 \leq \alpha_{NO_2} \leq 1.8) \tag{34}$$

indicating incomplete combustion with some carbon monoxide produced during the oxidation process. In the O_2 oxidation reaction, literature computes the loss of oxygen in the soot layer as

$$\dot{S}_{O_2} = -S_p \hat{\rho}_s Y_{s,O_2} k_{O_2} \tag{35}$$

where the hatted density variable indicates the average value within the layer. This is accomplished by summing the density over the number of discretizations and then dividing by the number of discretizations to get an average value in the layer.

In this equation, the Arrhenius reaction rate term is

$$k_{O_2} = A_{O_2} T_f \exp[-E_{O_2}/(R_u T_f)] \tag{36}$$

Using the molar reaction expression for O_2 oxidation along with the molecular weights, the loss of the soot on the layer is equal to

$$\dot{S}_{C_{(s)}} = -\frac{S_p \hat{\rho}_s Y_{s,O_2} k_{O_2} W_{C_{(s)}}}{\alpha_{O_2} W_{O_2}} \tag{37}$$

In order to get this term into the proper units for consistency with the soot loading term, the mass and density of the particulate matter need to be utilized (see Refs. [13,25–27,30,62]). This results in the following expression:

$$\chi = -\frac{S_p \hat{\rho}_s Y_{s,O_2} k_{O_2} W_{C_{(s)}}}{\alpha_{O_2} W_{O_2} \rho_d} \quad (1/s) \tag{38}$$

The combination of the two expressions results in an equation for soot mass per unit length on the surface:

$$\frac{dm_d}{dt} = \mathrm{s} - \chi m_d \tag{39}$$

which accounts for soot loading and oxidation in a transient manner. The thickness of the soot on the surface is calculated from geometric principles [54]:

$$t_d = \frac{1}{2}\left(d_m - \sqrt{d_m^2 - \frac{m_d}{\rho_d}}\right) \tag{40}$$

Note that the mass of the soot on the surface may vary in each numerical cell, but using the above equation normalized per length ensures that the thickness remains consistent.

For the mass equation in the soot layer, Eq. (4), the source term stemming from soot oxidation has to be determined. Since the mass added to the gas equals the mass of the soot that has been combusted, over the entire layer, this source term equals Eq. (37). In order to use it within the mass equation, it is split by the number of discretizations in the soot layer:

$$\dot{S}_{mass} = \frac{\dot{S}_{C_{(s)}}}{N_s - 1} \quad (\mathrm{kg\ C_{(s)}\ m^{-3}\ s^{-1}}) \tag{41}$$

While not explicitly derived, the inclusion of soot oxidation via the NO_2 pathway follows similar to the O_2 derivation presented.

2.5 Filter Energy Equation. In order to account for the temperature of the filter, Bissett used the traditional heat diffusion equation writing it as a function of the thicknesses of the wall and soot. The filter wall and soot layer assume to have the same temperature due to their proximity to each other and the fact that the soot is present within the filter wall due to deep bed filtration. Bissett's model included the effects of conduction in the wall $\dot{Q}_{cond}$, heat transfer from the gases in the channel $\dot{Q}_{conv}$, and the effects of soot oxidation on the energy of the wall $\dot{Q}_{reac}$. In 1989, Pattas and Samaras [66] formulate a discretized version of this equation and find an energy flux through the wall $\dot{Q}_{wall}$ not included in the original formulation; this relates back to the discrepancy in literature regarding the channel energy equations (see previous discussion and Refs. [10,14,15,28]). Based on the original channel energy equations, the enthalpy flow through the wall canceled itself out and, as a result, did not appear in this equation. A few years later, this equation was written in differential format

Table 1 Parameters used for isothermal and temperature step change simulations

Variable	Value	Variable	Value
Inlet velocity	24.8 m s^{-1}	Inlet pressure	1.0132 bars
EX-80 permeability	2×10^{-13} m^2	EX-80 Forscheimer	5×10^{8} m^{-1}
Channel diameter	2.11 mm	Channel length	12 in.
Wall thickness	0.432 mm	DPF diameter	5.66 in.
Cell density	100 cells $in.^{-2}$	Substrate density [58]	1300 kg m^{-3}
Pore diameter	12 μm	Substrate thermal conductivity	0.5 W m^{-1} K^{-1}
Substrate specific heat	600 J kg^{-1} K^{-1}	Porosity	50%
	Calculated parameters		
Total mass flow rate	0.075 kg s^{-1}	Inlet temperature	632.18 K
Number of cells	2516		

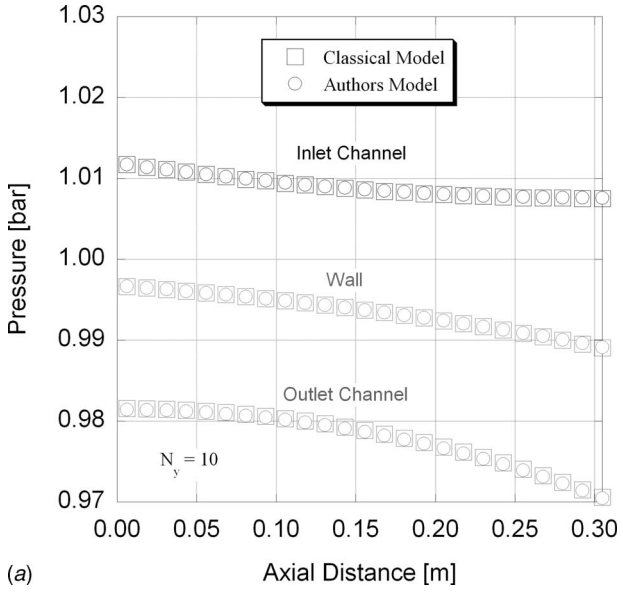

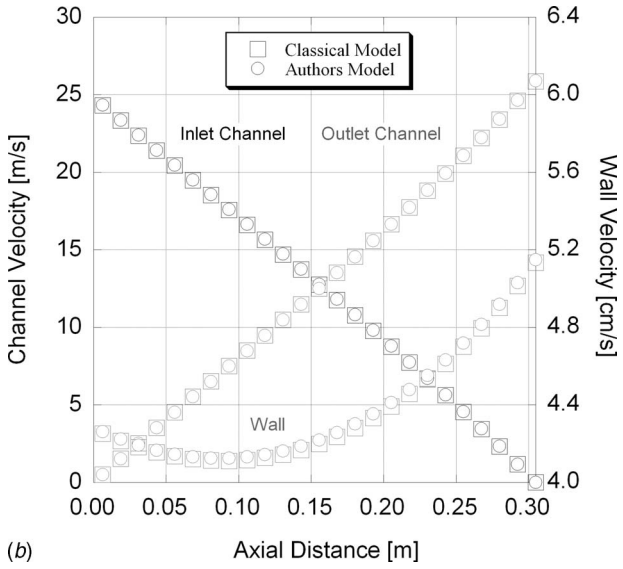

Fig. 6 Comparison between the classical flow model and area-conserved model of the authors for gas (*a*) pressure and (*b*) velocity during isothermal run

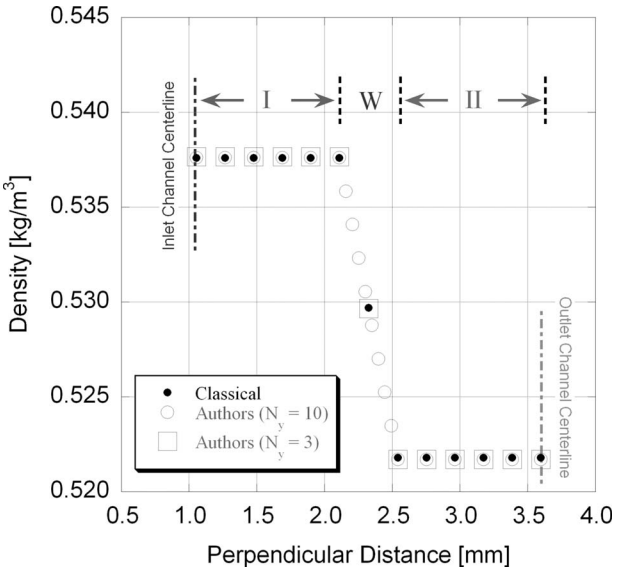

Fig. 7 Density comparison between the classical flow model and area-conserved model at halfway point in the axial direction during isothermal run

including this energy flux through the wall [10].

The current version of the filter energy equation can be now seen as variants of the following full description [24,27,56,61]:

$$(\rho_f c_f V_f + \rho_d c_d V_d)\frac{\partial T_f}{\partial t} = \dot{Q}_{\text{cond}} + \dot{Q}_{\text{conv}} + \dot{Q}_{\text{wall}} + \dot{Q}_{\text{reac}} + \dot{Q}_{\text{supply}} + \dot{Q}_{\text{multi}} + \dot{Q}_{\text{rad}} \quad (42)$$

The extension from Bissett's original model began when Romero et al. [67] decided to include the effects of thermal heaters to provide a more active regeneration process $\dot{Q}_{\text{supply}}$. Later, Konstandopoulos et al. [14] formulated a multidimensional version of a DPF $\dot{Q}_{\text{multi}}$, which is simplified into the classical flow model using a continuum description of the filter as explained in Ref. [12]. Because of this simplification, implementation of an effective thermal conductivity tensor accounts for multidimensional effects in the classical model. In the same paper, radiation heat transfer $\dot{Q}_{\text{rad}}$ between the walls is included in the multidimensional model but omitted from the classical flow model (see Bissett, Assumption 4). These terms are revisited a couple years later from the perspective of the classical flow model only [13,15]. The multidimensional version of the filter energy equation effectively eliminates Bissett's original assumptions of an adiabatic device with spatially uniform inlet conditions using ambient heat transfer boundary conditions and zones of different inlet flow conditions.

Traditionally, researchers write the filter energy equation as a function of wall and soot thicknesses; however, here the authors write it as a function of volumetric terms intended to account for the entire filter volume based on a 1D representation. This is similar to the methodology for modeling the monolith energy equation for 1D catalyst modeling [16]. In the model, the total empty channel volume (no soot) equals the volume of each channel times the number of channels written per axial length:

$$V_e = d_m^2 N_c \quad (43)$$

Utilizing the total DPF volume,

$$V_{\text{DPF}} = \frac{\pi D^2}{4} \quad (44)$$

an empty void fraction can be determined similar to monolithic catalyst modeling:

$$\varepsilon = \frac{V_e}{V_{\text{DPF}}} \quad (45)$$

As a result, the total volume of the solid filter is then equal to

$$V_f = (1-\varepsilon)V_{\text{DPF}} \quad (46)$$

When the soot is present, the total empty channel volume now accounts for the loss in gaseous volume:

$$V_{de} = \frac{N_c}{2}[(d_m - 2t_d)^2 + d_m^2] \quad (47)$$

Computation of a soot-based void fraction as a function of the soot loading equals

$$\varepsilon_d = \frac{V_{de}}{V_{\text{DPF}}} \quad (48)$$

and derivation of the total volume of particulate matter on the surface results in

$$V_d = (\varepsilon - \varepsilon_d)V_{\text{DPF}} \quad (49)$$

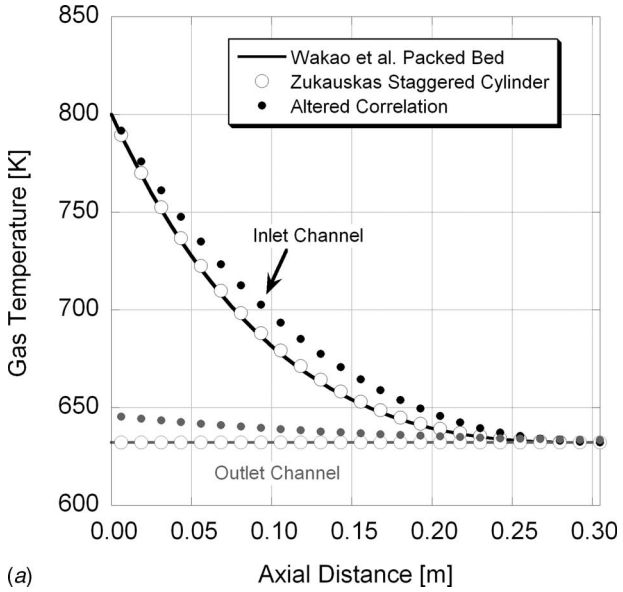

(*a*)

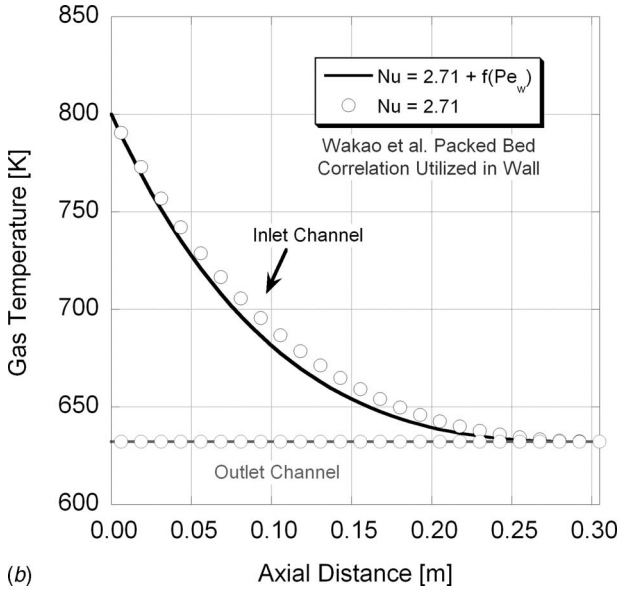

(*b*)

Fig. 8 (*a*). Comparison of heat transfer correlations during artificial step change numerical experiment and (*b*) effect of Peclet number on the heat transfer

Since the soot loading does not vary dramatically in the axial direction from node to node, the heat transfer due to conduction often removes this axial dependence:

$$\dot{Q}_{\text{cond}} = (\lambda_f V_f + \lambda_d V_d)\frac{\partial^2 T_f}{\partial z^2} \tag{50}$$

Because the gas in the inlet channel sees a different surface area than the outlet channel, the model must account for these varying areas in the heat transfer due to heat transfer and energy transfer:

$$\dot{Q}_{\text{conv}} = \left(\frac{N_c}{2}\right)[h_g S_{\text{I}}(T_{\text{I}} - T_s) + h_g S_{\text{II}}(T_{\text{II}} - T_w)] \tag{51}$$

$$\dot{Q}_{\text{wall}} = \left(\frac{N_c}{2}\right)(\rho_s u_s h_{\text{I}} S_{\text{I}} - \rho_w u_w h_w S_{\text{II}}) \tag{52}$$

Note that the heat transfer terms are now a function of the local gas values at the interface of the soot and inlet channel and the wall and outlet channel, respectively.

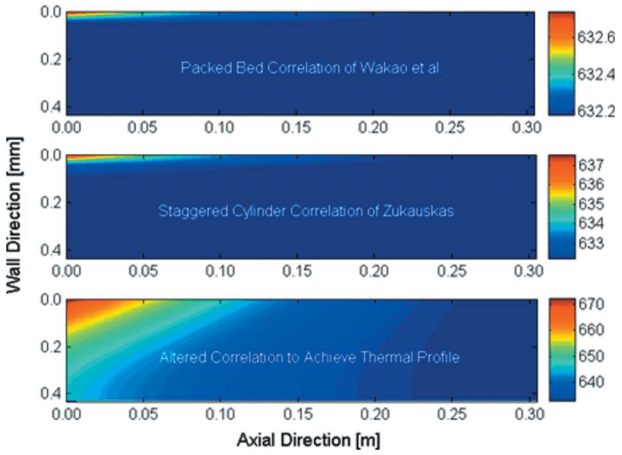

Fig. 9 Contour plots of different heat transfer correlations during temperature step change numerical experiment

Finally, the contributions due to combustion are a function of the soot oxidation as described in the previous section:

$$\dot{Q}_{\text{reac}} = -\left(\frac{N_c}{2}\right)\left(\frac{m_d \Delta H_{\text{reac}}}{\rho_d}\right)\dot{S}_{C_{(s)}} \tag{53}$$

where oxidation only occurs on half the number of total channels. This term includes the heat of reaction and its effect on the filter energy equation.

3 Boundary Conditions

According to Nield and Bejan [35], at the interface between a porous medium and a clear fluid the continuity of temperature can be imposed. To do so, the model enforces a local thermodynamic equilibrium at the interface of the channels and the wall at every axial distance point. The normal component of the heat flux derived from the first law of thermodynamics describes the governing equations at the surface:

$$\dot{Q}_{\text{in}} + \dot{m}_{\text{in}} H_{\text{in}} = \dot{Q}_{\text{out}} + \dot{m}_{\text{out}} H_{\text{out}} \tag{54}$$

At this interface, the area is the same between the inlet channel gas and the soot or porous wall and, as a result, the first law at this boundary is equal to

$$\rho_s u_s h_{\text{I}} + h_g(T_{\text{I}} - T_s) = \rho_s u_s h_s - k_g^* \frac{dT_s}{dy} - h_c(T_f - T_s) \tag{55}$$

where the left-hand side equals the heat flux to the boundary from the inlet channel. On the right-hand side, the terms represent the respective heat fluxes away from the boundary due to advection, conduction, and convection, respectively. Solving for the temperature derivative, we recover the boundary condition at $y=0$ for the wall energy:

$$\left.\frac{dT_s}{dy}\right|_{y=0} = \frac{1}{k_g^*}[\rho_s u_s(h_s - h_{\text{I}}) - h_c(T_f - T_s) - h_g(T_{\text{I}} - T_s)] \tag{56}$$

Following the same logic for the interface between the outlet channel and the wall, the boundary condition at $y=t_m+t_d$ can be determined:

$$\left.\frac{dT_w}{dy}\right|_{y=t_m+t_d} = \frac{1}{k_g^*}[h_g(T_{\text{II}} - T_w) - h_c(T_f - T_w)] \tag{57}$$

The above methodology follows that of the conservation of species as discussed in the papers by Haralampous et al.

At these boundaries, the pressure is equal to the respective channel pressures from a control volume analysis,

Table 2 Parameters used for soot loading simulations

Variable	Value	Variable	Value
Inlet pressure	1.0132 bars	Inlet temperature	583 K
DPF diameter	9 in.	DPF length	12 in.
Cell density	60 cells $in.^{-2}$	Wall thickness	31 mil
Mass flow rate	350 kg h^{-1}	Cell size [78]	2.5 mm
Inlet temperature	310 °C	Thermal conductivity [79]	9 W m^{-1} K^{-1}
Bulk density [79]	1600 kg m^{-3}	Specific heat [79]	750 J kg^{-1} K^{-1}
Particulate thermal conductivity [80]	2 W m^{-1} K^{-1}	Particulate specific heat [81]	889 J kg^{-1} K^{-1}
Pore diameter [79]	40 μm	Porosity [79]	50%
	Calculated parameters		
SiC loaded permeability	3.25×10^{-13} m^2	Particulate permeability	5.10×10^{-14} m^2
SiC empty permeability	2.00×10^{-12} m^2	Particulate density	75 kg m^{-3}
Void fraction	0.58	Number of cells	3817
Substrate density	2753 kg m^{-3}		

$$p_s|_{y=0} = p_{\mathrm{I}} \quad \text{and} \quad p_w|_{y=t_m+t_d} = p_{\mathrm{II}} \tag{58}$$

with the densities calculated according to the ideal gas law:

$$\rho_s|_{y=0} = p_s/RT_s \quad \text{and} \quad \rho_w|_{y=t_m+t_d} = p_w/RT_w \tag{59}$$

For the inlet channel, typically specification of the thermodynamic properties at the front face of the device occurs: ρ_{I}, T_{I}, and u_{I}. For the outlet channel, the stagnation condition for the velocity specifies the only known commodity at the left boundary:

$$u_{\mathrm{II}}|_{z=0} = 0 \tag{60}$$

While the pressure at the left wall can be calculated through an iteration technique similar to methods previously utilized in literature [10], a method of characteristics (MOC) analysis from fluid dynamics needs to be completed to calculate the temperature at this wall. This is because its value is a function of the flow from the wall and the left running wave (u-a) from the neighboring cell in the outlet channel. From previous efforts [16,68], the following governing equation at the wall can be written:

$$\frac{\partial p_{\mathrm{II}}}{\partial t} - a_{\mathrm{II}}^2 \frac{\partial \rho_{\mathrm{II}}}{\partial t} = \Delta_2 \tag{61}$$

To calculate the steady-state solution, the left-hand side of the equation is set equal to zero with the following components:

$$\Delta_2 = \frac{p_e}{\rho} S_{\mathrm{eng}} - \frac{u p_e}{\rho} S_{\mathrm{mom}} - \left[\frac{H-u^2}{\rho} p_e + \sum_j Y_{\mathrm{II}_j} p_{C_j} \right] S_{\mathrm{mass}} + \sum_j p_{C_j} S_j = 0 \tag{62}$$

From the DPF governing equations, the knowledge that u_{II} equals zero at the wall and omitting the species equations, the terms in the above equation are

$$S_{\mathrm{mass}} = \frac{\rho_w u_w S_{\mathrm{II}}}{A_{\mathrm{II}}}, \; S_{\mathrm{mom}} = 0 \; \text{ and } \; S_{\mathrm{eng}} = \frac{S_{\mathrm{II}}}{A_{\mathrm{II}}} [h_g (T_w - T_{\mathrm{II}}) + \rho_w u_w h_w] \tag{63}$$

Hence, the temperature at the wall in the outer channel is determined to be

$$T_{\mathrm{II}}|_{z=0} = T_w - \frac{\rho_w u_w}{h_g} (h_{\mathrm{II}} - h_w) \tag{64}$$

An iterative procedure is then required to calculate T_{II} at the boundary as h_{II} is also a function of T_{II}.

4 Numerical Methods

For the inlet and outlet channels, there exists a differential-algebraic system of equations. Similar to Bissett's work, the numerical code LSODI [69] can be used to solve for the resulting thermodynamic properties. In the soot and wall layers, the need for computational speed requires a numerical approximation. This is because solving the compressible version of the governing equations through these layers proved too tedious a numerical task.

From Darcy's law, use of an average velocity through each respective layer allows for an approximation of the pressure drop across each layer:

$$\Delta p_s \approx -\frac{\mu \bar{u}_s t_d}{K_d} \quad \text{and} \quad \Delta p_w \approx -\frac{\mu \bar{u}_w t_m}{K_m} \tag{65}$$

Since neglecting the Forscheimer effect typically occurs in DPF modeling, the authors feel that this is a reasonable assumption to make.

Using the ideal gas law and average temperatures, the pressure differential relates to the density drop in each layer:

$$\Delta \rho_s \approx \frac{\Delta p_s}{R\bar{T}_s} \quad \text{and} \quad \Delta \rho_w \approx \frac{\Delta p_w}{R\bar{T}_w} \tag{66}$$

This simplification results in an approximation of the compressibility effect in each layer. Since the viscosity does not change significantly in the layers, the pressure drop terms can be equated:

$$\Delta p_s = \Delta p_w \frac{K_m \bar{u}_s t_d}{K_d \bar{u}_w t_m} \tag{67}$$

Combining this result with the density approximation gives a relative scale of the density differences between the two layers:

$$\frac{\Delta \rho_s}{\Delta \rho_w} \approx \frac{K_m \bar{u}_s t_d \bar{T}_w}{K_d \bar{u}_w t_m \bar{T}_s} \tag{68}$$

Using the boundary conditions determined in the previous section,

$$\rho_s|_{y=0} - \rho_w|_{y=t_d+t_m} = \Delta \rho_s + \Delta \rho_w \tag{69}$$

the density drop across the soot layer equals

$$\Delta \rho_s = \frac{\rho_s|_{y=0} - \rho_w|_{y=t_d+t_m}}{1 + \dfrac{K_d \bar{u}_w t_m \bar{T}_s}{K_m \bar{u}_s t_d \bar{T}_w}} \tag{70}$$

Computation of the density drop across the wall layer uses the boundary conditions via Eq. (69).

Then, to compute the density values at each numerical discretization, the model assumes that the density varies linearly in each

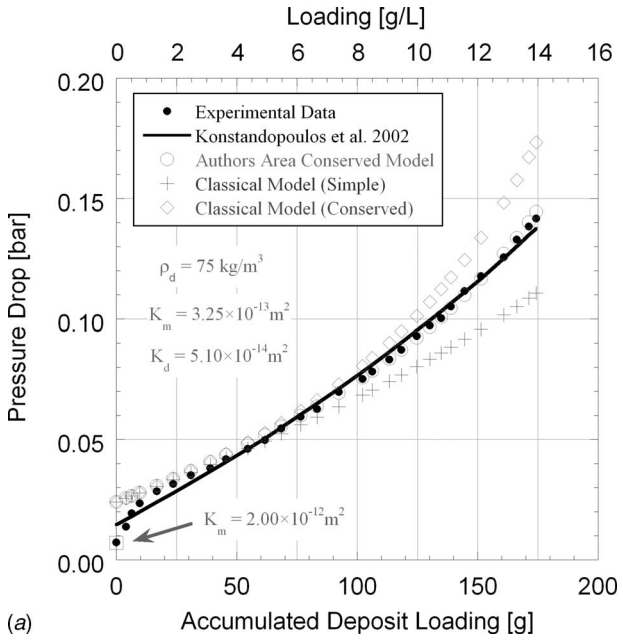

(*a*)

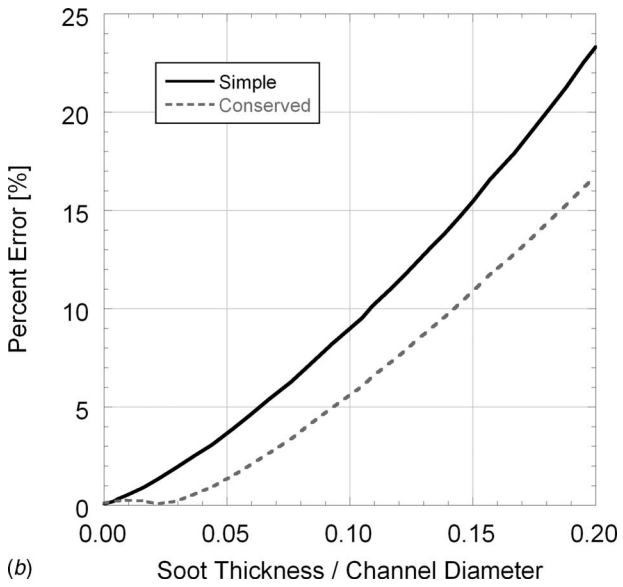

(*b*)

Fig. 10 (*a*) Pressure drop as a function of soot loading versus experimental data [77] and previous literature [74] results and (*b*) the percent error in approximating the flow through the wall using an average velocity

layer. Using this simplification, computation of the velocity and pressure profiles in each layer occurs in a first-order implicit method as follows (soot layer example only):

$$u_s|_i = \frac{\rho_s u_s|_{i-1} + \Delta y_s \dot{S}_{\text{mass}}|_i}{\rho_s|_i \left(1 + \frac{\Delta y_s}{A_s|_i}\frac{dA_s}{dy}\right)} \tag{71}$$

$$p_{s,i} = p_{s,i-1} - \left(\frac{\mu u_s}{K_d} + \beta_d \rho_s u_s^2\right)_i \Delta y_s \tag{72}$$

Note that by holding the total density drop across the layers consistent to the first laws of thermodynamics at the boundaries, Eq. (69), the model does not introduce any error to the overall flow rates entering and exiting the respective layers. Some compressibility effects are lost but at savings in numerical run time.

This iterative method of solving for the velocity will be compared to the classical method of utilizing only a single velocity and neglecting the effects of soot thickness on the mass equations; i.e., $S_{\text{I}}=S_{\text{II}}$. Through the use of Eq. (65), this velocity can be calculated as (ignoring Forscheimer effects)

$$\bar{u} = \frac{p_{\text{I}} - p_{\text{II}}}{\mu\left(\frac{t_m}{K_m} + \frac{t_d}{K_d}\right)} \tag{73}$$

This equation can be determined from using the non-area-conserved form of the soot and wall pressure (Eqs. (10) and (11)).

To better account for the area conservation, using an implicit first-order differentiation of the soot pressure equation results in

$$\bar{u} = \frac{(p_{\text{I}} - p_{\text{II}})S_{\text{I}}}{\mu\left(\frac{t_m S_{\text{I}}}{K_m} + \frac{t_d S_{\text{II}}}{K_d}\right)} \tag{74}$$

For this version, it is important to note that while the average velocity utilizes the soot thickness, the mass equations still utilize $S_{\text{I}}=S_{\text{II}}$ to ensure no mass accumulation in the layer (similar to Haralampous et al. as discussed in Sec. 2.1).

To solve the energy equation incorporating second-derivative terms, the model utilizes a variable differentiation formulation. This is to allow for a different numerical discretization in the soot layer as in the wall layer: $\Delta y_s \neq \Delta y_w$. Figure 5 illustrates a schematic of this variable differentiation, and the numerical implementation equals [70,71]

$$\frac{dT}{dy} = \frac{1}{\Delta y_+ + \Delta y_-}\left[\frac{\Delta y_-}{\Delta y_+}(T_{j+1} - T_j) + \frac{\Delta y_+}{\Delta y_-}(T_j - T_{j-1})\right] \tag{75}$$

$$\frac{d^2T}{dy^2} = \frac{2}{\Delta y_+ + \Delta y_-}\left[\left(\frac{T_{j+1} - T_j}{\Delta y_+}\right) - \left(\frac{T_j - T_{j-1}}{\Delta y_-}\right)\right] \tag{76}$$

for the first and second derivatives, respectively. The same number of nodes is used in each layer; however, because the wall thickness will be different than the soot thickness, this differentiation is required at the interface between the two layers; i.e., $\Delta y_- = t_d/N_s$ and $\Delta y_+ = t_m/N_s$. Solving for the temperature in the energy equations and substituting the above relationships allows for computation of the temperature profile in the soot and wall layers in a second-order implicit manner.

In order to compute the entrance wall velocity, the model utilizes an iterative procedure by first assuming an initial soot velocity: $u_s^*|_{y=0}$. Use of the constant pressure boundary condition at the interface of the wall and the outlet channel allows for a calculation of the deviation between the actual and predicted pressures:

$$\Delta p = p_w^*|_{y=t_m+t_d} - p_{\text{II}} \tag{77}$$

Differentiation of the traditional wall pressure equation in algebraic format allows the model to find a wall velocity correction term

$$\frac{\Delta p}{du} = -\mu\left(\frac{t_m}{K_m} + \frac{t_d}{K_d}\right) \tag{78}$$

A Newton–Raphson technique then updates the guess for the inlet soot velocity:

$$\Delta u_s^*|_{y=0} = -\frac{\Delta p}{\Delta p/du} \tag{79}$$

This iteration repeats until the deviation between the actual and the predicted pressure is less than a specified convergence criterion.

To complete the numerical procedures, solution of the soot mass equation occurs in an implicit manner,

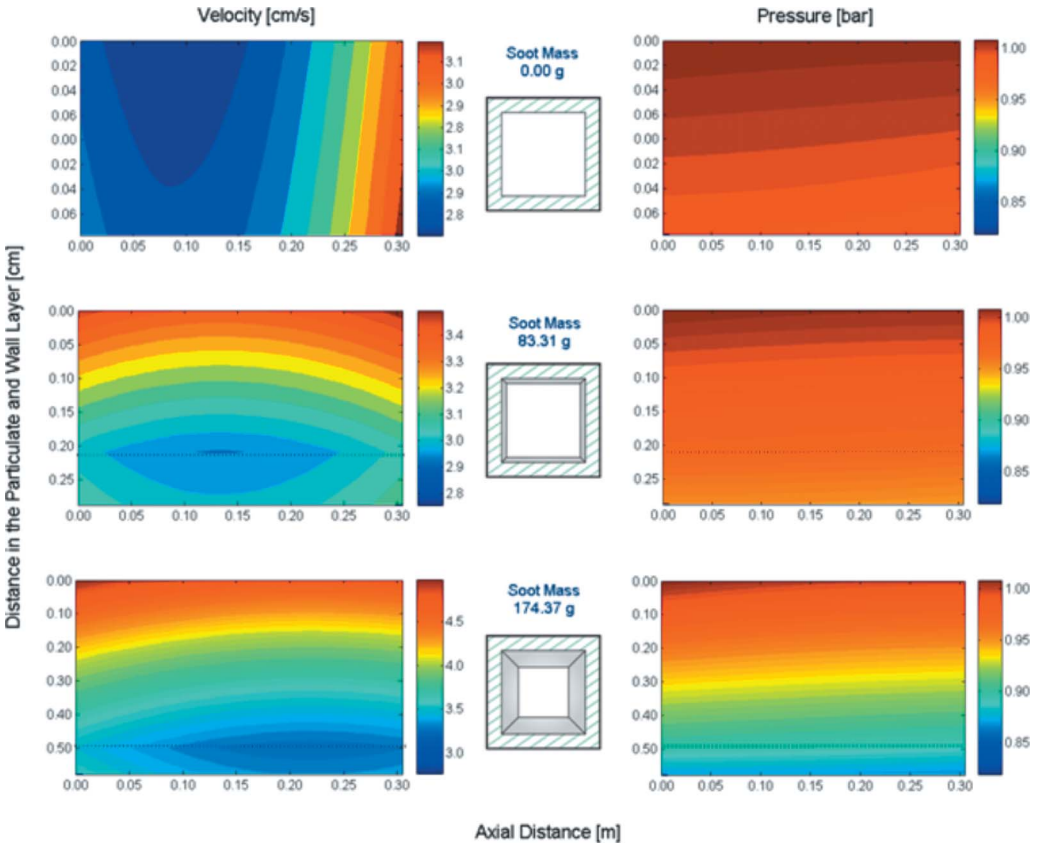

Fig. 11 Velocity and pressure contour plots in the soot and wall layers as a function of soot loading

$$m_d^{n+1} = \frac{m_d^n + \varsigma^{n+1}\Delta t}{1 + \chi^{n+1}\Delta t} \tag{80}$$

and the filter temperature equation is computed according to the forward-time centered space [72] method as previously discussed in catalyst modeling [16].

By using the linear density approximation and the Newton–Raphson technique for the initial soot velocity, the reduction in the numerical run time occurs to the point where it makes transient test procedures run possible. In the case that the gas temperature in the soot and wall layers is equal to the filter temperature, the numerical method presented will approximate compressibility since the density change varies directly with the pressure drop according to Eq. (66).

5 Results

The models to date typically only use one average value for density and velocity in the soot and wall layers, respectively, with most references using only one for both layers. The formulation presented in this paper calculates all thermodynamic properties in the wall as a function of distance based on the Navier–Stokes equations of motion using a linear density approximation. To compare the classical model with the version presented here, sample runs were made utilizing filter properties available in Ref. [73] and presented in Table 1. In this reference paper, there is no soot present, and run-time conditions are given. With respect to the reproduction of the classical model, the local wall pressure approximation of Haralampous et al. [13] is used:

$$\bar{p} = \tfrac{1}{2}(p_{\mathrm{I}} + p_{\mathrm{II}}) \tag{81}$$

As illustrated in Fig. 6, the axial values of pressure, velocity, and density compare very favorably between the two models with only a small discrepancy noted in the wall velocity. In Fig. 7, separation of the density values by the channels and wall illustrates the differences between the two models. Using the model presented here, there is a continual change in the density properties across the wall approximating the effects of compressibility. Since this was an isothermal run, the density at the interface of the inlet channel and wall $\rho_w|_{y=0}$ used in the mass flux term of the channel mass equations is equal to the density in the inlet channel because the pressure and temperature at the interface are the same as the inlet channel. This is also the case for the density at the interface of the outlet channel and the wall $\rho_w|_{y=t_m}$.

It is interesting to find that when the wall is discretized by only three nodes, one corresponding to the inlet/outlet channel boundaries and one for the middle of the wall, the middle wall node corresponds nearly exactly with the simple local pressure based classical model. This is because the pressure drop across the wall is nearly linear according to Darcy's law with only a small effect due to Forscheimer. Hence, using the average pressure in the classical formulation will give properties that accurately approximate the effects of the wall on the flow when the gas temperature does not vary significantly.

In order to check the assumption that the gas temperature in the wall instantly assumes the filter temperature, a sample simulation was run artificially raising the inlet temperature of the previous example to 800 K, whereas the filter temperature was held constant at 632.18 K. While this may not actually occur in practice, this numerical test illustrates if any effect is present due to conduction; i.e., it looks at the relationship of advection and conduction versus convection. Later in this paper, definitive proof occurs through a simulation involving an actual experimental test. Fig. 8(*a*) plots the channel results illustrating that both convective heat transfer correlations produce nearly the same results. The temperature of the gas leaving the filter wall is equal to the wall because the heat transfer coefficients are extremely large due to the small pore size. It took reducing the Zukauskas correlation by a factor of 25 in order to see any change in the results. Figure 9

corroborates this through contour plots of the gas temperature in the wall. The correlation of Wakao et al. shows that the thermal entrance length is insignificant, whereas the Zukauskus correlation demonstrates a very small entrance length. The altered correlation illustrates the implementation of the conduction term by showing more of a vertical temperature profile when the convective heat transfer is small. When comparing the magnitudes of the three terms in Eqs. (18) and (19), it was found that the magnitude of convection to advection is on the order of 10^5, whereas the magnitude of convection to conduction is on the order of 10^4. This illustrates that convection dominates the mode of heat transfer in the wall, validating the common assumption that $T_s = T_w = T_f$.

To determine the effect of wall velocity on heat transfer, previous efforts were rerun using the heat transfer correlation of Eq. (17) including and not including the Peclet number effects. Since this case had a relatively high wall flow velocity as illustrated by the inlet channel value, this is a good indication of any effect on the wall and channel temperatures. When including the Peclet number effects as illustrated in Fig. 8(*b*), the results show that the inlet channel temperature profile shifts as more heat transfer occurs closer to the inlet. This is because the Nusselt number is higher in the case of suction and transfers more heat to the wall in the entrance cells. This could possibly cause the soot regeneration event to shift toward the entrance and will be revisited in results presented later in this paper.

To demonstrate the effects of the soot on the flow, simulation runs were accomplished using data available in a paper by Konstandopoulos et al. [74] and presented in Table 2. Figure 10(*a*) demonstrates the calibration of the filter and soot permeabilities as a function of pressure drop versus soot loading. In this figure, two different filter permeabilities were determined with respect to an empty filter and a value that corresponds to the case when a significant amount of the soot is present. This is because as the soot accumulates with the wall from deep bed filtration, the filter permeability will decrease to reflect the change in pore size. There are models in literature to account for this effect [28,52–54,56,57]; however, incorporation of those models with respect to the equations presented in this paper is noted for future efforts. The model presented here does follow the experimental data quite well after deep bed filtration has finished.

In addition, Fig. 10(*a*) illustrates the pressure drop results when a singular velocity and pressure are utilized for the wall and soot layers via Eqs. (73), (74), and (81) as in the classical model interpretation. Figure 10(*b*) shows that the use of the non-area-conserved pressure equation to calculate the wall velocity results in a 5% error in pressure drop occurs when the soot layer is 6% of the channel diameter. However, utilizing the area-conserved pressure equation to calculate the wall velocity demonstrates that this 5% error is not reached until the soot layer is 10% of the channel diameter. From a DPF loading standpoint, this corresponds to a loading of around 8 g/l, which is a medium to heavy loaded filter to be avoided in actual operation. Since engineers must design the filters for all possible scenarios, this result is important and illustrates clearly when the use of area conservation must be considered. However, for normal DPF operating regimes using the proper pressure drop equation to account for the soot loading while still utilizing a singular wall velocity and pressure illustrates that the assumption of $t_d \ll d_m$ is quite valid.

In Fig. 11, wall velocity and pressure contour plots within the wall are illustrated as a function of soot loading with the drawings to scale (soot thickness versus channel diameter). We see that the wall velocity is no longer constant in the normal direction with about a 20% difference seen in the case of 174.37 g of the soot loaded within the filter. The pressure plots illustrate the difference in the two layers with a significant amount of the drop occurring within the soot layer because of the lower permeability of soot; i.e., higher flow resistance.

To demonstrate the effects of transient soot loading, a numerical experiment was set up to flow a uniform and random amount

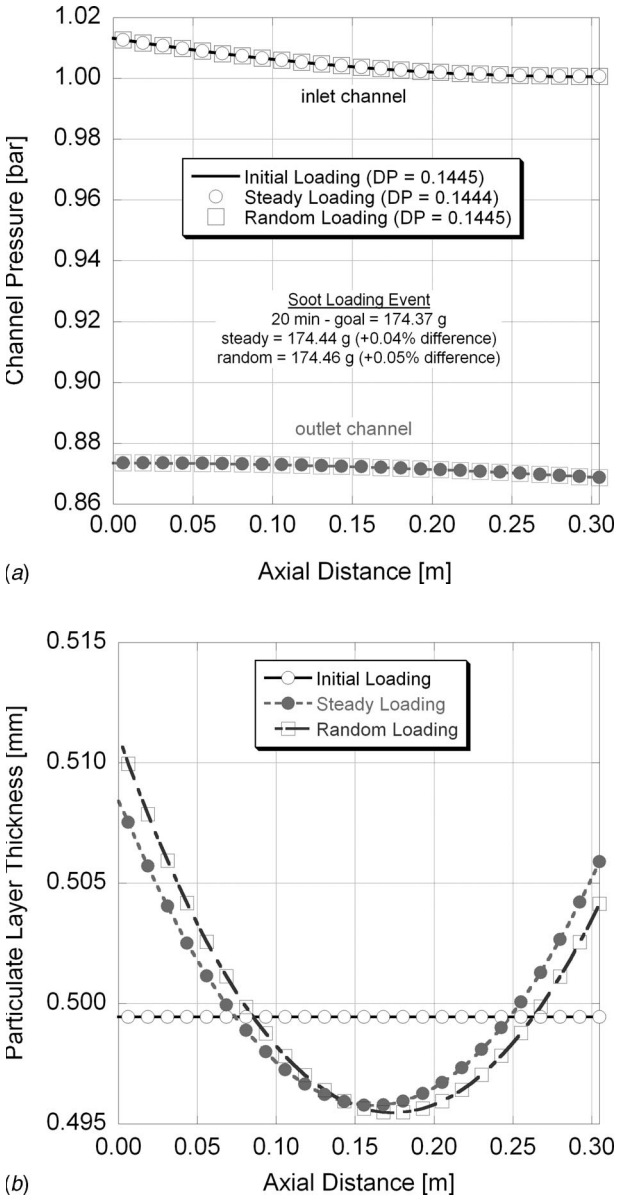

Fig. 12 Comparison of three different soot loading events with respect to (*a*) pressure and (*b*) particulate layer thickness

of soot into the filter as a function of the time; total amount on the surface to equal 174.37 g at the end of the test. The end goal was to see if the soot loading is nonuniform on the surface and if the model is able to account for the correct mass of the soot. In Fig. 12, the results show that while the random and uniform soot loading events have different thickness profiles, the deviations from the norm are only a few percent. Additionally, there is no significant difference in the pressure drop results as a function of loading. In both cases, the model showed excellent ability with respect to accuracy of the total loading.

To validate the oxidation component of the soot mass equation and the filter energy equation, two phases of a SiC DPF experimental test by Young et al. [75] were modeled. The first phase involved the warm-up of a loaded DPF by thermally heating an inlet flow containing only inert N_2. In the second phase, the flow rate was reduced, the heater turned off, and 18% O_2 was introduced into the feed stream (Table 3). Unfortunately, the experimental data in the paper for the second phase were only available down to 400°C. As a result, linear extrapolation of the inlet temperature profile occurred beyond that point until reaching room

Table 3 Parameters used for SiC warm-up, cooldown, and oxidation simulations

Variable	Value	Variable	Value
Cell density	28 cells cm^{-2}	Wall thickness	0.43 mm
Thermal conductivity	15 W m^{-1} K^{-1}	Bulk density	0.76 g cm^{-3}
DPF diameter	144 mm	DPF length	150 mm
Particulate thermal conductivity [80]	2 W m^{-1} K^{-1}	Particulate specific heat [81]	889 J kg^{-1} K^{-1}
Pore diameter	8 μm	Monolith type	B–SiC
Porosity	41%		
	Calculated parameters		
Number of cells	4560	Cell diameter [82]	1.46 mm
Substrate density	1885 kg m^{-3}	Specific heat	1025 J kg^{-1} K^{-1}
Particulate permeability	5.10×10^{-14} m^2	Particulate density	75 kg m^{-3}
SiC empty permeability	3.00×10^{-13} m^2	SiC loaded permeability	1.70×10^{-13} m^2
	Young et al. warm-up		
Volumetric flow rate	1500 l min^{-1}	Mass flow rate (STD)	0.0296 kg s^{-1}
Deposit loading	37.11 g	Inlet pressure	1.0132 bars
	Young et al. cool down and oxidation		
Volumetric flow rate	700 l min^{-1}	Mass flow rate (STD)	0.0138 kg s^{-1}
Inlet O_2 after 40 s	18%	Inlet pressure	1.0132 bars

temperature. The results in Fig. 13(*a*) illustrate that the model is able to capture the warm-up of the DPF. As a check of the heat transfer coefficients, this figure shows a comparison of the packed-bed correlation with the assumption of setting the gas temperature in the filter equal to the filter. The results show that there is not any difference between this assumption and the use of the packed-bed correlation. Even when using the altered correlation, the warm-up profile only deviates slightly from the packed-bed correlation.

In the same figure, the simulation and experimental results for the cooldown and oxidation test are given. The activation energy was set equal to 125 kJ/mol as found in Ref. [58], while the partial oxidation parameter was specified as the average value of those found in the literature, Eq. (33). In order to reach the specified conversion rate of 55% mentioned in the paper of Young et al., the authors calibrated the preexponential factor. Overall, the model is able to capture the temperature rise at the different positions along the DPF. However, the filter temperatures predicted by the simulation are higher than the experimental values. This could be because of the effects of a varying experimental flow rate, radial heat transfer, ambient heat transfer, and a lower exothermic reaction due to more CO creation than CO_2 (see Fig. 14). In addition, since the species equations were not included, the amount of oxygen towards the end of the DPF could be too high, causing a larger exotherm. It is important to note that previous results of an adiabatic 1D DPF model also show a higher temperature than experimentally found [76].

The experimental test of Young et al. was also utilized to determine whether or not the mass source term for the gas in Eq. (4) is required. Figure 15 shows that once the exothermic reactions start occurring, the exit mass flow rate starts to deviate in the case where the source term is omitted. During the conditions of the largest deposit conversion, a deviation of around 6% in the mass flow rate is encountered. As a result, the final conversion of deposit mass on the surface was around 1% higher by omitting this source term. This test also provided the final comparison of the importance of the Peclet number in the heat transfer correlations for the inlet and outlet channels. As illustrated in Fig. 16, the Nusselt numbers vary up to 6% over the length of the experiment. This is enough of a change to warrant including the small computational requirement of including a Peclet number calculation and use of either Eq. (16) or (17).

6 Conclusions

This paper describes a 1D based DPF model using area conservation in both channels and the soot and wall layers. This formulation accounts for the effects of changing gaseous area in the inlet channel and varying cross-sectional area of flow through the soot layer. A brief description of other variable area models available in literature was completed to illustrate how this model differs from their governing equations. Instead of using a one unique velocity value through either layer, the model presented here calculates the velocity profile through the wall to account for the different surface areas in the inlet and outlet channels. Since the mass equations in the surface layers are included in the model formulation, it remains consistent to the conservation of mass and no accumulation of mass is present. It was found that area conservation becomes important when the DPF becomes moderately loaded on the order of 8 g/l. A deviation in pressure drop through the filter of around 5% is found when using the classical model assumption of $t_d \ll d_m$.

The model also imposes thermodynamic equilibrium at the interface of the channels and soot and wall layer to capture the thermal entrance lengths. This was accomplished by using the first law of thermodynamics to calculate the normal heat flux to and from the wall layers. It was found that the gas temperature in the wall quickly becomes the filter temperature. Convection within the porous membrane is at least on the order of 10^4 times larger than advection and conduction, validating previous model assumptions that the gas temperature in the soot and wall layers is equal to the filter temperature. As a result, the authors have illustrated that the computational requirements needed to account for area conservation and the gas temperature in the wall are inefficient with respect to model predictions.

It was found that under conditions of high inlet flow rates, the temperature profile in the DPF shifts toward the front as the heat transfer increases because of suction. The change in the Nusselt number during an experimental test illustrates that the impact of suction and injection on the heat transfer can be around 6% and should be considered. In addition, the mass source term for the gas in the soot layer was determined to have a small impact on the mass flow rate through the DPF with a 6% deviation seen when not included in the model. This resulted in a small change in the total particulate conversion of around 1% and may be of more

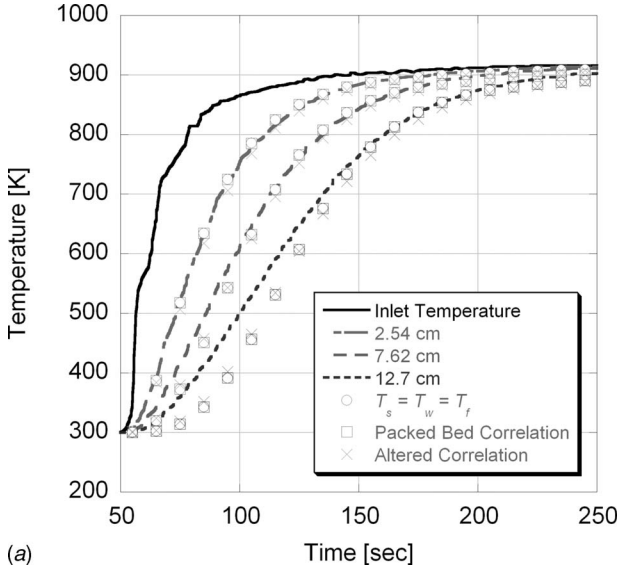

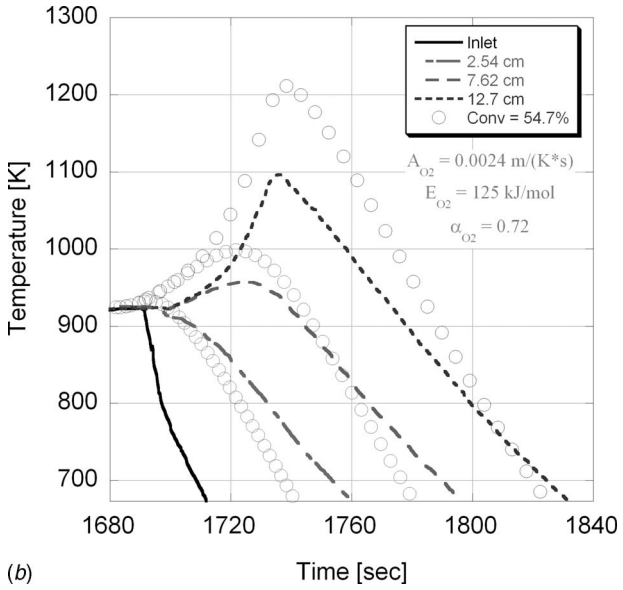

Fig. 13 Model versus experimental results for (*a*) warm-up of loaded SiC DPF containing only inert N_2 and (*b*) cooldown and oxidation test with 18% O_2

interest when cyclic soot loading and regeneration events are encountered. Finally, a transient soot loading model was included in order to capture the irregularities of loading on the surface. It was found that very little difference in the pressure drop is encountered when a uniform, steady, or random soot loading is utilized.

This paper illustrates a number of small changes in model results when a rigorous implementation of the model is considered according to the governing equations of fluid dynamics. Overall, the classical model assumptions are quite valid; however, as with any numerical model, a good understanding of the physics is required to make sure that the model is applied properly.

Nomenclature

a = speed of sound ($m\ s^{-1}$)
$\tilde{a}$ = surface area density (m^{-1})
A = cross-sectional area [m^2]
A_{O_2} = preexponential in O_2 Arrhenius rate law ($m\ K^{-1}\ s^{-1}$)

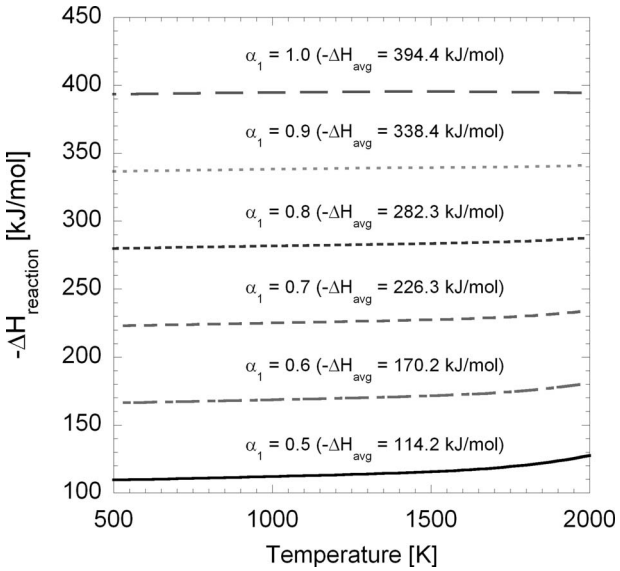

Fig. 14 Reaction enthalpy calculations of soot oxidation by O_2 at different partial oxidation factors

A_s = cross-sectional area in the soot layer per unit length (m)
A_w = cross-sectional area in the wall layer per unit length (m)
c = specific heat ($J\ kg^{-1}\ K^{-1}$)
c_p = constant pressure specific heat of gas ($J\ kg^{-1}\ K^{-1}$)
d = effective diameter (m)
d_m = channel diameter (m)
d_p = pore diameter (m)
D = diameter of the DPF (m)
D_p = diameter of a particle (m)
E_{O_2} = activation energy in O_2 Arrhenius rate law ($kJ\ mol^{-1}$)
F = friction factor of Bissett (28.454)
h = specific enthalpy ($J\ kg^{-1}$)
h_c = convective heat transfer coefficient in the soot and wall layers ($W\ m^{-2}\ K^{-1}$)

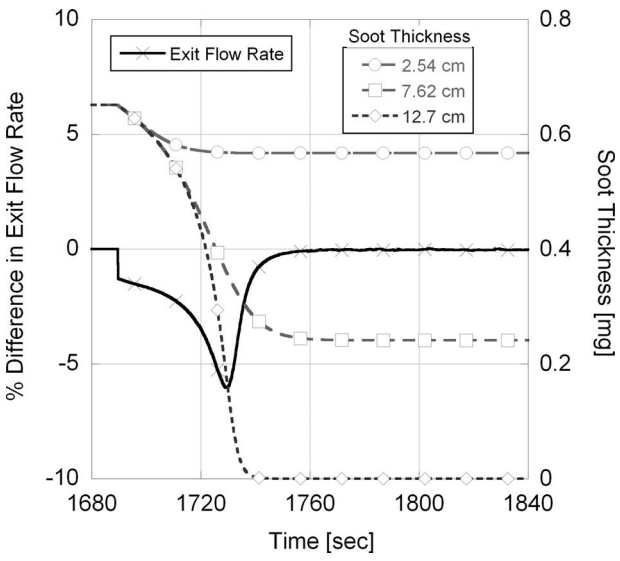

Fig. 15 Exit mass flow rate difference from omitting the gain in mass due to soot oxidation reactions in Eq. (4)

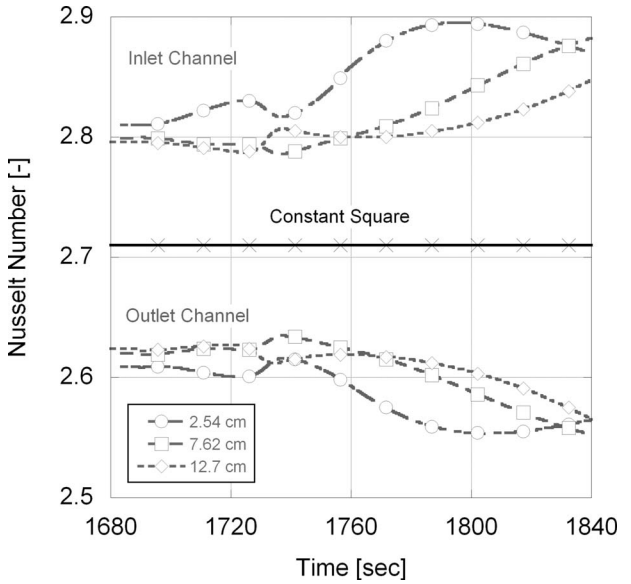

Fig. 16 Instantaneous Nusselt number in the inlet and outlet channels for the oxidation experiment

h_g = convective heat transfer coefficient in the channels ($W\ m^{-2}\ K^{-1}$)
H = total enthalpy ($J\ kg^{-1}$)
k = rate constant ($m\ s^{-1}$)
k_g = thermal conductivity of gas in the channels ($W\ m^{-1}\ K^{-1}$)
k_g^* = effective thermal conductivity of the gas in the soot and wall layers ($W\ m^{-1}\ K^{-1}$)
m = mass (kg)
$\dot{m}_{\text{in}}$ = total mass flow rate of gas ($kg\ s^{-1}$)
$\dot{m}_{\text{in/out}}$ = mass flow rate into/out of the wall boundary ($kg\ s^{-1}$)
$\dot{m}_{\text{soot}}$ = mass flow rate of the soot ($kg\ s^{-1}$)
N_{pore} = total number of pores
N_{part} = total number of particles
N_c = total number of channels
N_s = Number of discretizations in the soot layer
Nu = Nusselt number
p = pressure (Pa)
$\bar{p}$ = average pressure in soot and wall layer (Pa)
p_e = partial pressure with respect to energy ($kg\ m^{-3}$)
p_C = partial pressure with respect to concentrations ($m^2\ s^{-2}$)
Pe = Peclet number
Pr = Prandtl number
$\dot{Q}_{\text{cond}}$ = energy conduction within the wall ($W\ m^{-1}$)
$\dot{Q}_{\text{conv}}$ = energy convection due to gas in channels ($W\ m^{-1}$)
$\dot{Q}_{\text{multi}}$ = energy conduction due to multidimensional effects ($W\ m^{-1}$)
$\dot{Q}_{\text{rad}}$ = radiation energy within filter channels ($W\ m^{-1}$)
$\dot{Q}_{\text{reac}}$ = energy exotherm/endotherm due to soot/wall reactions ($W\ m^{-1}$)
$\dot{Q}_{\text{supply}}$ = active energy supply to wall ($W\ m^{-1}$)
$\dot{Q}_{\text{wall}}$ = energy flow through the wall ($W\ m^{-1}$)
$\dot{Q}_{\text{in/out}}$ = energy flux into/out of the wall boundary ($W\ m^{-1}$)
Re = Reynolds number
R_u = universal gas constant (8.3145) ($J\ mol^{-1}\ K^{-1}$)
S = surface area per unit length (m)
$\dot{S}_{C_s}$ = overall soot combustion rate ($kg\ C_{(s)}\ m^{-3}\ s^{-1}$)
S_{eng} = governing equations term for energy equations ($W\ m^{-3}$)
S_j = governing equations term for species equations ($kg\ m^{-3}\ s^{-1}$)
S_{mass} = governing equations term for mass equations ($kg\ m^{-3}\ s^{-1}$)
$\dot{S}_{\text{mass}}$ = discretized soot combustion rate ($kg\ C_{(s)}\ m^{-3}\ s^{-1}$)
S_{mom} = governing equations term for momentum equations ($kg\ m^{-2}\ s^{-2}$)
$\dot{S}_{O_2}$ = oxygen combustion rate ($kg\ O_2\ m^{-3}\ s^{-1}$)
S_p = specific surface area of the soot (5.5×10^7) (m^{-1})
t = time (s)
t_d = soot thickness (m)
t_m = filter wall thickness (m)
T = temperature (K)
u = velocity ($m\ s^{-1}$)
$\bar{u}$ = average velocity in soot and wall layer ($m\ s^{-1}$)
V = volume per axial length (m^2)
W = molecular weight ($g\ mol^{-1}$)
y = soot and wall (normal) distance (m)
Y = mass fractions
z = channel (axial) distance (m)

Greek Variables

α_{NO_2} = NO_2 partial oxidation factor
α_{O_2} = O_2 partial oxidation factor
α_g = thermal diffusivity of gas ($m^2\ s^{-1}$)
β = Forchheimer inertial coefficient (m^{-1})
χ = inverse of soot combustion time scale (s^{-1})
Δ = differential operator
Δ_2 = source term in the MOC
ΔH_{reac} = heat of reaction ($kJ\ mol^{-1}$)
ε = void fraction of clean DPF
ε_d = void fraction of loaded DPF
ε_p = porosity (%)
K = Darcy's law permeability (m^2)
λ = thermal conductivity ($W\ m^{-1}\ K^{-1}$)
μ = dynamic viscosity ($kg\ m^{-1}\ s^{-1}$)
θ = soot accumulation angle (°)
ρ = density ($kg\ m^{-3}$)
ς = mass flow rate of the soot to the surface per mesh interval ($kg\ C_{(s)} m^{-1}\ s^{-1}$)

Subscript and Subsubscript

a = heat transfer coefficient
b = heat transfer coefficient
$C_{(s)}$ = solid carbon, particulate or soot
d = soot
de = empty channel volume when the soot is present
DPF = entire diesel particulate filter
e = empty channel volume
f = filter
fd = fully developed
i = axial index number
I = inlet channel
II = outlet channel
j = species and normal index numbers
NM = total number of species
N_2 = nitrogen
NO_2 = nitrogen dioxide

O_2 = oxygen
PB = packed bed
s = soot
w = wall

References

[1] Howitt, J. S., and Montierth, M. R., 1981, "Cellular Ceramic Diesel Particulate Filter," SAE Paper No. 810114.
[2] General Motors, 1979, General Motors Response to EPA Notice of Proposed Rulemaking on Particulate Regulation for Light-Duty Diesel Vehicles Submitted to Environmental Protection Agency.
[3] Springer, K. J., and Stahman, R. C., 1977, "Removal of Exhaust Particulate From a Mercedes 300D Diesel Car," SAE Paper No. 770716.
[4] Tessier, L. P., et al., 1980, "The Development of a High Efficiency Diesel Exhaust Particulate Filter," SAE Paper No. 800338.
[5] Garner, C. P., and Dent, J. C., 1988, "A Thermal Regeneration Model for Monolithic and Fibrous Diesel Particulate Traps," SAE Paper No. 880007.
[6] Oh, S. H., et al., 1981, "Mathematical Modeling of Fibrous Filters for Diesel Particulates—Theory and Experiment," SAE Paper No. 810113.
[7] Shadman, F., and Bissett, E. J., 1983, "Analysis of Thermal Regeneration of Fibrous Diesel-Particulate Filters," Ind. Eng. Chem. Prod. Res. Dev., **22**, pp. 203–208.
[8] MacDonald, J. S., and Vaneman, G. L., 1981, "Experimental Evaluation of Fibrous Filters for Trapping Diesel-Exhaust Particulates," SAE Paper No. 810956.
[9] Bissett, E. J., 1984, "Mathematical Model of the Thermal Regeneration of a Wall-Flow Monolith Diesel Particulate Filter," Chem. Eng. Sci., **39**, pp. 1232–1244.
[10] Koltsakis, G. C., and Stamatelos, A. M., 1997, "Modes of Catalytic Regeneration in Diesel Particulate Filters," Ind. Eng. Chem. Res., **36**, pp. 4155–4165.
[11] Konstandopoulos, A. G., and Johnson, J. H., 1989, "Wall-Flow Diesel Particulate Filters—Their Pressure Drop and Collection Efficiency," SAE Paper No. 890405.
[12] Gropi, G., and Tronconi, E., 1996, "Continuous vs. Discrete Models of Nonadiabatic Monolith Catalysts," AIChE J., **42**(8), pp. 2382–2387.
[13] Haralampous, O. A., et al., 2003, "Partial Regenerations in Diesel Particulate Filters," SAE Paper No. 2003-01-1881.
[14] Konstandopoulos, A. G., et al., 2001, "Spatial Non-Uniformities in Diesel Particulate Trap Regeneration," SAE Paper No. 2001-01-0908.
[15] Kostoglou, M., et al., 2003, "Multi-Channel Simulation of Regeneration in Honeycomb Monolithic Diesel Particulate Filters," Chem. Eng. Sci., **58**, pp. 3273–3283.
[16] Depcik, C., and Assanis, D., 2005, "One-Dimensional Automotive Catalyst Modeling," Prog. Energy Combust. Sci., **31**(4), pp. 308–369.
[17] Bissett, E. J., 1985, "Thermal Regeneration of Particle Filters With Large Conduction," Math. Modell., **6**, pp. 1–18.
[18] Bissett, E. J., and Shadman, F., 1985, "Thermal Regeneration of Diesel Particulate Monolithic Filters," AIChE J., **31**, pp. 753–758.
[19] Lee, W.-T., 1992, "Local Preconditioning of the Euler Equations," Ph.D. thesis, University of Michigan, Ann Arbor, MI.
[20] Roe, P. L., 1986, "Characteristic-Based Schemes for the Euler Equations," Annu. Rev. Fluid Mech., **18**, pp. 337–365.
[21] Liu, J., et al., 1996, "Comparison Studies on the Method of Characteristics and Finite Difference Methods for One-Dimensional Gas Flow Through IC Engine Manifold," SAE Paper No. 960078.
[22] Onorati, A., et al., 1999, "Fluid Dynamic Modeling of the Gas Flow With Chemical Specie Transport Through the Exhaust Manifold of a Four Cylinder SI Engine," SAE Paper No. 1999-01-0557.
[23] Peters, B. J., 2003, "Numerical Simulation of a Diesel Particulate Filter During Loading and Regeneration," 2003 Spring Technical Conference of the ASME Internal Combustion Engine Division, Salzburg, Austria.
[24] Peters, B. J., et al., 2004, "Integrated 1D to 3D Simulation Workflow of Exhaust Aftertreatment Devices," SAE Paper No. 2004-01-1132.
[25] Haralampous, O. A., et al., 2004, "Study of Catalytic Regeneration Mechanisms in Diesel Particulate Filters Using Coupled Reaction-Diffusion Modeling," SAE Paper No. 2004-01-1941.
[26] Haralampous, O. A., and Koltsakis, G. C., 2004, "Oxygen Diffusion Modeling in Diesel Particulate Filter Regeneration," AIChE J., **50**(9), pp. 2008–2019.
[27] Haralampous, O. A., et al., 2004, "Reaction and Diffusion Phenomena in Catalyzed Diesel Particulate Filters," SAE Paper No. 2004-01-0696.
[28] Konstandopoulos, A. G., et al., 2005, "Progress in Diesel Particulate Filter Simulation," SAE Paper No. 2005-01-0946.
[29] Konstandopoulos, A. G., et al., 2003, "Simulation of Triangular-Cell-Shaped, Fibrous Wall-Flow Filters," SAE Paper No. 2003-01-0844.
[30] Haralampous, O. A., and Koltsakis, G. C., 2002, "Intra-Layer Temperature Gradients During Regeneration of Diesel Particulate Filters," Chem. Eng. Sci., **57**, pp. 2345–2355.
[31] Depcik, C., et al., 2005, "The Numerical Simulation of Variable-Property Reacting-Gas Dynamics: New Insights and Validation," Numer. Heat Transfer, Part A, **47**, pp. 27–56.
[32] Wooding, R. A., 1957, "Steady State Free Thermal Convection of Liquid in a Saturated Permeable Medium," J. Fluid Mech., **2**, pp. 273–285.
[33] Brinkman, H. C., 1947, "A Calculation of the Viscous Force Exerted by a Flowing Fluid on a Dense Swarm of Particles," Appl. Sci. Res., Sect. A, **1**, pp. 27–34.
[34] Brinkman, H. C., 1947, "On the Permeability of Media Consisting of Closely Packed Porous Particles," Appl. Sci. Res., Sect. A, **1**, pp. 81–86.
[35] Nield, D. A., and Bejan, A., 1999, *Convection in Porous Media*, Springer-Verlag, New York.
[36] Beck, J. L., 1972, "Convection in a Box of Porous Material Saturated With Fluid," Phys. Fluids, **15**, pp. 1377–1383.
[37] Koltsakis, G. C., and Stamatelos, A. M., 1997, "Catalytic Automotive Exhaust Aftertreatment," Prog. Energy Combust. Sci., **23**, pp. 1–39.
[38] Cheng, Y. C., and Hwang, G. J., 1995, "Experimental Studies of Laminar Flow and Heat Transfer in a One-Porous-Wall Square Duct With Wall Injection," Int. J. Heat Mass Transfer, **38**(18), pp. 3475–3484.
[39] Cheng, Y. C., et al., 1994, "Developing Laminar Flow and Heat Transfer in a Rectangular Duct With One-Walled Injection and Suction," Int. J. Heat Mass Transfer, **37**(17), pp. 2601–2613.
[40] Hwang, G. J., et al., 1997, "An Experimental Study of Laminar Heat Transfer in a One-Porous-Wall Square Duct With Suction Flow," Int. J. Heat Mass Transfer, **40**(2), pp. 481–485.
[41] Hwang, G. J., et al., 1993, "Developing Laminar Flow and Heat Transfer in a Square Duct With One-Walled Injection and Suction," Int. J. Heat Mass Transfer, **36**(9), pp. 2429–2440.
[42] Kinney, R. B., 1968, "Fully Developed Frictional and Heat Transfer Characteristics of Laminar Flow in Porous Tubes," Int. J. Heat Mass Transfer, **11**, pp. 1393–1401.
[43] Pederson, R. J., and Kinney, R. B., 1971, "Entrance-Region Heat Transfer for Laminar Flow in Porous Tubes," Int. J. Heat Mass Transfer, **14**, pp. 159–161.
[44] Raithby, G., 1971, "Laminar Heat Transfer in the Thermal Entrance Region of Circular Tubes and Two-Dimensional Rectangular Ducts With Wall Suction and Injection," Int. J. Heat Mass Transfer, **14**, pp. 223–243.
[45] Schmidt, F. M., and Newell, M. E., 1967, "Heat Transfer in Fully Developed Laminar Flow Through Rectangular and Isosceles Triangular Ducts," Int. J. Heat Mass Transfer, **10**, pp. 1121–1128.
[46] Yuan, J., et al., 2001, "Simulation of Fully Developed Laminar Heat and Mass Transfer in Fuel Cell Ducts With Different Cross-Sections," Int. J. Heat Mass Transfer, **44**, pp. 4047–4058.
[47] Calmidi, V. V., and Mahajan, R. L., 2000, "Forced Convection in High Porosity Metal Foams," ASME J. Heat Transfer, **122**, pp. 557–565.
[48] Ingham, D. B. et al., 2004, *Emerging Technologies and Techniques in Porous Media*, Kluwer Academic, Dordrecht.
[49] Lu, W., et al., 2006, "Thermal Analysis on Metal-foam Filled Heat Exchangers. Part I: Metal-Foam Filled Pipes," Int. J. Heat Mass Transfer, **49**, pp. 2751–2761.
[50] Zhao, C. Y., et al., 2004, "Thermal Transport in High Porosity Cellular Metal Foams," J. Thermophys. Heat Transfer, **18**(3), pp. 309–317.
[51] Boomsma, K., and Poulikakos, D., 2001, "On the Effective Thermal Conductivity of a Three-Dimensionally Structured Fluid-Saturated Metal Foam," Int. J. Heat Mass Transfer, **44**, pp. 827–836.
[52] Wakao, N., et al., 1979, "Effect of Fluid Dispersion Coefficients on Particle-to-Fluid Heat Transfer Coefficients in Packed Beds," Chem. Eng. Sci., **34**, pp. 325–336.
[53] Zukauskas, A. A., 1987, "Convective Heat Transfer in Cross-Flow," *Handbook of Single-Phase Convective Heat Transfer*, Wiley, New York.
[54] Konstandopoulos, A. G., et al., 2000, "Fundamental Studies of Diesel Particulate Filters: Transient Loading, Regeneration and Aging," SAE Paper No. 2000-01-1016.
[55] Masoudi, M., et al., 2001, "Validation of a Model and Development of a Simulator for Predicting the Pressure Drop of Diesel Particulate Filters," SAE Paper No. 2001-01-0911.
[56] Mohammed, H., et al., 2006, "An Advanced 1D 2-Layer Catalyzed Diesel Particulate Filter Model to Simulate: Filtration by the Wall and Particulate Cake, Oxidation in the Wall and Particulate Cake by NO_2 and O_2, and Regeneration by Heat Addition," SAE Paper No. 2006-01-0467.
[57] Zhang, Z., et al., 2002, "Modeling and Numerical Simulation of Diesel Particulate Trap Performance During Loading and Regeneration," SAE Paper No. 2002-01-1019.
[58] Kandylas, I. P., and Koltsakis, G. C., 2002, "Simulation of Continuously Regenerating Diesel Particulate Filters in Transient Driving Cycles," Proc. Inst. Mech. Eng., Part D (J. Automob. Eng.), **216**, pp. 591–606.
[59] Koltsakis, G. C., and Stamatelos, A. M., 1996, "Modeling Catalytic Regeneration of Wall-Flow Particulate Filters," Ind. Eng. Chem. Res., **35**, pp. 2–13.
[60] Koltsakis, G. C., and Stamatelos, A. M., 1996, "Modeling Thermal Regeneration of Wall-Flow Diesel Particulate Traps," AIChE J., **42**(6), pp. 1662–1672.
[61] Konstandopoulos, A. G., et al., 2003, "Multichannel Simulation of Soot Oxidation in Diesel Particulate Filters," SAE Paper No. 2003-01-0839.
[62] Guo, Z., and Zhang, Z., 2006, "Multi-Dimensional Modeling and Simulation of Wall-Flow Diesel Particulate Filter During Loading and Regeneration," SAE Paper No. 2006-01-0265.
[63] Aoki, H., et al., 1993, "Numerical Simulation Model for the Regeneration Process of a Wall-Flow Monolith Diesel Particulate Filter," SAE Paper No. 930364.
[64] Jacquot, F., et al., 2002, "Kinetics of the Oxidation of Carbon Black by NO_2. Influence in the Presence of Water and Oxygen," Carbon, **40**, pp. 335–343.
[65] Neeft, J. P. A., et al., 1997, "Kinetics of the Oxidation of Diesel Soot," Fuel, **76**(12), pp. 1129–1136.
[66] Pattas, K. N., and Samaras, Z. C., 1989, "Computational Simulation of the Ceramic Trap Transient Operation," SAE Paper No. 890403.

[67] Romero, A. F., et al., 1995, "Self Regenerating Catalyzed Diesel Aftertreatment System," SAE Paper No. 950367.
[68] Depcik, C., 2003, "Modeling Reacting Gases and Aftertreatment Devices for Internal Combustion Engines," Ph.D. thesis, The University of Michigan, Ann Arbor, MI.
[69] Hindmarsh, A. C., 2002, "Serial Fortran Solvers for ODE Initial Value Problems," http://www.llnl.gov/CASC/odepack/.
[70] Hirsch, C., 1988, *Numerical Computation of Internal and External Flows*, Wiley, Chichester.
[71] Hirsch, C., 1990, *Numerical Computation of Internal and External Flows*, Wiley, New York.
[72] Roache, P. J., 1972, *Computational Fluid Dynamics*, Hermosa, Albuerque, NM.
[73] Konstandopoulos, A. G., et al., 1999, "Optimized Filter Design and Selection Criteria for Continuously Regenerating Diesel Particulate Traps," SAE Paper No. 1999-01-0468.
[74] Konstandopoulos, A. G., et al., 2002, "Microstructural Properties of Soot Deposits in Diesel Particulate Traps," SAE Paper No. 2002-01-1015.
[75] Young, D. M., et al., 2002, "Silicon Carbide for Diesel Particulate Filter Applications: Material Development and Thermal Design," SAE Paper No. 2002-01-0324.
[76] Konstandopoulos, A. G., and Kostoglou, M., 1999, "Periodically Reversed Flow Regeneration of Diesel Particulate Traps," SAE Paper No. 1999-01-0469.
[77] Johnson, J. H., et al., 1997, "A Study of the Regeneration Characteristics of Silicon Carbide and Cordierite Diesel Particulate Filters Using a Copper Fuel Additive," SAE Paper No. 970187.
[78] Gantawar, A. K., et al., 1997, "A Study of the Regeneration Characteristics of a Silicon Carbide and Cordierite Diesel Particulate Filters Using a Copper Fuel Additive," SAE Paper No. 970188.
[79] Stobbe, P., et al., 1993, "SiC as a Substrate for Diesel Particulate Filters," SAE Paper No. 932495.
[80] Incropera, F. P., and DeWitt, D. P., 1990, *Fundamentals of Heat and Mass Transfer*, Wiley, New York.
[81] National Institute of Standards and Technologies, 2007, "NIST Chemistry Webbook," http://webbook.nist.gov/chemistry/.
[82] Day, J. P., 1990, "The Design of a New Ceramic Catalyst Support," SAE Paper No. 902167.

An Improved Phenomenological Soot Formation Submodel for Three-Dimensional Diesel Engine Simulations: Extension to Agglomeration of Particles into Clusters

Joan Boulanger
Gas Turbine Laboratory,
Institute for Aerospace Research,
National Research Council Canada,
1200 Montréal Road,
Ottawa, ON, K1A 0R6, Canada
e-mail: joan.boulanger@nrc-cnrc.gc.ca

W. Stuart Neill

Fengshan Liu

Gregory J. Smallwood

Institute for Chemical Process and Environmental Technology,
National Research Council Canada,
1200 Montréal Road,
Ottawa, ON, K1A 0R6, Canada

An extension to a phenomenological submodel for soot formation to include soot agglomeration effects is developed. The improved submodel was incorporated into a commercial computational fluid dynamics code and was used to investigate soot formation in a heavy-duty diesel engine. The results of the numerical simulation show that the soot oxidation process is reduced close to the combustion chamber walls, due to heat loss, such that larger soot particles and clusters are predicted in an annular volume at the end of the combustion cycle. These results are consistent with available in-cylinder experimental data and suggest that the cylinder of a diesel engine must be split into several volumes, each of them with a different role regarding soot formation.
[DOI: 10.1115/1.2939003]

Keywords: soot model, diesel engine, CFD

Introduction

This short note follows the presentation of a proposed soot model [1] that was essentially developed for engineering purposes, and extends it by introducing agglomeration using the elements exposed in a recent review [2]. This model was originally developed for estimating the soot volume fraction and the primary soot particle diameter. Agglomeration is far from being fully understood. This extension should thus be considered as a somewhat speculative and coarse interpretation of soot particle agglomeration in a cylinder. The qualitative focus may facilitate the comprehension of the in-cylinder pollutant formation process. However, it is important to note that the intent is not to provide comparisons with actual cases and measurements, given our incomplete fundamental knowledge of the processes involved. Rather, it is to assess the behavior and impact on modeling of such refinements and the type of information and scenario that may be accessed such that further experimental validations and practical use can be planned.

Soot Formation Submodel

The equations below correspond to the extended model (see Ref. [1] for the base line soot and oxidation models):

$$\frac{d(\rho n)}{dt} = a_0[\text{fuel}]e^{-T_a/T} + f(\rho n) - g(\rho n)(\rho N) - S'_{\text{ox}} \tag{1}$$

$$\frac{d(\rho N)}{dt} = a(\rho n) - b(\rho n)(\rho N) - H(d_{p_l} - d_{p_Z})(\rho(N - N'))^{4/3}(\rho Y_s(N - N')/N)^{2/3}\pi\left(\frac{6}{\rho_s \pi}\right)^{2/3}\bar{v}_r \tag{2}$$

$$\frac{d(\rho Y_s)}{dt} = \bar{v}_r \frac{\pi d_{p_i}^2}{4}(\rho N)[\text{fuel}]n_c \bar{M}_c + \rho_s a(\rho n)\frac{\pi d_{p_i}^3}{6} - NA_s S_{\text{ox}} \tag{3}$$

$$\frac{d(\rho Z_s)}{dt} = \bar{v}_r \frac{\pi d_{p_i}^2}{4}\rho(N - N')[\text{fuel}]n_c \bar{M}_c + \rho_s a(\rho n)\frac{\pi d_{p_i}^3}{6} \tag{4}$$

$$\frac{d(\rho N_c)}{dt} = H(d_{p_z} - d_{p_l})(\rho(N - N'))^{4/3}(\rho Y_s(N - N')/N)^{2/3} \times \pi\left(\frac{6}{\rho_s \pi}\right)^{2/3}\bar{v}_r - \bar{v}_r 4\sigma_c(\rho N_c)(\rho N_c) \tag{5}$$

Table 1 Kinetics in the soot model. For detailed information, see Ref. [1]. For ease, the basic kinetics from Ref. [3] on which this modeling is based is recalled in the caption: $d(\rho N)/dt = a(\rho n) - b(\rho n)(\rho N)$ and $d(\rho n)/dt = a_0[\text{fuel}]\exp(-T_{a_{n_0}}/T) + F(\rho n) - g_0(\rho n)(\rho N)$

T_a	21,000 K
a	10^5 (−)
f	100 (−)
g	10^{-15} m^3
b	8×10^{-14} m^3
a_0	2.3×10^{-3} Hz
ρ_s	1900 kg/m^3
D_0	1 nm

Contributed by the Internal Combustion Engine Division of ASME for publication in the JOURNAL OF ENGINEERING FOR GAS TURBINES AND POWER. Manuscript received April 30, 2007; final manuscript received February 15, 2008; published online August 22, 2008. Review conducted by Kalyan Annamalai. Paper presented at the 2006 Fall Conference of the ASME Internal Combustion Engine Division (ICEF2006), Sacramento, CA, November 5–8, 2006.

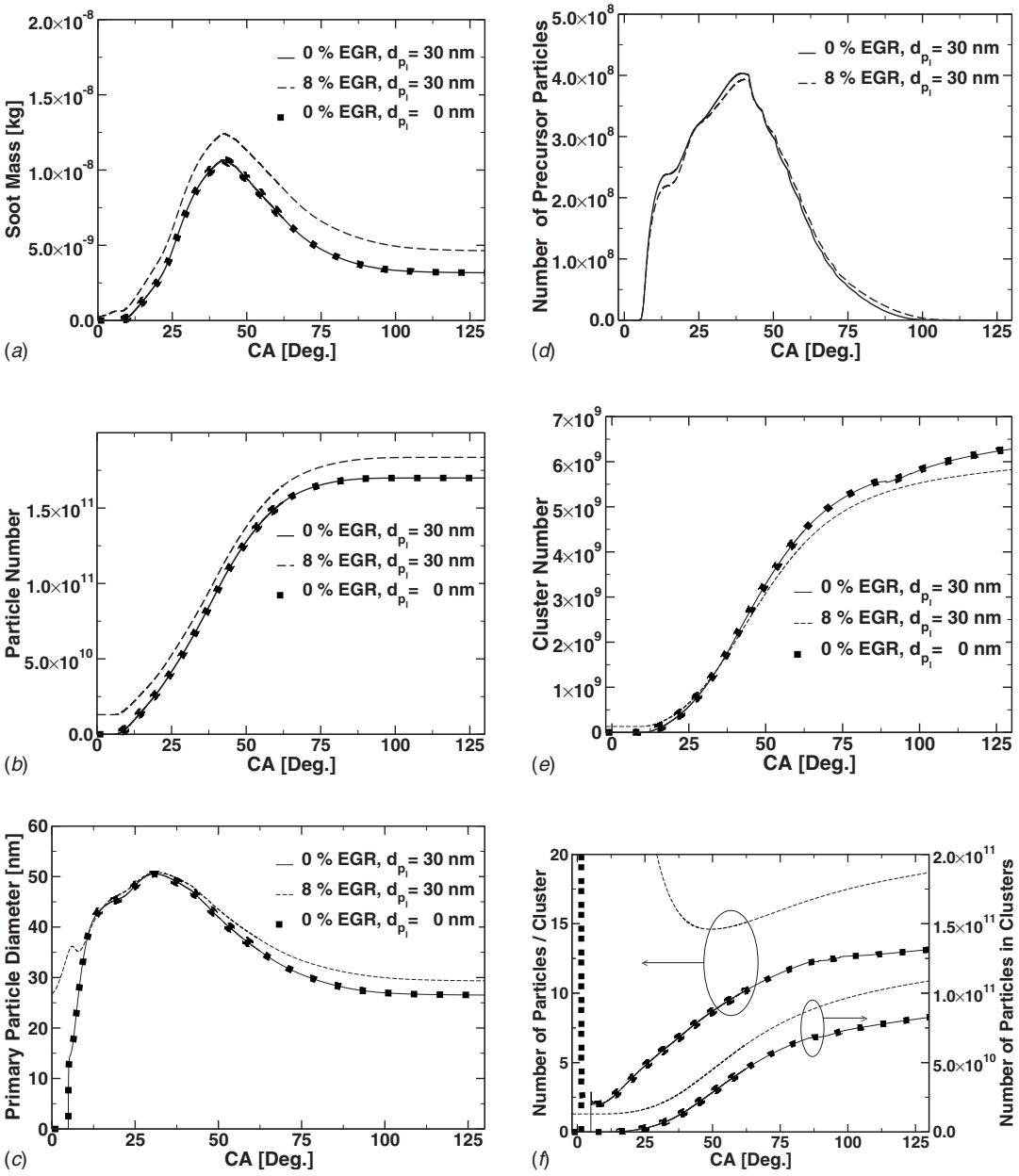

Fig. 1 Soot formation history in the cylinder sector: (*a*) mass, (*b*) primary particle number, (*c*) root mean cubic diameter, (*d*) precursor particle number, (*e*) cluster number, and (*f*) aggregated particles; line: 0% EGR, dashed: 8% EGR, and dots: 0% EGR, no threshold diameter (d_{pl}=0)

$$\frac{d(\rho N')}{dt} = 2H(d_{p_Z} - d_{p_l})(\rho(N-N'))^{4/3}(\rho Y_s(N-N')/N')^{2/3} \times \pi\left(\frac{6}{\rho_s \pi}\right)^{2/3} \bar{v}_r + \bar{v}_r(d_c/2 + d_p/2)^2 \pi\rho(N-N')(\rho N_c) \quad (6)$$

where f, g, a, and b are the parameters in Ref. [3] for Semenov-type equations; T_a is the activation temperature of the fuel pyrolysis step; ρ_s is the density of soot and Y_s is its mass fraction; d_{p_i} is the inception diameter of soot from radicals; a_0 is the preexponential factor estimating the rate of pyrolysis; [fuel] is the molar concentration of the hydrocarbon (HC) fuel; n_c is the number of carbon atoms in the HC molecule; $\bar{M}_c$ is the carbon molar weight; and $A_s S_{ox}$ and S'_{ox} are the oxidation terms. Details of these terms are provided in Ref. [1] and their values are quickly recalled in Table 1. The first equation is for the number density of active

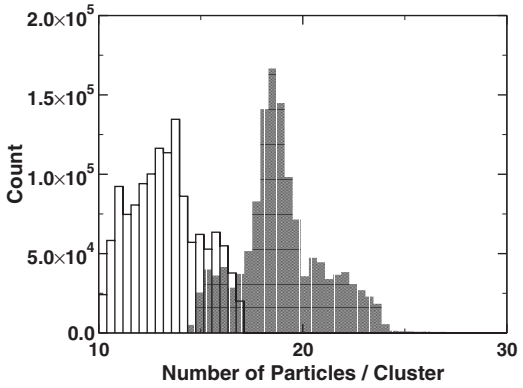

Fig. 2 Distribution of cluster size in terms of particle number; open 0% EGR, and shaded 8% EGR

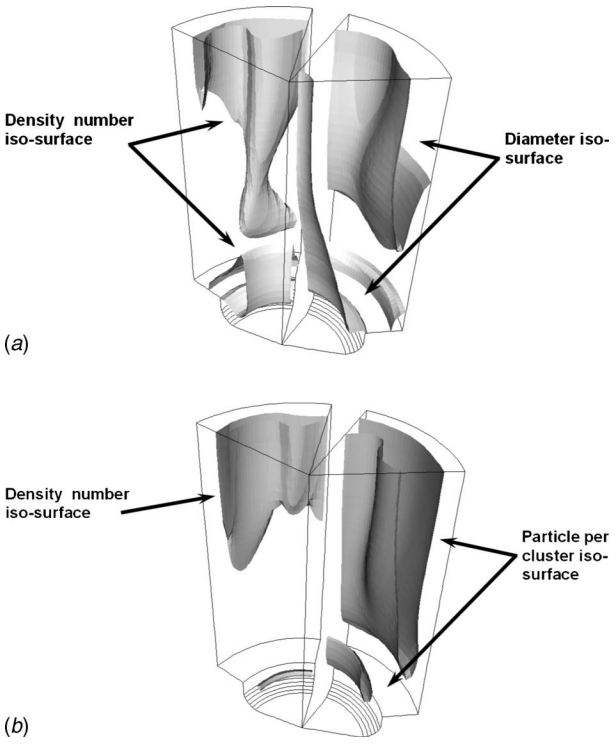

Fig. 3 (*a*) Primary particle location (EVO). Left: density number isosurface, 2.3×10^{14} m^{-3}; range (1.5×10^{13} m^{-3}, 3.3×10^{14} m^{-3}). Right: diameter isosurface. Internal 20 nm. External 30 nm. Range (0 nm, 42 nm), (*b*) Cluster location (EVO). Left: density number isosurface, 1.2×10^{13} m^{-3}; range (1.5×10^{11} m^{-3}, 1.6×10^{13} m^{-3}). Right: particles per cluster isosurface 14; range (4, 17). Note that the different sectors are the same computational sector representing different quantities.

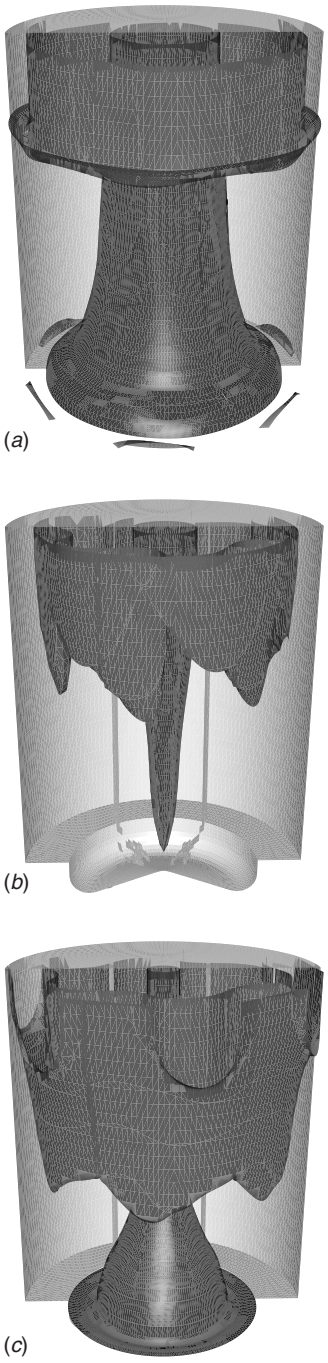

Fig. 4 (*a*) Primary particle diameter field. Internal isosurface: 17.5 nm. External isosurface: 35 nm. (*b*) Cluster size (number of particles) field. Internal isosurface: 7. External isosurface: 16. (c) Cluster size (apparent diameter (Ref. [5]), d_c) field. Internal isosurface: 20 nm. External isosurface: 120 nm.

radicals n (fuel molecule pyrolysis). The second equation is for the soot primary particle population N. A third equation based on kinetic theory describes the change in mass ρY_s of the primary particles through growth and coalescence. Evidence is reported in Ref. [4] through transmission electron microscopy (TEM) imaging that agglomeration may happen very early in the cylinder. Hence, new terms extending the model to agglomeration are expressed in the last three equations and the introduction of Heaviside function in the number density equation, Eq. (2). The principle for the present development is the following. A subpopulation N' of N particles is considered agglomerating into N_c clusters. The remaining $(N-N')$ particles are still free. Each time two free particles collide, they may coalesce (last term of Eq. (2)) or stick and form a structure (first term of Eq. (5)). The transition between coalescence and agglomeration is not obvious [2]. A sensible approach consists in saying that coalescence is no longer possible when the particle is too old, which means that it is solid and the surface is no longer active enough for growth such that it cannot be buried. Size might be a good indication of aging. However, oxidation and coalescence lead to a change in size, which is not related to chemical aging. Thus, a tracer is introduced. This tracer is a virtual soot mass fraction. It is based on free particles and surface growth only (without oxidation or coagulation). This is Eq. (4). When the tracer-particle diameter d_{p_Z} is bigger than a threshold diameter d_{p_l}, coalescence is switched off (last term of Eq. (2)) and agglomeration is switched on (first term of Eqs. (5) and (6)). These are the Heaviside functions. Each creation results in two initial particles per structure (first term of Eq. (6)). Structures may collide with free particles (second term of Eq. (6)) and increase their particle number. They may also collide with each other (second term of Eq. (5)) and form a single bigger cluster.

All collisions are assumed effective. They are based on basic kinetic theory to make the model simple and self-consistent. $\bar{v}_r$ is the relative velocity between two particles in Brownian motion. Its square is thus equal to the sum of their respective quadratic mean velocities. For modeling, the cluster collision surface, a disk equivalent to the projected surface, is retained. The projected surface, is the sum of the projected surfaces of the primary particles, according to Ref. [5]. This interesting discovery makes the model independent of the fractal parameters, which are acknowledged to

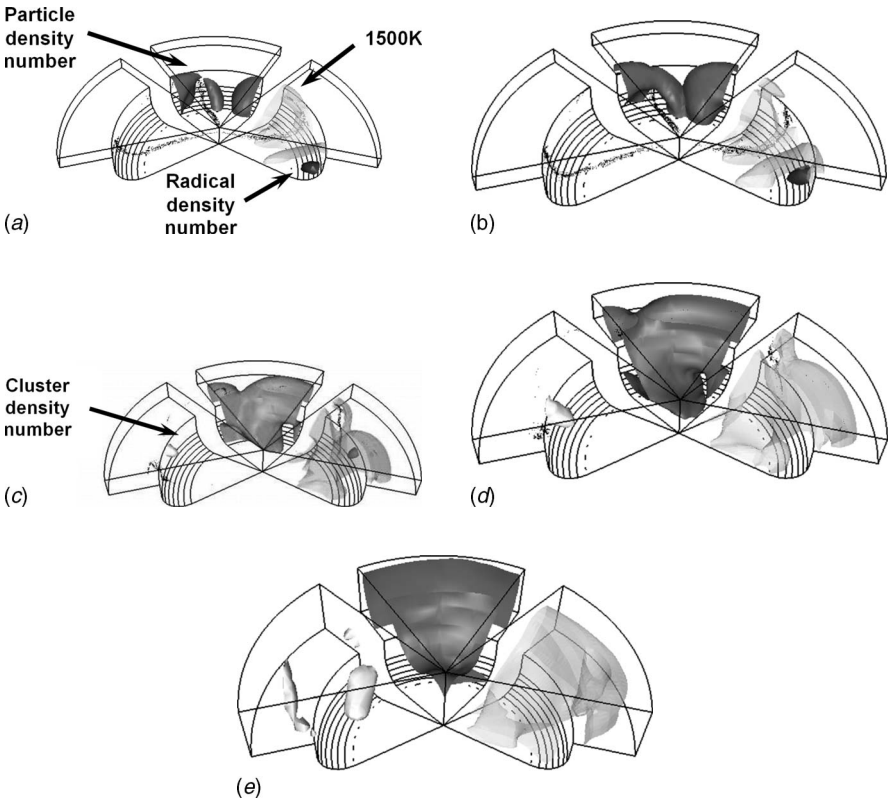

Fig. 5 Sequence of formation of the soot. Left: cluster density number isosurface, 1×10^{13} kg^{-1}. Middle: soot particle density number isosurface, 1×10^{13} kg^{-1}. Right: radical density number isosurface, 1×10^{13} kg^{-1}. Transparent isotemperature at 1500 K. (*a*) At radical appearance (CA=9.6 ATDC). (*b*) Close to end of injection (CA =11.7 ATDC). (*c*) At cluster appearance (CA=18.0 ATDC). (*d*) At radical disappearance (CA=22.1 ATDC). (*e*) At full evaporation (CA=34.7 ATDC). Note that the different sectors are the same computational sector representing different quantities.

vary with engine geometry, speed, and load. Thus, the projected surface/collision area is given by $\sigma_c=\pi d_c^2/4=N'/N_c\pi d_p^2/4$, where N'/N_c is the number of particles per cluster. d_c is the estimated diameter of the cluster and d_p is the diameter of the primary particle. Kinetic theory has limits for complicated structures like fractal aggregates. They may be animated by a complex movement not considered in the theory. Furthermore, their response to turbulent flow may be very different from small soot particles. Aggregation rate may thus be higher than predicted because of a nonrepresentative evaluation of the relative velocity. Empirical approaches have pointed out this problem in typical engine flows [6,7]. This is the reason why comprehensive approaches based on kinetic theory, as in Ref. [8], are of limited utility here. Corrections to augment the Brownian collision rate are very empirical at the present time. It is furthermore hard to believe that they are adapted to the considered configuration. Hence, an arbitrary factor of 100 from the Brownian collision rate appearing in the last term of Eq. (6) has been used to enhance particle clustering in order to maintain simplicity in the model. Tests have demonstrated that change in this factor has marginal impact on soot prediction (except, of course, cluster size) as it has no direct interaction with the soot mass growth. The chosen magnifying factor is arbitrary. Given limited knowledge of this process, it is believed that this qualitative approach is appropriate to highlight phenomena prior to any practical consideration and validation.

The reader is referred to Ref. [1] for the computational framework, tools, and configuration.

Results and Discussion

An overview of the simulation results is provided in Fig. 1. Numerous observations may be made: (i) cooled exhaust gas recirculation (EGR) increases soot emissions by enhancing both the particle number density and the particle size through a lower overall temperature regarding soot combustion during the expansion stroke and a higher equivalence ratio due to the presence of a vitiated mixture. These are the known prediction capabilities for this kind of model [1]; (ii) pyrolysis of fuel into soot precursors is known to be dependent on both temperature and fuel. This is properly accounted for as the formation of soot precursors is slightly delayed and is smaller for the EGR case. This leads to a time delay before the soot forms in the combustion chamber. The lower temperature in the cylinder for the EGR case slightly reduces the early formation of soot precursors. On the other hand, EGR leads to more soot precursors later in the expansion stroke; and (iii) the choice of a threshold diameter d_{p_l} to turn coagulation into agglomeration is of little importance in the chosen framework. This numerical artifact is due to the Brownian-based coagulation rate being too low, as discussed earlier. In addition to the fact that contemporary knowledge does not allow any solution for this issue, the extremely fast maturation of soot particles proposed (and still debated) in literature [2] may be explained, below.

EGR leads to a slightly smaller number of clusters being formed. This might be due to a reduced early collision frequency between free primary particles. This frequency is dependent on temperature. However, the number of particles per cluster is

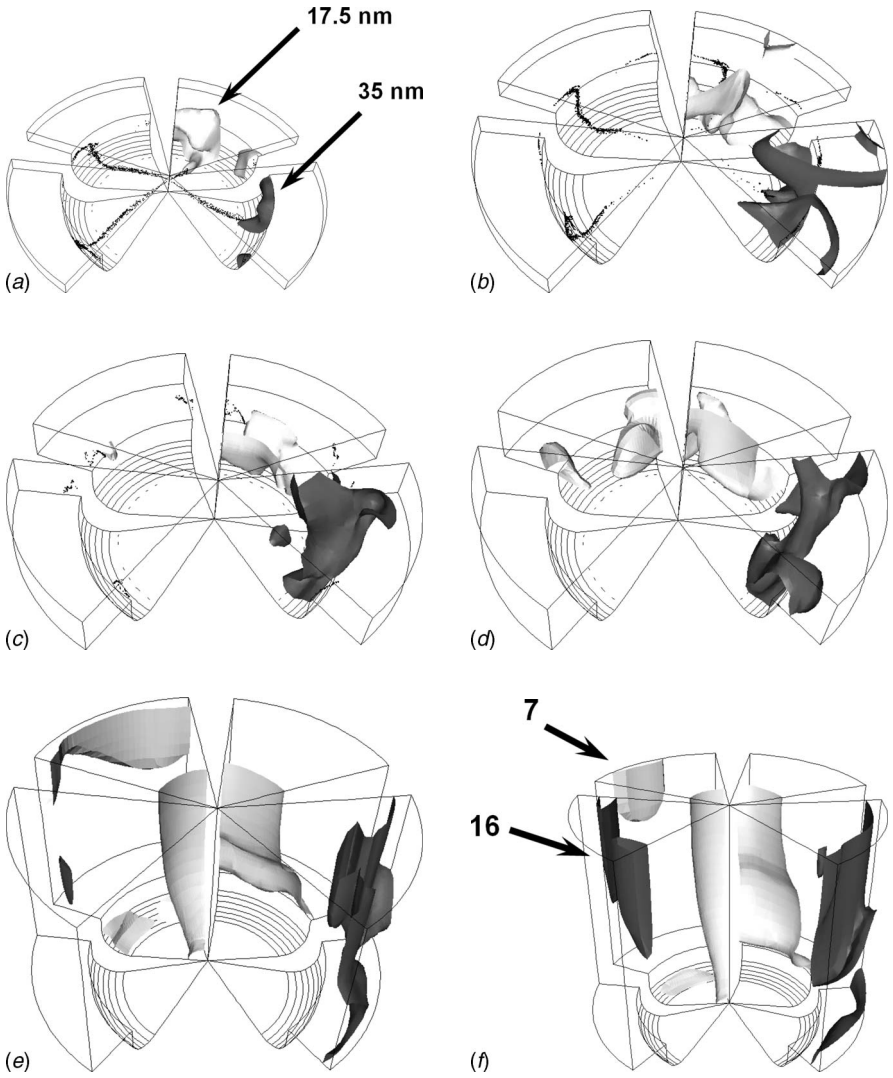

Fig. 6 Sequence of formation of the soot. From left to right. Particle per cluster isosurface=16. Particle per cluster isosurface=7. Primary particle size isosurface =17.5 nm. Primary particle size isosurface=35 nm. (*a*) Appearance of particles larger than 45 nm (CA=9.6 ATDC). (*b*) Close to the end of injection (CA=13.8 ATDC). (*c*) Appearance of clusters larger than seven particles (CA=26.3 ATDC). (*d*) End of evaporation (CA=34.7 ATDC). (*e*) Appearance of clusters larger than 16 particles (CA=72.7 ATDC). (*f*) CA=93.3 ATDC. Note that the different sectors are the same computational sector representing different quantities.

larger. The dashed upper curve in Fig. 1(*f*) for the EGR case predicts that the number of particles in a cluster decreases and then increases. This trend occurs because the soot clusters that are recirculated into the combustion chamber due to cooled EGR are assumed to be fully mature with an average size of 100 particles.

In contrast to the primary particle formation, the threshold diameter d_{p_l} to switch from coagulation to agglomeration is visible in cluster dynamics. In Fig. 1(*f*), the start of the cluster formation is revealed by the singularity on the left hand side of the graph. There are a few degrees crank angle between the 0 nm and 30 nm cases. This is negligible. Transition at 0 nm means that the particles are never able to merge. On the other hand, transition at 30 nm involves more mature particles after a long process of surface growth and notable changes of surface chemistry. This is consistent with the fast maturation of the primary particles, as discussed above, showing that the coagulation rate may be of limited importance. It is noted that the existence of soot particles at top dead center (TDC) in this case is simply due to the re-injection of the soot-containing exhaust gas (without filter) into the intake.

For the following figures, isovalues have been chosen arbitrarily to help the reader interpret the location of the species of interest. Furthermore, when a range of values is present in the caption, it is only for information purposes about the order of magnitude involved. This range is not represented in the picture.

Distribution of the cluster size at exhaust valve opening (EVO) predicted by the numerical simulation is given in Fig. 2. The distribution shape is about the same for the non-EGR and EGR cases. The overall size is thus shifted to EGR as more particles tend to agglomerate.

Figure 3 gives comparative information about soot particles and clusters at the end of the expansion stroke. Consistent with our previous communication [1], bigger particles are found close to the cylinder wall and head. The proposed model is thus able to reproduce the trends experimentally observed [9,10]. It allows one the interpretation that heat loss prevents the oxidation of primary particles. It has actually been shown that emission prediction in

the near-wall region is dramatically impacted by the surface temperature [11]. Oxidation is highly temperature dependent. The number density of particles is more important at the intermediate annular location in the cylinder, an area swept across by spray combustion. In regions close to the wall, where both particle diameter and number density are large, agglomeration is expected to be important. Figure 3(*b*) displays the presence of numerous agglomerated particles in this region. Both numerous clusters and numerous particles per cluster are found. Like the primary particle distribution, clusters tend to be larger close to the wall. This is consistent with the experiments as well. Growth, coagulation, and agglomeration are acknowledged to be simultaneous. It is thus admitted that some of the largest particles experimentally found may come from a more-or-less buried cluster, i.e., stuck particles are buried by surface growth.

A complete picture of the primary particle location with respect to size is provided in Fig. 4(*a*). A conical volume around the cylinder axis and embedding the bowl is filled with small particles. A crown of large particles is located close to the corner between the top and the wall. Small particles are explained because of oxidation. The interior of the cylinder volume is a well-mixed high-temperature zone throughout the combustion process. In contrast, the engine cooling system leads to heat losses at the boundaries. They are mainly located at the head and the wall. The oxidation of the soot is thus difficult in these regions. This leads to larger particles. The same formation history is exhibited by clusters, as shown in Figs. 4(*b*) and 4(*c*). Small clusters are present along the axis, consistent with the observations made about the results shown in Fig. 3. Numerous large particles have, however, agglomerated in a crown close to the top of the cylinder, according to the mechanism described previously. This provides the picture of particle formation at the end of the expansion stroke and before entering the exhaust pipe. Further agglomeration is expected to occur there.

A history of the soot formation is given in Fig. 5. The iso-1500 K defines a volume where the temperature is higher, as the transition criterion from ignition to combustion. In Fig. 5(*a*), radicals and soot particles are formed in rich, high-temperature zones. These zones are on the side of the spray and between the spray paths as swirl entrains a rich mixture fed with evaporating fuel. Over time, clouds of soot grow in the proximity of the spray, as shown in Fig. 5(*b*). Then, clusters begin to appear in the area where the density of soot particle is high, as shown in Fig. 5(*c*). This area is of an annular shape with a diameter roughly of the order of the bowl. The shape of this area is explained by the presence of evaporating spray, impacting close to the edge of the bowl and mixing with hot air. It is in this rich region where the soot is formed. During the expansion stroke, this region is simply stretched in the direction of the downward motion of the piston. The result is the field observed in Figs. 3 and 4. Figure 6 displays another picture of the described phenomena. Particles of the soot are formed very early, as exhibited in Fig. 6(*a*). They easily reach a large size in the rich, high temperature zone in the vicinity of the spray, Fig. 6(*b*). Clusters appear later and slowly grow, Figs. 6(*c*)–6(*e*). As mentioned before, they preferably appear and grow at an annular location that corresponds to a zone where numerous and large particles are found.

Acknowledgment

This research has been made possible by the funding received from the Government of Canada Program for Energy Research and Development (PERD/AFTER). The authors wish to thank Dr. S. C. Kong and Professor R. D. Reitz for providing the grid specification of the engine geometry and parameters. Dr. William Wallace is gratefully acknowledged for his fruitful comments regarding the improvement of the manuscript.

References

[1] Boulanger, J., Liu, F., Neill, W. S., and Smallwood, G. J., 2005, "An Improved Soot Formation Model for 3-D Diesel Engine Simulations," ASME J. Eng. Gas Turbines Power, **129**, pp. 877–884.
[2] Frenklach, M., 2002, "Reaction Mechanism of Soot Formation in Flames," Phys. Chem. Chem. Phys., **4**, pp. 2028–2037.
[3] Tesner, P., Snegiriova, T., and Knorre, V., 1971, "Kinetics of Dispersed Carbon Formation," Combust. Flame, **17**, pp. 253–260.
[4] Su, D. S., Müller, J.-O., Jentoft, R. E., Rothe, D., Jacob, E., and Schlögl, R., 2004, "Fullerene-Like Soot From EUROIV Diesel Engine: Consequences for Catalytic Automotive Pollution Control," Top. Catal., **30/31**, pp. 241–245.
[5] Brasil, A. M., Farias, T. L., and Carvalho, M. G., 1999, "A Recipe for Image Characterization of Fractal-Like Aggregates," J. Aerosol Sci., **30**, pp. 1379–1389.
[6] Khan, I. M., Wang, C. H. T., and Langridge, B. E., 1971, "Coagulation and Combustion of Soot Particles in Diesel Engines," Combust. Flame, **17**, pp. 408–419.
[7] Smith, O. I., 1981, "Fundamentals of Soot Formation in Flames With Application to Diesel Engine Particulate Emissions," Prog. Energy Combust. Sci., **7**, pp. 275–291.
[8] Kazakov, A., and Frenklach, M., 1998, "Dynamic Modeling of Soot Particle Coagulation and Aggregation: Implementation With the Method of Moments and Application to High-Pressure Laminar Premixed Flames," Combust. Flame, **114**, pp. 484–501.
[9] Shahad, H. A. K., 1989, "An Experimental Investigation of Soot Particle Size Inside the Combustion Chamber of a Diesel Engine," Energy Convers. Manage., **29**, pp. 141–149.
[10] Leipertz, A., and Dankers, S., 2003, "Characterization of Nano-Particles Using Laser-Induced Incandescence," Part. Part. Syst. Charact., **20**, pp. 81–93.
[11] Wiedenhoefer, J. F., and Reitz, R. D., 2000, "Modeling the Effect of EGR and Multiple Injection Schemes on I.C. Engine Component Temperatures," Numer. Heat Transfer, Part A, **37**, pp. 673–694.

Development and Application of a Complete Multijet Common-Rail Injection-System Mathematical Model for Hydrodynamic Analysis and Diagnostics

Andrea E. Catania
Alessandro Ferrari
Michele Manno

IC Engines Advanced Laboratory,
Politecnico di Torino,
C.so Duca degli Abruzzi, 24
10129 - Torino (Italy)

A rather complete mathematical model for a common-rail injection-system dynamics numerical simulation was developed to support experimentation, layout, and control design, as well as performance optimization. The thermofluid dynamics of the hydraulic-system components, including rail, connecting pipes, and injectors was modeled in conjunction with the solenoid-circuit electromagnetics and the mechanics of mobile elements. One-dimensional flow equations in conservation form were used to simulate wave propagation phenomena throughout the high-pressure connecting pipes, including the feeding pipe of the injector nozzle. In order to simulate the temperature variations due to the fuel compressibility, the energy equation was used in addition to mass conservation and momentum balance equations. Besides, the possible cavitation phenomenon effects on the mass flow rate through the injector bleed orifice and the nozzle holes were taken into account. A simple model of the electromagnetic driving circuit was used to predict the temporal distribution of the force acting on the pilot-valve anchor. It was based on the experimental time histories of the current through the solenoid and of the associated voltage that is provided by the electronic control unit to the solenoid. The numerical code was validated through the comparison of the prediction results with experimental data, that is, pressure, injected flow rate, and needle lift time histories, taken on a high performance test bench Moehwald-Bosch MEP2000-CA4000. The novel injection-system mathematical model was applied to the analysis of transient flows through the hydraulic circuit of a commercial multijet second-generation common-rail system, paying specific attention to the wave propagation phenomena, to their dependence on solenoid energizing time and rail pressure, as well as to their effects on system performance. In particular, an insight was also given into the model capability of accurately predicting the wave dynamics effects on the rate and mass of fuel injected when the dwell time between two consecutive injections is varied. [DOI: 10.1115/1.2925679]

Introduction

The diesel engine penetration has largely passed the 40% share of the European market of passenger cars and it is easy to predict a further growth in the next years over 50%. Such great success is mainly due to the late 1990s availability of technology breakthrough for the fuel delivery system, i.e., the common rail (CR), which has enhanced the direct-injection (DI) diesel engine potential in terms of fuel economy and fun to drive, granting a superior emission and noise-vibration-harshness (NVH) control, the traditional weak points of solution. The diesel engine NO_x and PM emission challenge continues in the next future toward zero emission level, so that injection-system layout optimization and control strategy enhancement are key objectives to pursue. To that end, it is fundamental to better understand the effects of operation variables and components on the dynamics of the new generation multijet CR systems. Thus, a complete and accurate simulation tool of these systems is very useful to the designer.

The CR features and potentialities in substantial improvements of DI diesel engine performance are described by many authors (e.g., Refs. [1] and [2]). In such a system, the generation of pressure level is independent of the fuel metering so that both the injection timing and length can be optimized for every working condition providing accuracy in the injected mass quantity. The fuel can be injected at very high (roughly constant) pressure for spray atomization, so as to promote its mixing with air, resulting in combustion improvement. Besides, it is possible to shape the energy conversion process in order to minimize the typical combustion noise of diesel engines and to further lower emissions and fuel consumption.

The electronically controlled multiple injection concept, by splitting the fuel injection up to five pulses, in conjunction with variable-swirl intake ducts and cooled exhaust gas recirculation (EGR), has been an effective strategy to achieve simultaneous reduction of NO_x and soot level emissions fulfilling the reduced engine-out emission levels imposed by EURO-4 legislation.

All these premises support a design approach finalized to manufacturing an injection system that is capable of operating repeatable injections of small and precise fuel amounts. Many research activities are oriented toward CR system improvements in order to reduce the dwell time between two consecutive injections. A constraint in reducing this dwell time is due to the pressure fluctuations, which arise as a consequence of injector opening and closing and which propagate inside the system, hindering the

Contributed by the Internal Combustion Division of ASME for publication in the JOURNAL OF ENGINEERING FOR GAS TURBINES AND POWER. Manuscript received April 14, 2007; final manuscript received October 15, 2007; published online August 25, 2008. Review conducted by Christopher J. Rutland. Paper presented at the 2005 Spring Conference of the ASME Internal Combusion Engine Division (ICES2005), Long Beach, CA, April 5-7, 2005.

achievement of the required accuracy and repeatability in the amount of fuel injected at each pulse when the dwell time varies. Using very close injections requires an adequate system dynamics that is strongly dependent on the hydraulic-system layout. Although the solenoid recharge-time typically allows actuation of two consecutive electric pulses above 100 μs time intervals, flow instabilities further increase such a limit to 1000 μs in order to keep a low standard deviation of the fuel amount injected over consecutive engine cycles when the dwell time is changed [2–4].

Numerical simulation offers the means of evaluating design and operation variable effects on the transient flows inside the CR systems with a significant reduction of experimental tests [5–7]. The system geometrical features and the impulsive character of its behavior do not allow a fully beneficial simulation when too simplified mathematical models are used ([5,8]).

One-dimensional (1D) pipe flow models offer the best ratio between benefits and computational cost, since they are capable of catching the macroscopical fluid dynamic phenomenon aspects taking full advantage of experimental tests. Numerical models of CR systems, based on 1D partial differential equations, were developed in Refs. [6] and [9]. However, all these models assume a constant rail pressure with respect to time and therefore, although they can provide good resolution in the simulation of single injection events, they cannot be applied for accurately simulating multiple injection events. In fact, the experimental pressure distribution versus time at each location of the rail-injector junctions shows a modulation corresponding to pressure oscillations versus time in the rail, which thus does not behave as an infinite capacity. If a constant rail pressure is assumed, the pressure waves caused by the opening and closing of one injector are not expected to affect the fluid dynamics of the pipes delivering the fuel from the rail to the other injectors, whereas experimental tests have shown that such an assumption can be critical [10]. Besides, the flow is usually taken to be isothermal or at least temperature variations are included by drastic simplifications [9], so that the reduced accuracy in sound-speed values can significantly lower the degree of accuracy in multiple injection simulation.

In the present work, a rather complete CR system numerical model, capable of accurately simulating multiple injections and their interactions, was developed and validated by experimental results, for the first time in the literature. The hydraulic and electromagnetic components of a commercial multijet CR injection system for diesel passenger cars, including pump-rail line, rail, rail-injector pipes, and electroinjectors, were modeled. Different injector configurations were also considered.

A 1D barotropic flow model was applied to the pipes connecting the rail with the injectors and with drilled passages inside the injectors. It takes temperature variations into account on the basis of a thermodynamic law of oil evolution deduced from experimental pressure time histories at different system points. The moving mechanical parts of injector were modeled by second order mass-spring-damper schemes. Finally, a simple and effective electromagnetic model was built for the solenoid control valve. It was based on the experimental time history of the electric current through the coil and on the time-dependent voltage that was applied by the ECU to the coil itself. This model was shown to predict reasonable values of the attraction force acting on the pilot valve, due to the general good agreement between the numerical and experimental results for the pressure and needle lift time distributions.

The results of prediction were analyzed to find cause-effect relationships and give explanations of the main nonstationary events conditioning the injection-system performance.

Experimental Facility

A high performance test bench Moehwald-Bosch MEP2000-CA4000 that is instrumented for fluid dynamic characterization of high-pressure electronically controlled fuel injection systems was applied for experimental investigation. This facility has a maximum shaft power of 35 kW and a maximum speed of 6100 rpm, with the capability of simulating fast injection-system transient operations and of choosing testing parameters so as to simulate the real engine operating conditions.

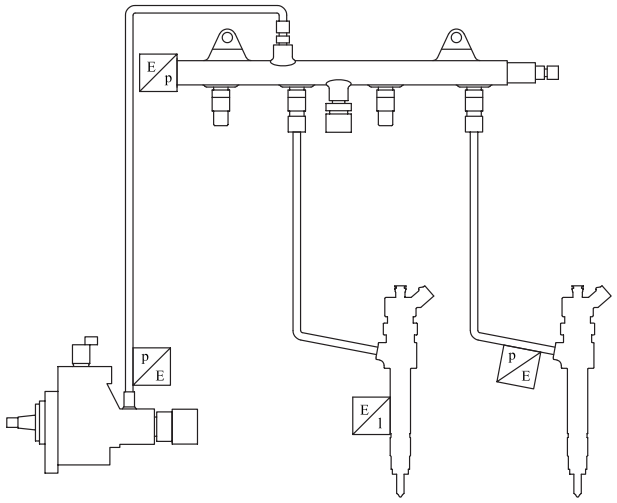

Fig. 1 Experimental hydraulic layout and transducers

With regard to the measurement instruments, an injection discharge-rate meter (EVI) was used to take injector flow rate traces by recording the pressure waves produced by an injection inside a loop connected with the injector nozzle. The recorded pressure time history is converted into fuel mass distribution [10]. The injector was equipped with an inductive needle-lift sensor. The injected quantity indicator EMI2 was employed to measure the amount of fuel injected for each pulse the full injection is split in. Three piezoresistive transducers recorded pressure and temperature distributions versus time in the rail, at the pump delivery outlet and at the injector inlet. A National Instruments data acquisition board and an acquisition program, which was developed by the authors in LABVIEW environment, were used to control the injection system. Further details on the experimental apparatus and on the measuring instruments are given in Ref. [10].

A new generation CR system for a 1900 cc JTD engine, with an electronic control unit (ECU) that is capable of managing up to five injections per engine cycle was installed on the bench. The experimental hydraulic layout of the considered system is shown in Fig. 1. This consists of a commercial high-pressure electronically controlled fuel injection system made up of a rotary pump, a rail, and four electroinjectors (Fig. 2). A three piston Bosch radial jet pump, having a displacement of 550 mm^3/rev, supplies the accumulator with ISO 4113 oil, which simulates the fuel. It is lubricated and cooled by the oil itself. A fluid pressure regulator is located at the delivery pump outlet. It is responsible for maintaining the level of the oil pressure in the accumulator at a prescribed value, and is controlled by the ECU on the basis of a pressure signal input coming from the rail.

For model validation, a rail trapped volume of 20 cm^3 and injector supply pipes of different internal diameters (2.4–3 mm) and lengths (125–300 mm) were considered. A rail-feeding pipe of fixed length and diameter, 265 mm and 2.4 mm, respectively, was considered for all the experimental tests, as the injection-system performance were virtually unaffected by the geometrical features of the pump-rail pipe.

Thermofluid Dynamic Model

The schematic of the hydraulic system was basically made up of chamber elements, i.e., volumes with all the characteristic dimensions of the same order, and pipe elements, i.e., volumes with one dimension prevailing over the others. In the chambers, pres-

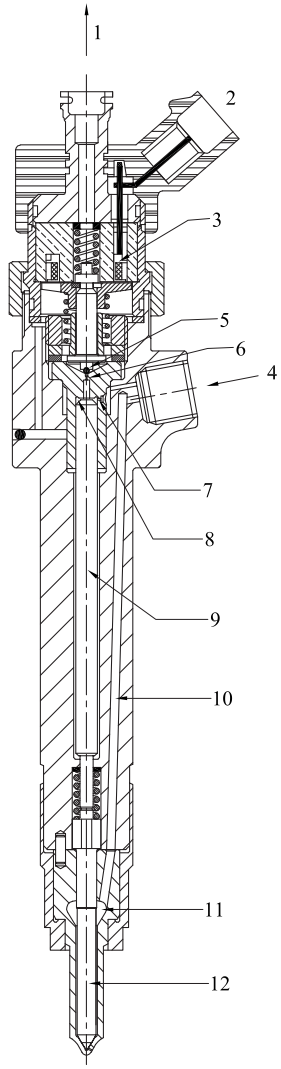

1 Fuel return (low pressure)
2 Electrical connection
3 Triggering element (solenoid valve)
4 Fuel inlet (high pressure)
5 Pilot-valve ball
6 Bleed orifice (hole A)
7 Feed orifice (hole Z)
8 Needle-valve control chamber
9 Needle-valve control plunger
10 Feed pipe to the nozzle
11 Delivery chamber
12 Nozzle needle

Fig. 2 Electroinjector

sure and temperature take uniform values that depend only on time, according to a lumped mass model. In the pipes, the thermofluid dynamic properties are allowed to vary with both time and axial coordinate, on the basis of a 1D approach.

The experimental time histories of pressure and temperature measured at the delivery pump outlet were provided as input to the model. These made it possible to include the action of the pressure regulator and the thermodynamic effects of the fluid compression in the pump. Since the rail is a tubular element, which is supplied with oil by the pump and delivers the oil to the injectors through pressure pipes, it was modeled as a set of chamber elements, at any pipe junction location, and of pipe elements connecting these chambers each other as well as with the rail sidewalls.

A filter was present at the inlet of every injector (Location 4 in Fig. 2), to remove solid impurities from the feeding oil. It was modeled as a concentrated resistance to the flow. Two chamber elements were located upstream and downstream from the filter, respectively.

The main feature of the injector is the presence of a control volume, at the top of the control plunger (Location 8 in Fig. 2), supplied by the inlet pipe through a calibrated hole, namely, Z (Location 7 in Fig. 2). The central unit drives an electromagnet that controls the injector opening: The solenoid excitation causes the lifting of the pilot-valve ball, which opens a discharge hole, namely, A (Location 6 in Fig. 2). This connects the control volume to the oil tank through the return pipe (1 in Fig. 2), determining a pressure decrease in the control volume itself.

A pipe conveys the oil from the injector inlet to the delivery chamber, which is connected to the multihole nozzle tip through an annular passage. The access to the injector holes is regulated by the needle lift: When the electromagnet is not excited, the pressures acting on the control-plunger and needle-valve unit, along with the action of the spring preload, maintain the needle closed. As soon as the electromagnet is excited, the pressure in the control volume very quickly decreases, so that, after a very short time from the rising of the current trough the solenoid, the needle lifts allowing the fuel injection. It is evident that part of the pressurized fuel supplied by the rail is discharged through the holes Z and A, whose dimensions determine the value of the pressure in the control volume and the major portion of the time lag between the pilot valve and needle lifting.

Different nozzle configurations including valve covered orifice (VCO), Minisac, and Microsac were modeled so as to cover the overall commercial range of second-generation multijet electroinjectors.

Pipe-Flow Governing Equations. Based on a conservative formulation, the pipe-flow model equations are written in the divergence form, that is, following a control volume approach for a constant cross section area pipe element, the conservation of mass and the momentum-balance equations can be written in the following differential form:

$$\frac{\partial \mathbf{w}}{\partial t} + \frac{\partial \mathbf{F}}{\partial x} = \mathbf{H} \tag{1}$$

where

$$\mathbf{w} = \begin{bmatrix} \rho \\ \rho u \end{bmatrix}, \quad \mathbf{F}(\mathbf{w}) = \begin{bmatrix} \rho u \\ \rho u^2 + p \end{bmatrix}, \quad \mathbf{H} = \begin{bmatrix} 0 \\ -\dfrac{4\tau_w}{d} \end{bmatrix} \tag{2}$$

t is the time variable and x is the spatial variable along the pipe axis; ρ, u, and p are the average cross-sectional density, velocity, and pressure of the liquid, and d is the internal diameter of the pipe. Due to the presence of impulsive phenomena, giving rise to high-frequency pressure oscillations, the wall shear stress τ_w was modeled according to the following expression:

$$\tau_w = \frac{1}{8} f \rho |u| u + \delta \frac{16}{d^2} \mu \int_0^t \frac{\partial u(x,\lambda)}{\partial t} W(t-\lambda) d\lambda \tag{3}$$

where the first term on the right hand side is the stationary part of τ_w evaluated using the Darcy–Weisbach friction coefficient f, whereas the second term represents the frequency dependent component of τ_w. This latter was estimated by a convolution integral taking the velocity fluctuation time history into account. The weighting function W is computed according to Zielke's model in the efficiently modified version proposed by Kagawa [11,12]. The coefficient δ is equal to 1 for laminar flow. In the case of turbulent flow, δ was estimated as the ratio of turbulent to laminar stationary friction coefficients, the former evaluated at the actual Reynolds number and the latter extrapolated to this by the Moody diagram.

The conservation equations of only the mass and momentum are generally sufficient to mathematically model the 1D flow of a compressible pure liquid provided that either an isothermal flow is assumed or the thermodynamic evolution of the fluid is specified. In such cases, because the temperature is either constant or linked to the fluid density, or pressure, by the process equation, the additional required state equation reduces to $p=p(\rho)$.

In order to take account of the thermal effects due to the liquid-fuel compressibility, which can play a significant role in high-pressure injection-system simulation, the energy equation was in-

troduced in Refs. [13] and [14]. The total (thermal and mechanical) energy conservation equation can be written in the following divergence form:

$$\frac{\partial(\rho h_0 - p)}{\partial t} + \frac{\partial(\rho h_0 u)}{\partial x} = \rho(\dot{q} + \dot{l}_w) - \frac{4\tau_w}{d}u \tag{4}$$

h_0 is the total (or stagnation) enthalpy per unit mass of the fluid system, i.e., $h_0 = h + u^2/2$, $\dot{q}$ is the heat transfer rate per unit mass from the pipe boundaries to the system, and $\dot{l}_w$ is the viscous power dissipation per unit mass within the system. By combining Eq. (4) with the continuity equation and with the following conservation equation of the mechanical energy (that is obtained multiplying each term of the momentum-balance equation by u):

$$\frac{1}{2}\rho\left(\frac{\partial u^2}{\partial t} + u\frac{\partial u^2}{\partial x}\right) = -u\left(\frac{\partial p}{\partial x} + \frac{4\tau_w}{d}\right) \tag{5}$$

one derives the so-called "heat equation" from Eq. (4),

$$\frac{dh}{dt} - \frac{1}{\rho}\frac{dp}{dt} = \dot{q} + \dot{l}_w \tag{6}$$

By introducing the entropy, Eq. (6) gives rise to the following thermodynamic relation among the fluid state variables in any elemental process:

$$Tds = dh - \frac{dp}{\rho} \tag{7}$$

where T is the local temperature and s is the entropy per unit mass of the system. To take the heat exchanges with the walls and the effects of viscous power dissipation into account, a polytropiclike thermodynamic evolution was considered. In this case, Eq. (7) yields the following thermodynamic relation among the fluid state variables:

$$dh - \frac{dp}{\rho} = cdT \tag{8}$$

where c is the constant specific heat of the polytropic evolution.

For a pure liquid, the enthalpy fundamental equation in differential form can be easily verified to be [13]

$$dh = c_p dT + (1 - \beta T)\frac{dp}{\rho} \tag{9}$$

Thus, from Eqs. (8) and (9), keeping $a_T = \sqrt{E_T/\rho}$ in mind, the following adimensional equation is obtained linking pressure and temperature variations:

$$\frac{dp}{E_T} = \frac{c_p - c}{\beta a_T^2}\frac{dT}{T} \tag{10}$$

Equation (10) was used to close the pipe-flow model, i.e., Eq. (1), together with the state equation of the liquid fluid. This latter was written in the following differential form:

$$\frac{d\rho}{\rho} = \frac{dp}{E_T} - \beta dT \tag{11}$$

where

$$\beta = \frac{1}{v}\left(\frac{\partial v}{\partial T}\right)_p = -\frac{1}{\rho}\left(\frac{\partial \rho}{\partial T}\right)_p \tag{12}$$

is the *volumetric coefficient of thermal expansion* or the *thermal expansivity*, and

$$E_T = -v\left(\frac{\partial p}{\partial v}\right)_T = \rho\left(\frac{\partial p}{\partial \rho}\right)_T \tag{13}$$

is the *isothermal bulk modulus of elasticity* of the fluid. The test-oil ISO 4113 physical properties (namely, bulk modulus of elasticity, speed of sound, thermal expansivity, kinematic viscosity, specific heat at constant pressure and ratio between specific heats at constant pressure and at constant volume), were modeled by analytical functions of pressure and temperature. These were derived from the interpolation of accurately determined experimental data up to 1500 bars. Nevertheless, their results at higher pressure, namely, up to 2000 bars, showed very good agreement with the experimental data behavior at such high pressures [13,14]. This allows one to be confident of the model reliability at pressures up to 2000 bars and over.

Since two independent relations exist, namely, Eqs. (10) and (11), that link pressure, temperature, and density, the system is monovariant, i.e., only one intensive thermodynamic property is needed to describe the internal state of the fluid. Therefore, in order to obtain the expression of the pressure wave propagation speed for the considered polytropic evolution, one can calculate the pressure gradient in Eq. (1) as follows:

$$\frac{\partial p}{\partial x} = \frac{dp}{d\rho}\frac{\partial \rho}{\partial x} \tag{14}$$

and rewrite Eq. (1) in the form

$$\frac{\partial \mathbf{w}}{\partial t} + \mathbf{A}\frac{\partial \mathbf{w}}{\partial x} = \mathbf{H} \tag{15}$$

where

$$\mathbf{A} = \begin{bmatrix} 0 & 1 \\ \dfrac{dp}{d\rho} - u^2 & 2u \end{bmatrix} \tag{16}$$

is the Jacobian matrix of the partial differential equation system. Hence, the values of the pressure wave propagation speed are provided by the following eigenvalues of the matrix $\mathbf{A}$:

$$\lambda_{1,2} = u \pm \sqrt{\frac{dp}{d\rho}} \tag{17}$$

so that the sound speed is given by

$$a = \sqrt{\frac{dp}{d\rho}} \tag{18}$$

The pressure derivative in Eq. (18) is calculated for the considered polytropic evolution. Introducing Eqs. (10) and (11) into Eq. (18), with a few analytical steps (as shown in the Appendix), one obtains

$$a = \sqrt{\frac{c - c_p}{c - c_v}}a_T \tag{19}$$

Therefore, in the developed numerical model, the pressure waves propagate along the pipes with the velocities given by Eq. (17) in which the sound speed is computed according to Eq. (19). The value of the specific heat c was experimentally derived from pressure wave propagation measurements in an ad hoc rail-injector pressure pipe using two piezoresistive transducers with a natural frequency of above 40 kHz, when installed through clamp adapters. These were located at a known distance δl from each other, long enough (more than 1 m) so as to make virtually negligible the error in the propagation speed evaluation. Figure 3 reports the pressure time history recorded by the two transducers, one located close to the injector inlet (Transducer A) and the other close to the rail connector (Transducer B). In the initial phase, the wave propagation phenomena induced by the electroinjector travel only from the injector toward the rail with velocity equal to $\lambda = u - a$. The pressure Pattern B shows a delay with respect to that registered by Transducer A. In particular, as soon as the pressure in the rail-injector pipe starts to decrease because of the rarefaction wave induced by the pilot-valve opening, the fluid velocity u is yet very low so that there is no lack of accuracy in setting $|\lambda| \approx a$. Therefore, by measuring the time interval δt in Fig. 3, it is possible to work the sound speed out as $a = \delta l/\delta t$. Since the oil mean pressure and temperature in the pipe portion between the

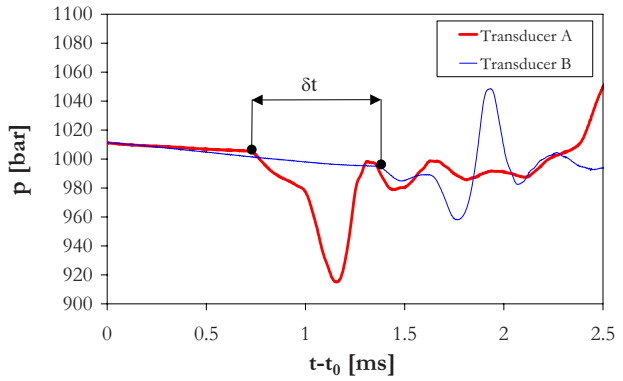

Fig. 3 Pressure wave speed evaluation scheme

transducers are known (the piezoresistive transducers also record the fluid temperature), the isothermal sound speed a_T, the specific heat at constant pressure c_p, and volume c_v can be calculated [14]. Hence, one can determine the polytropic specific heat c from Eq. (19). At all analyzed conditions, a value of c corresponding to a polytropic coefficient

$$m = \frac{c - c_p}{c - c_v} \tag{20}$$

between $m=1$ (i.e., isothermal) and $m=c_p/c_v$ (isentropic) was shown to provide good consistency with experimental data.

Chamber Thermodynamic Equations. With reference to any chamber j in the mathematical model, the mass conservation equation writes

$$\dot{m}_{\text{in},j} - \dot{m}_{\text{out},j} = \frac{d\rho_j}{dt} V_j + \rho_j \frac{dV_j}{dt} \tag{21}$$

where $\dot{m}_{\text{in},j}$ and $\dot{m}_{\text{out},j}$ are the mass flow rates coming into and going out of the chamber j, respectively; V_j is the chamber volume and ρ_j is the density of the fluid in the chamber. If the chamber j is connected to a pipe, the flow rate at the interface is worked out by solving the pipe model partial differential equations (PDE) and then it is applied to the chamber as a boundary condition, in agreement with the characteristic approach. When a restriction presenting a discharge area A is located between the two chambers j and $j+1$, the volumetric flow rate Q through the discharge area can be expressed by

$$Q = \frac{\Delta p}{|\Delta p|} \mu A \sqrt{\frac{2}{\bar{\rho}} |\Delta p|} \tag{22}$$

where $\Delta p = p_j - p_{j+1}$ and $\bar{\rho}$ is a mean density evaluated along an isenthalpic evolution from p_j to p_{j+1}. Because the diesel-oil Joule–Thompson coefficient is sensibly different from zero, the temperature increase through the restriction was evaluated by Eq. (9) taking $dh=0$. Unsteady discharge coefficients were used for the needle-seat-passage and for nozzle holes, according to the procedure in Refs. [15] and [16]. For other restrictions, μ was evaluated taking the effects of the flow Reynolds number into account, instead of considering the simple case of constant μ [17], by the following expression:

$$\mu = \mu_{\max} \tanh\left(\frac{\text{Re}}{\text{Re}_{\text{cr}}}\right) \tag{23}$$

where Re is the Reynolds number of the flow at the discharge section A of the restrictor, Re_{cr} is the critical Reynolds number, and $\mu_{\max}$ is the discharge coefficient value for fully developed turbulent flow. The hyperbolic-tangent function modulates the value of μ so that for $\text{Re} \gg \text{Re}_{\text{cr}}$ the discharge coefficient is virtually constant, whereas for $\text{Re} \ll \text{Re}_{\text{cr}}$, it is almost linear with Re,

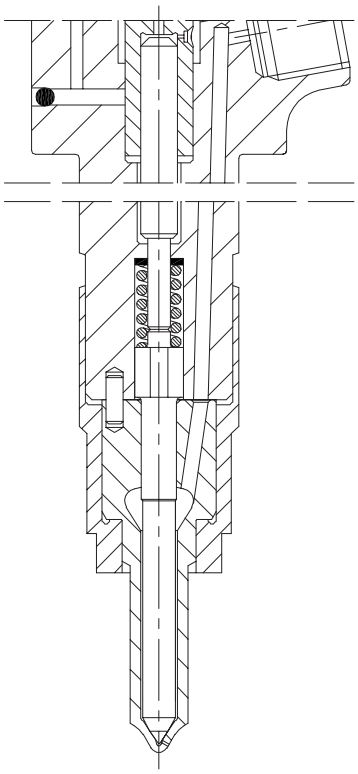

Fig. 4 Control plunger and nozzle

leading to a linear dependence of the volumetric flow rate on the pressure drop across the restrictor, as actually is for pure laminar flows. Values of Re_{cr} range from 1000, for simple geometries of the orifice, to 150 for complex restrictor designs. The value of $\mu_{\max}$ is dependent on the geometric features of the orifice and also on the fluid properties in the vena contracta, i.e., more specifically, including the possible presence of vaporous cavitation phenomena. The cavitation effect in the discharge flow was taken into account modifying the value of $\mu_{\max}$ following the procedure developed in Ref. [18].

Because the fluid velocity inside the chambers is taken to be virtually nil, the momentum equation can be disregarded, so that, for completing the chamber model, only the energy equation and the fluid state equation have to be added to the continuity equation, that is, to Eq. (21).

Following the Eulerian approach, the total energy equation can be written in the form

$$c_{\text{ch}} \frac{dT_j}{dt} - p_j \frac{dV_j}{dt} = \frac{d}{dt}(\rho_j V_j e_j) + \dot{m}_{\text{out},j} h_j - \dot{m}_{\text{in},j} h_{0_{\text{in},j}} \tag{24}$$

where p_j, T_j, e_j, and h_j are the mean pressure, temperature, internal energy, and enthalpy per unit mass in the chamber j, respectively, and $h_{0_{\text{in},j}}$ is the total specific enthalpy at the chamber inlet. The heat exchange with the walls, including the effect of the viscous power dissipation, is taken into account through the specific heat c_{ch}, which is a model fitting parameter [14].

Mechanical Model

Figure 4 shows an enlargement of the main electroinjector mechanical system. The needle valve and the control piston were modeled as two degree of freedom mechanical systems whose behavior is described by two independent Newton's dynamic equilibrium equations, including hydraulic, mechanical, as well as electromagnetic forces.

With reference to the schematic reported in Fig. 5, the mass-spring-damper ordinary differential equations referring either to

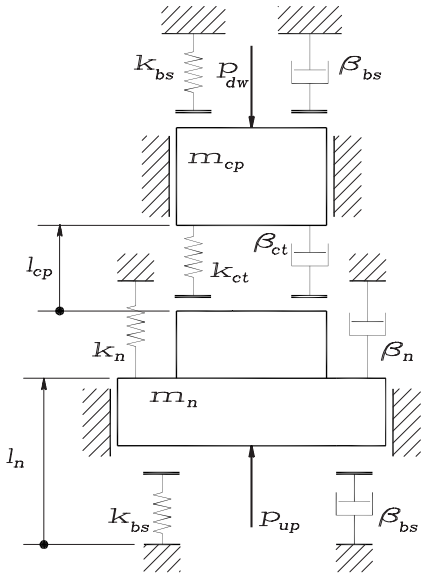

Fig. 5 Second order dynamic model for control plunger and needle

the whole system of the control plunger and needle or only to the control plunger are, respectively, written as follows:

$$(m_n + m_{\mathrm{cp}})\frac{d^2 l_n}{dt^2} + (\bar{\beta}_n + \bar{\beta}_{\mathrm{cp}} - \delta\beta_{\mathrm{ct}})\frac{dl_n}{dt} + (\bar{k}_n + \bar{k}_{\mathrm{cp}} - \delta k_{\mathrm{ct}})l_n + m_{\mathrm{cp}}\frac{d^2 l_{\mathrm{cp}}}{dt^2} + (\bar{\beta}_{\mathrm{cp}} - \delta\beta_{\mathrm{ct}})\frac{dl_{\mathrm{cp}}}{dt} + (\bar{k}_{\mathrm{cp}} - \delta k_{\mathrm{ct}})l_{\mathrm{cp}} + \bar{F}_{0_n} + \bar{F}_{0_{\mathrm{cp}}} = \sum_k p_k S_k \tag{25}$$

$$m_{\mathrm{cp}}\left(\frac{d^2 l_n}{dt^2} + \frac{d^2 l_{\mathrm{cp}}}{dt^2}\right) + (\bar{\beta}_{\mathrm{cp}} - \delta\beta_{\mathrm{ct}})\frac{dl_n}{dt} + \bar{\beta}_{\mathrm{cp}}\frac{dl_{\mathrm{cp}}}{dt} + (\bar{k}_{\mathrm{cp}} - \delta k_{\mathrm{ct}})l_n + \bar{k}_{\mathrm{cp}} l_{\mathrm{cp}} + \bar{F}_{0_{\mathrm{cp}}} = \sum_k p_k S_k \tag{26}$$

where

$$l_n < 0, \quad \bar{k}_n = k_n + k_{\mathrm{bs}}, \quad \bar{\beta}_n = \beta_n + \beta_{\mathrm{bs}}, \quad \bar{F}_{0_n} = F_{0_n}$$

$$l_n \geq 0, \quad \bar{k}_n = k_n, \quad \bar{\beta}_n = \beta_n, \quad \bar{F}_{0_n} = F_{0_n}$$

$$l_{\mathrm{tot}} < l_{\max}, \quad \bar{k}_{\mathrm{cp}} = \delta k_{\mathrm{ct}}, \quad \bar{\beta}_{\mathrm{cp}} = \delta\beta_{\mathrm{ct}}, \quad \bar{F}_{0_{\mathrm{cp}}} = 0$$

$$l_{\mathrm{tot}} \geq l_{\max}, \quad \bar{k}_{\mathrm{cp}} = \delta k_{\mathrm{ct}} + k_{\mathrm{bs}}, \quad \bar{\beta}_{\mathrm{cp}} = \delta\beta_{\mathrm{ct}} + \beta_{\mathrm{bs}}, \quad \bar{F}_{0_{\mathrm{cp}}} = -k_{\mathrm{bs}} l$$

with

$$\beta_n = 2\zeta_n\sqrt{k_n m_n}, \quad \delta = \frac{1 - \mathrm{sign}(l_{\mathrm{cp}})}{2}$$

$l_{\max}$ and l_{tot} being, respectively, the maximum allowed stroke, that is, a constant value, and the sum of l_n and l_{cp}. The stiffness k_{ct} and the damping β_{ct} were introduced to model the force that the needle and the control piston apply to each other when they are in contact.

The pilot valve (Fig. 6) is made up of two mobile elements, namely, the pin and the anchor. When the solenoid is excited by the current, the anchor is attracted toward the magnet drawing the pin, which is integral with the anchor during the lifting. However, as soon as the pin element reaches its stroke-limiter seat, the anchor is allowed to swing with respect to the pin, in order to damp the counterstroke of the pin on the basement and thus avoid oscillations of such an element, which, due to the very low pin lift, could produce the closure of the bleed orifice. Both pin and anchor elements were treated as harmonic oscillators according to the schematic of Fig. 7. Newton's equations for the whole device (pin and anchor) and for the anchor only are, respectively, expressed by

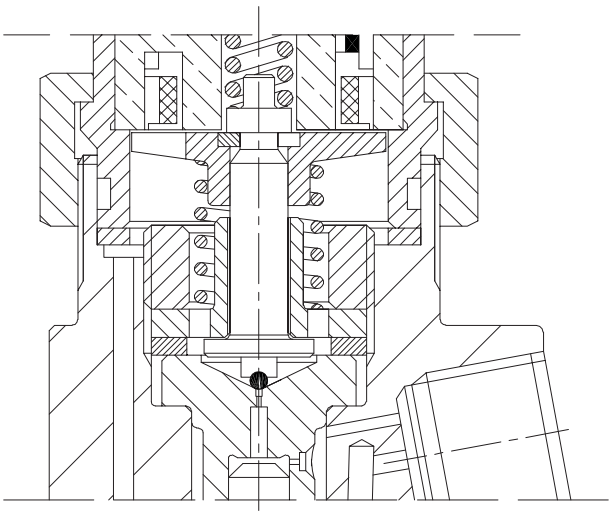

Fig. 6 Pilot valve

$$(m_a + m_p)\frac{d^2 l_p}{dt^2} + (\beta_a + \bar{\beta}_p)\frac{dl_p}{dt} + (k_a + \bar{k}_p)l_p - m_a\frac{d^2 l_a}{dt^2} - (\bar{\beta}_a - \delta\beta_{\mathrm{ct}})\frac{dl_a}{dt} - (\bar{k}_a - \delta k_{\mathrm{ct}})l_a + \bar{F}_{0_p} - \bar{F}_{0_a} = \sum_k p_k S_k + F_E \tag{27}$$

and

$$m_a\left(\frac{d^2 l_a}{dt^2} - \frac{d^2 l_p}{dt^2}\right) + \bar{\beta}_a\frac{dl_a}{dt} - \beta_a\frac{dl_p}{dt} + \bar{k}_a l_a - k_a l_p + \bar{F}_{0_a} = \sum_k p_k S_k - F_E \tag{28}$$

where

$$l_a < 0, \quad \bar{k}_a = k_a + k_{\mathrm{ct}}, \quad \bar{\beta}_a = \beta_a + \beta_{\mathrm{ct}}, \quad \bar{F}_{0_a} = F_{0_a}$$

$$l_a \geq 0, \quad \bar{k}_a = k_a, \quad \bar{\beta}_a = \beta_a, \quad \bar{F}_{0_a} = F_{0_a}$$

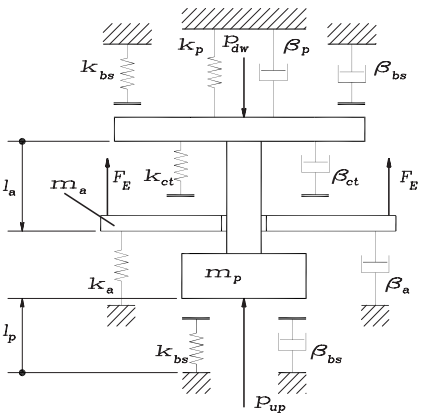

Fig. 7 Second order dynamic model for pilot valve

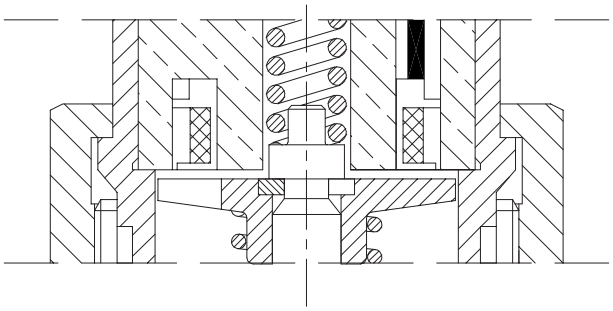

Fig. 8 Pilot-valve anchor and solenoid

$$l_p < 0, \quad \bar{k}_p = k_p + k_{\text{bs}}, \quad \bar{\beta}_p = \beta_p + \beta_{\text{bs}}, \quad \bar{F}_{0_p} = F_{0_p}$$

$$l_p < l_{p_{\max}}, \quad \bar{k}_p = k_p, \quad \bar{\beta}_p = \beta_p, \quad \bar{F}_{0_p} = F_{0_p}$$

$$l_p \geq l_{p_{\max}}, \quad \bar{k}_p = k_p + k_{\text{bs}}, \quad \bar{\beta}_p = \beta_p + \beta_{\text{bs}}, \quad \bar{F}_{0_p} = F_{0_p} - k_{\text{bs}} l_{p_{\max}}$$

with

$$\beta_a = 2\zeta_a \sqrt{k_a m_a}, \quad \delta = \frac{1 - \text{sign}(l_a)}{2}$$

$l_{p\max}$ being the maximum pin lift. The quantity F_E represents the electromagnetic attractive force generated by the electric current flowing through the solenoid. All the masses, the stiffness, and the maximum lifts relative to each of the two degree of freedom systems were experimentally determined.

Electromagnetic Circuit Model

A solenoid circuit model of practical implementation was set up to provide the electromagnetic force acted on the anchor. The electromechanical behavior of the solenoid (Fig. 8) can be modeled by a lumped parameter approach as follows:

$$V - N\frac{d\Phi}{dt} - RI = 0 \tag{29}$$

where R is the solenoid electrical resistance, I is the electrical current through the solenoid, V is the voltage applied to it, and N and Φ are the solenoid turns and the magnetic flux through each turn, respectively. Applying the energy equation to the anchor-coil system, one obtains

$$VIdt = RI^2 dt + F_E dx + dU_m \tag{30}$$

where VI is the electric power to the system; $F_E dx$ is the mechanical work done by the electromagnetic force on the anchor, being $dx = dl_p - dl_a$; and dU_m is the change of the system magnetic energy.

Combining Eqs. (29) and (30) with the following expression of the magnetic energy U_m stored in the system:

$$U_m = \frac{1}{2} N\Phi I \tag{31}$$

one has

$$F_E dx = \frac{1}{2}(NId\Phi - N\Phi dI) \tag{32}$$

Hopkinsow's law for the equivalent magnetic circuit of the pilot-valve control system is expressed by the following equation:

$$NI = \Re\Phi \tag{33}$$

where $\Re = \Re(x)$ is the total reluctance of the system, linearly varying with the coordinate x as is above defined in differential form. Differentiating Eq. (33) and multiplying both sides of the resultant

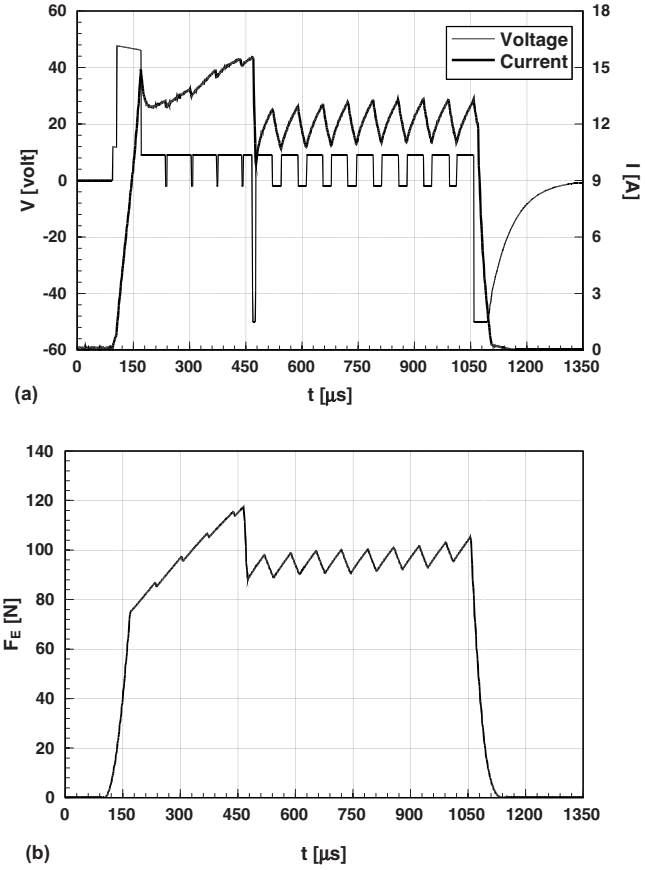

Fig. 9 Electromagnetic model: (*a*) voltage and current at solenoid and (*b*) electromagnetic force on pilot valve

equation by Φ, from the application again of Hopkinsow's law, the following relation comes out:

$$\Phi^2 d\Re = \Phi N dI - NId\Phi \tag{34}$$

Equations (32) and (34) yield the following expression for the magnetic force acting on the anchor:

$$F_E = -\frac{1}{2}\Phi^2 \frac{d\Re}{dx} \tag{35}$$

The only parts of the circuit reluctance, which are variable with x, are the reluctances due to the gap between the magnet and the anchor (Fig. 8), so that the derivative of $\Re$ with respect to x reduces to

$$\frac{d\Re}{dx} = -\frac{1}{\mu_0}\left(\frac{1}{\Sigma_1} + \frac{1}{\Sigma_2}\right) \tag{36}$$

being μ_0 the magnetic constant and Σ_1, Σ_2 the cross sections of the magnetic circuit. These sections are delimited: on the one side, by the internal diameters of the recirculation passage and of the solenoid, and on the other side, by the external diameters of the solenoid and of the anchor.

In order to calculate the electromagnetic force from Eq. (35), the magnetic flux of the circuit has to be determined. Recording both the current and voltage time histories (Fig. 9(*a*)), the magnetic flux can be derived as a function of time from Eq. (29) by

$$\Phi(t) = \frac{1}{N}\int_0^t [V(t) - RI(t)]dt \tag{37}$$

where the instant $t=0$ corresponds to the solenoid excitation initial time. The resistance R and the number N of the solenoid turns were experimentally determined. Equations (35)–(37) were used

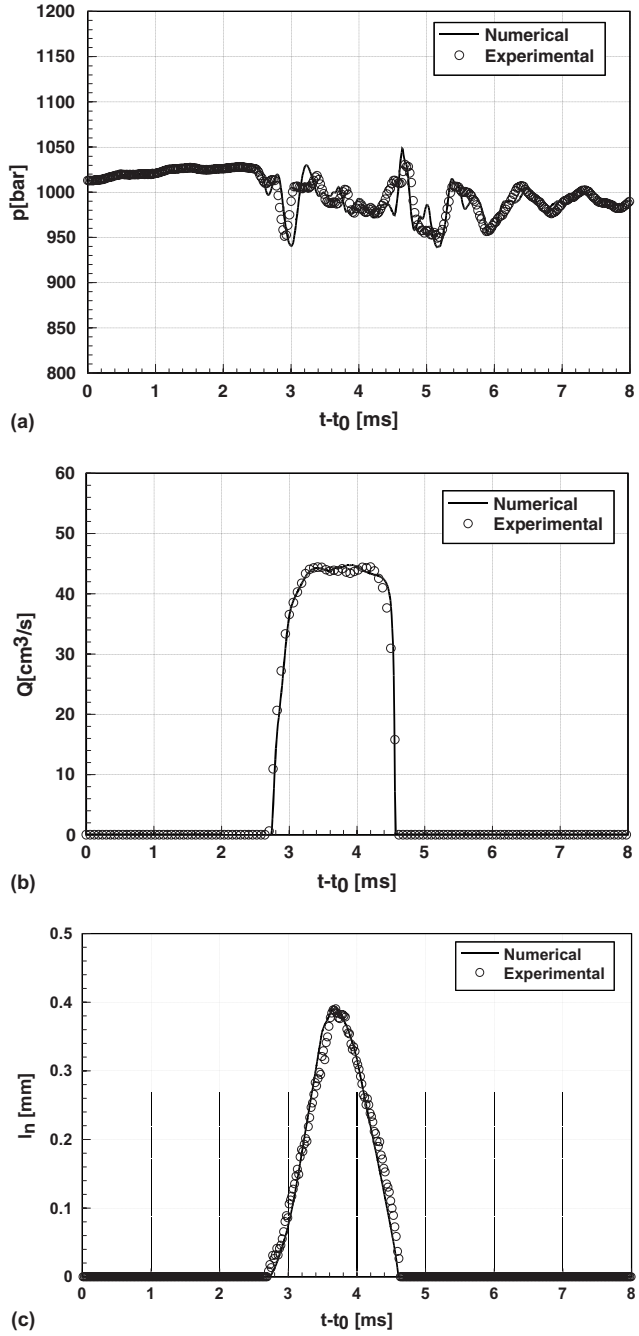

Fig. 10 Single injection (p_{rail}=1000 bars, ET=1085 μs): (*a*) pipe pressure at injector inlet, (*b*) injection flow rate, and (*c*) needle lift

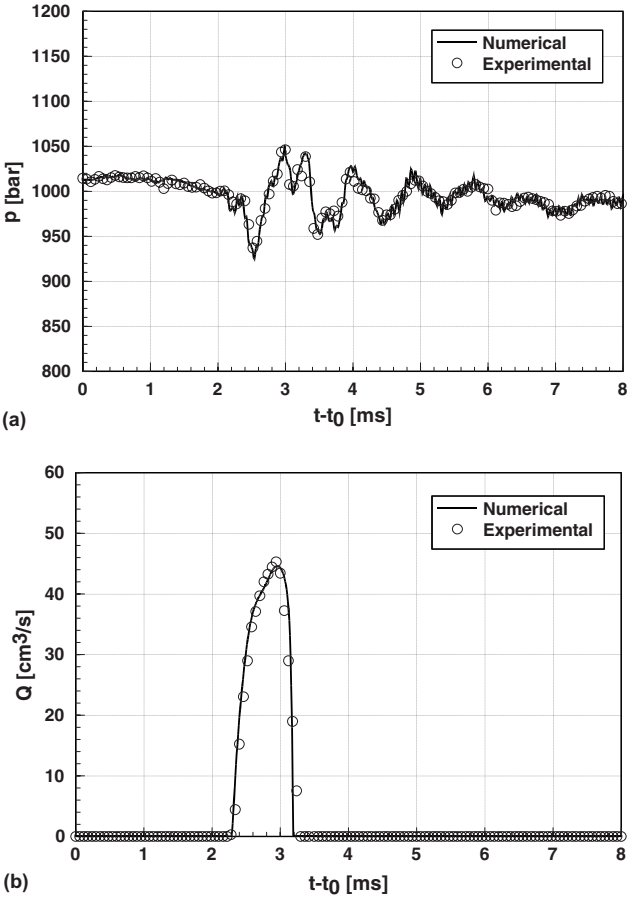

Fig. 11 Single injection (p_{rail}=1000 bars, ET=600 μs): (*a*) pipe pressure at injector inlet and (*b*) injection flow rate

in the numerical code for evaluating the time distribution of the force F_E acting on the control-system anchor (Fig. 9(*b*)). It is worth pointing out that Eqs. (35) and (37) are of general application, whereas Eq. (36) depends on the geometry of the magnetic circuit and thus on the valve configuration. The time pattern of the force in Fig. 9(*b*) is quite similar to that of the solenoid current in Fig. 9(*a*). Therefore, in order to apply a different force profile to the anchor, one should design the temporal pattern of the current to the solenoid so as to make it similar to the desired force time distribution.

Numerical Algorithm

The mass and momentum conservation equations for the pipe flow were discretized by the high-resolution finite-volume scheme SLIC [19] with a *minmod* slope limiter. The numerical scheme in its conservation form writes

$$\mathbf{w}_j^{n+1} = \mathbf{w}_j^n - \frac{\Delta t}{\Delta x}\left(\mathbf{\Phi}_{j+1/2}^{n+1/2} - \mathbf{\Phi}_{j-1/2}^{n+1/2}\right) + \Delta t \mathbf{H}_j^{n+1/2} \tag{38}$$

where the subscript j designates the spatial grid locations, the superscript n designates the time level, and $\mathbf{\Phi}$ is the numerical flux vector. A slope-limited linear spatial reconstruction of the conservative variables $\mathbf{w}$ is performed at time level n, and then a time upgrading step is carried out to obtain the values of the same variables at time $(n+1/2)$, i.e., $\mathbf{w}^{n+1/2}$, which are required by the SLIC scheme to compute the numerical flux function $\mathbf{\Phi}^{n+1/2}$ in Eq. (38).

For the discretization of the chamber continuity and energy equations, as well as of the dynamics equations for the electroinjector mobile elements, the multistep Adams–Moulton method of the fourth order accuracy [20] was applied.

Results

Figures 10–15 illustrate the CR injection-system performance, showing the comparison between prediction and experimental results for different working conditions of solenoid energizing time (ET) and of nominal rail pressure (p_{rail}), as well as of dwell time (DT) in the case of multiple injections. The engine speed of 2000 rpm, which is an intermediate value in the speed range, was taken for all conditions in the present work. As a matter of fact, a relatively low speed effect on the injector dynamics was experimentally assessed in Ref. [10]. Two distinct nozzle configurations

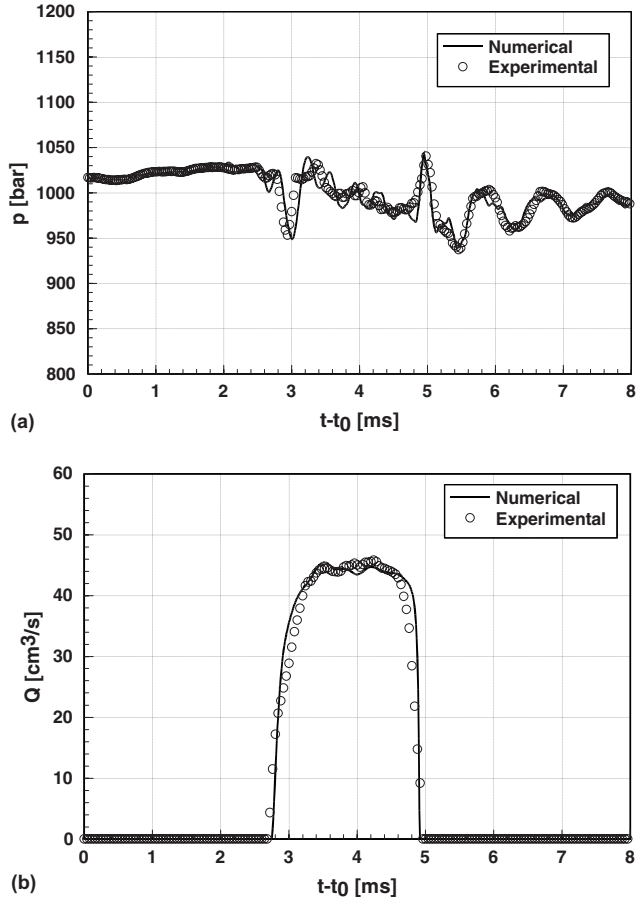

Fig. 12 Single injection (p_{rail}=1000 bars, ET=1300 μs): (*a*) pipe pressure at injector inlet and (*b*) injection flow rate

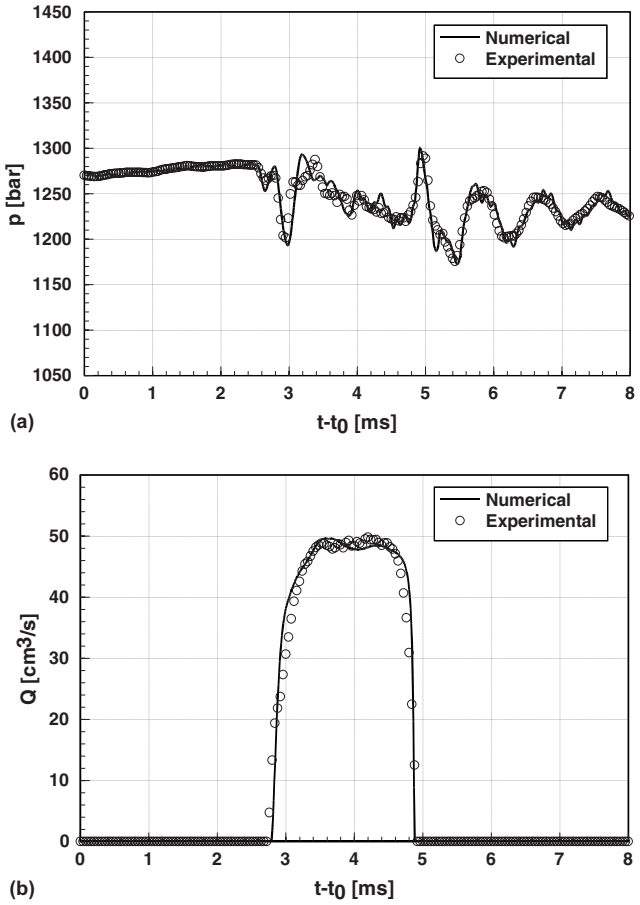

Fig. 13 Single injection (p_{rail}=1250 bars, ET=1300 μs): (*a*) pipe pressure at injector inlet and (*b*) injection flow rate

were analyzed. In particular, Figs. 10–14 report the results for a VCO electroinjector, whereas Fig. 15 refers to a Minisac electroinjector.

The diagrams report the pressure time history (Figs. 10(*a*), 11(*a*), 12(*a*), 13(*a*), 14(*a*), 14(*c*), 15(*a*), and 15(*c*)) at the inlet of the electroinjector, the injection flow rate (Figs. 10(*b*), 11(*b*), 12(*b*), 13(*b*), 14(*b*), 14(*d*), 15(*b*), and 15(*d*)), and the needle lift (Fig. 10(*c*)). Figures 10–13 refer to a single injection and Figs. 14 and 15 refer to multiple injections. For convenience, the relative time $t-t_0$, with respect to a reference instant t_0, is taken as abscissa. The theoretical time distributions are reported through solid lines and the experimental results are plotted by circle symbols.

The generally good agreement between the predicted and measured distributions shown by these figures indicates a quite satisfactory accuracy degree of the injection-system mathematical model in capturing the most important features of the flow phenomena.

The primary nonstationary events shown in the figures for a single injection under different operating conditions have the same explanations, although there are differences in intensity and phase, depending on the values of ET and p_{rail}.

In Fig. 10(*a*), the first pressure drop occurring at $t-t_0 \approx 2.6$ ms is a result of the propagation of the depression event arising in the needle-valve control chamber due to the opening of the pilot valve. Then, as the needle starts to lift, the pressure level rises in this chamber as a consequence of its volume reduction. Such a compression is conveyed to the rail by pressure waves traveling toward it. At the same time, the fuel injection that is caused by the needle lift gives rise to a depression in the injector delivery chamber, which propagates toward the rail, too. Due to the difference in path lengths, the compression wave coming from the control chamber precedes the depression wave, so that in Fig. 10(*a*) the pressure pattern, after a drop due to the pilot-valve opening, shows a rise first ($t-t_0 \approx 2.8$ ms) and then a fall again ($t-t_0 \approx 3.0$ ms). Such a peculiarity can also be observed in the other examined situations.

The depression in the delivery chamber draws the fuel from the injector drilled pipe to the nozzle. As the pressure continues to decrease, the flow rate to the delivery chamber grows. When this flow rate exceeds the injected flow rate because of greater drilled pipe section with respect to the restricted nozzle flow area, the pressure in the delivery chamber stops falling and begins to rise, thus approaching the value preceding the injection start. In Fig. 10(*a*), this compression wave at the injector inlet was found to be almost in phase with the other compression wave, arising from the reflection, at the rail, of the depression wave related to the injector opening. Hence, the pressure increase up to $\approx$1030 bars ($t-t_0 \approx 3.3$ ms in Fig. 10(*a*)) has to be ascribed to both effects.

The subsequent peak that is present both in the theoretical and experimental pressures at $t-t_0 \approx 3.7$ ms is due to the pilot-valve closure, after the needle and control pistons have reached their maximum lift. A water hammer takes place in the control chamber, giving rise to this pressure peak that propagates to the rail. When the needle reaches its stroke end for high ET the peak is stronger, due to the reduced control chamber volume.

The water hammer, which arises at the needle closure, that is, around $t-t_0 \approx 4.6$ ms when the flow rate collapses in Fig. 10(*b*), causes the pressure peak shown in Fig. 10(*a*) at $t-t_0 \approx 4.7$ ms. The time delay between the injection end and the appearance of

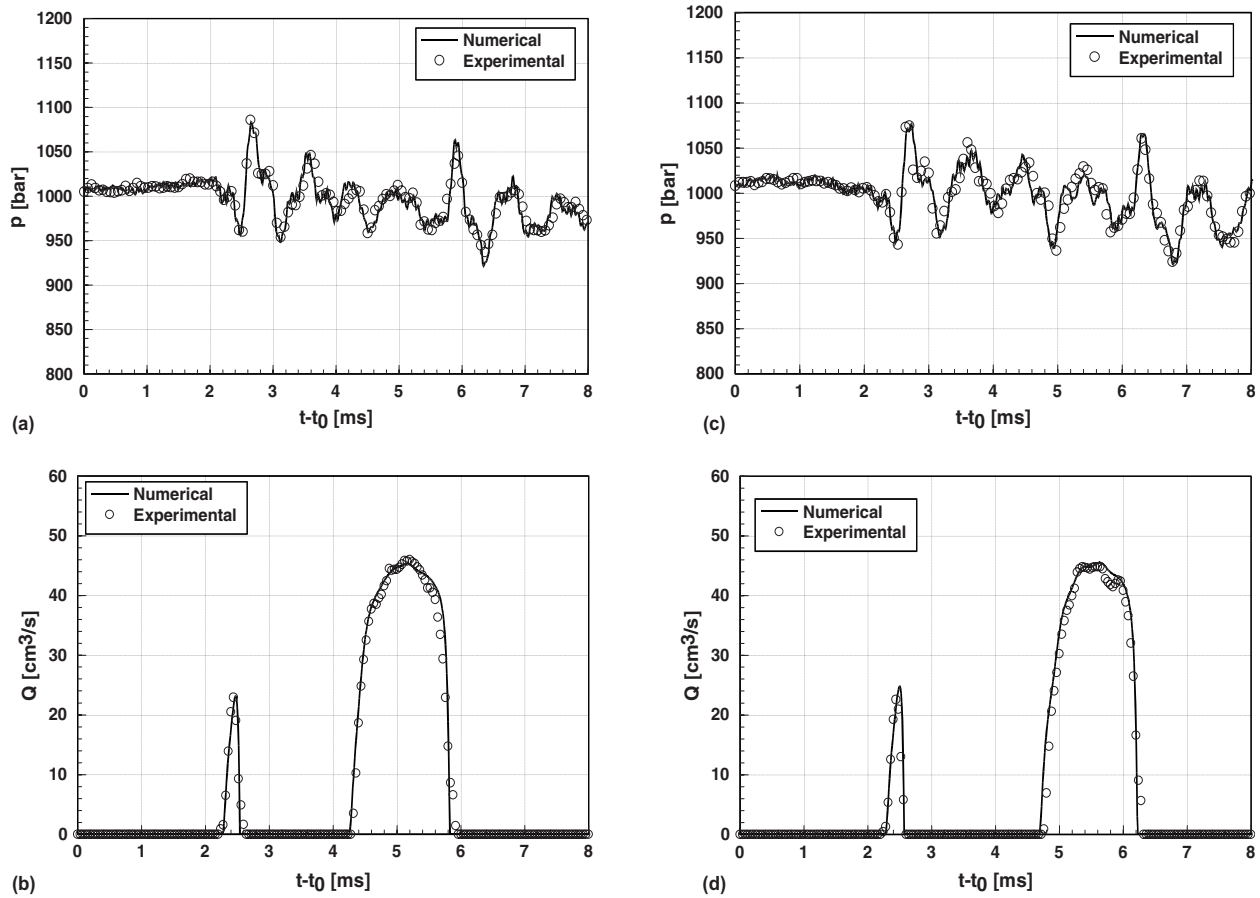

Fig. 14 Pilot and main injections (p_{rail}=1000 bars, ET_{pil}=300 μs, ET_{main}=900 μs): (*a*) pipe pressure at injector inlet (DT =1700 μs), (*b*) injection flow rates (DT=1700 μs), (*c*) pipe pressure at injector inlet (DT=2050 μs), and (*d*) injection flow rates (DT=2050 μs)

this peak depends on the pressure wave propagation velocity. Since the sound speed grows with the pressure, it reduces with the rail pressure increase (Fig. 13).

The water-hammer onset at the injection end produces a regime of pressure waves, which travel inside the closed system and whose kinetic energy is gradually dissipated by friction actions. These pressure waves give rise to fluctuations having a time period that is related to the natural frequencies of the system. The characteristic frequency of these oscillations depends on the geometric features of system components as well as on the fluid mean pressure and temperature. A simple but effective lumped parameter model for evaluating the system characteristic frequency has been developed in Ref. [10], taking the effects of both geometry and working conditions into account.

Figure 10(*b*) reports the flow rate distribution versus time. The temporal extension of the injection phase is higher than the ET value (i.e., 1.5–2 times ET) because in this case the delay of the injector closure with respect to the current drop is much higher than the nozzle opening delay with respect to the current rise.

Figure 10(*c*) validates the needle mass-spring-damper model, which is capable of predicting both the rising and falling needle velocities with a good precision. As can be inferred, for these values of p_{rail} and ET, the needle does not reaches its maximum lift, that is, 0.43 mm for the tested electroinjector. The flow-rate and needle-lift patterns are different because of high-pressure-wave dynamics; in fact, from the maximum needle lift on, the flow rate is kept high by a pressure wave reaching the injector delivery chamber.

Figures 11(*a*) and 11(*b*) report the same variables as those in Figs. 10(*a*) and 10(*b*) for a lower ET (600 μs) and for the rail pressure of 1000 bars. In Fig. 11(*a*), the pressure peak ($t-t_0 \approx 3.0$ ms) after the depression caused by the injection is due to the compression wave coming from the rail, whereas the subsequent peak is caused by the water hammer produced by the needle closure. These two peaks are now closer than in Fig. 10(*a*) because of the shorter ET, which moves the second peak toward the first one. The third peak, which occurs in Fig. 11(*a*) at $t-t_0 \approx 3.6$ ms, has the following explanation: The water hammer due to the needle closure produces a compression wave that propagates through the injector feed pipe. In correspondence with the inlet injector filter, the compression is partially transmitted through the filter and partially reflected as a compression wave toward the delivery chamber. When this latter wave reaches the nozzle tip, the pressure rises there. Thus, being the injector closed, a pressure increase propagates again along the feed pipe toward the rail, producing the above mentioned slight peak in Fig. 11(*a*), at $t-t_0 \approx 3.6$ ms.

In Fig. 11(*b*), the flow rate peak is in phase with the pressure peak present at $t-t_0 \approx 3.0$ ms in Fig. 11(*a*). The compression wave coming from the rail arrives at the delivery chamber when the needle is going to start its closure phase and thus maintains the flow rate still rising, which causes a dissymmetry in the shape of the diagram with respect to its maximum in Fig. 11(*b*).

The CR system performance close to full load conditions (ET =1300 μs) were investigated for a rail pressure of 1000 bars and 1250 bars, respectively (Figs. 12 and 13). In Figs. 12(*a*) and 13(*a*), the water hammer caused by the injector closure is significantly late ($t-t_0 \approx 5.0$ ms) with respect to the injection-induced depression, in comparison to the previous cases, because of the larger ET. The free pressure oscillations are more intense than in

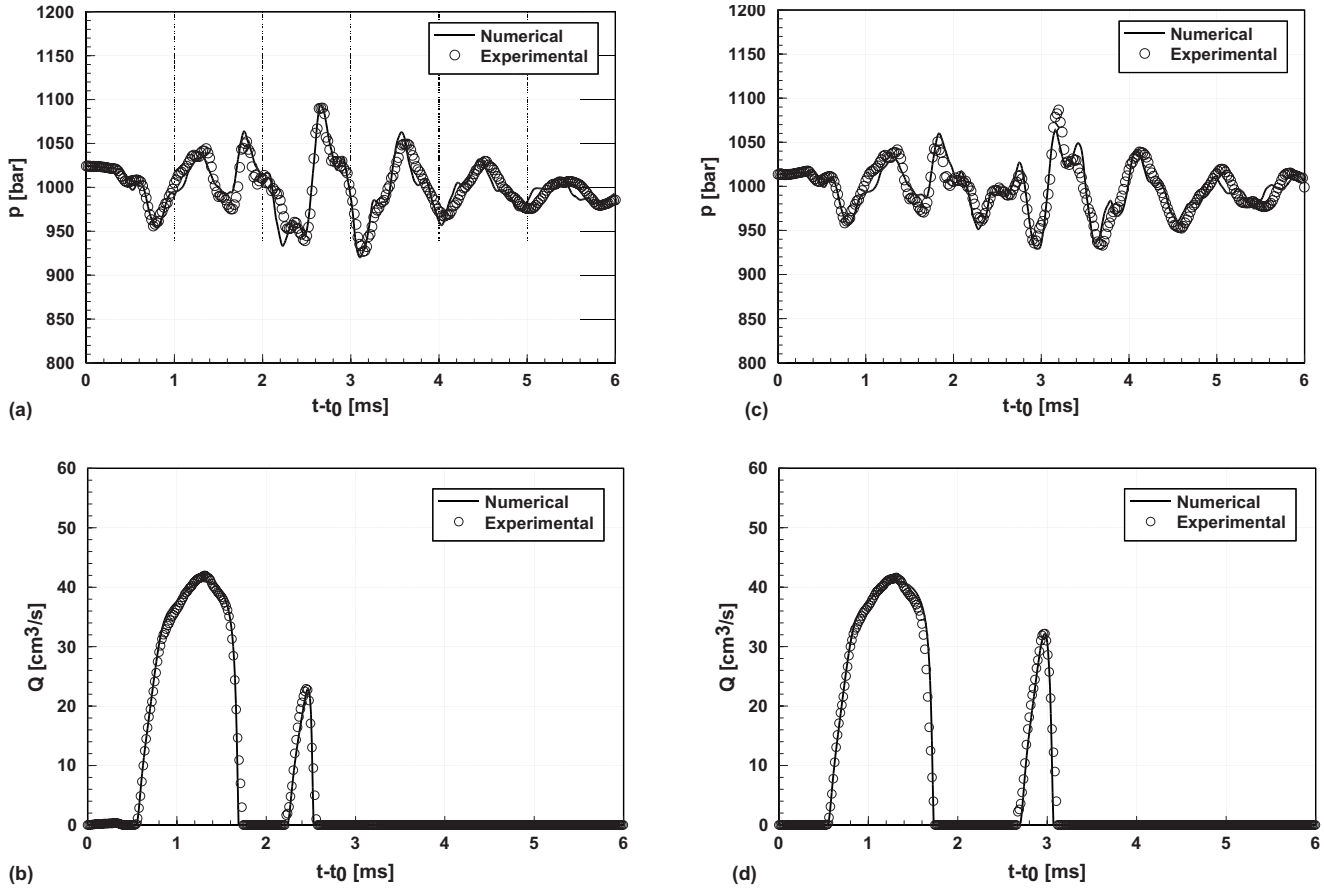

Fig. 15 Main and post injections (p_{rail}=1000 bars, ET_{main}=800 μs, ET_{post}=400 μs): (*a*) pipe pressure at injector inlet (DT =850 μs), (*b*) injection flow rates (DT=850 μs), (*c*) pipe pressure at injector inlet (DT=1350 μs), and (*d*) injection flow rates (DT =1350 μs)

Fig. 10(*a*) due to the larger extension of the injection event and to the rail pressure increase (Fig. 13(*a*)). It is worth pointing out that, as in the above test cases, the adopted model to take viscous power dissipation into account, including frequency dependent friction, proved to be capable of correctly predicting the attenuation of the measured pressure fluctuations. More specifically, by neglecting the nonstationary term in the expression of the wall shear stress (Eq. (3)), an excessively poor damping of the pressure fluctuations in the system was obtained, because of the high frequency dynamics, which is a distinctive feature of CR systems. The flow rate distributions in Figs. 12(*b*) and 13(*b*), exhibiting a roughly trapezoidal shape, present some oscillations in the region of their highest values because of the pressure waves traveling throughout the electroinjector feeding pipe. It can be inferred from these figures that the main effect of the rail pressure growth is a rise in the injected volume. As previously stated, the model accuracy at much higher p_{rail} values is assured by the ample pressure validation range of the oil physical property analytical expressions employed.

Figures 14 and 15 refer to multiple injection shots. In particular, the diagrams of Fig. 14 represent two situations where a pilot and a main injection are effectuated with different dwell times (DT =1700 μs and DT=2050 μs, respectively) and constant energizing times (ET_{pilot}=300 μs, ET_{main}=900 μs) at same nominal rail pressure (p_{rail}=1000 bars). In Figs. 14(*a*) and 14(*c*), the pressure peak following the depression induced by the pilot injection is sensibly higher than the analogous peaks shown in the former pressure plots relative to single injection events. In fact, the height of this peak is around 80 bars over the initial pressure level, whereas in the previous pictures, it was always less than 50 bars. A resonance phenomenon due to the synergic effects of both the reflection-induced compression wave traveling from the rail and the water-hammer compression wave coming from the injection chamber is responsible for such a particularly large peak amplitude, which produces very intense oscillations, in spite of the small ET_{pilot} value. These can cause significant variations in the fuel-injected quantity during the main injection, depending on the dwell time, and even hydraulic instabilities at particularly low dwell times.

Figures 14(*b*) and 14(*d*) show sensible differences in the injected fuel volume during the main pulse ($V \approx 59.5$ mm^3, for DT=1700 μs and $V \approx 55$ mm^3, for DT=2050 μs, $\Delta V \approx 4.5$ mm^3). Such differences are related to the fact that the dwell times were selected so that the main injections start when a maximum and a minimum pressure peak are present in the delivery chamber, respectively [10].

In general, resonance phenomena can occur when injections with small energizing time, such as pilot injections, are carried out because these tend to anticipate the injector-closure water hammer with respect to injections with large energizing times. The synergic phasing of the water-hammer compression effect with the compression wave coming from the rail, in the injector delivery chamber, can take place in commercial CR layouts. For these the compression wave traveling through the drilled injector passage from the rail takes 400–700 μs to go back and forth along its path, the exact value depending on injector inlet pipe length and diameter.

Figure 15 refers to a Minisac nozzle electroinjector. A main and a postinjection were performed at the same working conditions of nominal rail pressure (p_{rail}=1000 bars) and energizing times

(ET_{main}=800 μs, ET_{post}=400 μs), but at two different dwell times (namely, DT=850 μs in Figs. 15(*a*) and 15(*b*) and DT=1350 μs in Figs. 15(*c*) and 15(*d*)). The maximum flow rate values during the main injection are sensibly lower than those of Figs. 10(*b*), 12(*b*), 14(*b*), and 14(*d*) although the nominal rail pressure level is the same (1000 bars). This is due to the fact that the nozzle configuration has been changed, the Minisac generally injecting a lower fuel amount than the VCO under the same working conditions. All of the previously observed main nonstationary events are still present for the Minisac nozzle, the explanations of them being the same.

As can be inferred, in Figs. 15(*a*) and 15(*c*) the pressure fluctuations induced by the main injection are less intense than those caused by the pilot injection in Figs. 14(*a*) and 14(*c*), owing to the absence of resonance phenomena. This turns out in a reduced difference between the injected fuel volume during the postinjection for distinct dwell times ($V \approx 3.9$ mm^3, for DT=850 μs and $V \approx 7.1$ mm^3, for DT=1350 μs, $\Delta V = 3.2$ mm^3) in comparison to the case of Figs. 14(*b*) and 14(*d*). However, the percentage deviation for the postinjected fuel volume oscillations (Figs. 15(*b*) and 15(*d*)) is much higher (namely, 58%) than the correspondent one (7%) related to the main injected volume fluctuations (Figs. 14(*b*) and 14(*d*)). This fact can be explained by observing that the mean volume of the fuel injected during the postinjection in Figs. 15(*b*) and 15(*d*) is much lower than that injected during the main injection in Figs. 14(*b*) and 14(*d*). Percentage deviations higher than 58% can be obtained if shorter ET_{post} and DT between main and postpulses are adopted.

Since the trend in modern diesel and HCCI engines is to extend the fuel injection to an increasing pulse number with shorter ET and DT [21] for improving combustion efficiency and reducing pollutant emissions at the same time, the issue of disturbances induced by pressure waves on the amount of fuel injected at each shot turns out to be an important challenge in future development of high-pressure injection systems.

Conclusion

An overall mathematical model of a multijet CR injection system was developed, including the thermofluid dynamics of hydraulic components, the mechanics of mobile elements, and the electromagnetics of the solenoid circuit.

Particular care was devoted to the modeling of nonstationary wave propagation phenomena because their accurate prediction is of fundamental importance for the design of the hydraulic-system layout and of new multiple-injection control strategies, aimed at performance optimization. To that end, in addition to the temperature variations caused by the compressibility of the liquid fuel, the balance between viscous power dissipation and heat transfer across the walls was included by introducing a constant polytropic specific heat, which was fitted on the basis of experimental tests. Owing to the presence of high-frequency oscillations caused by the strongly impulsive dynamics that is typical of CR systems, the frequency dependent wall friction had to be introduced for predicting the sensible pressure wave attenuation, according to experimental observations. With reference to the electromagnetic circuit, the practical procedure followed for evaluating the attraction force that the solenoid applied to the pilot valve, using easily obtainable experimental data, gave physically consistent results.

The comparison of predictions and experimental results on a commercial multijet CR system of latest solenoid-type generation showed a generally good agreement for the considered various working conditions of nominal rail pressure, solenoid energizing time, and, in the case of multiple injections, dwell time between two consecutive pulses. This substantiated the quite satisfactory accuracy degree of the injection-system mathematical model in capturing the essential features of flow phenomena.

The thorough analysis of the main dynamic events gave a physical explanation of cause and effect relationships between the pressure wave propagation and performance, highlighting the significant role of the hydraulic-system layout on them. It also stressed the importance of properly modeling the dynamics of the rail for correctly predicting the injected fuel quantities in multiple injections.

Acknowledgment

This research was financially supported by Fiat Research Center, Fiat-GM Powertrain and Mur (Ministry of University and Research) under the COFIN 2004 Program. The invaluable technical assistance of S. Canale, G. Bonetto, F. Guglielmo, and E. Rigon of Fiat Research Center is also gratefully acknowledged.

Nomenclature

- a = speed of sound
- $\mathbf{A}$ = Jacobian matrix
- c = specific heat
- d = pipe diameter
- DT = dwell time
- E = bulk modulus of elasticity, sensor electrical output
- ET = energizing time
- f = friction coefficient
- F = force, spring force
- $\mathbf{F}$ = flux vector
- h = enthalpy per unit mass
- $\mathbf{H}$ = source vector
- k = spring rate
- I = electric current
- l = lift, axial distance between mobile elements
- $\dot{l}_w$ = viscous power dissipation per unit mass
- L = length of pipe and injector-drilled passage
- m = mass
- N = solenoid turn number
- p = pressure, average cross-sectional pressure
- $\dot{q}$ = heat transfer rate per unit mass
- Q = volumetric flow rate
- R = resistance
- $\Re$ = circuit magnetic reluctance
- s = entropy per unit mass
- S = surface area perpendicular to the lift axis
- t = time
- T = temperature
- u = average cross-sectional velocity
- U_m = magnetic energy
- v = specific volume or volume per unit mass
- V = volume, injected volume, voltage
- $\mathbf{w}$ = conservative variable vector
- x = axial coordinate, distance along the pipe axis
- β = thermal expansivity, damping
- Δt = time increment
- Δx = distance increment
- θ = cam angle
- λ = Jacobian matrix eigenvalue
- μ = dynamic viscosity, discharge coefficient, permeability
- ρ = density, average cross-sectional density
- Σ_1, Σ_2 = magnetic-circuit cross sections
- τ_w = wall shear stress
- $\Phi/\mathbf{\Phi}$ = magnetic flux/numerical flux vector
- ζ = damping factor

Subscripts

- 0 = reference value, total enthalpy per unit mass
- a = anchor
- bs = basement
- ch = chamber
- cp = control plunger

cr = critical
ct = contact
dw = downward
E = electromagnetic
n = needle
M = maximum value
p = at constant pressure, pin element
T/v = at constant temperature/volume
up = upward

Appendix: Sound-Speed Formula for a Polytropic Evolution in Liquid Flows

Substituting Eq. (8) into Eq. (9), one obtains

$$cdT = c_p dT - \beta T \frac{dp}{\rho} \tag{A1}$$

Equation (A1) can be rewritten as follows:

$$\frac{dT}{dp} = \frac{\beta T}{\rho(c_p - c)} \tag{A2}$$

Another relation for dT/dp can be achieved by rearranging Eq. (11),

$$\frac{dT}{dp} = \frac{1}{\beta E_T} - \frac{1}{\beta \rho}\frac{d\rho}{dp} \tag{A3}$$

Taking in mind that $a^2 = dp/d\rho$ and $a_T^2 = E_T/\rho$, from Eq. (A3), the following expression can be easily obtained:

$$\frac{dT}{dp} = \frac{1}{\beta\rho}\left(\frac{1}{a_T^2} - \frac{1}{a^2}\right) \tag{A4}$$

By equating Eq. (A4) to Eq. (A2), one obtains

$$\frac{\beta T}{\rho(c_p - c)} = \frac{1}{\beta\rho}\left(\frac{1}{a_T^2} - \frac{1}{a^2}\right) \tag{A5}$$

Equation (A5) can be solved with respect to the ratio of a to a_T leading to

$$\frac{a_T^2}{a^2} = 1 - \frac{a_T^2 \beta^2 T}{c_p - c} = 1 - \frac{E_T \beta^2 T}{\rho(c_p - c)} \tag{A6}$$

The specific heat at constant volume of a substance is defined as

$$c_v = \left(\frac{\partial e}{\partial T}\right)_v \tag{A7}$$

Being $e = h - pv$, from Eqs. (9) and (A7), it follows that

$$c_v = c_p - \frac{\beta T}{\rho}\left(\frac{\partial p}{\partial T}\right)_v \tag{A8}$$

On the other hand, for an isochoric evolution, Eq. (11) reduces to

$$\left(\frac{\partial p}{\partial T}\right)_v = \beta E_T \tag{A9}$$

which, by substitution into Eq. (A8), leads to

$$c_v = c_p - \frac{\beta^2 E_T}{\rho} T \tag{A10}$$

Finally, combining Eq. (A10) with Eq. (A6), one obtains

$$\frac{a_T^2}{a^2} = 1 - \frac{c_p - c_v}{c_p - c} \tag{A11}$$

that is equivalent to

$$a = \sqrt{\frac{c_p - c}{c_v - c}}\, a_T$$

References

[1] Stumpp, G., and Ricco, M., 1996, "Common-Rail: An Attractive Fuel Injection System for Passenger Car DI Engines," SAE Paper No. 960870.
[2] Flaig, U., Polach, W., and Ziegler, G., 1999, "Common Rail System for Passenger Car DI Diesel Engines; Experiences With Application for Series Production Projects," SAE Paper No. 1999-01-0191.
[3] Bianchi, G. M., Pelloni, P., Corcione, F. E., and Luppino, F., 2001, "Numerical Analysis of Passenger Car HSDI Diesel Engine With 2nd Generation of Common-Rail Injection System: The Effect of the Multiple Injections on Emissions," SAE Paper No. 2001-01-1068.
[4] Piepont D. A., Montgomery, D. T., Reitz R. D., and Ziegler, G., 1994, "Reducing Particulate and NO_x Using Multiple Injections and EGR in a D.I. Diesel Engine," SAE Paper No. 940897.
[5] Wickman, D. D., Tanin, K. V., Senecal, P. K., Reitz, R. D., Gebert, K., Barkhimer, R. L., and Beck, N. J., 2000, "Methods and Results from the Development of a 2600 bar Diesel Fuel Injection System," SAE Paper No. 2000-01-0947.
[6] Amoia, V., Ficarella, A., Laforgia, D., De Matthaeis, S., Genco, C., and Young, F. R., 1997, "A Theoretical Code to Simulate the Behavior of an Electro-Injector for Diesel Engines and Parametric Analysis," SAE Paper No. 970349.
[7] Lasa, M., Heinkel, H. M., Moser, E., and Rothfuβ, R., 2000 "Expeditious Design of Mechatronic Systems Using a VHDL-AMS Based Standard Element Library—A Common Rail Example," SAE Paper No. 2000-01-0581.
[8] Wickman, D. D., Tanin, K. V., Das, S., Reitz, R. D., Gebert, K., Barkhimer, R. L., and Beck, N. J., 1998, "An Evaluation of Common-Rail Hydraulically Intensified Diesel Fuel Injection System Concepts and Rate Shapes," SAE Paper No. 981930.
[9] Catalano, L. A., Tondolo, V. A., and Dadone, A., 2002, "Dynamic Rise of Pressure in the Common-Rail Fuel Injection System," SAE Paper No. 2002-01-0210.
[10] Catania, A. E., Ferrari, A., Manno, M., and Spessa, E., 2008, "Experimental Investigation of Dynamics Effects on Multiple-Injection Common Rail System Performance," ASME J. Eng. Gas Turbines Power, **130**(3), p. 032806.
[11] Zielke, W., 1968 "Frequency-Dependent Friction in Transient Pipe Flow," ASME J. Basic Eng., **90**, pp. 109–115.
[12] Kagawa, T., Lee, I. Y., Kitagawa, A., and Takenaka, T., 1983 "High Speed and Accurate Computing Method of Frequency-Dependent Friction in Laminar Pipe Flow for Characteristics Method," Trans. Jpn. Soc. Mech. Eng., Ser. B, **49**, pp. 2638–2644.
[13] Catania, A. E., Ferrari, A., Manno, M., and Spessa, E., 2006, "A Comprehensive Thermodynamic Approach to the Acoustic Cavitation Simulation in High-Pressure Injection Systems by a Conservative Homogeneous Two-Phase Barotropic Flow Model," ASME J. Eng. Gas Turbines Power, **128**, pp. 434–445.
[14] Catania, A. E., Ferrari, A., Manno, M., and Spessa, E., 2008, "Temperature Variations in the Simulation of High-Pressure Injection-System Transient Flows Under Cavitation," Int. J. Heat Mass Transfer, **51**, pp. 2090–2107.
[15] Catania, A. E., Dongiovanni, C., Mittica, A., Badami, M., and Lovisolo, F., 1994, "Numerical Analysis Versus Experimental Investigation of a Distributor-Type Diesel Fuel-Injection System," ASME J. Eng. Gas Turbines Power, **116**, pp. 814–830.
[16] Catania, A. E., Dongiovanni, C., Mittica, A., Negri, C., and Spessa, E., 1997, "Experimental Evaluation of Injector-Nozzle-Hole Unsteady Flow-Coefficients in Light Duty Diesel Injection Systems," *Proceedings of the Ninth International Pacific Conference on Automotive Engineering Motor Vehicle and Environment*, SAE-Indonesia, Vol. 1, pp. 283–290.
[17] AMESim Manual, version 3.0.1, Imagine, Roanne, France.
[18] Von Kuensberg Sarre, C., Kong, S.-C., and Reitz, R. D., 1999, "Modeling the Effects of Injector Nozzle Geometry on Diesel Sprays," SAE Paper No. 1999-01-0912.
[19] Toro, E. F., 1997, *Riemann Solvers and Numerical Methods for Fluid Dynamics: A Practical Introduction*, Springer-Verlag, Berlin.
[20] Butcher, J. C., 1987, *The Numerical Analysis of Ordinary Differential Equations*, Wiley, New York.
[21] Catania, A. E., Ferrari, A., and Spessa, E., 2008, "Numerical-Experimental Study and Solutions to Reduce the Dwell Time Threshold for Fusion-Free Consecutive Injections in a Multijet Solenoid-type CR Systems," ASME ICED Spring Technical Conference, Paper No. ICES2006-1369, ICES2006 best paper award, ASME J. Eng. Gas Turbines Power, in press.

Comparison of Primary Flow Measurement Techniques Used During Combined Cycle Tests

W. Cary Campbell[1]
e-mail: wlccampb@southernco.com

Warren H. Hopson
e-mail: whhopson@southernco.com

Mark A. Smith
e-mail: maasmith@southernco.com

Southern Company Services,
42 Inverness Center Parkway,
Birmingham, AL 35242

One of the most significant contributors to the overall uncertainty of a performance test of a combined cycle steam turbine is the uncertainty of the primary flow measurement. ASME performance test codes provide many alternative methods for determining flow. In two actual combined cycle tests performed in 2005, the following three alternate methods were used to determine the high-pressure (HP) steam flow into the combined cycle steam turbines: (1) Derivation from measured HP feedwater flow using calibrated PTC 6 throat tap nozzles, (2) derivation from low-pressure (LP) condensate using calibrated PTC 6 throat tap nozzles, and (3) derivation from LP condensate using calibrated orifice metering sections. This paper describes the design, calibration, and installation of each flow meter involved, the methods used to calculate the HP steam flow, the estimated uncertainty of the HP steam flow derived using each method, and the actual test results using each method. A comparison of the methods showed that there are distinct advantages with one of the methods and that very low uncertainties in HP steam flow can be achieved if sufficient attention is applied to the design, calibration, and installation of all flow meters involved. Note that the information in this paper was originally published in ASME Paper PWR2006-88074 and presented at the 2006 ASME Power Conference in Atlanta, GA. For detailed diagrams, figures, and tabulations of data and analysis, please refer to the published proceedings from that conference. [DOI: 10.1115/1.2720544]

Introduction

In April–May 2005, combined cycle steam turbine performance acceptance tests were performed on two identical units at the Plant McIntosh Combined Cycle Facility, located in Rincon, Georgia—approximately 30 miles northwest of Savannah. The units are co-owned by the Savannah Electric and Georgia Power subsidiaries of the Southern Company. The tests were performed by the Generating Plant Performance section of Southern Company Services, Inc. using test techniques and procedures that had been developed over the preceding five year period. The Southern Company had commissioned and tested fourteen 2-on-1 combined cycle units since the year 2000 and the McIntosh unit tests were the last two planned for this construction period. In previous tests, the high-pressure (HP) steam flow used in each steam turbine acceptance test had been derived solely from HP feedwater (FW) flows measured using inspectable PTC 6-1996 flow nozzles [1], along with inspectable calibrated wall tap flow nozzles on the superheat spray lines. The results of these tests were acceptable; however, due to difficulty in inspecting the feedwater flow nozzles after each test, it was decided to utilize removable PTC 6-1996 flow nozzles in the condensate lines for the McIntosh tests. Since the HP feedwater flow nozzles had already been procured for this unit, and each heat recovery steam generator (HRSG) also contained a condensate flow orifice meter tube, the installation of the condensate test nozzle provided an opportunity to compare three alternate methods of primary flow measurement during these tests.

Cycle Description

Units 10 and 11 at Plant McIntosh each consist of two GE 7FA gas turbines and one Alstom steam turbine. Each steam turbine receives HP, intermediate-pressure (IP), and low-pressure (LP) steam from two Deltak HRSG's. Rated output of each unit is approximately 500 MW at base load and 630 MW with full duct-burner heat input and steam injection to the gas turbines. Rated steam turbine output is approximately 280 MW at full load.

HP Steam Flow Derivation Techniques

The HP steam flow into the HP turbine was derived in three ways. Details, advantages, and disadvantages of each method are as discussed below.

HP Feedwater Flow Method. In this method, the HP steam flow is derived from the measurements of HP feedwater flow leaving the feedpumps of each HRSG and HP de-superheating spray flows. The total HP steam flow entering the HP turbine is the sum of all HP feedwater and HP de-superheating flows.

The HP feedwater flows were measured using one welded-in inspectable PTC 6 flow nozzle per HRSG or two per unit. Each HP feedwater flow nozzle had four tap sets and at least two which met PTC 6-1996 calibration requirements. Differential pressures were measured across the two best tap sets per nozzle.

HP de-superheating spray flows were measured using inspectable wall tap flow nozzles. HRSG blowdown was isolated during the tests so no corrections were necessary for those flows.

All meters were calibrated prior to installation and inspected prior to the tests. Both sets of meters were in service during initial steam blows; however, pre-test inspections showed no damage or deposits. Post-test inspections of the HP feedwater flow nozzles were also performed after the tests and showed no damage or deposits.

The advantages of this method are that it uses very few meters and it utilizes liquid flow measurements. This reduces the uncertainties associated with steam flow measurements due to the application of an expansion factor, steam density, and the difficulty in establishing water legs in differential steam pressure sensing line tubing.

Disadvantages of this method are the high cost of the inspectable PTC 6 nozzles and the difficulty of inspecting the nozzles in place. At high test loads, actual Reynolds numbers of the HP

[1]Corresponding author.

Manuscript received October 12, 2006; final manuscript received January 2, 2007; published online August 26, 2008. Review conducted by Dilip R. Ballal. Paper presented at the ASME Power 2006 (PWR2006), May 02–04, 2006, Atlanta, GA.

feedwater nozzles were also outside of the calibrated range and the discharge coefficients had to be extrapolated using PTC 6 procedures [2].

Condensate Flow Methods. HP steam flow into the steam turbine can also be determined by performing a mass balance around the steam turbine cycle itself. This method requires accurate measurement of the LP condensate flow leaving the turbine cycle and measurement or derivation of all other flows entering or leaving the turbine cycle.

LP condensate can be determined either by measuring the total condensate leaving the steam turbine cycle or by summing the condensate flows into each HRSG. Each of these two methods was used during these tests as discussed below.

Total Condensate Flow Nozzle Method. As part of an agreement with our steam turbine vendor, we agreed to use PTC 6-1996 condensate flow test nozzles as the primary flow meters for the tests. One flanged meter tube section was procured for each unit. Each meter tube and nozzle section was designed, built, calibrated, and installed according to PTC 6-1996 [3]. Each nozzle had four tap sets with at least two required to meet the PTC 6-1996 calibration requirements. The meters were temporarily installed in the common condensate pump discharge line immediately before the tests and removed immediately after the tests. The meters were not in place during any steam blows or routine plant operation. Each meter had an integral recovery cone designed according to PTC 6-1996.

The other flows necessary to calculate HP steam flow from condensate were either measured directly or derived from other HRSG inlet and outlet flows. The feed pumps do not require flow measurement of the seal water flows due to being supplied with mechanical seals. HRSG blowdown and condenser makeup were out of service during the base load tests. Makeup and gas turbine steam injection were in service during the peak load tests; however, since blowdown was isolated, the makeup flow equaled the steam injection flow and their effects on the steam turbine cycle mass balance was nullified.

LP steam flow could be determined either by direct measurement or by derivation from LP condensate. Due to the high number of instruments involved and the high uncertainty estimated from the LP condensate based approach, it was decided to directly measure the LP steam flow. The meters used were model HHR flow tubes manufactured by Fluidic Techniques, Inc. These meters have an elliptical inlet similar to a PTC 6 nozzle but are of a more pre-fabricated design. They have a built-in recovery cone, two tap sets, and a 1 in. [2.54 cm] inspection latrolet. Each meter was calibrated and inspected immediately before and after the tests. The meters were in service during the initial steam blows; however, pre- and post-test inspections showed no damage or deposits.

Hot reheat and cold reheat flows needed for the HP steam flow calculation do not need to be measured—only the difference between them is required. This was determined by measurement of IP feedwater, reheat spray, and gas turbine power augmentation steam injection flows (when in service). HRSG blowdowns were out of service during the tests, so no corrections were necessary for these flows.

The advantages of this method for determining the HP steam flow are the ease in inspecting the flow nozzle section, the capability to be installed and removed immediately before and after the tests, low head loss so the meter can be calibrated at the highest possible Reynolds numbers, operation within the tested Reynolds numbers during the tests, and measurement of total unit condensate flow with one meter.

The main disadvantage of this approach is the number of other flowrates that must be added or subtracted from the LP condensate flow to derive the HP steam flow. Another apparent disadvantage is the increased sensitivity of the derived HP steam flow due to the fact that the condensate flow is actually higher than the HP steam flow. This occurs in a combined cycle unit because IP and LP steam flows are being added to the steam turbine rather than flow being extracted to feedwater heaters as in a conventional fossil fired or nuclear steam turbine.

Condensate Flow Orifice Method. Total LP condensate flow was also determined by summing the LP condensate flows into the economizer section of each HRSG. These flows were measured using orifice flow meter tubes which were provided by the HRSG vendor. These orifice meter tubes were designed and installed according to the requirements of ASME MFC-3M [3]. Since they were needed for our HRSG acceptance tests, they also were calibrated.

The advantages of using orifice meters are their low cost, ease of inspection, and their use of flange tap pressure tap holes. Unlike throat tap nozzles, these flange taps are not as sensitive to the sharpness and quality of the pressure tap holes.

Some disadvantages of using orifice meters for primary flow measurement are their high head loss and the need for concentric orientation of the orifice plate. Since these meters were intended for plant utilization over a wide variety of flow rates, the orifice beta ratios were sized to produce a maximum differential pressure (DP) of approximately 200 in. H_2O [498 mbar] during peak load operation. It is not practical to shut down the unit and change orifice plates during a performance test, so the same orifice plates were used during the base load tests. The DPs produced at base load were lower than 100 in. H_2O [249 mbar], which is lower than PTC 6 recommendations.

The meter's sensitivity to concentric orientation requires extreme care when removing, inspecting, and re-inserting the orifice plate. When the orifice plates were removed for inspection, precise measurements were made to ensure that they were reinserted within 1/64 in. [0.397 mm] of the concentricity during the initial calibration and according to ASME PTC 19.5 requirements [4].

Cycle Leakage Flows. A complete cycle isolation walkdown was performed before each test sequence. All valves that were found to be leaking were either isolated or attempts were made to measure them. All HP, IP, and LP steam bypass valves were isolated during the tests. Downstream temperatures were monitored before and after isolating these valves to confirm they were sufficiently isolated. Total cycle losses were calculated by monitoring condenser hotwell drop during the tests. During the base load tests total cycle losses were kept below 0.2% of HP steam flow. Corrections for unaccounted cycle losses were applied to HP, IP, reheat (RH), and LP steam flows in proportion to the ratio of each flow to the total condensate flow.

Data Acquisition Techniques

Static and differential pressures across all flow meters were measured using 0.1% accuracy class transmitters which have built in temperature compensation. All DP transmitters were calibrated near the expected line static pressure to minimize static pressure range shifts and zeroed at actual line static pressures prior to the tests.

Temperatures used in flow calculations were measured using continuous lead thermocouples and Kaye ice point references.

Test data was recorded using the SCS Performance Test System (PTS). The PTS uses distributed data acquisition boxes to receive analog signals from all test instruments, perform analog to digital conversion, and transmit the data to a central personal computer where on-line calibration corrections are applied and instantaneous flow calculations are performed.

All instruments were calibrated at the SCS Metrology Lab immediately before and after the tests to standards traceable to NIST. Calibration corrections were applied for all instruments and data acquisition channels on-line by the PTS software. Compensations were applied for all known errors and offsets rather than accepting the stated uncertainties or specifications of each instrument. This transfers the majority of the bias uncertainty of the instrument to the uncertainty of its calibration standard.

Flow Meter Designs

HP Feedwater Flow Nozzles. The HP feedwater flow nozzles were supplied by the HRSG vendor Deltak, per SCS specifications, and were manufactured by Crane Manufacturing, Inc. These nominal 10 in. [25.4 cm] diameter meter sections met all ASME PTC 6-1996 design requirements for primary flow and included welded ends, 5 in. [12.7 cm] flanged inspection ports, four throat tap sets, integral recovery cone, and an upstream plate type flow straightener.

Each of the four HP feedwater flow nozzles needed for the two units was calibrated at Alden Laboratory in Worcester, MA prior to permanent welded-in installation. All four tap sets of each nozzle were calibrated at a minimum of 20 test points.

The slopes of the actual calibration curves are all within the PTC 6 criteria for "slope independence," including the revised criteria published in the response to technical inquiry (Question 6) published in the February, 1999 edition of Mechanical Engineering magazine [5]. These nozzles are the most recent and perhaps the best PTC 6 nozzles built according to SCS specifications which require strict conformance to PTC 6 requirements and proof of performance prior to acceptance from the vendors. If a minimum of two tap sets do not meet at least the revised PTC 6 criteria, the meters are rejected and must either be retrofitted or replaced. Our insistence on meeting these requirements and the improvements in our vendor's manufacturing processes have resulted in all 28 PTC-6 HP feedwater nozzles required for our combined cycle unit testing since the year 2000 meeting the PTC 6-1996 requirements [1].

The conformance to PTC 6 requirements ensures that the meter's performance during actual unit testing will be reliable and predictable at a wide range of mass flowrate and Reynolds numbers. During our combined cycle unit tests, we had steam turbine guarantees at two test conditions. For our base load test case (at design throttle pressure), the expected throat Reynolds number was within the actual Alden range of calibration flows. For our peak load guarantee case (duct fired at maximum throttle pressure), the test Reynolds numbers were outside of the calibration range and the discharge coefficients were determined from a curve fitted equation extrapolated according to PTC 6-1996 procedures [2].

The HP feedwater flow nozzles were situated on horizontal piping upstream of the HP feedwater regulating valve on each HRSG. The nozzles were oriented with the best two tap sets in the horizontal plane or on top of the pipe and with the inspection ports in the top two quadrants for ease of inspection. During testing, the flowrates indicated by each tap set were compared to ensure that they were well within the PTC 6 -1996 code limit of 0.2% [6]. A consistent difference in tap set readings was also used as a method to verify that no damage occurred to a tap set during testing.

Condensate Flow Nozzles. The 12 in. [30.48 cm] condensate flow nozzles for each unit were manufactured by Fluidic Techniques per SCS specifications. Each of these meter tubes also meet all PTC 6-1996 design requirements for primary flow measurement [1]. Each meter tube include a flanged inlet, nozzle section, and outlet section, four throat tap sets, pressure recovery cone, and an upstream plate type flow straightener.

Each condensate flow nozzle was calibrated at Alden Laboratory with at least two of the four tap sets meeting the calibration criteria required in PTC 6-1996 [2].

As with the HP feedwater flow nozzles, the expected throat Reynolds number was within the actual Alden range of calibration flows for our base load test case (at design throttle pressure). For the peak load guarantee case (duct fired at maximum throttle pressure), the test Reynolds numbers were slightly outside of the calibration range and the discharge coefficients were determined from a curve fitted equation extrapolated according to PTC 6-1996 procedures [2].

Since this meter would only be installed temporarily and contained a recovery cone, the meter was sized to produce a very high resolution differential pressure (765 in. H_2O [1906 mbar] at peak load conditions). The calculations were checked to ensure enough condensate pumping capacity was available for the extra pressure loss; no problems were encountered on the actual tests with either one pump (base load) or two pump (full pressure) operation.

The meter was installed in horizontal piping after the gland steam condenser and prior to the split to the individual HRSG's. Sufficient upstream pipe length was included within the meter tube (17 pipe diam.) to meet all minimum uncertainty requirements; however, extra upstream length of 20 pipe dia. was included upstream of the meter tube to ensure no additional uncertainty questions would arise.

As with the HP feedwater flow nozzles, the flowrates indicated by each tap set were compared to ensure that they were well within the PTC 6 -1996 code limit of 0.2% [6].

Condensate Flow Orifice Meters. The individual HRSG 10 in. [25.4 cm] LP condensate flow orifice meter tubes were supplied by Deltak, per SCS specification, and were manufactured by Crane Manufacturing, Inc. These are flange tap orifice meter tubes with two tap sets. One tap set for each meter was calibrated at Alden Laboratory. No calibration performance was guaranteed, however, the shape and slope of each calibration curve are evaluated to ensure that they are close to the theoretical curve derived from ASME MFC-3M-1989 [3]. The actual calibration data regression curve is also compared to the extrapolated discharge coefficient curve created using the procedure contained in PTC 19.5-2004 [7]. The actual data regression line was very close to the MFC 3M and PTC 19.5 curves; however, it appeared to have a slightly more negative slope. It also tended to curve less sharply at low flows than the predicted curves. Fortunately, during our tests, actual Reynolds numbers were within the range of the calibration data and extrapolation methods were not a concern.

The meter sections are located in the horizontal piping prior to the HRSG LP condensate regulating valve. No flow straighteners were necessary since the meters were situated after approximately 123 pipe dia. (103 ft. [31.4 m]) of straight piping.

Superheat Spray Flow Nozzles. The individual HRSG 2.5 in. [6.35 cm] superheat spray flow nozzles were supplied by Deltak, per SCS specifications, and manufactured by Crane Manufacturing, Inc. These are typical wall tap flow nozzles. One tap set of each meter was calibrated at Alden Laboratory. The slope of the calibration curve was very close to the theoretical curve derived from ASME MFC-3M-1989 [8] and with the expected normal and maximum flows either in or close to the Alden obtainable Reynolds numbers. One interesting item of note is that the meters were made to be inspectable (using a borescope) by SCS specification of a 45 deg threaded plugged Latrolet® on the upstream side.

The meter sections were installed at the end of a straight horizontal piping run of 22 pipe dia. thus no flow straighteners were required.

IP Feedwater Flow Meters. The individual HRSG 6 in. [15.24 cm] IP feedwater flow orifice meters were supplied by Deltak, per SCS specification, and manufactured by Crane Manufacturing, Inc. These were flange tap orifice meter tubes with two tap sets. One tap set of each meter was calibrated at Alden Laboratory and the performance was compared to MFC 3M-1989 [3] and PTC 19.5-2004 [7] expectations. The slopes of the calibration curves were very close to the theoretical curves with the expected base load and peak load guarantee points within the Alden obtainable range of calibration Reynolds numbers.

The meter sections were located in horizontal piping prior to the HRSG IP feedwater regulating valves and no flow straighteners were required.

Reheat Spray Flow Nozzles. The individual HRSG 2 in.

[5.08 cm] reheat spray flow nozzles were supplied by Deltak, per SCS specifications, and manufactured by Crane Manufacturing, Inc. These were wall tap flow nozzles similar in design to the HP superheat spray nozzles. One tap set of each meter was calibrated at Alden Laboratory. The slope of the calibration curves were very close to the theoretical curves derived from ASME MFC-3M-1989 [8] and with the expected normal and maximum flows either in or close to the Alden obtainable Reynolds numbers. These meters were also made to be inspectable (using a borescope) by SCS specification of a 45 deg threaded plugged Latrolet® on the upstream side.

The meter sections were installed at the end of a long straight horizontal piping run of 55 pipe diam. so no flow straighteners were required.

LP Steam Flow Meters. The individual HRSG 18 in. [45.72 cm] LP steam flow tubes were supplied by Deltak, per SCS specifications, and manufactured by Fluidic Techniques. Their HHR model flow tubes feature an elliptical inlet throat tap flow nozzle combined with an integral pressure recovery cone and have two tap sets. One tap set of each meter was calibrated at Alden Laboratory with water. Although there is no ASME expected performance for these proprietary flow devices, the slope of the calibration curves were compared to the PTC 19.5 predictions for laminar and turbulent flow [9] and PTC 6-1996 throat tap nozzles [2,5]. These nozzles did not meet PTC 6-1996 requirements [2] but did exhibit similar performance. The best fit was obtained by using the PTC 6-1996 equation format [2] with a variable C_x. Extrapolation was not a concern as the expected normal and maximum flows were within the in the Alden obtainable Reynolds numbers. These meters were also made to be inspectable (using a borescope) by SCS specification of a 45 deg threaded plugged Latrolet® on the upstream side. The meter sections did not have flow straighteners since they were installed in a straight horizontal piping run with 18 pipe dia. of straight pipe upstream of the meters.

Other Flows. Other flow meters were provided in the plant design for control system inputs and direct monitoring of steam flows out of each HRSG. While these flow meters were not used for the primary steam turbine acceptance test flows, they were used for monitoring of the stability of drum levels and steam flows leaving each HRSG section. These flow meters were purchased as uncalibrated meters; however, many were calibrated in place during our tests by comparison to the flows derived from the calibrated primary flow elements.

Actual Performance Test Data

Test Conditions. Steam turbine capacity tests were conducted at two basic conditions:

1. Base load: Two gas turbines operating at base load with no supplemental HRSG fuel input or gas turbine steam injection. The expected base load steam turbine capacity is approximately 190 MW with an expected total HP steam flow of 876 klb/h [110.4 kg/s].
2. Peak load: Two gas turbines operating at base load with full supplemental HRSG fuel input and gas turbine steam injection. The expected peak load steam turbine capacity is approximately 280 MW with an expected total HP steam flow of 1579 klb/h [199.0 kg/s].

Pairs of tests were conducted at each operating condition to verify test repeatability. A small reduction in HP steam flow ($\sim$5%) was made between test runs to require the unit to reestablish new steady state conditions and to demonstrate repeatability of test results.

Test Preparations. Immediately prior to the start of the steam turbine capacity tests, the unit was shutdown to allow for the temporary installation of the LP condensate nozzle. During this unit outage, the other calibrated flow elements that had been in service from the time of the original unit startup were visually inspected for damage and deposits. These pre-test inspections revealed no deposits and no significant damage. The damage found was limited to some small nicks in the leading edges of several orifice plates.

Orifice plate inspections were accomplished by the complete removal of each plate for inspection. The plates were shipped installed in their meter tubes in their as-calibrated positions. Because the meter tubes do not provide a mechanical position registration, each plate's orientation was measured at eight circumference points with a feeler gage from the outside flange faces to the outside plate edge to establish the plates as-calibrated position. Plates were reinstalled back to their individual as-found positions after inspection. Plate inspections included visual and tactile checks for edge damage and roughness as well as checking for plate flatness. All inspections were witnessed by a vendor representative and detailed written and photographic documentation was compiled for each meter.

Nozzle inspections were accomplished using the supplied inspection ports and included boroscopic, photographic, and mirror based visual inspection. In the case of the HP FW nozzles, it was also possible to perform a limited tactile inspection.

Immediately upon completion of the primary test week, the unit was again shut down to allow removal of the temporary LP condensate nozzle and to perform the post-test flow meter inspections.

While removing the LP condensate nozzle on Unit 10 it was discovered by the inspection engineer that the pipe fitters had left a stack of 6 in. [15.24 cm] cutting wheel disks in the piping upstream of the nozzle's flow straightener plate. This plate had acted as a strainer and prevented the disks from traveling to the nozzle's throat. The as-found position of the cutting disks indicated that they had remained in a generally stacked configuration during operation and had reduced the available flow passing area of the 12 in. [30.48 cm] diameter straightener plate by possibly 25%. A thorough visual inspection revealed that there was no apparent damage to the straightener or the nozzle. Nevertheless, due to the possibility that these disks had influenced the flow profile entering the flow nozzle, it was agreed by all parties to reassemble the LP condensate nozzle and retest the unit to verify the resulting impact on both the flow measurement and the steam turbine corrected performance.

Interestingly, the results of the retest indicated no significant difference in the HP steam flows derived using each method. The difference between the LP condensate and HP feedwater flow nozzle derived HP steam flows varied by only 0.07%, while the difference between the LP condensate nozzle and orifice flows was only 0.03% compared to the previous two tests conducted with the cutting disks in place. It was thus concluded by all parties that the disks had not significantly impacted the accuracy of the LP condensate nozzle. In fact, this iteration showed that the repeatability of the LP condensate nozzle performance was remarkably consistent, despite the disassembly and reassembly of the meter tube and the reinstallation of DP transmitters and tubing.

No other significant post-test meter inspection findings were made on either unit.

Summary of Test Results

Table 1 shows a comparison of actual LP condensate flow measurements by the two different flow methods. As can be seen, the Unit 10 condensate measurement methods agreed within 0.33%. This compares favorably with the estimated measurement uncertainty range of 0.23% and 0.38% for the two methods. For the Unit 11 test, the methods have a difference of 0.80%. This bias error between the nozzle and orifices was present for all of the Unit 11 tests and does not compare favorably with the estimated uncertainties.

Table 1 Comparison of LP condensate flow methods

	Unit 10	Unit 10 Retest	Unit 11
LP condensate flow			
Nozzle, klb/h	1103	1112	1096
Orifices, klb/h	1100	1108	1087
Difference, %	−0.33	−0.31	−0.80
Est. LP cond. flow uncertainties			
Nozzle, ±%	0.23	0.23	0.23
Orifices, ±%	0.38	0.38	0.38

Table 2 compares the three different main steam flow derivation methods. As can be seen, the LP condensate nozzle and HP FW nozzles compare quite closely: to within 0.20%. This is well within the estimated uncertainty bandwidths of these two flow methods. The LP orifice method shows a much larger difference with the LP condensate nozzle for all tests, clearly exceeding the estimated uncertainty bandwidths. Due to the close agreement between the two PTC 6 nozzle methods, it was concluded that the LP orifice method has significant metering errors or that the post-test uncertainty estimate for this method does not adequately model all of the actual error sources. The LP condensate orifice meters were designed, calibrated, and installed according to all required codes; however, since the agreed upon test procedure required that the common LP condensate flow nozzle would be used as the primary flow measurement device for the test, no extended attempts were made to resolve the inconsistency between the LP condensate flow orifice meters and the LP condensate and HP feedwater flow approaches.

Estimated Measurement Uncertainty

Analysis Techniques. Measurement uncertainty analysis was used as a key aid in the design of the initial test procedure design and as a primary means of demonstrating that the test results were repeatable and met the required accuracy goals. ASME PTC 19.1-1998 "Test Uncertainty" [10] was used as the guiding standard for all of the uncertainty modeling.

Pre-test uncertainty modeling was used to aid SCS in the selection of measurement methods and accuracy specification requirements for all instruments used to support the test, whether temporary test instruments or embedded permanent plant instruments. It was specifically used to determine and justify the calibration of 21 of each combined cycle unit's 31 flow elements.

Post-test uncertainty modeling was performed on each of the steam turbine acceptance tests. This modeling consisted of adding to the pre-test models the actual test recorded instrument variability's (random error component) and any bias (systematic) error adjustments suggested by the actual test circumstances. Also included was the actual number of measurement observations (i.e., data scan count) for each test.

Table 2 Comparison of HP steam flow derivation methods

	Unit 10	Unit 10 Retest	Unit 11
HP steam flow			
LP nozzle, klb/h	869	881	872
LP orifices, klb/h	865	877	863
HP nozzles, klb/h	869	881	870
Flow difference from LP nozzle			
LP orifices, %	−0.42	−0.39	−1.00
HP nozzles, %	−0.07	0.00	−0.20
Est. HP steam flow uncertainties			
LP nozzle, ±%	0.14	0.14	0.14
LP orifices, ±%	0.33	0.33	0.34
HP nozzles, ±%	0.36	0.36	0.36

Correlation of Systematic Uncertainties. PTC 19.1 guidelines were strictly adhered to in constructing the uncertainty models including the use of "correlated systematic uncertainties" as covered in Section 8 of the PTC. Correlated systematic errors occur when error sources are not independent, such as calibrating all test thermocouples against the same calibration standard or calibrating most of the primary flow elements in the same flow laboratory. Since this is a common issue in a 2-on-1 combined cycle plant design and with almost all of the temporarily installed test instruments, correlation errors had to be specifically dealt with in the models.

To deal with correlation, the uncertainty models were created to handle correlation as an additional bias term. This was done by splitting the base equation for B_r, the total systematic uncertainty of the result (from PTC 19.1-1998 Eq. 8.2), into two parts, as shown below for an example with three uncertainty elements

$$B_r = [(\theta_1 B_1)^2 + (\theta_2 B_2)^2 + (\theta_3 B_3)^2 + 2\theta_1\theta_2 B_1 B_2 + 2\theta_1\theta_3 B_1 B_3 + 2\theta_2\theta_3 B_2 B_3]^{0.5}$$

$$B_r = [\Sigma(\text{Squared Uncorrelated Terms}) + \Sigma(\text{Correlated Terms})]^{0.5}$$

If B_r has no correlated terms, the last three terms in the base equation fall out and B_r can be arrived at simply as the root sum square of the three elemental independent terms. When, as in the above example where the three bias terms are correlated, the final three terms of the base equation can be calculated and summed together to form a single correlated bias term. Thus, our uncertainty models carry a correlated bias error line item to specifically report the total correlated error component.

To further simplify the calculation of correlation, in most instances, all elemental bias terms were considered fully correlated when most arose from use of the same calibration standards and laboratory. For example, two flow meters were considered to be completely correlated when their primary flow elements and sensing instruments were all calibrated in the same labs.

Primary Flow Meter Uncertainties

LP Condensate Flow Nozzle. The single tap total uncertainty for the LP condensate flow nozzle was ±0.23% of reading for a 95% confidence limit. The total flow measurement uncertainty, after averaging the two individual tap set readings together, is, after round-off, still ±0.23%. No significant uncertainty reduction is gained by reading both tap sets. This result is somewhat counter-intuitive as it is typically assumed that averaging would help reduce the uncertainty. In this case, because of the complete correlation of the elemental errors for both tap sets, the correlated bias term, the last elemental error source listed on the table, essentially negates the advantage of reading multiple tap sets.

LP Condensate Flow Orifice Meters. The uncertainty calculation for LP condensate flow using the LP orifice measurements yielded an uncertainty of 0.38%. This is slightly different from the common LP condensate flow nozzle in that, for this case, there are two separate flow elements reading approximately 50% of the total flow instead of two tap sets reading the same flow on the same flow element. Again, as in the earlier case, there is no significant improvement in the uncertainty of the total flow reading by using two separate meters that are completely correlated.

The primary difference in uncertainty between the twin code orifice meters and the single code nozzle is the amount of differential pressure head measurement generated by the two meter types and the consequent reduction in bias error in the differential pressure measurement. Since the LP condensate flow orifice meters were designed for permanent plant installation over a wide

range of flows, the orifice plate beta ratios were sized to produce DPs in the range of 80 to 200 in. H_2O [199 to 498 mbar] for the lowest possible total head loss. This need for flexibility resulted in low DP readings during the steam turbine base load tests, high standard deviations in measured DPs, and high precision uncertainty values. The test LP condensate flow nozzle did not have this problem since it had a recovery cone and could be sized to produce DPs in the 300 to 700 in. H_2O [747 to 1744 mbar] range.

HP Feedwater Flow Nozzles. The uncertainty calculations for the two PTC 6 HP flow nozzles yield an estimate of 0.36% for the total HP FW flow measurement. The uncertainty of each HP feedwater flow meter is higher than that of the LP condensate flow nozzle. This is due to the lower differential pressure generated plus an additional uncertainty error for possible in-service damage. Table 4.10 (Item C) of ASME PTC 6 Report-1985 [11] shows a 0.1% difference in uncertainty for a meter which was in service between the time of calibration and test, and its conditions may have changed, although there is no evidence of deterioration. Our HP feedwater flow meters were in service from the initial startup of the steam turbine to the time of the test; therefore, even though they were inspected after the test and showed no evidence of deterioration, we commercially agreed with the steam turbine vendor to add a 0.1% additional uncertainty for the possibility that a change in meter performance may have occurred during the time between calibration and the tests.

HP Steam Flowrate Uncertainties

HP steam flow to the steam turbine was calculated using each of the three primary flow methods discussed in this paper. The estimated uncertainties of the HP steam flow derived from each method are discussed below:

LP Condensate Flow Nozzle Method. The uncertainty calculation for HP steam flow derived using the LP condensate nozzle yielded an overall estimated uncertainty of 0.14%. Of particular interest in this calculation was a negative correlation bias error term. It is possible to have the correlation term yield a negative value, as the PTC 19.1-1998, Section 8, Case 3, example calculation clearly demonstrates [10]. For a combined cycle steam turbine test, the negative bias occurs because the LP condensate flow is larger than the HP steam flow since IP and LP steam flow are added to the HP flow before exiting the cycle as condensate. This negative correlation greatly reduces the final total bias for both LP condensate flow methods, giving them a distinct uncertainty advantage over the HP feedwater flow method. This is a nonintuitive result that can best be arrived at by careful uncertainty modeling, thus clearly demonstrating the value of pre-test modeling to help optimize the test method for maximum accuracy.

LP Condensate Flow Orifice Method. The calculation of HP steam flow uncertainty for the LP condensate orifice method yielded an estimated uncertainty of 0.33%. Here again, there is a negative value correlation term but the value here has a much smaller impact on the final bias result. It should again be pointed out that as shown in Table 2 the actual test results do not support the low value of this uncertainty calculation. The actual discrepancies between the LP condensate orifice meter flows and the LP condensate and HP feedwater flow nozzle were larger than the estimated uncertainties. Apparently, either some major error sources have not been properly included in the estimated uncertainty analysis or a consistent error existed in our LP condensate orifice meter flow methods. The most likely explanation is the low DP produced by the orifice meters and their sensitivity to small errors in DP readings.

HP Feedwater Flow Nozzle Method. The HP steam flow uncertainty for the HP FW nozzle method was is 0.36%. This method had a positive correlation term and a corresponding higher uncertainty than the LP condensate nozzle method. Compared to the LP condensate flow nozzle method, these two steam flow measurement methods produced extremely close results—well within their uncertainty bandwidths.

Conclusions

Combined cycle tests performed on two units with three different methods for estimating HP steam flow to the steam turbine agreed between 0% and 0.2% when using ASME PTC 6 throat tap flow nozzles in both the HP feedwater and LP condensate lines. The agreement between these methods was much better than the uncertainties of 0.14% and 0.36% estimated using ASME PTC 19.1 procedures when using a common LP condensate PTC 6 flow nozzle and HP feedwater PTC 6 nozzles. The HP steam flow derived from LP condensate flow orifice meter tubes were not within estimated uncertainty bands.

These results illustrate that very low uncertainties in combined cycle unit HP steam flow and steam turbine test results can be achieved when using ASME PTC 6 throat tap nozzles and when appropriate attention is paid to the design, calibration, installation, and use of all flow meters involved.

Recommendations

In order to achieve the lowest possible uncertainty of HP steam flow measurement and steam turbine output performance uncertainty during an ASME PTC 6.2 [12] combined cycle test, the following practices are recommended:

1. Use LP total condensate flow as the primary flow measurement.
2. Measure total LP condensate flow using an ASME PTC 6 throat tap nozzle meter tube [1].
3. Design, calibrate, and evaluate throat tap nozzle meter tubes according to ASME PTC 6 requirements [1].
4. Size the nozzle beta ratio to obtain differential pressures between 200 and 1000 in. H_2O [498 to 2491 mbar] during actual steam turbine test runs.
5. Include a recovery cone in the design so that higher flows can be obtained during calibration and to minimize head loss during operation.
6. Pay particular attention to throat tap holes sharpness during nozzle manufacture.
7. Witness the calibration and require that at least two tap sets meet PTC 6 requirements [2,5] before acceptance.
8. Temporarily install and remove the meter tube immediately before and after the tests.
9. Integrate the meter tube in the plant design to obtain required upstream pipe lengths and ease of installation and removal.
10. Calibrate all secondary flow meters used in the HP, IP, and LP steam flow derivations.
11. When using HP feedwater flow nozzles, minimize inspection port length to ease inspection.
12. Provide inspection plugs or ports on all meters used in the steam turbine acceptance tests.
13. Inspect all meters before and after the tests to minimize assumed uncertainty impacts.
14. When using orifice plates, include different size alignment pins in the design to ensure concentricity and repeatable orientation during plate removal, inspection, and reinsertion.
15. Perform a thorough pre-test uncertainty analysis to allow evaluation and optimization of test procedure design.
16. Include correlation of biases in uncertainty analyses.
17. Minimize variations in primary flows during testing.
18. Compensate for known deviations from calibration standards for data acquisition systems and test instruments.
19. Attempt to substantiate all uncertainty calculation inputs.
20. Minimize arbitrary uncertainty assumptions.

Acknowledgment

We appreciate the contributions of Crane Manufacturing, Inc., Tulsa, OK, Fluidic Techniques, Inc., Mansfield, TX, and Alden Research Labs, Inc, Worcester, MA.

References

[1] ASME, 1996, "Performance Test Code 6 on Steam Turbines," ASME Performance Test Code No. PTC 6-1996, pp. 36–55.
[2] ASME, 1996, "Performance Test Code 6 on Steam Turbines," ASME Performance Test Code No. PTC 6-1996, pp. 42–44.
[3] ASME, 1995, "Measurement of Fluid Flow in Pipes Using Orifice, Nozzle, and Venturi," ASME Standard No. MFC-3M-1989, pp. 14–32.
[4] ASME, 2004, "Flow Measurement," ASME Performance Test Code No. PTC 19.5-2004, pg. 32.
[5] ASME, 1999, "Technical Inquiry on PTC 6-1996—Steam Turbines, Question 6," Mechanical Engineering Magazine, February, pp. 81–82.
[6] ASME, 1996, "Performance Test Code 6 on Steam Turbines," ASME Performance Test Code No. PTC 6-1996, pg. 55.
[7] ASME, 2004, "Flow Measurement," ASME Performance Test Code No. PTC 19.5-2004, pp. 39–42.
[8] ASME, 1995, "Measurement of Fluid Flow in Pipes Using Orifice, Nozzle, and Venturi," ASME Standard No. MFC-3M-1989, pp. 32–36.
[9] ASME, 2004, "Flow Measurement," ASME Performance Test Code No. PTC 19.5-2004, pp. 44–49.
[10] ASME, 1998, "Test Uncertainty," ASME Performance Test Code No. PTC 19.1-1998.
[11] ASME, 1997, "Guidance for Evaluation of Measurement Uncertainty in Performance Tests of Steam Turbines," ASME Performance Test Code Report No. PTC 6 Report-1985, pg. 26.
[12] ASME, 2004, "Steam Turbines in Combined Cycles," ASME Performance Test Code No. PTC 6.2-2004.